Probabilistic Fatigue Methodology for Aircraft Landing Gear

By

JOSHUA GEORGE HOOLE

Department of Aerospace Engineering
UNIVERSITY OF BRISTOL

A dissertation submitted to the University of Bristol
in accordance with the requirements of the degree of
DOCTOR OF PHILOSOPHY in the Faculty of Engineering.

MARCH 2020

Word count: 78,615

Copyright Permissions and Redaction Statement

The stress-life materials dataset for 4340 steel presented within this thesis has been reproduced with the kind permission of IHS ESDU.

The automatic dependent surveillance-broadcast datasets and Flightradar24® screenshots within this thesis have been reproduced with the kind permission of Flightradar24®.

Excerpts of SAE AIR5914 are included within this thesis under Copyright Clearance Center License ID: 1035779-1.

Specific elements of this thesis have been redacted due to copyright. Redacted elements are either highlighted explicitly in the text, or are marked with [REDACTED].

Abstract

Aircraft landing gear comprise of safety-critical structural components that are exposed to large cyclic loads over long in-service design lives. To prevent the occurrence of fatigue crack initiation, fatigue analysis methods are employed to identify the 'safe-life' at which the component must be retired, to guarantee the structural integrity of the component. However, the engineering parameters relating to the fatigue design of landing gear components, including material properties and loading, demonstrate significant variability. This variability is currently mitigated using design conservatism.

Design conservatism can ultimately lead to over-weight components and as a result, probabilistic design approaches have been proposed to better represent design parameter variability within fatigue analysis processes. Unfortunately, a large number of inhibiting factors, or 'blockers', currently prevent the wider-scale implementation of probabilistic fatigue design approaches.

The aim of this research is to develop a probabilistic fatigue methodology that overcomes the blockers to a probabilistic design approach. It is hypothesised that careful selection of a Monte Carlo Simulation based methodology, definition of systematic processes and frameworks, along with the exploitation of recent advances in surrogate modelling and 'big-data' sources, can help to combat the blockers to probabilistic design.

Following application of the developed probabilistic fatigue methodology to landing gear component case studies, it was demonstrated that probabilistic methodologies can support the fatigue design of landing gear components through identifying the conservatism in existing practices, along with highlighting areas of component over-design. From implementing the methodology, it was observed that the proposed methodology could overcome the blockers to probabilistic design concerning *computational expense*, *required assumptions*, *availability of data*, *accuracy of data characterisatio*n and the large amount of *required knowledge* to implement such approaches. The remaining blockers to probabilistic design approaches therefore concern the development of reliability targets and the engineering mindset change required to implement such approaches.

AUTHOR'S DECLARATION

I declare that the work in this dissertation was carried out in accordance with the requirements of the University's Regulations and Code of Practice for Research Degree Programmes and that it has not been submitted for any other academic award. Except where indicated by specific reference in the text, the work is the candidate's own work. Work done in collaboration with, or with the assistance of, others, is indicated as such. Any views expressed in the dissertation are those of the author.

SIGNED: ..... DATE: .....

TABLE OF CONTENTS

List of Tables

List of Figures

NOMENCLATURE

Due to this thesis combining elements of structural analysis, statistics and surrogate modelling, the re-use of nomenclature is unavoidable due to the conventions of each field. As a result, the nomenclature used within this thesis is clearly defined in the text.

Acronyms

.csv - *Comma Separated Variable*

1D - *1-Dimensional*

2P - *2-Parameter*

3D - *3-Dimensional*

3P - *3-Parameter*

A-D - *Anderson-Darling*

ADS-B - *Automatic Dependent Surveillance-Broadcast*

AMV - *Advanced Mean Value*

ANN - *Artificial Neural Network*

CDF - *Cumulative Density Function*

CI - *Confidence Interval*

CPU - *Central Processing Unit*

DoE - *Design of Experiments*

EASA - *European Aviation Safety Agency*

ECDF - *Empirical Cumulative Distribution Function*

EFC - *Equivalent Fatigue Cycle*

E-N - *Strain-Life*

ESDU - *Engineering Sciences Data Unit*

FAA - *Federal Aviation Administration*

FF - *Full-Factorial*

FMECA - *Failure Mode, Effects and Criticality Analysis*

FORM - *First Order Reliability Method*

FOSM - *First Order Second Moment*

FPI - *Fast Probability Integration*

GPD - *Generalised Pareto Distribution*

GPR - *Gaussian Process Regression*

GSA - *Global Sensitivity Analysis*

HxSy - *Hole 'x' Slice 'y'*

HCF - *High Cycle Fatigue*

HPC - *High Performance Computing*

ICDF - *Inverse Cumulative Density Function*

ID - *Identification Number*

IS - *Importance Sampling*

K-L - *Kullback-Leibler*

LCF - *Low Cycle Fatigue*

LF - *Likelihood Function*

LHS - *Latin Hypercube Sampling*

LSA - *Limit State Approximation*

LSF - *Limit State Function*

MCS - *Monte Carlo Simulation*

MLE - *Maximum Likelihood Estimation*

MLG - *Main Landing Gear*

MPC - *Multi Point Constraint*

Acronyms (*Continued*)

MPP - *Most Probable Point*

MQ - *MultiQuadratic*

MTOW - *Maximum TakeOff Weight*

NM - *Nelder-Mead*

OWE - *Operational Weight Empty*

PDF - *Probability Density Function*

PPLR - *Probability Plotting and Linear Rectification*

P-S-N - *Probability-Stress-Life*

RAM - *Random Access Memory*

RBDO - *Reliability-Based Design Optimisation*

RBF - *Radial Basis Function*

RET - *Rapid Exit Taxiway*

RSM - *Response Surface Method*

RTO - *Rejected TakeOff*

SAE - *Society of Automotive Engineers*

SAT - *Shock Absorber Travel*

S-N - *Stress-Life*

SND - *Standard Normal Distribution*

SORM - *Second Order Reliability Method*

SSI - *Stress-Strength Interference*

T/D - *TouchDown*

U - *Upper*

UL - *Upper Left*

UR - *Upper Right*

Symbols - *Stress and Fatigue Analysis*

t - *Plate Thickness*

W - *Plate Width*

ϕ - *Keyhole Diameter*

L - *Plate Load Offset*

A - *Plate Loaded Area*

c - *Plate Moment Arm*

I -*Plate Second Moment of Area*

OR - *Outer Radius*

IR - *Inner Radius*

w_g - *Fuse Groove Width*

d_g - *Fuse Groove Depth*

r_g -*Fuse Groove Radius*

db_w - *Drag Brace Flange Width*

db_h - *Drag Brace Web Height*

db_{tw} - *Drag Brace Web Thickness*

db_{tf} - *Drag Brace Flange Thickness*

db_l - *Drag Brace Centroid Height*

P_p - *Plate Load*

M_p - *Plate Moment*

F_1 - *Axial Load*

F_2, F_3 - *Shear Loads*

F_4, F_5 - *Bending Moments*

F_6 - *Torsional Moment*

σ - *Direct Stress*

σ_{F_1} - *Direct Stress due to* F_1

σ_{F_4} - *Direct Stress due to* F_4

σ_{F_5} - *Direct Stress due to* F_5

S - *Shear Load*

τ - *Shear Stress*

τ_{F_2} - *Direct Stress due to* F_2

τ_{F_3} - *Direct Stress due to* F_3

τ_{F_6} - *Direct Stress due to* F_6

σ_{UTS} - *Ultimate Tensile Strength*

Symbols - *Stress and Fatigue Analysis (Continued)*

E - *Young's (elastic) Modulus*

σ_{eq} - *von Mises Equivalent Stress*

K_t - *Stress Concentration Factor*

σ_a - *Stress Amplitude*

σ_m - *Mean Stress*

σ_0 - *Fully-Reversed Stress Amplitude*

σ_{FL} - *Fatigue Limit*

P - *S-N Curve Coefficient*

q - *S-N Curve Exponent*

n - *Number of Applied Cycles*

N_f - *Number of Cycles to Failure*

PoS - *Probability of Survival*

$N_{f_{PoS}}$ - N_f *from P-S-N Curve*

$N_{f_{S-N}}$ - *Statistically Generated* N_f

d - *Accumulated Fatigue Damage for* σ_0

D_T - *Accumulated Fatigue Damage at Safe-Life*

D_{fail} - *Miner's Rule Failure Criterion*

μ_f - *Pin Joint Friction Coefficient*

$U1$ - *Displacement Along x Direction*

$U2$ - *Displacement Along y Direction*

$U2$ - *Displacement Along z Direction*

$R1$ - *Rotation About x Direction*

$R2$ - *Rotation About y Direction*

$R3$ - *Rotation About z Direction*

Symbols - *Statistics and Statistical Characterisation*

$f(x)$ - *PDF Evaluated at 'x'*

$F(x)$ - *CDF Evaluated at 'x'*

δ - *Threshold Parameter*

λ - *Shape Parameter*

σ - *Scale Parameter*

x_i - *Data Point*

N - *Sample Size*

μ_X - *Mean of Variable 'X'*

s_X - *Standard Deviation of Variable 'X'*

Φ_{SND} - *Standard Normal CDF*

c_v - *Coefficient of Variation*

cov - *Covariance of 'x' and 'y'*

γ - *Sample Skewness*

CL - *Confidence Level*

α - *Significance Level*

ρ - *Pearson Correlation Coefficient*

r - *PPLR Correlation Coefficient*

R_c - *Cumulative Relative Frequency*

$A0$ - *PPLR Regression Intercept*

$A1$ - *PPLR Regression Slope*

X_T - *Transformed Dataset*

S_{X_T} - *Standard Deviation of Transformed Dataset*

$R_{C,T}$ - *Transformed Cumulative Relative Frequency*

$S_{R_{C,T}}$ - *Standard Deviation of Transformed Cumulative Relative Frequency*

χ^2 - *Chi-Squared*

χ^2_s - *Chi-Squared Test Statistic*

χ^2_c - *Chi-Squared Critical Value*

O_j - *Observed Frequency in Bin 'j'*

E_j - *Expected Frequency in Bin 'j'*

A^2 - *Anderson-Darling Test Statistic*

Symbols - *Statistics and Statistical Characterisation (Continued)*

A_c^2 - *Anderson-Darling Critical Value*

$F_{ECDF}(x)$ - *ECDF Evaluated at 'x'*

$RMSE$ - *Root Mean Square Error*

N_t - *Tail Dataset Sample Size*

t - *Tail Dataset Threshold*

F_{GPD} - *Generalised Pareto Distribution CDF*

Symbols - *Probabilistic and Sensitivity Analysis*

$P[x]$ - *Probability of Event 'x'*

L - *Load or 'Stress' Distribution*

C - *Capacity or 'Strength' Distribution*

β - *Reliability Index*

G - *Limit State Function*

μ_G - *Mean of Limit State Function*

σ_G - *Standard Deviation of Limit State Function*

N_{MCS} - *Number of MCS Iterations*

N_{fail} - *Number of MCS 'Failure' Iterations*

RN - *Random Decimal Number*

RI - *Random Integer*

p_f - *Probability of Failure*

R - *Reliability*

p_{acc} - *Acceptable Probability of Failure*

R_T - *Reliability Target*

$P_{f_{dist}}$ - p_f *Estimate from SSI*

$P_{f_{MCS}}$ - p_f *Estimate from MCS*

σ_{MCS} - *Standard Deviation of MCS Result*

$P_{f_{MCS+2\sigma}}$ - *MCS* p_f *Estimate at Two Standard Deviations*

$P_{f_{tail}}$ - p_F *Estimate from Tail-Fitting*

$p_{f_{feature}}$ - *Feature-Level* p_f *Estimate*

$p_{f_{component}}$ - *Component-Level* p_f *Estimate*

$p_{f_{assembly}}$ - *Assembly-Level* p_f *Estimate*

TE - *Total Effect Sensitivity Index*

TE_j - *TE when Variable '*x_j*' is Fixed*

$f_0(y)$ - *Parent Distribution PDF at 'y'*

$f_{x_j}(y)$ - *Distribution PDF at 'y' when Variable '*x_j*' is Fixed*

y_l - *K-L Entropy Lower Integration Limit*

y_u - *K-L Entropy Upper Integration Limit*

Symbols - *Surrogate Modelling*

MAE - *Maximum Absolute Error*

$RMSE$ - *Root Mean Square Error*

MPE - *Maximum Percentage Error*

y - *Model Output Value*

$\hat{y}$ - *Predicted Output Value*

$\boldsymbol{X}$ - *Matrix of Training Data Values*

$\boldsymbol{y}$ - *Vector of Output Values*

S - *Sample Size of Dataset*

S_T - *Sample Size of Training Dataset*

S_V - *Sample Size of Validation Dataset*

N_I - *Number of Input Parameters*

FF_l - *Full-Factorial Design of 'l' levels.*

β - *RSM Coefficient*

ψ - *Radial Basis Function (RBF)*

$\boldsymbol{w}$ - *RBF Weight Vector*

$\boldsymbol{\Psi}$ - *RBF Gram Matrix*

Symbols - *Surrogate Modelling (Continued)*

r_e - *Euclidean Distance*

σ_{MQ} - *MultiQuadratic RBF Parameter*

GP - *Gaussian Process*

μ_{GP} - *Gaussian Process Basis Function*

$\boldsymbol{K}$ - *Gaussian Process Covariance Matrix*

k - *Gaussian Process Kernel Function*

σ_f - *Gaussian Process Parameter*

l - *Gaussian Process Length Scale*

σ_n - *Gaussian Process Noise Parameter*

Symbols - *Landing Gear Loads*

M - *Aircraft Mass*

n_x - *Drag Load Factor*

n_y - *Side Load Factor*

n_z - *Vertical Load Factor*

F_X - *Global Drag Load*

F_Y - *Global Side Load*

F_Z - *Global Vertical Load*

F_x - *Drag Load at Axle Tip*

F_y - *Side Load at Axle Tip*

F_z - *Vertical Load at Axle Tip*

M_x - *Axle Tip Side Load Moment*

M_y - *Axle Tip Drag Load Moment*

M_z - *Axle Tip z-axis Moment*

ID 11 - *Right Turn*

ID 12 - *Left Taxi*

ID 66 - *Straight Taxi*

ID 41 - *Deceleration / Braking*

ID 42 - *Acceleration*

ID 31 - *Tail-Right Pushback*

ID 32 - *Tail-Left Pushback*

ID 511 - *Right Runway Entry*

ID 512 - *Left Runway Entry*

ID 521 - *Right Backtrack Entry*

ID 522 - *Left Backtrack Entry*

ID 111 - *Takeoff Roll*

ID 333 - *Landing Touchdown*

ID 444 - *Landing Roll*

ID 711 - *Right Runway Exit*

ID 712 - *Left Runway Exit*

ID 721 - *Right High Speed Exit*

ID 722 - *Left High Speed Exit*

ID 731 - *Right Backtrack Exit*

ID 732 - *Left Backtrack Exit*

ID 81 - *Right Turn Onto Stand*

ID 82 - *Left Turn Onto Stand*

Units

mm - *Dimension, millimetre*

° - *Angle, degree*

rad - *Rotation, radian*

ft - *Altitude, feet*

Kn - *Groundspeed, knots*

ms^{-2} - *Acceleration, metres a second*^{2}

g - *Gravitational Acceleration, 9.81* ms^{-2}

N - *Force/Load, newton*

Nmm - *Moment, newton-millimetre*

MPa - *Stress and Modulus, megapascal* ($MNmm^{-2}$)

GB - *Computational Memory, gigabyte*

CHAPTER 1

BACKGROUND AND MOTIVATION

Aircraft landing gear must provide reliable performance under some of the most demanding conditions within aircraft operations. This thesis focuses on component reliability within structural design. Fatigue design and analysis plays a fundamental part in ensuring the structural integrity of landing gear in-service. However, the engineering parameters relating to fatigue design demonstrate significant variability, which currently must be mitigated using design conservatism and safety factors. Probabilistic approaches to design have been proposed to better represent the variability in design parameters, with a view to increasing the efficiency and safety of structural components in-service. Despite the potential utility of probabilistic approaches, they are yet to be used on a wide-scale within engineering design. Beyond providing the necessary background on fatigue design, this chapter asks the question of: "why are probabilistic design approaches not more widely exploited?". This chapter also lays out the proposed research questions that are aimed at increasing the utility of probabilistic approaches for fatigue design.

1.1 Fatigue of Aircraft Landing Gear and Probabilistic Design

Aircraft landing gear comprise of the sophisticated structure and systems required to provide directional control of the aircraft during ground operations (e.g., taxiing, takeoff and landing) and also to support the weight of aircraft on the ground [1, 2]. The design of landing gear requires expertise from all areas of mechanical, structural and manufacturing engineering [3], resulting in a complex and unique assembly [1], such as the landing gear of a civil transport aircraft shown in Figure 1.1.

FIGURE 1.1. Main landing gear of a wide-body civil aircraft.
Original images attributed to Julian Herzog and are used under the GNU Free Documentation License Version 1.2 GFDL and Creative Commons Attribution 4.0 International License CC-BY-4.0.
Source: Wikimedia Commons [A] [B]

Concerning the structural design of landing gear assemblies and components, landing gear must be designed to sustain the high static loads experienced during ground manoeuvres such as landing touchdown, as well as the repeated cyclic loads from taxiing, braking and turning [1, 2, 4, 5]. Repeated application of cyclic loads (which result in cyclic stresses within components) can cause the failure of structures, even if the magnitude of the stresses are well below the static strength of the component material [6, 7]. The failure mechanism through which this achieved is known as fatigue, and encompasses the accumulation of fatigue damage and the initiation and subsequent propagation of cracks within materials under cyclic loading [6–8].

Fatigue failure and design is often concerned with estimating crack initiation as a result of the applications of a large number ($> 10^5$) of cyclic stresses in the elastic domain of the material during High Cycle Fatigue (HCF). Landing gear components are exposed to HCF from the repeated loads applied to the landing gear during ground manoeuvres. However, due to the large load variations that occur during the ground-air-ground cycle of a flight, landing gear components are also exposed to Low Cycle Fatigue (LCF) [9], which typically results in materials being cycled in the plastic domain, with shorter expected fatigue lives in the order of $< 10^4$ cycles [6]. As a result, landing gear fatigue design and analysis must consider both LCF and HCF.

Fatigue failures have been documented since the mid-1800s by engineers and scientists such as Braithwaite, Rankine and Wöhler [10] and designing against fatigue has continued to remain a high priority within all fields of engineering ever since [6, 11]. The consequences of fatigue failure can range from the economic impacts of replacing failed components in-service, to catastrophic accidents resulting from the complete failure of structures [6, 8].

Regarding aircraft landing gear, historic studies have suggested that landing gear exhibit a higher rate of fatigue failure in-service when compared to other types of aircraft structural assemblies [12–14], with 43% of landing gear failures being as a direct result of fatigue [15]. A more recent study by Schmidt has demonstrated that the occurrence of fatigue failures in landing gear has reduced over the last six decades such that one to two component failures due to fatigue are expected per year in civil transport aircraft [16]. Whilst this failure rate will appear low in comparison to other engineering sectors, due to the single load-path nature of landing gear structural assemblies, fatigue failure of landing gear components can result in catastrophic events (e.g. loss of the aircraft, or loss of life) [16]. Landing gear structural assemblies are therefore a safety-critical aspect of all aircraft [1].

Even though it has also been suggested that the majority of landing gear fatigue failures occur during less critical ground manoeuvre phases (e.g. historically, 82% of fatigue failures were observed during taxiing [14]) and that only a limited number of fatigue failures result in a catastrophic accident [16], the economic impact of landing gear fatigue failures can be significant. As a landing gear structural failure can cause damage to the remainder of the aircraft, landing gear fatigue failures have resulted in aircraft being written-off and scrapped, resulting in significant economic and operational impacts for the aircraft operator [17–19]. In other cases, the need to replace landing gear components that have failed prematurely due to fatigue across a fleet of military transport aircraft has been shown to cost in excess of $150 million USD through re-design and replacement of components [20].

The objective of mitigating fatigue failure in landing gear components is to ensure the structural integrity of the safety-critical landing gear assembly throughout the intended design life, to prevent the occurrence of catastrophic accidents. As with other aspects of aerospace structural design, this must be achieved whilst minimising the component weight, to reduce aircraft fuel burn and operating costs, especially when considering that the landing gear remains unused once the aircraft is in-flight [1, 4]. This design challenge is poetically demonstrated by the quote from Conway: "*The landing gear of an aircraft has been described on the one hand as the essential intermediary between the aeroplane and catastrophe, and on the other hand, the obstacle between the aircraft and freedom*" [3].

In order to mitigate fatigue failure in landing gear components, they are designed using a 'safe-life' philosophy [1, 21]. The 'safe-life' (also known as a 'life-limit') of a component represents the design life at which the component must be retired from service, regardless of whether evidence of fatigue crack initiation and propagation is present in the component or not [1, 21].

For aircraft landing gear, the safe-life is typically defined in terms of the number of flight cycles (e.g. 60,000 flights) [2, 4]. A safe-life philosophy infers a crack-free in-service life, and therefore, landing gear fatigue design only considers fatigue as a failure mode during fatigue damage accumulation up to crack initiation [1, 21].

A safe-life philosophy is required for aircraft landing gear due to their safety-critical function, single-load path configuration and widespread utilisation of high-strength metallic alloys, which typically have a low fracture toughness and therefore exhibit rapid propagation of fatigue cracks following initiation [1]. These characteristics of landing gear structural components mean that aircraft landing gear cannot currently be reliably inspected in-service for crack propagation prior to catastrophic component failure and as a result, a crack-free life is required [1, 21].

Safe-Life Fatigue Design and Analysis

Fatigue design is the process of selecting the final component design, as defined by material selection, component properties, intended loading in-service, etc., with the aim of mitigating fatigue failure of the component during its intended design life [22]. Fatigue design is achieved by making decisions regarding the component design based upon the results of assessing whether a proposed component design will satisfy the requirement for a crack-free in-service life [11].

In order to assess whether a proposed component design will satisfy the requirement for a crack-free in-service life, safe-life fatigue analysis methods are employed [21]. This is in harmony with the modern approach to engineering design, where analysis and simulation processes are extensively used to assess whether a proposed design satisfies the design requirements [23]. The final landing gear component design is also tested during a full-scale fatigue test of the landing gear assembly [5, 24].

The safe-life fatigue analysis process represents the 'toolbox' of methods and processes employed to simulate the fatigue damage accumulation that will occur within components when in-service. As stated by Osgood "*all machine and structural designs are problems in fatigue...*" and therefore, the safe-life fatigue analysis process shares many similarities with the fatigue analysis methods used across different industrial sectors [22]. The safe-life fatigue analysis process is based upon classical crack initiation analysis methods, such as a Stress-Life (S-N) approach, based upon S-N curves and Miner's rule for damage accumulation [16, 21]. Strain-Life (E-N) analysis approaches, which are more representative of LCF, can also be used within the safe-life fatigue analysis process [9].

The cornerstone of S-N fatigue analysis is the generation of S-N curves, which establish the fatigue 'response' of the component material [6]. The material fatigue response represents how the number of cycles to failure 'N_f' varies with the applied cyclic stress amplitude 'σ_0'. An example of an S-N curve is shown in Figure 1.2 [6, 25]. S-N curves are usually derived using fully-reversed (i.e. zero mean stress 'σ_m') uniaxial cyclic testing of material coupons at different σ_0 values and the N_f value to cause failure is recorded for each coupon [6]. Repeated coupons

are tested at each selected σ_0, which demonstrate significant variability within the S-N dataset as shown in Figure 1.2 [25]. Whilst safe-life fatigue analysis is typically based upon uniaxial testing of coupons, multiaxial testing of specimens representative of component geometries is also performed to a limited extent within the field of fatigue design and analysis [6, 22].

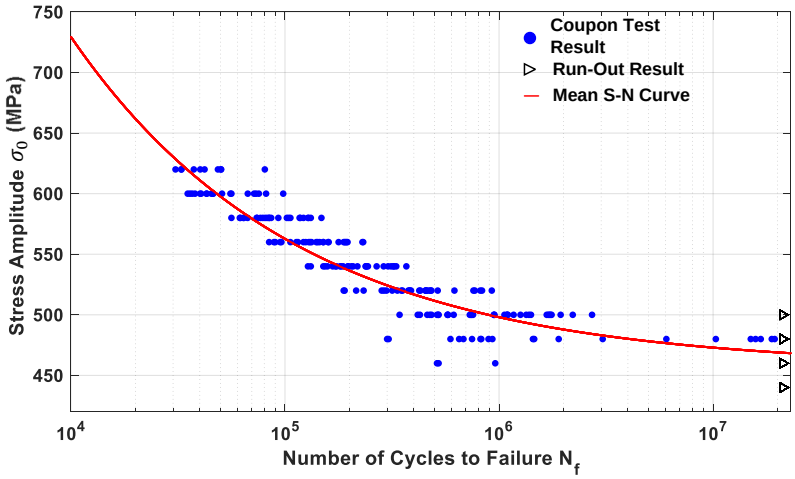

FIGURE 1.2. An example of an S-N curve for 4340 high tensile steel. Reproduced with permission from IHS ESDU [25].

The loading for the component is then considered. The component loading is typically defined in the form of a load-time history, which details the magnitude and sequence of individual loading events applied to the component [7, 26]. The applied loading is intended to be representative of the loading that the component will be exposed to in-service and is often in the form of loading spectra derived using load measurements from in-service components [7]. The load-time history is then converted into a stress-time history based upon the component geometry through either analytical (e.g. hand-calculation style) stress analysis or stress analysis performed using linear Finite Element Analysis (FEA) [7]. Cycle counting methods such as 'rainflow counting' are then used to extract the stress cycles resulting from the load-time history, resulting in the definition of stress cycles with a stress amplitude 'σ_a' and mean stress level 'σ_m' [6, 7].

The next stage of the S-N fatigue analysis process is to convert the extracted stress cycles from rainflow counting into equivalent fully-reversed stress cycles 'σ_0' such that they are compatible with the S-N dataset and S-N curve [7]. A range of mean stress corrections are presented in the literature, with the Goodman mean stress correction being the most prevalent. The Goodman mean stress correction is shown in Equation 1.1, where σ_{UTS} is the ultimate tensile strength of the material [7].

$$\sigma_0 = \frac{\sigma_a}{1 - \frac{\sigma_m}{\sigma_{UTS}}} \tag{1.1}$$

Using the S-N curve, the N_f for each of the fully-reversed stress cycles σ_0 can be identified. The fatigue damage accumulated 'd' by each σ_0 can be computed using Miner's rule for linear damage accumulation shown in Equation 1.2, where 'n' is the number of times the σ_0 stress cycle is applied [6, 7].

$$d = \frac{n}{N_f} \tag{1.2}$$

The total damage 'D_T' resulting from the extracted stress cycles is computed using Equation 1.3. Failure is assumed to occur when $D_T = 1$, as this represents that all of the available fatigue life within the material has been consumed [6, 7]. As result, the Miner's rule failure criterion is $D_{fail} = 1$ [6, 7].

$$D_T = \sum d = \sum \frac{n}{N_f} \tag{1.3}$$

Within landing gear safe-life fatigue analysis, the load-time history typically represents the load-time history for the design safe-life. As a result, providing the D_T value is shown to be less than D_{fail}, it can be inferred that the component will remain crack-free for the design safe-life. In the context of fatigue design, D_T can be considered as the 'performance function' of the safe-life fatigue analysis process and therefore, provides an assessment of whether the landing gear component will satisfy the requirement of a crack-free safe-life. A flowchart summarising the S-N approach to the safe-life fatigue analysis process is shown in Figure 1.3.

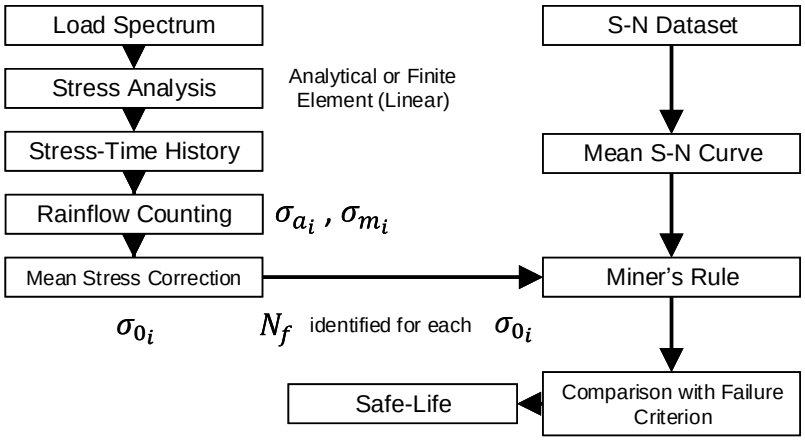

FIGURE 1.3. The S-N fatigue analysis process.

Variability and Uncertainty in Fatigue Design

As highlighted by the quote from Shigley and Mischke, "*variation is omnipresent*" and therefore, all engineering parameters, including component design parameters and parameters relating to the in-service environment, should be expected to demonstrate variability or 'scatter' [23, 27]. The presence of variability in design parameters and operating conditions is acknowledged in a wide range of engineering and structural design reference texts [6, 7, 22, 28–35]. Variability originates from 'randomness' in the value that engineering parameters take, and in the context of structural and fatigue design is expected to be observed in engineering parameters relating to component material properties, the component geometry and the loads that are applied to the component in-service [30]. Variability in engineering parameters can be represented by the coefficient of variation 'c_v', which is computed as the standard deviation (i.e. the statistical measure of variability) divided by the mean value of the parameter.

Firstly, regarding material properties, the S-N datasets generated for safe-life fatigue analysis demonstrate that materials show significant variability in the N_f for a given stress amplitude [36]. As visualised previously in Figure 1.2, the variability in the number of cycles to failure for a material at a given stress amplitude can vary by two orders of magnitude [6, 36], representing a significant source of variability in fatigue design. Therefore, the value of N_f within S-N datasets can show variability of the order $c_v = 25\%$ to $c_v = 75\%$ [37]. The c_v values for N_f are significantly higher than the variability observed in static material properties, such as for σ_{UTS} of $c_v \approx 5\%$ [22]. It is typical to observe that the variability in N_f increases with reducing stress amplitude [6]. For the high tensile strength steels used in landing gear components, S-N datasets also show variability in the fatigue limit 'σ_{FL}', which represents the stress amplitude below which the material can be theoretically cycled indefinitely without failure[1] [7, 22]. The value of σ_{FL} is also derived from experimental testing and is expected to demonstrate variability [6, 35]. Whilst the variability in cyclic material properties is typically larger, static material properties such as σ_{UTS} and Young's (Elastic) Modulus 'E' also exhibit variability [29, 31].

During the manufacture of components, many forming, machining, assembly and joining processes are required. Each process performed will have its own individual sources of variability and these will ultimately result in variability of the component dimensions (e.g. thicknesses, widths, hole diameters, cross-sectional properties, etc.), with typical c_v values in the range of 0.1% to 1% [31]. Component dimensional variability will consequently alter the stresses generated in a component under load, and can also impact the stress concentration caused by specific engineering features [29].

Significant variability is also present in the loads that a component will be exposed to in-service [38, 39]. Variability in in-service loads can be decomposed into the variability in the magnitude of the applied loads, the occurrence of specific loads (i.e. the number of load applications) and the sequence in which the loads are applied to the component [36, 38]. The

[1] When using Miner's rule it is assumed stress amplitudes below σ_{FL} do not accumulate fatigue damage [7, 22].

variability in the magnitude of applied loads across engineering design range from $c_v = 1\%$ to $c_v = 50\%$, with landing gear touchdown loads typically demonstrating a $c_v \approx 10\%$ [29, 40].

To account for variability in engineering parameters within fatigue design, and to ensure components retain their structural integrity in-service, a deterministic approach has been used [6, 8]. Within a deterministic approach, design conservatism along with large safety factors are used to mitigate the presence of variability, by setting engineering design parameters to single, 'safe' values [8]. The aerospace sector has employed a deterministic approach to safe-life fatigue design since the 1940s and 1950s [41]. A more detailed consideration of the safety factors used within safe-life fatigue design is presented in Chapter 2.

Whilst inherent 'randomness' results in variability within design parameters (known as *aleatoric* uncertainty [42]), lack-of-knowledge can also be present in analysis methods and performance functions, resulting in uncertainty in the results generated from such processes. Lack-of-knowledge, known as *epistemic* uncertainty, can be reduced by increased data collection or improved analysis methods and models and is therefore also known as 'model-based' uncertainty [42]. Consequently, epistemic uncertainty typically manifests itself in design approaches as engineering assumptions.

On the other hand, aleatoric uncertainty or design parameter variability cannot be reduced as the 'randomness' observed in certain design parameters is an inherent physical property [42]. This thesis focuses solely on representing variability or aleatoric uncertainty within fatigue design, and the reader is directed to Sandberg et al for a further discussion of epistemic uncertainty in the context of fatigue design [43]. It is therefore assumed that the S-N fatigue analysis processes detailed within this chapter is 'perfect' and free from model-based or epistemic uncertainty.

Probabilistic Fatigue Design and Analysis

The presence of variability in design parameters and in-service operating conditions will always result in the finite risk of an in-service component failing to achieve its design purpose and requirements [28, 30, 31, 44]. Within structural design, this is typically observed as the structure failing in-service as the result of an applied 'load' (e.g. applied stress) exceeding a given 'capacity' (e.g. ultimate tensile stress) [30, 44]. As both the load 'L' and capacity 'C' can be expected to exhibit variability [44], they can be represented using probability distributions (e.g. Normal, Weibull, etc.) as shown in Figure 1.4.

Figure 1.4 provides the classical definitions of the probability of failure 'p_f' and the reliability 'R' of a component in the context of structural design. As can be seen from Figure 1.4, there is a probability that the load L will exceed the capacity C. As failure occurs when $L \geq C$, this probability represents the p_f of the component. Reliability is defined as the probability that the component load will not exceed the capacity and is therefore related to p_f [30]:

$$R = 1 - p_f \tag{1.4}$$

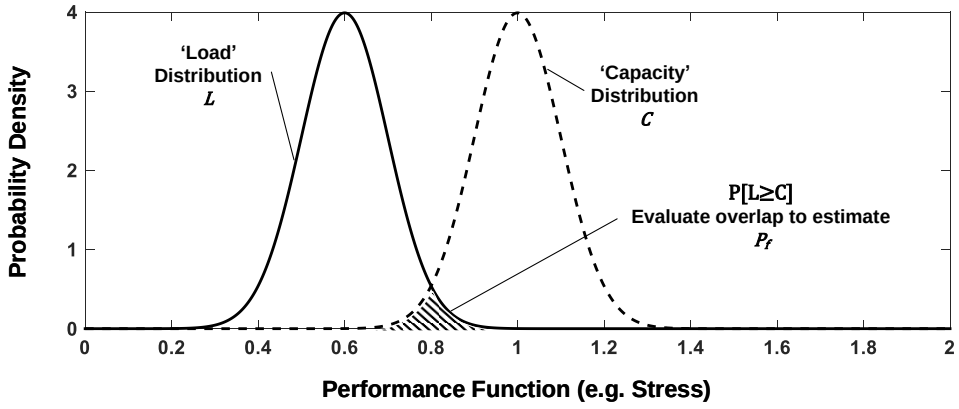

FIGURE 1.4. Concept of 'Load' and 'Capacity' in reliability analysis.

In the example of safety-critical structural components, R is typically used as a measure of the 'safety' of the structure, as structural failure could result in a catastrophic accident [30].

Probabilistic design is an approach whereby design decisions regarding components are made based upon the p_f or R values for a proposed design [45]. Probabilistic design approaches are often employed to ensure that safety-critical components retain their structural integrity in-service, by ensuring proposed designs achieve an acceptable p_f or target R [45]. Due to the widespread use of analysis and simulation methods for assessing whether proposed designs will satisfy design requirements, along with the prohibitive economic cost of repeated full-scale component testing, the generation of p_f and R values to support probabilistic design has been focused predominately at analytically-based probabilistic methodologies [23, 45].

Probabilistic methodologies aim to statistically characterise the variability in the design parameters of an analysis process using probability distributions (e.g. Normal, Weibull, etc.), and then propagate the variability through the existing analysis process using probabilistic analysis methods, such as Monte Carlo Simulation or the First Order Reliability Approach [46]. The probabilistic analysis method enables the variability to be propagated to the process output or performance function, enabling estimates of p_f or R to be generated for the component design [39]. The probabilistic analysis methods are packaged within a probabilistic analysis framework and the relationship between these elements and probabilistic design is shown in Figure 1.5.

In the context of safe-life fatigue design, a probabilistic approach would aim to base design decisions on the probability of the component design failing to satisfy the crack-free safe-life requirement by failing before the design life. This definition of p_f could be assessed by applying a probabilistic fatigue methodology to the safe-life fatigue analysis process, in order to identify the probability of the accumulated fatigue damage in a component D_T exceeding the failure criterion of D_{fail}.

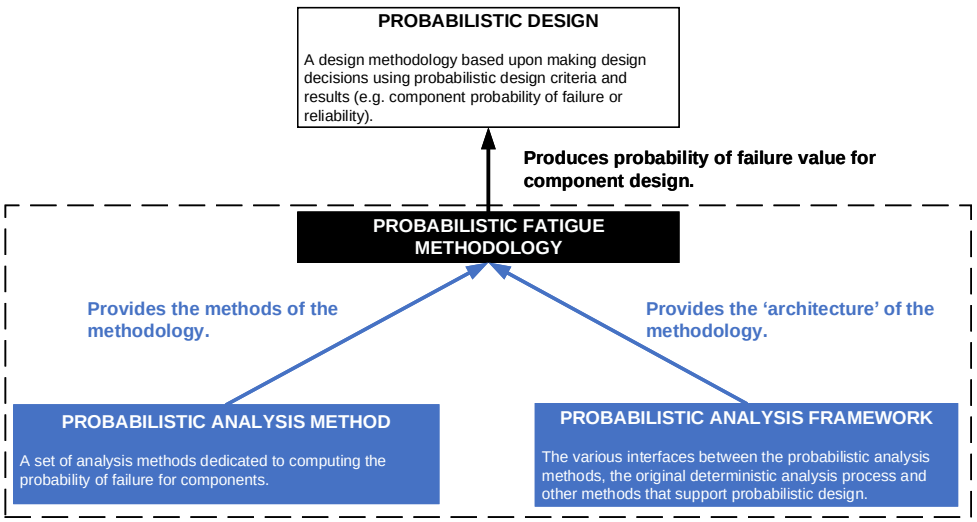

FIGURE 1.5. Definition of a probabilistic fatigue methodology via its relationship to probabilistic design, probabilistic analysis methods and probabilistic analysis frameworks.

The justification for developing probabilistic design approaches in fatigue design can be decomposed into improved failure mode modelling, the incorporation of reliability into the design process and challenging the use of conservatism and safety factors in the existing deterministic design process [23, 45–47].

Firstly, the many sources of variability in fatigue design demonstrate that fatigue as a failure mode is inherently variable [6]. Probabilistic approaches offer the only route to capturing and retaining the sources of variability within the design and analysis process, potentially improving the modelling of fatigue as a failure mode and increasing the confidence in the analysis methods used for fatigue design. Concerning landing gear fatigue design, previous studies have demonstrated that approximately 20% of landing gear fatigue failures are as a result of poor design [15, 16] and therefore, improvements to design approaches could increase the safety of landing gear assemblies.

The implementation of probabilistic design also has an advantage over the deterministic approach based upon safety factors, due to its ability to challenge the conservatism currently required within fatigue design [45]. Based on the deterministic approach, it is not possible to quantify 'how' conservative existing safety factors are, potentially leading to:

- **Over-design:** The use of safety factors can potentially result in components that are over-designed, increasing component weights and reducing the efficiency of the structure [8, 48]. This is especially a consideration for aircraft landing gear, as they are effectively 'dead-weight' when the aircraft is airborne [1, 4].

- **Under-design:** The use of safety factors and design conservatism may not guarantee the safety of a structure, as it does not permit the safety of the structure to be quantified. As an example, the safe-life philosophy requires crack-free component lives and yet landing gear are observed to fail due to fatigue in-service [16]. Therefore, it could be suggested that the existing approach based on safety factors does not provide sufficient structural safety.

A probabilistic framework enables the conservatism and level of safety of a structural design to be quantified using p_f or R values [31, 45] and could therefore support a challenge of the conservatism currently required. A challenge of the existing conservatism would increase component efficiency, whilst ensuring components retain their structural integrity in-service. An existing criticism of a deterministic design approach based upon safety factors is that they are often introduced to ensure components do not fail in-service, yet components are still observed to fail in-service, consequently demonstrating that a quantifiable p_f and R for components does exist and should therefore be quantified to provide a measure of the safety of the structure [31, 32].

Finally, probabilistic design methods enable p_f or R to be used as metrics to compare and optimise designs. For example, aerospace structural design, including landing gear components, must meet minimum weight requirements yet with a high level of safety [45]. This can be achieved by optimising designs to minimise weight, whilst also achieving a reliability requirement in a process known as Reliability-Based Design Optimisation (RBDO) [49, 50]. In addition, the incorporation of p_f and R as design metrics into the design stage can highlight features and locations of components which demonstrate an insufficient reliability, preventing costly re-design and component replacement, by facilitating design modification prior to entry into service [45].

Inhibiting Factors: 'Blockers' to Probabilistic Approaches

Despite the significant advantages offered by implementing probabilistic approaches to design, and that the mathematical and statistical methods that under-pin such an approach have been mature for at least the last four decades, the adoption of probabilistic approaches has been limited across the field of engineering [23, 51]. The reluctance of the engineering sector to perform probabilistic design is as a result of a series of inhibiting factors that have prevented the wide-scale implementation of such approaches [23], and these factors are known as 'blockers'. The key blockers to implementing probabilistic approaches to design currently presented in the literature are:

- **Computational Expense:** Probabilistic approaches typically require an increased computational expense when compared to the existing deterministic-based process. This can both be in the form of the computational resource required and the time taken to perform the probabilistic analysis. Probabilistic approaches can therefore slow down the design process [23, 45, 46, 52–54].

- **Simplifications/Assumptions of Deterministic Analysis Process:** Modern structural design approaches are heavily based on analysis and simulation methods, which often consist of complex physics-of-failure models [7, 23, 45, 47]. Probabilistic approaches often require simplifications of the existing deterministic design and analysis process for implementation. Such simplifications and assumptions must be made *a-priori* before performing the probabilistic analysis. This can result in scepticism regarding the results from probabilistic approaches [45, 46, 54, 55].

- **Availability of Data:** The data required to characterise the variability in design parameters is often not available or would be too costly to generate. As a result, it can be challenging to justify the accuracy of probabilistic methods if they fail to capture all sources of variability [23, 54].

- **Accuracy of Data Characterisation:** Practicing engineers typically have a limited background in statistical methods [23, 45, 46] and therefore, may fail to accurately characterise the variability in design parameters by failing to challenge long-held statistical assumptions or by selecting probability distributions based on mathematical convenience [28, 37]. Such an approach naturally reduces the accuracy of probabilistic approaches [45, 55].

- **Required Knowledge:** The development of a probabilistic approach requires the understanding and implementation of a large number of statistical, mathematical and computational techniques and this can represent an immense resource burden on engineers wishing to implement such approaches [23, 53]. As such techniques are considered novel within engineering design, practicing engineers may lack confidence in the required methods, resulting in scepticism regarding the accuracy of probabilistic approaches [54].

In order to overcome these blockers, previous researchers, such as Goh et al [23, 54] and Safie et al [47, 56] have highlighted the need for systematic approaches and frameworks to support probabilistic design from both the standpoint of knowledge consolidation and methodology implementation. In addition, recent advances in probabilistic analysis methods have presented an opportunity to reduce the computational expense of probabilistic design approaches, while retaining any complexity present in the original deterministic design process [57]. Such approaches are known as surrogate modelling methods and they can be used to produce a computationally efficient representation of a computationally expensive element of an analysis process (e.g. FEA) [57]. Finally, as the engineering sector moves into the age of 'big-data', which consists of datasets that are large in size and are often generated autonomously by in-service components [58–60], there is the potential opportunity to challenge the blocker of data availability when implementing and utilising probabilistic methods.

Another observation is that the blockers to probabilistic design approaches relate directly to the probabilistic methodology used, rather than the concept of probabilistic design itself. As a result, it is proposed that focusing on improvements to the probabilistic analysis methods and framework will provide an effective route to overcoming the blockers to probabilistic design.

Whilst examples of the application of probabilistic approaches to fatigue design have been widely presented in the literature [39, 57], the use of probabilistic fatigue design approaches is not yet routine [11, 23, 51, 61]. Therefore, the overcoming of the blockers to probabilistic design will be demonstrated through the use of fatigue analysis case studies. As probabilistic analysis methods and design approaches have only been applied to the static structural design of landing gear components and assessment of landing gear loads [62–65], the use of landing gear component fatigue design case studies to support the demonstration of the probabilistic fatigue methodology provides a novel application of probabilistic analysis methods. However, as the fatigue design and analysis approaches for aircraft landing gear components are similar to the classical approaches used across the engineering sector [7, 21], the findings from the case studies will also be applicable to other fatigue design and analysis cases.

1.2 Problem Statement

Fatigue design is a vital step in ensuring that safety-critical structural components, such as aircraft landing gear, retain their structural integrity in-service to prevent catastrophic accidents and economic consequences from component failure. The engineering parameters related to fatigue failure and design include material properties, component dimensions and the expected in-service loading of the component, all of which demonstrate variability. Design conservatism and safety factors are currently used to account for this variability, which may lead to components that are either over or under-designed, respectively reducing the efficiency or safety of components in-service. Probabilistic design approaches have been proposed to better represent the variability in design parameters. However, a number of blockers currently prevent the wide-scale implementation of probabilistic design approaches. It is proposed that improvements to the probabilistic analysis methods used within such an approach, based upon recent advancements in the probabilistic and aerospace structural design communities, could overcome these blockers. The following research questions summarise the research problem addressed in this thesis:

- *Can a probabilistic fatigue methodology be successfully applied to safe-life landing gear components, in order to compute the probability of failure related to a component safe-life*?
- *Can a probabilistic fatigue methodology be used to support the existing safe-life fatigue analysis process and fatigue design?*

- *Can careful selection of a probabilistic analysis method, along with the construction of a systematic probabilistic analysis framework, result in a probabilistic fatigue methodology that overcomes the blockers to probabilistic design approaches?*
- *Can recent advances in probabilistic approaches and aerospace structural design, such as surrogate modelling and 'big-data' sources, assist probabilistic fatigue methodologies in overcoming the blockers to probabilistic design approaches?*

1.2.1 Research Aim and Objectives

Based on the research questions posed above, the aim of this research is to develop a probabilistic fatigue methodology to support the fatigue design of safe-life components. To achieve this aim, the following objectives are proposed:

1. To review existing probabilistic analysis methods and their previous application to fatigue design.
2. To select a specific probabilistic analysis method for fatigue design, taking into consideration the current blockers to probabilistic design approaches.
3. To define a probabilistic analysis framework and systematic probabilistic analysis processes which can overcome the current blockers to probabilistic design approaches.
4. To investigate the utilisation of surrogate modelling and big-data sources in a probabilistic methodology for fatigue design.
5. To demonstrate the proposed probabilistic fatigue methodology on case studies in safe-life fatigue design, concerning aircraft landing gear structural components.

1.2.2 Research Methodology

As with all pieces of individual research, a systematic research methodology is required to achieve the research aim and objectives of this thesis. Systematic research methodologies require the stages of *observations*, *hypothesis formation*, *hypothesis testing*, *hypothesis evaluation* and *hypothesis acceptance* or *rejection*.

The *observations* stage is embodied in the problem statement in Section 1.2, leading to *hypothesis formulation* in the form of the four hypotheses posed as research questions in the same section.

In order to perform *hypothesis testing*, the research objectives detailed in Section 1.2.1 were realised through the definition of a probabilistic fatigue methodology and its subsequent application to landing gear component fatigue analysis case studies. The *hypothesis testing* can be further decomposed into the following activities:

1. A review of the current practices, guidelines and blockers concerning probabilistic approaches, coupled with a critical review of existing practices for mitigating variability in fatigue design parameters.

2. Selection of a probabilistic analysis method based on considerations concerning the application of the method, strengths and limitations of the candidate methods and the existing blockers to probabilistic design approaches.

3. Integration of the selected probabilistic analysis method within a probabilistic analysis framework, to form the probabilistic fatigue methodology.

4. Definition of a systematic statistical characterisation process for design parameters and its demonstration on an S-N dataset.

5. Generation of landing gear ground manoeuvre statistics from a big-data source to support the representation of variability in landing gear loading within the probabilistic fatigue methodology.

6. Assessment of various surrogate modelling methods to replace the FEA models used within fatigue design for loading and stress analysis, along with the definition of a surrogate model selection process.

7. Demonstration of the probabilistic fatigue methodology on landing gear component case studies of differing complexity, with regards to loading, geometry and utilisation of analytical or FEA-based stress analysis.

Hypothesis evaluation then returns to the four original research questions and uses the results and observations from *hypothesis testing*, coupled with additional information from the literature and existing practices, to provide an answer to each of the research questions, ultimately resulting in either *hypothesis acceptance* or *rejection*. The evaluation of the research questions will also be performed by considering the wider application of probabilistic fatigue methodology within fatigue design, to highlight future opportunities for the exploitation of this research.

1.3 Original Contributions of Thesis

Across the work performed in this thesis to satisfy the research aim and answer the research questions, the following novel research contributions have been identified:

- A critical review of both the existing practices for accounting for variability in fatigue design and the previous implementation of probabilistic analysis methods within safe-life fatigue design.
- Development of a probabilistic fatigue methodology, based upon a Monte Carlo Simulation method, that overcomes the current blockers to probabilistic design approaches.
- Development and execution of systematic processes for the implementation of probabilistic methodologies. The developed processes concern systematic statistical characterisation, surrogate model selection and a general probabilistic analysis framework.
- Extensive utilisation of surrogate modelling methods to reduce the computational expense of performing probabilistic fatigue analysis.
- Characterisation of landing gear ground manoeuvre variability from the real-time tracking of in-service aircraft using a big-data source.
- Successful demonstration of the probabilistic fatigue methodology on case studies concerning landing gear components of differing geometrical, loading and analysis complexity.

Whilst the probabilistic fatigue methodology is demonstrated using safe-life landing gear component case studies within this thesis, the research contributions highlighted above also impact the wider field of probabilistic design and analysis, as will be explored throughout the following chapters.

1.3.1 Publications Arising from this Research

The research work presented within this thesis has been disseminated within the public domain across a series of papers, book chapters and presentations. The list below details the dissemination activities performed and highlights the relevant chapters within this thesis that each item of dissemination supports.

Author Contribution Statement: For all publications as lead author, J. Hoole performed the technical work and produced the related manuscript.

Journal Papers

J. Hoole, P. Sartor, J. D. Booker, J. E. Cooper, X. V. Gogouvitis, and R. K. Schmidt, *Systematic statistical characterisation of stress-life datasets using 3-Parameter distributions*, International Journal of Fatigue, Vol. 129, 2019. The contents of this paper can be found in Chapter 4.

J. Hoole, P. Sartor, J. D. Booker, J. E. Cooper, X. V. Gogouvitis, and R. K. Schmidt, *Landing Gear Ground Maneuver Statistics from Automatic Dependent Surveillance-Broadcast Transponder Data*, AIAA Journal of Aircraft (Submitted September 2019, under peer-review as of February 2020). The contents of this paper can be found in Chapter 5.

Book Chapters

J. Hoole, P. Sartor, J. D. Booker, J. E. Cooper, X. V. Gogouvitis, and R. K. Schmidt, *Probability Distribution Type for the Accumulated Damage from Miner's Rule in Fatigue Design*, in "Mechanical Fatigue of Metals - Experimental and Simulation Perspectives", edited by José A.F.O. Correia, Abílio M. P. De Jesus, António Augusto Fernandes and Rui Calçada, Springer, 2019. The contents of this book chapter can be found in Chapters 2 and 3.

J. Hoole, P. Sartor, J. D. Booker, J. E. Cooper, X. V. Gogouvitis, A. Ghouali, and R. K. Schmidt, *A Framework to Implement Probabilistic Fatigue Design of Safe-Life Components*, in "ICAF 2019 - Structural Integrity in the Age of Additive Manufacturing", edited by Antoni Niepokolczycki and Jerzy Komorowski, Springer, 2019. The contents of this book chapter can be found in Chapter 3.

Conference Papers

N. Zentuti, J. D. Booker, J. Hoole, R. A. W. Bradford, and D. Knowles, *Probabilistic Structural Integrity*, Proceedings of the TAGSI-FESI Symposium, Cambridge, U.K., April 18th, 2018. J. Hoole contributed a short summary of probabilistic fatigue methodologies to this paper.

J. Hoole, P. Sartor, J. D. Booker, J. E. Cooper, X. V. Gogouvitis, and R. K. Schmidt, *Evaluating the Impact of Conservatism in Industrial Fatigue Analysis of Life-Limited Components*, Proceedings of the 12th International Fatigue Conference (Fatigue2018), Poitiers, France, May 27th - June 1st, 2018. The contents of this paper can be found in Chapter 2 and Appendix A.

J. Hoole, P. Sartor, J. D. Booker, J. E. Cooper, X. V. Gogouvitis, and R. K. Schmidt, *Comparison of Surrogate Modelling Methods for Finite Element Analysis of Landing Gear Loads*, Proceedings of AIAA SciTech2020, Orlando, Florida, U.S.A, January 6th-10th, 2020. The contents of this paper can be found in Chapter 6.

Presentations

Landing Gear Ground Maneuver Statistics from ADS-B Transponder Data, SAE Aerospace Landing Gear Systems A-5 Committee, Cologne, Germany, October 15th-16th, 2019.

A Framework to Implement Probabilistic Fatigue Design for Landing Gear Structures, HBM Prenscia Technology Day: Overcoming Real World Fatigue Testing and Simulation Challenges, Sheffield, U. K., November 19th, 2019.

1.4 Thesis Structure

This thesis contains nine further chapters, which are summarised below:

Chapter 2: Literature Review

This chapter provides a comprehensive literature review of the practices currently used to manage variability in fatigue design, along with reviewing the previous application of probabilistic methodologies to the safe-life fatigue analysis process. The chapter also considers the selection process for the probabilistic analysis method, based on the strengths and limitations of the identified candidate methods. The critical review of existing practices resulted in the conference paper "*Evaluating the Impact of Conservatism in Industrial Fatigue Analysis of Life-Limited Components*", whilst the definition of the probabilistic analysis method is presented in the book chapter "*Probability Distribution Type for the Accumulated Damage from Miner's Rule in Fatigue Design*".

Chapter 3: Proposed Probabilistic Analysis Framework

A wide range of additional methods are required to support a probabilistic methodology and as a result, this chapter will identify such methods. Background is provided on surrogate modelling methods, computation of probability of failure values and sensitivity analysis approaches. The chapter concludes with the construction of the probabilistic analysis framework to be used within the probabilistic fatigue methodology. The framework and discussion points from this chapter have been presented within the book chapter "*A Framework to Implement Probabilistic Fatigue Design of Safe-Life Components*".

Chapter 4: Enhanced Statistical Characterisation Process for Materials Data

Chapter 4 defines and demonstrates a novel systematic statistical characterisation process to be used to characterise the variability in Stress-Life material datasets. The characterisation process is demonstrated on a rich material dataset for 4340 steel. This chapter also details how material design parameter variability is incorporated into the probabilistic fatigue methodology. The majority of this chapter has contributed to the journal paper "*Systematic statistical characterisation of stress-life datasets using 3-Parameter distributions*".

Chapter 5: Landing Gear Load-Time Histories from Big-Data Sources

A novel data collection activity is presented based upon the 'real-time' tracking of aircraft to characterise the variability in ground manoeuvre occurrence and sequencing for aircraft landing gear. From the range of statistics generated from the data collection, the consequences and impact on the existing fatigue design practice for landing gear load spectra are explored. This chapter also

describes how loading variability is incorporated into the probabilistic fatigue methodology. The data collection methodology and generated ground manoeuvre variability statistics resulted in the submitted manuscript "*Landing Gear Ground Maneuver Statistics from Automatic Dependent Surveillance-Broadcast Transponder Data*".

Chapter 6: Surrogate Modelling of Landing Gear Loads

This chapter reviews the wide range of surrogate modelling methods that have come to maturity. Each of the candidate surrogate modelling methods are evaluated across two case studies concerning a main landing gear finite element loads model. Systematic processes for surrogate model training and selection are also presented. The technical work performed in this chapter has been presented in the conference paper "*Comparison of Surrogate Modelling Methods for Finite Element Analysis of Landing Gear Loads*".

Chapter 7: Lower Side-Stay Case Study

This chapter demonstrates the implementation of the probabilistic fatigue methodology on a case study comprising of the lower side-stay assembly from the main landing gear of a wide-body civil aircraft. This case study aims to explore the application of the probabilistic fatigue methodology to components that are loaded in a simple manner. Sensitivity analysis is also performed to identify the fatigue design drivers of the assembly.

Chapter 8: Drag Brace Case Study

To further demonstrate and evaluate the probabilistic fatigue methodology, Chapter 8 applies the methodology to a case study regarding the lower drag brace from the main landing gear of a wide-body civil aircraft. The drag brace case study considers the application of the probabilistic fatigue methodology to a component that demonstrates geometrical, loading and analysis complexity, along with the surrogate modelling of finite element stress models.

Chapter 9: Discussion

The discussion chapter evaluates how the novel work presented over the preceding chapters achieves the research aim. This chapter also evaluates how the proposed probabilistic fatigue methodology contributes to overcoming the blockers to a probabilistic approach to design.

Chapter 10: Conclusions and Further Work

This chapter presents the conclusions of the thesis and recommendations for further research activities.

CHAPTER 2

LITERATURE REVIEW

Design conservatism and safety factors are currently used to mitigate the variability observed in fatigue design parameters. This chapter provides a critical review of the existing approaches to fatigue design conservatism and safety factors across different engineering sectors, to highlight the deficiencies in performing fatigue design based upon a deterministic approach and conservatism. This chapter also identifies the potential probabilistic analysis methods available for application within a probabilistic fatigue methodology. For newcomers to the field of probabilistic approaches, the wide range of available and mature methods can be bewildering. However, during the course of this chapter it is demonstrated that through careful consideration of the application of the probabilistic method and the strengths and limitations of each probabilistic analysis method, the path to selecting a probabilistic analysis method can be made clearer. Regarding the research questions proposed as the start of this thesis, this chapter asks: "can the careful selection of a probabilistic analysis method help to overcome the blockers to a probabilistic approach to fatigue design?".

2.1 Literature Review Scope

Within the literature, there are a number interpretations and definitions of 'probabilistic fatigue', which can be grouped into the following categories:

- **Probabilistic Fatigue Design:** The application of probabilistic analysis methods to existing deterministic analysis processes to compute p_f values to support design decisions [46], as is the focus of this thesis.
- **Statistical Methodologies:** A fully-defined and integrated design and analysis process, which differs significantly from existing design and analysis processes, such as the approach proposed by Castillo and Fernádez-Canteli, which requires alternative definitions of S-N curves and Miner's rule for damage accumulation [66].
- **Stochastic Fatigue:** This field concerns the modelling of material defects and the physics-of-failure of fatigue using probabilistic and statistical methods [67–69]. In addition, 'stochastic fatigue' is also used to describe where the loading applied to structures is purely random and is evaluated using frequency-domain techniques [70, 71].

As this thesis is concerned with probabilistic approaches to fatigue design, statistical methodologies and stochastic fatigue approaches will be neglected from the literature review. In addition, probabilistic approaches to design have been developed to consider both crack initiation (i.e. the safe-life fatigue analysis process) and crack propagation (i.e. a 'damage tolerant' approach) within the literature [48]. The scope of this thesis is limited to literature concerning the application of probabilistic analysis methods to fatigue analysis processes based upon Miner's rule for damage accumulation up to crack initiation. However, due to their generalised nature, the probabilistic analysis methods identified in the literature review could also be applied to crack-propagation based fatigue design and analysis [44].

2.2 Existing Management of Variability in Fatigue Design

Across the different engineering sectors, the variability and uncertainty in component safe-life values and accumulated fatigue damage is currently accounted for using conservatism within the fatigue design and analysis process [8]. The conservatism applied during the fatigue analysis process effectively reduces the available safe-life of a component and typically takes the form of statistical reductions on material properties or as deterministic 'safety factors' [8]. The incorporation of conservatism into the fatigue analysis process ensures that components retain their structural integrity in-service and is usually prescribed in the relevant design standards for each industrial sector. However, the utilisation of conservatism within the fatigue analysis process can lead to the potential safe-life of a component not being fully exploited due to retiring a component from service at an earlier safe-life. Conservatism can also result in components

being 'over-sized' and heavier, increasing the total life-cycle cost of a component and reducing the overall performance of the structure [8].

Concerning the typical characteristics of safe-life landing gear components from the perspective of fatigue design and analysis, they are single load-path, monolithic (i.e. no weldments) and manufactured from high tensile strength steels, which are not routinely inspected in-service. In addition, S-N fatigue analysis is performed for safe-life landing gear components. These characteristics are also demonstrated by components in engineering sectors outside of landing gear, including nuclear, wind energy and steel structures as shown in Table 2.1.

TABLE 2.1. Engineering sectors that perform safe-life fatigue analysis, along with regulatory documents and typical components.

Engineering Sector	**Design Requirements**	**Advisory Material**	**Typical Components**
Large Aircraft	EASA CS25 [24]	EASA AMC25 [24]	Aircraft Landing Gear [21, 24]
Light Aircraft	FAA Part 23 [72]	FAA AC23 [72]	Fuselage and Wing Structures [72]
Nuclear	AMSE III NB [73]	-	Piping and Boilers [73]
Wind Turbines	BS61400-1 [74]	-	Turbine Blades, Hubs, Towers [74]
Offshore Structures	DNVGL-RP-C203 [75]	DNVGL-OS-C101 [76]	Offshore Platforms, Jackets and Piles [75]
Steel Structures	Eurocode 3 [77]	-	Steel Bridges [77]

From reviewing the design standards for each engineering sector shown in Table 2.1, there are a wide range of methods that enable conservatism to be introduced into the fatigue analysis process for safe-life components. These methods can be differentiated into statistically-derived reductions and deterministic safety factors. There are six common methods to introduce conservatism into safe-life fatigue analysis processes as identified during the review of the design requirements and advisory material in Table 2.1:

1. A safety factor on the component safe-life (either to reduce the estimated component safe-life, or demonstrate that the component must sustain multiple design lives beyond the in-service safe-life).

2. A safety factor used to reduce the Miner's rule failure criterion D_{fail}.

3. A safety factor used to increase the stress levels applied to the component.

4. A statistically-derived reduction of the S-N curve used for fatigue analysis.

5. A deterministic reduction on the S-N curve that reduces the σ_0 for a given N_f value (i.e. shifting the S-N curve 'down').

6. A deterministic reduction on the S-N curve that reduces the N_f for a given σ_0 value (i.e. shifting the S-N curve 'left').

Figure 2.1 demonstrates the stage in the safe-life fatigue analysis process that each type of conservatism is applied. The statistically derived reduction of the S-N curve is based upon reducing the N_f for a given σ_0 based directly on the variability observed during material coupon testing.

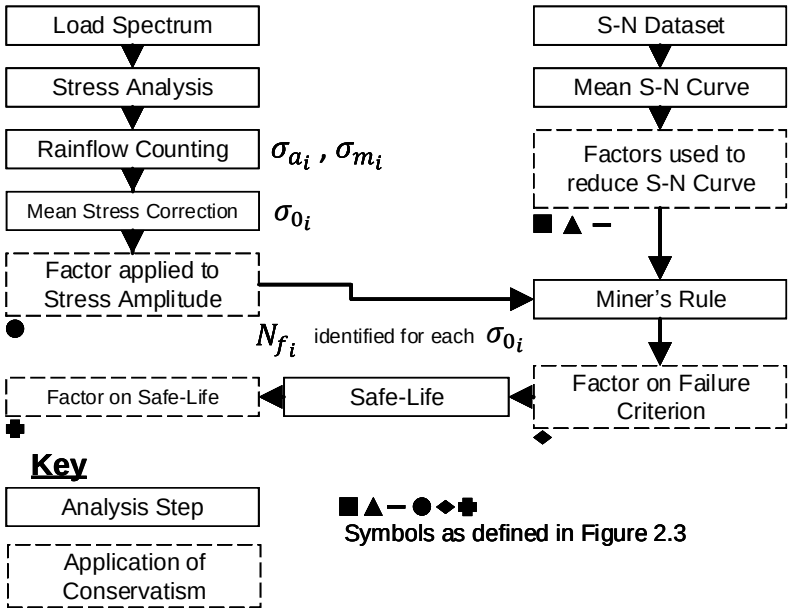

FIGURE 2.1. Methods for applying conservatism in safe-life fatigue analysis.

Statistically reduced S-N curves are defined by a Probability of Survival 'PoS' and a Confidence Level 'CL'. The PoS represents the proportion of material specimens that would be expected to survive at a given σ_0 and the CL is required to account for the statistical uncertainty resulting from using sample data rather than the full population. Closed-form methods are available for constructing S-N curves of a given PoS/CL based on an S-N dataset [78], and a PoS/CL value of 50/50 represents the mean S-N curve. PoS/CL S-N curves are commonly referred to as Probability-S-N (P-S-N) curves, design, working or characteristic S-N curves. Figure 2.2 shows S-N curves of different PoS/CL values, along with the S-N curves generated when deterministic factors on σ_0 and N_f are applied (referred to as factors on "stress" and "life" respectively).

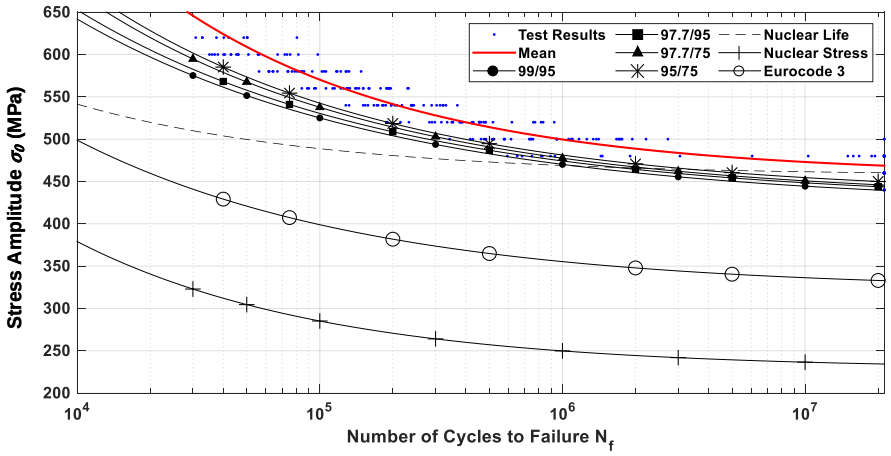

FIGURE 2.2. S-N curves of differing PoS/CL values and S-N curves resulting from deterministic factors on σ_0 and N_f. S-N dataset reproduced with permission from IHS ESDU [25].

A comprehensive review of the fatigue design standards for each engineering sector shown previously in Table 2.1 permitted a comparison of the conservatism currently applied by each sector as shown in the matrix in Figure 2.3. The findings shown in the matrix in Figure 2.3 enhance the observations of previous work that reviewed the conservatism applied to fatigue analysis in the steel, offshore and nuclear sectors [55, 79, 80]. Each populated cell in Figure 2.3 shows the area of variability accounted for by each conservatism approach, along with the method of application and magnitude of the conservatism applied by each sector.

Within Figure 2.3 any conservatism value marked with an asterisk '*' shows that a single safety factor is used to account for multiple areas of variability or uncertainty. For example, Figure 2.3 shows that the light aircraft sector uses a **single** safety factor of 8 applied to the component safe-life, which is intended to collectively mitigate the variability in S-N curve material scatter and loading, along with accounting for uncertainty in the selected S-N material coupon, environmental degradation of materials and uncertainty in analysis methods [72].

From reviewing Figure 2.3, it can be observed that the areas of variability accounted for vary significantly across the different engineering sectors. The only area consistently accounted for is the variability within S-N datasets, as shown by the fully populated row in Figure 2.3. Based on the fact that all sectors account for S-N dataset variability, it can therefore be expected that variability in S-N datasets is considered as one of primary sources of variability in fatigue design and analysis. The nuclear sector appears to provide the most comprehensive conservatism approach for accounting for variability in materials data, through accounting for surface finish/material treatment effects, environmental effects and the size effect [73][1].

[1]The size effect is a statistical effect in which larger components demonstrate lower fatigue lives than material specimens, due to there being a greater probability of fatigue-inducing defects in a large volume of material [22].

■ "Stress" factor applied to stress amplitude on S-N curve
▲ "Life" factor applied to number of cycles to failure on S-N curve
▬ PoS/CL statistical reduction on mean S-N Curve
● Factor applied to stress cycle amplitude
◆ Factor applied to Miner's rule failure criterion
✚ Factor applied to component life-limit
* Conservatism applied to multiple areas of variability / uncertainty

	Area of Variability or Uncertainty	Engineering Sector: Large Aircraft (EASA CS25)	Light Aircraft (FAA Part 23)	Nuclear (ASME III NB) [A]	Wind Turbines (BS61400-1) [B]	Offshore Steel Structures (DNVGL-RP-C203)	Steel Structures (Eurocode 3)
Materials Data	S-N curve material scatter	▬ 99/95	✚ >8*	■ 2* ▲ 2*	▬ 97.7/95	▬ 97.7/75	▬ 95/75
	Deviation of properties from design data				● 1.1*		
	Difference between coupon/specimen used to generate S-N curve and component	✚ 3*	✚ >8*		● 1.1*		
	Effect of surface finish and material treatment			■ 2* ▲ 4*			
	Size effect			▲ 2.5			
	Environmental degradation / no environmental protection applied to component	✚ 3*		■ 2* ▲ 4*			
Loading	Loading Variability	✚ 3*	✚ >8*		● 1[C]	◆ 10*[E]	
	Accuracy of stress concentration factors		✚ >8*				
Geometry	Variability or uncertainty in component dimensions.				● 1.1*		
	Inaccurate assessment of component resistance (e.g. structural sections)				● 1.1*		
Component	Consequence of failure for component / level of required safety	✚ 3*			● 1.15[D]	◆ 10*[E]	■ 1.35[F]
	Inspectability of components					◆ 10*[E]	
Analysis	Uncertainty in analysis methods		✚ >8*			◆ 10*[E]	
	Uncertainty in conversion factors				● 1.1*		

A: Only the most conservative of either the "stress" factor or "life" factor on the S-N curve is applied.
B: Assuming Steel material (other conservatism values are provided for other materials).
C: This conservatism is used to account for loading uncertainty and deviation during static design.
D: Class 2 "non fail-safe" components whose failure may lead to the failure of a major wind turbine part.
E: Either a multiplication of the accumulated damage or as a divisor on the Miner's rule failure criterion.
F: Required for a safe-life component (i.e. un-inspected) with a high consequence of failure.

FIGURE 2.3. The different conservatism approaches used by various engineering sectors for safe-life fatigue analysis, including the areas of variability accounted for, the method of conservatism application and the magnitude of the conservatism applied.

Most sectors, excluding nuclear and steel structures, also currently account for variability in the loading applied to the component as shown in Figure 2.3. This observation also suggests that variability in component loading is considered a significant source of variability within the fatigue

design and analysis of safe-life components. The other source of variability typically discussed within fatigue analysis is variability in component dimensions, although it is interesting to note that this is only currently accounted for using conservatism within the wind turbine sector [74].

Concerning the method of application of conservatism within safe-life fatigue analysis, there is little consistency across the engineering sectors. As can be seen in Figure 2.3, the large aircraft sector and Eurocode3 steel structures employ both a P-S-N curve with a safety factor on the component safe-life, whereas light aircraft structures only use a safety factor on the component safe-life to introduce conservatism. The offshore sector uses a P-S-N curve and a safety factor applied to D_{fail}, whilst the wind turbine sector introduces yet another approach, utilising a P-S-N curve and a safety factor applied to increase the applied component stresses. The nuclear sector is based exclusively on deterministic safety factors. It can therefore be seen from the matrix in Figure 2.3 that there is significant inconsistency in the method(s) used to apply conservatism across the different sectors.

Figure 2.3 also demonstrates that the methods of conservatism application also vary considerably for each individual area of variability. For example, Figure 2.3 shows that S-N dataset variability is accounted for using: statistically-reduced P-S-N curves, deterministic safety factors applied to the S-N curve, as well as a safety factor applied to the component safe-life. Likewise, variability in the applied loading is accounted for using: a safety factor applied to component stress, a safety factor applied to D_{fail}, or using a safety factor on the component safe-life. Figure 2.3 also shows that a conservatism method is often used that does not directly address the source of variability. For example, the wind turbine sector uses a safety factor on the applied component stresses to account for material property variability, which one would expect to be accounted for using conservatism applied to material properties directly.

The final source of inconsistency across the engineering sectors highlighted in the matrix in Figure 2.3 is the magnitude of conservatism applied. From Figure 2.3, it can be seen that the PoS/CL values for statistically-reduced P-S-N curves and the magnitude of safety factors varies significantly across the engineering sectors. It can therefore be proposed that the overall conservatism introduced to fatigue design and analysis of safe-life components varies significantly between the sectors (the impact of the different conservatism approaches is quantified using a case study in Appendix A).

The significant inconsistency across the sectors shown previously in Table 2.1 regarding the areas of variability accounted for using conservatism, along with the method of conservatism application and conservatism magnitude, contradicts the observation that each sector is performing similar design and analysis approaches on similar components. As each sector is performing fatigue design and analysis of safety-critical safe-life components with similar characteristics, it would be expected that the conservatism approaches would be similar across the different sectors. It is therefore evident that a more harmonised approach to safe-life fatigue analysis, with respect to accounting for design parameter variability, is required within the engineering community.

In addition, the matrix in Figure 2.3 demonstrates that in many sectors, a mixture of statistically-derived conservatism and deterministic safety factors is employed. As a result, the overall conservatism applied to an analysis process to account for variability in different design parameters cannot be directly compared due to the utilisation of different conservatism methods. This is further compounded in cases where a single safety factor is used to account for multiple areas of variability, as is performed in most engineering sectors, and as a result, the conservatism represented in each safety factor cannot be directly apportioned to specific design parameters. Ultimately, this means that engineers cannot calibrate or relate safety factors to the observed variability in design parameters. It is a common criticism in the literature that deterministic safety factors fail to account for information that is available about variability in design parameters [32].

The situation is further complicated in sectors which also use safety factors to account for areas that do not relate to design parameter variability, such as uncertainty in the analysis methods used or the consequence of the component failure. As a result, engineers cannot be certain of the areas of the component fatigue design and analysis to which the conservatism applied is over or under-conservative and therefore, a true understanding of the conservatism applied during analysis cannot be formed. Therefore, a fatigue analysis approach is required that directly accounts for the variability present in design parameters, such that the level of conservatism (or safety) introduced by safety factors can be quantified. The inability to quantify the actual level of safety introduced to a structure through the use of safety factors can result in over-design (or in some instances un-conservative design), as described by Haugen [31].

Other criticisms of safety factor based approaches to accounting for variability in engineering design are widespread within the literature. Svensson and Johnnesson summarise that whilst safety factors are typically based on empirical and in-service experience, the full justification for the magnitude of safety factors is usually unknown [29, 38, 81]. Within the aerospace sector, the magnitude of safety factors often have a long-standing history[2] and coupled with inclusion of safety factors into regulatory requirements [38, 81], the challenging of safety factors is seldom performed [32]. This results in an engineering mindset that if the prescribed conservatism approach for fatigue analysis is applied, that the component will indeed be safe. However, components are observed to fail in-service therefore demonstrating that the design conservatism and safety factors are failing to guarantee the structural integrity of components. In addition, the belief that a component is safe as a result of design conservatism and safety factors can lead to the presence of the finite probability of component failure, and its root causes, being neglected during design [32]. In a similar manner, as the level of safety introduced by a conservatism approach cannot be quantified, the changing of the safety factor value, or applying the same safety factor to different designs, will result in different amounts of conservatism being applied to a component [81]. Finally, a common observation within the literature is that prescribed

[2]e.g. The 1.5 safety factor on static loading currently used in aerospace structural design was developed during the 1930s [45].

conservatism approaches do not represent the radical developments in analysis methods (e.g. FEA, improved materials characterisation, etc.) which have occurred since the inception of the conservatism approaches. As a result, the prescribed conservatism approaches prevent the advancements in structural analysis methods to be fully exploited [32, 38].

2.3 Probabilistic Fatigue Analysis Methods

The justifications provided for implementing a probabilistic approach to design presented in Chapter 1 align with the limitations and criticisms of the existing deterministic fatigue design approach based upon conservatism and safety factors identified in the previous section. Firstly, probabilistic analysis methods enable the reliability, and therefore, safety, of a component to be quantified. This is also achieved by directly representing the variability in fatigue design parameters using the statistical characterisation of design parameter datasets using probability distributions. Finally, probabilistic analysis methods are typically 'general' in their application as they 'wrap-around' the existing analysis process [46, 61]. This quality of probabilistic analysis processes means that a unified approach to representing variability in fatigue design parameters could be implemented across the engineering community, as the probabilistic analysis methods are insensitive to the specific fatigue design and analysis processes used by each sector.

Whilst a probabilistic design approach can be shown to overcome the limitations of the existing fatigue design approach based upon deterministic analysis and conservatism, there are a wide range of probabilistic analysis methods presented within the literature and therefore, care must be taken when selecting the specific probabilistic analysis method to implement [23, 28]. As a result, this section will perform a wide review of probabilistic analysis methods previously adopted for safe-life fatigue design, with a view to selecting a probabilistic analysis method that can help overcome the current blockers to a probabilistic approach for safe-life fatigue design.

2.3.1 Stress-Strength Interference Method

The classical approach to performing probabilistic analysis in structural design is known as the Stress-Strength Interference (SSI) method, which builds directly upon the concepts of 'load' and 'capacity' described in Chapter 1 [29, 30, 44]. The SSI approach aims to compute the joint probability of the interference between the 'load' and 'capacity' distributions as shown previously in Figure 1.4, as the joint probability represents the probability that 'load' will exceed the 'capacity'. If the probability distributions of 'load' and 'capacity' are statistically independent (i.e. one does not influence the other), the interference joint probability is equal to p_f, and can be shown to be [30, 44]:

$$p_f = P[L \geq C] = \int_{-\infty}^{\infty} F_C(x) f_L(x) dx \tag{2.1}$$

In Equation 2.1, 'x' is the value of the performance function (e.g stress), '$F_C(x)$' is the Cumulative Density Function (CDF) of the 'capacity' and '$f_L(x)$' is the Probability Density Function (PDF) of the 'load'. For various combinations of 'load' and 'capacity' probability distributions, closed-form solutions to Equation 2.1 are available [30, 32, 44]. Alternatively, if the 'load' PDF and 'capacity' CDF have been defined, numerical integration techniques can be used to produce an estimate of p_f [29].

Within the context of structural design and analysis, the 'load' typically represents a 'stress' and the 'capacity' typically represents a 'strength' (e.g. ultimate tensile strength) [44]. Concerning safe-life fatigue design and analysis, the 'stress' distribution shown in Figure 2.4a represents the variability in the accumulated fatigue damage 'D_T' from fatigue analysis based on Miner's rule and the 'strength' distribution represents the variability in the Miner's rule failure criterion 'D_{fail}' [67, 82]. In the situation whereby a deterministic failure criterion is used (i.e. $D_{fail} = 1$, see Figure 2.4b), Equation 2.1 reduces to the form in Equation 2.2, which is simply the evaluation of the CDF of the 'stress' distribution, '$F_L(x)$':

$$p_f = P[D_T \geq D_{fail}] = 1 - \int_{-\infty}^{D_{fail}} f_L(x)dx = 1 - F_L(D_{fail}) \tag{2.2}$$

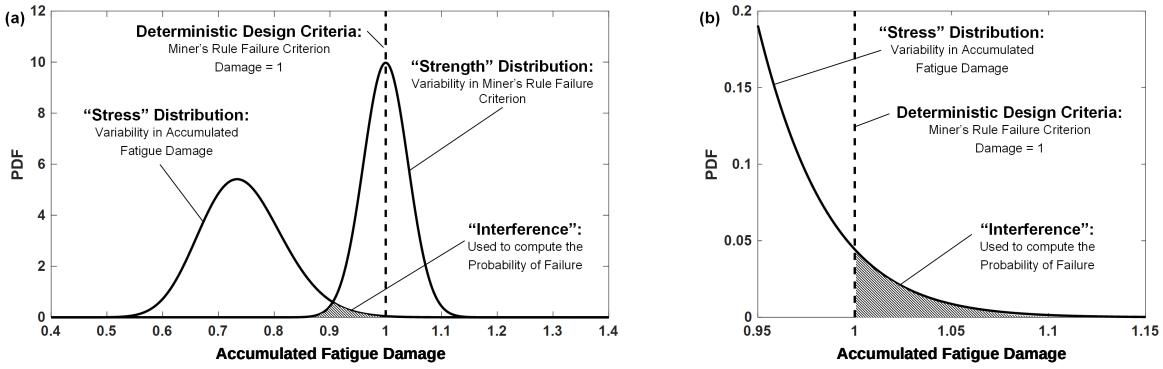

FIGURE 2.4. Application of the SSI approach to safe-life fatigue analysis for: (a) a variable failure criterion and (b) a deterministic failure criterion.

The SSI approach has been widely applied to safe-life fatigue analysis based on Miner's rule across the last three decades. Initially applied to offshore components by Wirsching in the 1980s [83, 84], the SSI method was also utilised for the probabilistic S-N analysis of automotive components in the 1990s [85–87]. The SSI method has also been applied to safe-life fatigue analysis by Zhao [88] and Zhao et al [89].

The SSI method has also seen extensive utilisation in recent years, within the work of Beretta et al and Zhu et al for turbine components which are assessed using a safe-life fatigue analysis process. Within the approaches proposed by Berreta et al [90–92] and Zhu et al [93–99], it

is assumed that the accumulated damage D_T distribution is represented by the Log-Normal distribution type, with a deterministic D_{fail} failure criterion [91, 93]. The SSI approach has also been applied to the probabilistic fatigue analysis of railway components [100].

Whilst the SSI approach is based directly on the 'load' and 'capacity' definition of reliability, along with only requiring a limited statistical background to understand its simple and intuitive basis [29, 44, 101], the disadvantage of the SSI method is that it requires the definition of the probability distribution types and parameters for the 'stress' and 'strength' distributions [57]. In many applications of the SSI approach to probabilistic safe-life fatigue analysis, the probability distributions assumed (typically Normal or Log-Normal) for the 'stress' and 'strength' distribution are selected with limited justification [87, 91, 93]. In some instances, the assumption of a Log-Normal 'stress' distribution has been utilised to simplify the calculation processes within the SSI approach and even the most recent application of the SSI approach to safe-life fatigue analysis by Zhou et al has required an assumed 'stress' probability distribution type [102].

Therefore, previous applications of the SSI approach to safe-life fatigue analysis have required the probability distribution type for the accumulated damage D_T 'stress' distribution to be defined *a-priori*, before conducting the probabilistic fatigue analysis. Due to the complexity of the current safe-life fatigue analysis process for aircraft landing gear [9], it is expected that the presence of complex loading spectra, rainflow cyclic counting and the specific S-N curve shapes could result in a complex probability distribution type for the D_T 'stress' distribution. Therefore, a probabilistic fatigue analysis approach that does not require the definition of the 'stress' probability distribution type *a-priori* is required, to ensure accurate p_f estimates from the SSI approach. This is highlighted by recent work performed by Zhang et al, which assumed a symmetrical Normal distribution for the 'stress' distribution *a-priori*, despite the actual variability in the 'stress' distribution demonstrating skew following the probabilistic fatigue analysis [103]. The assumption of the Normal distribution could lead to inaccuracy in the p_f estimates derived from the SSI approach due to the inaccurate characterisation of the skew in the 'stress' distribution.

An alternative SSI approach for safe-life fatigue analysis identified in the literature is based upon the concept of an Equivalent Fatigue Cycle (EFC). In the SSI approach for the fatigue analysis of rocket engine components proposed by Ferlin et al [104], the full variable-amplitude loading spectrum applied to the component is converted to an equivalent single constant-amplitude stress cycle (i.e. the EFC) using Miner's rule. The use of EFC therefore assumes that all fatigue damage is accumulated at a single location on the S-N curve. However, the variability observed in S-N datasets is not constant across the complete S-N curve (as the value N_f increases, the variability in N_f is expected to increase dramatically [6]). As a result, the assumption of an EFC does not enable the true nature of the variability within S-N datasets to be accurately represented within an SSI approach. EFCs were utilised in an SSI approach in the fatigue analysis of automotive components [85, 86], by Zhao et al [89] and by Bucas et al [105].

2.3.2 Limit State Approaches

A 'Limit State Function' (LSF) represents the design boundary where a structural component transitions from being safe (e.g. D_T<1) to an unsafe or failed state (e.g. $D_T \geq 1$). In terms of the 'load' random variable 'L' and the 'capacity' random variable 'C', the LSF 'G' takes the form [44]:

$$G = C - L \tag{2.3}$$

As L and C are random variables, G is also a random variable, and positive values of G represent that the structure is safe, whilst negative values of G represent that the component has failed [30]. Computing p_f estimates using an LSF differs from the SSI approach as it identifies the probability of the LSF being negative [44]:

$$p_f = P[G \leq 0] = P[C \leq L] \tag{2.4}$$

However, the definition of the LSF in Equation 2.3 only represents the case where L and C are defined by single random variables. In the case where multiple random variables define the LSF, Limit State Approximation (LSA) methods have been developed [44, 106].

LSA methods were developed during the 1960s in the form of the Cornell safety index, also known as the First Order Second Moment (FOSM) approach [30, 44, 106]. FOSM computes a reliability index 'β', which is based upon the mean 'μ_G' and standard deviation 'σ_G' of the LSF [44]:

$$\beta = \frac{\mu_G}{\sigma_G} \tag{2.5}$$

In the case where the LSF is defined by multiple random variables, a Taylor series expansion of the LSF is performed, evaluating each random variable at their mean values and the reliability index β is subsequently computed [44]. The p_f estimate can then be generated using Equation 2.6, which uses the CDF of the Standard Normal Distribution (SND) 'Φ_{SND}' [44].

$$p_f = P[G \leq 0] = \Phi_{SND}\Big(-\frac{\mu_G}{\sigma_G}\Big) = \Phi_{SND}(-\beta) = 1 - \Phi_{SND}(\beta) \tag{2.6}$$

FOSM has been extended to account for the observation that it is typically values at the extremes or 'tails' of the design parameter and L and C random variables that lead to failure conditions (e.g. the 'worst case' loading combined with the 'worst case' capacity), which is not accurately captured by using the FOSM Taylor series expansion about the mean random variable values [46]. First Order Reliability Methods (FORM) have been developed to account for distribution tail values by converting the LSF into a 'normalised' space, which produce SNDs that represent the design parameter random variables [30]. Figure 2.5 presents an LSF in the normalised space of two input design parameters [30]. As the LSF moves closer to the origin of the normalised space, the failure region grows larger. Therefore, the smallest distance between the LSF and the origin represents the combination of random variable values that maximises

the value of p_f [30]. This location is known as the Most Probable Point (MPP) and the distance between the origin and the MPP is the reliability index β. Optimisation methods are often required to identify the location of the MPP [46].

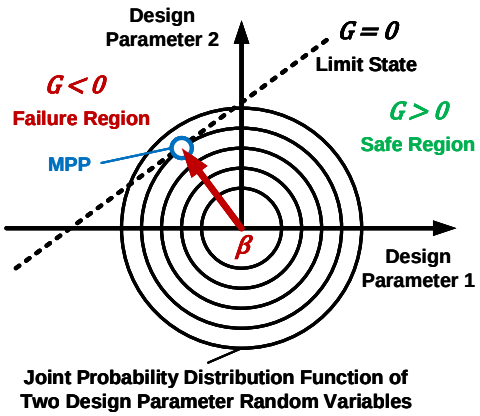

FIGURE 2.5. The FORM approach for computing the β reliability index, shown in the normalised space for two input design parameters.

As for the FOSM approach, Φ_{SND} is used to estimate the p_f based on the reliability index (known as the Hasofer-Lind reliability index) [30]. The FORM approach requires the assumption *a-priori* that the LSF is linear at the MPP [44]. The Second Order Reliability Method (SORM) has been developed to account for cases where the LSF is non-linear, by assuming the LSF is quadratic at the MPP [30]. The FORM/SORM approaches also require the LSF to be explicit (i.e. a closed-form equation between the random variables exists), which is not possible with numerical solution process such as FEA or fatigue cycle counting [107]. Advanced Mean Value (AMV) [108] and Fast Probability Integration (FPI) [109] have been proposed to apply FORM/SORM to analysis situations with implicit LSFs, by using evaluations of the implicit LSF (i.e. from the original deterministic analysis process) to identify the MPP [108, 109].

LSA methods have been widely applied to the probabilistic fatigue analysis of safe-life components. The FOSM approach for probabilistic fatigue analysis has been previously applied to offshore structures [110, 111] and steel structures [112, 113]. FORM/SORM approaches have also been widely applied to safe-life fatigue analysis, including rotorcraft components [114], nuclear piping and pressure vessels [115] and wind turbine components [116–119]. Reliability Index β based approaches also form the fatigue substantiation process detailed within the design codes/regulatory material of the offshore [111] and steel structures (Eurocode 3) [75, 77] sectors.

Despite LSA methods being widely accepted, to the extent of being included in industrial fatigue design codes [75, 77], there are a significant number of limitations of LSA methods that impact the accuracy of p_f estimations generated using such methods. Firstly, LSA approaches neglect the distributional information of the design parameter random variables, through the

assumption of Normal random variables [23]. This could result in reduced accuracy of p_f estimates when the random variables demonstrate skewed behaviour, which is expected within probabilistic fatigue analysis (e.g. the variability in S-N datasets is typically characterised using skewed Log-Normal distributions [6] and loads within landing gear design typically follow a highly-skewed distribution [12, 14]). Whilst Rackwitz-Fiessler methods have been proposed to transform skewed distributions to Normal distributions [30], this still only provides an approximation of the distribution type for the design parameter random variables. In addition, LSA methods require an *a-priori* assumption of the LSF, which cannot be made in new analysis cases, especially if an implicit LSF exists as a result of numerical analysis methods (e.g. FEA). As for SSI, a probabilistic analysis approach is required that does not make *a-priori* assumptions of the existing analysis process, to support the generation of accurate p_f estimates. It has also been suggested in the literature that the reliance of LSA methods on the SND CDF to estimate p_f values from a reliability index β can result in inaccurate p_f estimates when the p_f is less than 1×10^{-5} [45].

The implementation of LSA methods also highlights some further limitations of the approach. LSA methods often require the assumption of an EFC as for the SSI approach [119], therefore failing to accurately account for variability observed in S-N datasets. Likewise, the introduction of the normalised space and MPP in FORM/SORM is a statistically abstract concept and not easily linked back to the definition of structural reliability in the form of 'load' and 'capacity'. This is further complicated by the requirement of additional methods (AMV, FPI) to account for implicit LSFs therefore reducing the suitability of applying LSA methods by engineers that have a limited statistical background [23].

2.3.3 Monte Carlo Simulation

Monte Carlo Simulation (MCS) is a probabilistic approach based upon repeated evaluations of the existing analysis process used in the deterministic approach [57]. It is important to distinguish that an MCS does not perform repetitions of the deterministic design approach (i.e. including design parameter conservatism and safety factors), but rather, repeatedly evaluates the models and performance functions within the deterministic analysis approach, each time with randomly sampled values for the input design parameters. Within an MCS approach to probabilistic fatigue analysis, the variability in the input design parameters is represented using probability distributions [57]. An MCS approach then randomly samples values from each of the input design parameter probability distributions and conducts the existing analysis process to produce a corresponding output value [57]. This process is repeated for typically thousands or millions of iterations, with new input design parameter samples being generated and new output values being calculated for each iteration [23]. Over a sufficient number of iterations, the variability present in the input design parameters will be propagated through to the output value [57]. In the context of safe-life fatigue analysis, the input design parameters concern the fatigue design

parameters (e.g. component dimensions, material properties, loading spectrum, etc.) and the output value is the accumulated damage from Miner's rule D_T.

Estimates for the value of p_f from an MCS are computed by identifying the number of MCS iterations 'N_{fail}' that result in a 'failure' condition (e.g. $D_T \geq D_{fail}$) out of the total number of MCS iterations 'N_{MCS}'. The $P_{f_{MCS}}$ estimate can then be computed using Equation 2.7 [44]:

$$P_{f_{MCS}} = \lim_{N_{MCS} \to \infty} \frac{N_{fail}}{N_{MCS}} \tag{2.7}$$

Many examples of the application of MCS approaches to safe-life fatigue analysis are presented within the literature, including nuclear [120], automotive [121] and turbine components [57, 122]. An MCS approach to the probabilistic fatigue analysis of safe-life components has also been performed extensively for rotorcraft components throughout the last three decades [123–129]. The enduring and wide-spread use of MCS approaches to the probabilistic fatigue analysis of safe-life components is typically as a result of the conceptual simplicity of the approach, as MCS approaches simply 'wrap-around' and perform evaluations of the existing analysis process [61], rather than relying on complex statistical methods, as is the case with LSAs. In addition, the 'wrap-around' nature of MCS approaches means that the existing deterministic analysis process can be used 'as-is', without requiring any *a-priori* assumptions or simplifications regarding the analysis process or the variability within the input design parameters [23]. The combination of retaining the full complexity of the original analysis process with a simple to understand and implement probabilistic approach, results in MCS providing an attractive choice for engineers wishing to perform probabilistic fatigue analysis [23, 45].

Concerning safe-life components in the aerospace sector, Ocampo et al have performed extensive work concerning the definition of an MCS-based framework for the probabilistic fatigue analysis of safe-life light aircraft components [39, 130]. Safe-life components for light aircraft have a similar S-N fatigue analysis process to aircraft landing gear, based upon load-time histories, cycle counting, the use of P-S-N curves and the application of Miner's rule [39, 72]. In order to enhance the work performed by Ocampo et al, further development of MCS-based approaches to the probabilistic fatigue analysis of safe-life components in the aerospace sector would require the inclusion of the FEA models used to perform the loads and stress analysis for landing gear components.

The primary limitation of MCS-based probabilistic fatigue analysis approaches is the computational expense required to compute the p_f estimate using Equation 2.7. For convergence to be achieved within an MCS approach, typically 10^6 MCS iterations must be performed, with typical guidance requiring 10^{k+1} MCS iterations for a target p_f of 10^{-k} [114]. For safe-life fatigue analysis, based on FEA load and stress analysis and rainflow cycle counting of load time histories, the required number of MCS iterations could result in a prohibitive computational expense due to the large Central Processing Unit (CPU) run-time required [57].

Targeted Sampling

In order to reduce the computational expense of performing MCS-based probabilistic fatigue analysis, a number of sampling methods have been proposed that 'target' the generation of random samples to specific areas of the input design parameter probability distributions. The targeting of samples can result in a p_f estimate from MCS converging with a fewer number of iterations compared to a 'pure' MCS approach. Firstly, Latin Hypercube Sampling is a stratified sampling approach, which divides each input probability distribution into a series of bins which have an equal probability of being sampled from [131]. LHS ensures that each bin is sampled from once, whilst MCS can result in multiple samples in some bins and no samples in other bins, potentially increasing the number of MCS iterations for convergence compared to LHS [131]. LHS has been used in the probabilistic fatigue analysis of pressure vessels by Halfpenny et al [61].

Importance Sampling (IS) has also been proposed as a means to reduce the computational expense of MCS-based probabilistic fatigue analysis. IS uses sampling distributions to target the MCS random samples around the MPP, which would be identified by using an LSA method, theoretically reducing the number of MCS iterations required for the convergence of the p_f value [30]. Echard et al [57, 132], Zhao et al [114] and Frewen et al [133] have demonstrated the application of IS to the safe-life fatigue analysis of aerospace components. However, IS approaches require additional statistical concepts to be understood and implemented within the probabilistic approach. Assumptions about the existing analysis process may also be required, such as for the IS approach proposed by Echard et al [57], which is based upon the EFC assumption. Additional statistical complexity and the need to modify the existing fatigue analysis process reduces the potential utility of such approaches for engineers with a limited statistical background [23]. In addition, IS results in the MCS iterations being focused around the MPP, which may be falsely identified using an LSA approach, resulting in inaccurate p_f estimates [30]. In a similar fashion, IS prevents input design parameter variability away from the MPP to be evaluated, potentially reducing the utility of results from a probabilistic approach for assessing design performance at maximum and minimum values of design parameters [30].

Utilisation of Surrogate Modelling

An alternative approach to implementing novel sampling methods within an MCS-based probabilistic fatigue analysis approach is the utilisation of surrogate modelling to reduce the computational expense of MCS approaches. Surrogate models (also known as meta-models or emulators) can be used to replace the computationally intensive elements of the safe-life fatigue analysis process, such as FEA models for loads and stress analysis. The purpose of surrogate modelling methods is to replace the computationally expensive element (known as a 'model') with an alternative surrogate model that requires less computational resource to evaluate, whilst still accurately representing the relationship between the input and output values of the original

model [57]. Surrogate modelling methods require 'training' data, which is used to construct the surrogate model and 'validation' data which is used to test the accuracy of the surrogate model output when provided with new and 'unseen' input values [134]. Training and validation data is produced by performing evaluations of the original model (e.g. the original component FEA stress analysis) [134].

There are a wide range of potential surrogate modelling methods reported in the literature, from simple 'curve-fitting' response surfaces [46], to non-parametric Gaussian Process Regression and machine learning-based Artificial Neural Networks [135]. Response surfaces have been used to replace FEA models in the safe-life fatigue analysis of automotive components [136] and Echard et al, Huchet et al and Teixeira et al have all presented the use of Gaussian Process Regression within probabilistic fatigue analysis approaches [57, 137, 138]. From the literature it is evident that when compared to novel sampling methods (e.g. LHS, IS, etc.), there has been a more limited application of surrogate modelling methods to fatigue design and are yet to be widely exploited [138, 139]. However, as surrogate modelling methods could be used to accurately represent computationally expensive elements of the safe-life fatigue analysis process, they offer a route to performing probabilistic fatigue analysis which does not require any simplification or *a-priori* assumptions of the original analysis process. As a result, surrogate modelling should be considered as a route to implementing MCS-based probabilistic fatigue analysis methods.

High Performance Computing

The final approach available to reduce the computational expense of MCS-based probabilistic fatigue analysis is the employment of High Performance Computing (HPC) methods. HPC in the context of this thesis concerns the implementation of parallel processing methods, whereby the probabilistic fatigue analysis is distributed over multiple CPU processing cores [140]. Due to the iterative nature of MCS, individual MCS iterations can be performed on single CPU cores [140]. For example, a 4-core processor could perform four MCS iterations in parallel, potentially reducing the CPU run-time of MCS-based probabilistic fatigue analysis. The utilisation of parallel processing is now possible on standard desktop computers and Ocampo et al have previously demonstrated the successful use of parallel processing during the MCS-based probabilistic fatigue analysis of safe-life components [140].

2.3.4 Hybrid Approaches

The final probabilistic fatigue analysis method identified within the literature was a hybrid MCS-SSI approach. Within such an approach, an MCS is used to generate output values, which can then be statistically characterised to provide the 'stress' (or load) distribution within an SSI approach [57]. The p_f estimate is then generated in the same manner as for a standard SSI approach [57].

Zhu et al previously demonstrated an MCS-SSI hybrid approach within the probabilistic fatigue analysis of safe-life turbine components [94]. However, the utilisation of MCS-SSI was to demonstrate that the 'stress' distribution within the probabilistic fatigue analysis conformed to the *a-priori* assumption that the 'stress' distribution was represented by a Log-Normal distribution [94]. It is proposed that an MCS-SSI approach could be used to generate output values for the accumulated damage D_T using an MCS, and then statistical characterisation methods would be employed to identify the 'stress' distribution type, rather than assuming a distribution type *a-priori*. It is expected that convergence of p_f values generated using an MCS-SSI approach will occur significantly faster than a 'pure' MCS approach and this will be explored within this thesis.

Echard et al highlighted challenges concerning the number of MCS iterations used within an MCS-SSI hybrid approach [57]. Echard et al state that typically only a limited (e.g. hundreds) of MCS iterations are available due to the computational expense of each MCS iteration [57]. This is also highlighted by the MCS-based probabilistic fatigue analysis of turbine components by Zhu et al and Narayanan et al, where limited ($N_{MCS} < 5,000$) MCS iterations were performed [94, 122]. However, within these previous studies, surrogate modelling methods were not used to replace computationally expensive elements of the fatigue analysis process (e.g. FEA stress analysis). As a result, it is proposed that if surrogate modelling methods were incorporated into the MCS-SSI approach, the number of MCS iterations could be increased, potentially resulting in more accurate p_f estimates, for a lower computational expense than a 'pure' MCS.

2.3.5 Guidance for Probabilistic Analysis Method Selection

As demonstrated within the review of the literature, there is a limited consensus regarding which probabilistic fatigue analysis methods are most appropriate for safe-life components, as SSI, LSA and MCS-based approaches have all been used successfully across many different applications. The literature review has also highlighted that all of the probabilistic methods have been used consistently across the previous three decades, therefore demonstrating that in the field of probabilistic fatigue analysis that the 'state-of-the-art' is also the current art.

Therefore, as the current literature does not provide a clear indication of the method to be employed within a probabilistic fatigue methodology for safe-life components, other considerations must be accounted for. Summarising the extensive work performed by Goh et al [23], the selection of a probabilistic analysis method is a complex interaction between:

- **Intended application:** *How accurate, fast and robust must the probabilistic analysis method be?*

- **The characteristics of the existing analysis process:** *Is the existing process highly dimensional, highly non-linear and does it contain any computationally expensive models or numerical solution processes?*

- **The characteristics of the input probability distributions:** *Are datasets characterised by Normal or skewed distributions? Do correlations exist between design parameters?*
- **The strengths and limitations of each method**

Goh et al provide a series of 'primers' to further support probabilistic method selection based on the considerations above [23]. Level I methods concern the deterministic analysis method with safety factors, Level II methods are approximation methods such as LSAs, and Level III are 'exact' methods based on MCS approaches [23]. Goh et al suggest that Level III methods should be utilised when implementing a probabilistic method for performing structural reliability assessments [23], which includes a probabilistic fatigue methodology.

2.4 Summary

Currently within fatigue design, variability in design parameters is accounted for within deterministic fatigue analysis using conservatism and safety factors. However, such an approach results in the inability to quantify the conservatism 'designed-in' to the component, potentially resulting in economic consequences from over-design or safety implications from un-conservative design. Due to the existing use of conservatism to account for variability in safe-life fatigue analysis, it can be concluded that an alternative design and analysis approach is required that satisfies each of the following criteria:

- An approach that can quantify the fatigue reliability of a component, such that the level of safety factored into the component safe-life is quantifiable.
- An approach that directly represents the variability present within fatigue design parameters.
- An approach that is insensitive to the fatigue design application or engineering sector, such that a harmonised approach to accounting for variability in fatigue design and analysis can be developed.
- An approach that is insensitive to the specific safe-life fatigue analysis methods currently utilised, such that future improvements in structural analysis methods can be incorporated in the fatigue methodology.

Probabilistic design approaches enable the component reliability to be quantified, using probabilistic analysis methods such as SSI, LSAs or MCS in order to overcome the current limitations of the deterministic safe-life fatigue analysis approach based on conservatism and safety factors. Across the literature there is little consensus and consistency regarding which probabilistic analysis method(s) should be applied to estimate p_f and R values for safe-life components. Therefore, based upon the method classifications provided by Goh et al [23], the probabilistic analysis

method type can be down-selected based upon the characteristics of the existing deterministic analysis process. As it is expected that the input design parameter probability distribution types for landing gear fatigue analysis will demonstrate non-Normal skew characteristics (e.g. the Log-Normal distribution of N_f in S-N datasets [6]), the primers produced by Goh et al suggest that Level II methods are not suitable for the probabilistic fatigue analysis of safe-life landing gear components [23]. Likewise, due to the implicit nature of the safe-life fatigue analysis process of landing gear components (resulting from FEA load and stress analysis), the linearity of the LSF cannot be characterised *a-priori*, further supporting the rejection of Level II methods.

The rejection of Level II methods ultimately leaves Level III, or MCS-based approaches, as the sole type of probabilistic analysis method that could be applied to the safe-life fatigue analysis process. This is further supported by Goh et al stating that Level III methods should be used for structural reliability assessments [23]. The selection of Level III methods therefore contributes to overcoming the blocker relating to the *a-priori* simplifications and assumptions of the existing deterministic analysis process often required when implementing probabilistic design approaches, as MCS approaches evaluate the existing analysis process 'as-is' due to their wrap-around nature.

The down-selection to Level III methods still leaves a large number of MCS-based probabilistic analysis methods to select from. The final down-selection of the probabilistic analysis method for safe-life landing gear components can therefore be based on the relevant 'blockers' that inhibit the implementation of probabilistic methods initially presented in Chapter 1:

- **Computational Expense:** 'Pure' MCS requires a potentially prohibitive computational expense and therefore, an MCS-based approach must either use LHS, IS, surrogate modelling or an MCS-SSI hybrid approach.

- **Required Assumptions:** As it is required to retain the existing safe-life fatigue analysis process 'as-is' to ensure accurate p_f estimates and reduce scepticism of probabilistic results, MCS-based approaches which require assumptions to be made about the original analysis process should not be used. Investigations into the failure of adoption of probabilistic methods have highlighted that retaining the existing deterministic analysis process is vital for the successful implementation of probabilistic design approaches [54]. As a result, MCS using IS should not be employed as it is based upon LSA/MPP approaches and may require an EFC assumption, which will not accurately represent the variability present in S-N datasets.

- **Accuracy of Data Characterisation:** All MCS-based approaches enable any probability distribution type to be used to characterise the variability in design parameters, and therefore, all MCS-based approaches can successfully challenge this blocker. However, IS 'targets' the sampling at specific locations of the probability distribution, potentially reducing the accuracy of the representation of the input design parameter variability in the probabilistic fatigue analysis.

- **Required Knowledge:** MCS approaches are intuitive to understand as they are simply based on repeated evaluations of the existing models and performance function employed within the deterministic analysis process [45]. However, the employment of surrogate modelling methods would require additional methods to be understood and the utilisation of IS would require the understanding of additional statistical concepts.

Therefore, when considering the 'blockers' to the widespread implementation of probabilistic methods above, it can be observed that an MCS approach using IS fails to successfully challenge the majority of the blockers. In addition, a pure MCS cannot be used due to computational expense and therefore, either an LHS, MCS supported by surrogate modelling or MCS-SSI approach is required.

It is proposed that an MCS-SSI approach, supported with surrogate modelling of the FEA models within the safe-life fatigue analysis process could provide a computationally efficient approach. An MCS-SSI hybrid approach will retain the full complexity of the original analysis process, through accurate statistical characterisation of design parameters and the SSI 'stress' distribution, as well as constructing accurate surrogate models. The MCS-SSI approach also has the benefit of combining the two most intuitive probabilistic methods, with the simplicity of the MCS approach coupled with the simple nature of the SSI approach, which can be directly related back to the definition of structural reliability. Figure 2.6 shows a high-level flowchart of the proposed MCS-SSI approach developed from these arguments.

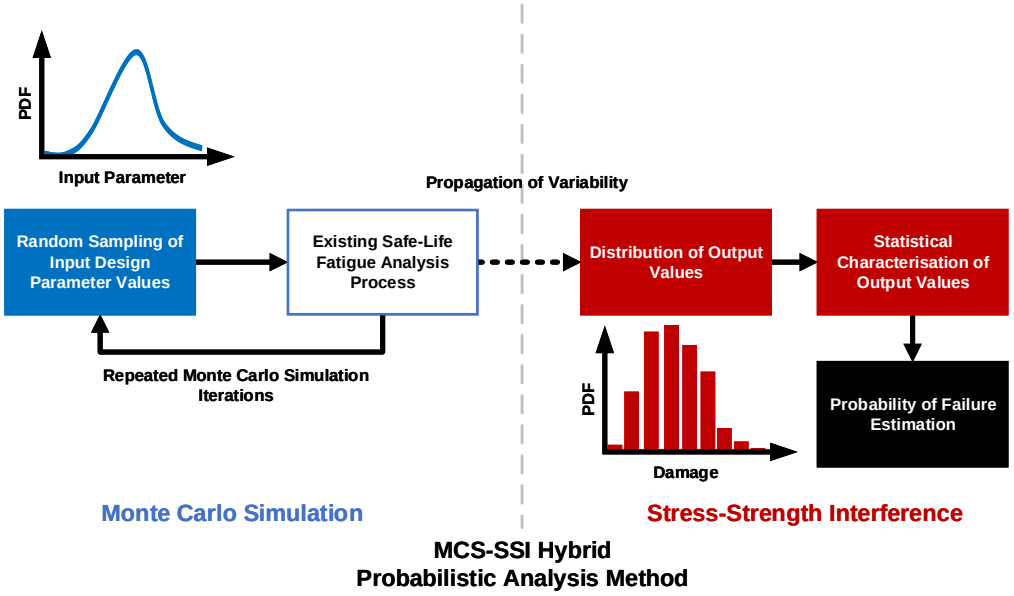

FIGURE 2.6. A visualisation of the MCS-SSI hybrid probabilistic analysis approach.

A hybrid MCS-SSI approach enables a challenging of the current blockers to implementing probabilistic fatigue design approaches, including: reducing *computational expense* (through the use of surrogate models and SSI), not requiring *a-priori assumptions and simplifications of the existing fatigue analysis process* and increasing the *accuracy of data characterisation* within the methodology (both through the use of MCS). In addition, as MCS and SSI are conceptually simple compared to LSA approaches, the blocker of *required knowledge* is reduced in impact through the careful selection of the probabilistic analysis method for use within the probabilistic fatigue methodology. The matrix in Table 2.2 summarises how the selection of the MCS-SSI probabilistic analysis method can help overcome the blockers to a probabilistic fatigue design approach.

TABLE 2.2. The blockers to probabilistic design approaches overcome using the MCS-SSI hybrid probabilistic analysis approach.

Blocker	Blockers overcome due to use of MCS-SSI
Computational Expense	Use of MCS to generate 'stress' distribution of SSI approach (rather than to directly calculate p_f) reduces the computational expense compared to a 'pure' MCS.
Required Assumptions of Existing Process	Use of MCS enables the full complexity of the existing analysis process to be retained due to the 'wrap-around' nature of MCS.
Availability of Data	N/A
Accuracy of Data Characterisation	Use of MCS enables any probability distribution type to be incorporated into the probabilistic fatigue methodology to represent the variability in design parameters.
Required Knowledge	MCS and SSI are conceptually simple probabilistic analysis methods when compared to LSAs. This is beneficial for engineers with a limited background in statistical methods.

The quote from Siddall [28] regarding probabilistic analysis method selection: "*choice of the best method for a given analysis is rather difficult*" may at first be valid when confronted by the wide range of candidate probabilistic analysis methods and the lack of guidance and consistency regarding their application within the literature. However, this chapter has demonstrated that through consideration of the intended application, individual strengths and limitations of each method and the current blockers to a probabilistic design approach, the careful selection of a probabilistic analysis method can be achieved. In addition, this chapter has demonstrated how careful selection of the probabilistic analysis method is part of the research effort in overcoming the blockers to probabilistic approaches. Over the following chapters, the MCS-SSI hybrid probabilistic analysis method will be integrated into a probabilistic analysis framework and demonstrated on a series of landing gear safe-life component case studies.

CHAPTER 3

PROPOSED PROBABILISTIC ANALYSIS FRAMEWORK

Whilst selecting a probabilistic analysis method may appear to provide the means to execute a probabilistic approach to fatigue design, a probabilistic analysis framework is still required to integrate the probabilistic analysis method with the existing analysis process and the other methods required to support a probabilistic approach. This chapter defines a probabilistic analysis framework that overcomes the blockers to a probabilistic design approach. Combining the probabilistic analysis method and the probabilistic analysis framework results in the complete definition of the probabilistic fatigue methodology. The remaining chapters within this thesis aim to populate the probabilistic fatigue analysis framework with the methods and processes required to successfully implement a probabilistic fatigue methodology for safe-life components.

3.1 The Need for a Framework

The previous chapter identified that an MCS-SSI hybrid probabilistic analysis approach could help overcome the blockers to a probabilistic design approach. In addition to the selection of the MCS-SSI probabilistic analysis method, a probabilistic analysis framework is required to integrate the probabilistic analysis method with the existing deterministic safe-life fatigue analysis process and other methods required to implement a probabilistic approach to design. Typical guidance on integrating probabilistic approaches into design processes states that the probabilistic approach must be based upon the existing design and analysis process [46, 54]. In addition, Safie and Fox suggest that a systematic process for conducting probabilistic fatigue analysis could support the wider utilisation of probabilistic approaches in fatigue design, by providing guidelines for engineers to follow when implementing probabilistic approaches [47]. Concerning general engineering practice, during the development of novel approaches to design or analysis, systematic approaches based upon frameworks are recommended to support the understanding of new approaches within existing design and analysis applications [54, 141].

The definition of a probabilistic analysis framework also retains the general nature of the proposed probabilistic fatigue methodology, as frameworks prevent the utilisation of probabilistic analysis methods becoming focused and tailored directly to the specific case study that they are being applied to. The consideration of 'bespoke' probabilistic approaches solely in the limited context of specific case studies is a common criticism of the demonstration of probabilistic analysis methods in the literature [46, 51, 54]. Analysis frameworks on the other hand, enable probabilistic methodologies to retain their flexibility when being applied to future design tasks, increasing their wider utility within engineering design [45].

Probabilistic analysis frameworks have been described previously within the literature in both flowchart [46] and proforma formats [23], and this chapter aims to extend this previous work by incorporating recent developments within the probabilistic analysis fields, such as big-data sources and surrogate modelling, with a view to overcoming the blockers to probabilistic design approaches. This chapter will also demonstrate how the various methods of a probabilistic fatigue methodology interact with one another by providing a high-level representation of the framework. A detailed-level analysis flow and architecture is then presented, which is used to demonstrate the individual steps required within the probabilistic fatigue methodology.

3.2 Additional Methods to Implement Probabilistic Fatigue Methodology

In order to define a probabilistic fatigue methodology, the other methods and tools required to implement a probabilistic fatigue analysis method must be reviewed. This collection of methods and tools concerns statistical characterisation of design parameters, surrogate modelling of FEA models within the fatigue analysis process and the methods used to provide p_f and R estimates.

3.2.1 Statistical Characterisation

The first group of additional methods required to implement a probabilistic approach are statistical characterisation methods. These methods are used to 'fit' and 'select' the probability distribution types to be used to represent the variability in design parameters. 'Fitting' is the process of estimating the distribution parameters for the PDF of a candidate probability distribution and can be performed using graphical probability plotting or optimisation-based maximum likelihood estimation methods [33]. 'Selection' of the final distribution type is then performed using goodness-of-fit tests, such as Chi-Squared and Anderson-Darling, in order to accept or reject a candidate distribution [33]. As the accuracy of p_f estimates generated by a probabilistic analysis method is directly dependent on the accuracy of the statistical characterisation of the design parameters, it is recommended a robust and systematic approach to statistical characterisation is used. This goal can be achieved using multiple fitting and goodness-of-fit tests for validation, to ensure the correct selection of the probability distribution type, resulting in the accurate characterisation of design parameter variability.

A systematic approach to statistical characterisation can also assist engineers in implementing probabilistic design approaches, through increasing engineers' confidence in implementing statistical characterisation methods in a 'step-by-step' approach [23, 28], to assist in 'down-selecting' the probability distribution type for different design parameters. Due to the need for a systematic statistical characterisation process, the development and demonstration of such a process will be presented in the context of S-N datasets in Chapter 4.

3.2.2 Surrogate Modelling

Within the existing safe-life fatigue analysis process, FEA models are employed to compute internal loads and stresses within components. As fatigue analysis typically requires loads and stress analysis to be performed for many individual cyclic load levels, the computational expense of running a full FEA model within a probabilistic fatigue approach can be significant, if not prohibitive. This is especially the case for an MCS-based approach, which requires repeated evaluations of the existing deterministic fatigue analysis process to generate p_f and R estimates.

Surrogate modelling methods, as introduced briefly in Section 2.3.3, can be used to accurately represent the input-output relationship of FEA models within the safe-life fatigue analysis process, with a view to reducing the computational expense of an MCS-based probabilistic analysis method.

The simplest surrogate modelling method is known as the Response Surface Method (RSM). RSM is a polynomial surface across N_I dimensions, where N_I is the number of input parameters to the model [46]. The polynomial equation (typically either quadratic or cubic) defining the RSM is fitted to training data (i.e. evaluations of the FEA model) using least squares regression [46]. The advantage of RSM is that it is quick to train (typically < milliseconds) and intuitive to use

due to its similarity to 'curve-fitting' of experimental data [142]. The limitation of RSM however, is that it cannot be applied to models with significant non-linearity or high dimensionality [143].

To improve the ability of surrogate models to represent models with high dimensionality or high non-linearity, non-parametric regression methods have been developed which do not rely on assuming an existing polynomial surface shape. Non-parametric regression methods construct a surrogate model by combining a series of 'basis' functions with assigned weights to produce a smooth-fit to the training data [134]. Such methods include Radial Basis Functions (RBFs) [142] and Gaussian Process Regression (GPR) [134]. GPR and RBF typically require larger training datasets and longer training times (typically minutes).

The final class of surrogate modelling methods are machine-learning methods, such as Artificial Neural Networks (ANNs). ANNs replicate the behaviour of the human brain in order to 'learn' the relationship between training data input and output values [135]. The ANN architecture is made up of a series of layers of 'neurons' which are comprised of a transfer function (usually sigmoid) along with weights [135]. The ANN is trained using sophisticated optimisation processes that adjust the weights for each neuron in order to minimise the error between the training data output values and the output values predicted by the ANN [135]. ANN methods are suitable for high dimensional models, along with highly non-linear models [142]. The limitation of an ANN approach is the increased time and experience required to define the ANN architecture (e.g. number of neurons) and training time required to produce the neuron weights (typically hours) [142].

Whilst there are numerous reference texts providing detail on the advantages and disadvantages of the different surrogate modelling methods [142–144], there is yet to be a systematic process for selecting the surrogate modelling method for a novel application. The development of such a process will be explored in the context of the FEA models used to support the safe-life fatigue analysis of landing gear components in Chapter 6.

3.2.3 Sensitivity Analysis

Probabilistic design approaches can also include sensitivity analysis methods, which permit the identification of design drivers [131, 145–148]. Sensitivity analysis methods apportion the variability in the output of an analysis process (e.g. D_T accumulated damage) to the variability in specific input design parameters [131, 148]. This permits a 'ranking' of input design parameters with respect to their relative contribution to the analysis process output [147]. The results from sensitivity analysis can therefore be used to identify design drivers which have the greatest impact on the variability observed in accumulated fatigue damage D_T. Future work can then be focused at the design drivers to better characterise or control the variability present in the design drivers [148]. Through improved characterisation or control of design parameter variability, the conservatism currently required for specific design parameters within fatigue design and analysis

could be challenged, as the use of sensitivity analysis methods may highlight areas of the safe-life fatigue analysis process where existing safety factors are either under or over conservative [145].

The results from sensitivity analysis can also be fed-back into the probabilistic analysis method and surrogate modelling methods in a process known as parameter 'screening' [147]. Parameter screening identifies the input parameters that do not provide a significant contribution to the output variability and fixes such parameters to nominal deterministic values when conducting the probabilistic analysis and training of the surrogate model [147]. The use of parameter screening can reduce the amount of training data required for surrogate models and potentially increases the rate of convergence for a probabilistic analysis method [146, 147]. The combination of both of these factors could result in a reduction in the computational resource required to implement a probabilistic fatigue methodology.

Probabilistic Variance-Based Sensitivity Analysis (VBSA) methods have been developed in order to apportion the variance (a statistical measure of variability related to standard deviation) in the analysis process output to the variance in the probability distributions that characterise the variability in design parameters [131]. The finite difference variance equation approach provides a method based upon the derivative of the process output with respect to a change in each input parameter and the variance in each input parameter [29]. Sobol indices are an alternative measure of how the variance in the process output changes when each input parameter is fixed to a single value one-at-a-time [146, 149][1]. VBSA methods have been previously applied to the fatigue analysis of safe-life rotorcraft components [151] and safe-life light aircraft structures [145].

The limitation of VBSA methods is that as they only assess variance, VBSA methods may not produce accurate results when the probability distributions that characterise the variability in the input and output parameters are highly-skewed (i.e. non-Normal) [131]. This is of particular concern in fatigue analysis, where S-N datasets are typically characterised using Log-Normal and Weibull distributions [6] and loads data is often characterised using a highly skewed distribution [12, 14].

Global Sensitivity Analysis (GSA) methods focus on quantifying how the probability distribution shape of the process output varies as the input design parameters are fixed to a nominal deterministic value one-at-a-time, in a process known as 'omission' sensitivity [147, 148, 152, 153]. A greater 'change' in the output probability distribution shape infers that the fixed design parameter provides a greater contribution to variability in the process output [152, 153]. The use of GSA methods permits the sensitivity of highly-skewed output distributions to highly-skewed input distributions to be identified [131]. GSA methods are considered 'global' approaches as they explore the entire potential input space of design parameters [146].

[1]The author has previously applied Sobol indices to the safe-life fatigue analysis of landing gear components during an MEng project [150].

3.3 Probabilistic Analysis Framework

As this chapter has demonstrated, there are a wide range of additional methods required to implement a probabilistic fatigue methodology. Figure 3.1 shows a high-level probabilistic analysis framework that visualises the many interactions that exist between each of the required methods. Figure 3.1 also highlights how the required methods interact with the existing safe-life fatigue analysis process. Figure 3.1 also shows that specific elements of the framework can be decomposed into further required steps. These additional steps are detailed in their own flowcharts within relevent chapters of this thesis, as shown in Figure 3.1, such as the required statistical characterisation and surrogate model selection processes defined in Figures 4.1 and 6.18 respectively.

Figure 3.1 also shows how all of the methods required to implement the probabilistic fatigue methodology within the framework treat the existing safe-life fatigue analysis process as a 'black-box'. Therefore, the probabilistic framework is superimposed onto the existing analysis process by 'wrapping-around' the process, rather than intending to replace the existing deterministic analysis process. This complies with the guidance provided in the literature regarding the successful implementation of probabilistic approaches and the development of novel design approaches, specifically concerning the need to base the probabilistic approach on the existing deterministic analysis process [23, 45, 46, 54]. In addition, the framework shown in Figure 3.1 is general in nature and could be directly applied to other analysis methods within engineering design.

3.3.1 Computational Resource Considerations

Figure 3.1 also highlights that the probabilistic fatigue methodology must account for computational resource considerations. Firstly, the computational run-time of the methodology is directly proportional to the number of MCS iterations performed. Methods for defining the number of MCS iterations are typically based on achieving convergence of the MCS results, based upon pre-defined criteria as previously discussed in Section 2.3.3. However, the available computational resource is rarely available to achieve converged MCS results [57] and therefore, the number of MCS iterations is also often defined based on achieving an acceptable MCS error for the expected p_f of the component under analysis [114]. The approach for computing MCS is error is presented later in Section 3.5.1.1 and as the convergence of an MCS is application and case study specific, MCS iteration selection is more easily discussed in the context of specific components under analysis. Therefore, the selection of the number of MCS iterations for the probabilistic fatigue methodology is further addressed in Section 7.1.1.

A lesser-discussed computational challenge of MCS-based probabilistic analysis is the computational memory demand for handling the large data files associated with repeated MCS iterations, especially when large load-time histories are constructed within probabilistic fatigue analysis [140].

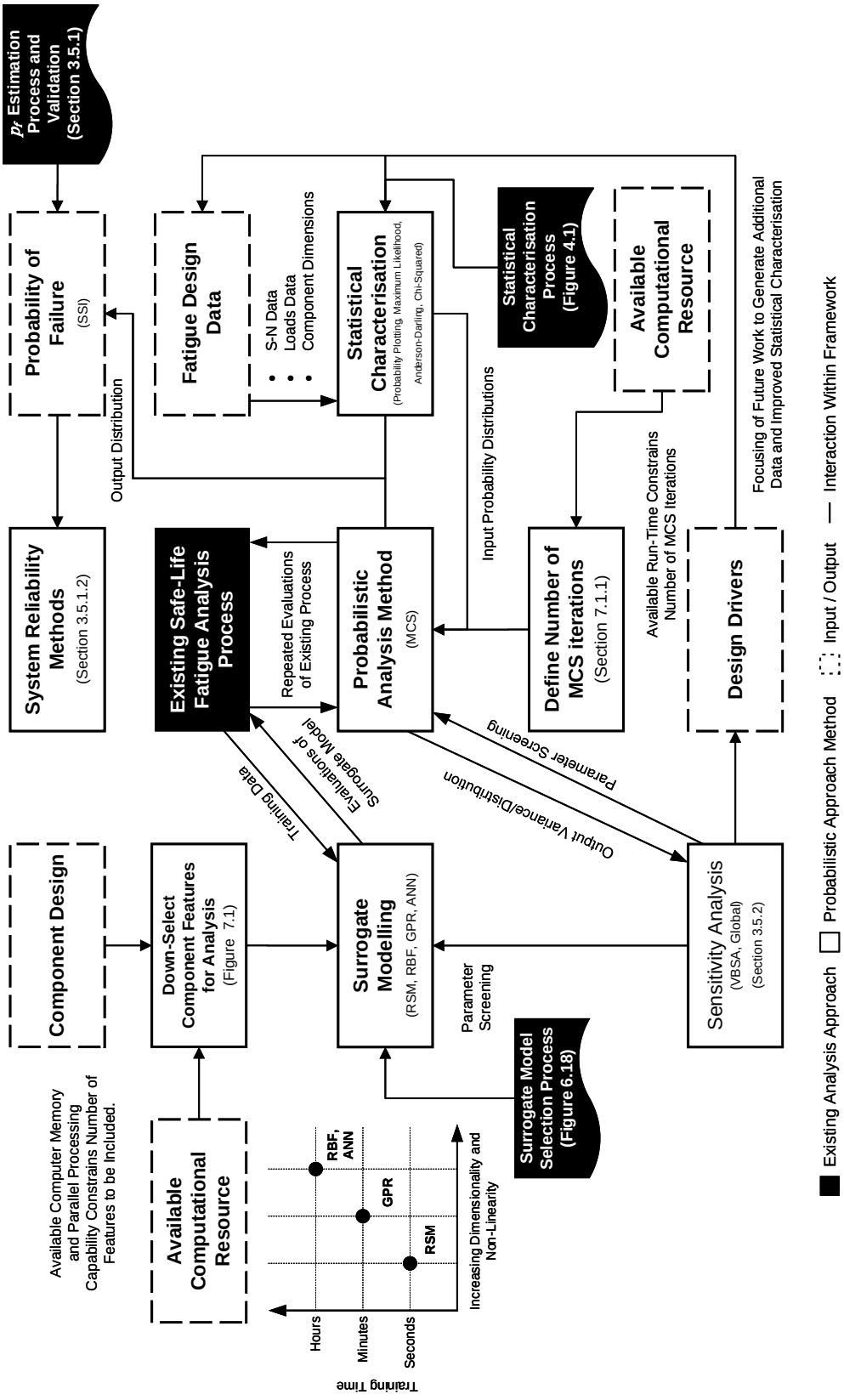

FIGURE 3.1. The proposed probabilistic analysis framework to implement the MCS-SSI probabilistic analysis method within the probabilistic fatigue methodology. The framework also highlights the interaction between the various methods required for a probabilistic methodology.

The constraint of available memory for MCS approaches is further compounded when parallel processing, as introduced in Section 2.3.3, is used to assess multiple engineering features of components within a probabilistic approach simultaneously. Such parallel processing can rapidly consume the available computational memory resource available, limiting the amount of parallelisation that can be performed, increasing the computational run-time of the methodology.

Consequently, Figure 3.1 demonstrates that when assessing a component using the probabilistic fatigue methodology, a process is required to identify and down-select the engineering features of the component to include in the probabilistic analysis. Rather than performing the probabilistic analysis at all locations across the component, the down-selection of features that are expected to show a quantifiable p_f to include within the probabilistic analysis will reduce the memory demand and corresponding run-time of the methodology.

A systematic process for down-selecting engineering features for inclusion in probabilistic analysis has been defined based upon identifying stress and fatigue 'hot-spots'. As such a process is more clearly demonstrated on a component case study, the full description of the down-selection process is presented in Section 7.1.2 and demonstrated within the case studies in Sections 7.2.3 and 8.1.4.

3.4 Overcoming Blockers to Probabilistic Design using a Probabilistic Analysis Framework

During the definition of the probabilistic analysis framework shown previously in Figure 3.1, it was observed that the utilisation of a probabilistic analysis framework could be used to overcome some of the blockers to implementing probabilistic design approaches. The probabilistic analysis framework in Figure 3.1 can be enhanced by introducing recent developments within the fields of probabilistic design and structural design in the form of big-data sources and by utilising the methods within the probabilistic analysis methods within other engineering design activities.

3.4.1 Big-Data Sources

One of the blockers identified within Chapter 1 was that the generation of the datasets required for the statistical characterisation of design parameters within a probabilistic design approach is either too costly or not currently possible [45]. Recent advances within the engineering sector regarding big-data are enabling the generation and capture of datasets that can support a probabilistic fatigue methodology. An example of a big-data source relevant to the safe-life fatigue analysis process is the online tracking of aircraft in-service using services such as FlightRadar24® [154], which can provide operational statistics to support studies into the variability in aircraft operations. Likewise, as 'real-time' data streaming of aircraft loads continues to mature [58], the incorporation of actual in-service aircraft loads into a probabilistic fatigue methodology becomes more of a possibility. These advances could improve the accuracy of the p_f estimates

from a probabilistic fatigue methodology through richer datasets that can be used to improve the statistical characterisation of design parameters. As a result, the exploitation of big-data sources in the context of probabilistic design approaches could help overcome the current blockers of limited availability of data, along with the accuracy of the statistical characterisation of design parameters. The use of big-data sources for probabilistic analysis methodologies will be explored in the context of landing gear loading spectra in Chapter 5.

3.4.2 Required Knowledge and Resources

Another blocker to the wide-scale implementation of probabilistic analysis methodologies and design approaches is the significant technical knowledge that is required to implement such approaches [23, 45, 46]. As highlighted over the previous chapters, there is a wide range of methods that are required to be understood and implemented. Naturally, this represents a high resource burden on engineers wishing to implement probabilistic design approaches and analysis methodologies.

The definition and use of analysis frameworks can support a reduction in the level of technical knowledge that engineers must consolidate to implement a probabilistic design approach and analysis methodology, through demonstrating clearly how each method required within the framework interacts with one another. In addition, the use of systematic processes for statistical characterisation, surrogate model generation and selection can also reduce the technical knowledge required, by guiding engineers step-by-step through the individual methods required for a probabilistic analysis methodology. The visual representation of a methodology using flowcharts also highlights the 'flow' of information throughout the methodology, simplifying the steps required to develop the methodology into a computational code.

Alternatively, the high resource burden required to understand and implement probabilistic analysis methodologies can be reduced through identifying other design tasks and activities that could benefit from the individual methods required within the probabilistic analysis framework.

Firstly, the ever-increasing use of 'big-data' within engineering design will require the robust, systematic and rapid statistical characterisation of datasets. Therefore, the statistical characterisation methods and processes implemented for the probabilistic fatigue methodology could also be used to characterise the datasets from the anticipated increase in the exploitation of big-data sources. One of the challenges of big-data sources is the sheer volume of data, which can be challenging to physically store and interpret [59, 60]. The use of statistical characterisation methods can reduce large batches of data into single statistical measures (e.g. probability distributions, pie charts, etc.), condensing the volume of the information and data to be stored from the big-data source.

The use of optimisation methods within design is widespread across the engineering field, including the aerospace sector [49]. As optimisation approaches (especially RBDO) often require repeated evaluations of computationally expensive FEA models, the surrogate modelling methods required within the probabilistic fatigue methodology could also be used to support optimisation-based design. For example, an FEA model of a component could be replaced with an RSM, such that the optimisation process is conducted using the surrogate model, reducing the computational expense. This reduction in computational expense could also permit a greater number of optimisation iterations to be performed. In addition, a working understanding of optimisation methods is required to successfully implement the maximum likelihood estimation statistical characterisation methods and the training methods required for surrogate models within the probabilistic fatigue analysis framework. Therefore, it can be seen that a probabilistic fatigue methodology and optimisation-based approach to design are closely linked and reliant on the methods used within each approach.

Finally, combining the need for rapid evaluations of computationally expensive models and the utilisation of big-data sources, is the recent advancement of 'digital twins' for the in-service monitoring of components [58]. Within a digital twin, a mathematical model of an in-service component is updated based upon in-service data in real-time (e.g. monitoring the fatigue damage accumulation in a component based on the actual in-service loads applied to the component) [58]. The surrogate modelling methods required for a probabilistic fatigue methodology could therefore also be employed within a digital twin approach, with the aim of reducing the computational expense of performing real-time assessment and monitoring of components in-service.

Figure 3.2 shows the interaction between the probabilistic fatigue analysis framework and the other aspects of engineering design that the methods within the framework can be utilised within (specific links to additional steps required within each block are shown previously in Figure 3.1). Figure 3.2 therefore demonstrates that there are significant opportunities for the technical knowledge and methods required for a probabilistic fatigue methodology to be utilised and exploited in other aspects of engineering design and component monitoring, increasing the useful return from the resources required to develop and implement a probabilistic fatigue methodology. As this effectively reduces the resource burden for implementing a probabilistic approach, the 'buy-in' from engineers and management that is vital for the successful adoption of probabilistic approaches [23, 45, 46, 54] could be increased as a result of the definition of the probabilistic analysis framework. The redeployment of surrogate modelling methods to other engineering activities is especially relevant to this thesis, as surrogate modelling methods represent a trade-off between additional required knowledge and the reduction in computational expense they provide within an MCS-SSI approach.

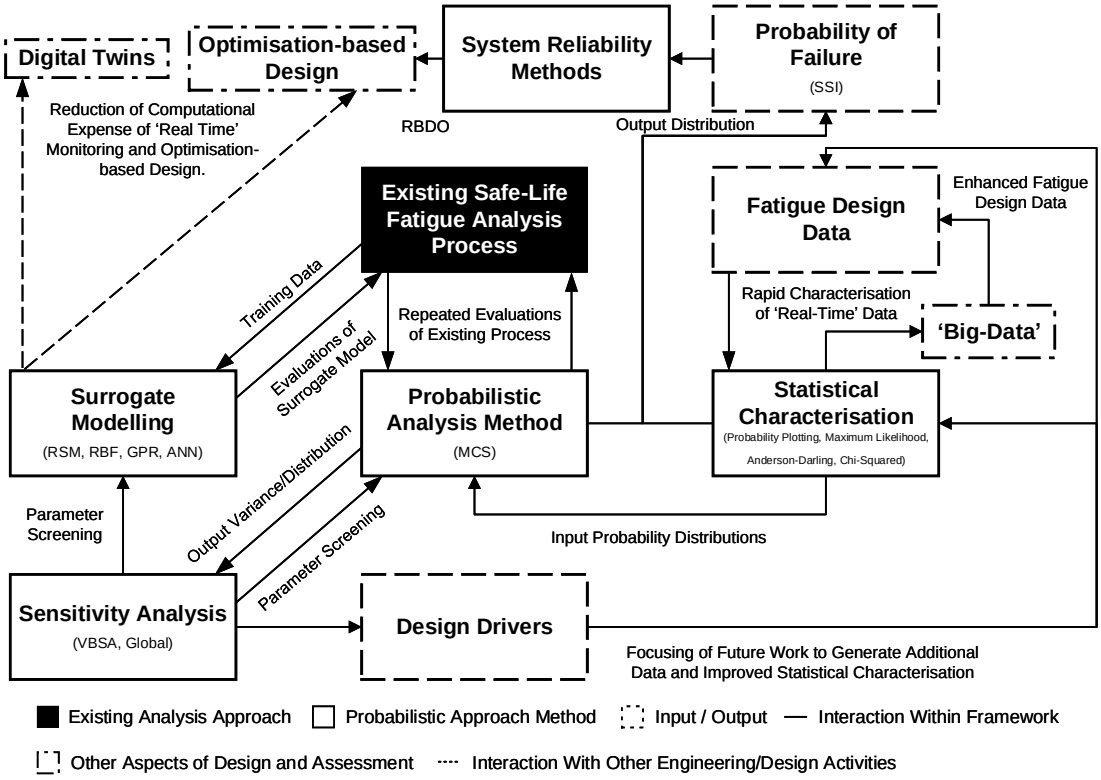

FIGURE 3.2. A demonstration of how the defined probabilistic analysis framework can help overcome the blockers to probabilistic approaches to fatigue design.

3.5 Probabilistic Fatigue Methodology Implementation

Whilst the probabilistic analysis framework provides the visualisation of how the different methods and processes within the probabilistic fatigue methodology interact, additional consideration must be made regarding the construction of the flow of the probabilistic fatigue analysis process, to support the implementation of the methodology in a computational code.

In order to implement the high-level probabilistic fatigue analysis framework shown previously in Figure 3.1, the probabilistic analysis 'flow' or 'architecture' was considered in greater detail, with the aim of producing a detailed-level framework for the probabilistic fatigue methodology. Figure 3.3 shows how the MCS-SSI hybrid probabilistic analysis approach can be decomposed into three stages: *random sampling, fatigue analysis* and *post processing*. Figure 3.3 demonstrates how the variability in the statistically characterised design parameters is converted to variability in the accumulated damage D_T. Figure 3.4 provides a detailed flowchart of the MCS-SSI probabilistic analysis architecture, which is also divided into the stages of *random sampling, fatigue*

analysis and *post processing*. The flowcharts in Figure 3.3 and Figure 3.4 assume that statistical characterisation of design parameters and the development FEA surrogate models has been performed. The computational code required to implement Figure 3.4 was developed within a MATLAB® environment.

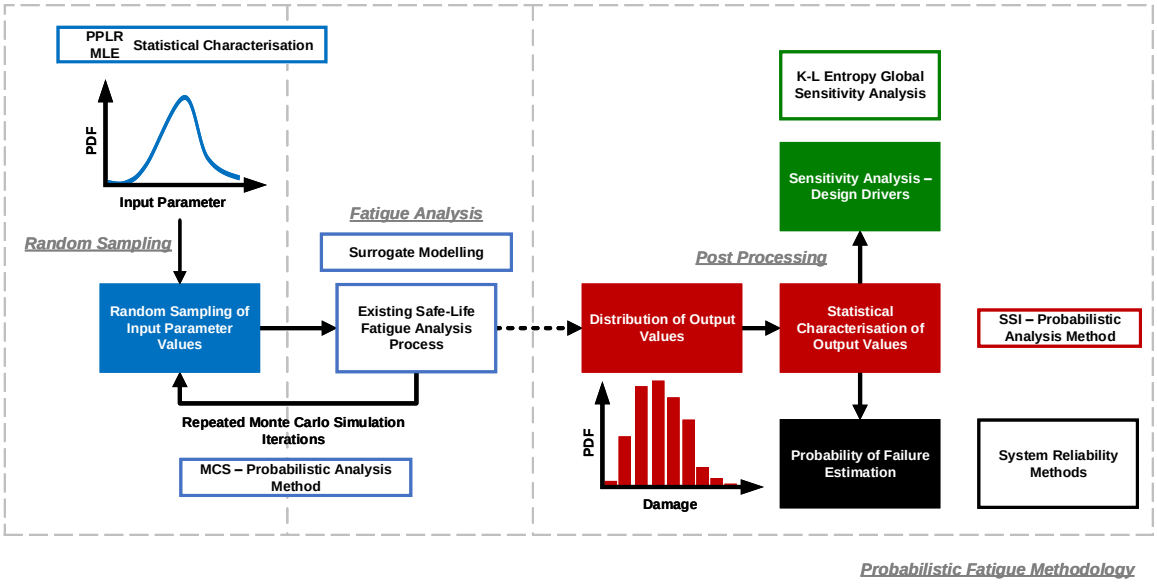

FIGURE 3.3. A high-level flowchart of the proposed probabilistic fatigue methodology, based upon the MCS-SSI hybrid probabilistic analysis method.

The first stage of the MCS-SSI probabilistic analysis approach randomly samples values from the probability distributions used to statistically characterise the variability in each of the input design parameters, including loading, cyclic material properties (i.e. the S-N curve), static material properties and component geometry. Random sampling is performed using an approach called Inverse Cumulative Density Function (ICDF) sampling. ICDF sampling randomly generates a uniformly-distributed random number between $[0, 1]$ and evaluates this number using the ICDF defined for each design parameter [61][2]. Additional sampling methods for generating the S-N curve and load-time history are presented in Chapters 4 and 5 respectively. For each iteration of the MCS, a new S-N curve and load-time history for the component is randomly generated as shown in Figure 3.4.

[2]The ICDF is directly sourced from the CDF used to statistically characterise the variability in the design parameter.

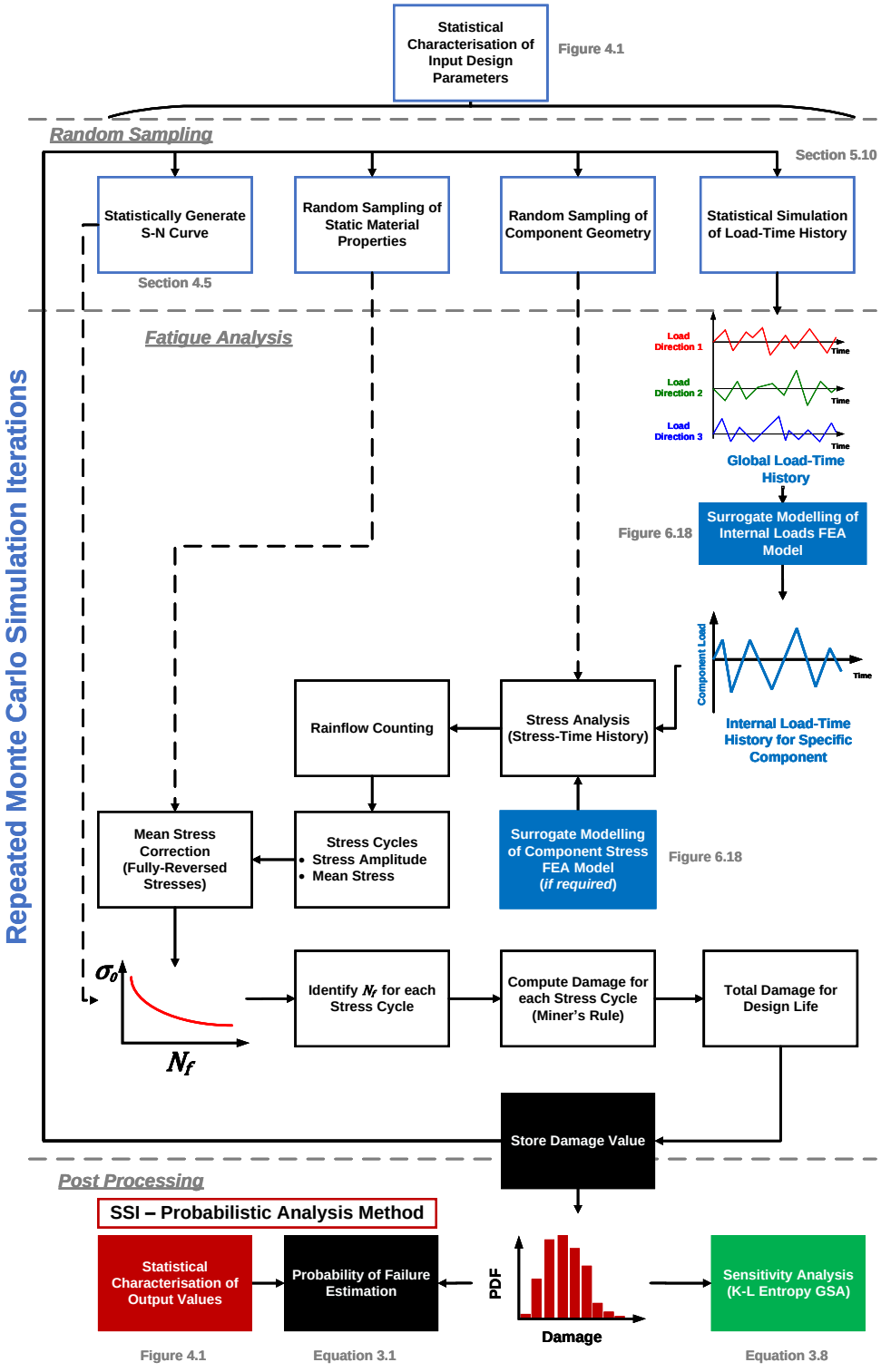

FIGURE 3.4. A detailed flowchart of the proposed probabilistic fatigue methodology, based upon the MCS-SSI hybrid probabilistic analysis method.

The *fatigue analysis* stage of the MCS-SSI probabilistic analysis approach is then performed, following the S-N fatigue analysis process shown previously in Figure 1.3 in Chapter 1. If required, the load-time history is converted to component internal loads using a surrogate model of the FEA loads model. Stress analysis is then used to convert the internal component loads into a component stress-time history, also using a surrogate model if necessary. The stress-time history is then converted to fully-reversed σ_0 stress amplitudes using rainflow counting and the Goodman mean stress correction. The N_f is then identified for each σ_0 from the randomly generated S-N curve and Miner's rule is finally used to compute the total damage D_T in the component resulting from the load-time history.

The MCS is then repeated for many iterations, each time resulting in the computation of a new D_T value. The D_T values can then be statistically characterised to permit the computation of p_f estimates in the *post processing* stage of the MCS-SSI probabilistic analysis method.

3.5.1 Post Processing: *Probability of Failure Estimates*

The execution of the MCS will propagate the variability in the design parameters to the accumulated damage value D_T. Therefore, the variability in D_T can also be statistically characterised using a probability distribution. This distribution represents the 'stress' distribution in the SSI approach. Once the probability distribution type has been selected and fitted to the D_T values, the p_f estimate derived from the distribution '$P_{f_{dist}}$' can be computed using Equation 3.1, providing the failure criterion D_{fail} is deterministic [29, 30, 46]. In Equation 3.1, '$F(D_{fail})$' represents the CDF of the D_T 'stress' distribution evaluated at the deterministic failure criterion. $P_{f_{dist}}$ is therefore the p_f estimate generated using the MCS-SSI hybrid probabilistic analysis approach and is visualised previously in Figure 2.4b in Chapter 2 and in Figure 3.5.

$$P_{f_{dist}} = 1 - F(D_{fail}) \tag{3.1}$$

Due to the use of random sampling in the MCS-SSI hybrid probabilistic analysis method, p_f estimates will be subjected to statistical uncertainty (i.e. if another MCS-based probabilistic analysis was conducted, it should be expected that the p_f values would differ slightly, as the random sampling used within MCS would lead to a different D_T values). As a result, confidence intervals must be used to express the uncertainty in the p_f values [33, 46, 155]. A confidence interval is the range of values that a statistical parameter can be expected lie within and these are constructed using closed-form equations or parametric bootstrap simulation methods [33, 156]. A confidence interval is constructed at a given confidence level, which by convention is 95% [33]. A confidence level of 95% represents that if many applications of the probabilistic analysis method were performed, 95% of the analyses would result in p_f values that lie within the constructed confidence interval [33]. As a result, confidence intervals enable an 'upper-bound' to the p_f estimate to be generated [155].

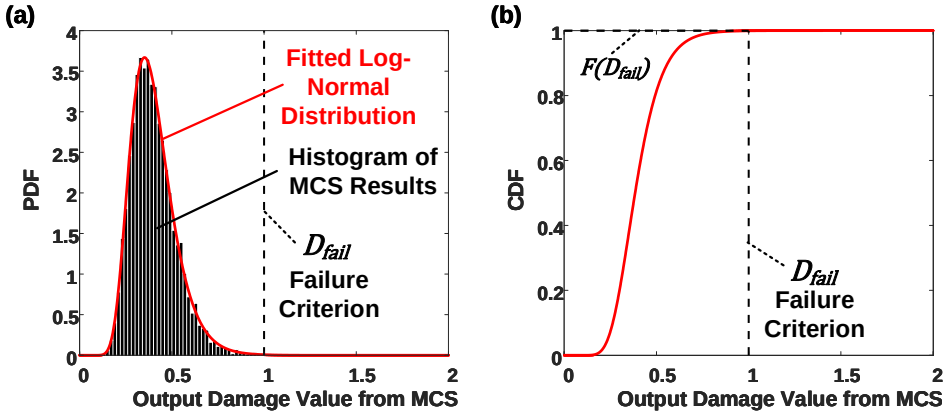

FIGURE 3.5. Computation of the $P_{f_{dist}}$ estimate using (a) statistical characterisation of MCS output values and (b) evaluation of the CDF of the fitted distribution.

3.5.1.1 Validation of p_f Estimates

In order to provide validation of the $P_{f_{dist}}$ estimates, it is proposed that other p_f estimation methods based upon the MCS-SSI approach could be used. $P_{f_{MCS}}$ estimates based directly on the number of MCS iterations that result in a 'failure' iteration (i.e. $D_T \geq D_{fail}$) can be computed using Equation 2.7 from Chapter 2 [30]. This value can then be compared to the $P_{f_{dist}}$ estimate for validation. Confidence intervals can also be constructed for $P_{f_{MCS}}$ using Equation 3.2, where σ_{MCS} is the standard deviation of the $P_{f_{MCS}}$ value as computed using Equation 3.3, where N_{MCS} is the number of MCS iterations [155]. A confidence interval of $\pm 2\sigma_{MCS}$ is approximately equivalent to a 95% confidence interval [33].

$$P_{f_{MCS+2\sigma}} = P_{f_{MCS}} + 2\sigma_{MCS} \tag{3.2}$$

$$\sigma_{MCS} = \sqrt{\frac{P_{f_{MCS}}(1 - P_{f_{MCS}})}{N_{MCS}}} \tag{3.3}$$

Tail-Fitting Methods

An additional method for generating p_f estimates uses 'tail-fitting'. Tail-fitting focuses on producing a probability distribution that only characterises the 'tail' (i.e. extreme value statistics [157, 158]) of a dataset [159, 160]. Tail-fitting has been proposed for probabilistic design as an approach for generating more accurate p_f values, as they focus statistical characterisation efforts on MCS results that are in the vicinity of the failure criterion [159, 160]. The fundamental concept behind tail-fitting is to isolate the data points of a dataset that lie in the 'tail' of the dataset and fit a dedicated probability distribution to the isolated tail data [159, 160]. This concept is visualised in Figure 3.6 and tail-fitting is typically used as it is hypothesised that fitting a

dedicated distribution to a tail dataset could result in more accurate statistical characterisation of the dataset in the tail region.

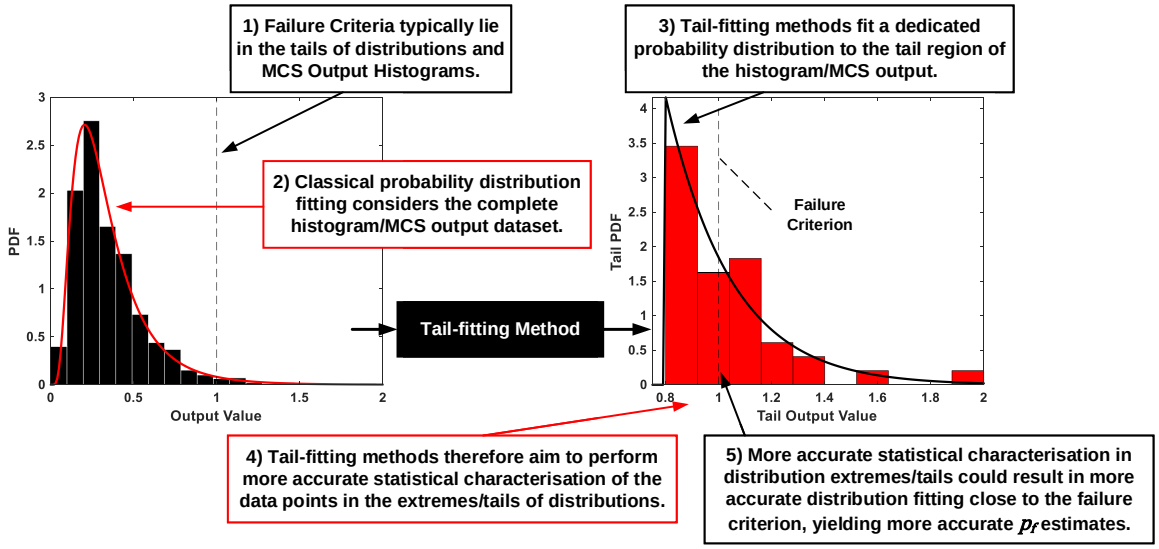

FIGURE 3.6. The concept of tail-fitting probability distributions with a view to increasing the accuracy of statistical characterisation close to failure criteria in order to increase the accuracy of p_f estimates.

The Generalised Pareto Distribution (GPD) is the probability distribution type most widely used to statistically characterise the tail datasets and is not to be confused with the Pareto Front approach that is widely used in optimisation methods [159, 160]. The PDF and CDF of the GPD are shown in Equations 3.4 and 3.5 respectively. The PDF and CDF of the GPD contain shape 'λ', scale 'σ' and threshold 'δ' distribution parameters (see Appendix B for the definition of these parameters) [159, 160].

$$f(x;\lambda,\sigma,\delta) = \begin{cases} \left(\frac{1}{\sigma}\right)\left(1+\lambda\frac{(x-\delta)}{\sigma}\right)^{-1-\frac{1}{\lambda}}, & if\ \lambda \neq 0 \\ \left(\frac{1}{\sigma}\right)\exp\left\{-\frac{(x-\delta)}{\sigma}\right\}, & if\ \lambda = 0 \end{cases} \tag{3.4}$$

$$F(x;\lambda,\sigma,\delta) = \begin{cases} 1-\left(1+\lambda\frac{(x-\delta)}{\sigma}\right)^{-\frac{1}{\lambda}}, & if\ \lambda \neq 0 \\ 1-\exp\left\{-\frac{(x-\delta)}{\sigma}\right\}, & if\ \lambda = 0 \end{cases} \tag{3.5}$$

The tail data points are isolated from the tail dataset by defining a threshold 't', above which the data points are selected to be in the tail dataset. A typical criterion for setting the value of t is to ensure that the tail dataset size 'N_t' is equal to $1.5\sqrt{N_{MCS}}$ [159, 160].

The complete method and equations for computing p_f estimates from GPD tail-fitting (denoted '$P_{f_{tail}}$') are detailed in Appendix B, but conceptually the process can be described as:

1. Identify the failure criterion value (e.g. $D_{fail} = 1$) and isolate the tail dataset from the MCS output based upon the selected threshold t value.
2. Identify the proportion of the MCS output that lies within the tail dataset.
3. Fit the GPD distribution to the tail dataset.
4. Evaluate the fitted GPD CDF at the failure criterion value. This demonstrates the proportion of the tail dataset that lies above the failure criterion.
5. As the the tail dataset is only a subset of the total MCS output, $P_{f_{tail}}$ is computed by scaling the proportion of the tail dataset that is above the failure criterion (Step 4) with respect to the proportion of the MCS output that lies in the tail dataset (Step 2).

It is proposed that the $P_{f_{tail}}$ estimate values can also be used to provide validation of the $P_{f_{dist}}$ estimates. Based on a review of the literature, it is believed that GPD tail-fitting approaches are yet to be specifically applied in a probabilistic fatigue methodology for safe-life components, and therefore, their utility will be assessed within the case studies in Chapters 7 and 8.

3.5.1.2 System Reliability

The existing deterministic safe-life fatigue design approach typically takes a 'hot-spot' approach, whereby the component feature (e.g. lug, cut-out, radii, etc.) with the highest or most-critical D_T value is used to define the safe-life of the component [9]. Whilst this is acceptable for deterministic design and analysis approaches, which assume that the complete component consists of the 'worst case' design parameters for material properties, loading and geometry, it should be noted that in a probabilistic approach, multiple component features can contribute to the component-level p_f.

As a result, a probabilistic approach must be able to combine p_f values across component features to produce a component-level p_f. This also highlights an advantage of using a probabilistic approach over a deterministic approach, as a probabilistic fatigue methodology would permit a component safe-life value to be defined accounting for all features of the component, rather than solely the hot-spot. The toolbox of methods used to combine p_f values are known as 'system reliability' methods [30, 161]. As safe-life components are required to have a crack-free life, the failure of any component feature results in failure of the component and this is therefore known as a 'series' system [30]. If it is assumed that component design parameters and fatigue damage accumulation are statistically independent across the component, the component-level p_f is simply the summation of the p_f for each component feature [161]:

$$p_{f_{component}} = \sum p_{f_{feature}} \tag{3.6}$$

In a similar manner, the structural assembly-level (e.g. a complete landing gear assembly) p_f could be estimated using Equation 3.7. Equation 3.7 is valid for series assemblies, where failure of a single component results in the failure of the assembly, as is the case of single-load path structures such as aircraft landing gear.

$$p_{f_{assembly}} = \sum p_{f_{component}} \tag{3.7}$$

The introduction of system reliability methods also highlights two additional advantages of probabilistic fatigue analysis methods over the existing deterministic processes:

- Through assessing all component features, rather than a 'hot-spot' approach, probabilistic approaches enable high-risk areas of component designs to be identified and provide a more complete assessment of the proposed design [45].
- If p_f estimates were available for other failure modes (e.g. tensile overload/static rupture), these could be aggregated with the fatigue p_f to provide a component p_f estimate that accounted for all failure modes of the component. Probabilistic approaches are currently the only way in which component performance functions can be constructed that account for all failure modes [45].

3.5.2 Post Processing: *Kullback-Leibler Sensitivity Analysis*

The final element of post processing that can be performed on the output of the probabilistic analysis methodology is the utilisation of sensitivity analysis methods to identify design drivers, as introduced in Section 3.2.3. GSA methods are typically based on density[3] or 'entropy' sensitivity analysis approaches, which focus on how the shape of the PDF for the output value changes when the variability in each design parameter is fixed to a nominal deterministic value [147]. Figure 3.7 provides a hypothetical GSA case, whereby the greatest deviation from the 'parent' distribution (where all design parameters are permitted to vary), represents that the fixed design parameter has a greater influence on the output variability than the other design parameters [131, 147, 148].

The quantification of the change in the PDF is typically referred to as the 'entropy' and entropy provides a metric for discriminating between two different PDFs [147]. The Kullback-Leibler (K-L) entropy been proposed as a method for ranking design parameters when conducting sensitivity analysis [152, 153]. The K-L entropy provides a 'Total Effect' (TE) sensitivity value, which represents the contribution to the output variability of the design parameter, when accounting for the variability in the design parameter and any interactions it may have with other design parameters [147].

[3]The term 'density' refers to quantifying changes in the PDF or probability density when fixing design parameter variability [131, 147].

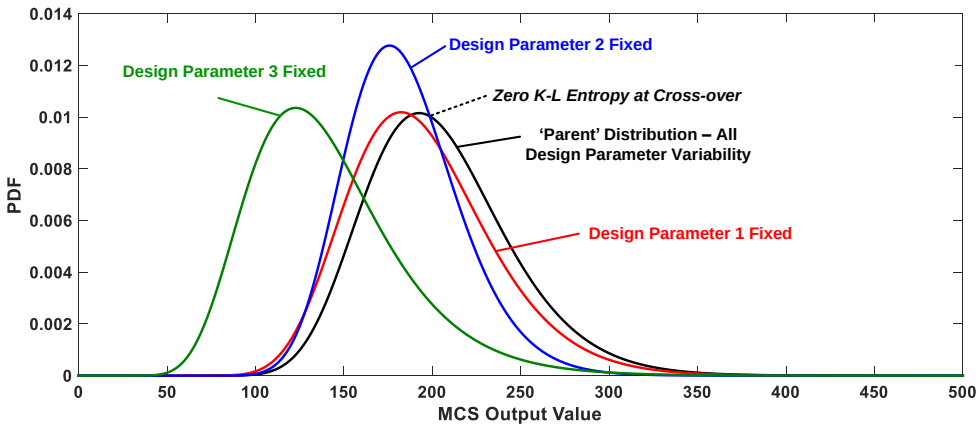

FIGURE 3.7. Demonstration of the principles behind GSA and the K-L entropy sensitivity analysis method.

The K-L TE can be computed using Equation 3.8, where '$f_0(y)$' is the 'parent' PDF of the output value and '$f_{x_j}(y)$' is the PDF of the output value when design parameter 'x_j' is fixed to a nominal deterministic value [152, 153]. The K-L entropy is then computed using numerical integration methods within the region of interest of the output value from y_l to y_u. The K-L entropy value is zero when two PDFs provide the same value for a given y, and the K-L value increases as the difference between the two PDF values increases. The K-L entropy GSA approach has been recently adopted for performing the probabilistic sensitivity analysis of offshore wind turbines by Teixeira et al [162].

$$TE_j = \int_{y_l}^{y_u} f_0(y) \times \left| log\left[\frac{f_{x_j}(y)}{f_0(y)}\right]\right| dy \tag{3.8}$$

The K-L entropy sensitivity analysis method was selected for the probabilistic fatigue methodology because it can be applied directly to the D_T values and probability distributions generated from the MCS-SSI hybrid probabilistic analysis method [147, 152, 153]. Therefore, the K-L sensitivity analysis method is simple to implement within the proposed probabilistic analysis framework.

3.6 Summary

Within a probabilistic fatigue methodology, there are a large number of individual methods that are required to be understood and implemented. These methods span techniques relating to statistical characterisation, surrogate modelling, probabilistic analysis and sensitivity analysis and also interact with one another across throughout the execution of a probabilistic methodology.

As a result, probabilistic analysis frameworks are required to visualise the interrelationship between each individual method and to highlight the 'flow' of information between each method.

The definition of probabilistic analysis frameworks can therefore reduce the resource burden required for engineers to understand and implement a probabilistic approach. The probabilistic analysis framework proposed supports the overcoming of the *required knowledge* blocker to implementing probabilistic design approaches. The need for a systematic process for statistical characterisation and surrogate model construction has also been identified and both will be considered in the following chapters.

The definition of a probabilistic analysis framework has also highlighted other design tasks and activities in which the methods required for a probabilistic analysis methodology can be utilised. The redeployment of the methods required for probabilistic approaches to other engineering activities effectively increases the useful 'return' from the resources required to develop and implement a probabilistic approach. As this effectively reduces the resource burden for implementing a probabilistic approach, the 'buy-in' from engineers and management could be increased as a result of the definition of the probabilistic analysis framework in this chapter. Therefore, the proposed framework further contributes to overcoming the *required knowledge* blocker to implementing probabilistic design approaches, as summarised in the matrix in Table 3.1.

This chapter has also detailed the analysis 'flow' or steps required to conduct the probabilistic fatigue methodology using an MCS-SSI hybrid method. The identification of the probabilistic fatigue analysis steps will support the development of the MATLAB® computational code required to perform the landing gear component case studies in Chapters 7 and 8.

TABLE 3.1. The blockers to probabilistic design approaches overcome by defining the probabilistic analysis framework.

Blocker	Blockers overcome due to definition of analysis framework
Computational Expense	N/A
Required Assumptions of Existing Process	N/A
Availability of Data	N/A
Accuracy of Data Characterisation	N/A
Required Knowledge	• Framework simplifies understanding of methodology through demonstrating interrelationships between the methods required to support the probabilistic methodology. • Framework demonstrates utility of individual methods outside of probabilistic approach.

CHAPTER 4

ENHANCED STATISTICAL CHARACTERISATION PROCESS FOR MATERIALS DATA

Significant variability is present in the S-N datasets used for fatigue design and analysis, observed as the 'scatter' in the number of cycles to failure demonstrated during material specimen testing. The variability in S-N datasets is typically characterised based upon long held statistical assumptions and a limited choice of probability distribution types, potentially resulting in inaccurate or conservative characterisation of the S-N dataset variability. Engineers also typically have a limited background in statistical characterisation methods, further compounding the issue.

This chapter demonstrates the development and implementation of a systematic statistical characterisation process, with the aim of ensuring that the probability distribution type with the best-fit to the design parameter dataset is selected to characterise the variability in design parameters. The impact of the systematic statistical characterisation process on both deterministic and probabilistic fatigue analysis processes is also investigated. As a result, this chapter also identifies how an enhanced and systematic statistical characterisation process can contribute to overcoming the blockers to a probabilistic design approach.

4.1 Variability in Stress-Life (S-N) Datasets

As first introduced in Chapters 1 and 2, significant variability is observed in the number of cycles to failure 'N_f' for a given σ_0 stress level in S-N datasets. The variability present in N_f is observed as a result of material specimen testing, during which the recorded N_f values for different coupons can vary by up to two orders of magnitude and the variability typically increases with a reducing stress level [163]. For a typical S-N dataset, N_f values will be available at a number of discrete σ_0 levels. Within S-N datasets, N_f data points at discrete σ_0 stress levels can either be 'complete' (i.e. all specimens were observed to fail) or 'censored/run-out' (i.e. where some specimen tests were stopped prior specimen failure[1]). It should be noted that this chapter only considers complete S-N datasets and further discussion on the statistical characterisation of censored datasets is provided by Sehn, Mann et al and Toasa Caiza et al [163–165].

The presence of variability in S-N datasets must be captured within a probabilistic fatigue methodology by statistically characterising the variability in N_f using probability distributions. Statistical characterisation of the variability in N_f is also currently required during deterministic fatigue design in order to produce design or 'P-S-N' curves.

4.1.1 3-Parameter Probability Distributions

Due to the need to statistically characterise the variability in N_f within deterministic fatigue analysis, the fatigue design community have developed existing practices for statistically characterising S-N datasets, typically using Log-Normal and Weibull distributions to represent the variability in N_f [36, 166]. Both 2-Parameter (2P) and 3-Parameter (3P) versions of the Log-Normal and Weibull distributions exist [29, 33, 163], although it is typically only 2P distributions which are routinely used to characterise the variability in N_f [7, 22, 36, 163, 166]. The 3P distributions differ from the 2P distributions through the introduction of a location parameter 'δ'. The δ parameter acts as a 'threshold' value, below which the probability of a value occurring is nil [29, 33]. In the context of the statistical characterisation of N_f, the δ parameter represents the minimum number of cycles to failure, thus inferring that there is a lower bound to the fatigue life of a material at a given σ_0 [36]. Both the 2P and 3P distributions retain the shape 'λ' and scale 'σ' parameters and therefore, the 3P distributions are equivalent to the 2P distributions when $\delta = 0$. The 3P Log-Normal and 3P Weibull PDFs are shown in Equations 4.1 and 4.2 respectively [29]. δ, λ and σ are collectively referred to as the PDF distribution parameters.

$$f(x;\lambda,\sigma,\delta) = \frac{1}{(x-\delta)\lambda\sqrt{2\pi}}\exp\left\{-\frac{[ln(x-\delta)-\sigma]^2}{2\lambda^2}\right\} \tag{4.1}$$

$$f(x;\lambda,\sigma,\delta) = \frac{\lambda}{\sigma}\left(\frac{x-\delta}{\sigma}\right)^{\lambda-1}\exp\left\{-\left(\frac{x-\delta}{\sigma}\right)^{\lambda}\right\} \tag{4.2}$$

[1] This is typical at low stress amplitudes where the high N_f can be prohibitive to achieve.

The application of both 3P Log-Normal and 3P Weibull distributions to characterise N_f from S-N datasets has been presented by previous work within the literature. Work performed by Zhao et al presented one of the earliest investigations into the use of 3P distributions to statistically characterise N_f within a steel S-N dataset, using classical probability plotting methods for distribution fitting [167]. Zhao et al identified that the 3P Weibull distribution provided an improved fit to the S-N dataset, when assessing the Goodness-of-Fit using correlation coefficients [167]. Schijve demonstrated the applicability of 3P Log-Normal and 3P Weibull distributions to steel S-N datasets using probability plotting methods for distribution fitting [36]. More recent work by Wei et al provided an investigation into comparing 2P and 3P Weibull distributions when applied to S-N datasets, using probability plotting methods for distribution fitting and the Anderson-Darling Goodness-of-Fit test [168]. Based on the results of the Anderson-Darling test, it was concluded that the 3P Weibull distribution provided a better fit to the S-N dataset than the 2P Weibull distribution [168]. Finally, Khameneh and Azadi investigated the statistical characterisation of S-N datasets using a combination of probability plotting and maximum likelihood estimation methods, along with the Anderson-Darling test for performing a Goodness-of-Fit test [169]. Within this work, the 3P Weibull distribution was selected as the distribution that provided the best-fit to the S-N dataset [169]. It has been suggested that the 3P Weibull distribution may provide a better fit to N_f due to the additional δ threshold parameter [163].

The presence of a minimum N_f value due to the 3P δ threshold value has also been supported from a physical standpoint [36]. Schijve and Wei et al suggest that the inclusion of a threshold parameter is realistic, as the zero threshold of the 2P distributions theoretically infers that the material could fail before loading has occurred [36, 168]. The 3P Weibull distribution has also been used based on physical justification within the model proposed by Castillo and Fernández-Cantelli, where it is suggested that a Weibull distribution is more appropriate to model N_f variability compared to a Log-Normal distribution, as a result of the 'weakest link' principle [66].

The review of the literature has highlighted that the 3P distributions can be expected to provide an improved fit to S-N datasets when statistically characterising the variability in N_f, along with there being a physical basis for selecting 3P distributions over 2P distributions. In addition, as the introduction of the δ parameter increases the minimum possible N_f from zero when using a 3P distribution, it is proposed that 3P distributions could result in reduced conservatism in design P-S-N curves, providing they are shown to provide the best-fit to the S-N dataset. From the perspective of a probabilistic fatigue methodology, the literature also demonstrated that a 3P distribution regularly provides an improved fit to the S-N dataset over a 2P distribution and as a result, 3P distributions should be considered when statistically characterising the variability in N_f when implementing the probabilistic fatigue methodology.

However, the previous literature has typically only characterised the variability in N_f at a single σ_0 stress level, rather than at all stress levels present within an S-N dataset. Therefore, a quantification of the reduction in conservatism when constructing P-S-N curves using 3P

distributions is yet to be performed. In addition, the distribution fitting and selection methods used within the literature often utilise only probability plotting methods, rather than the more statistically-rigorous maximum likelihood estimation approach. The common practice demonstrated in the literature also fails to perform validation of the distribution fitting and selection using multiple methods. Reference texts on data analysis recommend that multiple fitting methods are to be used to achieve a robust approach to statistical characterisation [33, 170] and as a result, a statistical characterisation process that combines probability plotting and maximum likelihood distribution fitting is required.

4.2 Systematic Statistical Characterisation Process

The proposed systematic statistical characterisation process is shown in Figure 4.1 and is decomposed into 'Fitting' and 'Selection' of probability distributions. 'Fitting' is the process of generating PDF distribution parameter estimates. The 'Selection' process tests each candidate distribution for Goodness-of-Fit (GoF), in order to down-select the final distribution type, by either accepting or rejecting the distribution. The process aims to maximise the amount of evidence that can be generated to support the selection of one candidate distribution over another.

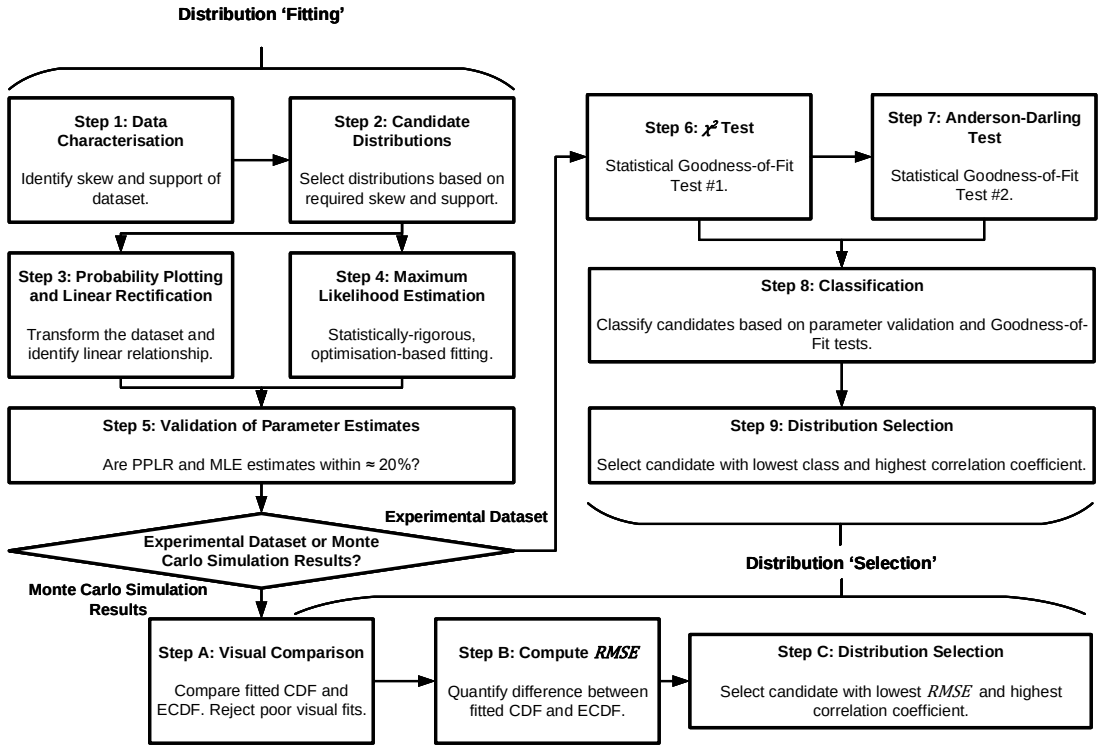

FIGURE 4.1. The proposed systematic statistical characterisation process based upon multiple distribution fitting and selection methods for validation.

4.2.1 The Need for a Systematic Statistical Characterisation Process

The need for developing a novel systematic statistical characterisation process within the probabilistic fatigue methodology can be considered from the perspectives of: *probabilistic fatigue methodology, existing S-N dataset characterisation practice* and *blockers to probabilistic design*. Regarding the probabilistic fatigue methodology specifically, accurate statistical characterisation of design parameter variability is vital for generating accurate p_f estimates. However, for a given dataset, there are often a number of competing candidate distribution types and it can be challenging to identify the correct distribution to be used to characterise the design parameter [38, 166]. As a result, a systematic and robust approach to statistical characterisation is required.

Considering existing practices for S-N dataset statistical characterisation, typically only a single fitting method and single GoF test is performed to select one candidate distribution over another. As 3P distributions are non-trivial from a fitting perspective [37], it is vital to perform validation of the distribution parameter estimates to ensure accurate values are used. This can be achieved using multiple fitting methods and GoF tests within the process. The use of multiple fitting methods also permits the limitations of each fitting method and GoF test to be mitigated.

The use of a systematic statistical characterisation process can also help overcome the blockers to a probabilistic design approach. Engineers often do not have a significant statistical background [23, 171], and a systematic process can help support the users' confidence in implementing statistical characterisation by guiding users through the same process each time, by providing rules to guide the decision making required to down-select the final distribution type [172]. In addition, it has been suggested that when selecting probability distributions to characterise the variability in design parameters, certain probability distributions (typically, Normal and Log-Normal) are often selected out of a desire for mathematical simplicity and convenience [28, 37]. A systematic process enables a wide range of candidate distributions to be considered prior to down-selection. Therefore, a systematic statistical characterisation process permits a review and challenge of long held statistical beliefs and assumptions [28].

The results of statistical characterisation must often be shared with other engineers, management, customers or regulatory bodies. Therefore, it is desirable to include intuitive or 'visual' methods within the statistical characterisation process, such that results can be shared with other stakeholders and to increase confidence in distribution parameter estimates.

4.2.2 Required Steps for the Systematic Statistical Characterisation Process

The systematic statistical characterisation process shown previously in Figure 4.1 demonstrates how the process goes from selecting candidate distributions, through distribution fitting using multiple methods, prior to selecting the final distribution type based on the results from the GoF tests. This section will briefly introduce the methods required within the process. In the wider context of probabilistic approaches to design, the statistical characterisation process could be applied to all continuous datasets.

Step 1: Dataset Characterisation

The first step of the process is to characterise the 'support' and the 'skew' of the dataset. 'Support' is usually driven by physical limitations and is the possible range of values that the dataset can take [33]. For S-N datasets, the support is typically $[0, +\infty]$ (2P distributions) or $[\delta, +\infty]$ (3P distributions). 'Skew' is the measure of how asymmetrical a dataset is about the mean value (as shown by a long distribution 'tail'). The sample skew of a dataset 'γ' can be computed using Equation 4.3 for a sample size 'N'. 'x_i' is the value of a data point, 'μ_X' is the mean and 's_X' is the sample standard deviation of the dataset [167]:

$$\gamma = \frac{\frac{1}{N}\sum_{i=1}^{N}(x_i - \mu_X)^3}{s_X^3} \tag{4.3}$$

A positive γ value indicates positive or 'right' skew, with a right-hand tail (as is typical for S-N datasets [36]), whilst a negative γ value infers the opposite [167].

Step 2: Candidate Distributions

After identifying the required support and sample skew of the dataset, candidate distributions can be proposed. The candidate distributions should consist of distribution types that are capable of representing the dataset support and skew. Any distributions that are currently assumed for the design parameter should also be included to challenge existing assumptions regarding statistical characterisation [28].

Step 3: Probability Plotting and Linear Rectification

Probability plotting is a widely-used tool in reliability engineering that can be used identify whether a dataset belongs to an assumed distribution type [29, 170]. Probability plotting transforms data points using empirically-derived ranking equations (which estimate the cumulative relative frequency 'R_c') and linear rectification equations for each distribution type. Further information on ranking equations is provided in the statistical primer in Appendix B. If a transformed dataset shows a linear relationship on the probability plot, the dataset can be suggested to originate from the selected distribution as shown in Figure 4.2. The intercept '$A0$' and slope '$A1$' coefficients of the linear regression of the transformed data points can then be converted into distribution parameter estimates using equations provided in reference texts [29, 35, 170].

The correlation coefficient 'r' can be used to quantify how linear the transformed data points are on the probability plot [29]. The correlation coefficient is computed using Equation 4.4. A value of $r = 1$ infers a perfect correlation in the probability plot. In Equation 4.4, '$cov(X_T, R_{C,T})$' represents the covariance of the transformed data points and ranking values, and 'S_{X_T}' and '$S_{R_{C,T}}$' are the sample standard deviation of the transformed data points and rank values respectively.

$$r = \frac{cov(X_T, R_{C,T})}{S_{X_T} S_{R_{C,T}}} \tag{4.4}$$

This approach to distribution fitting will be referred to as PPLR (Probability Plotting and Linear Rectification) for the remainder of this thesis. The strength of PPLR is that it is a visual and intuitive method [170]. The limitation of the PPLR approach is the reliance on assuming a ranking equation to estimate R_c. There are a wide range of ranking equations presented within the literature [29, 170] and therefore, it is recommended that the ranking equation that maximises the value of r is used to generate the PPLR distribution parameter estimates.

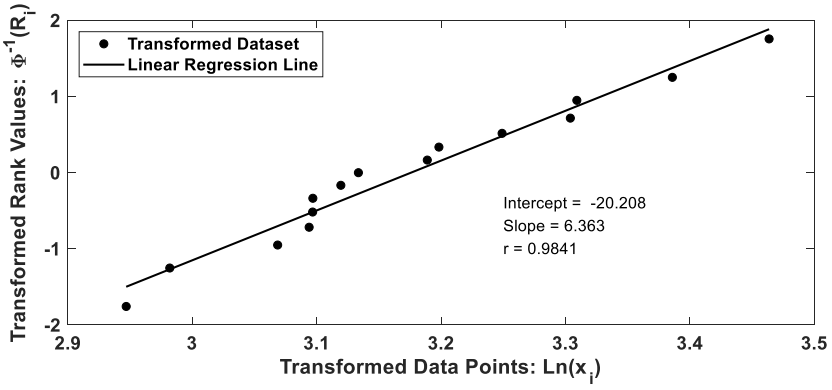

FIGURE 4.2. An example of PPLR distribution fitting for a 2P Log-Normal distribution.

Step 4: Maximum Likelihood Estimation

Maximum Likelihood Estimation (MLE) methods are a statistically rigorous approach to estimating distribution parameters [33]. The core philosophy of the MLE approach is to select distribution parameter estimates that maximise the probability of the dataset being observed from random samples from the distribution (known as the 'likelihood') [33]. Likelihood Functions (LFs) are available in reference texts and are maximised using numerical solution processes and optimisation methods (see Appendix B) [33]. The strength of the MLE approach is that for large sample sizes, the distribution parameter estimates are unbiased and the statistical uncertainty of MLE values can be assessed [33]. However, the limitation of the MLE approach is the reliance on the non-trivial task of maximising the complex LF equations [164]. This can lead to a lack of convergence or convergence to a local maximum LF value, rather than the global maximum, resulting in inaccurate distribution parameter estimates. Therefore, PPLR methods are required to validate the distribution parameter estimates from MLE.

Step 5: Distribution Parameter Validation

Following distribution fitting using PPLR and MLE, two sets of distribution estimates will be available. In order to validate the distribution parameter estimates, the percentage difference between the PPLR and MLE estimates should be computed. Good agreement between the two sets of distribution parameter estimates would infer that the candidate distribution type provides an accurate characterisation of the variability in the design parameter.

From previous studies in the literature, it has been demonstrated that when using different fitting methods to fit a single distribution type to a dataset, the distribution parameter estimates can vary significantly, by up to 20% [29]. As a result, 'validation' of distribution parameter estimates is defined as the maximum difference between the PPLR and MLE distribution parameter estimates being less than or equal to 20%.

Step 6: Chi-squared Goodness-of-Fit Test

The first GoF test within the process is the Chi-squared (χ^2) test, which compares the frequency of observations within the dataset with the expected frequency from the fitted probability distribution, by considering the dataset across n_{bin} bins constructed using prescribed rules, which are detailed in Appendix B [173]. The χ^2 test statistic 'χ^2_s' is computed using Equation 4.5, where 'O_j' is the observed frequency in each bin and 'E_j' is the expected frequency in each bin from the fitted CDF (see Appendix B for further detail) [173]:

$$\chi^2_s = \sum_{j=1}^{n_{bin}} \frac{(O_j - E_j)^2}{E_j} \tag{4.5}$$

The χ^2_s value is then compared to a critical value 'χ^2_c' sourced from statistical tables and the candidate distribution is rejected if $\chi^2_s \geq \chi^2_c$ [173]. The critical value is generated at a specific significance level 'α' (convention dictates $\alpha = 5\%$). The strength of the χ^2 GoF test is its ability to generate χ^2_c values for any distribution type, whilst the limitation of the test is that it is accurate only for large sample sizes and should not be be used when $N < 15$ and should be used with caution for $N < 50$ [28, 29]. Therefore, an additional GoF test is required to provide validation for the χ^2 GoF test for the typical sample sizes of S-N dataset [174].

Step 7: Anderson-Darling Goodness-of-Fit Test

The second GoF test in the process is the Anderson-Darling (A-D) test, which also compares the difference between the expected frequency from the dataset and the CDF [173]. The A-D GoF test statistic 'A^2' is compared to a critical value 'A^2_c' at a given α value. Guidance on computing A^2 is provided in Appendix B. Tabulated A^2_c values are available for Normal, 2P Log-Normal and 2P Weibull distributions, but are not available for 3P distributions [175] and must therefore be estimated using a parametric bootstrap approach [176]. Parametric bootstrap approaches randomly sample from the fitted distribution, re-fit the distribution to the sample and compute

the A^2 statistic over many iterations (typically 10,000) [175]. The A_c^2 value is then estimated by finding the $1-\alpha$ percentile of the bootstrap A^2 values [175, 176]. A distribution is rejected if $A^2 \geq A_c^2$. A limitation of the A-D test is the requirement to generate A_c^2 values using a parametric bootstrap, which when coupled with a complex MLE numerical solution approach can take a few hours of CPU run-time to perform 10,000 bootstrap iterations.

Step 8: Distribution Classification

One of the most significant challenges during statistical characterisation is the synthesis of all of the information generated during distribution fitting and GoF testing, in order to select the distribution that most accurately characterises the dataset. To support the down-selection of the final distribution type in a systematic manner, a series of novel classifications that consolidate the results of distribution fitting and GoF tests have been proposed, as shown in Table 4.1.

TABLE 4.1. Candidate distribution classifications when the χ^2 GoF test can be performed for a sample size of $N \geq 15$.

Class	Validated Estimates?	PPLR - GoF Results		MLE - GoF Results	
		χ^2	A-D	χ^2	A-D
1	Yes	Accept	Accept	Accept	Accept
2	No	Accept	Accept	Accept	Accept
2	Yes	3 Accept, 1 Reject - *reduced validation across GoF tests*			
3	No	3 Accept, 1 Reject - *reduced validation across GoF tests*			
4	All other cases, including incorrect skew or support.				

The classifications shown in Table 4.1 are based on the amount of evidence available to support a candidate distribution providing the best-fit to the dataset. Therefore, distributions that have validated distribution parameter estimates and are accepted by all GoF tests will have the lowest classification. All other classifications represent a 'loss' of supporting evidence. Table 4.2 shows the classifications to be used when $N < 15$ and the χ^2 GoF test cannot be used. The use of classifications synthesises all of the results from fitting and GoF tests (up to 25 elements of information) into a single value for each candidate distribution.

TABLE 4.2. Candidate distribution classifications when the χ^2 GoF test cannot be performed for a sample size of $N < 15$.

Class	Validated Estimates?	A-D GoF for PPLR	A-D GoF for MLE
1	Yes	Accept	Accept
2	No	Accept	Accept
3	Yes	Only 1 Test Accepts	
4	All other cases, including incorrect skew or support.		

Following classification, the lowest possible class should be identified. If only Class 4 distributions are available, a wider search for other candidate distributions should be conducted. Class 3 distributions may be used as an approximation to the dataset but should warrant further

investigation. Both Class 1 and Class 2 distributions can be considered as suitable distributions, with Class 1 being preferable to Class 2. The existing practice for statistically characterising N_f within the literature [36, 167, 168] only uses one fitting method and one GoF test for distribution selection, and is therefore equivalent to Class 4. As a result, the minimum acceptable classification of Class 2 represents increased statistical rigor when characterising S-N datasets.

Step 9: Final Distribution Selection

If only one distribution type is available in the lowest of Class 1 or 2, it should be selected as the final distribution type. If multiple candidate distributions are present within the lowest class, the correlation coefficient value r from PPLR can be used to rank the remaining distributions. A candidate distribution in the lowest class with the largest r value should be selected as the final distribution type.

Statistical Characterisation of Monte Carlo Simulation Output

As the probabilistic fatigue methodology framework defined in Chapter 3 is based upon a hybrid MCS-SSI approach, a systematic statistical characterisation process must also be available to down-select the probability distribution type for the 'stress' distribution generated by the MCS. The number of data points within the MCS output will be significantly larger (typically thousands or millions of data points) than the typical sample sizes demonstrated by experimental datasets for material properties (typically tens of data points).

Whilst PPLR and MLE distribution fitting methods can be used to fit distributions to large sample sizes, the A-D and χ^2 GoF tests cannot be reliably used to assess the GoF of the candidate distributions for cases where the sample size is large. This is due to the observation that the sensitivity of the GoF tests increases with the sample size (i.e. the number of MCS iterations performed), to the point where the A-D, χ^2 and other small-sample GoF tests will reject distributions despite providing an acceptable fit to the dataset [177, 178]. As the r correlation coefficient from PPLR is not affected negatively by sample size, it can be used to assess the GoF for distributions applied to datasets generated by an MCS.

Therefore, an alternative GoF testing approach is required, based upon the Empirical Cumulative Density Function (ECDF). The ECDF is a step-function which approximates the CDF of a dataset for each data point 'x_i', and the value of the ECDF 'F_{ECDF}' can be computed using Equation 4.6 [173]:

$$F_{ECDF}(x_i) = \frac{\text{Number of Data Points} \leq x_i}{N} \tag{4.6}$$

Within the systematic statistical characterisation process shown previously in Figure 4.1, alternative distribution selection steps are specified for cases where the process is to be applied to the output from an MCS. **Step A** performs a visual comparison between the ECDF of the MCS

dataset and the CDF of the fitted distribution, to qualitatively identify whether a good fit has been achieved, especially in the tails of the distribution. Candidate distributions with a poor visual fit (including incorrect support or skew) can be rejected. Figure 4.3 provides an example of a good and poor fit to an ECDF.

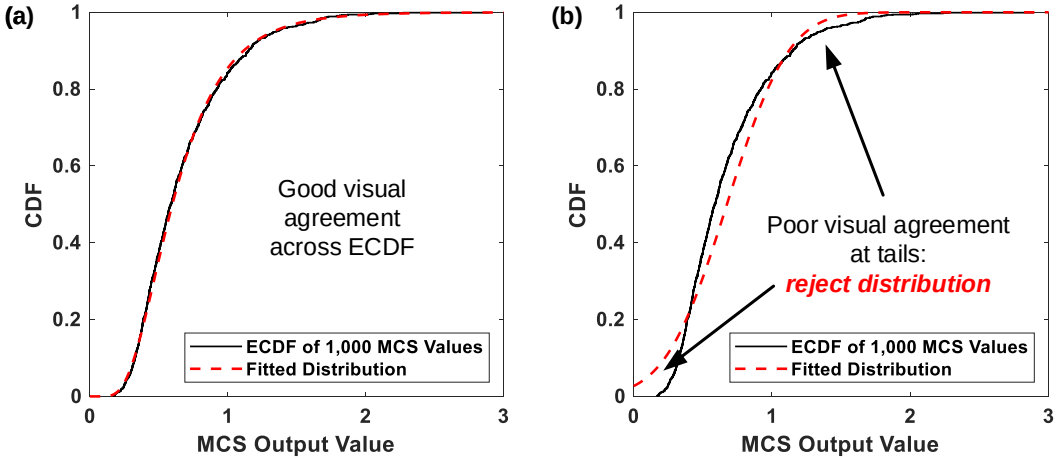

FIGURE 4.3. Examples of visually comparing ECDF and CDF for candidate distributions that provide (a) a good fit and (b) a bad fit to the output from an MCS.

In **Step B** the visual agreement between the ECDF and the candidate distribution CDF can be quantified using the Root Mean Square Error ($RMSE$), which compares the value of cumulative density for a given MCS result between the ECDF and the CDF. $RMSE$ can be computed using Equation 4.7, where 'x_i' is a given result from the MCS iterations (i.e. a D_T damage value). A lower value of $RMSE$ infers an improved fit of the CDF to the ECDF.

$$RMSE = \sqrt{\frac{\sum_{i=1}^{N_{MCS}} (\text{Value from CDF at } x_i - \text{Value from ECDF at } x_i)^2}{N_{MCS}}} \tag{4.7}$$

As shown in Figure 4.1, the stage **Step C** selects the final distribution type by selecting the candidate distribution with the lowest $RMSE$ and highest r value. As the $RMSE$ and r are GoF measures rather than 'accept/reject' GoF tests, classifications for each candidate distribution cannot be defined[2]. Whilst the remainder of this chapter concerns statistical characterisation of experimental datasets, the application of the statistical characterisation process shown in Figure 4.1 to the output from an MCS will be shown during case studies in Chapters 7 and 8.

[2]Future work should explore the possibility of generating critical values for $RMSE$ and r based upon the parametric bootstrap methods that are used to generate A-D A_c^2 critical values.

4.3 Statistical Characterisation of 4340 Steel S-N dataset

The S-N dataset shown previously in Figure 1.2 in Chapter 1 represents the S-N dataset for 4340 steel [25], which is a high strength steel typical of the materials used within aircraft landing gear components [21, 179]. The Engineering Sciences Data Unit (ESDU) 4340 steel S-N dataset is generated from the fully-reversed rotating-bending testing of material coupons [25]. Within the S-N dataset, sample sizes vary from $N = 10$ to $N = 42$, with the majority of σ_0 stress levels having samples sizes between $N = 25$ and $N = 30$ [25]. Due to these smaller sample sizes from the experimental datasets, Figure 4.1 shows that Steps 1 to 9 should be used to down-select the distribution type for N_f at each σ_0 stress level.

4.3.1 Demonstration of Process on a Single Stress Level

Considering the 4340 steel S-N dataset at the stress level of $\sigma_0 = 520$ MPa, the support and skew of the dataset were identified within Step 1 of the systematic statistical characterisation process. The sample skew value of $\gamma = 0.948$ suggests that the dataset shows positive skew. As the expected support for N_f is either $[0, +\infty]$ or $[\delta, +\infty]$ [36], the 2P Log-Normal, 3P Log-Normal, 2P Weibull and 3P Weibull distributions were selected as candidate distributions.

The probability plots from the PPLR distribution fitting in Step 3 are shown in Figure 4.4. It can be seen from Figure 4.4 that all candidate distributions presented linear relationships on the probability plots. Figure 4.4 also demonstrates that the 3P Weibull distribution minimised the deviation in the linear relationship at the lower tail of the 2P Weibull probability plot. This suggests an improved fit to the dataset when using a 3P distribution, supporting the presence of a δ threshold parameter. The PPLR distribution parameter estimates are shown in Table 4.3.

Step 4 of the statistical characterisation process performed MLE fitting of the distributions and the resulting parameter estimates are also given in Table 4.3. Table 4.3 also shows that the maximum percentage difference between PPLR and MLE parameter estimates varied significantly across the different candidate distributions, from 4.853% to 48.612%. Using the 20% difference as the threshold validation, the results inferred that the 2P Log-Normal and 2P Weibull distributions are the only candidate distributions with validated parameter estimates (Step 5). It can be seen from Table 4.3 that the δ parameter estimates for the 3P distributions varied significantly to one other. This result is consistent with the work of Schijve, who also observed inconsistency between the δ values for 3P Log-Normal and 3P Weibull distributions [36].

Table 4.4 shows the results of the χ^2 GoF test from Step 6 of the process. The 'A' prefix demonstrates that the GoF test accepted the candidate distribution and an 'R' prefix with *italic* values shows that the GoF test rejected the candidate distribution. It can be seen from Table 4.4 that the 3P Weibull distribution when fitted using a PPLR approach was the only candidate distribution to be rejected by the χ^2 GoF test at $\alpha = 5\%$. The 3P Weibull distribution fitted using MLE was accepted by the χ^2 GoF test at $\alpha = 5\%$.

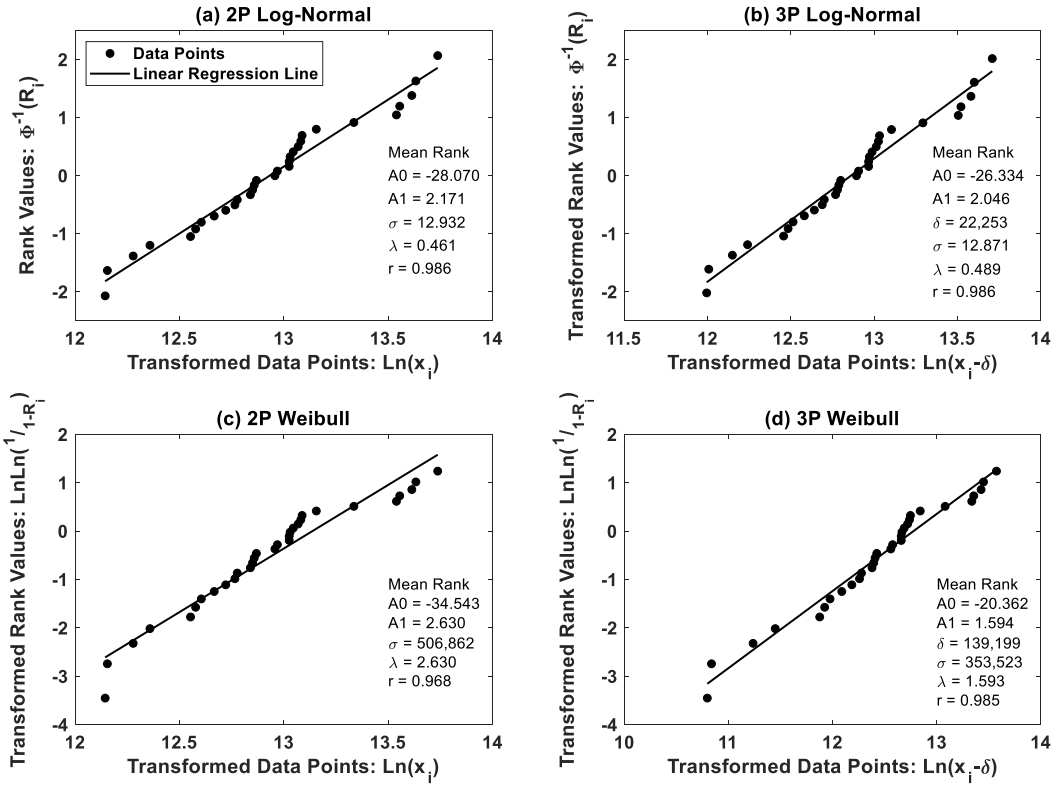

FIGURE 4.4. PPLR distribution fitting for N_f at $\sigma_0 = 520$ MPa for: (a) 2P Log-Normal, (b) 3P Log-Normal, (c) 2P Weibull and (d) 3P Weibull distributions.

TABLE 4.3. The distribution parameter estimates for N_f at $\sigma_0 = 520$ MPa.

Distribution	Fitting Method (*Rank Equation*)	Distribution Parameter Estimate			Maximum Difference
		Threshold δ	Scale σ	Shape λ	
2P Log-Normal	PPLR (*Mean*)	-	12.932	0.461	10.333%
	MLE	-	12.932	0.418	
3P Log-Normal	PPLR (*Mean*)	22,253	12.861	0.472	48.612%
	MLE	43,304	12.809	0.464	
2P Weibull	PPLR (*Mean*)	-	504,751	2.767	4.853%
	MLE	-	508,269	2.508	
3P Weibull	PPLR (*Mean*)	146,676	342,490	1.603	21.187%
	MLE	176,620	298,760	1.408	

The results from the A-D GoF test are also shown in Table 4.4 from Step 7. It can be seen that the 2P Weibull distribution, when fitted with PPLR and MLE was rejected at $\alpha = 5\%$. This also highlights the importance of validating GoF tests, as the rejection of the 2P Weibull distribution by the A-D test contradicts the results of the χ^2 GoF test. In a similar fashion, the PPLR-fitted 3P Weibull distribution was accepted by the A-D GoF test despite being rejected by the χ^2 GoF test.

TABLE 4.4. GoF test results for candidate distributions for N_f at $\sigma_0 = 520$ MPa.

Distribution	Fitting Method (*Rank Equation*)	χ^2_s	χ^2_c $\alpha = 5\%$	A^2	A^2_c $\alpha = 5\%$	r	Class
2P Log-Normal	PPLR (*Mean*)	4.055	A 5.992	0.445	A 0.752	0.986	**1**
	MLE	2.810	A 5.992	0.386	A 0.752	-	
3P Log-Normal	PPLR (*Mean*)	3.012	A 5.992	0.429	A 0.601	0.986	**2**
	MLE	1.831	A 5.992	0.383	A 0.649	-	
2P Weibull	PPLR (*Mean*)	3.535	A 5.992	0.990	R *0.757*	0.968	**4**
	MLE	3.648	A 7.815	0.904	R *0.757*	-	
3P Weibull	PPLR (*Mean*)	9.516	R *3.842*	0.521	A 0.885	0.985	**3**
	MLE	2.686	A 5.992	0.509	A 0.891	-	

The final column of Table 4.4 shows the classification of each candidate distribution for Step 8 of the process, based upon the classifications defined in Table 4.1. Table 4.4 shows that the 2P Log-Normal distribution was Class 1, the 3P Log-Normal distribution was Class 2 (due to unvalidated distribution parameter estimates), the 2P Weibull distribution was Class 4 (due to A-D GoF test rejecting both PPLR and MLE estimates) and the 3P Weibull distribution was Class 3 (due to unvalidated parameter estimates and χ^2 rejecting the PPLR estimates). Therefore, when considering only the stress level at $\sigma_0 = 520$ MPa, the 2P Log-Normal distribution should be selected as the final distribution for N_f, due to having the lowest class number. The 3P Log-Normal distribution was rejected due to the large difference (48.612%) between the δ threshold parameter from PPLR and MLE, resulting in unvalidated distribution parameter estimates.

4.3.2 Statistical Characterisation of Complete 4340 Steel S-N Dataset

The systematic statistical characterisation process was also applied to the remaining stress levels within the S-N dataset at σ_0 =620, 600, 580, 560 and 540 MPa (identified as Stress Level 1, 2, 3, 4 and 5 respectively). The results from distribution fitting, GoF testing and classification are shown in Tables 4.5 and 4.6, including Stress Level 6 at $\sigma_0 = 520$ MPa as characterised in Section 4.3.1 for completeness. The statistical characterisation results from Tables 4.5 and 4.6 will be reviewed to identify the candidate distribution that best characterises the variability in N_f for the 4340 steel S-N dataset. The utility of the distribution classifications is highlighted by the sheer size of Tables 4.5 and 4.6, as all of the information for a candidate distribution is consolidated within a single classification number. The clearest approach to reviewing the vast amount of information in Tables 4.5 and 4.6 is to focus on each candidate distribution type individually. Only the A-D GoF test could be performed at Stress Level 1 due to the sample size of $N = 10$.

TABLE 4.5. Distribution parameter estimates and GoF test results for N_f at Stress Level 1, 2 and 3 of the 4340 steel S-N dataset.

Stress Level 1:	$\sigma_0 = 620$ MPa	Sample Size N:		10	Sample Skew γ:	1.528	Best Fit Distribution:			**2P Log-Normal**	
Distribution	Fitting Method (*Rank Equation*)	Distribution Parameter Estimate			Max Difference	χ^2_s	χ^2_c $\alpha = 5\%$	A^2	A^2_c	r	Class
		Threshold δ	Scale σ	Shape λ							
2P Log-Normal	PPLR (*EV*)	-	10.645	0.300	4.590%	-	-	0.404	A 0.752	0.959	**1**
	MLE	-	10.665	0.286		-	-	0.384	A 0.752	-	
3P Log-Normal	PPLR (*EV*)	25,795	9.552	0.743	25.584%	-	-	0.252	A 0.635	0.982	**2**
	MLE	29,337	9.195	1.011		-	-	0.308	A 1.001	-	
2P Weibull	PPLR (*EV*)	-	48,562	3.717	15.990%	Incorrect Skew Behaviour. Reject 2P Weibull Distribution.					**4**
	MLE	-	49,602	3.205							
3P Weibull	PPLR (*Hazen*)	30,167	45,010	0.935	59.542%	Exponential Distribution. Reject 3P Weibull Distribution.					**4**
	MLE	30,800	111,251	0.630							
Stress Level 2:	$\sigma_0 = 600$ MPa	Sample Size N:		17	Sample Skew γ:	0.761	Best Fit Distribution:			**3P Log-Normal**	
Distribution	Fitting Method (*Rank Equation*)	Distribution Parameter Estimate			Max Difference	χ^2_s	χ^2_c $\alpha = 5\%$	A^2	A^2_c	r	Class
		Threshold δ	Scale σ	Shape λ							
2P Log-Normal	PPLR (*Mean*)	-	10.903	0.351	16.012%	6.253	R *5.992*	0.390	A 0.752	0.981	**2**
	MLE	-	10.903	0.303		3.448	A 5.992	0.392	A 0.752	-	
3P Log-Normal	PPLR (*Mean*)	26,745	10.136	0.713	15.335%	3.750	A 5.992	0.253	A 0.626	0.990	**2**
	MLE	31,590	9.857	0.796		4.719	R *3.842*	0.277	A 0.630	-	
2P Weibull	PPLR (*Mean*)	-	63,416	3.348	2.350%	Incorrect Skew Behaviour. Reject 2P Weibull Distribution.					**4**
	MLE	-	63,202	3.428							
3P Weibull	PPLR (*Hazen*)	33,711	25,148	1.207	41.284%	3.280	A 5.992	0.205	A 1.002	0.992	**4**
	MLE	35,096	17,800	0.860		MLE Produces Exponential Distribution.					
Stress Level 3:	$\sigma_0 = 580$ MPa	Sample Size N:		26	Sample Skew γ:	0.503	Best Fit Distribution:			**3P Weibull**	
Distribution	Fitting Method (*Rank Equation*)	Distribution Parameter Estimate			Max Difference	χ^2_s	χ^2_c $\alpha = 5\%$	A^2	A^2_c	r	Class
		Threshold δ	Scale σ	Shape λ							
2P Log-Normal	PPLR (*Mean*)	-	11.394	0.309	11.506%	2.247	A 5.992	0.349	A 0.752	0.987	**1**
	MLE	-	11.394	0.277		2.563	A 5.992	0.398	A 0.752	-	
3P Log-Normal	PPLR (*Mean*)	32,771	10.897	0.489	18.280%	3.067	A 3.842	0.285	A 0.616	0.989	**2**
	MLE	40,102	10.732	0.517		4.318	R *3.842*	0.353	A 0.616	-	
2P Weibull	PPLR (*Mean*)	-	101,850	3.871	0.821%	Incorrect Skew Behaviour. Reject 2P Weibull Distribution.					**4**
	MLE	-	101,837	3.903							
3P Weibull	PPLR (*Mean*)	51,936	45,682	1.400	12.577%	1.722	A 3.815	0.253	A 0.940	0.992	**1**
	MLE	55,015	40,578	1.330		1.884	A 3.815	0.264	A 0.911	-	

TABLE 4.6. Distribution parameter estimates and GoF test results for N_f at Stress Level 4, 5 and 6 of the 4340 steel S-N dataset.

Stress Level 4:	$\sigma_0 = 560$ MPa	Sample Size N:		28	Sample Skew γ:	0.413	Best Fit Distribution:			**3P Weibull**	
Distribution	Fitting Method (*Rank Equation*)	Distribution Parameter Estimate			Max Difference	χ^2_s	χ^2_c $\alpha = 5\%$	A^2	A^2_c	r	Class
		Threshold δ	Scale σ	Shape λ							
2P Log-Normal	PPLR (*Mean*)	-	11.848	0.320	10.405%	2.077	A 5.992	0.234	A 0.752	0.992	**1**
	MLE	-	11.849	0.290		1.498	A 5.992	0.238	A 0.752	-	
3P Log-Normal	PPLR (*Mean*)	0	11.848	0.320	18.280%	Inconsistent δ parameter. Reject 3P Log-Normal Distribution.					**4**
	MLE	13,798	11.740	0.317							
2P Weibull	PPLR (*Mean*)	-	161,041	3.791	0.903%	Incorrect Skew Behaviour. Reject 2P Weibull Distribution.					**4**
	MLE	-	161,065	3.826							
3P Weibull	PPLR (*Mean*)	72,364	83,901	1.589	16.223%	3.320	A 5.992	0.243	A 1.013	0.993	**1**
	MLE	80,325	72,189	1.471		1.602	A 3.842	0.294	A 0.898	-	
Stress Level 5:	$\sigma_0 = 540$ MPa	Sample Size N:		28	Sample Skew γ:	0.518	Best Fit Distribution:			**3P Weibull**	
Distribution	Fitting Method (*Rank Equation*)	Distribution Parameter Estimate			Max Difference	χ^2_s	χ^2_c $\alpha = 5\%$	A^2	A^2_c	r	Class
		Threshold δ	Scale σ	Shape λ							
2P Log-Normal	PPLR (*Mean*)	-	12.280	0.325	10.533%	1.566	A 5.992	0.286	A 0.752	0.991	**1**
	MLE	-	12.280	0.294		1.368	A 5.992	0.315	A 0.752	-	
3P Log-Normal	PPLR (*Mean*)	54,037	11.972	0.439	20.553%	1.266	A 3.842	0.237	A 0.673	0.992	**2**
	MLE	68,017	11.871	0.432		1.042	A 3.842	0.270	A 0.607	-	
2P Weibull	PPLR (*Mean*)	-	248,920	3.697	3.235%	Incorrect Skew Behaviour. Reject 2P Weibull Distribution.					**4**
	MLE	-	249,202	3.580							
3P Weibull	PPLR (*Mean*)	110,601	130,134	1.617	15.184%	1.657	A 3.842	0.234	A 0.916	0.993	**1**
	MLE	122,587	112,979	1.458		3.574	A 5.992	0.228	A 0.901	-	
Stress Level 6:	$\sigma_0 = 520$ MPa	Sample Size N:		31	Sample Skew γ:	0.948	Best Fit Distribution:			**2P Log-Normal**	
Distribution	Fitting Method (*Rank Equation*)	Distribution Parameter Estimate			Max Difference	χ^2_s	χ^2_c $\alpha = 5\%$	A^2	A^2_c	r	Class
		Threshold δ	Scale σ	Shape λ							
2P Log-Normal	PPLR (*Mean*)	-	12.932	0.461	10.333%	4.055	A 5.992	0.445	A 0.752	0.986	**1**
	MLE	-	12.932	0.418		2.810	A 5.992	0.386	A 0.752	-	
3P Log-Normal	PPLR (*Mean*)	22,253	12.871	0.489	48.612%	3.012	A 5.992	0.429	A 0.601	0.986	**2**
	MLE	43,304	12.809	0.464		1.831	A 5.992	0.383	A 0.649	-	
2P Weibull	PPLR (*Mean*)	-	506,862	2.630	4.853%	3.535	A 7.815	0.990	R *0.757*	0.968	**4**
	MLE	-	508,269	2.508		3.648	A 7.815	0.904	R *0.757*	-	
3P Weibull	PPLR (*Mean*)	139,199	353,523	1.593	21.187%	9.516	R *3.842*	0.521	A 0.885	0.985	**3**
	MLE	176,620	298,760	1.408		2.686	A 5.992	0.509	A 0.891	-	

2P Log-Normal Distribution

From Tables 4.5 and 4.6, it can be seen that the 2P Log-Normal distribution was predominately a Class 1 distribution across the six stress levels as it was accepted by both GoF tests at $\alpha = 5\%$ with validated distribution parameter estimates (i.e. PPLR and MLE parameter estimates are within 20%). The only instance where the 2P Log-Normal distribution was higher than Class 1 was at Stress Level 2, due to the rejection by the χ^2 GoF test for the PPLR distribution parameter estimates. The 2P Log-Normal distribution also has high r correlation coefficient values across the stress levels. The consistency of the 2P Log-Normal distribution to be a Class 1 distribution suggests that the 2P Log-Normal distribution could provide accurate statistical characterisation of the variability in N_f across the S-N dataset. This observation is in agreement with the existing and commonly held assumption that N_f is 2P Log-Normally distributed [37].

2P Weibull Distribution

The 2P Weibull distribution was classified at all stress levels as Class 4 as shown in Tables 4.5 and 4.6. This classification was as a result of both the PPLR and MLE fitting process producing λ shape estimates that are in excess of $\lambda = 3$, resulting in distributions that will demonstrate symmetric or negative skew [180] at Stress Levels 1 to 5. This contradicts the positive γ sample skew values computed for each dataset. At Stress Level 6, the 2P Weibull distribution was rejected by the A-D test at $\alpha = 5\%$ for both the PPLR and MLE distribution parameter estimates. Therefore, the 2P Weibull distribution does not provide accurate statistical characterisation of the N_f values across the 4340 S-N dataset.

3P Log-Normal Distribution

From Tables 4.5 and 4.6, it can be seen that the 3P Log-Normal distribution was predominately a Class 2 distribution across the 6 stress levels, although it was Class 4 for Stress Level 4 due to inconsistent PPLR and MLE location parameter estimates. Despite having larger r correlation coefficient values compared to the 2P Log-Normal distribution, which suggest an improved fit to the dataset, the percentage difference between the PPLR and MLE distribution parameter estimates typically exceeded the 20% threshold, resulting in unvalidated parameter estimates at Stress Levels 2 to 6. The MLE distribution parameter estimates for the 3P Log-Normal distribution were also rejected by the χ^2 GoF test at $\alpha = 5\%$ for Stress Levels 2 and 3.

The most significant observation regarding the 3P Log-Normal distribution from Tables 4.5 and 4.6 was the instability and inconsistency of the δ threshold parameter estimates. Firstly, it can be observed for Stress Level 4 that the PPLR δ threshold parameter estimate was equal to zero and therefore, the 3P Log-Normal distribution was equivalent to the 2P Log-Normal distribution. In addition, it can be seen that the threshold parameter value did not continually increase for a reducing σ_0 value, as shown in Figure 4.5. It would be expected that the minimum

N_f value defined by the δ value would increase with reducing σ_0 in a similar manner to the mean N_f increasing with reducing σ_0 (i.e. the classical S-N curve response). As can be seen in Figure 4.5, the δ threshold parameter increases from Stress Level 1 to Stress Level 3, but then rapidly decreased and fluctuated across Stress Levels 4, 5 and 6. The instability in the δ threshold parameter and high class numbers means that the 3P Log-Normal distribution should not be used to characterise the N_f values within the 4340 S-N dataset.

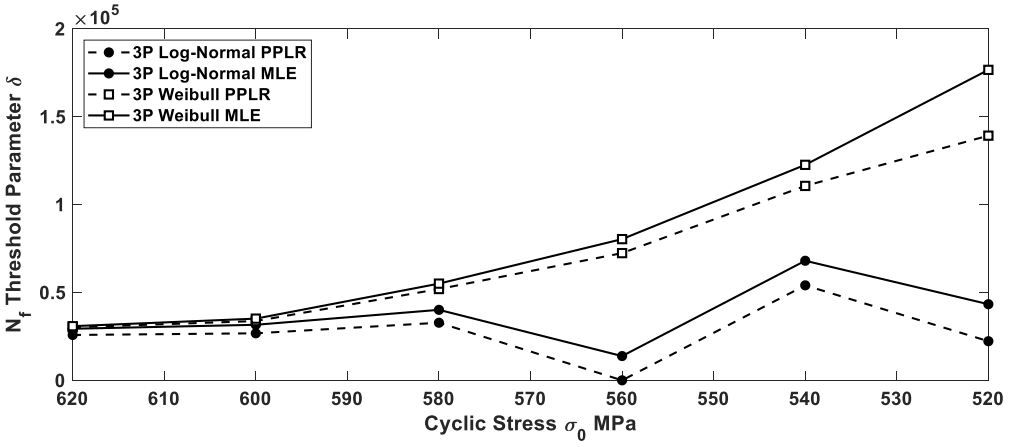

FIGURE 4.5. Variation of the δ threshold parameter with reducing σ_0 for the 3P Weibull and 3P Log-Normal distributions.

3P Weibull Distribution

Regarding the 3P Weibull distribution, Tables 4.5 and 4.6 show that for half of the characterised Stress Levels (3, 4 and 5), the 3P Weibull distribution was a Class 1 distribution, with r correlation coefficients that were higher than the other Class 1 candidate distribution, which was the 2P Log-Normal distribution. Table 4.5 and 4.6 therefore show that the 3P Weibull distribution provided the best-fit for the variability in N_f at half of the stress levels within the S-N dataset. In addition, Figure 4.5 shows that the δ threshold parameter was significantly more stable, showing a continual increase in minimum N_f value for reducing σ_0, compared to the unstable behaviour of the 3P Log-Normal distribution δ threshold parameter.

However, at Stress Levels 1, 2 and 6, the 3P Weibull distribution was classified as either Class 4 or Class 3 and this was expected to be as a result of challenges regarding the fitting of the 3P Weibull distribution. For Stress Level 1, an Exponential distribution was produced by both PPLR and MLE methods (i.e. $\lambda \leq 1$) and the 3P Weibull distribution was therefore rejected due to incorrect skew behaviour. The incorrect skew behaviour is expected to be as a result of the smaller sample size of $N = 10$. At Stress Level 2, PPLR fitting produced a 3P Weibull distribution with a high r correlation coefficient and was accepted by both GoF tests, whilst MLE fitting

produced an Exponential distribution. This suggests that the MLE optimisation process had converged to a local maximum for the 3P Weibull LF. Had the global maximum for the LF been identified, it would be expected that the 3P Weibull distribution would have also been Class 1 and provided the best-fit to the variability in N_f at Stress Level 2. For Stress Level 6, the PPLR-fitted distribution was rejected by the χ^2 GoF test, whilst the MLE-fitted distribution was accepted by both GoF tests. This contradiction between the GoF results for the two fitting methods could be as a result of the ranking equation used within PPLR being only an approximation of the cumulative frequency R_c of the dataset for probability plotting.

Based on the results in Tables 4.5 and 4.6, when the 3P Weibull distribution had been successfully fitted to the S-N dataset with validated distribution parameter estimates, it was seen to have the highest r correlation coefficient from PPLR and should therefore be considered as a final candidate distribution, along with the 2P Log-Normal distribution, for the S-N dataset. The identification of the 3P Weibull distribution providing the most accurate characterisation of the variability in N_f in S-N datasets is supported by the previous findings of Zhao et al [167], Wei et al [168] and Khameneh and Azadi [169].

4.4 Application of Statistical Characterisation to Deterministic Fatigue Analysis

As the selection of the probability distribution type to characterise the variability in N_f is required for both deterministic and probabilistic fatigue design, this section will demonstrate the impact of using the systematic statistical characterisation process on the construction of P-S-N curves as used in deterministic fatigue design. The applicability of results from the systematic statistical characterisation process also demonstrates how activities required for implementing a probabilistic approach can also support the existing deterministic design and analysis approach.

4.4.1 Impact of 3P Weibull Distribution on P-S-N Curves

The first investigation regarding deterministic design considered the N_f value required to achieve a given PoS at each σ_0 stress level for both the 2P Log-Normal and 3P Weibull distributions ($N_{f_{Pos}}$), which is computed using the distribution ICDF. Figure 4.6 shows the 2P Log-Normal and 3P Weibull distributions fitted to the Stress Level 6 N_f values and the presence of the δ threshold parameter can be clearly seen. Figure 4.7 shows the original 4340 steel S-N dataset [25], with the $N_{f_{PoS}}$ values at 99% PoS for both the 2P Log-Normal and 3P Weibull distribution for Stress Levels 2 to 6[3]. A Basquin-type S-N curve [6, 8] was also fitted to the $N_{f_{PoS}}$ values, using minimum fitting (i.e. where all points lie on, or on the conservative side of the S-N curve), to provide a 99% PoS P-S-N curve. The fatigue limit σ_{FL} was defined for 99% PoS based on a mean

[3]Stress Level 1 has been omitted due to the small sample size.

value of σ_{FL} = 457 MPa and a standard deviation of 13 MPa, by applying the 'Probit' method to the 4340 steel S-N dataset [6, 35]. The 99% PoS $N_{f_{PoS}}$ values are also shown in Table 4.7.

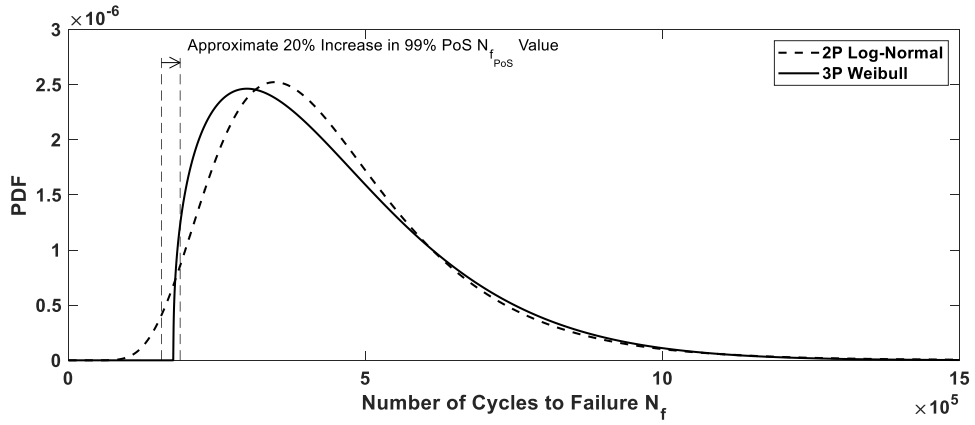

FIGURE 4.6. A comparison of the 2P Log-Normal and 3P Weibull distributions at Stress Level 6.

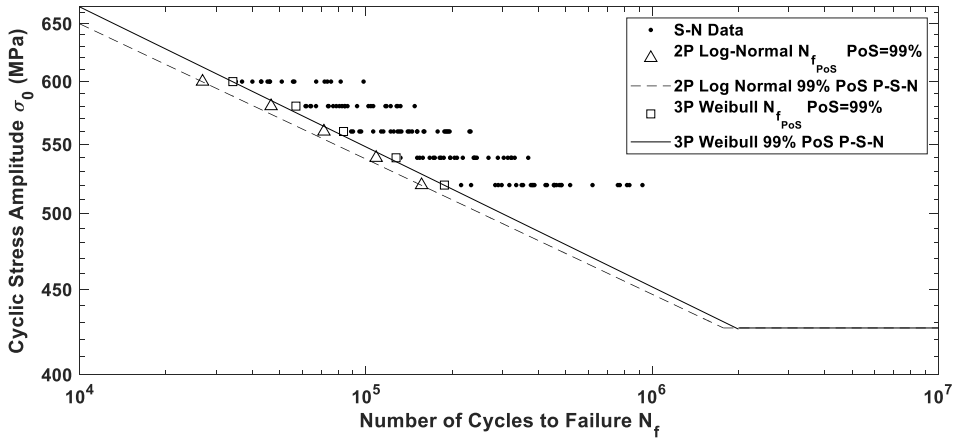

FIGURE 4.7. 99% PoS P-S-N curves constructed using 2P Log-Normal and 3P Weibull S-N dataset for 4340 steel. S-N dataset reproduced with permission from IHS ESDU [25].

It can be seen from Table 4.7 and Figure 4.6 that the 3P Weibull 99% PoS $N_{f_{PoS}}$ values were approximately 20% larger than those of the 2P Log-Normal distribution. This suggests that the 3P Weibull distribution, when successfully fitted to the S-N dataset, provides a reduction in the conservatism of the 99% PoS P-S-N curve of 20%. This can be clearly seen by the 99% PoS P-S-N curves in Figure 4.7, where the 3P Weibull P-S-N curve will estimate higher N_f values than the 2P Log-Normal P-S-N curve at a given σ_0 stress level.

TABLE 4.7. N_f values for 99% PoS P-S-N curves constructed from 2P Log-Normal and 3P Weibull N_f distributions for 4340 steel.

Stress Level	σ_0 (MPa)	99% PoS $N_{f_{PoS}}$ Value		$N_{f_{PoS}}$ Increase for 3P Weibull
		2P Log-Normal	3P Weibull	
2	600	26,854	34,267	27.605%
3	580	46,610	56,291	20.770%
4	560	71,315	83,490	17.072%
5	540	108,560	127,408	17.362 %
6	520	156,426	187,999	20.184%

4.4.2 Impact of 3P Weibull Distribution on Component Safe-Life

In order to further investigate the impact of using 3P Weibull distributions to construct P-S-N curves for deterministic fatigue analysis, a case study was defined in order to quantify the difference in a component safe-life when using P-S-N curves constructed with both 2P Log-Normal and 3P Weibull distributions. The Society of Automotive Engineers (SAE) keyhole benchmark shown in Figure 4.8 was used as a representative component geometry, assuming a stress concentration of $K_t = 3$ at the keyhole notch [181]. The SAE 'transmission' load-time history also shown in Figure 4.8 was used as the case study loading spectrum [181], where 'P_p' is the applied loading and 'M_p' is the corresponding moment. The Basquin-type 99% PoS P-S-N curves shown previously in Figure 4.7 were used to represent the cyclic material properties of the component.

[REDACTED]

FIGURE 4.8. SAE keyhole geometry and 'transmission' load-time history [181, 182].

Fatigue damage accumulation was computed using the S-N fatigue analysis process described in Chapter 1. The accumulated damage D_T from Miner's rule when using each P-S-N curve is shown in Table 4.8. Assuming a failure criterion of $D_{fail} = 1$, the component safe-life could be

computed as the inverse of D_T (i.e. the number of times that the 'transmission' loading spectrum could be applied prior to component retirement) and is shown in Table 4.8 for both the 2P Log-Normal and 3P Weibull P-S-N curves.

TABLE 4.8. Fatigue analysis results for the SAE keyhole geometry case study when using 2P Log-Normal and 3P Weibull N_f distribution P-S-N curves.

Fatigue Analysis Result	99% PoS $N_{f_{PoS}}$ Value		Change for 3P Weibull
	2P Log-Normal	3P Weibull	
Accumulated Damage D_T	8.95×10^{-5}	7.28×10^{-5}	-18.569%
Safe-Life	11,172	13,739	22.977%

From Table 4.8, it can be seen that the use of the 3P Weibull P-S-N curve resulted in a 23% increase in the component safe-life value, which is consistent with the 20% increase in 99% PoS $N_{f_{PoS}}$ values from the P-S-N curves shown previously in Table 4.7. Therefore, the 3P Weibull distribution has also been shown to reduce the conservatism in component safe-life values compared to the 2P Log-Normal distribution.

4.4.2.1 Advantages and Challenges of the 3P Weibull Distribution for P-S-N Curves

The use of the 3P Weibull distribution to statistically characterise the variability in N_f values within the 4340 steel S-N dataset was shown to reduce conservatism within both P-S-N curves and component safe-life values by approximately 20%. This reduction in conservatism could result in components with longer design safe-life values, or permit higher cyclic stresses within the component. Higher component stresses could result in reduced component mass (due to smaller required sectional areas) and therefore, the use of 3P Weibull distributions to characterise the variability in N_f within S-N datasets could increase the efficiency of components designed using a deterministic safe-life fatigue analysis process. Alternatively, the 2P Log-Normal distribution was shown to also accurately represent the variability in N_f and therefore, could be retained if designers wish to incorporate conservatism into the design of safety-critical components.

However, the utilisation of the 3P Weibull distribution to characterise the variability in N_f for the construction of P-S-N curves faces challenges regarding the fitting and GoF testing of 3P Weibull distributions. As demonstrated in Section 4.3.2, the fitting of 3P Weibull distributions can be sensitive to small sample sizes and can lead to poorly-fitting distributions as a result of incorrect convergence of the MLE fitting process. In addition, computationally-expensive bootstrap methods must be used to estimate GoF test critical values. This is further compounded if the 3P Weibull distribution was to be used to characterise the variability in N_f for S-N datasets that contain censored or run-out data points, as such approaches are reliant on LF functions that are significantly more complicated to evaluate [33, 164].

Concerning deterministic fatigue design, the construction of P-S-N curves also requires the definition of the confidence level 'CL'. As tabulated values (or closed-form solutions) are not available for constructing CL values for 3P Weibull distributions, a parametric bootstrap

approach would also be required [183], further increasing the computational expense of utilising 3P Weibull distributions to construct P-S-N curves.

4.5 Application of Statistical Characterisation Results to the Probabilistic Fatigue Methodology

In the context of probabilistic design, the purpose of statistically characterising the variability in N_f is to represent the variability observed in S-N datasets within the probabilistic fatigue methodology. As a result, an approach is required to represent the variability within the S-N datasets (i.e. data points from material specimen testing) within the repeated evaluations of the existing fatigue analysis process. This section demonstrates how S-N dataset variability is propagated through the probabilistic fatigue methodology.

4.5.1 Statistical Simulation of S-N Curves

In order to represent the variability present in the S-N dataset within the probabilistic fatigue methodology, an approach based upon the statistical simulation of P-S-N curves using randomly sampled PoS values was employed. Such an approach is widely used in MCS-based probabilistic fatigue methodologies, including work performed by Ocampo et al and Zhu et al [39, 94]. Within the MCS-SSI probabilistic analysis method, a new P-S-N curve with a randomly sampled PoS value will be generated. The process for achieving this is as follows:

1. **Randomly Sample PoS:** A uniform random number generator is used to randomly sample a value 'RN' between $[0,1]$. This value represents $1-\frac{PoS}{100}$, therefore defining the randomly sampled PoS value for the P-S-N curve.

2. **ICDF Sampling of N_f:** Using the value of RN, the ICDF for N_f at each σ_0 level within the S-N dataset is evaluated. This generates a random sample of N_f at each σ_0.

3. **ICDF Sampling of σ_{FL}:** The RN value is also used to perform ICDF sampling of the σ_{FL} value.

4. **Fitting of P-S-N Curve:** The existing S-N curve type used for deterministic fatigue analysis [163] is then fitted to the randomly sampled N_f and σ_{FL} values.

The above sequence of steps is repeated for each MCS iteration, each time producing a new P-S-N curve. Over repeated MCS iterations, the variability present within the S-N dataset (in the form of the statistically characterised N_f values at each σ_0 level and σ_{FL}) will be propagated through to the collection of statistically simulated S-N curves.

4.5.1.1 Demonstration and Verification of Approach

Based upon the statistical characterisation of the 4340 steel S-N dataset performed using the systematic statistical characterisation process, the 2P Log-Normal distribution can be used to represent the variability in the N_f values. The distribution parameters of the 2P Log-Normal distributions are shown for each σ_0 stress level in Table 4.9. σ_{FL} is characterised as a Normal distribution with a mean value of 457 MPa and a standard deviation of 13 MPa.

TABLE 4.9. Statistical characterisation of N_f for the 4340 steel S-N dataset as used to statistically simulate P-S-N curves.

Stress Level	σ_0 (MPa)	Distribution Type	N_f Distribution Parameters	
			σ	λ
1	620	2P Log-Normal	10.645	0.300
2	600	2P Log-Normal	10.905	0.351
3	580	2P Log-Normal	11.394	0.309
4	560	2P Log-Normal	11.848	0.320
5	540	2P Log-Normal	12.280	0.325
6	520	2P Log-Normal	12.932	0.417

The S-N curve type for the 4340 steel S-N dataset used within deterministic design is a 'power law' in the form shown in Equation 4.8 [25], where 'P' and 'q' are the S-N curve parameters to fit:

$$\sigma_0 = PN_f^q + \sigma_{FL} \tag{4.8}$$

Figure 4.9 shows the statistical generation of five P-S-N curves, with randomly sampled PoS values of 2.7%, 20.0%, 56.8%, 82.7% and 91.6% for the 4340 steel S-N dataset.

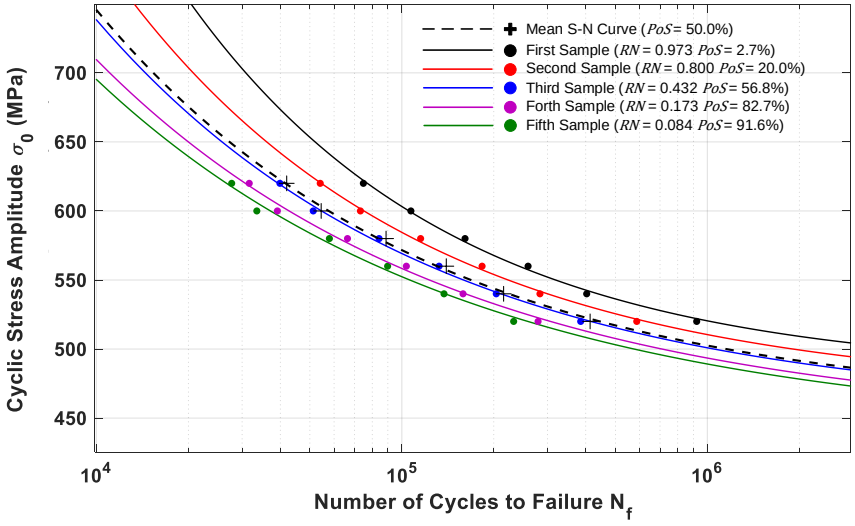

FIGURE 4.9. Statistical simulation of five P-S-N curves.

It can be seen from Figure 4.9 that it is assumed that the N_f values across different σ_0 stress levels are perfectly correlated (i.e. a material specimen that demonstrates a 'poor' fatigue life at one stress level will also demonstrate a 'poor' fatigue life at another stress level). In addition, it is assumed that the σ_{FL} is also perfectly correlated with the N_f values (i.e. a material specimen with a low fatigue life will also demonstrate a low σ_{FL}). Whilst these are the assumptions currently made during the construction of P-S-N curves for deterministic design [6], previous work within the literature suggests that in reality, the correlation between N_f values at different stress levels (and likewise between N_f values and σ_{FL}) would lie somewhere between statistically independent (i.e. perfectly uncorrelated) and perfectly correlated [69]. However, this correlation is yet to quantified due to the destructive nature of material specimen testing.

Increasing the number of statistically simulated P-S-N curves to 100 results in Figure 4.10. As both the N_f values and σ_{FL} are characterised by distributions that demonstrate central tendency (i.e. a 'peak' in probability density about the mean value), it is expected that the statistically simulated S-N curves will also cluster around the mean S-N curve. This can be observed in Figure 4.10, which demonstrates a higher density of P-S-N curves around the mean S-N curve. This qualitatively suggests that the underlying variability in the S-N dataset is being propagated through to the statistically simulated P-S-N curves.

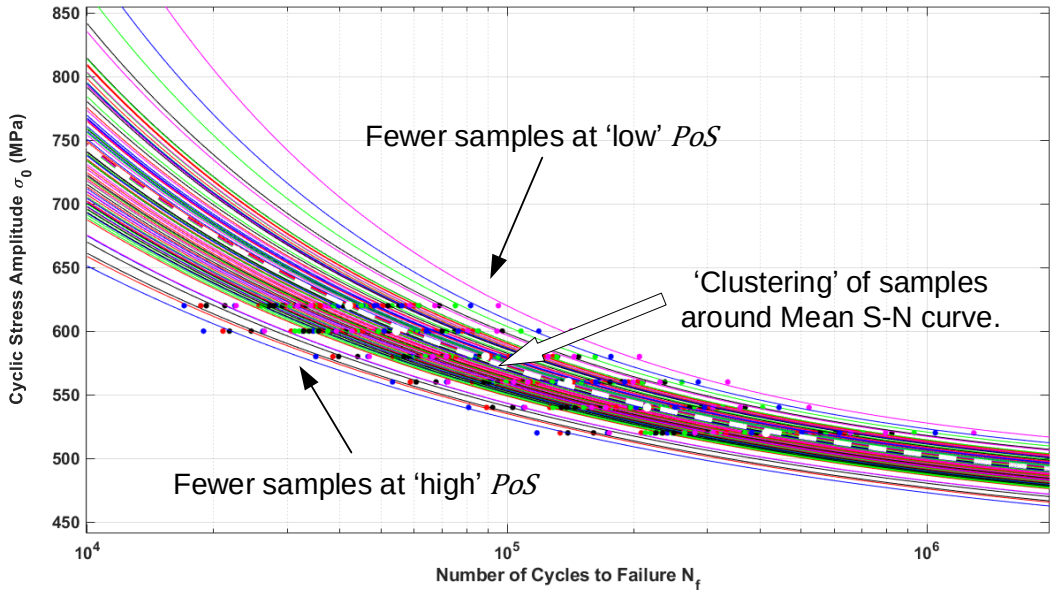

FIGURE 4.10. Statistical simulation of 100 P-S-N curves.

In order to verify that the underlying variability in the S-N dataset is being propagated through to the statistically simulated P-S-N curves, the variability in the N_f values 'read-off' from the statistically simulated P-S-N curves '$N_{f_{S-N}}$' can be characterised. Statistical simulation of 10,000 P-S-N curves was performed and the $N_{f_{S-N}}$ values were recorded from each S-N curve at each of the original σ_0 stress levels within the S-N dataset. The variability in the $N_{f_{S-N}}$ values was then characterised using a 2P Log-Normal distribution, resulting in the distribution parameter values shown in Table 4.10.

TABLE 4.10. Verification of the P-S-N statistical simulation process by comparing N_f 2P Log-Normal distribution parameter estimates for the original S-N dataset and values 'read-off' from the 10,000 statistically simulated P-S-N curves.

(Stress Level) σ_0	(1) 620 MPa		(2) 600 MPa		(3) 580 MPa	
Distribution Parameter	σ	λ	σ	λ	σ	λ
S-N dataset N_f	10.645	0.300	10.905	0.351	11.394	0.309
10,000 P-S-N $N_{f_{S-N}}$	10.635	0.322	10.961	0.318	11.335	0.317
Percentage Difference	**-0.093%**	**7.370%**	**0.509%**	**-9.521%**	**-0.514%**	**2.690%**
(Stress Level) σ_0	(4) 560 MPa		(5) 540 MPa		(6) 520 MPa	
Distribution Parameter	σ	λ	σ	λ	σ	λ
S-N dataset N_f	11.848	0.320	12.280	0.325	12.932	0.417
10,000 P-S-N $N_{f_{S-N}}$	11.778	0.325	12.319	0.349	13.016	0.412
Percentage Difference	**-0.591%**	**1.575%**	**0.315%**	**7.405%**	**0.652%**	**-1.214%**

It can be seen that when comparing the original N_f distribution parameters from the original S-N dataset and the $N_{f_{S-N}}$ distribution parameters from the 10,000 P-S-N curves in Table 4.10, that the percentage difference for the distribution parameters at all stress levels is below 10%. It is suggested that the slight deviation in the distribution parameter estimates is due to the use of an assumed S-N curve shape, rather than as a result of the statistical simulation process. The use of an assumed S-N curve shape can lead to fitted P-S-N curves lying away from the randomly sampled N_f values as shown previously in Figure 4.9, resulting in slight differences in the variability in $N_{f_{S-N}}$ values compared to the N_f of the S-N dataset. Therefore, as the difference in distribution parameter estimates is as a result of the assumed S-N curve type (which is an assumption required for deterministic fatigue design and analysis), the statistical simulation process for P-S-N curves successfully propagates the underlying variability in S-N datasets into statistically simulated P-S-N curves.

Finally, as the systematic statistical characterisation process demonstrated that the 3P Weibull distribution also provides accurate characterisation of the variability in N_f within the 4340 steel S-N dataset, the P-S-N statistical simulation process can also be constructed using 3P Weibull distributions for N_f. The impact on the probabilistic fatigue methodology of selecting 3P Weibull distributions to characterise the variability in N_f will be investigated in the case studies in Chapters 7 and 8.

4.6 Assessment of Systematic Statistical Characterisation Process

Following the application of the results from the S-N dataset characterisation to both deterministic and probabilistic approaches to fatigue design, a review of the proposed process can be made. Firstly, the application of the systematic statistical characterisation process has highlighted how a reduction in the conservatism within existing deterministic fatigue analysis processes can be achieved with improved statistical characterisation of S-N datasets, as facilitated by the systematic statistical characterisation process.

Concerning a probabilistic approach to fatigue design, the systematic statistical characterisation process, through the use of the classifications defined in Tables 4.1 and 4.2, permitted the large amount of information related to distribution fitting and testing for a dataset (approximately 25 individual elements for each candidate distribution) to be synthesised into a single class number, simplifying the distribution selection process. The use of a systematic statistical characterisation process therefore assists in overcoming the *required knowledge* blocker to a probabilistic approach to fatigue design, by consolidating the required statistical characterisation methods into a systematic process. In addition, the use of distribution selection guidelines related to the distribution classifications can support engineers with a limited statistical background in down-selecting the candidate distribution that most accurately represents the variability in a design parameter.

The application of the systematic statistical characterisation process to an S-N dataset also enabled the identification of the 3P Weibull distribution as the most accurate distribution to characterise the variability in N_f values. As a result, the statistical characterisation process also supports the overcoming of the *accuracy of data characterisation* blocker, by providing a systematic process to ensure the most accurate candidate distribution type is selected for a design parameter. In a similar manner, the utilisation of the systematic statistical characterisation process also permitted the challenging of the long held assumption that the variability of N_f within S-N datasets is best characterised using a 2P Log-Normal distribution. As a result, the development and implementation of the systematic statistical characterisation process enables existing assumptions within deterministic analysis processes to be challenged. Both of these attributes result in a more accurate statistical characterisation of the variability in design parameters, ultimately contributing to improved accuracy of p_f estimates generated using the probabilistic fatigue methodology.

4.7 Summary

Significant variability is observed in the number of cycles to failure N_f for a given stress level σ_0 within the S-N datasets used for fatigue design and analysis. The variability in N_f is currently characterised using a limited range of distributions, including 2P Log-Normal and 2P Weibull

distributions. However, the selection of the distribution type to statistically characterise N_f is often performed out of a desire for mathematical simplicity. In addition, it has been proposed in the literature that 3P distributions, which introduce a δ threshold parameter, could better characterise the variability in N_f, through the defining a minimum number of cycles to failure for a material at a given stress level.

Existing statistical characterisation practices only perform limited validation of selected probability distributions. When coupled with the limited statistical background that engineers typically possess, it is evident that additional guidance is required to ensure that the most accurate probability distribution type is selected to represent the variability in design parameters within a probabilistic fatigue methodology. As a result, a systematic statistical characterisation process was developed, based upon multiple distribution fitting and testing methods.

The application of the systematic statistical characterisation process to an S-N dataset for 4340 steel demonstrated that the 3P Weibull distribution provided the most accurate characterisation of the variability in N_f values. The utilisation of 3P Weibull distributions to characterise the variability in N_f within deterministic fatigue design also demonstrated that conservatism could be reduced in both P-S-N curves and a component safe-life by approximately 20%.

Concerning a probabilistic approach to fatigue design, the systematic statistical characterisation process enables the most accurate distribution type to be selected for design parameters, ensuring the generation of accurate p_f values and as a result, overcoming the *accuracy of data characterisation* blocker. Other blockers to probabilistic design approaches that can also be overcome through utilisation of the process, are highlighted in Table 4.11.

TABLE 4.11. The blockers to probabilistic design approaches overcome by defining and implementing a systematic statistical characterisation process.

Blocker	Blockers overcome due to systematic statistical characterisation process
Computational Expense	N/A
Required Assumptions of Existing Process	N/A
Availability of Data	N/A
Accuracy of Data Characterisation	• Enables a wide range of candidate distributions to be considered and down-selects to the most accurate distribution type. • Permits the challenging of long held statistical assumptions regarding design parameters.
Required Knowledge	• Consolidates required statistical characterisation methods into a systematic process. • Supports engineers with a limited statistical background by providing distribution down-selection guidance.

The systematic statistical characterisation process consolidates the methods required for statistical characterisation into a single and systematic process, reducing the knowledge required to implement such processes. In addition, the systematic statistical characterisation process supports engineers with a limited statistical background by providing down-selection guidance, to ensure that the most accurate candidate probability distribution type is selected. Both of these attributes of the process contribute to overcoming the *required knowledge* blocker to a probabilistic approach to design.

The accurate statistical characterisation of the 4340 S-N dataset therefore enabled the statistical simulation of P-S-N curves within the probabilistic fatigue methodology, which successfully propagates the variability within the S-N datasets into the probabilistic fatigue analysis method.

CHAPTER 5

LANDING GEAR LOAD-TIME HISTORIES FROM BIG-DATA SOURCES

Landing gear loads demonstrate variability in the occurrence and sequencing of ground manoeuvres, along with variability in the loading magnitude associated with each ground manoeuvre. Whilst extensive characterisation of the variability in loading magnitudes is currently performed within the existing deterministic safe-life fatigue analysis process, a probabilistic fatigue methodology would also require characterisation of the variability in ground manoeuvre occurrence and sequencing. Current practice for characterising the variability in aircraft ground manoeuvres requires in-service loads monitoring of aircraft to be performed. Unfortunately, as such studies are typically limited to single airframes due to the expense of loads monitoring, only limited data is currently available to characterise the variability in ground manoeuvre occurrences. In addition, data is not currently available regarding the variability of ground manoeuvre sequencing observed for aircraft in-service. However, recent advances during the 'digital age' of the aerospace industry have resulted in 'big-data' sources becoming available, which provide the necessary data to characterise the variability in aircraft ground manoeuvre occurrence and sequencing, based upon the 'real-time' tracking of a global aircraft fleet.

This chapter presents novel algorithms used to identify and characterise ground manoeuvres from the real-time tracking of aircraft using Automatic Dependent Surveillance-Broadcast transponders. This original work represents the first application of such datasets to support aircraft structural design. Through the generation of statistics concerning aircraft ground manoeuvre occurrence and sequencing variability, load-time histories can be statistically simulated for landing gear structural assemblies. Based on an assessment of the impact of big-data sources for landing gear load-time histories on both deterministic and probabilistic fatigue design methodologies, this chapter aims to explore whether the exploitation of big-data sources can help to overcome the current blockers to a probabilistic approach to design.

5.1 Variability in Landing Gear Loads

The loads applied to landing gear include vertical, side and drag loads from all ground manoeuvres during pushback, taxi, takeoff, touchdown and the landing roll. Landing gear loads are typically defined as 'global' loads at the tyres using load factors. Load factors are measured in units of gravitational acceleration 'g' and are defined in three directions, 'n_x' (drag), 'n_y' (side) and 'n_z' (vertical) as shown in Figure 5.1.

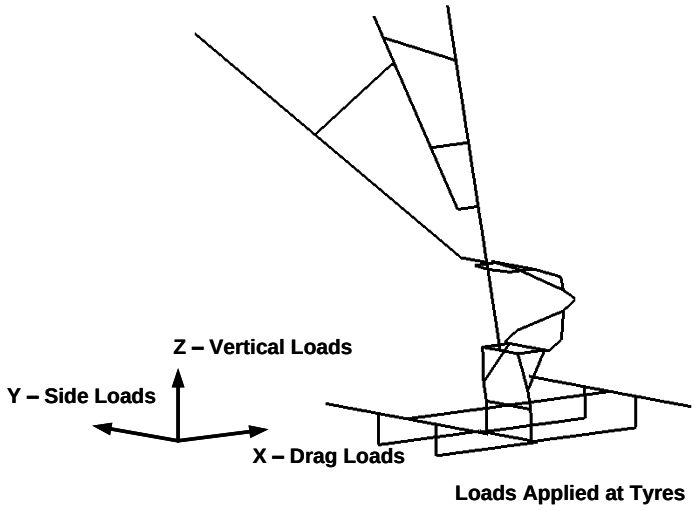

FIGURE 5.1. Landing gear loading directions.

Across a single flight, the landing gear is exposed to many different types of ground manoeuvres, which result in different combinations of drag, side and vertical loads on the landing gear [12, 14]. A compilation of the typical loads that must be accounted for during fatigue design is provided in Table 5.1. Load factors can be converted to the global drag 'F_X', side 'F_Y' and vertical 'F_Z' loads (in Newtons, N) applied to the landing gear, based upon the aircraft mass 'M', using Equations 5.1 through 5.3. It should be noted that the unloaded 'static' condition of the landing gear on the ground is 0 g for both drag and side loads and 1 g for vertical loads. After takeoff, the vertical load factor reduces to 0 g.

$$F_X = n_x \times M \tag{5.1}$$

$$F_Y = n_y \times M \tag{5.2}$$

$$F_Z = (1 + n_z) \times M \tag{5.3}$$

Table 5.1: Typical landing gear loads from ground manoeuvres that must be accounted for when performing fatigue design and analysis [12, 14].

Loading Type	Description of Loading
Turns	Turns occur whilst the aircraft is taxiing before takeoff and after landing and includes entry and exit to the runway. Turns result in side loads and torsional loads on the landing gear. Multiple turns can occur within a single flight.
Braking	Braking occurs whilst the aircraft is taxiing before takeoff and after landing and is performed to decelerate prior to entering a turn, or bringing the aircraft to a stop or 'holding-short' of runways or occupied taxiways. Braking results in drag loads being applied to the landing gear. Multiple braking actions can occur within a single flight.
Taxiing	During taxiing, 'bump' vertical loads can be applied to the landing gear. See below.
Bump Loads	Bump loads are vertical loads applied to the landing gear as it taxis over rough surfaces or obstacles. Bump loads can occur whilst taxiing (including turning and braking) and during the takeoff and landing rolls. Multiple bump loads can occur within a single flight.
Engine Run-up	Prior to commencing the takeoff roll, the engines will be spooled-up with the landing gear brakes on. The engine run-up results in landing gear drag and vertical loads.
Takeoff Roll	As the aircraft accelerates down the runway, bump loads may be experienced due to the roughness of the runway surface (or other items such as runway centre-line lights). Side loads may also be encountered due to crosswinds.
Takeoff Rotation	During rotation, the vertical loads on the landing gear will change.
Landing Touchdown	Landing touchdown will result in large vertical loads being applied to the landing gear. Landings can be symmetrical (i.e. both landing gear contact the runway at the same time) or asymmetrical (i.e. one landing gear contacts the runway first). Side loads can also occur during the landing touchdown, as a result of drift during touchdown, which may be caused by crosswinds.
Spin-up and Spring-back	'Spin-up' is the drag force associated with the rotational acceleration of the tyres from stationary to the landing speed of the aircraft. During spin-up, the landing gear assembly deflects rearwards and the resulting elastic energy is then released during 'spring-back' once the tyres have spun-up to the required rotational speed. Spring-back results in a force applied to the landing gear in the opposite direction to the spin-up drag force (i.e. in the direction of the aircraft movement).
Lift Dump	Spoilers are deflected on the upper surface of the wing to reduce the lift of the wing after touchdown to ensure that 'weight-on-wheels' is achieved to support braking. Therefore, the deployment of spoilers increases the vertical load on the landing gear.
Landing Roll	During the landing roll, large braking forces will be applied to the landing gear, through wheel brakes, thrust reversers and spoiler deployment. The landing roll results in large drag loads on the landing gear. Bump loads due to the runway surface may also occur.
Pushback and Turn onto Stand	Typically on departure from the gate, the aircraft must be reversed using a ground tug. Pushback results in drag loads acting on the main landing gear and nose landing gear. Taxiways are typically arranged perpendicular to the gate and therefore, the pushback may also require a turn to be performed in reverse. Following the flight, the aircraft returns to the gate under its own power. Often a tight turn is required to leave the taxiway to align with the arrival gate.
Towing	Following a flight, aircraft may need to be repositioned (e.g. to another gate, maintenance hangar, etc.) and this is achieved using a ground tug.
Braked Turns and Pivot Turns	Braked turns will introduce drag loads during turns. Braked turns are often performed when a tight turn is required, resulting in one main landing gear remaining stationary as the aircraft 'pivots' about the stationary landing gear. Pivoting can result in large torsional loads within the stationary landing gear.
Extension and Retraction	Loads will be applied in discrete locations on the landing gear (e.g. retraction actuator mounts) as the gear is retracted and extended.
Self-excited Oscillations	Landing gear can demonstrate often complex dynamic loading under certain conditions. These often result in large and rapid torsional loads ('shimmy').

Within the fatigue design and analysis of landing gear, load-time histories are constructed that detail the sequence of the loads (in terms of the load factors) for the design safe-life of the landing gear [9]. Due to the nature of aircraft operations, the loads that the landing gear will carry in-service will vary significantly from flight-to-flight [1, 14]. The variability present within the in-service landing gear loads can be decomposed into the following three areas, as visualised in Figure 5.2:

1. Loading magnitude for a given ground manoeuvre (e.g. how 'hard' a landing is due to variability in the aircraft touchdown rate [184]).

2. Manoeuvre occurrence (e.g. how many left turns are performed during each taxi phase).

3. Manoeuvre sequencing (e.g. the probability that a right turn will follow a left turn).

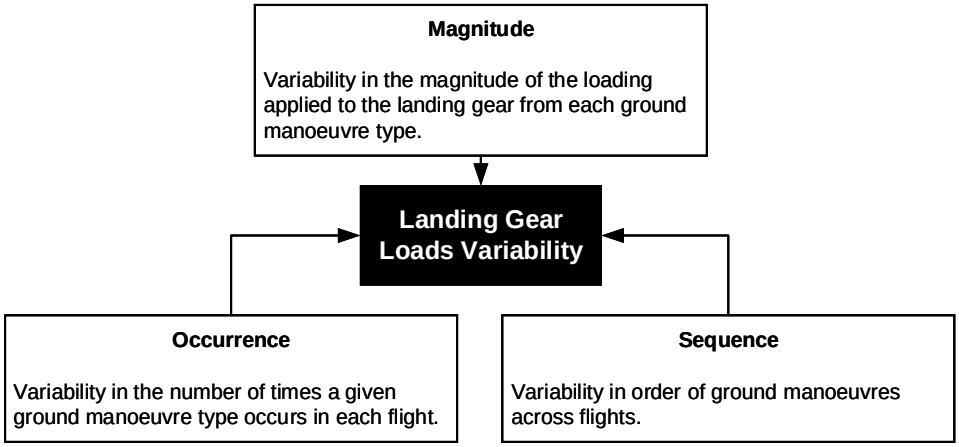

FIGURE 5.2. Sources of variability in landing gear loads.

Within the existing practice for the construction of load-time histories (also known as the load spectrum) in deterministic fatigue design and analysis, variability in the loading magnitude is represented in the form of exceedance curves for each ground manoeuvre type [12, 14]. Figure 5.3a shows an example of an exceedance curve, which provides the expected load factor values for a ground manoeuvre and the number times a higher load factor is expected to be observed (known as the exceedance).

Exceedance curves are then partitioned in a process known as 'blocking', which identifies the number of repetitions of specific load factor values for each manoeuvre type, as shown in Figure 5.3b [186, 187]. An assumed sequence of manoeuvres is then used to construct the load-time history. In some instances, a standardised load spectrum may be employed for the fatigue design and analysis of landing gear components [188].

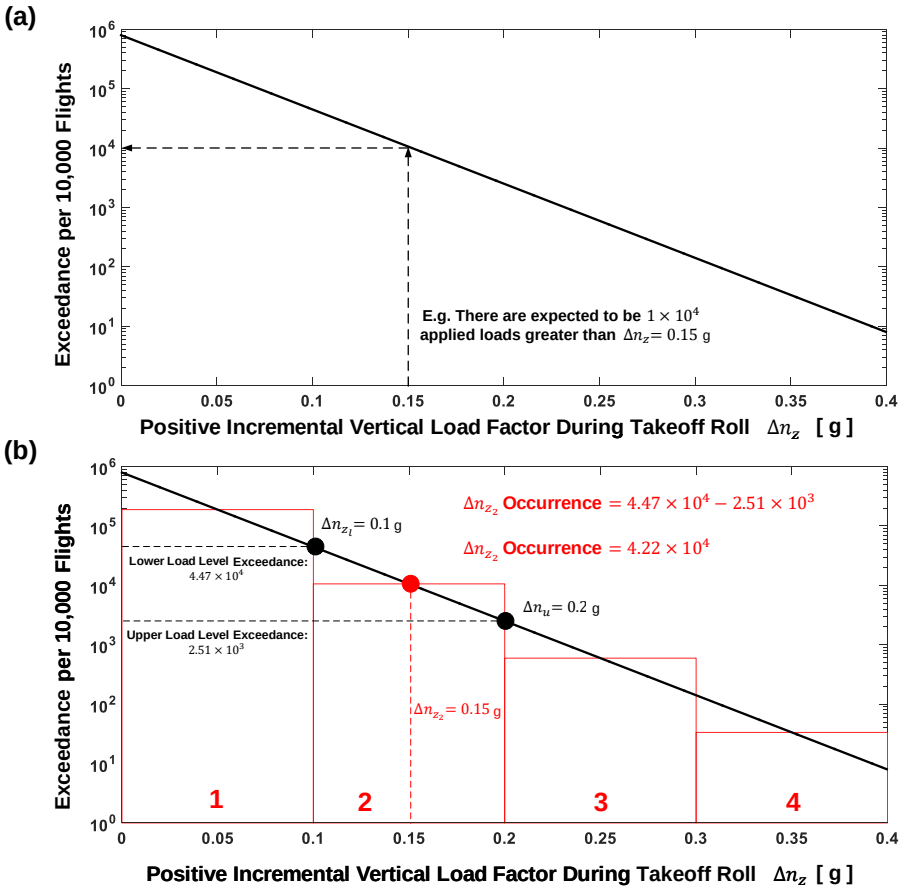

FIGURE 5.3. An example of an (a) exceedance curve and (b) blocking approach [185].

5.1.1 Limitations of Existing Practice

Whilst the variability in the loading magnitude for ground manoeuvres is currently well-characterised and widely incorporated into the existing deterministic fatigue analysis process, significant assumptions must be made regarding the variability of ground manoeuvre occurrence and sequencing within the construction of landing gear load spectra and load-time histories [134, 188, 189]. A visualisation of a typical assumed manoeuvre sequence is shown in Figure 5.4.

The variability in both ground manoeuvre occurrence and sequencing is a direct result of the aircraft taxi routes at departure and arrival airports and as a result, is dependent on a significant number of factors, not limited to:

- Departure and arrival airport.
- Airport geometry and aircraft compatibility.
- Weather (for takeoff/landing runway direction).

- Airport traffic and local air traffic control taxi procedures.
- The aircraft operator's typical gate locations.

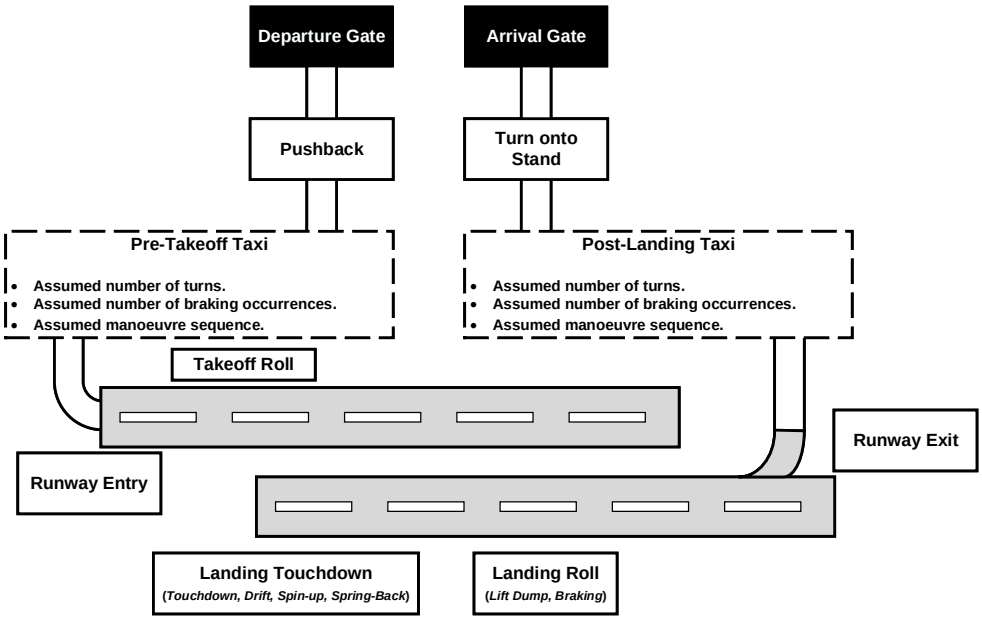

FIGURE 5.4. An example of an assumed ground manoeuvre sequence.

It is therefore anticipated that the ground manoeuvre occurrence and sequencing for aircraft in routine service will show significant variability. However, the variability in ground manoeuvre occurrences has only been characterised to a limited extent in previous studies. Previous studies, based on in-service loads monitoring of individual aircraft, only provide average values of ground manoeuvre occurrences (e.g. 4 turns during pre-takeoff taxi) and do not provide information regarding the per-flight variability of ground manoeuvre occurrences [12, 14, 188]. In addition, there is currently no data in the public domain that characterises the variability in ground manoeuvre sequencing.

As a result of the limited data to characterise the variability in ground manoeuvre occurrence and sequencing, additional data is required to completely represent the variability present in landing gear loads within the probabilistic fatigue methodology. The inclusion of ground manoeuvre occurrence and sequencing variability will increase the accuracy of the p_f estimates for landing gear components assessed using the probabilistic fatigue methodology. The statistical simulation of landing gear load-time histories will permit the variability in loading magnitude, manoeuvre occurrence and manoeuvre sequence to be incorporated into the probabilistic fatigue methodology.

Concerning the existing safe-life fatigue analysis process that is repeatedly evaluated by the probabilistic methodology, the inclusion of manoeuvre occurrence and sequencing variability can

increase the accuracy of the damage values estimated using Miner's rule. The 'rainflow' counting method utilised within the safe-life fatigue analysis process extracts the cyclic stress amplitudes for a component based upon the order in which they occur as a result of the sequence of loads within the load-time history [7, 9]. As a result, the removal of the need to assume a standard sequence of manoeuvres for the construction of the load-time history, will result in load-time histories that are more representative of the in-service loading of landing gear components. This improved representation of manoeuvre and load sequencing will lead to more accurate stress cycles extracted by rainflow counting, ultimately resulting in more accurate D_T damage values from Miner's rule. This in turn will result in more accurate p_f estimates when implementing the probabilistic fatigue methodology, as a result of a more representative fatigue analysis process.

Finally, the generation of data regarding the variability in ground manoeuvre occurrence and sequencing can provide validation of the existing assumptions required to construct landing gear load spectra and load-time histories for deterministic fatigue design and analysis.

The remainder of this chapter details a novel data collection study concerning the variability in aircraft ground manoeuvre occurrence and sequencing based upon a 'big-data' source. The characterisation of the variability in manoeuvre occurrence, sequencing and loading magnitude is then incorporated into a process that statistically simulates load-time histories for aircraft landing gear.

5.2 Big-Data Sources for Aircraft Ground Manoeuvres

During the digital age of the aerospace industry, the availability of 'real-time' data from in-service aircraft has grown considerably [58, 190]. While in-service data was typically only available from specifically instrumented aircraft (e.g. FAA statistical loads [191]), recent advances have resulted in aircraft tracking data becoming available within the public domain for entire aircraft fleets. Automatic Dependent Surveillance-Broadcast (ADS-B) transponders provide 'real-time' information regarding a number of parameters of an in-service aircraft across a flight [192]. The ADS-B transponder is interrogated by a ground-based receiver and the ADS-B transponder 'broadcasts' a wide range of data, including aircraft speed, altitude, heading and location [192].

Flightradar24® is an online service that performs tracking of aircraft based upon ADS-B transponder data [154]. Flightradar24® provides coverage of civil aircraft fleets across the globe, and generates high-fidelity aircraft tracks across complete aircraft flights. An example ground track for a flight from Flightradar24® is shown in Figure 5.5 [154].

It can be observed in Figure 5.5 that the ground track has sufficient fidelity to identify the taxi route of the aircraft, including all taxiway turns. Typically, ground tracks are available from aircraft pushback to the takeoff roll and from the landing roll to the aircraft returning to the stand/gate. Therefore, ADS-B data files provide a big-data source for gathering data relating to landing gear ground manoeuvres. The ground tracks are generated from comma separated

variable (.csv) files, which contain the aircraft position in latitude and longitude, heading, ground speed in knots (Kn) and calibrated altitude in feet (ft) [154]. Within the .csv files, each data row represents a new ADS-B broadcast point, marked by a unique timestamp.

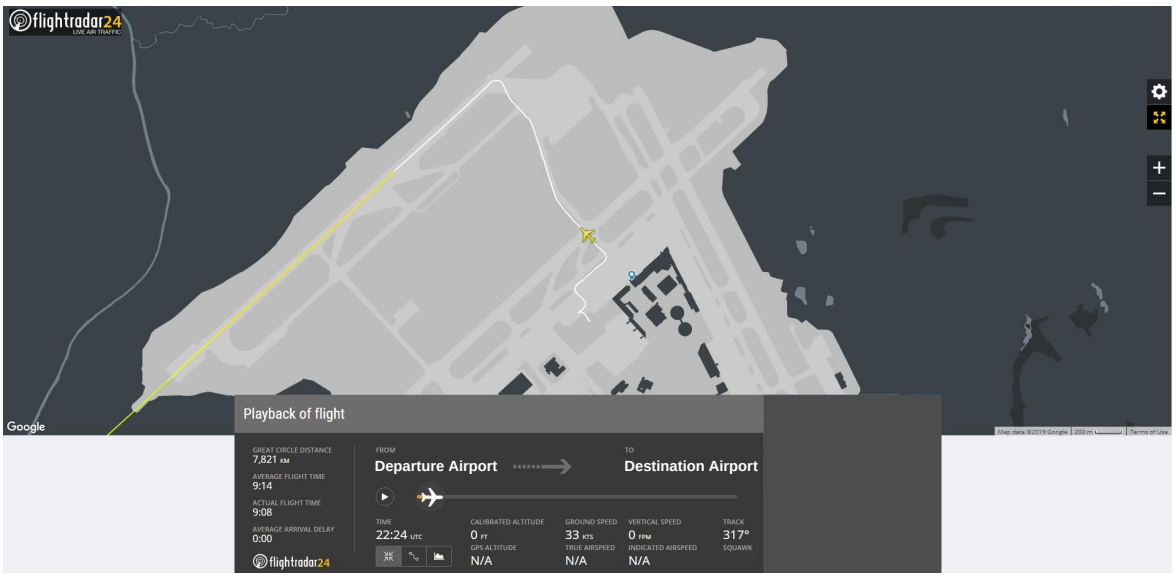

FIGURE 5.5. An example of a Flightradar24® ADS-B ground track, reproduced with permission from Flightradar24® [154].

Figure 5.6 shows a time plot for how the aircraft heading (referred to as 'direction' in the .csv files) and speed change with respect to the timestamp (i.e. each broadcast from the ADS-B transponder and each row in the .csv data file). The x-axis in Figure 5.6 only represents the sequence of broadcasts and is not representative of the time between each ADS-B broadcast. Heading/direction and speed changes can be clearly observed in Figure 5.6 and these represent the ground turns and braking applications performed by the aircraft during that specific flight.

Due to the data contained within the Flightradar24® ADS-B .csv data files, it is proposed that the following information can be extracted for each flight defined by an ADS-B .csv data file:

- Number of turns for pre-takeoff and post-landing taxi phases.
- Number of braking actions for pre-takeoff and post-landing taxi phases.
- Direction of pushback from gate.
- Direction of turn onto stand for arrival at stand/gate.
- Runway entry direction and type (e.g. standard or backtrack pivoting entrance).
- Runway exit direction and type (e.g. low speed or high speed exit).

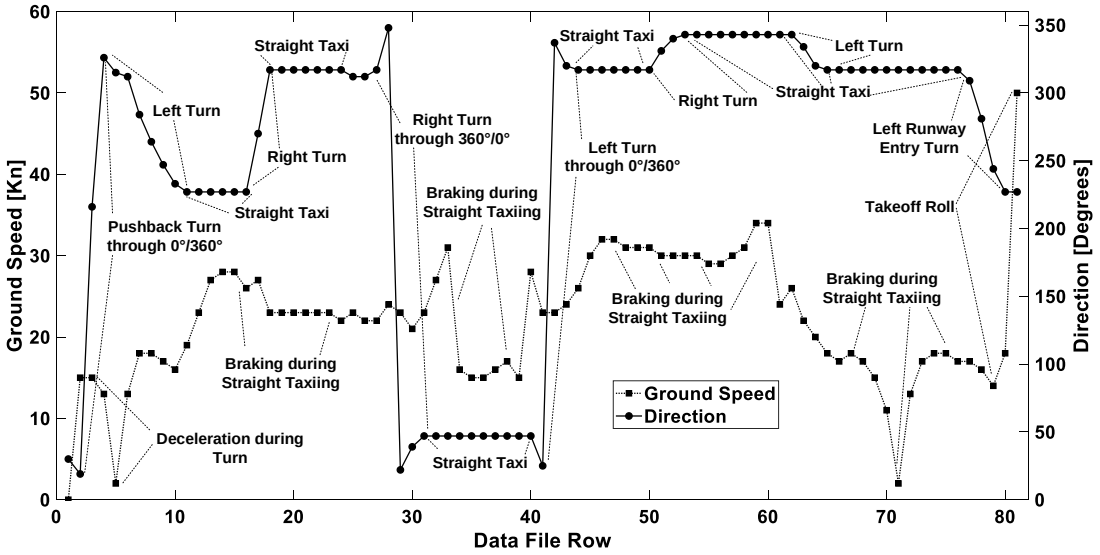

FIGURE 5.6. Heading/direction and speed values from ADS-B broadcasts in an ADS-B data file. ADS-B data file reproduced with permission of Flightradar24® [154].

A data collection study composed of multiple flights (from multiple ADS-B .csv data files) could therefore be used to generate statistics that characterise the per-flight variability in the occurrence of specific ground manoeuvres. In addition, if the ground manoeuvre occurrences are extracted in the order in which they occur for each flight, sequencing variability can also be characterised by identifying the manoeuvres preceding and following specific manoeuvre types.

Previous work in the literature has used ADS-B datasets to optimise aircraft flight paths during the approach and landing phase [193]. Other applications of ADS-B datasets have considered the optimisation of aircraft taxi routes [194–197] and departure sequencing at specific airports, along with other elements of air traffic management [198–200]. Wider applications have included the identification of aircraft and flight characteristics from ADS-B data [201, 202], aircraft fleet management [203, 204], along with the studying of aircraft emissions and noise [205–207]. ADS-B datasets have also been used to support investigations into aircraft accidents [208, 209] and to study meteorological conditions [210, 211]. Sun et al provide algorithms which extract performance parameters from takeoff to landing for civil aircraft based upon ADS-B data [212]. The proposed utilisation of ADS-B datasets to identify ground manoeuvres being performed by aircraft aims to complement the previous work conducted by Sun et al [212].

Therefore, the proposed use of ADS-B datasets within a probabilistic fatigue methodology presents a novel application of ADS-B data for ground manoeuvre identification and statistical characterisation. Based upon the review of the literature, the proposed work also represents the first application of ADS-B data to support the design of aerospace structures, specifically the fatigue design of landing gear components.

5.3 Algorithms for ADS-B Data Collection and Processing

In order to identify ground manoeuvres from the ADS-B data files, a series of algorithms are required to convert the broadcast points in the .csv file into a flight 'strip' that details the manoeuvres that occurred within the pre-takeoff and post-landing taxi phases of the flight. This was achieved by defining novel algorithms, based on conditional or '`if`' statements, that identify ground manoeuvres based upon heading/direction and speed changes as shown previously in Figure 5.6. The collection of flight strips for an aircraft fleet are then to be processed in order to generate statistics regarding the per-flight variability in manoeuvre occurrence and sequencing, as shown in the flowchart in Figure 5.7.

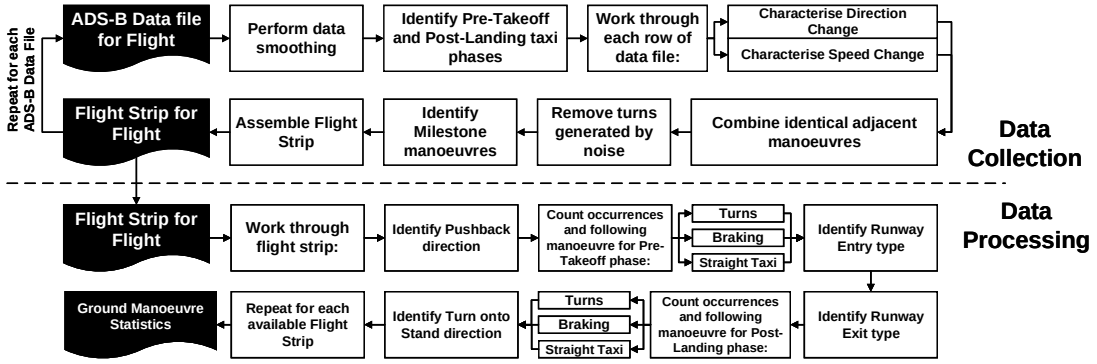

FIGURE 5.7. A flowchart of the proposed ADS-B data collection and processing approach.

5.3.1 Data Collection

The flowchart in Figure 5.7 shows that the generation of ground manoeuvre statistics is decomposed into 'Data Collection' and 'Data Processing'. Data Collection concerns the algorithms that are applied to each individual ADS-B .csv file to identify the specific manoeuvres and manoeuvre sequencing observed within the specific flight relating to the ADS-B .csv file.

Identification of Pre-Takeoff and Post-Landing Phases

The first step of the data collection process is to identify the pre-takeoff and post-landing taxi phases of the ADS-B data file. The pre-takeoff taxi phase is defined from the first broadcast row to the broadcast row which immediately precedes the first broadcast row within the data file that has a non-zero altitude (i.e. the aircraft has become airborne). The post-landing taxi phase is identified as the first broadcast row with a zero-altitude following the airborne rows of the data file to the last row of the data file.

Heading and Speed Change

The pre-takeoff and post-landing broadcast ADS-B data rows are then worked through row-by-row in order to identify whether the aircraft heading/direction and speed has changed with respect to the previous data row. Heading/direction changes, which are computed by comparing the aircraft heading of the current data row with the previous data row, are used to identify turns. The turn direction is characterised using the 'compass' shown in Figure 5.8, which establishes the turn direction using a series of conditional statements based upon the start and end values of the heading/direction change. It is assumed that the aircraft will take the shortest path around the compass and this is considered an appropriate assumption due to typical airport geometries, which result in individual turns usually being no greater than 180° (turns on airport taxiways are typically 30° to 90°). Following the application of the compass during row-by-row characterisation, an Identification (ID) code is applied to each row, either 11 (right turn), 12 (left turn) or 66 (straight taxi). Numeric ID codes, rather than strings or characters, are used to simplify the data processing.

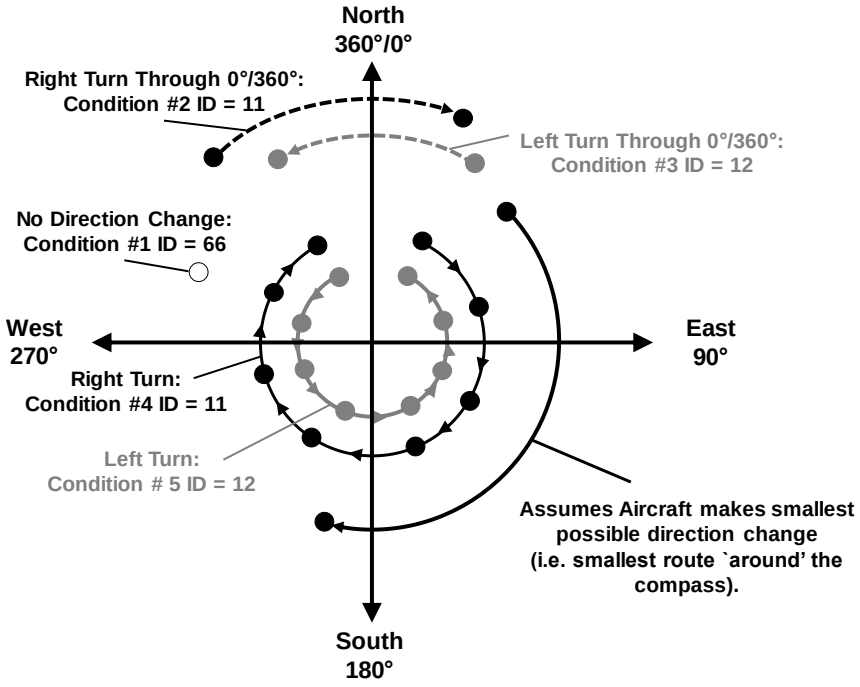

FIGURE 5.8. The compass approach used to characterise heading/direction changes in ADS-B data files.

The row-by-row characterisation of the ADS-B data files also identifies the speed change between data broadcast rows. A deceleration is marked with the ID 41. An example of a completed row-by-row characterisation of an ADS-B .csv file is shown in Figure 5.9 for a pre-takeoff taxi phase.

Timestamp	UTC	Callsign	Latitude	Longitude	Altitude	Speed	Direction	Direction Change	Speed Change	
					0	0	28	66	42	Constant Speed: ID = 42
					0	0	28	66	42	
					0	9	25	12	42	
					0	10	50	11	42	Straight Taxi: ID = 66
					0	9	75	11	41	
					0	9	92	11	42	
					0	9	104	11	42	Right Turn: ID = 11
	Data Removed due to Sensitivity				0	9	115	11	42	
					0	10	118	11	42	
					0	18	160	11	42	Acceleration: ID = 42
					0	27	205	66	42	
					0	30	205	66	42	
					0	32	205	66	42	
					0	14	196	12	41	Braking/Deceleration: ID = 41
					0	10	171	12	41	
					0	11	163	12	42	
					0	18	163	66	42	Left Turn: ID = 12

FIGURE 5.9. Row-by-row manoeuvre characterisation of an ADS-B data file.

Due to the potential for multiple ADS-B broadcasts every second [154], it is expected that individual turning and braking manoeuvres could be split across several broadcast data rows. As a result, the ADS-B data file is again evaluated row-by-row and manoeuvres that are adjacent and identical are combined. It should be noted that braking manoeuvres are only combined during straight taxi manoeuvres, as the data within the ADS-B data file cannot identify whether decelerations during turns are as a result of braking or the turning manoeuvre itself. The combination of manoeuvres results in the pre-takeoff manoeuvre sequence shown in Figure 5.10.

Identical Adjacent Manoeuvres Combined

Provides Start and End Rows in Original Data File for Future Reference

Timestamp	UTC	Callsign	Latitude	Longitude	Altitude	Speed	Direction	Manoeuvre ID	Start Row	End Row
					0	0	28	66	1	2
					0	9	25	12	3	3
					0	10	50	11	4	11
	Data Removed due to Sensitivity				0	27	205	66	12	14
					0	14	196	12	15	17
					0	18	163	66	18	18

FIGURE 5.10. The process of combining adjacent identical manoeuvres within an ADS-B data file.

5.3.1.1 ADS-B Data Smoothing

During the development of the algorithms, it was observed that reception noise within the ADS-B data file could result in the identification of turns which were not performed when comparing the ADS-B data file to the original Flightradar24® visual ground track. It was determined that the incorrect identification of manoeuvres was as a direct result of 'noise' within the ADS-B data files.

The first source of noise was found to be as a result of small fluctuations of heading/direction value from row-to-row, typically of 1° to 2°. These small deviations in heading would be charac-

terised as a turn, while comparison with the Flightradar24® ground track would show that the aircraft was taxiing on a straight taxiway. Therefore, a minimum turn angle of 5° was defined as a threshold for identifying a turn manoeuvre and this threshold successfully eliminated the false identification of manoeuvres from this source of ADS-B data noise.

Another source of noise was identified within the ADS-B data files which showed that the aircraft speed was zero, but with a constantly changing heading/direction value (i.e. the aircraft was continually pivoting in the spot). Therefore, an additional algorithm was developed that would screen the ADS-B data files prior to row-by-row characterisation and remove elements of the data files within which the aircraft heading changed while the aircraft speed was zero.

5.3.1.2 Characterisation of Milestone Manoeuvres

Within the taxi route of an aircraft, there are a series of 'milestone' manoeuvres that mark the transition of the aircraft from one ground taxi phase to the next [188]. The first of these is the pushback of the aircraft from the gate, which often involves the aircraft performing a turn in reverse. Prior to the takeoff roll, the aircraft typically enters the runway by performing a turn and this marks the end of the pre-takeoff taxi phase. Following the touchdown and landing roll, the aircraft vacates the runway and this turn represents the start of the post-landing taxi phase. Finally, the aircraft typically vacates a taxiway to turn onto the arrival stand or gate and this represents the final ground manoeuvre of the flight. Additional algorithms were developed to characterise each milestone manoeuvre. The characterisation of milestone manoeuvres is required as such manoeuvres typically result in different loading being applied to the landing gear, compared to standard taxiway turns.

Pushback

In order to identify the aircraft pushback, the aircraft must be observed to be travelling in reverse. As ADS-B data files only represent the magnitude of the aircraft ground speed, an alternative algorithm was required to identify whether the aircraft was undergoing pushback. To identify if the aircraft was travelling in reverse, the latitude and longitude positions from the ADS-B data file could be used to compute the bearing (°) between two broadcast data rows. If the bearing was found to be greater than 90° different than the aircraft heading (i.e. the direction that the aircraft nose is pointing), it was assumed that the aircraft was travelling in a direction opposite to the aircraft nose and therefore, pushback was occurring. Pushbacks are classified as ID 31 for a tail-right pushback or ID 32 for tail-left pushback. The pushback algorithm is visualised in Figure 5.11.

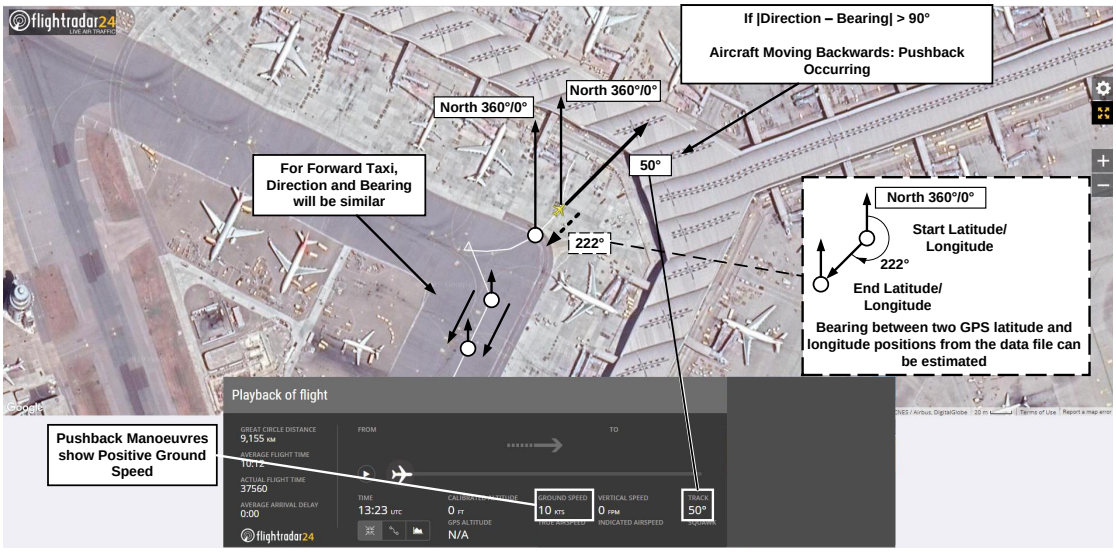

FIGURE 5.11. Visualisation of the pushback characterisation algorithm from ADS-B data files, with original ground tracks sourced from Flightradar24®. Screenshot reproduced with permission of Flightradar24® [154].

Runway Entry

Within the ADS-B data files, it was observed that the takeoff roll could be identified as a straight taxi manoeuvre with a high taxi speed (> 50 Kn). Therefore, for each pre-takeoff flight strip, the last observed turn prior to the takeoff roll was assumed to be the runway entry turn. The turn direction could be identified from the ID number and would then be updated to either ID 511 for a right runway entry or ID 512 for a left entry. Runway entries are often 'tight' or pivoting turns and as a result, induce different loads on landing gear structures compared to a standard taxiway turn.

Another type of runway entry is a runway 'backtrack', which is often required at smaller airports. During a runway backtrack, the aircraft enters the runway and taxis in the direction opposite to the intended takeoff direction. At the end of the runway, the aircraft performs a tight 180° pivot turn to align with the takeoff direction. Such runway entries are identified by comparing the latitude and longitude of the aircraft with known backtrack locations for the aircraft fleet. It was assumed that if an aircraft passed within a 100 m radius 'catchment' zone and demonstrated a 180° turn immediately prior to the takeoff roll, a backtrack runway entry was performed. The identification of backtrack turns is important due to the large torsional loads introduced into the landing gear during the 180° pivot turn [12, 14, 188]. The identification code ID 521 represents a right backtrack turn and ID 522 represents a left backtrack turn.

Runway Exit

Within ADS-B data files, the landing roll is observed as a high speed straight taxi manoeuvre at the start of the post-landing taxi phase. Therefore, it was assumed that the turn manoeuvre immediately following the landing roll is the runway exit manoeuvre.

Aircraft are able to vacate runways using taxiways that are either perpendicular to, or are between 30° and 45° from, the landing runway direction. The latter turn types are usually performed using Rapid Exit Taxiways (RETs), which permit the aircraft to vacate the runway at a higher speed [213]. In order to identify whether an aircraft performed a high speed runway exit using a RET, the aircraft speed at the start of the runway exit turn was identified. During development of the algorithm, it was found that turn entry speeds greater than 30 Kn were observed for aircraft using RETs and therefore, this was set as the threshold speed for identifying whether a standard runway exit, or high speed runway exit was performed. The loads applied to landing gear differ significantly between standard and high speed runway exits [191]. The runway exit turn angle was found not to provide a reliable way of characterising runway exit types, as aircraft often perform an additional taxiway turn immediately after they have vacated the runway.

A backtrack runway exit can also be performed, during which the aircraft continues the landing roll to the end of the runway, prior to performing a tight 180° pivot turn. This is identified in the same manner as backtracks during runway entry. The following ID codes were used to represent the runway exit type and direction in each flight strip:

- Standard Exit: ID 711 (right), ID 712 (left).
- High speed Exit: ID 721 (right), ID 722 (left).
- Backtrack Exit: ID 731 (right), ID 732 (left).

Turn onto Stand

From reviewing ADS-B data files and comparing them to Flightradar24® visual ground tracks, it was observed that aircraft would turn onto their arrival stand/gate and either come to a complete stop or show a low aircraft speed of < 15 Kn. Therefore, in the event that the final manoeuvre has a maximum speed of less than 15 Kn, it was assumed that this condition was the aircraft arriving on stand. The direction of the turn onto stand manoeuvre is identified by the ID of the final turning manoeuvre in the flight strip. ID 81 represents a right turn onto stand and ID 82 represents a left turn onto stand. The identification of the turn onto stand direction is required, as due to the congested nature of aircraft gates and ramp areas, the turn onto stand is typically a tight or pivoting turn, resulting in larger torsional loads in the landing gear.

5.3.2 Data Processing: Generation of Manoeuvre Statistics

Following the identification of the milestone manoeuvres, the flight strip can then be assembled. An example of a completed flight strip is shown in Figure 5.12 and represents the manoeuvres that occur for a flight and the sequence in which they occur. The start row and end row shown in Figure 5.12 represent the data rows and ADS-B broadcasts in the original ADS-B data file.

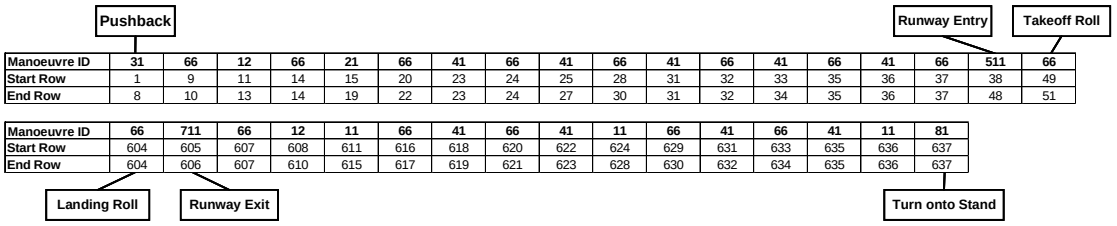

Manoeuvre ID	31	66	12	66	21	66	41	66	41	66	41	66	41	66	41	66	511	66
Start Row	1	9	11	14	15	20	23	24	25	28	31	32	33	35	36	37	38	49
End Row	8	10	13	14	19	22	23	24	27	30	31	32	34	35	36	37	48	51

Manoeuvre ID	66	711	66	12	11	66	41	66	41	11	66	41	66	41	11	81
Start Row	604	605	607	608	611	616	618	620	622	624	629	631	633	635	636	637
End Row	604	606	607	610	615	617	619	621	623	628	630	632	634	635	636	637

FIGURE 5.12. Complete flight strip from characterisation of the manoeuvres within an ADS-B data file.

For the flight strip shown in Figure 5.12, the number of pre-takeoff and post-landing turn and braking manoeuvres can be counted. This process, when repeated for multiple flights, enables the identification of how the number of turning and braking manoeuvres varies on a per-flight basis across a fleet of aircraft. In addition, over the repeated flights, a 'tally' for each milestone manoeuvre type and turn direction can also be recorded.

Finally, the manoeuvre sequencing for each flight strip can be identified. For each type of manoeuvre, a tally is kept of the manoeuvre that immediately follows it (except for the runway entry and turn onto stand, whereby it is the manoeuvre that precedes these manoeuvres that is of interest). From the tally values, the proportional share of the manoeuvres either following or preceding a certain type of manoeuvre can be computed.

5.4 Demonstration of ADS-B Data Collection and Processing

The algorithms described within the previous section were implemented within a MATLAB® environment, which read the ADS-B data files and applied the algorithms to produce a corresponding flight strip for each ADS-B data file. A MATLAB® script was then used to tally values from each flight strip to produce the ground manoeuvre occurrence and sequencing statistics.

5.4.1 Dataset Assembly

The dataset to be used to generate the ground manoeuvre statistics was based upon a fleet of a wide-body civil aircraft. A wide-body civil aircraft was selected due to the availability of existing data on wide-body aircraft ground manoeuvres (albeit limited with respect to variability) from Ladda and Struck [14] and the FAA statistical loads program [191]. At the time of writing, the

selected wide-body aircraft fleet performs approximately 2,500 flights a week [154], and operates into and from both small and medium sized airports, along with large international airports.

The route network for each operator of the wide-body civil aircraft was identified using Flightradar24® and the ADS-B reception was evaluated at each departure and arrival airport [154]. It was observed that limited reception was available at certain airports (especially at stand/gate locations). As this limited reception resulted in inaccurate ground tracks, these routes were omitted form the dataset. The aircraft utilisation on the remaining routes was then identified. If the wide-body aircraft type was used on a given route five times a week, five ADS-B data files for the route were randomly selected from across the period of a single year. The random sampling of flights in a manner that is proportional to the actual aircraft type utilisation in-service was performed to produce ground manoeuvre statistics that would be representative of the entire wide-body civil aircraft fleet. The random sampling of flights resulted in 1,265 ADS-B data files and the resulting routes are shown in Figure 5.13a. The final dataset consisted of the flights across 262 individual routes and flights operating from 79 different airports. Figure 5.13b shows the ground tracks across the wide-body civil aircraft fleet at a single airport and due to the high fidelity of the ADS-B data files, key elements of the airport geometry can be identified.

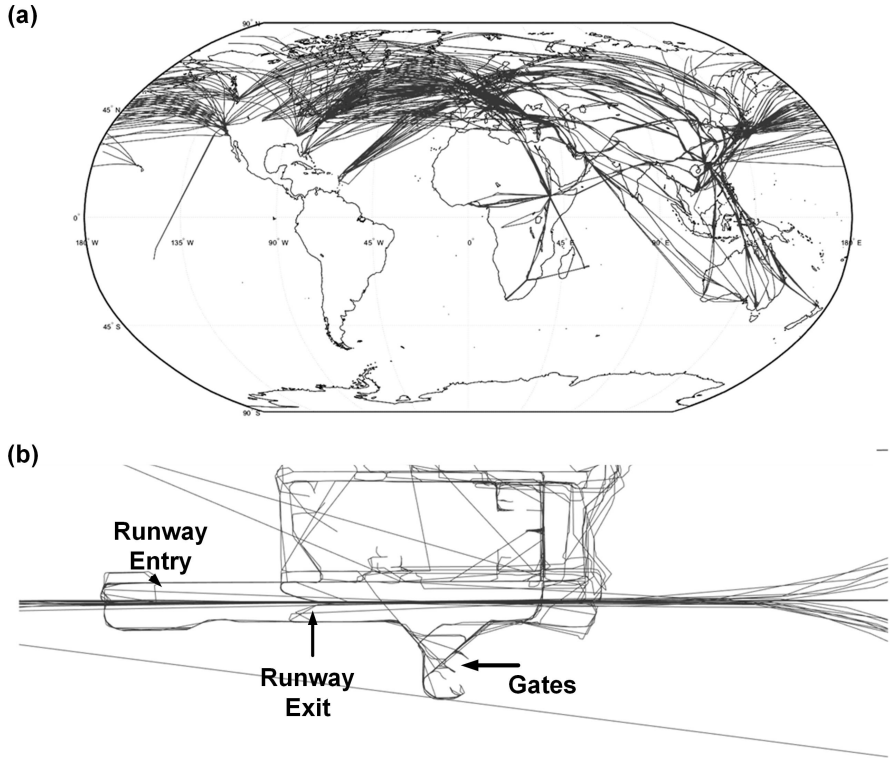

FIGURE 5.13. (a) The route network of the wide-body civil aircraft included in the ADS-B dataset. (b) A demonstration of the fidelity of the ADS-B ground tracks, which trace out the key features of an airport geometry.

5.5 Ground Manoeuvre Occurrence Statistics

Following the implementation of the algorithms for processing the ADS-B data files and the dataset assembly, the data collection and processing algorithms were applied to produce ground manoeuvre statistics for the wide-body civil aircraft.

5.5.1 Pre-Takeoff Taxi Phase Ground Manoeuvres

Figure 5.14 shows a histogram representing the total number of pre-takeoff turns per-flight and the frequency with which they were observed across the 1,265 flights of the assembled dataset for the wide-body aircraft fleet. The mode (i.e. most common) number of pre-takeoff turns was found to be three pre-takeoff turns per-flight, which demonstrates good agreement with the previous studies into wide-body aircraft ground manoeuvres, which suggest that four pre-takeoff turns per-flight is typical [14, 191]. The minimum number of pre-takeoff turns was zero, representing flights that entered the runway directly from pushback, which is possible when operating from smaller airport geometries. The maximum number of pre-takeoff turns was 26 and an investigation into this result highlighted that the aircraft had performed a Rejected TakeOff (RTO), which would be expected to result in additional pre-takeoff turns. Figure 5.14 also shows that a significant number of flights have greater than five pre-takeoff turns, and these flights were found to be operating from large international airports.

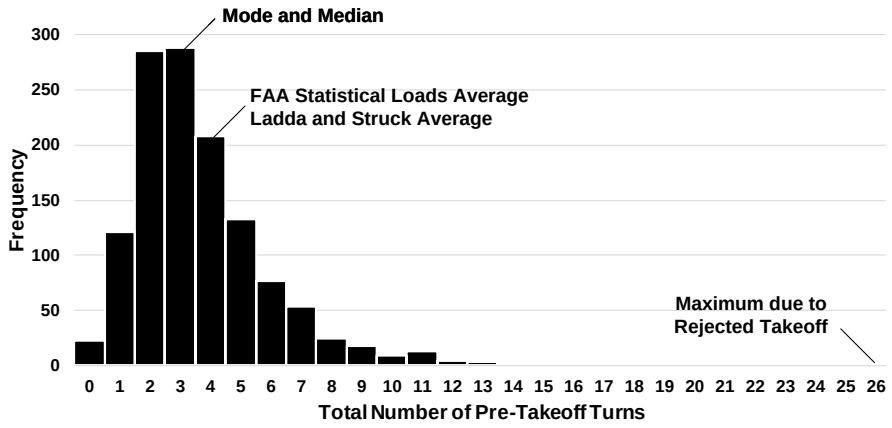

FIGURE 5.14. A histogram of the number of pre-takeoff turns for a wide-body civil aircraft.

The pre-takeoff turns across the flights of the demonstration dataset can also be decomposed into the number of pre-takeoff left and pre-takeoff right turns for each flight, as shown in Figures 5.15a and 5.15b respectively. The mode number of occurrences for both turn directions is one and the median is two, highlighting a positive skew in the histograms. Figure 5.15c shows that the share between left and right turns during the pre-takeoff taxi phase is approximately equal.

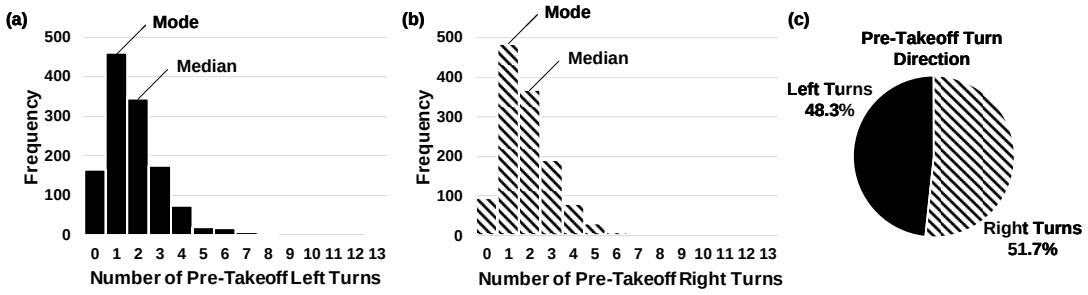

FIGURE 5.15. Pre-takeoff turn direction statistics for a wide-body civil aircraft: (a) histogram of number of pre-takeoff left turns, (b) histogram of number of pre-takeoff right turns and (c) the proportional share between turn direction for pre-takeoff turns.

Figure 5.16 shows the total number of pre-takeoff braking applications per-flight and the frequency with which they were observed across the 1,265 flights of the assembled dataset. The mode and median number of pre-takeoff braking applications were three and four respectively, showing consistency with the previous studies into wide-body aircraft ground manoeuvres [14, 191], as well as highlighting the positive skew in the histogram.

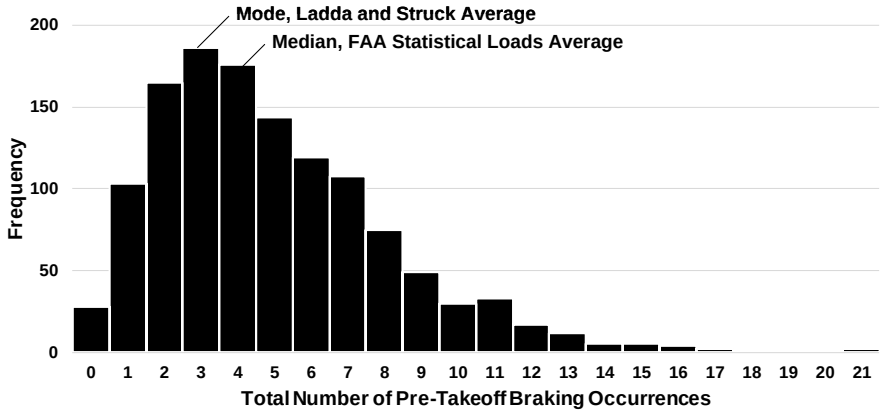

FIGURE 5.16. A histogram of the number of pre-takeoff braking occurrences for a wide-body civil aircraft.

5.5.2 Post-Landing Taxi Phase Ground Manoeuvres

Figure 5.17 shows the total number of post-landing turns per-flight and the frequency with which they were observed across the 1,265 flights of the assembled dataset. The mode and median values were found to be two and three respectively, demonstrating the positive skew in the

dataset. The mode number of turns post-landing was found to be smaller than the mode number of turns pre-takeoff. This is to be expected as the pre-takeoff taxi out to the runway will require the aircraft to taxi to the threshold at the end of the runway, rather than routing directly from where the aircraft vacates the runway following landing, as aircraft typically do not use the full runway length on landing for every flight. The more direct taxi routing post-landing could result in fewer turns being performed by the aircraft prior to turning onto the arrival stand/gate.

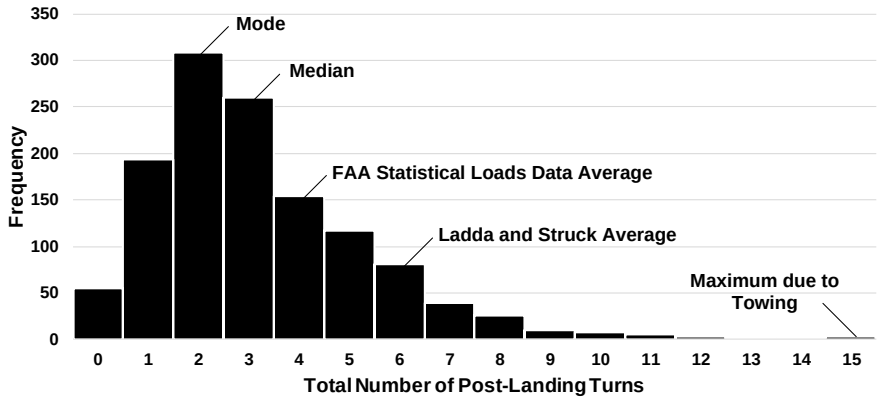

FIGURE 5.17. A histogram of the number of post-landing turns for a wide-body civil aircraft.

Figure 5.17 also shows that the mode number of post-landing turns is significantly lower than the turning occurrences suggested by the in-service monitoring of a wide-body civil aircraft performed by Ladda and Struck [14] and the FAA statistical loads programme [191]. It is expected that this is as a result of the previous studies being reliant on the instrumentation and monitoring of specific aircraft, which could bias the statistics to the routes that the specific aircraft was operated on. For example, the statistics presented by Ladda and Struck are based on the monitoring of an individual aircraft operated by a single airline, which may not be representative of the operational service of an entire wide-body civil aircraft fleet [14]. The minimum number of turns was found to be zero, corresponding to flights arriving at smaller airports, where the aircraft taxies directly onto stand after vacating the runway. The maximum number of turns was found to be 15 as a result of the aircraft being towed from the arrival gate.

The post-landing turns can also be decomposed into the number of post-landing left and right turns for each flight as shown respectively in Figures 5.18a and 5.18b. The mode and median number of post-landing turns in each direction per-flight is one. Figure 5.18c shows that the share between post-landing left and right turn directions is also approximately equal.

Figure 5.19 shows the variability in post-landing braking occurrences per-flight across the 1,265 flights of the ADS-B dataset. Figure 5.19 demonstrates strong agreement with the pre-takeoff braking applications shown previously in Figure 5.16, as for both pre-takeoff and post-landing taxi phases, the mode and median values were three and four braking occurrences

respectively. These values also show good agreement with the previous studies on wide-body aircraft ground manoeuvres as highlighted in Figure 5.19.

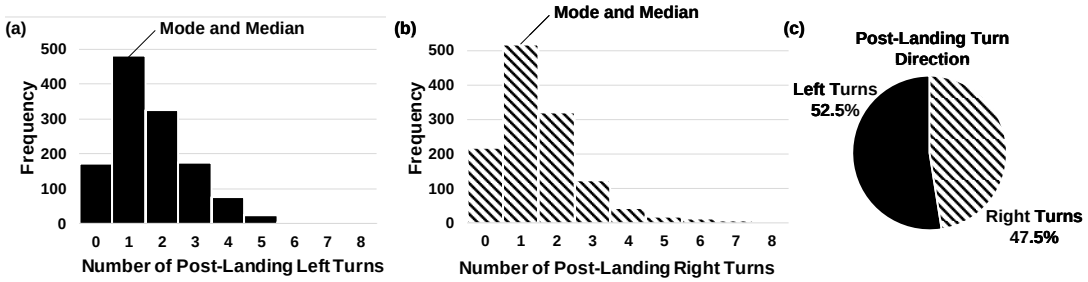

FIGURE 5.18. Post-landing turn direction statistics for a wide-body civil aircraft: (a) histogram of number of post-landing left turns, (b) histogram of number of post-landing right turns and (c) the proportional share between turn direction for post-landing turns.

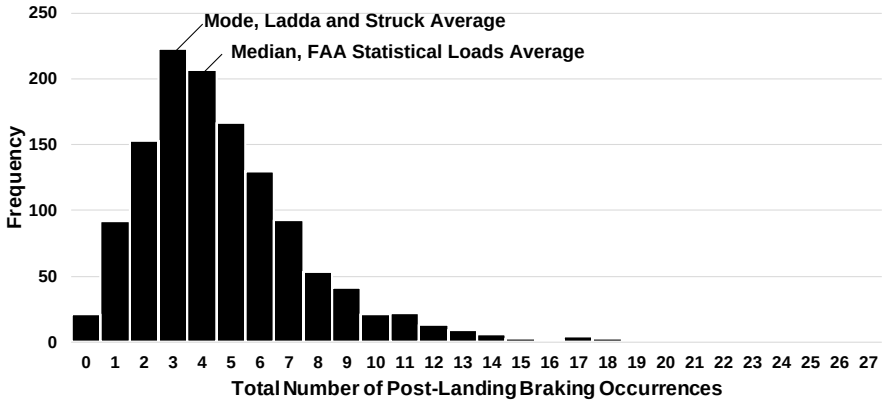

FIGURE 5.19. A histogram of the number of post-landing braking occurrences for a wide-body civil aircraft.

5.5.3 Share of Turns and Braking Manoeuvres across Flight

In order to identify whether more turning or braking manoeuvres occur during the pre-takeoff or post-landing taxi phases, the total number of turning and braking occurrences were computed for both taxi phases. Figure 5.20a shows the share of pre-takeoff and post-landing turning manoeuvres across the 1,265 flights within the ADS-B dataset. 53.2% of turns were found to occur during the pre-takeoff phase, while the remaining 46.8% of turns were performed post-landing. Figure 5.20b demonstrates that the braking occurrences are also approximately equal across the pre-takeoff and post-landing phases.

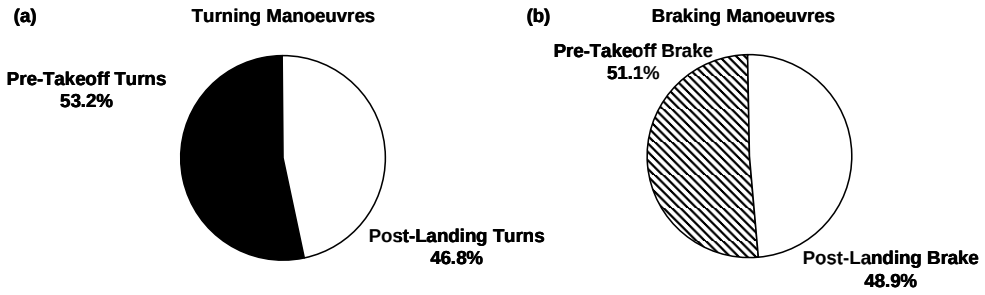

FIGURE 5.20. The proportional share of (a) turning manoeuvres and (b) braking occurrences across pre-takeoff and post-landing taxi phases for a wide-body civil aircraft.

5.5.4 Correlation between Turning and Braking Manoeuvres

Based on the observation of an equal share of turning directions, it was hypothesised that the number of left turns and right turns observed during a taxi phase would be correlated (i.e. if a larger number of left turns was observed during a pre-takeoff taxi phase, a larger number of right turns would also be expected in the pre-takeoff taxi phase).

Figure 5.21a shows a contour plot representing how the number of pre-takeoff right turns varies with the number of pre-takeoff left turns, where a lighter shade in the contour plot represents a more commonly observed combination of left and right turns from the flights in the ADS-B dataset. From Figure 5.21a it can be observed that the most common combination of turns was one left turn and one right turn during the pre-takeoff taxi phase. Figure 5.21a also highlights that there is a slight 'stretch' in the contour plot, suggesting that as the number of pre-takeoff left turns increases, so does the number of pre-takeoff right turns. This trend can be quantified using the Pearson correlation coefficient 'ρ', which can be computed using Equation 5.4 between two variables 'x' and 'y' [156]. The correlation between the number of pre-takeoff left turns and pre-takeoff right turns is $\rho = 0.660$, suggesting a moderate correlation (as $\rho > |0.8|$ is considered a 'strong' correlation and correlations below $\rho = |0.5|$ are considered 'weak' [156]).

$$\rho = \frac{\sum_{i=1}^{N} y_i(x_i - \mu_x)}{\left[\sum_{i=1}^{N}(y_i - \mu_y)^2 \sum_{i=1}^{N}(x_i - \mu_x)^2\right]^{\frac{1}{2}}} \tag{5.4}$$

Figure 5.21b shows the contour plot representing the correlation between the number of left turns and right turns during the post-landing taxi phase and displays a similar relationship to the pre-takeoff taxi phase. Based on the Pearson correlation coefficient of $\rho = 0.619$, it can also be suggested that there is a moderate correlation between the number of left and right turns during the post-landing taxi phase. Contingency tables, which provide the frequency for each combination of number of left and right turns are provided in Appendix C for both the pre-takeoff and post-landing taxi phases.

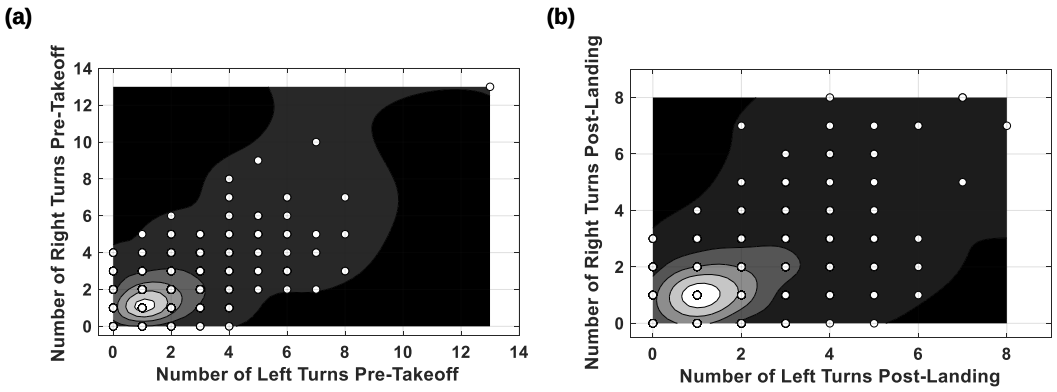

FIGURE 5.21. Contour plots highlighting: (a) the correlation between pre-takeoff left and right turns and (b) the correlation between post-landing left and right turns.

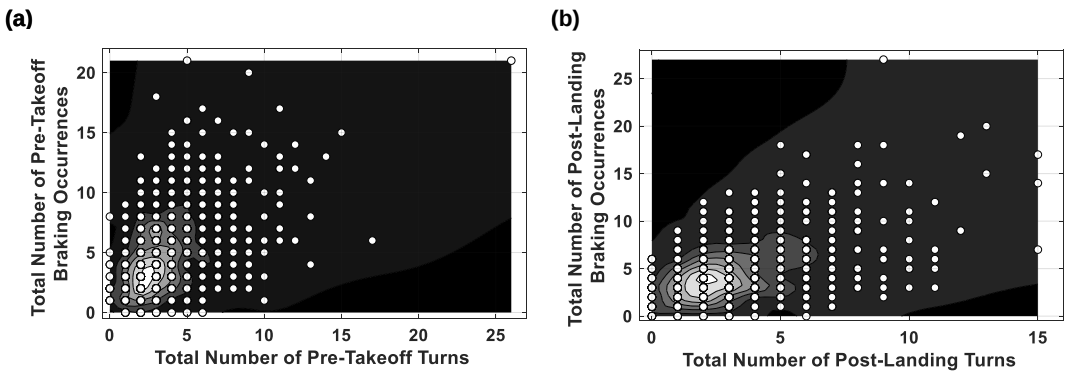

FIGURE 5.22. Contour plots highlighting: (a) the correlation between pre-takeoff turning and braking occurrences and (b) the correlation between post-landing turning and braking occurrences.

It was also hypothesised that a correlation may exist between the total number of turns and total number of braking occurrences during a taxi phase, as it would be expected that aircraft would decelerate prior to performing a turn. Therefore, the correlation between turning and braking occurrences for the pre-takeoff and post-landing taxi phases was also investigated. Figure 5.22a shows a contour plot of the number of pre-takeoff braking occurrences compared with the total number of pre-takeoff turns. The contour plots highlight that the most commonly observed combination was two pre-takeoff turns with two pre-takeoff braking occurrences. While the contour plot demonstrates a potential relationship of increasing number of braking occurrences for increasing number of turns, the correlation coefficient value of $\rho = 0.452$ suggests that only a weak correlation is present.

Figure 5.22b shows the correlation between the number of post-landing braking occurrences and the total number of post-landing turns. It can be observed from Figure 5.22b that the most commonly observed combination was two turns and four braking occurrences during the post-landing taxi phase. The correlation coefficient of $\rho = 0.503$ demonstrates that again, only a weak correlation is observed between the number of braking manoeuvres and total number of turns.

5.5.5 Occurrence Statistics of Milestone Manoeuvres

Following the characterisation of the variability in turning and braking manoeuvre occurrences, the proportional share of milestone manoeuvre types was identified for pushback, runway entry, runway exit and turn onto stand manoeuvres. Figure 5.23 shows the proportional share of manoeuvre type for each of the milestone manoeuvres.

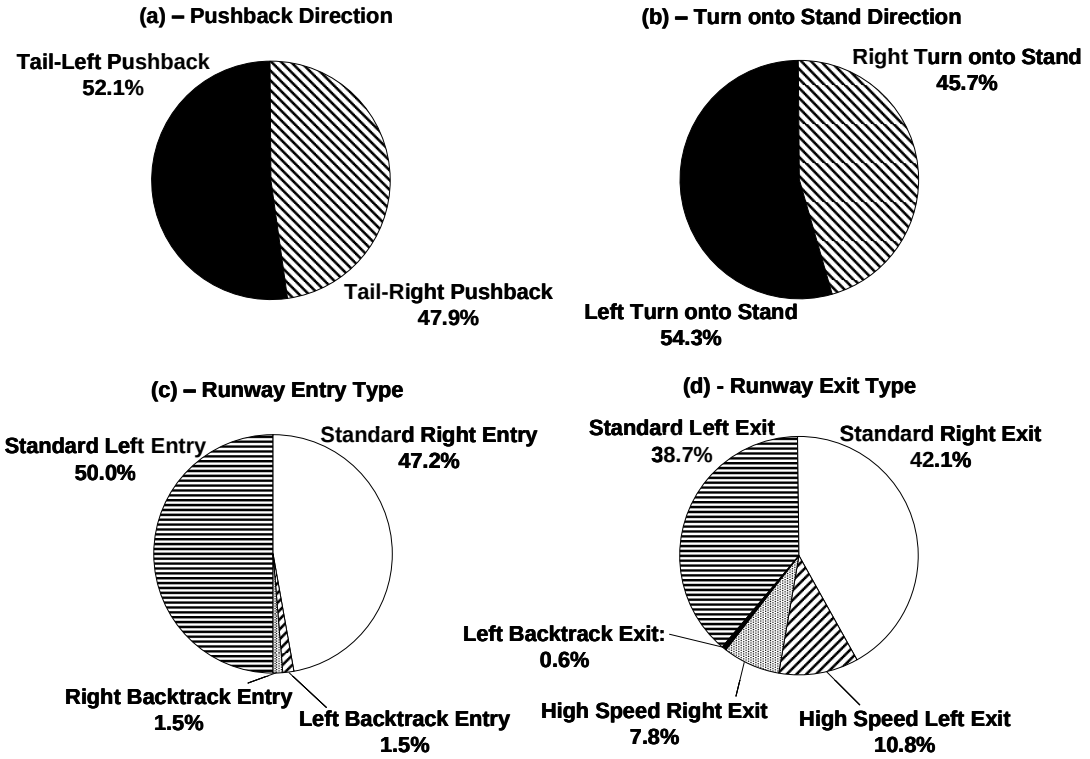

FIGURE 5.23. Proportional share of milestone manoeuvres for a wide-body civil aircraft: (a) pushback direction, (b) turn onto stand direction, (c) runway entry type and direction and (d) runway exit type and direction.

Figure 5.23a shows that the direction of aircraft pushback is approximately equal, with 52.1% and 47.9% of pushback manoeuvres being tail-left and tail-right respectively. The slight discrepancy in the equal share is expected to be as a result of the 283 flights which did not provide pushback data (22.4% of the collected dataset). Figure 5.23b presents the share of turn onto stand direction, with 54.3% of flights performing a left turn onto stand. In a similar manner to the pushback manoeuvre, it was expected that the share between left and right turn onto stand directions would be approximately equal and the resulting discrepancy is expected to be as a result of the 16.3% flights of the dataset which failed to provide information regarding the turn onto stand direction. As a result, across the pushback and turn onto stand manoeuvres, the turn direction across the wide-body aircraft fleet is approximately equal.

Figure 5.23c shows the runway entry type and it can be observed that the vast majority (97.2%) of flights within the ADS-B dataset performed a standard runway entry, with the direction of the runway entry being approximately equally shared between left and right runway entries. The 2.8% of flights performing a backtrack runway entry shows good agreement with the wide-body aircraft route network, of which 3.3% of routes (based on their proportion of the weekly fleet utilisation) operate out of airports that may require a runway backtrack prior to takeoff [154]. It can also be observed from Figure 5.23c that the left and right turn directions have an approximately equal share of the runway backtrack entry manoeuvres.

Finally, Figure 5.23d shows the proportional share of the runway exit type and direction across the 1,265 flights in the assembled ADS-B dataset. 80.8% of runway exits were found to be standard runway exits (i.e. low speed turns) with left and right turn directions having an equal proportion. High speed runway exits using RETs were only observed for 18.5% of flights. This result may be as a consequence of the selected wide-body aircraft, which operates into a significant number of airports that do not have RETs [154]. In addition, an aircraft may vacate using an RET, but a slower exit speed than the runway exit algorithm threshold of 30 Kn. Only 0.6% of flights demonstrated a backtrack exit from the runway. While 3.3% of wide-body aircraft route network was observed to operate into airports that may require a runway backtrack, the aircraft were typically observed to vacate the runway at an earlier taxiway, removing the need to perform a runway backtrack. It can be observed from Figure 5.23d that the turn directions for both standard and high speed runway exits are approximately equal in proportion across the wide-body aircraft fleet.

5.6 Ground Manoeuvre Sequencing Statistics

The statistics relating to the sequencing of manoeuvres were generated by considering the tally of manoeuvres either preceding or following a specific type of manoeuvre across the 1,265 flights in the ADS-B dataset. The interpretation of the tally value enables the proportional share of a given manoeuvre occurring after a specific manoeuvre (e.g. identifying the probability of a right

turn occurring directly after a left turn in the pre-takeoff taxi phase) to be quantified.

Figure 5.24 shows the proportional share of manoeuvres occurring after pre-takeoff and post-landing turns across the flights within the assembled dataset. Figures 5.24a and 5.24b show the ratio of manoeuvres following pre-takeoff left and right turns respectively. It can be observed from Figures 5.24a and 5.24b that the majority of pre-takeoff turns are followed by a straight taxi manoeuvre, regardless of the turn direction. A similar observation can be made for post-landing turns from Figures 5.24c and 5.24d, where the greatest proportion of manoeuvres following a post-landing turn is a straight taxi manoeuvre. For all taxi phases and turn directions, Figure 5.24 demonstrates that a turn in the opposite direction to the original turn (i.e. a 'turn reversal', such as a left turn directly into a right turn) only occurs in approximately 20% to 30% of turning manoeuvres.

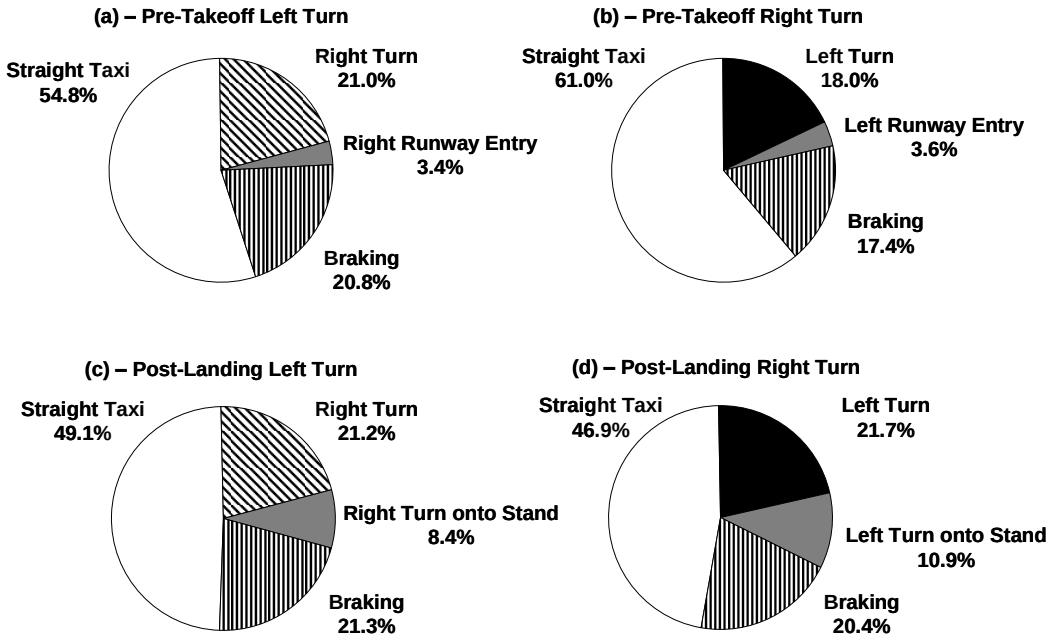

FIGURE 5.24. Proportional share of manoeuvres following turning manoeuvres for a wide-body civil aircraft: (a) manoeuvres following a pre-takeoff left turn, (b) manoeuvres following a pre-takeoff right turn, (c) manoeuvres following a post-landing left turn and (d) manoeuvres following a post-landing right turn.

From further consideration of Figures 5.24a and 5.24b, it can be seen that the proportional share of following manoeuvres is similar for both left and right turns. The same observation can be made regarding post-landing turns in Figures 5.24c and 5.24d, suggesting that the sequencing of manoeuvres after a turn is insensitive to the turn direction. However, from Figure 5.24, it can be observed that the proportions for manoeuvres following turns does vary when comparing between the pre-takeoff and post-landing taxi phases. For example, a comparison of subplots (a) and (b) with subplots (c) and (d) in Figure 5.24, shows that pre-takeoff turns are followed by

a greater proportion of straight taxi manoeuvres compared to post-landing turns. As a result, it can be suggested that manoeuvre sequencing after turns is sensitive to whether the turn is performed during the pre-takeoff or post-landing taxi phase.

Figure 5.25 shows the manoeuvres following straight taxi and braking manoeuvres across both the pre-takeoff and post-landing phases. Figures 5.25a and 5.25b show the proportional share of manoeuvres following pre-takeoff and post-landing straight taxi manoeuvres respectively. It should be observed from comparing Figures 5.25a and 5.25b that the proportional share of manoeuvres are similar across the pre-takeoff and post-landing phases, and left and right turn directions are observed in approximately equal proportions. This suggests that for straight taxi manoeuvres, the sequencing of manoeuvres is insensitive to the taxi phase. On the other hand Figures 5.25c and 5.25d suggest that for braking manoeuvres, the sequencing of manoeuvres is sensitive to taxi phase, as Figure 5.25d shows that a greater proportion of post-landing braking manoeuvres are followed by turns, when comparing the post-landing taxi phase to the pre-takeoff taxi phase.

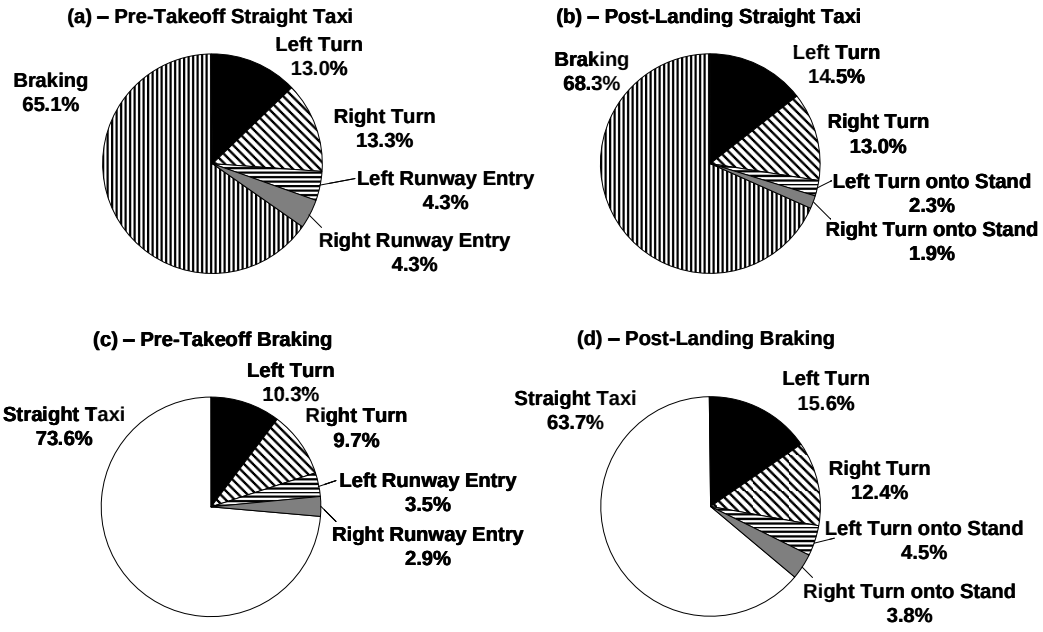

FIGURE 5.25. Proportional share of manoeuvres following straight taxi and braking manoeuvres for a wide-body civil aircraft: (a) manoeuvres following pre-takeoff straight taxi, (b) manoeuvres following post-landing straight taxi, (c) manoeuvres following pre-takeoff braking and (d) manoeuvres following post-landing braking.

From across Figure 5.25, it can be seen that regardless of taxi phase, the majority of manoeuvres following a straight taxi manoeuvre are braking manoeuvres and vice-versa. This observation suggests that there are extended sequences of manoeuvres during which the aircraft continually changes from a straight taxi to a braking manoeuvre before accelerating back into a

straight taxi manoeuvre. Flights demonstrating such behaviour were identified in the assembled ADS-B dataset and through the use of the Flightradar24® visual ground tracks, it was concluded that an aircraft alternating between straight taxi and braking manoeuvres was as a result of the aircraft 'queuing' behind other aircraft at locations such as the runway entry.

Appendix D provides the sequencing statistics for manoeuvres preceding the runway entry and turn onto stand milestone manoeuvres, along with the sequencing statistics for manoeuvres following the pushback and runway exit milestone manoeuvres. From the range of pie charts shown in Appendix D, it can be observed that the sequencing of manoeuvres either preceding or following specific milestone manoeuvres is insensitive to the turning direction of each milestone manoeuvre type.

5.7 Verification of ADS-B Data Collection and Processing Algorithms

In order to perform verification of the novel algorithms developed to process the ADS-B data files, the flight strips generated using the algorithms could be validated by comparing the identified manoeuvres with the original ADS-B data file and Flightradar24® visual ground track for each flight. For verification, 10% of the dataset (130 flights) from the assembled ADS-B data files were randomly selected and for each flight the following results were reviewed:

- Identification of the correct milestone manoeuvres.
- Identification of the correct manoeuvre sequence, including both turns and braking for both pre-takeoff and post-landing taxi phases.

Validation of the milestone manoeuvres, turn direction and sequencing identification was performed using the Flightradar24® user interface as visualised in Figure 5.26. The ability of Flightradar24® to map data files directly onto satellite images of airport layouts greatly aided this verification task [154]. The extraction of the correct turn and braking manoeuvre occurrence and sequence could also be validated using a plot of heading/direction and speed changes from the ADS-B data file as highlighted in Figure 5.26.

Table 5.2 shows the results from verification, where 'accuracy' is defined as the proportion of the verification dataset where the generated flight strip agreed with the Flightradar24® user interface and the ADS-B data file plot. Table 5.2 shows that algorithms were able to successfully identify the milestone manoeuvres for the majority of the verification data files. Reduced accuracy was observed for pushback and turn onto stand manoeuvres. The reduced accuracy for identifying pushback manoeuvres also resulted in lower accuracy for the sequencing of the pre-takeoff taxi manoeuvre sequence, as errors in pushback manoeuvre characterisation would propagate through to the pre-takeoff taxi phase.

Table 5.2 also shows that the algorithms are currently only able to produce a completely correct flight strip in less than half of the verification flights. This inaccuracy suggests that in their current form, the algorithms would be unsuitable for the in-service monitoring of individual aircraft. However, as the accuracy is significantly higher for identifying manoeuvre sequences and manoeuvre types independently in the pre-takeoff and post-landing taxi phases, ADS-B data files and the current algorithms are suitable for generating ground manoeuvre statistics for the wide-body civil aircraft fleet, when assuming that there is no correlation between the manoeuvre statistics for the pre-takeoff and post-landing taxi phases.

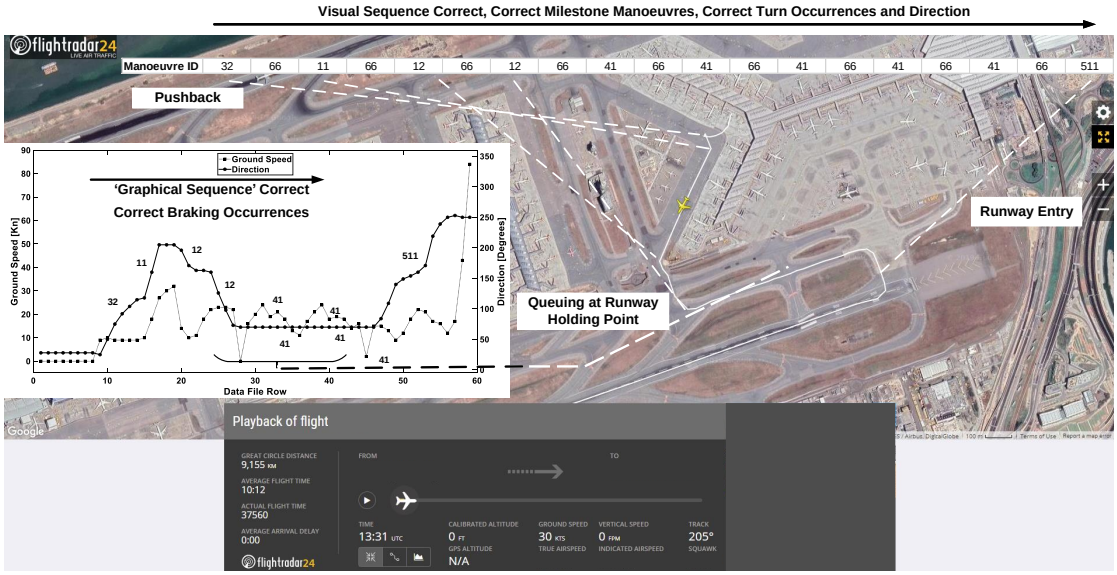

FIGURE 5.26. Visualisation of the ADS-B processing algorithm verification approach, using ground tracks from Flightradar24®. Screenshot reproduced with permission of Flightradar24® [154].

TABLE 5.2. Verification results for the ADS-B processing algorithms based on 10% of the assembled ADS-B dataset.

Verification Task for Flight	Accuracy
Correct Pushback Direction	82.3%
Correct Runway Entry Type and Direction	93.1%
Correct Runway Exit Type and Direction	96.2%
Correct Turn onto Stand Direction	83.1%
Correct Pre-Takeoff Sequence	75.4%
Correct Post-Landing Sequence	86.2%
Complete Flight Correct	47.7%

5.8 Utilisation of Big-Data Sources for Deterministic Fatigue Design

Beyond the intended application of the ground manoeuvre occurrence and sequencing statistics in the statistical simulation of landing gear load-time histories, the statistics generated across Sections 5.5 and 5.6 can also be used to evaluate the existing assumptions and guidance employed in the construction of landing gear load spectra for deterministic fatigue design and analysis.

Firstly, it was observed that across all types of turning manoeuvres that the turning direction was equally shared between left and right turns from the statistics generated from the ADS-B dataset. This result supports a current assumption made within the deterministic fatigue analysis of landing gear components, during which it is assumed that the number of left and right turns across the load spectrum are equal [188]. In addition, existing practice assumes that the total number of manoeuvres within the landing gear load spectrum is shared equally between pre-takeoff and post-landing taxi phases [188], and such an assumption is supported by the ADS-B derived statistics shown in previously in Figure 5.20.

The statistics generated across Sections 5.5 and 5.6 represent the global fleet of the wide-body civil aircraft across a number of different operators. It is recommended that future work investigates how the generated statistics change when focusing on single operators and individual aircraft as it is hypothesised that the route networks and operational practices of different operators will bias the ground manoeuvre statistics. For example, previous studies based upon the in-service monitoring of specific aircraft have suggested that aircraft may not perform an equal number of left and right turns across flights [214]. However, it is expected that this observation is as a result of monitoring specific aircraft (rather than the global fleet), resulting in a bias of the collected ground manoeuvre statistics. As a result, the generation of ground manoeuvre statistics from ADS-B data files of specific operators or aircraft could help to identify whether specific route networks significantly impact the landing gear ground manoeuvre statistics.

There are however, elements of the ground manoeuvre statistics generated from the ADS-B dataset which contradict existing deterministic fatigue design practices. The histograms generated for the number of turning and braking occurrences per-flight in Figures 5.14, 5.16, 5.17 and 5.19 all demonstrated that the mode and median number of manoeuvre occurrences were consistent with previous studies. Despite this agreement, the presence of the positive skew in the manoeuvre occurrence histograms contradicts the assumption made in existing design practice that an average number of turns occur for every flight [14, 188]. The use of an average number of turns per-flight would require the assumption of a symmetric distribution, where every number of turns greater than the average value is also represented below the average value. As a result, the current assumption of an average number of turns would fail to account for flights that will have a large number of turns (i.e. in the extreme tail of the skewed distribution) when constructing landing gear load spectra for deterministic fatigue design.

Concerning the assumed sequencing of manoeuvres required in landing gear load spectra, existing practice assumes that every turn performed by an aircraft is followed immediately by a turn in the following direction (i.e. a 'turn reversal') [188]. However, the sequencing statistics shown previously for turning manoeuvres in Figure 5.24 demonstrated that a turn reversal can only be expected to occur in 20% to 30% of turning manoeuvres. As a result, there is the potential for the existing practice of assuming turn reversals to be conservative. This is due to the loads applied to the landing gear being fully reversed across the two turns, resulting in larger stress amplitudes and increased fatigue damage accumulation in the landing gear, compared to the case where the turning loads on the landing gear are removed as the aircraft returns to straight taxi (i.e. to the 'unloaded' condition from the perspective of turning loads).

This section has demonstrated how the big-data source and statistics required to support a probabilistic fatigue methodology can also be used to evaluate and challenge the assumptions and practices used within the existing deterministic fatigue design and analysis process. In a similar manner to the improved statistical characterisation process of materials data presented in Chapter 4, this chapter has demonstrated the utility of the resources and approaches required for probabilistic design in supporting the existing deterministic design process.

5.9 Loading Magnitude Variability from In-Service Loads

Whilst the characterisation of the variability in ground manoeuvre occurrence and sequencing has required the novel application of ADS-B data files, the variability in the loading magnitude for specific ground manoeuvres can be characterised using the exceedance curves currently used for deterministic fatigue design and analysis. This section explores the characterisation of the variability in loading magnitude for landing gear loads.

5.9.1 Aircraft Mass

During in-service operation, the mass 'M' of the aircraft will vary as a result of variability in the fuel and payload carried by the aircraft for different flights. Existing data on mass variability is available for wide-body civil aircraft, which demonstrates that the mass of aircraft in-service can vary from the aircraft's Maximum TakeOff Weight (MTOW) down to the minimum of the Operational Weight Empty (OWE - i.e. no payload or fuel) [191]. Figure 5.27 shows histograms demonstrating the variability in the takeoff and landing masses for a wide-body civil aircraft based on in-service monitoring of the aircraft for a specific operator [191].

Figure 5.27c shows a contour plot of the observed combinations of takeoff and landing masses for the wide-body civil aircraft [191], in which a lighter shade represents a more common combination. The 'stretch' in the contour plot infers that a correlation exists between the takeoff

and landing masses, suggesting that a higher takeoff mass will result in a higher landing mass. Based on the contingency tables provided for the wide-body civil aircraft masses [191], $\rho = 0.820$ inferring a strong correlation between the takeoff and landing masses.

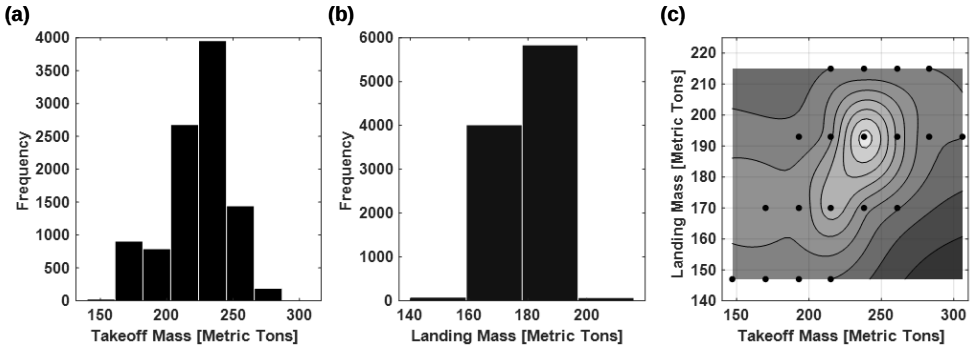

FIGURE 5.27. Variability in wide-body aircraft (a) takeoff mass and (b) landing mass. (c) shows a contour plot that highlights the correlation between takeoff and landing mass [191].

5.9.2 Manoeuvre Load Factor and 'Fine Blocking' Approach

As introduced in Section 5.1, the exceedance curves employed within deterministic fatigue design and analysis represent the variability in the load factor for each type of ground manoeuvre. As a result, the variability in the manoeuvre load factor can be statistically characterised by reverse-engineering the exceedance curve to generate a load factor dataset that would result in the original exceedance curve. This is achieved using the principle of exceedance curve blocking employed within the construction of landing gear load spectra for deterministic fatigue design.

The existing definition of blocks from exceedance curves results in identifying the load factor at the centre of block, and the number of times the load factor is applied by considering the minimum exceedance value and the maximum exceedance value, as shown previously in Figure 5.3b [186, 187]. Therefore, if the block size is reduced to one exceedance, the resulting load factor at the centre of each block can be taken to be a pseudo data point for the load factor. Figure 5.28 demonstrates the 'fine blocking' process, which converts the exceedance curve into a histogram that demonstrates the variability in the load factor magnitude for the specific ground manoeuvre.

Exceedance curves, based on the in-service monitoring of loads for a wide-body civil aircraft, are available in the public domain [12, 14, 191] and the full list of available exceedance curves is given in Appendix E.

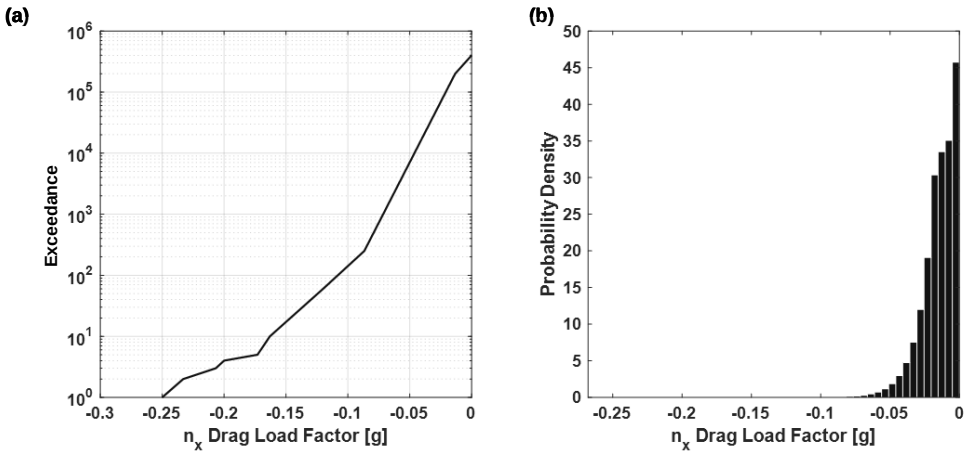

FIGURE 5.28. Demonstration of fine blocking of exceedance curves, (a) shows the original exceedance curve [191] and (b) shows the pseudo dataset created by fine blocking.

5.10 Statistical Simulation of Landing Gear Load-Time Histories

The aim of the statistical simulation of landing gear load-time histories is to generate load-time histories for the complete landing gear design safe-life (i.e. 50,000 flights), which over repeated MCS iterations will demonstrate the observed per-flight variability in ground manoeuvre occurrence, sequencing and the variability in loading magnitude for each ground manoeuvre. Within the hybrid MCS-SSI approach, one complete load-time history will be simulated for each MCS iteration. This section will demonstrate how the ground manoeuvre occurrence and sequencing statistics generated from the ADS-B dataset can be combined with exceedance curves to successfully generate load-time histories on a per-flight basis for a wide-body civil aircraft.

Figure 5.29 shows the overall process used to statistically simulate the load-time histories for the wide-body civil aircraft. It can be seen from Figure 5.29 that the process first requires the sampling of the manoeuvre occurrences for a flight, followed by the sequencing of the sampled manoeuvres, prior to randomly sampling the load factors for each manoeuvre within the sequence.

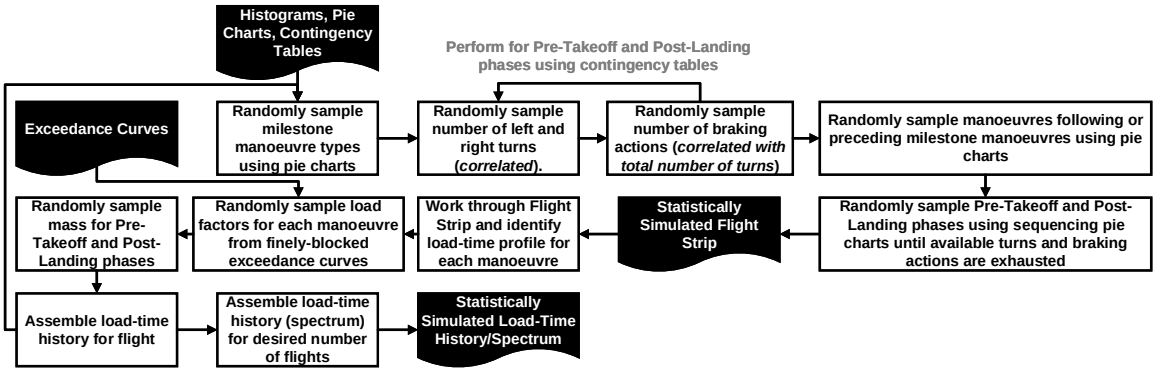

FIGURE 5.29. Proposed process for the statistical simulation of landing gear load-time histories.

5.10.1 Random Sampling of Ground Manoeuvre Occurrence and Sequence

Firstly, the occurrence of the manoeuvres for a flight must be randomly sampled based upon the statistics generated from the ADS-B dataset. The milestone manoeuvres are sampled first using a process called proportional sampling, which ensures that the proportional share values shown previously in the pie charts in Section 5.5.5 are represented over repeated MCS iterations. Table 5.3 shows the proportional share for the runway entry manoeuvre based upon the pie chart shown previously in Figure 5.23c.

TABLE 5.3. Proportional sampling values for runway entry type based on the pie charts from Figure 5.23c.

Runway Entry Type	Percentage Share	Proportional Share	Cumulative Proportion Bin
Standard Left (ID = 512)	49.960%	0.49960	[0,0.49960]
Standard Right (ID = 511)	47.194%	0.47194	[0.49960,0.97154]
Backtrack Left (ID = 522)	1.344%	0.01344	[0.97154, 0.98398]
Backtrack Right (ID = 521)	1.502%	0.01502	[0.98398, 1]

In order to randomly sample the runway entry type for a flight, a uniformly-distributed random number RN is generated between $[0,1]$ and the cumulative proportion 'bin' (e.g. for a standard left entry the bin is $[0,0.49960]$) that the value of RN falls into provides the runway entry type to be used for the current flight. This process is repeated for all of the milestone manoeuvres, therefore providing random samples of the turn directions for the pushback and turn onto stand manoeuvres, as well as the type and direction for the runway entry and exit manoeuvres.

The number of turns is then randomly sampled for the pre-takeoff and post-landing taxi phases. In order to represent the correlation between the number of left and right turns for both

taxi phases, correlated random sampling is used based upon the contingency tables shown in Appendix C. Appendix F provides a worked example of the correlated random sampling process, which is based on the random sampling a number of left turns, followed by generating a random sample for the number of right turns using the conditional probability for the number of right turns, given the value of the randomly sampled number of left turns. Correlated random sampling is also performed to randomly sample the number of braking occurrences based upon the total number of turning manoeuvres for each taxi phase. Appendix F also demonstrates the correlated random sampling of braking manoeuvres.

Following the use of proportional sampling and correlated random sampling, a flight can then be defined in terms of the randomly sampled milestone manoeuvres, turning occurrences and braking occurrences for both taxi phases.

The random sampling of the manoeuvre sequencing can then be performed using proportional sampling based upon the pie charts shown in Figures 5.24 and 5.25 and Appendix D. For example, using the pie chart for manoeuvres following a tail-left pushback shown in Appendix D, the cumulative proportion bins in Table 5.4 can be used to randomly sample, using RN ,the manoeuvre that immediately follows the tail-left pushback.

TABLE 5.4. Proportional sampling values for manoeuvre sequencing after tail-left pushback from Appendix D.

Following Manoeuvre	Percentage Share	Proportional Share	Cumulative Proportion Bin
Straight Taxi (ID = 66)	70.312%	0.70312	[0,0.70312]
Left Turn (ID = 21)	20.084%	0.20083	[0.70312,0.90396]
Braking (ID = 41)	9.604%	0.09604	[0.90396, 1]

In some instances, not all manoeuvres will be available to follow a certain manoeuvre. For example if no left turns are available within a taxi sequence, the proportional sampling tables must be updated to reflect the unavailability of a left turn manoeuvre, as shown in Table 5.5.

TABLE 5.5. Proportional sampling values for manoeuvre sequencing after tail-left pushback from Appendix D when no left turns are available

Following Manoeuvre	Percentage Share	Proportional Share	Cumulative Proportion Bin
Straight Taxi (ID = 66)	87.591%	0.87591	[0,0.87591]
Braking (ID = 41)	12.409%	0.12409	[0.87591, 1]

The manoeuvre sequence is constructed starting with defining the manoeuvres following and preceding the milestone manoeuvres using proportional sampling based upon the pie charts in Appendix D. The following manoeuvre sequence is then constructed using proportional sampling based upon the sequencing statistics shown previously in the pie charts in Figures 5.24 and 5.25, until all of the randomly sampled turning and braking occurrences have been exhausted. This results in the generation of a flight strip defined in terms of the manoeuvre ID numbers, as shown in Figure 5.30 (where ID 111 represents the takeoff roll, ID 333 is the landing touchdown

and ID 444 represents the landing roll). Appendix F provides a worked example of statistically simulating the manoeuvre occurrences and sequences for a flight.

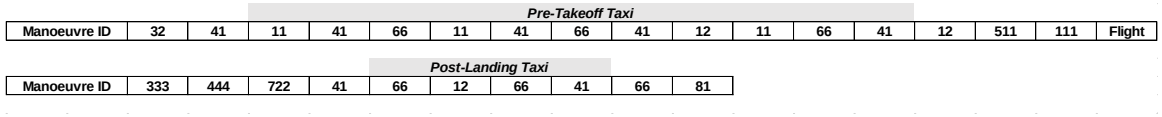

FIGURE 5.30. Example of a statistically simulated ground manoeuvre sequence.

5.10.2 Verification of Approach

In order to verify the statistical simulation of the manoeuvre occurrence and sequencing, 250,000 flights were statistically simulated and the resulting flight strips were processed using the algorithms constructed for the ADS-B data processing to evaluate the tally of manoeuvre occurrences and sequencing. This enabled the construction of contingency tables and pie charts such that the results from the statistically simulated flights could be compared back to the original ADS-B derived statistics.

Appendix F provides the complete error metrics when comparing the statistically simulated occurrence and sequencing statistics with the ADS-B derived values. From Appendix F it can be observed that the error in manoeuvre occurrences varied from 0.4% up to 32.3%. The maximum error of 32.3% concerns the correlated random sampling of takeoff turns and braking occurrences, for a combination of four pre-takeoff turns and two pre-takeoff brake occurrences which occurred in 2.5% of the statistically simulated flights compared to only 1.9% of flights in the ADS-B dataset. However, as this difference is small, it is expected that this is as a result of sampling error and would be reduced over an increased number of statistically simulated flights.

Regarding manoeuvre sequencing, Appendix F also demonstrates that the percentage error for manoeuvre sequencing statistics varies from 9.4% to 34.6%. The maximum error of 34.6% occurs for the manoeuvres following a pre-takeoff left turn, where in the statistically simulated flights, 14.2% of pre-takeoff turns were followed by a right turn, compared to 21.7% of turns in the ADS-B dataset. Rather than sampling error, this larger percentage difference in the manoeuvre sequencing is thought to be due to the pre-defining of the manoeuvres that follow and precede the milestone manoeuvres, resulting in turning and braking manoeuvres being unavailable to follow a turn or other manoeuvres later in the ground manoeuvre sequence. Future proposed sequencing simulation approaches that could potentially reduce the error in the manoeuvre sequencing statistics are discussed at the end of this chapter.

5.10.3 Random Sampling of Ground Manoeuvre Loading Magnitude

Following the statistical simulation of the manoeuvre occurrence and sequencing for a flight, the load factors associated with each manoeuvre in the flight can be randomly sampled. The generation of random samples for load factors is achieved by histogram sampling of the pseudo datasets generated from the fine blocking of the exceedance curves for wide-body civil aircraft listed in Appendix E. An example of histogram sampling is shown in Figure 5.31.

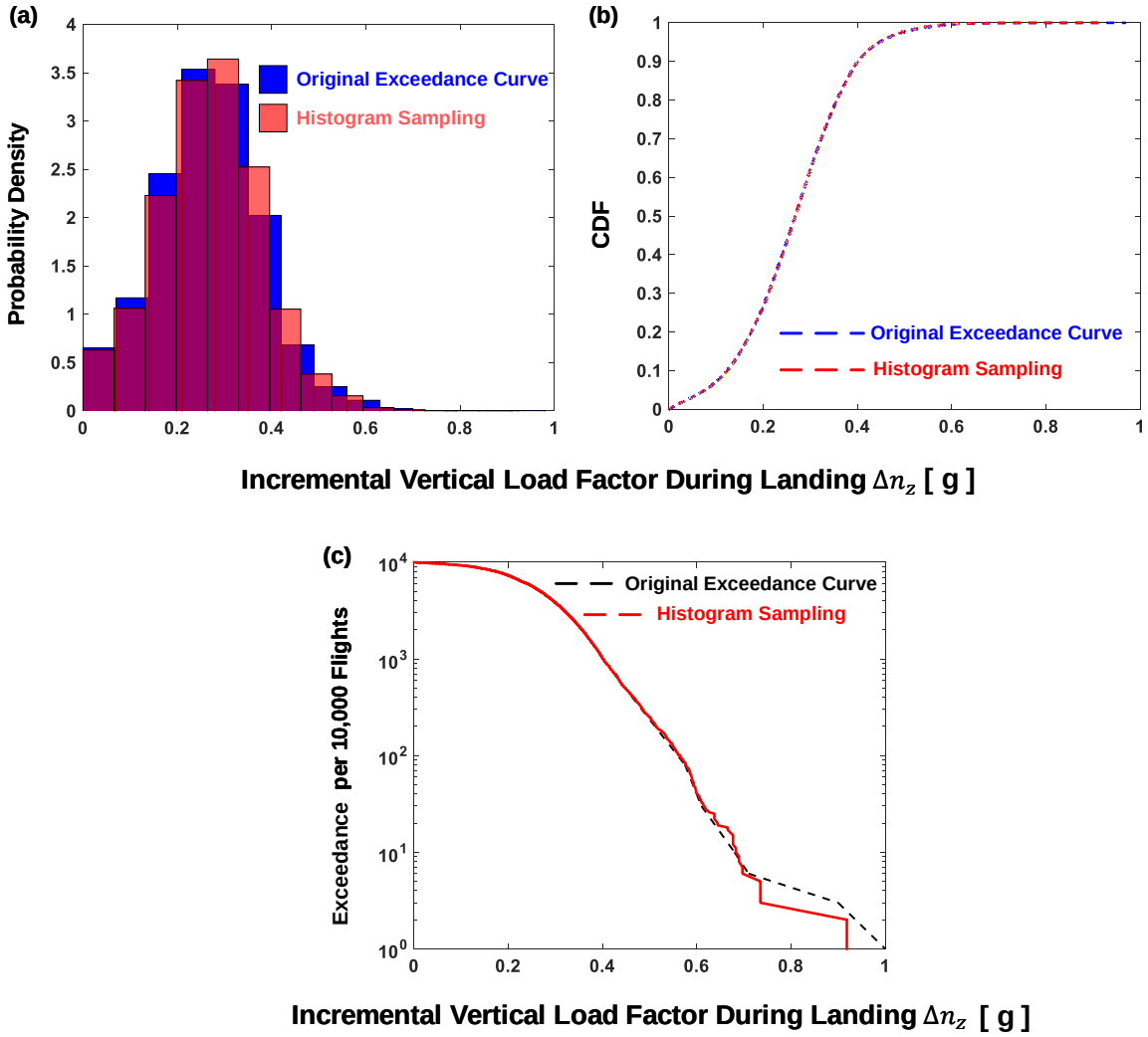

FIGURE 5.31. Demonstration of histogram sampling of load factors: (a) Comparison of the histograms from histogram sampling and pseudo dataset generated from fine blocking of the original exceedance curve, (b) comparison of the CDFs generated from the histograms and (c) a comparison of the exceedance curve generated from histogram sampling and the original exceedance curve [191].

The fine blocking of the exceedance curves will result in typically thousands of pseudo data points, each representing possible values of the load factor for each manoeuvre. By arranging the pseudo data points from smallest to largest value, a random integer 'RI' can be sampled from a uniformly-distributed random number generator and the RI value represents the position in the ordered pseudo dataset. As a result, histogram sampling provides a way of randomly sampling the load factor magnitude for a manoeuvre based upon the exceedance curve for the given manoeuvre. Repeated histogram sampling will recover the pseudo data set and the original exceedance curve, as shown in Figure 5.31. The deviation between the exceedance curves at low exceedance values (i.e. 'rare' high magnitude loads) shown in Figure 5.31 can be reduced by increasing the number of samples generated from histogram sampling and is expected to be minimal for the large number of flights to be simulated within a typical landing gear design safe-life.

The takeoff and landing mass for the flight is also randomly sampled using correlated random sampling based upon the contingency table that details the mass variability for a wide-body civil aircraft [191]. The method used for correlated random sampling is the same as the approach for generating correlated random samples for the turning and braking occurrences, as demonstrated in Appendix F.

5.10.3.1 Assumed Load Factor-Time Profiles

All ground manoeuvres in the randomly sampled manoeuvre sequence can be represented as short sections of load-time history. These sections are known as the load-time profile for each manoeuvre. For example, a braking manoeuvre can be represented as an increase up to the randomly sampled n_x drag load factor, followed by a decrease back to the unloaded stated (i.e. [0 g $\rightarrow n_x \rightarrow$ 0 g]) [188]. Existing practice for the construction of landing gear load-time histories provides the load-time profiles to be used for each ground manoeuvre type [188].

However, certain manoeuvres result in complicated combinations of loading directions, such as landing touchdown. During landing touchdown, the landing gear is exposed to vertical n_z loads, drag n_x loads (from spin-up and spring-back) and side n_y loads (from landing drift) [63]. Therefore, the load-time profiles must be defined across all three loading directions and may span many positions in the load time history, as visualised in Figure 5.32.

Within the more complicated load-time profiles, such as the touchdown profile in Figure 5.32, the load factor values are still generated using histogram sampling. In some instances, load factors are correlated across the loading directions, such as the correlation between spin-up and spring-back loads [12].

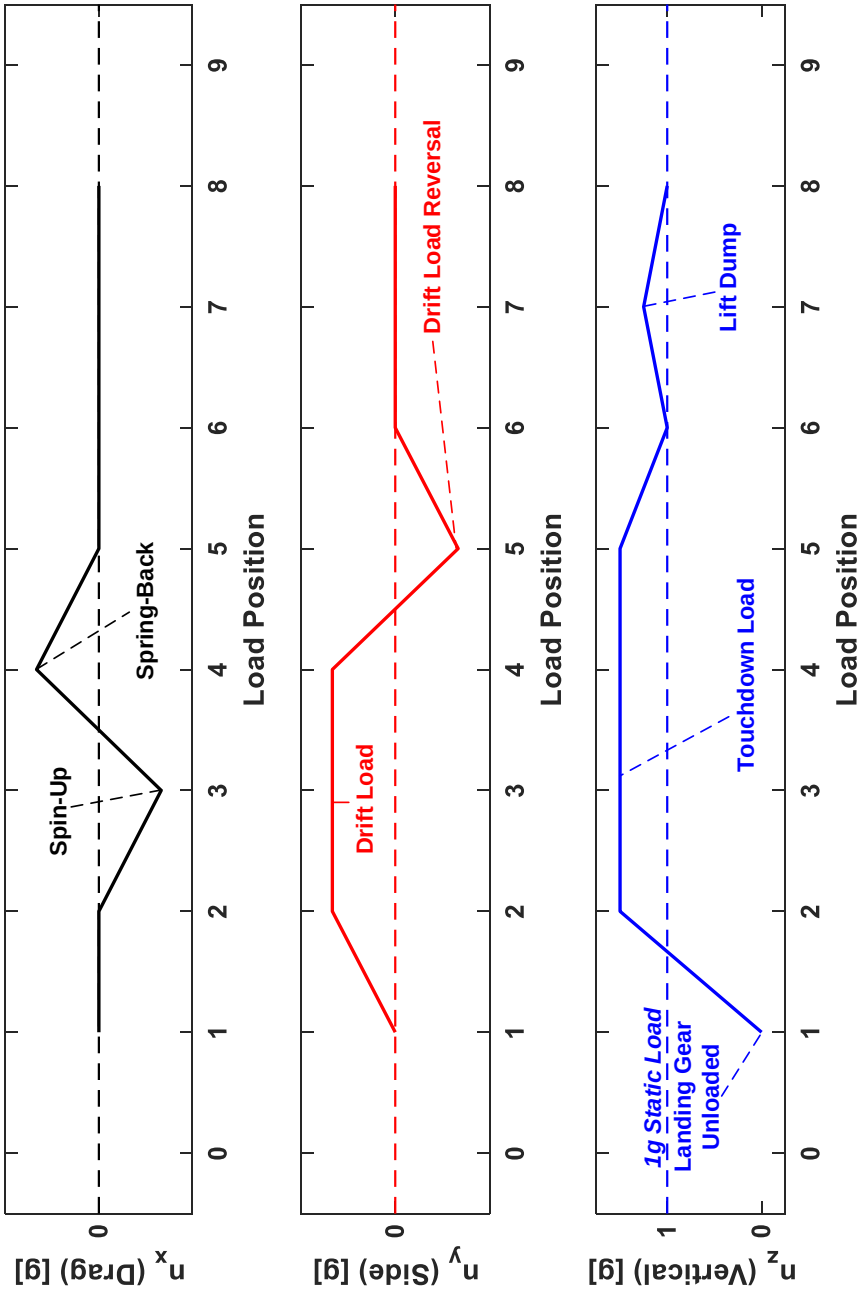

FIGURE 5.32. Load-time profile for the landing touchdown manoeuvre across the n_x, n_y and n_z loading directions.

5.10.4 Output of Load-Time History Statistical Simulation

Following the random sampling of the load factors for each required load-time profile of the randomly sampled manoeuvre sequence, the load-time history for the statistically simulated flight can be assembled. The load-time history provides the sequence of n_x, n_y and n_z load factor values during the pre-takeoff and post-landing taxi phases. Figure 5.33 shows a statistically simulated load-time history for a single flight.

It is important to note that whilst the sequence of loads shown in Figure 5.33 is commonly referred to as a 'load-time history', the rainflow counting methods employed for S-N fatigue analysis do not account for the specific time (e.g. seconds) between loads[1] and only account for the sequence or order in which loads occur [7]. Consequently, the x-axis of all load-time history plots in this thesis have the unit of 'load position', and this integer value represents the position of a specific load within the overall sequence of loads. Such a definition is required to ensure that ground manoeuvres which result in combined load factors (e.g. landing drift) apply the required load factors in the correct sequence in the loading history.

Figure 5.33 demonstrates the primary landing gear manoeuvre load factors, including push-back, turns, braking, touchdown (including spin-up and spring-back) and bump loads, along with the randomly sampled takeoff and landing mass. The flight shown in Figure 5.33 consists of 27 individual manoeuvres (this ranges from between 25 to 60 per-flight) and comprises of approximately 80 individual load factors (this ranges from 50 to 150 per-flight). It should be noted that the due to the sampling of load factor magnitudes from existing datasets, the n_x drag load factors within the load-time histories are defined in the opposite direction to the sign convention shown for the landing gear assembly in Figure 5.1. As a result, the n_x drag load factors shown in the load-time histories must be multiplied by a factor of -1 prior to further analysis, to ensure that the positive n_x direction represents drag loads.

The statistical simulation of flights can be repeated,as shown for five consecutive flights shown in Figure 5.34. The individual flights can be identified in Figure 5.34 from the changing mass values and the n_z unloading as the aircraft takes off. It should be observed from Figure 5.34 that each flight has a different number of side and drag loads, therefore demonstrating the random sampling of the turn and braking manoeuvre occurrence and sequencing.

Finally, the statistical simulation process can be used to simulate the load-history for an entire landing gear design safe-life of 50,000 flights. Figure 5.35 shows the resulting load-time history for a 50,000 flight design safe-life, which comprises of approximately five million individual load factor levels. The load time history generated in Figure 5.35 encapsulates the variability in manoeuvre occurrence, sequencing and the variability in loading magnitude for each manoeuvre. The CPU run-time required to statistically simulate the load-time history was 6.75 seconds when implemented in MATLAB® environment[2].

[1] i.e. strain-rate effects are neglected.

[2] Computer Specifications: 4-core processor (3.40 GHz) with 16.0 GB RAM.

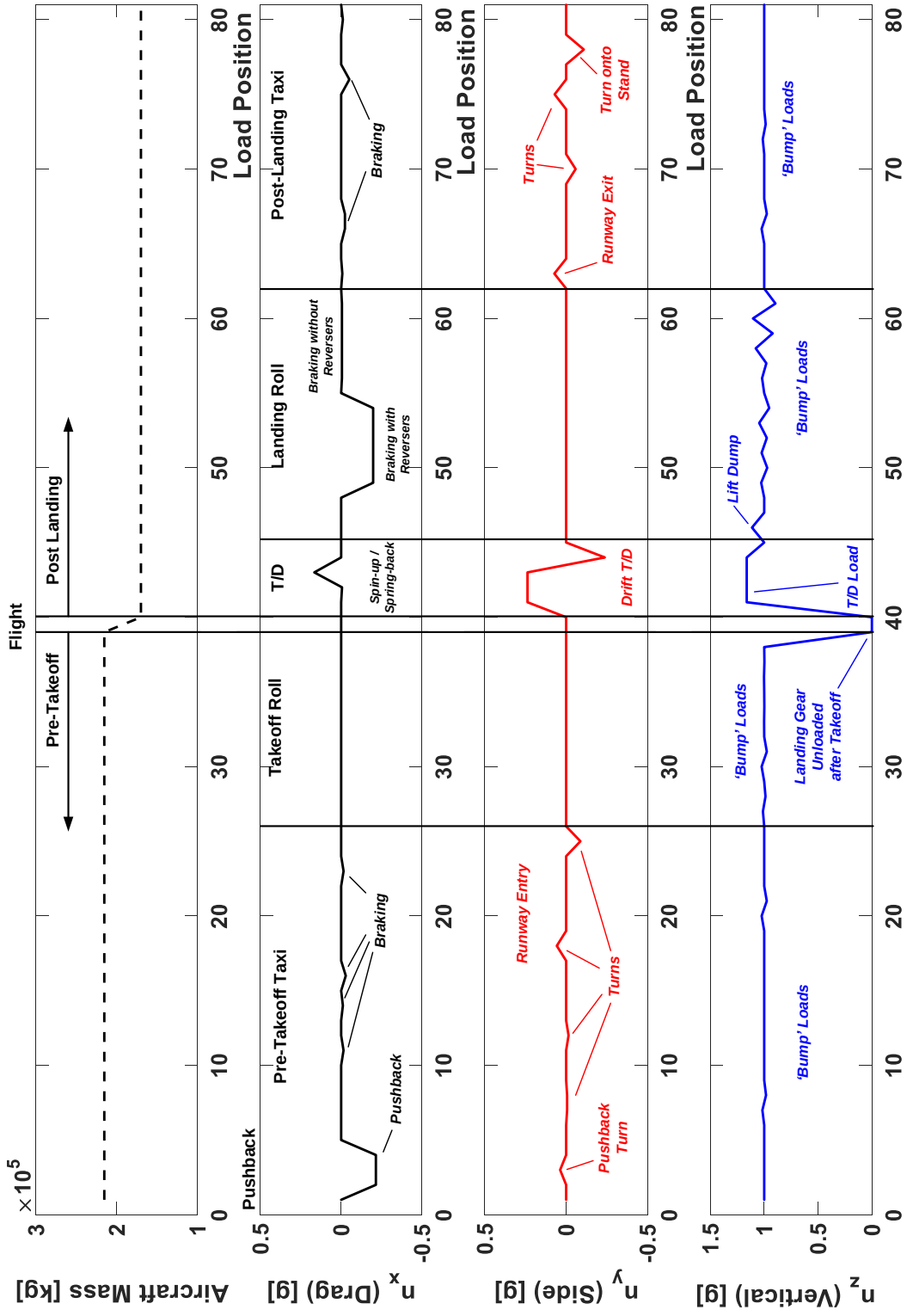

FIGURE 5.33. Statistically simulated load-time history for one flight (T/D = *TouchDown*).

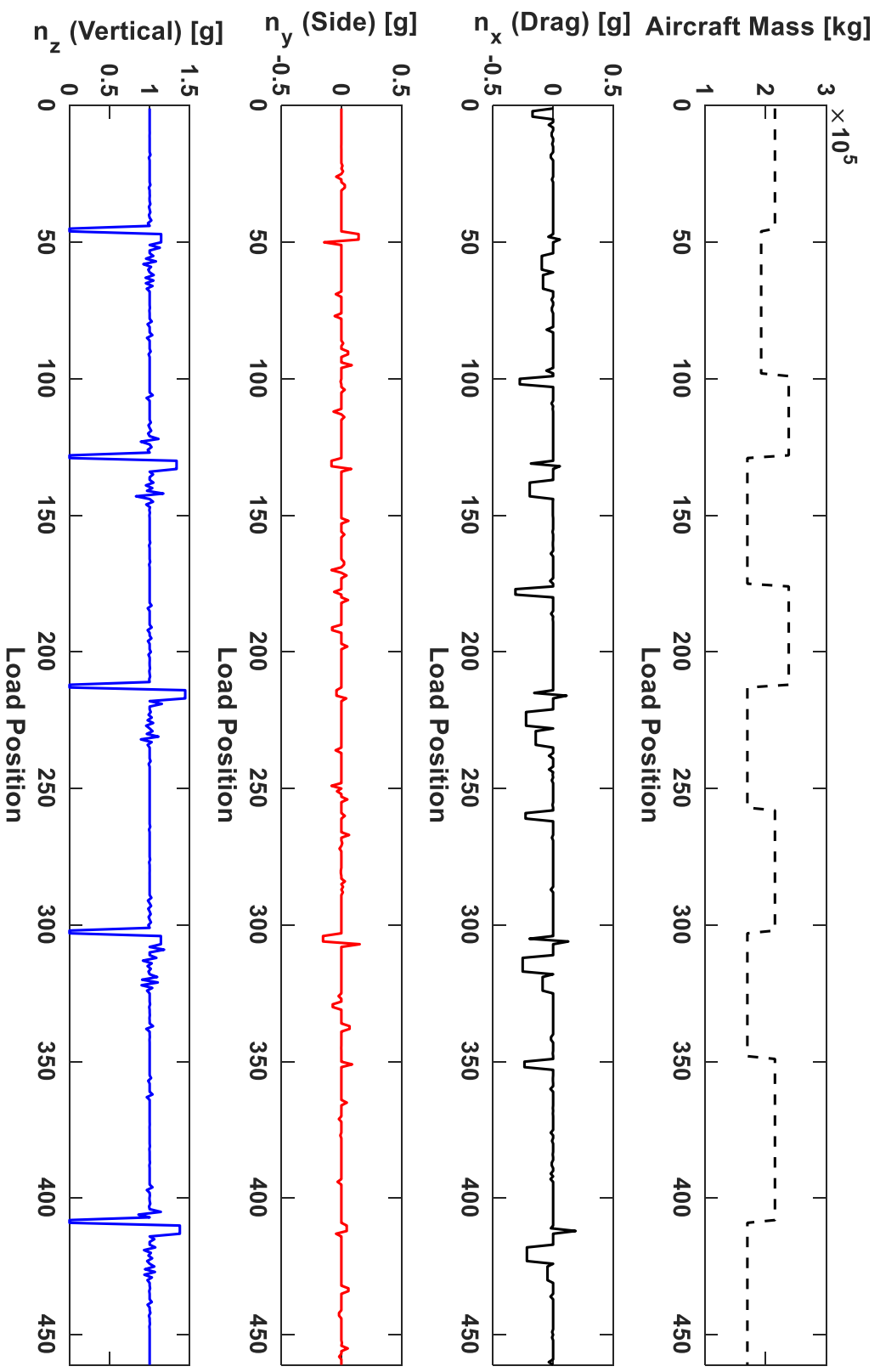

FIGURE 5.34. Repeated statistical simulation of load-time histories to produce five flights.

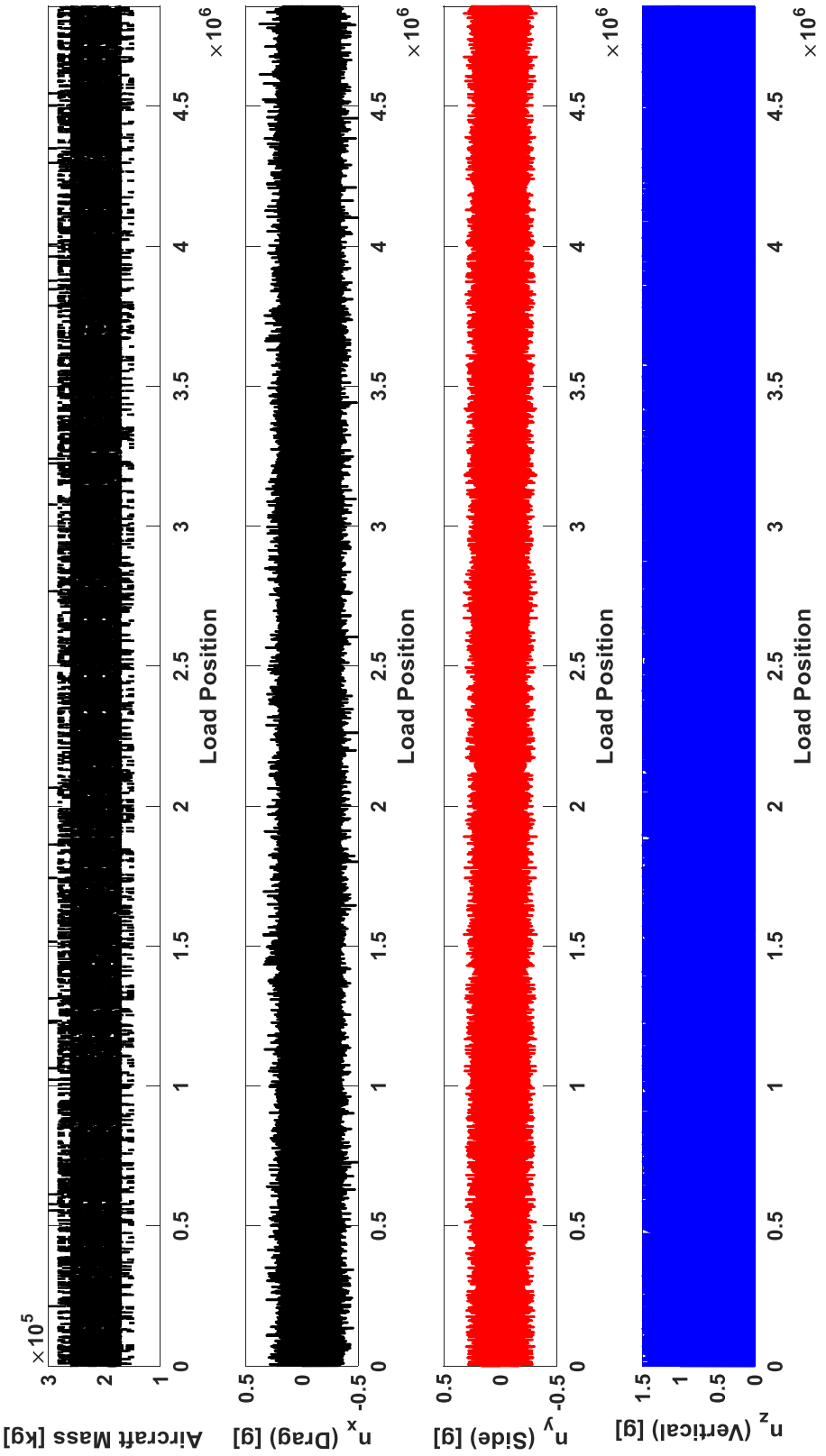

FIGURE 5.35. Repeated statistical simulation to produce a design life load-time history.

5.10.5 Limitations of Statistical Simulation of Load-Time Histories

Based upon the verification performed for the ADS-B data collection process and the statistical simulation process in Sections 5.7 and 5.10.2 respectively, there are a number of current limitations of the ADS-B data collection and load-time statistical simulation processes. These limitations ultimately reduce the accuracy of the representation of the variability in landing gear load-time histories included within the probabilistic fatigue methodology.

5.10.5.1 Availability of Data

A number of limitations regarding ADS-B data will result in potential inaccuracy or 'biasing' of the statistics shown in Sections 5.5 and 5.6. Firstly, ADS-B coverage is not currently available for all routes and operators of the wide-body civil aircraft, and as a result, the statistics shown within this chapter will be biased towards the available routes. This source of bias may result in the statistics for landing gear ground manoeuvres failing to represent the complete wide-body aircraft fleet, especially when major hubs of the aircraft operators do not have ADS-B receiver coverage. However, ADS-B receivers are continually being activated and therefore, it is expected that gaps in ADS-B coverage will reduce in the future.

5.10.5.2 Sources of Error in ADS-B Data

As highlighted in Section 5.3.1.1, data smoothing is required to remove 'noise' from the ADS-B data files and 41.5% of flights in the verification dataset were found to contain noisy data files. ADS-B data files could also contain data jumps, where aircraft rapidly transition from one location to another. Such behaviour was observed in the ADS-B datasets collected during this study, and have also been highlighted as a source of ADS-B error by Tabassum and Semke and Ali et al [215, 216]. The cause of ADS-B data jumps are still under investigation [215, 216]. As data jumps result in the aircraft latitude and longitude position changing, it is expected that this could result in errors in the characterisation of ground manoeuvres reliant on latitude and longitude positions, such as the aircraft pushpack (see Section 5.3.1.2). One way in which data jumps could be removed during ADS-B dataset processing is to compute the distance (based on latitude and longitude) between ADS-B broadcast points. If the distance between an ADS-B broadcast point and the following broadcast point is significantly bigger than the distance between the ADS-B broadcast points that precede and follow the selected broadcast point, the broadcast point can be identified as a data jump and removed from the ADS-B dataset.

Another source of error within ADS-B datasets is 'dropout' of the ADS-B signal, which can be considered as a large time difference between broadcasts from the ADS-B transponder on the aircraft. ADS-B signal dropouts result in 'missing data points' in the ADS-B dataset. Missing data points ultimately reduce the fidelity of the ADS-B dataset and can therefore result in

ground manoeuvres that occur during the dropout period failing to be identified by the algorithms detailed in Section 5.3.

Dropouts or missing data points were observed in 45.4% of flights in the verification dataset. In the work performed by Ali et al, it is suggested that the probability of observing loss or corruption of ADS-B aircraft position information is approximately 10% [217]. It is proposed that the significantly higher observed number of flights with missing data points within the study presented in this chapter is as a result of focusing on aircraft taxi phases. On the ground, the ADS-B signal may experience increased interference due to other aircraft and sources of electromagnetic interference [218]. Therefore, it is suggested that ADS-B datasets generated by aircraft during taxi phases may show larger errors compared to when the aircraft is airborne.

Dropouts can occur for a multitude of technical and operational reasons (e.g. transponder failure, ground-based interference, errors in the global positioning information provided to the ADS-B transponder etc. [217]) and therefore, it is easier to assess the fidelity of ADS-B datasets by quantifying the time between subsequent ADS-B broadcasts, known as the step time.

A review of the ADS-B datasets collected in Section 5.4.1 identified that approximately 60% of ADS-B broadcasts were within 10 seconds or less of another broadcast. Figure 5.36 shows a histogram of the frequency of observed step times across the 1,265 collected ground tracks. Large step times (e.g. > 60 seconds) were observed in situations where the aircraft ground speed remained zero for an extended period of time.

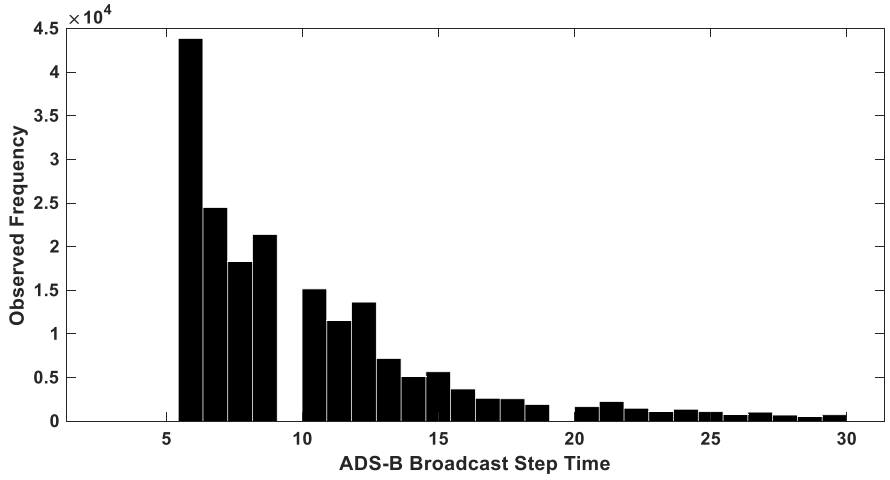

FIGURE 5.36. Observed frequencies of ADS-B step time between the broadcast points of 1,265 pre-takeoff and post-landing taxi phases.

Work performed by Verbraak et al suggested that 90% of ADS-B broadcasts should occur within 10 seconds or less [219]. One possible cause for the larger step time for the 1,265 ADS-B datasets collected in Section 5.4.1 is that the work performed in this chapter has focused on the

processing of ASD-B datasets generated during aircraft taxi, rather than in flight. Verbraak et al have demonstrated that as the number of aircraft in the coverage area of an ADS-B receiver increases, so does the broadcast step time [219]. As aircraft taxi phases occur at airports, there are expected to be significantly more aircraft within the ADS-B receiver coverage area, resulting in much larger broadcast step times than would be expected once the aircraft is in flight.

Therefore, it is evident that inherent errors present within the ADS-B datasets, from data jumps, missing data points and dropouts resulting from large broadcast step times, can result in incorrect ground manoeuvre identification. This is as a result of incorrect manoeuvre identification from missing data points/location jumps or from ADS-B dropouts. From reviewing previous ADS-B data quality studies, it is anticipated both these error sources are exacerbated when focusing specifically on aircraft taxi phases.

It is proposed that future work could aim to further assess the validity of using ADS-B datasets to identify and characterise aircraft ground manoeuvres by comparing the ground tracks generated from ADS-B datasets with those generated from existing ground-based radar. Such an approach has already been demonstrated during flight tests by Zhang et al [220]. Another proposed approach is to compare the manoeuvres extracted by the processing of ADS-B datasets for a given flight, with the data from the aircraft flight data recorder sourced from the aircraft of the specific flight. Such an approach would provide further validation that the algorithms developed in Section 5.3 can successfully identify and extract aircraft ground manoeuvres.

5.10.5.3 Data Processing Errors and Error Cascade

The algorithms for ADS-B data processing also currently contain limitations regarding accurate characterisation of the pushback direction and reliably identifying the turn direction for 180° turns. This is as a result of the compass approach visualised previously in Figure 5.8 failing to provide sufficient information in all cases to define the direction of the turn. As a result, future work is proposed that would validate turn directions based upon computing the bearing between the start and end locations of the aircraft turn, using the latitude and longitude of the aircraft.

The method used to identify the sequence of ground manoeuvres for a flight is also susceptible to an error cascade, where one incorrectly characterised ground manoeuvre will result in an incorrect manoeuvre sequence. An example of this is the impact of incorrectly characterising the pushback direction on the pre-takeoff manoeuvre sequence, as discussed previously in Section 5.7. It is proposed that a way in which to mitigate the error cascade is to continually validate the extracted manoeuvres from the algorithms defined in Section 5.3 with the approach based on defining turn directions using bearings computed from latitude and longitude positions. Any flights showing a disagreement in the two manoeuvre identification processes can then be further investigated.

The error cascade present in extracted manoeuvre sequences can also be related to the inherent errors present within the ADS-B dataset due to dropouts and data jumps as discussed in the previous subsection. Therefore, in order to mitigate the effect of ADS-B data error sources on the correct identification of ground manoeuvres, an approach that relates the aircraft position from ADS-B broadcasts to the known airport geometry could be considered. From this, the position of the aircraft during the ADS-B dropout can be inferred through comparison with the possible taxi routes that the aircraft could have taken during the ADS-B dropout. Such an approach would naturally require a large database of known airport geometries, however, there has been recent success in relating ADS-B derived ground tracks to known airport geometries, as described by Brownlee et al [196].

Consequently, it is clear that in order to overcome the existing limitations of identifying and characterising ground manoeuvres from ADS-B datasets, further work is required in the following areas:

- Further investigation into ADS-B data error sources specifically concerned with aircraft taxi phases.
- Validation of ADS-B ground tracks with ground-based radar and data from flight data recorders from aircraft on specific flights.
- Increased validation and verification within the manoeuvre characterisation algorithms, through the use of latitude and longitude based manoeuvre characterisation and relating ADS-B derived ground tracks to known airport geometries.

5.10.5.4 Limitations of Statistical Simulation Process

Concerning the load-time history statistical simulation process, there are a number of limitations resulting from the use of sampling from contingency tables and histogram sampling. The use of contingency tables results in the statistical simulation process only being able to randomly sample turning and braking occurrences that have been previously observed in the assembled ADS-B dataset and therefore, may not be representative of all of the turning and braking combinations that could be observed in-service. In a similar nature, the histogram sampling of load factor values restricts the possible load factor values to those generated from the fine blocking process. However, both of these areas could be mitigated with increased data collection.

Another limitation of the statistical simulation process are the errors observed in the manoeuvre sequencing in Section 5.10.2 and Appendix F. As the milestone manoeuvres are used as a starting point for the ground manoeuvre sequences, this can result in unrepresentative taxi sequences, leading to the larger percentage errors for the manoeuvre sequencing statistics. An alternative approach that could be considered within future work is to generate a set of sequencing statistics for every observed combination of turning occurrences (e.g. an individual set of pie charts would define the manoeuvre sequencing for a flight with two left and two right

pre-takeoff turns with four braking occurrences). It is anticipated that such an approach would improve the accuracy of the statistical simulation process by reducing the bias introduced by pre-assigning the manoeuvres which follow or precede the milestone manoeuvres.

Missing Manoeuvres from Statistical Simulation Process

Additional data is also required to represent the full range of landing gear manoeuvres within the statistical simulation methodology. Loading resulting from in-service events such RTOs, towing, braked turns and torsional loads is currently not able to be included within the statistical simulation process as a result of a lack of data for the occurrence of each of these manoeuvres. In addition, within the statistical simulation of load-time histories, it is assumed that the load factors are statistically independent (i.e. uncorrelated). However, it is expected that certain loading conditions will demonstrate a correlation between the load factors for different ground manoeuvres. For example, Buxbaum suggests that correlation exists between the n_x, n_y and n_z load factors during landing touchdown [12], although the quantification of this correlation would require additional in-service loads monitoring of MLG assemblies. Finally, it is anticipated that correlation will exist for the manoeuvre occurrence and sequencing between flights, as it is expected that wide-body aircraft will operate 'return' journeys, where they repeatedly operate from the same airports. Therefore, a much wider ADS-B data collection activity would be required to characterise any manoeuvre correlation that occurs between flights, by tracking individual aircraft across a series of consecutive flights.

5.11 Summary

Aircraft landing gear are exposed to cyclic loads from the ground manoeuvres that aircraft perform in-service. Variability is observed in the magnitude of the loads associated with each ground manoeuvre, along with the per-flight variability concerning the occurrence and sequencing of ground manoeuvres. While data is widely available to characterise the variability in loading magnitude, assumptions are currently required regarding ground manoeuvre occurrence and sequencing when constructing load spectra and load-time histories for landing gear components.

Big-data sources, such as 'real-time' aircraft tracking using ADS-B transponder data, provide the required information to characterise the variability in ground manoeuvre occurrence and sequencing for wide-body civil aircraft. This chapter has presented a novel approach for generating landing gear ground manoeuvre statistics using ADS-B data files, through detailing the algorithms developed to identify and characterise ground manoeuvres based upon speed and heading changes observed in the ADS-B data files. The work presented within this chapter is the first application of ADS-B datasets to support aircraft structural design presented in the public domain.

From implementing the algorithms on an assembled dataset of 1,265 flights across a global wide-body aircraft fleet, the following statistics and observations were generated:

- For wide-body civil aircraft, the mode number of pre-takeoff turns was found to be three per-flight, and the number of post-landing turns was found to be two per-flight, showing good agreement with previous studies based upon in-service loads monitoring of wide-body aircraft.
- For wide-body civil aircraft, the mode number of braking occurrences for both pre-takeoff and post-landing taxi phases was both found to be three per-flight, showing consistency with previous studies based upon in-service loads monitoring of wide-body aircraft.
- The share of left and right turn directions across all turning manoeuvre types was found to be equal.
- For wide-body aircraft, braking manoeuvres are most commonly followed by a straight taxi manoeuvre and vice versa, as a result of aircraft queuing during taxi.

The statistics generated from the ADS-B datasets were used to evaluate the assumptions currently required within the construction of load spectra for landing gear components. Firstly, the observation of an equal share between left and right turn directions across all turning manoeuvres supports the current practice of assuming an equal number of left and right turns across flights and design safe-lives for landing gear components. However, from the ADS-B derived sequencing statistics it was observed that turn-reversals (e.g. a left turn, immediately followed by a right turn) only occur in 20% to 30% of turning manoeuvres, suggesting that current practice of assuming every turning manoeuvre is a turn-reversal is potentially conservative. Finally, existing practice assumes that an average number of turning and braking manoeuvres is performed for each flight in the load spectra. The histograms for turning and braking occurrences generated for the wide-body civil aircraft from the ADS-B dataset contradict this assumption by demonstrating positive skew. The positive skew in the histograms suggests that the current practice of assuming average manoeuvre occurrences will not adequately account for flights that demonstrate a large number of manoeuvres, such as when aircraft operate at large international airports.

Concerning the probabilistic fatigue methodology, the use of a big-data source in the form of the ADS-B data files has enabled the inclusion of ground manoeuvre occurrence and sequencing variability within the probabilistic fatigue methodology. The ground manoeuvre occurrence and sequencing variability is incorporated into the probabilistic fatigue methodology through the statistical simulation of load-time histories, which provides a randomly sampled design safe-life load-time history for a landing gear structural assembly. As a result, the use of big-data sources within the probabilistic fatigue methodology contributes to overcoming the *availability of data* blocker to a probabilistic approach to design, through generating datasets and statistics

regarding ground manoeuvre occurrence and sequencing for a global aircraft fleet, which was not previously feasible using traditional in-service loads monitoring approaches. In addition the use of a big-data source challenges the *accuracy of data characterisation* blocker, through providing a more thorough statistical characterisation of the variability in ground manoeuvre occurrences, beyond the average values available from previous studies. Finally, characterisation of the ground manoeuvre occurrence and sequencing variability from a big-data source helps to overcome the *simplifications/assumptions of deterministic analysis process* blocker, through removing the need to make assumptions regarding the occurrence and sequencing of manoeuvres within the existing deterministic safe-life fatigue analysis process. Table 5.6 summarises how the use of big-data sources can help overcome the blockers to a probabilistic approach to design.

TABLE 5.6. The blockers to probabilistic design approaches overcome by exploiting big-data sources.

Blocker	Blockers overcome due to exploitation of big-data sources
Computational Expense	N/A
Required Assumptions of Existing Process	Assumptions regarding loading occurrence and sequencing are no longer required in the deterministic and probabilistic fatigue methodologies.
Availability of Data	'Real-time' tracking and monitoring of structures enables datasets and statistics regarding loading occurrence and sequencing to be generated, which was not previously feasible.
Accuracy of Data Characterisation	Characterisation of the variability in loading occurrence has been extended beyond the average values previously available, to account for skew within the occurrence histograms.
Required Knowledge	N/A

CHAPTER 6

SURROGATE MODELLING OF LANDING GEAR LOADS

The computation of landing gear component loads, based upon the global loads applied to a landing gear assembly, is a complex task as a result of the geometry, layout and joints present within the structural assembly. Existing practice requires the use of computationally expensive finite element models to convert global landing gear loads into internal component loads. The utilisation of finite element models represents a significant computational expense in the existing deterministic fatigue analysis process and as a result, presents a potentially prohibitive computational expense within a probabilistic fatigue methodology. This expense is particularly evident when considering the millions of individual loads that will be required to be assessed from the statistically simulated load-time histories, in order to represent ground manoeuvre occurrence and sequencing variability in the probabilistic fatigue methodology.

Surrogate modelling methods have been proposed as a route to generating more computationally-efficient representations of finite element models. This chapter will explore whether it is possible to generate accurate representations of the input-output relationships of complex landing gear finite element load models, to ensure that the statistically simulated load-time histories can be converted into internal component loads within the probabilistic fatigue methodology. Through using two case studies of differing complexity, this chapter will also identify trends in the accuracy and required training resource of different types of surrogate models, with a view to providing guidance to support the wider utilisation of surrogate models in engineering design and analysis. The following chapter will also conclude by highlighting how the wider adoption of surrogate modelling methods can help overcome the blockers to a probabilistic approach to design.

6.1 Landing Gear Beam Models

The landing gear loads introduced in Chapter 5 represent 'global' load factors which result in drag F_X, side F_Y and vertical F_Z loads being applied to the tyres of the landing gear [221, 222]. In order to conduct stress analysis of specific components within the landing gear structural assembly for static and fatigue analysis, the global loads applied at the tyres must be converted to internal component loads [222].

Whilst landing gear structural assemblies are typically single-load path and statically determinate, the geometry and mechanical joints present within landing gear assemblies results in analysis complexity when converting the global loads to the internal loads of a specific component. As a result, linear static FEA models of landing gear structural assemblies are employed to convert global loads to internal loads. These FEA models typically comprise of 1D beam finite elements (i.e. capable of carrying axial, shear, bending and torsional loads) and are therefore referred to as either beam models or 'stick' models [63, 221, 222]. An example of an FEA beam model for a 4-wheel Main Landing Gear (MLG), as typically employed on wide-body aircraft, is shown in Figure 6.1, which also shows the structural elements of the MLG structural assembly.

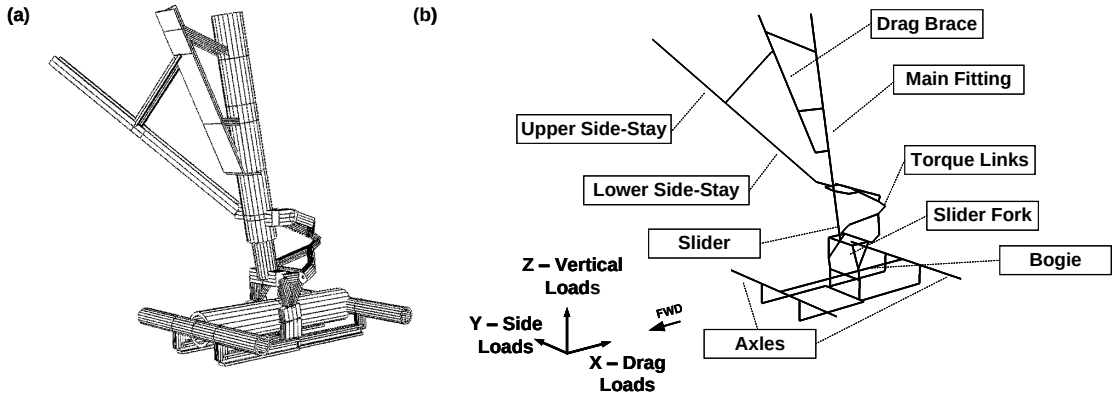

FIGURE 6.1. A 1D beam FEA model of a 4-wheel MLG shown with (a) a 3D beam representation and (b) key structural elements of the assembly.

FEA beam models are required to convert global loads to internal component loads due to the structural complexity of landing gear assemblies:

- **Geometrical Complexity:** MLG assemblies comprise of many individual structural components, with varying sectional and material properties.
- **Loading Complexity:** MLG assemblies are exposed to a complex and combined loading of F_X, F_Y and F_Z.
- **Joints:** To achieve MLG shock absorption, retraction and stowage, MLG assemblies consist of a large number of mechanical joints.

- **Airframe Attachment/Boundary Conditions:** The airframe attachment of the MLG can result in complex boundary conditions.

The primary dimensions of the MLG assembly are shown in Figure 6.2 and are representative of the geometry of an in-service wide-body civil aircraft MLG, sourced from public domain photographs of MLG assemblies. During linear static internal loads analysis, the shock absorber can be assumed to be fixed for simplicity, and this is represented by the fixed Shock Absorber Travel (SAT) of 450 mm shown in Figure 6.2. The FEA beam model was constructed in ABAQUS® using Python™ scripting [223, 224].

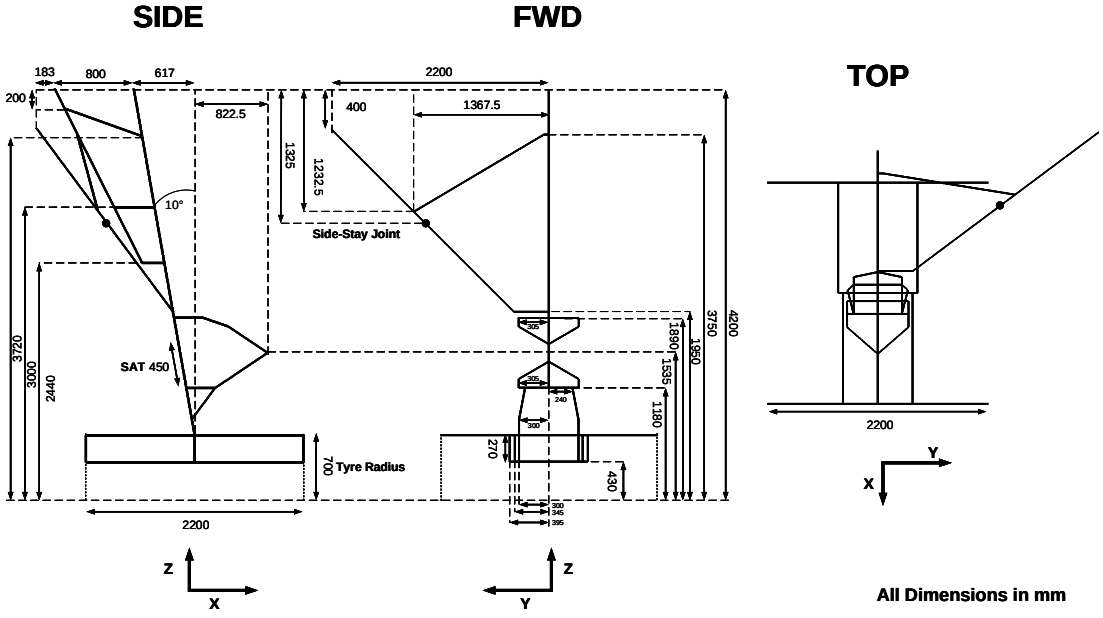

FIGURE 6.2. The primary dimensions of the FEA MLG beam model.

Representative sectional properties of the MLG assembly were sourced from scaling public domain photographs of wide-body civil aircraft MLG. For the modelling of mechanical joints (predominately pin joints) across the MLG structural assembly, Degree of Freedom (DoF) releases were implemented at each joint using the appropriate ABAQUS® 'connector' elements. DoF releases permit two beam elements (i.e. structural components) in the assembly to move independently of one another, in a motion that is representative of the actual mechanical joint [26]. DoF releases permit the load transfer across mechanical joints to be represented within the FEA beam model. The DoF releases used by van Ginneken [225] were implemented within the FEA MLG beam model. To represent the boundary conditions of the airframe attachment of the MLG at the side-stay and main fitting locations, pinned boundary conditions were assumed for the FEA MLG beam model, as previously performed by Caputo et al and Heerens [221, 226].

Global loads are applied to the MLG assembly at the tyres, assuming an equal share of the F_X, F_Y and F_Z loads between both MLGs and across all four tyres. The F_X, F_Y and F_Z loads are computed using Equations 5.1 through 5.3 in Chapter 5 based upon the aircraft mass M and the load factors n_x, n_y and n_z. To introduce loads into the MLG beam model, the loads F_x, F_y and F_z at each individual tyre are computed, by dividing the global load by a factor of 8, to account for two MLG and four tyres on each MLG. As the loads within the FEA MLG beam model are applied at the axle stub, the moments (M_x, M_y, M_z) resulting from the tyre radius offset from the axle, are also applied at the axle, neglecting any non-linear response from the tyres.

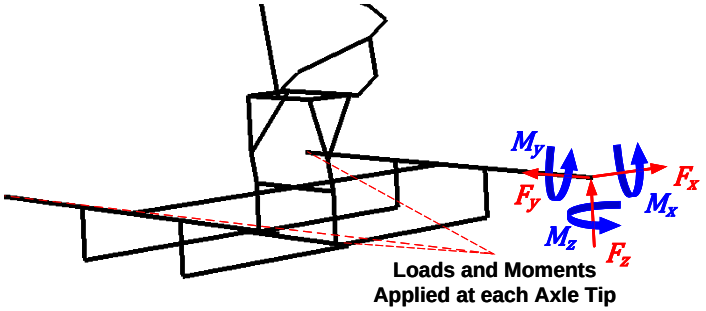

FIGURE 6.3. The method of loading for the FEA MLG beam model.

The MLG beam model was meshed using seeding conditions from current practice [221] and B31 type elements (Linear Beam in 3D space) for linear static analysis. A single evaluation of the FEA MLG beam model was found to require on average 20 seconds of CPU run-time[1].

6.1.1 The Need for Surrogate Modelling of Landing Gear Beam Models

The statistical simulation of load-time histories demonstrated in Chapter 5 highlighted that a single design safe-life of 50,000 flights is composed of approximately five million individual load-factor levels. As a result of the 20 second CPU run-time for performing a single evaluation of the linear static FEA MLG beam model, the conversion of global loads to internal component loads represents a significant computational expense for fatigue design and analysis. This computational burden is further compounded when considering the probabilistic fatigue methodology based upon an MCS-SSI approach. An MCS-SSI approach would require thousands of statistically simulated design safe-life load-time histories to be evaluated using the FEA MLG beam model, representing a prohibitive and infeasible computational resource burden.

Surrogate models, as introduced across Chapters 1 to 3, enable a model to be constructed that provides an accurate representation of the input and output relationship of a computationally expensive model, whilst requiring significantly less computational resource to evaluate [57]. The surrogate model can then be evaluated as a replacement for the original computationally

[1]Computer Specifications: 4-core processor (3.40 GHz) with 16.0 GB RAM.

expensive model [57]. In the context of the FEA MLG beam model, the surrogate model would be able to produce predictions of internal component loads based upon given values of the load factors and aircraft mass, without requiring the direct evaluation of the linear static original FEA MLG beam model. The use of a surrogate model to replace the linear static FEA MLG beam model within the probabilistic fatigue methodology would therefore significantly reduce the computational expense of implementing the MCS-SSI approach.

6.2 Surrogate Modelling Process

In order to construct a surrogate model, a range of candidate surrogate modelling methods are available. Figure 6.4 shows the process required to generate a surrogate model. Each surrogate modelling method consists of individual 'tuneable' parameters. The purpose of the process in Figure 6.4 is to identify the specific values of the tuneable parameters that minimise the error between the predicted output values from the surrogate model and the output of the original model for the same given input values [134, 143].

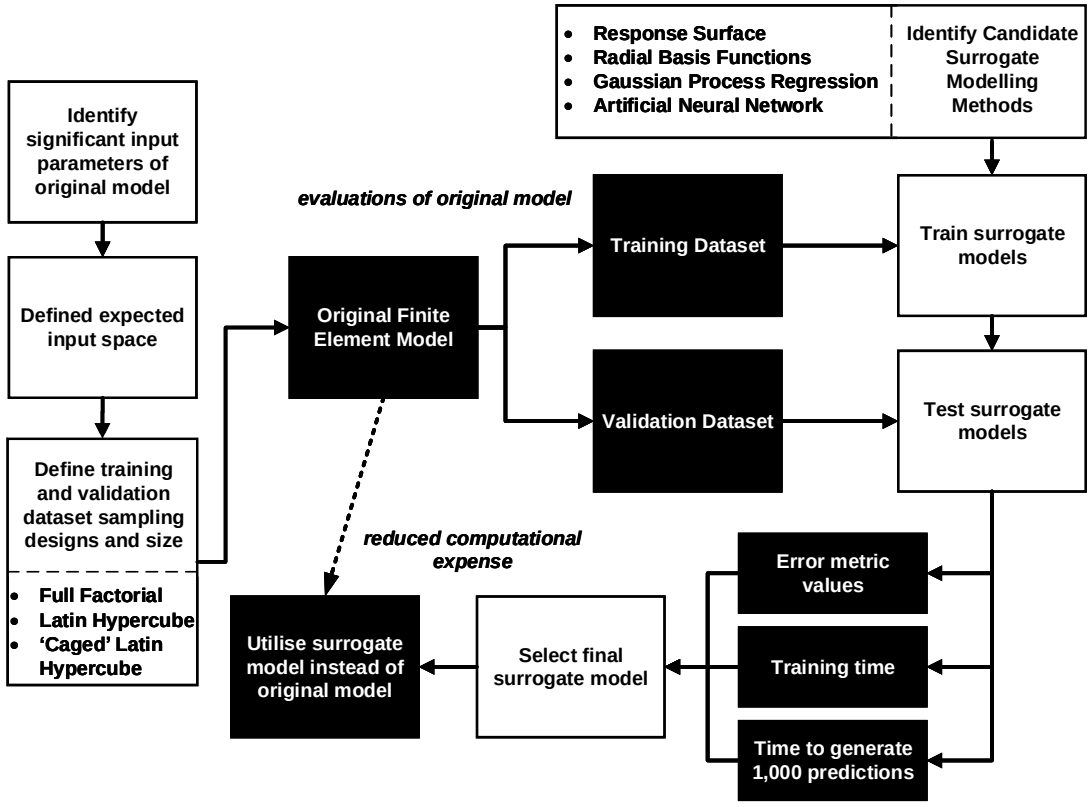

FIGURE 6.4. An overview of the surrogate modelling process adopted.

The process for constructing a surrogate model can be decomposed into training and testing. 'Training' of the surrogate model is the process of selecting the values of the tuneable parameters, based upon known input and output values of the original model [134, 143]. 'Testing' of the surrogate model aims to evaluate the accuracy of the predicted output values from the surrogate model, along with the time required to train and evaluate the surrogate model [134, 143].

An important concept within surrogate modelling is 'generalisation' [143]. Generalisation is the term used to describe how the surrogate model behaves 'between' the known input and output values used to train the surrogate model [144]. The aim of surrogate modelling is to produce a smooth and accurate interpolation between the known input and output values used for training [227]. The opposite to generalisation is 'over-fitting' whereby the surrogate model is forced to be accurate at the known input values used for training, at the expense of accuracy for new or 'unseen' input values [144].

The remainder of this section aims to describe the surrogate modelling process adopted (as shown in Figure 6.4) and provides the necessary background on each of the candidate surrogate modelling methods.

6.2.1 Generation of Training and Validation Data

The first stage of the surrogate modelling process is to generate the input and output values from the original model to produce the surrogate model training dataset [134, 143]. In order to generate the training dataset, the maximum and minimum values for all of the model inputs must be identified to produce the 'expected input space'. Concerning the FEA MLG beam model, the maximum and minimum values for the load factors were identified for a wide-body civil aircraft based on in-service loads monitoring [191]. This resulted in the expected input space consisting of n_x $[-0.5\text{ g}, +0.5\text{ g}]$, n_y $[-0.5\text{ g}, +0.5\text{ g}]$, n_z $[-0.5\text{ g}, +1.5\text{ g}]$ and the aircraft mass varying between MTOW and OWE (305,000 kg and 135,000 kg respectively) [191].

Training datasets can be systematically constructed using approaches in common with the Design of Experiments (DoE) [142]. Full Factorial (FF) design splits the expected input space into a series of levels and generates a training data point at each intersection between the levels as shown in Figure 6.5a [46, 142]. Within engineering design, extreme values often provide important design points (i.e. 'robust' design [61]) and as a result, FF design is favourable as it ensures that minimum and maximum values (and the combination thereof) are included within the training dataset.

However, FF design suffers from the 'curse of dimensionality' whereby the training dataset size becomes prohibitively large to evaluate using the original model as the number of input parameters (i.e. dimensionality) increases [142]. As a result, Latin Hypercube Sampling (LHS) has been proposed to generate training datasets that encompass the expected input space, while having a smaller sample size than FF design. LHS design is achieved by partitioning the input space into equal-width bins and generating random samples such that a training data point is

observed in each bin for each input parameter as shown in Figure 6.5b [131]. LHS for training data generation is therefore similar to the use of LHS for generating random samples within the probabilistic analysis methods discussed in Chapter 2.

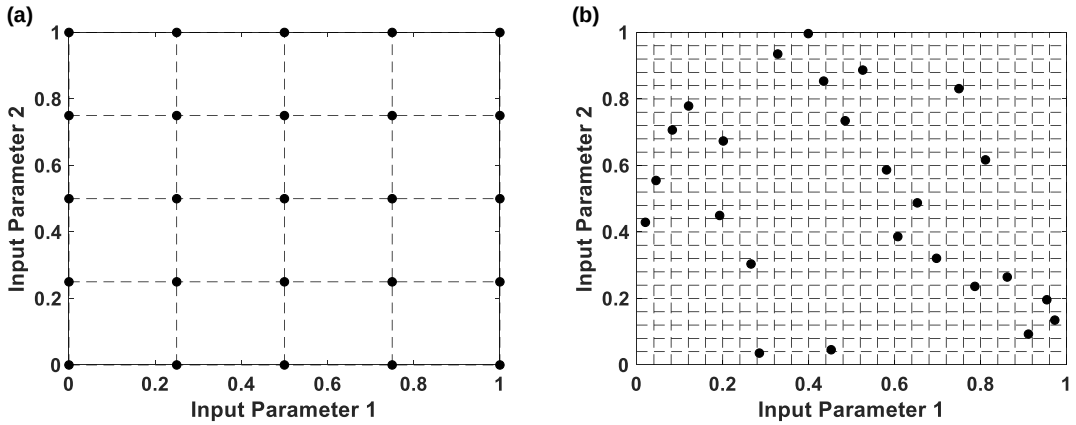

FIGURE 6.5. (a) An example of a Full Factorial design with 25 data points. (b) An example of a Latin Hypercube design with 25 datapoints.

The use of LHS design fails to guarantee that minimum and maximum values will be included within the training dataset. Therefore, it is proposed that a hybrid approach between FF and LHS (known a 'Caged-LHS'), which adds a 2-level FF design to the LHS design training data, should be used to ensure minimum and maximum input parameter values and combinations are represented in the training dataset. A visualisation of a Caged-LHS design for three input parameters is shown in Figure 6.6.

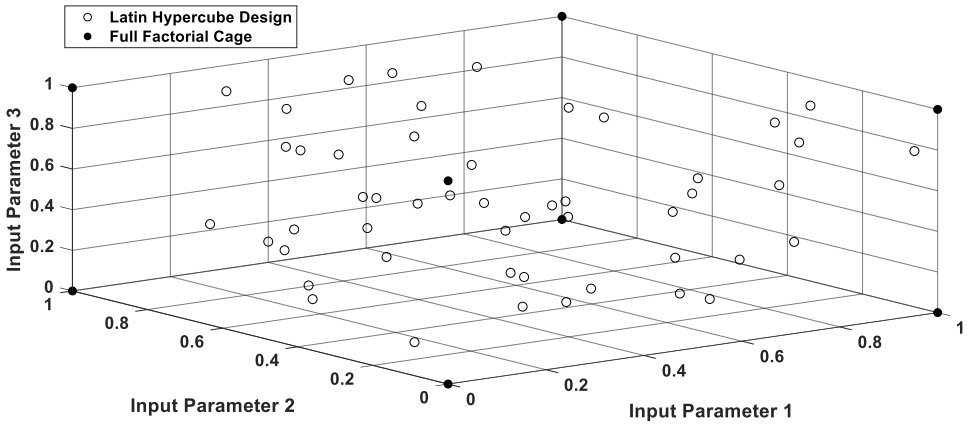

FIGURE 6.6. A demonstration of Caged-Latin Hypercube design for 3 input parameters.

The definition of the training dataset size was performed by considering the computational resource (i.e. CPU run-time) required to evaluate the original FEA MLG beam model. An 'overnight' resource period was defined (8 hours), during which the computational resource would not be required for other engineering activities. A 'full-day' resource period was also constructed (approximately 32 hours: two overnight periods and a working day). Based on the CPU run-time for a single evaluation of the FEA MLG beam model of 20 seconds, this would permit 1,500 and 5,000 evaluations of the FEA MLG beam model for the overnight and full-day resource periods respectively.

Following the definition and identification of the available resource period, either FF, LHS or Caged-LHS design is then used to generate the input values of the training dataset. These input values are then evaluated by the original model (e.g. FEA MLG beam model) to provide corresponding output values, to complete the generation of the training dataset.

In order to test the trained surrogate model, a validation dataset must also be generated. For validation datasets, the 'space-filling' nature of LHS design should be exploited, to ensure that the accuracy of the surrogate model is tested at input values away from the training dataset values [143]. The size of the validation dataset can range from 10% to 25% of the training dataset [63]. As the validation dataset is not used to train the surrogate model, it is often referred to as 'unseen' data. It is conventional to scale the input and output values of the training and validation datasets between $[0,1]$, to ensure that input parameters with significantly different orders of magnitude do not dominate the surrogate model [143].

6.2.2 Testing of Surrogate Models

Following the training of the surrogate models, each candidate surrogate model must be tested. Testing of surrogate models includes evaluating their accuracy, with respect to the original model and an assessment of the time required to train and generate new predictions from the surrogate model.

The accuracy of a surrogate model is assessed using error metrics. The error metrics quantify the difference between the output value of the original model 'y' and the predicted output value '$\hat{y}$' from the surrogate model for a given set of input values [134]. The Maximum Absolute Error (MAE), Maximum Percentage Error (MPE) and the Root Mean Square Error ($RMSE$) error metrics are shown in Equations 6.1 to 6.3 and can be generated for either training or validation datasets of sample size 'S'. Within Equations 6.1 to 6.3, 'i' is an individual data point in the dataset [136, 228].

$$MAE = \max[|\hat{y}_i - y_i|] \text{ for } i = 1 \text{ to } S \tag{6.1}$$

$$MPE = \max\left[\frac{|\hat{y}_i - y_i|}{|y_i|} \times 100\%\right] \text{ for } i = 1 \text{ to } S \tag{6.2}$$

$$RMSE = \sqrt{\frac{\sum_{i=1}^{S}(\hat{y}_i - y_i)^2}{S}} \tag{6.3}$$

Both the MAE and MPE provide an indication of the maximum error within a surrogate model and as a result, can be used to reject candidate surrogate modelling methods which do not satisfy a specified error criterion. Significant challenges exist in the definition of 'acceptable' error criterion and this chapter will explore the definition of such values. As a starting point, a target of $MPE < 5\%$ is used as an acceptable error criterion, as this represents an accuracy criterion that is similar to the 5-10% error typically observed in FEA models [61, 229].

Another important element when testing surrogate models is the identification of the time required to train the surrogate model. The training of surrogate models is often dependent on complex statistical methods and optimisation processes [143]. Therefore, the time required to train each candidate surrogate model should be evaluated in order to identify if specific surrogate modelling methods have a lower overall computational expense. This evaluation metric can be computed by measuring the CPU run-time required to define the tuneable parameters of the surrogate model.

The time required to generate predictions from the trained surrogate model should also be recorded in order to identify whether one candidate model is faster to evaluate than another. As the surrogate model is to be used within the probabilistic fatigue methodology, within which it will be required to be evaluated for millions of load factor combinations, any additional reduction in CPU run-time that can be achieved by selecting a specific surrogate modelling method over another should be exploited. This evaluation metric can be computed by measuring the CPU run-time to generate 1,000 predictions for a series of unseen input values.

Following the training and testing, the final candidate surrogate model can be selected with a view to achieving the smallest error metric values and the shortest CPU run-time to train and evaluate the surrogate model.

6.2.3 Surrogate Modelling Methods

Candidate surrogate modelling methods span classical 'curve-fitting' approaches through to sophisticated machine learning methods. This subsection aims to provide a brief introduction to each of the candidate surrogate modelling methods considered for the FEA MLG beam model. Surrogate models are typically reliant on the generation of large matrices, and these are shown as **bold** in equations. Matrices typically take the dimension of $S \times S$ and can therefore be large for the training datasets required for surrogate model training.

6.2.3.1 Response Surface Method

As introduced in Chapter 3, the Response Surface Method (RSM) approach uses an N_I dimensional polynomial surface, usually based upon quadratic or cubic surfaces [142]. As the 'shape'

of the surface (i.e. quadratic or cubic) must be defined prior to training, RSM is known as a parametric approach.

A quadratic RSM for two input parameters ($N_I = 2$) is defined by the polynomial in Equation 6.4, where 'x' are the input variables and 'β' are the coefficients of the RSM. The β coefficients are the tuneable parameters of the RSM surrogate model and are computed using least squares regression applied to the training dataset [142].

$$\hat{y} = \beta_0 + \beta_1 x_1 + \beta_2 x_2 + \beta_3 x_1^2 + \beta_4 x_2^2 + \beta_5 x_1 x_2 \tag{6.4}$$

6.2.3.2 Radial Basis Functions

Whilst RSM methods are rapid to train and intuitive to understand due to their similarity to 'curve-fitting', they can result in inaccurate surrogate models for highly non-linear and highly dimensional models [142]. To overcome these limitations, non-parametric approaches have been proposed, which do not rely on an assumed polynomial surface shape [143]. Radial Basis Function (RBF) surrogate models are based upon the concept of combining a series of 'basis' functions with assigned weights to generate a smooth fit to the training data [143]. An RBF model can be represented using Equation 6.5, where '$\boldsymbol{\Psi}$' is known as the 'gram matrix' and consists of the basis functions 'ψ' evaluated between each data point in the training dataset. $\boldsymbol{w}$ is the weights vector and '$\boldsymbol{y}$' is a column vector of the output values of the training dataset.

$$\boldsymbol{y} = \boldsymbol{\Psi w} \tag{6.5}$$

A wide range of basis functions are presented within the literature [143] and this thesis considers the use of the MultiQuadratic (MQ) basis function. The MQ basis function is shown in Equation 6.6, where 'r_e' is the Euclidean distance between a pair of data points in the training dataset and 'σ_{MQ}' is the tuneable parameter of the basis function [143]. The process for populating the weights vector is provided by Forrester et al [143, 144].

$$\psi(r_e) = \left(r_e^2 + \sigma_{MQ}^2\right)^{-\frac{1}{2}} \tag{6.6}$$

In order to tune the value of σ_{MQ}, the MQ RBF surrogate model must be trained using the training dataset for different values of σ_{MQ}. Optimisation methods, such as Nelder-Mead (NM) can be used to minimise the MAE metric for the training dataset [144, 230, 231]. The value of σ_{MQ} that minimises the MAE value is selected as the final σ_{MQ} for the MQ RBF surrogate model.

6.2.3.3 Gaussian Process Regression

Gaussian Process Regression (GPR) is a non-parametric surrogate modelling method, which is based upon statistical concepts related to multivariate Normal distributions [63, 134, 227].

Within GPR, it is assumed that the input-output relationship of a model can be represented using a Gaussian Process 'GP' as shown in Equation 6.7 [134], where '$\boldsymbol{X}$' is a matrix of the training dataset input values. A GP is essentially a distribution across possible functions [63, 134, 227].

$$\boldsymbol{y} = f(\boldsymbol{X}) \approx GP(\mu_{GP}, \boldsymbol{K}) \tag{6.7}$$

Within Equation 6.7, '$\boldsymbol{K}$' is known as the covariance matrix, and controls the shape of the multivariate Normal distributions that form the GP [134, 227]. μ_{GP} in Equation 6.7 is the basis function of the GP and represents a constant 'offset' of the model [134]. Convention in the literature dictates that this value is typically set to zero and will therefore be neglected as a tuneable parameter when training GPR surrogate models [134].

The $\boldsymbol{K}$ matrix is composed of 'kernel' functions 'k', which quantify the correlation between the data points within the training dataset [227]. In GPR, the kernel functions are used to control the correlation between data points in the training dataset, such that data points that are close to one another exhibit a strong correlation (i.e. take similar values), whilst observations which are distant should demonstrate weaker correlation [227]. The definition of $\boldsymbol{K}$ ultimately results in generalisation being achieved with a smooth interpolation between training data points (i.e. observations that are close to one another have similar values, rather than sudden and large changes in value).

The most commonly applied kernel function is the 'squared exponential' function shown in Equation 6.8, where 'x_j' and 'x_k' are two different training data points, whilst 'σ_f' and 'l' are the tuneable parameters of the GPR [134]. 'σ_n' is an additional term that accounts for noise within the training dataset [134, 227]. The $\boldsymbol{K}$ matrix is composed of kernel functions for all possible combinations of data points in the training dataset.

$$k(x_j, x_k) = \sigma_f^2 \exp\left[\frac{-(x_j - x_k)^2}{2l}\right] + \sigma_n^2 \tag{6.8}$$

In order to tune the σ_f and l parameters, maximum likelihood methods (as presented in Rasmussen and Williams [227]) are used to fit the GPR surrogate model to the training dataset. As the application of surrogate models in this thesis concern deterministic outputs from the FEA MLG beam model, the value of σ_n was set to a negligible value (e.g. $< 1 \times 10^{-6}$) to represent 'noiseless' GPR [227].

6.2.3.4 Artificial Neural Networks

The final candidate surrogate modelling method considered are Artificial Neural Networks (ANNs). ANNs are a non-parametric surrogate modelling approach and are considered the classical approach to 'machine learning', whereby a surrogate model 'learns' the relationship between the input and output values for the original model [232].

ANNs are designed to mimic the human brain using a series of 'neurons' linked together, as shown in Figure 6.7. Each neuron is composed of a transfer function (typically tan-sigmoid). A weight is a multiplication factor and a bias is an addition factor applied to the links between neurons. The weight and bias values are the tuneable parameters of the ANN surrogate model and are found using sophisticated optimisation approaches known as 'back-propagation', such as the Levenberg-Marquardt method [232].

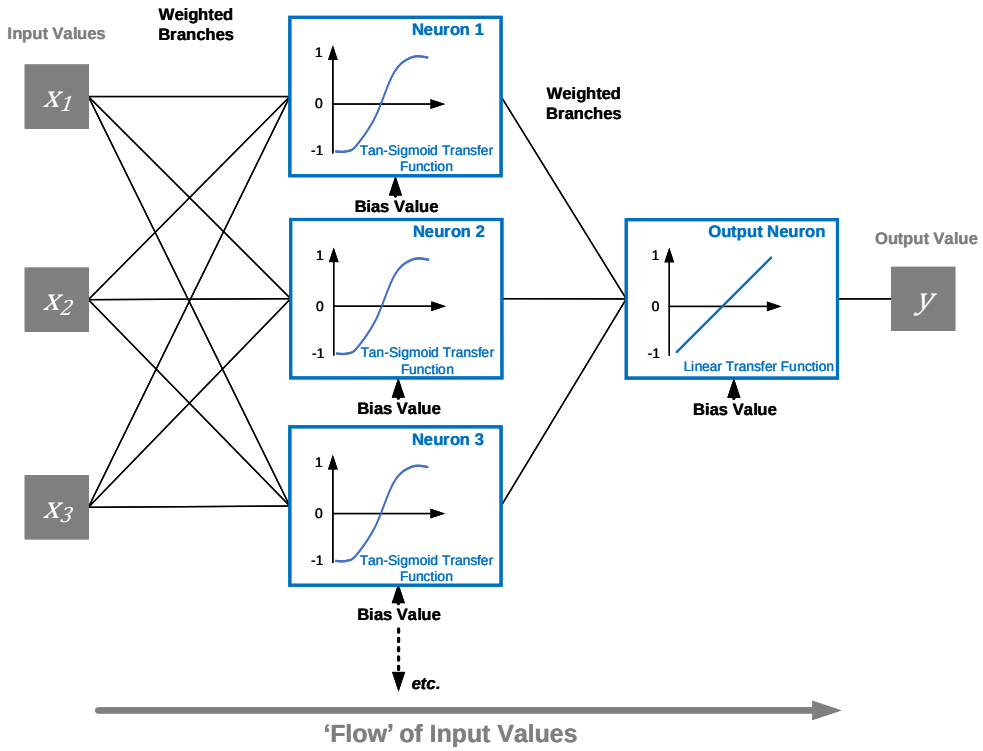

FIGURE 6.7. A visualisation of a single-layer Artificial Neural Network.

The advantage of ANNs is the flexibility afforded by the architecture of the ANN, as the number of neurons and layers of neurons can be adjusted [135]. As a result, the architecture of the ANN is also a tuneable element of the ANN surrogate model. Within the surrogate modelling of the linear static FEA MLG beam model, it was assumed that only a single layer of tan-sigmoid neurons was available and therefore, only the number of neurons within the layer was tuneable. The number of neurons is selected by performing a 'sweep' of different numbers of neurons and selecting the number of neurons that minimises the MAE metric for the training dataset. It should be noted that the initial values of weight and bias are randomly selected for each training run, leading to different ANN surrogate models and MAE values for the same number of neurons [232]. Therefore, two ANNs were constructed at each sweep value and the specific ANN that resulted in the minimum MAE value was selected.

6.2.3.5 Previous Utilisation of Surrogate Models

As surrogate modelling methods are general in nature, their demonstrated application within the literature is vast. As a result, this subsection intends to briefly review the application of surrogate modelling methods specifically to deterministic and probabilistic fatigue methodologies.

Despite Venter et al demonstrating the application of RSM surrogate models to replace computationally expensive fatigue analysis processes in the late 1990s [136], the utilisation of surrogate modelling methods in deterministic fatigue design has only become more common in the latter half of the 2010s, as highlighted by Teixeira et al [138]. Teixeira et al further support the need to introduce surrogate modelling on a wider scale within fatigue analysis due to the various computationally expensive elements present within fatigue analysis, such as FEA stress analysis and cycle counting [138].

As a result, Teixeira et al have demonstrated the use of GPR in both the deterministic and probabilistic fatigue methodologies employed for wind turbine components [138, 139, 233]. Within this recent work, GPR surrogate models were used to represent the input-output relationship between fatigue design parameters and accumulated damage values and therefore, the GPR surrogate models were used to represent the entire S-N fatigue analysis process [138, 139, 233]. Brandt et al and Huchet et al have also demonstrated the use of GPR surrogate models to represent the fatigue analysis process of wind turbine components in deterministic and probabilistic fatigue methodologies [234, 235].

Other examples of the use of surrogate modelling methods in probabilistic fatigue methodologies include the use of GPR for rocket engine components [57, 132], and ANNs for wind turbine and jet engine components [236, 237]. It is interesting to note that the existing practice in the literature typically uses surrogate models to represent the entire fatigue analysis process, resulting in all stages of the fatigue analysis process being represented by a 'black-box'. It proposed in the MCS-SSI probabilistic fatigue methodology to construct dedicated surrogate models of each computationally expensive element of the S-N fatigue analysis process, as it is hypothesised that this will result in more representative and accurate surrogate models. In addition, existing guidance on implementing probabilistic approaches to design recommends that the existing deterministic analysis process is left unchanged to ensure familiarity with engineers and to increase the 'buy-in' to such approaches [46, 54]. As a result, it is proposed that the use of surrogate modelling for elements of the fatigue analysis process, rather than generating a 'black-box' of the fatigue analysis process, could increase acceptance from engineers of the probabilistic methodology, as the overall fatigue analysis process can still be used 'as-is'.

Landing Gear Design

From the review of the literature, it is apparent that surrogate modelling methods have been predominately applied to wind turbine components in the context of fatigue design. However, surrogate modelling methods have seen a wider application in the general area of landing gear

design, focused mainly on using surrogate models to predict landing gear loads from dynamic drop tests. Holmes et al and Cross et al presented the application of GPR surrogate models to predict landing gear component loads from measured flight parameters [134, 238]. Cross et al also demonstrated the utility of ANN methods in the same application [135].

Tartaruga et al have used GPR to construct surrogate models of landing gear assemblies in order to reduce the computational expense of performing dynamic and vibrational analysis of landing gear structures [239].

Finally, Sartor et al have used GPR surrogate models to represent the analysis process used following a hard landing in order to identify design drivers [63, 240]. The use of a surrogate model supported sensitivity analysis to identify the flight parameters that provided the most significant contribution to loads and stresses within landing gear components [63, 240]. As a result, Sartor et al have produced a surrogate model of an analysis process that contains the FEA MLG beam model [63, 240].

While previous work has therefore considered the application of surrogate models within the sphere of landing gear design, this thesis presents the first example of surrogate models that are dedicated solely to the FEA MLG beam model. The development of dedicated surrogate models for the FEA MLG beam model is also consistent with the desire to produce individual surrogate models for elements of the safe-life fatigue analysis process, as discussed previously in the context of utilising surrogate models in probabilistic fatigue methodologies. In addition, previous work in the literature typically focuses on individual surrogate modelling methods. As a result, the following sections will compare a range of candidate surrogate modelling methods, in order to provide an assessment of the accuracy and computational expense of each surrogate modelling approach. This will be achieved by applying the RSM, RBF, GPR and ANN surrogate modelling methods to two separate FEA MLG beam model case studies, of differing complexity.

6.3 Surrogate Modelling of Side-Stay Axial Load

The first application of surrogate modelling methods to the FEA MLG beam model concerns the side-stay component. The side-stay caries F_Y side loads applied to MLG into the airframe structure. The lower side-stay for the linear static FEA MLG beam model is shown in Figure 6.8. Due to the joints which mount the lower side-stay to the main fitting, the lower side-stay is only capable of carrying axial loads along the length of the side-stay. As a result of the MLG configuration shown previously in Figure 6.1, the only global load that can generate an axial load 'F_1' in the side-stay is an F_Y side load resulting from an n_y side load factor.

As a result of the loading conditions and side-stay/main fitting joint, the beam model of the lower side-stay can be reduced to a two-input parameter model (aircraft mass M and n_y) with a single output parameter (axial side-stay load, F_1). Due to the beam model sign convention, a positive value of n_y will result in a negative F_1 value (i.e. compression in the side-stay).

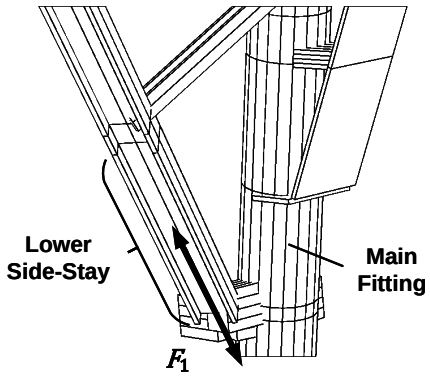

FIGURE 6.8. The lower side-stay component within the FEA MLG beam model, highlighting the F_1 side-stay axial load.

6.3.1 Training Data

For the generation of training and validation datasets from the FEA MLG beam model, an 'overnight' resource block was allocated, permitting a maximum of 1,440 evaluations of the original FEA beam model. The expected input space was defined between the MTOW and OWE for M and between ± 0.5 g for n_y [191], as shown in Figure 6.9.

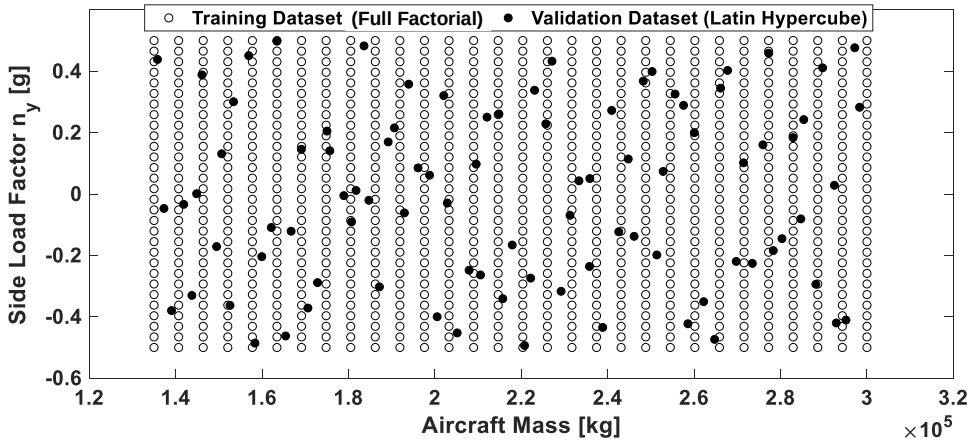

FIGURE 6.9. The Full Factorial training dataset (S_T = 900) and Latin Hypercube validation dataset (S_V = 90) for the lower side-stay surrogate model.

An FF design was selected for the training dataset. Based on the permissible number of original FEA model evaluations, 30 levels were used within the FF design, resulting in a training dataset sample size of $S_T = 900$. The validation dataset was constructed using LHS design with a sample size of $S_V = 90$ (i.e. 10% of the training dataset). The input values of the training

and validation dataset are shown in Figure 6.9. The original FEA MLG beam model was then evaluated for each data point to provide the F_1 side-stay axial load, in order to provide output values for the training and validation datasets.

6.3.2 Surrogate Models

The quadratic RSM, cubic RSM, MQ RBF, GPR and ANN surrogate models were trained using the FF training dataset. All training of the surrogate models was performed in a MATLAB® environment, using dedicated MATLAB® toolboxes for GPR and ANN training, and self-written code for the RSM and MQ RBF, based upon methods described by Forrester et al [144].

The quadratic RSM was composed of six β coefficients, while the cubic RSM was composed of nine β coefficients. The value of the β coefficients was identified using least squares regression.

The MQ RBF surrogate model for the lower side-stay was trained using NM optimisation, resulting in a value of $\sigma_{MQ} = 0.171$ minimising the MAE for the surrogate model predictions for the training dataset.

The maximum likelihood approach was used to train the GPR, resulting in $\sigma_f = 5.680$, $l = 19.090$ and the σ_n noise factor was minimised to a value of 1×10^{-6}.

Finally, a sweep through the number of neurons for the ANN surrogate model identified that the MAE for the training dataset could be minimised when using between 20 and 60 neurons in the single layer. This value was further refined to 51 neurons.

6.3.2.1 Error Metrics

The candidate surrogate models were then used to generate predictions $\hat{y}$ based upon the input values of the training and 'unseen' validation datasets. Table 6.1 shows the MAE and $RMSE$ for both the training and validation datasets. The minimum values for each error metric are highlighted in **bold**.

TABLE 6.1. Error metrics for the surrogate models of the lower side-stay F_1 axial load.

Surrogate Model	Training Dataset		Validation Dataset	
	MAE (N)	$RMSE$ (N)	MAE (N)	$RMSE$ (N)
Quadratic RSM	**5.016**	**1.321**	**4.011**	**1.394**
Cubic RSM	7.482	1.626	5.785	1.697
MQ RBF	10.22	4.184	102.3	12.19
GPR	6.218	1.525	5.068	1.465
ANN	7.866	1.967	6.988	1.974

It can be observed from Table 6.1 that the quadratic RSM, GPR and ANN surrogate models all provide similar MAE and $RMSE$ values for training and validation datasets. Table 6.1 also shows that the absolute error in the F_1 side-stay axial load is < 10 N for the RSM, GPR and ANN surrogate models. The RSM, GPR and ANN MAE values were therefore negligible compared to the typical side-stay loads, which are in the order of 1×10^5 N. As a result, MPE values were

not computed as they would also be negligible. The lower $RMSE$ values also suggested that the RSM, GPR and ANN surrogate models provide low errors across the expected input space. The quadratic RSM was found to provide the lowest MAE and $RMSE$ values for both the training and validation datasets.

Table 6.1 shows that the MQ RBF surrogate model provided significantly higher MAE and $RMSE$ values for the validation dataset when compared to the other surrogate modelling methods. However, it can be observed that the MQ RBF provides MAE and $RMSE$ values that are consistent with the other surrogate models for the training dataset. As a result, it can be suggested that the σ_{MQ} value defined during training resulted in an 'over-fit' of the MQ RBF surrogate model to the training data, resulting in poor generalisation and consequently low accuracy for the validation dataset.

6.3.2.2 Training and Evaluation Time

The CPU run-time[2] required to train the different candidate surrogate models is shown in Table 6.2. The training time includes the time required for optimising σ_{MQ} values for the MQ RBF and the time required to optimise the number of neurons in the ANN. The minimum times for training and generation of 1,000 predictions are highlighted in **bold**.

TABLE 6.2. Training and evaluation times for the lower side-stay surrogate models based upon recorded CPU run-time.

Surrogate Model	Training Time (seconds)	1,000 Predictions (seconds)
Quadratic RSM	**0.026**	**0.004**
Cubic RSM	0.033	0.006
MQ RBF	210.892	0.046
GPR	2.821	0.010
ANN	4.834×10^3	0.016

It can be seen from Table 6.2 that the quadratic RSM and cubic RSM required the lowest training time, in the order of 10^{-2} seconds. The GPR surrogate model required approximately three seconds to perform the maximum likelihood training of the σ_f and l parameters. The MQ RBF required over 200 seconds to identify the optimum value of σ_{MQ}, 1.141 seconds of which was dedicated to identifying the $\boldsymbol{w}$ weights vector when $\sigma_{MQ} = 0.171$. Finally, the ANN required over 4,500 seconds (approximately 1.3 hours) to optimise the number of neurons ($\approx$ 28 seconds of which was dedicated to training the weights and bias values for the final 51-neuron ANN). As a result, it can be observed that the MQ RBF and ANN surrogate modelling methods, which require optimisation of parameter values or architecture prior to training, have a significantly larger computational expense related to training, when compared to RSM and GPR surrogate modelling methods.

[2]Computer Specifications: 4-core processor (3.40 GHz) with 16.0 GB RAM.

Table 6.2 also shows the CPU run-time required to produce 1,000 predictions for unseen input values. It can be observed from Table 6.2 that all candidate surrogate modelling methods required less than 10^{-2} seconds to generate 1,000 predictions, with the quadratic RSM having the lowest CPU run-time of 4×10^{-3} seconds.

6.3.2.3 Selection of Surrogate Model

The quadratic RSM was selected as the final surrogate model for computing the F_1 axial side-stay loads. The quadratic RSM was selected due to providing the smallest MAE and $RMSE$ values for the candidate surrogate models across both the training and validation datasets. The quadratic RSM also had the shortest CPU run-time for training and generation of 1,000 predictions for unseen input values. As a result, the quadratic RSM provided both the most accurate surrogate model, along with the lowest required computational resource burden.

The final quadratic RSM surrogate model is shown in Figure 6.10, along with the training and validation dataset. It can be seen from Figure 6.10 that there is good visual agreement between the training and validation data points and the RSM, supporting the low MAE and $RMSE$ values shown previously in Table 6.1. Figure 6.10 also suggests that the response surface is planar, infering that the F_1 axial side-stay load has a simple linear relationship to both the aircraft mass M and n_y.

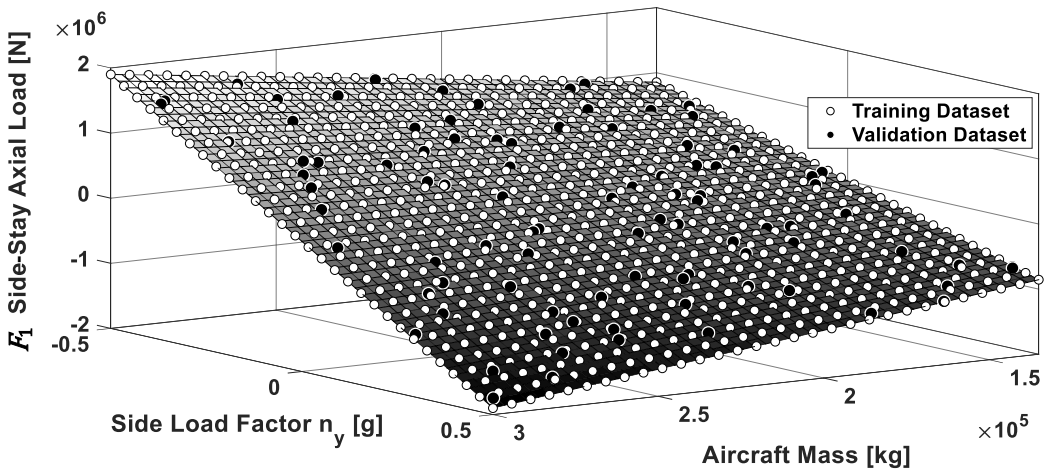

FIGURE 6.10. The quadratic RSM surrogate model for the lower side-stay. The training and validation datasets are also shown.

The β coefficients for the quadratic RSM are shown in Table 6.3, where it can be seen that the squared terms of M and n_y are negligible and these can therefore be neglected from the surrogate model. This further supports the linear and potentially planar nature of the relationship between the side-stay F_1 axial load and the input values of M and n_y. In addition, as it is only F_Y side

loads than result in F_1 side-stay axial loads, and as the FEA MLG beam model performs linear static analysis, a linear relationship should exist between F_1 and the input parameters n_y and M.

TABLE 6.3. Response surface β coefficients for the lower side-stay F_1 axial load quadratic RSM surrogate model.

RSM Coefficient	Value	Input Parameter
β_0	0.725	Constant
β_1	0.275	M
β_2	-0.450	n_y
β_3	-4.476×10^{-15}	M^2
β_4	4.219×10^{-14}	n_y^2
β_5	-0.550	$M \times n_y$

Common practice identified within the literature suggests that a linear response should be considered in the first instance when constructing surrogate models [241, 242]. As Figure 6.10 suggests that a linear relationship exists between F_1 and M and n_y, a linear RSM was investigated for the lower side-stay surrogate model. A linear RSM takes the form of a first order polynomial as shown in Equation 6.9 [242]. For the F_1 axial side-stay load, a linear response surface can be described using Equation 6.10.

$$\hat{y} = \beta_0 + \beta_1 x_1 + \beta_2 x_2 + ... \tag{6.9}$$

$$F_1 = \beta_0 + \beta_1 M + \beta_2 n_y \tag{6.10}$$

Based on least squares regression of the training dataset shown previously in Figure 6.9, the resulting linear response surface coefficients are shown in Table 6.4. The corresponding MAE and $RMSE$ values for the linear RSM are shown in Table 6.5.

TABLE 6.4. Response surface β coefficients for the lower side-stay F_1 axial load linear RSM surrogate model.

RSM Coefficient	Value	Input Parameter
β_0	0.862	Constant
β_1	-4.996×10^{-16}	M
β_2	-0.725	n_y

TABLE 6.5. Error metrics for the linear RSM of the lower side-stay F_1 axial load.

Training Dataset		Validation Dataset	
MAE (N)	$RMSE$ (N)	MAE (N)	$RMSE$ (N)
5.226×10^5	1.862×10^5	4.810×10^5	1.831×10^5

Table 6.5 shows that a linear RSM results in significantly higher MAE values compared to the quadratic RSM as shown previously in Table 6.1. Figure 6.11 shows the linear RSM compared to the training data, and demonstrates the poor fit to the training dataset. The negligible β value for the M parameter shown in Table 6.4 from least squares regression is as a result of minimising the error of the linear RSM at the maximum/minimum value combinations of M and n_y.

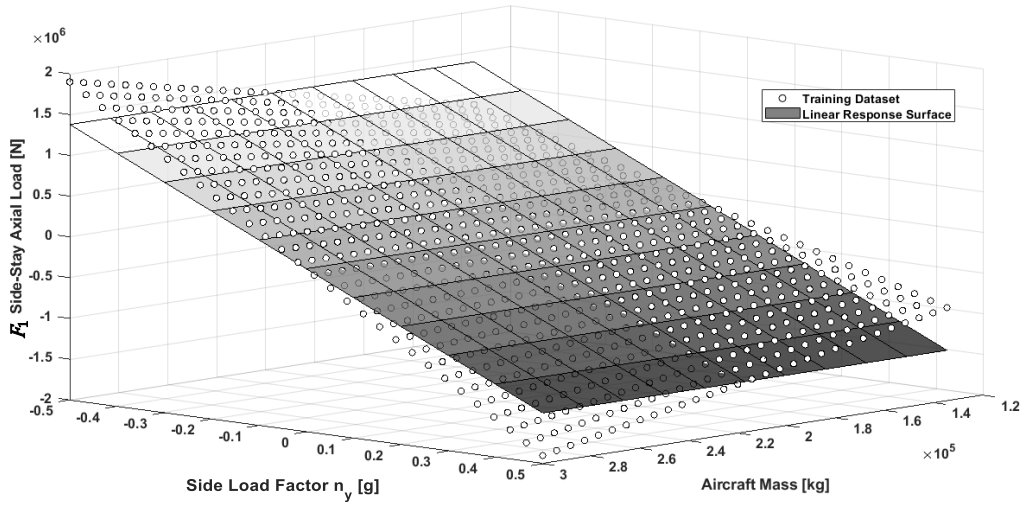

FIGURE 6.11. The linear RSM surrogate model for the lower side-stay. The training dataset is also shown.

The poor fit of the linear RSM (as visualised by the 'twist' present in the training dataset values across the expected input space in Figure 6.11) is as a result of the conversion of aircraft mass and the n_y side load factor into to the global F_Y side load applied to the MLG beam model. Based on Equation 5.2, the F_Y side load is the *product* of M and n_y, rather than a linear or additive computation. Consequently, a linear response surface should not be expected to provide accurate modelling of the F_1 side-stay axial load, as by definition such a surface is only a linear combination (i.e. $y = ax_1 + bx_2 + ...$) of M and n_y and neglects any product terms between M and n_y. The contribution of the product term between M and n_y to the F_1 axial side-stay load is also highlighted by the non-zero quadratic RSM β_5 value for $M \times n_y$ as shown previously in Table 6.3.

Consequently, a linear RSM would require the addition of the product term between M and n_y. Such a surface is referred to as a linear response surface with first order interactions [242, 243][3]. For the F_1 side-stay axial load, a linear RSM with first order interactions can be presented as shown in Equation 6.11, where β_3 represents the first order interaction. Least squares regression resulted in the β values shown in Table 6.6 with the corresponding MAE and $RMSE$ values shown in Table 6.7.

[3]Across the literature, a linear RSM with first order interactions in inconsistently classified as both a linear and a quadratic RSM [242].

$$F_1 = \beta_0 + \beta_1 M + \beta_2 n_y + \beta_3 M n_y \tag{6.11}$$

TABLE 6.6. Response surface β coefficients for the lower side-stay F_1 axial load linear RSM surrogate model with first order interactions.

RSM Coefficient	Value	Input Parameter
β_0	0.725	Constant
β_1	0.275	M
β_2	-0.450	n_y
β_3	-0.550	$M \times n_y$

TABLE 6.7. Error metrics for the linear RSM of the lower side-stay F_1 axial load with first order interactions.

Training Dataset		Validation Dataset	
MAE (N)	$RMSE$ (N)	MAE (N)	$RMSE$ (N)
5.016	1.321	4.012	1.394

It can be observed from Tables 6.6 and 6.7 that the β values and error metrics are consistent with those for the full quadratic RSM shown previously in Tables 6.1 and 6.3 and therefore, the F_1 side-stay axial load can be represented using a linear RSM with first order interactions.

Alternatively, as the global F_Y side load could be computed using Equation 5.2 prior to evaluating the FEA MLG beam model, the surrogate model could ultimately be reduced to only represent input parameter and one output parameter. The following training datapoints were generated from the linear static FEA MLG beam model:

1. Maximum F_Y side load from maximum values of M and $n_y = 0.5$ g.
2. Unloaded condition (i.e. $F_Y = 0$ N).
3. Minimum F_Y side load from maximum values of M and $n_y = -0.5$ g.

A linear response in the form shown in Equation 6.12 was fitted to the three training data points using least squares regression, resulting in a value of $\beta_1 = -1.291$ with a zero-valued β_0. Figure 6.12 shows the corresponding linear response, which demonstrates good agreement with the three training data points.

$$F_1 = \beta_0 + \beta_1 F_Y \tag{6.12}$$

The linear response in Figure 6.12 was also tested using the global F_Y side load values computed using Equation 5.2 from the validation dataset shown previously in Figure 6.9. The resulting $MAE = 6.731$ N is consistent with the error metrics for the quadratic RSM shown previously in Table 6.1. Therefore, by computing the global F_Y side load prior to evaluating the

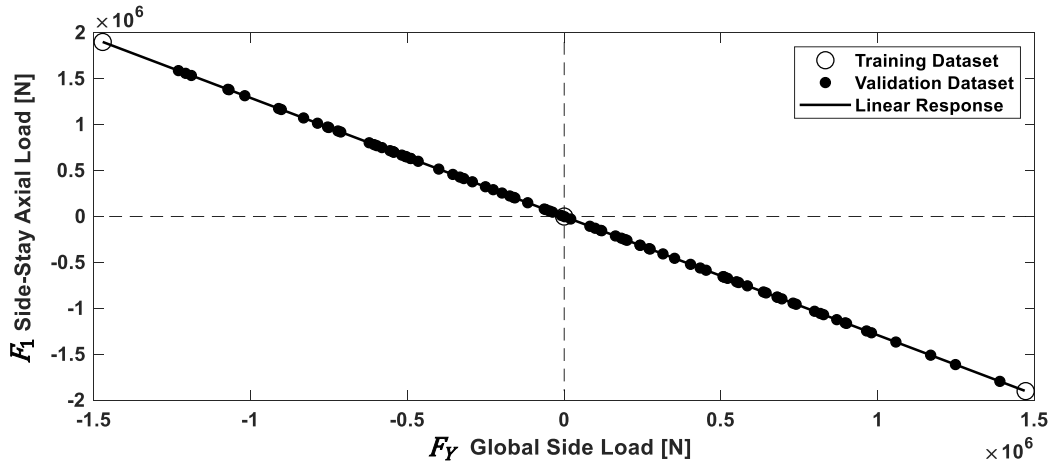

FIGURE 6.12. The linear response between the F_1 axial side-stay load and F_Y global side load. The training and validation datasets are also shown.

FEA MLG beam model, rather than performing this computation within the FEA MLG beam model itself, the training dataset sample size can be reduced to just three points due to the linear response of the FEA MLG beam model.

Therefore, it is recommend when constructing surrogate models that additional focus is placed on the input parameters to identify if any mathematical operations are required to combine the input parameters prior to evaluating the computationally expensive FEA model. Such additional work can reduce the required complexity of the surrogate model and required training dataset size, compared to including such mathematical operations within the FEA model. In addition, it is recommended that both a linear RSM and linear RSM with first order interactions are considered prior to evaluating other more complex surrogate modelling approaches, consistent with existing common practice [241, 242].

6.4 Surrogate Modelling of Drag Brace Internal Loads

The second application of surrogate modelling methods to the linear static FEA MLG beam model concerns the lower drag brace of the MLG as shown in Figure 6.13. As the lower drag brace is part of the single-piece forging of the main fitting, the lower drag brace is able to carry F_1 axial loads, shear loads (F_2, F_3), bending moments (F_4, F_5) and a torsional moment 'F_6'. The positive direction of each of these internal loads is shown in Figure 6.13. As a result of the internal loads that the drag brace can carry, the global loads that result in internal loads in the drag brace are F_X, F_Y and F_Z, resulting from the n_x, n_y and n_z load factors respectively.

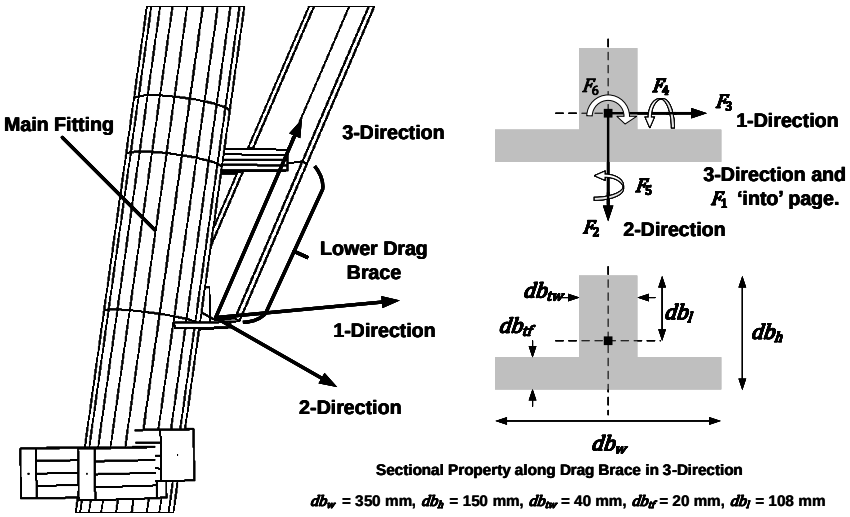

FIGURE 6.13. The drag brace of the FEA MLG beam model, highlighting the internal loading directions.

In addition to the load factors, other parameters within the FEA MLG beam model were considered as potential input parameters. A sensitivity study was conducted, within which all dimensional parameters and material properties for each component within the MLG structural assembly were varied between defined maximum and minimum values. Maximum and minimum values for the dimensional parameters were set at ±3 standard deviations (a typical design tolerance) using standard deviation values for typical manufacturing processes sourced from Haugen [31]. Material properties, specifically the 4340 steel elastic modulus ($E = 2.05 \times 10^5$ MPa) for each component [25], were varied between ±6 standard deviations. The aircraft mass and load factors were assumed to be bounded by the maximum values specified in Section 6.2.1 [191].

The sensitivity study was performed by evaluating the FEA MLG beam model for each maximum and minimum value of the input parameters, whilst retaining all other input parameters at their nominal values, resulting in an additional 267 evaluations of the FEA MLG beam model. Significant input parameters were defined as those that resulted in a greater than 1% change in the drag brace internal loads when set to minimum or maximum values. The sensitivity study highlighted that the aircraft mass, load factors, drag brace dimensions (shown in Figure 6.13), inner and outer radii of both the slider and the main fitting, and the elastic moduli of the slider and main fitting were significant parameters.

As a result of the sensitivity study, the FEA MLG beam model of the drag brace internal loads could be represented as a 15-input parameter model (aircraft mass, three load factors, five drag brace dimensions, two slider dimensions, two main fitting dimensions, slider modulus and main fitting modulus), with six output parameters (i.e. each of the internal loads shown in Figure 6.13). Therefore, the dimensionality of the drag brace beam model was significantly higher than that of

the lower side-stay beam model. In addition, it was expected that the underlying relationship between the global loads and the internal loads of the drag brace would be significantly more complex (i.e. non-linear) than the side-stay, as a result of the drag brace geometry, position in the MLG assembly and the presence of bending and torsional loads.

6.4.1 Training Data

For the generation of the training and validation datasets for the drag brace, a 'full-day' resource block was allocated, permitting a maximum of 5,760 evaluations of the original FEA MLG beam model. A longer resource block was assigned when compared to the lower side-stay surrogate model, as it was hypothesised that the increased complexity and dimensionality of the drag brace warranted a larger training sample size, with a view to producing a more accurate surrogate model. The maximum and minimum values used in the sensitivity study represented the expected input space.

An FF design was rejected for generating a training dataset as even a two-level FF design (i.e. only minimum and maximum values) would require 2^{15} (32,768) FEA MLG beam model evaluations[4] [142]. Therefore, an LHS design of sample size S_T = 5,000 was used to generate the training dataset. The LHS design was 'caged' using a two-level FF design of the input variables which resulted in a $\geq 5\%$ change in the drag brace internal loads during the sensitivity study (aircraft mass, load factors and main fitting modulus), resulting in 32 further evaluations of the original FEA MLG beam model.

A validation dataset of sample size $S_V = 500$ was generated using LHS design. The FEA MLG beam model was then evaluated for each of the training and validation datasets, producing values for F_1, F_2, F_3, F_4, F_5 and F_6 for each data point.

6.4.2 Surrogate Models

The training of the candidate surrogate models was conducted in the same manner as for the lower side-stay beam model. However, for the drag brace, as the original FEA MLG beam model has six output parameters, six RSM, MQ RBF and GPR surrogate models had to be constructed, one for each internal load of the drag brace. The architecture of the ANN enables the six outputs to be represented using a single ANN.

The quadratic RSM surrogate model was composed of six surfaces, each defined by 136 β coefficients, whilst the cubic RSM required 816 β coefficients for each of the six surfaces. The increase in the number of β coefficients highlights the increase in dimensionality and complexity of the drag brace component compared to the lower side-stay.

[4]For FF design, the number of data points is computed using $FF_l^{N_I}$, where FF_l is the number of levels in the FF design and N_I is the dimensionality of the model [142].

The MQ RBF surrogate model (comprised of six individual MQ RBF models for each internal load) was again trained using NM optimisation, resulting in the σ_{MQ} values for each internal load as shown in Table 6.8.

TABLE 6.8. MQ RBF surrogate model parameters for each internal load of the drag brace component.

Internal Load	σ_{MQ}
F_1	7.750
F_2	10.550
F_3	8.150
F_4	7.750
F_5	10.750
F_6	10.550

The maximum likelihood approach produced six GPR surrogate models and the corresponding σ_f and l values are shown for each internal load in Table 6.9. In all instances the noise factors were minimised to a negligible value of $\sigma_n = 1 \times 10^{-6}$.

TABLE 6.9. GPR surrogate model parameters for each internal load of the drag brace component.

Internal Load	σ_f	l	σ_n
F_1	5.660	68.516	1×10^{-6}
F_2	5.660	71.952	1×10^{-6}
F_3	7.252	39.664	1×10^{-6}
F_4	5.597	66.378	1×10^{-6}
F_5	4.573	26.660	1×10^{-6}
F_6	5.616	45.911	1×10^{-6}

Regarding the ANN, significant difficulty was experienced in achieving successful convergence for the Levenberg-Marquardt back-propagation, potentially as a result of specifying too many neurons (500) within the ANN architecture, with respect to the training dataset size of $S_T = 5,000$ [244]. An additional complication from such a large number of neurons and S_T was the long training time of 25 hours. Consequently, the ANN was neglected from the remainder of the drag brace case study. Additional guidance for the future construction of ANNs is provided in Section 6.7.3.

6.4.2.1 Error Metrics

The candidate surrogate models were then used to generate predictions based upon the input values of the training and validation dataset. Tables 6.10 and 6.11 show the MAE and $RMSE$ respectively for the training dataset across each of the internal loads. The minimum error metric values are shown in **bold**.

Tables 6.10 and 6.11 show that the error metrics for the training dataset are consistently larger for the drag brace when compared to those in Table 6.1 for the lower side-stay, highlighting

the increase in complexity of loading on the drag brace component. In addition, it can be observed that the error metrics for the F_4 bending moment are significantly larger than the other internal loads, regardless of the surrogate modelling method used. This is expected to be as a result of the increased magnitude of bending moments (10^8 Nmm) compared to axial or shear loads (10^5 N), along with the potentially more complex and non-linear relationship between the 15 input parameters and the F_4 bending moment.

TABLE 6.10. MAE error values for the training dataset for the drag brace surrogate models regarding each internal load.

Surrogate Model	Training Data MAE					
	F_1 (N)	F_2 (N)	F_3 (N)	F_4 (Nmm)	F_5 (Nmm)	F_6 (Nmm)
Quadratic RSM	9.0×10^3	1.4×10^3	514.4	1.2×10^6	7.0×10^3	2.9×10^4
Cubic RSM	456.0	22.0	36.0	1.3×10^4	6.5×10^3	867.9
MQ RBF	**33.8**	**4.8**	0.9	$\mathbf{2.1 \times 10^3}$	99.4	27.4
GPR	71.8	11.2	**0.2**	5.9×10^3	**2.1**	**22.1**

TABLE 6.11. $RMSE$ error values for the training dataset for the drag brace surrogate models regarding each internal load.

Surrogate Model	Training Data $RMSE$					
	F_1 (N)	F_2 (N)	F_3 (N)	F_4 (Nmm)	F_5 (Nmm)	F_6 (Nmm)
Quadratic RSM	1.3×10^3	136.3	79.1	1.4×10^5	1.1×10^4	4.8×10^3
Cubic RSM	40.6	2.2	4.8	$\mathbf{1.2 \times 10^3}$	788.1	112.1
MQ RBF	30.7	**1.5**	0.8	1.6×10^3	84.2	7.7
GPR	**19.9**	2.9	**0.1**	1.9×10^3	**0.3**	**5.4**

Tables 6.10 and 6.11 also show that for the majority of the training data error metrics across the internal loads, that either the GPR or the MQ RBF surrogate model provided the minimum MAE and $RMSE$ values. On the other hand, the quadratic RSM provides the largest error values for the training dataset, suggesting that a non-parametric surrogate modelling approach is required to represent the complexity of the drag brace FEA MLG beam model.

Tables 6.12 and 6.13 show the MAE and $RMSE$ values for the validation dataset across each of the internal loads for each candidate surrogate modelling method. The minimum error metrics are shown in **bold**.

It can be observed from Tables 6.12 and 6.13 that the MAE and $RMSE$ values for the validation dataset are at least an order of magnitude larger than for the training dataset. Tables 6.12 and 6.13 also show that the quadratic RSM provided large MAE and $RMSE$ values for the F_4 internal bending moment. The large error values for the F_4 bending moment for the quadratic RSM suggests that the underlying relationship between the input parameters and the F_4 bending moment is highly non-linear and as a result cannot be approximated using a quadratic surface. The MAE and $RMSE$ error metrics for the training and validation datasets shown across Tables 6.10 to 6.13 are visualised in Figure 6.14.

TABLE 6.12. MAE error values for the validation dataset for the drag brace surrogate models regarding each internal load.

Surrogate Model	Validation Data MAE					
	F_1 (N)	F_2 (N)	F_3 (N)	F_4 (Nmm)	F_5 (Nmm)	F_6 (Nmm)
Quadratic RSM	8.1×10^3	863.0	664.6	1.1×10^6	8.5×10^4	4.3×10^4
Cubic RSM	$\mathbf{6.7 \times 10^3}$	**769.0**	**453.2**	2.9×10^5	$\mathbf{2.3 \times 10^4}$	1.2×10^4
MQ RBF	6.9×10^3	786.2	466.3	$\mathbf{2.8 \times 10^5}$	2.4×10^4	$\mathbf{1.2 \times 10^4}$
GPR	6.9×10^3	781.1	463.9	2.9×10^5	2.4×10^4	1.2×10^4

TABLE 6.13. $RMSE$ error values for the validation dataset for the drag brace surrogate models regarding each internal load.

Surrogate Model	Validation Data $RMSE$					
	F_1 (N)	F_2 (N)	F_3 (N)	F_4 (Nmm)	F_5 (Nmm)	F_6 (Nmm)
Quadratic RSM	2.0×10^3	223.8	154.9	1.7×10^5	1.3×10^4	6.2×10^3
Cubic RSM	$\mathbf{1.6 \times 10^3}$	**185.2**	**127.3**	7.6×10^4	$\mathbf{6.5 \times 10^3}$	$\mathbf{3.6 \times 10^3}$
MQ RBF	1.7×10^3	185.3	127.7	$\mathbf{7.5 \times 10^4}$	6.5×10^3	3.6×10^3
GPR	1.6×10^3	185.4	127.5	7.5×10^4	6.5×10^3	3.6×10^3

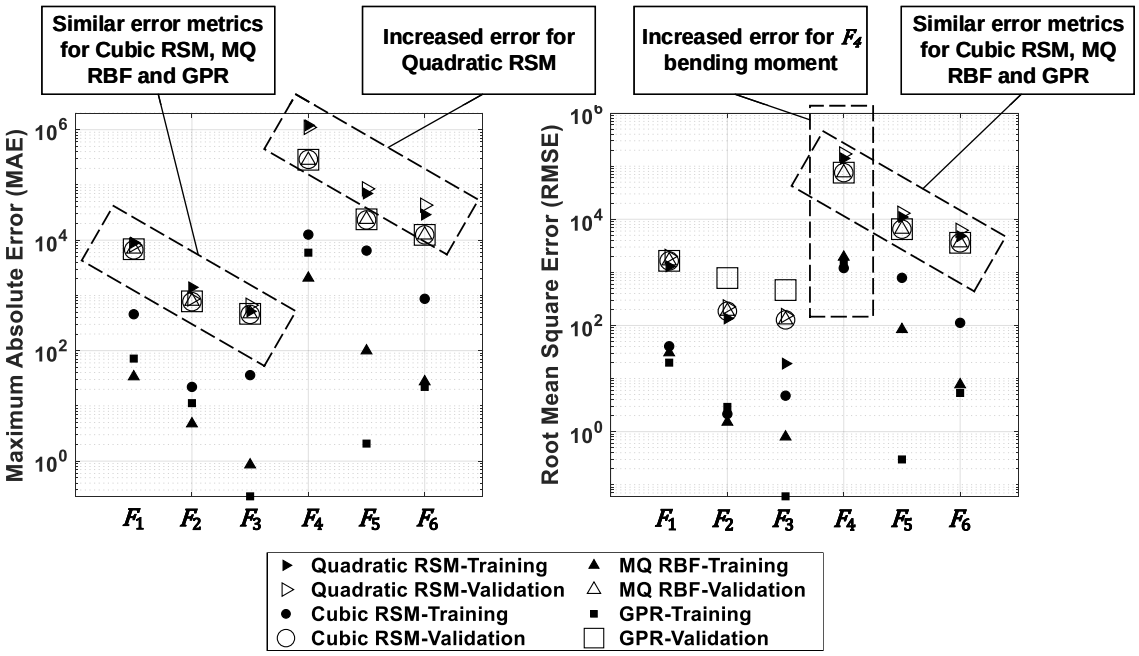

FIGURE 6.14. A visualisation of the MAE and $RMSE$ error metrics for the drag brace candidate surrogate models for each internal load.

From Figure 6.14 and Tables 6.12 and 6.13 it can be observed that the cubic RSM, MQ RBF and GPR surrogate models all provide similar MAE and $RMSE$ error values for the validation dataset. Therefore, the MPE for the validation dataset was also computed for these candidate surrogate models, resulting in the values shown in Table 6.14. The minimum values for each drag brace internal load are shown in **bold**.

TABLE 6.14. MPE error values for the validation dataset for the cubic RSM, MQ RBF and GPR drag brace surrogate models across the drag brace internal loads.

Surrogate Model	Validation Data MPE (%)					
	F_1	F_2	F_3	F_4	F_5	F_6
Cubic RSM	**0.326**	1.703	2.325	34.006	26.013	0.879
MQ RBF	0.920	1.102	2.475	**27.840**	6.065	1.735
GPR	0.578	**0.693**	**2.219**	38.907	**4.137**	**0.855**

It can be observed from Table 6.14 that the majority of the MPE values for the RSM, MQ RBF and GPR surrogate models are below the acceptance threshold of 5%. Once again, the F_4 bending moment results in the greatest MPE error, with values of approximately 30%. For the majority of internal loads, the GPR surrogate model was shown to provide the minimum MPE value (although it did demonstrate the largest MPE value for F_4). It should be noted that the cubic RSM surrogate model results in a larger MPE value for F_5 when compared to the MQ RBF and GPR surrogate models.

6.4.2.2 Training and Evaluation Time

The CPU run-time[5] required to train the different candidate surrogate models is shown in Table 6.15, with the minimum values shown in **bold**. It can be seen from Table 6.15 that again, the quadratic RSM and cubic RSM required the shortest training time, both below one second. The training of the MQ RBF required 1.706×10^4 seconds ($\approx$ 5 hours) in order to optimise the values of σ_{MQ} and compute the values of the $\boldsymbol{w}$ vector for each internal load. The GPR surrogate model required approximately 25 minutes to train.

TABLE 6.15. Training and evaluation times for the drag brace surrogate models based upon recorded CPU run-time.

Surrogate Model	Training Time (seconds)	1,000 Predictions (seconds)
Quadratic RSM	**0.061**	**0.002**
Cubic RSM	0.823	0.719
MQ RBF	1.706×10^4	19.400
GPR	1.510×10^3	0.199

[5]Computer Specifications: 4-core processor (3.40 GHz) with 16.0 GB RAM.

Table 6.15 also shows the CPU run-time required to produce 1,000 predictions for unseen input values, with minimum values shown in **bold**. It can be observed from Table 6.15 that the time required to produce 1,000 predictions has increased for all candidate surrogate modelling methods, highlighting the increase in complexity of the surrogate models. It can be observed from Table 6.15 that the MQ RBF surrogate model now requires nearly 20 seconds of CPU run-time to produce 1,000 predictions.

6.4.2.3 Selection of Surrogate Model

Based upon the error metric values shown previously in Tables 6.10 to 6.13, the quadratic RSM was rejected as it presented MAE and $RMSE$ values that were significantly higher than the other candidate methods. As shown previously in Figure 6.14 and Table 6.14, the cubic RSM, MQ RBF and GPR surrogate models were observed to have similar MAE, $RMSE$ and MPE values for the validation dataset.

Therefore, the selection of the surrogate modelling method for the drag brace of the FEA MLG beam model was based upon the time required to produce 1,000 predictions for unseen values. This selection criteria was chosen because in the context of the probabilistic fatigue methodology, it is imperative that the reduction in computational expense permitted by the use of surrogate modelling is maximised, especially considering the millions of load factor levels generated during the statistical simulation of load-time histories as presented in the previous chapter. As a result, the 20 seconds required to produce 1,000 predictions from the MQ RBF was deemed unacceptable as this would still represent a full day of CPU run-time to compute the internal loads of a single statistically simulated load-time history. Therefore, the MQ RBF surrogate model was rejected as a candidate surrogate modelling method.

As the GPR surrogate model was approximately three times faster to generate 1,000 predictions than the cubic RSM, whilst still having similar error metric values to the cubic RSM surrogate model, the GPR surrogate model was selected as the final surrogate model for the drag brace FEA MLG beam model.

6.4.2.4 Investigation of Surrogate Model Error

As the error metrics for the drag brace surrogate model were significantly larger than those observed for the lower side-stay surrogate model, an investigation into the error present within the drag brace GPR surrogate model was conducted. From Section 6.4.2.1, it was identified that the F_1 axial loads showed an $MAE = 10^3$ N, shear loads (F_2, F_3) showed an $MAE = 10^2$ N, bending moments (F_4, F_5) showed an $MAE = 10^5$ Nmm and the F_6 torsional moment showed an $MAE = 10^4$ Nmm.

One of the limitations of using MAE as an error metric is that it is challenging to define the value of an 'acceptable' absolute error, especially if the output from the surrogate model is not the final output of the overall analysis process within which the surrogate model is intended to

be used. In the case of the FEA MLG beam model, the internal load value would then be used to compute a component stress. As a result, component stress values, rather than the magnitude of the internal loads, represent the 'practical' engineering output value from the analysis process. Therefore, the change in sectional stress within the drag brace component was computed based upon each of the MAE values, using classical stress analysis methods [245].

Table 6.16 shows the MAE for the GPR surrogate model, along with the corresponding change in sectional stress (either direct stress 'σ' or shear stress 'τ'). As can be seen from Table 6.16, the change in stress values resulting from the MAE of the GPR surrogate model is less than 1.5 MPa. As this is a small change in the sectional stress, the MAE values of the GPR surrogate model were deemed acceptable.

TABLE 6.16. Change in drag brace sectional stress resulting from GPR surrogate model MAE.

Internal Load	Validation Data MAE	Change in Sectional Stress (MPa)
F_1	6.9×10^3 N	$\sigma_{F_1} = \pm 0.563$
F_2	781.1 N	$\tau_{F_2} = \pm 0.064$
F_3	463.9 N	$\tau_{F_3} = \pm 0.038$
F_4	2.9×10^5 Nmm	$\sigma_{F_4} = \pm 0.945$
F_5	2.4×10^4 Nmm	$\sigma_{F_5} = \pm 0.058$
F_6	1.2×10^4 Nmm	$\tau_{F_6} = \pm 1.345$

The other area of error investigated within the GPR surrogate model was the high MPE = 38.907% for the F_4 bending moment shown in Table 6.14. Firstly, the validation dataset was used to identify the region of output values at which the high MPE values occur. Figure 6.15a shows the percentage error values compared to their associated F_4 values and it can be seen that the largest percentage errors are centred around $F_4 = 0$ Nmm (i.e. an unloaded state in the drag brace). Due to the MPE formula shown in Equation 6.2, the 'sensitivity' of the error metric increases dramatically for values approaching zero, which can result in challenges when evaluating a model output that has an output range from 0 Nmm to 1×10^8 Nmm. In addition, Figure 6.15 shows that there are only six validation data points that exceed the 5% MPE target.

Figure 6.15b shows the F_4 percentage error values with their corresponding absolute error values. It can be observed from Figure 6.15b that the largest percentage error will not be expected to produce a large absolute error. For the MPE value of 38.907%, the corresponding absolute error is 2.2×10^4 Nmm. Using classical stress analysis [245], this would result in only a sectional stress change in the drag brace of $\sigma_{F_4} = \pm 0.073$ MPa. As a result, the 38.907% error in the GPR surrogate was also deemed acceptable.

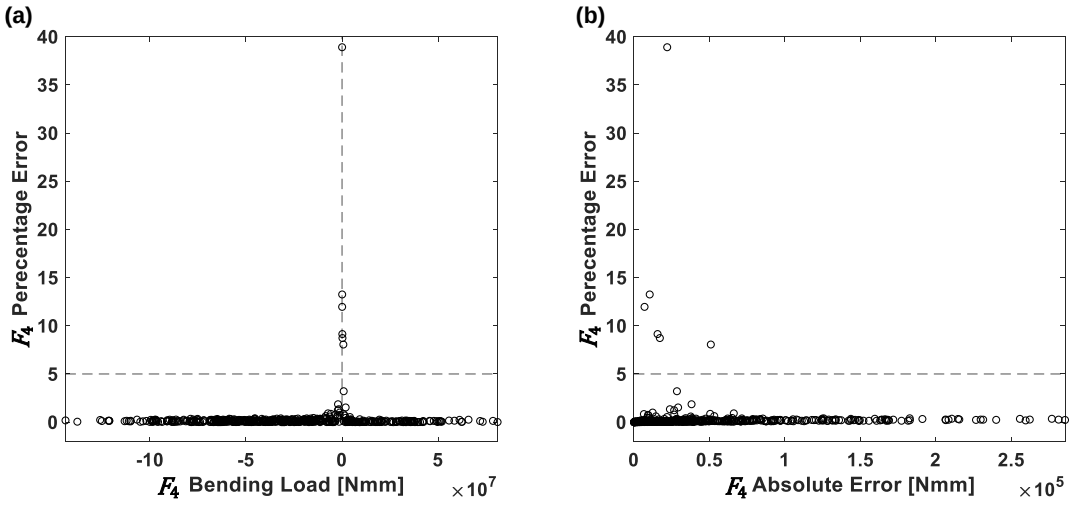

FIGURE 6.15. (a) The F_4 percentage errors compared to the corresponding F_4 bending load and (b) the F_4 percentage errors compared to the corresponding F_4 absolute error values.

6.5 Utilisation of Surrogate Models within Probabilistic Fatigue Methodology

The FEA MLG beam model case studies have successfully demonstrated that surrogate modelling methods can be used to significantly reduce the computational expense of evaluating the original FEA MLG beam model, whilst still accurately representing the relationship between the input and output parameters of the original model. For the RSM surrogate model of the lower side-stay, a single evaluation takes 4×10^{-6} seconds compared to the 20 seconds required for the original linear static FEA MLG beam model[6]. In a similar fashion, the GPR surrogate model for the drag brace only requires 2×10^{-4} seconds to produce a prediction for an 'unseen' combination of load factors. Therefore, whilst surrogate models will replace the existing FEA MLE beam model within the probabilistic fatigue methodology, the accuracy of the surrogate models permits the full complexity of the FEA MLG beam model to be retained within the probabilistic fatigue methodology, whilst reducing the computational expense of generating internal component loads.

The dramatic reduction in the CPU run-time required to generate internal component loads from global MLG assembly loads offered by surrogate modelling will be utilised in the probabilistic fatigue methodology to convert the statistically simulated load-time histories into internal component load-time histories. Figure 6.16 shows the axial lower side-stay loads predicted for a single flight, based upon a statistically simulated load-time history and the utilisation of the

[6]Computer Specifications: 4-core processor (3.40 GHz) with 16.0 GB RAM.

RSM surrogate model. Figure 6.17 shows the use of the RSM to predict the lower side-stay loads of 1,000 statistically simulated flights. The definition of the unit of 'load position' for the x-axes of Figures 6.16 and 6.17 is as defined previously in Section 5.10.4. The RSM requires 0.2 seconds to convert the statistically simulated design safe-life load-time history of 50,000 flights into internal component loads. This significant reduction in the computational expense of generating internal loads for components using surrogate models will ultimately facilitate the use of the load-time history statistical simulation approach within the probabilistic fatigue methodology. As a result, the use of surrogate models enables the incorporation of ground manoeuvre occurrence and sequencing variability, along with loading magnitude variability, within the probabilistic fatigue methodology, increasing the accuracy of estimates of p_f and R for safe-life landing gear components.

Returning to the probabilistic analysis framework defined in Chapter 3, the presented surrogate modelling methods could also be used to support engineering activities relating to design optimisation and digital twins, as the surrogate models only represent the input-output relationship of the FEA MLG beam model and are as a result, general in nature. The surrogate models could also be used to reduce the computational expense of the existing deterministic fatigue analysis process, resulting in more optimised designs, as proposed by Teixeira et al [138]. The knowledge developed in this chapter will be exploited for the surrogate modelling of FEA stress models, as will be shown in the case studies presented in Chapters 7 and 8.

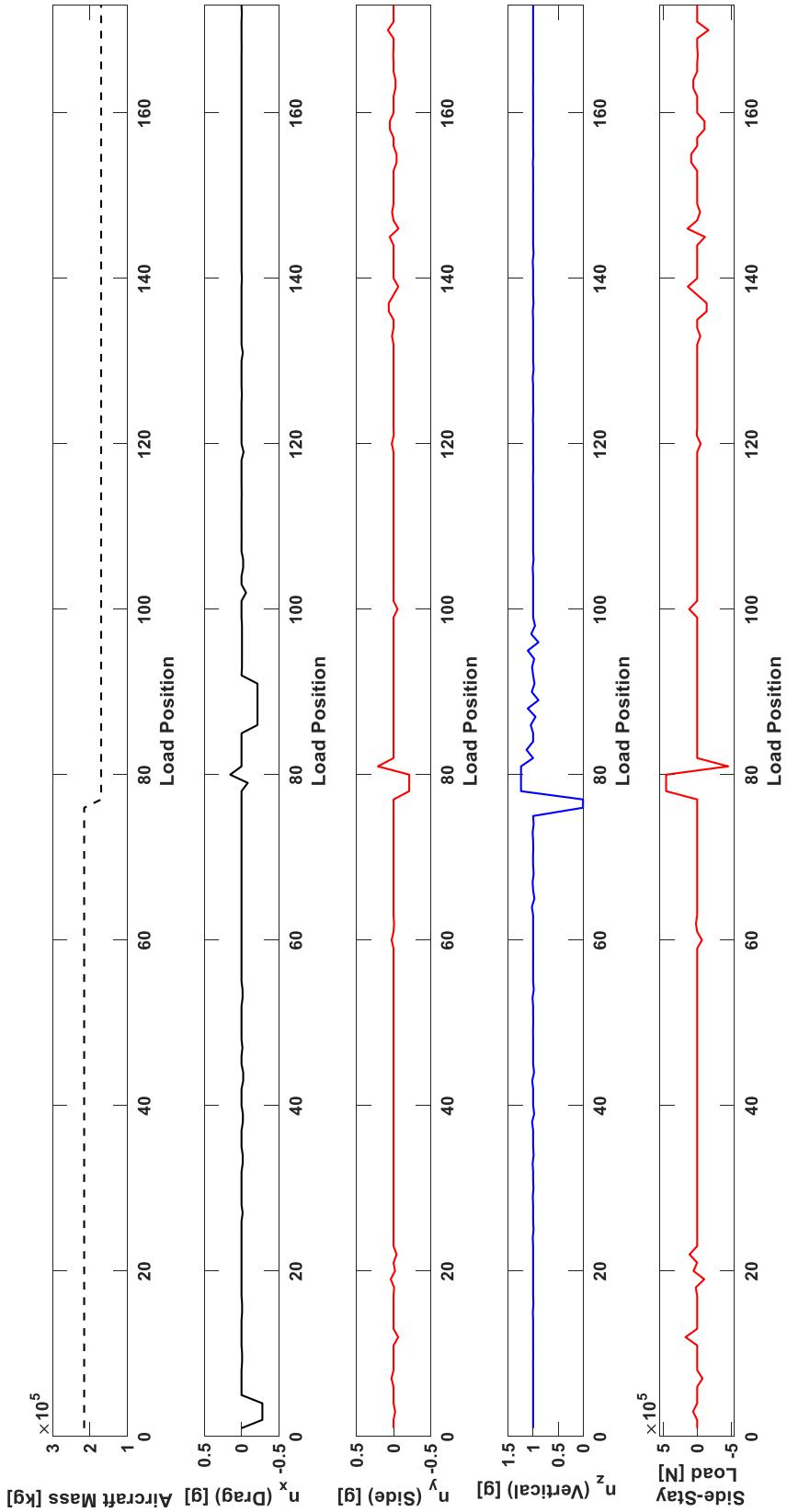

FIGURE 6.16. Utilisation of the RSM to predict side-stay loads for a single flight from the statistical simulation of a load-time history.

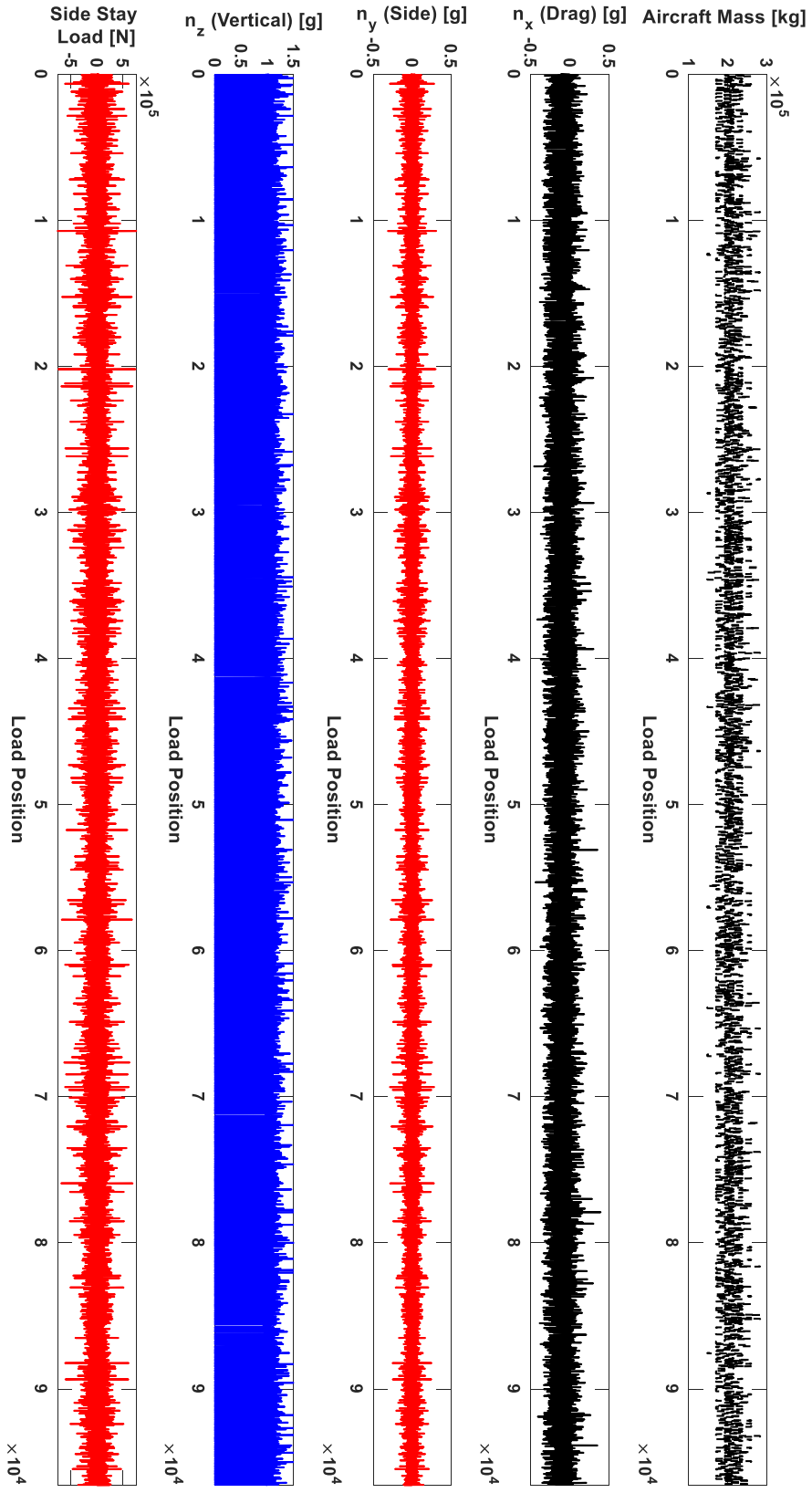

FIGURE 6.17. Utilisation of the RSM to predict side-stay loads for 1,000 flights from the statistical simulation of a load-time history.

6.6 Surrogate Modelling Trends from Case Studies

Across the application of surrogate models to the lower side-stay and drag brace, a number of observable trends were identified, concerning surrogate model accuracy, training time and evaluation time. These trends are expected to be as a result of the increase in complexity and dimensionality from the lower side-stay to the drag brace component, along with the increased training sample size used for the drag brace surrogate model. It is important to note that these trends are observed with respect to the application of surrogate modelling methods to linear elastic and linear static FEA only.

Firstly, the magnitude of the MAE and $RMSE$ metrics for the validation dataset increased by at least 2 orders of magnitude from the lower side-stay to the drag brace surrogate models. For the F_1 axial load, the MAE for the validation dataset was seen to increase from 4 N for the linear RSM to approximately 7×10^3 N for the GPR surrogate model of the drag brace. This increase in error is expected to be as a result of an increase in the underlying complexity of the relationship between the input and output parameters of the FEA MLG beam model when considering the drag brace component. The increase in complexity is also highlighted by the quadratic RSM failing to provide an accurate representation of the drag brace internal loads, suggesting that these loads have a highly non-linear relationship to the input parameters.

It can also be observed across the two case studies that the training time increased for all of the surrogate modelling methods, by at least an order of magnitude. This increase is as a result of the increased output dimensionality of the drag brace internal loads (i.e. requiring 6 surrogate models to be generated, rather than the single model required for the lower side-stay), along with the increase in the training dataset sample size. With an increase in training dataset sample size, larger matrices must be constructed and manipulated within the surrogate modelling methods, increasing the CPU run-time for training. From the evaluation of the training time across the lower side-stay and drag brace surrogate models, the following generalisation of the training time for each surrogate modelling method can be made: RSM - *seconds*, GPR - *minutes*, RBF - *hours*. It is suggested in the literature that the successful definition and training of ANNs can typically take *hours* [142]. This trend in training time for each surrogate modelling method can be used to support other practitioners in the selection of surrogate modelling methods for FEA models based on the resource period available for training.

A similar trend is also observed for the time to produce 1,000 predictions from each surrogate model. Again, as the size of the matrices within the surrogate model grew larger, due to dimensionality and increased training dataset sample size, the time required to evaluate the surrogate model also increased. This is best observed by considering the cubic RSM, which required 0.006 seconds to produce 1,000 predictions from an RSM defined by nine β coefficients. However, for the drag brace RSM, this increased to 0.719 seconds, due to the RSM being defined by 4,896 β coefficients. The larger number of β coefficients results in a greater computational expense when performing the matrix manipulation required to evaluate the RSM surrogate model [46].

Across the lower side-stay and drag brace FEA MLG beam models, it was observed that the MQ RBF surrogate modelling method, which required an optimisation process to define tuneable parameters prior to training, resulted in error values that were larger than the RSM and GPR surrogate modelling methods. For the lower side-stay, the MQ RBF surrogate model was shown to provide high error values compared to all of the other candidate methods. It is expected that this is as a result of the MQ RBF being 'over-fitted' to the training dataset, resulting in a poor-fit to the validation dataset. This suggests that the σ_{MQ} value selected may not have been the global minimum and as a result, the NM optimisation may have converged to a local minimum.

As a result, optimisation-reliant surrogate modelling methods introduce added training complexity, which not only increases the training time for the surrogate model, but may also result in an inaccurate surrogate model due to the challenges of the complex matrix manipulation and optimisation methods required for training. Hence, the expected trade-off between increased surrogate model accuracy and increased training time has not been observed when developing surrogate models for the FEA MLG beam model. Therefore, it is proposed that the optimisation-reliant RBF surrogate modelling method is not considered in the first instance when constructing surrogate models for linear elastic and static FEA, as it is possible to expend significant time and computational resource, only to construct an inaccurate surrogate model.

On the other hand, the cubic RSM was shown to provide consistent error metrics with the GPR and MQ RBF surrogate models, even for the more complex drag brace beam model. This demonstrates that the comparatively simple and widely-adopted RSM approach can provide accurate surrogate modelling for higher dimensional and non-linear responses of FEA models. The RSM approach also provides the shortest training time of all of the candidate surrogate modelling methods. In addition, RSM's similarity to curve-fitting methods can increase confidence in the constructed surrogate model, increasing 'buy-in' from engineers, which is especially crucial when adopting novel analysis methods in new applications [46, 54]. As a result, it is recommended that when developing surrogate models for linear static FEA, that RSM surrogate models are constructed in the first instance, prior to implementing more sophisticated approaches, with a view to minimising the resource required to implement accurate surrogate models.

6.7 Proposed Surrogate Modelling Selection Process for Linear Static Finite Element Analysis

Based upon the trends observed from applying surrogate modelling methods to the FEA MLG beam model, a surrogate model selection process for linear static FEA models is proposed to support practitioners and those new to the field of surrogate modelling. The process is shown as a flowchart in Figure 6.18 and aims to exploit the simplicity, low required knowledge and training burden of RSM methods, whilst mitigating the risk of expending significant time and computational resource on training sophisticated surrogate modelling methods.

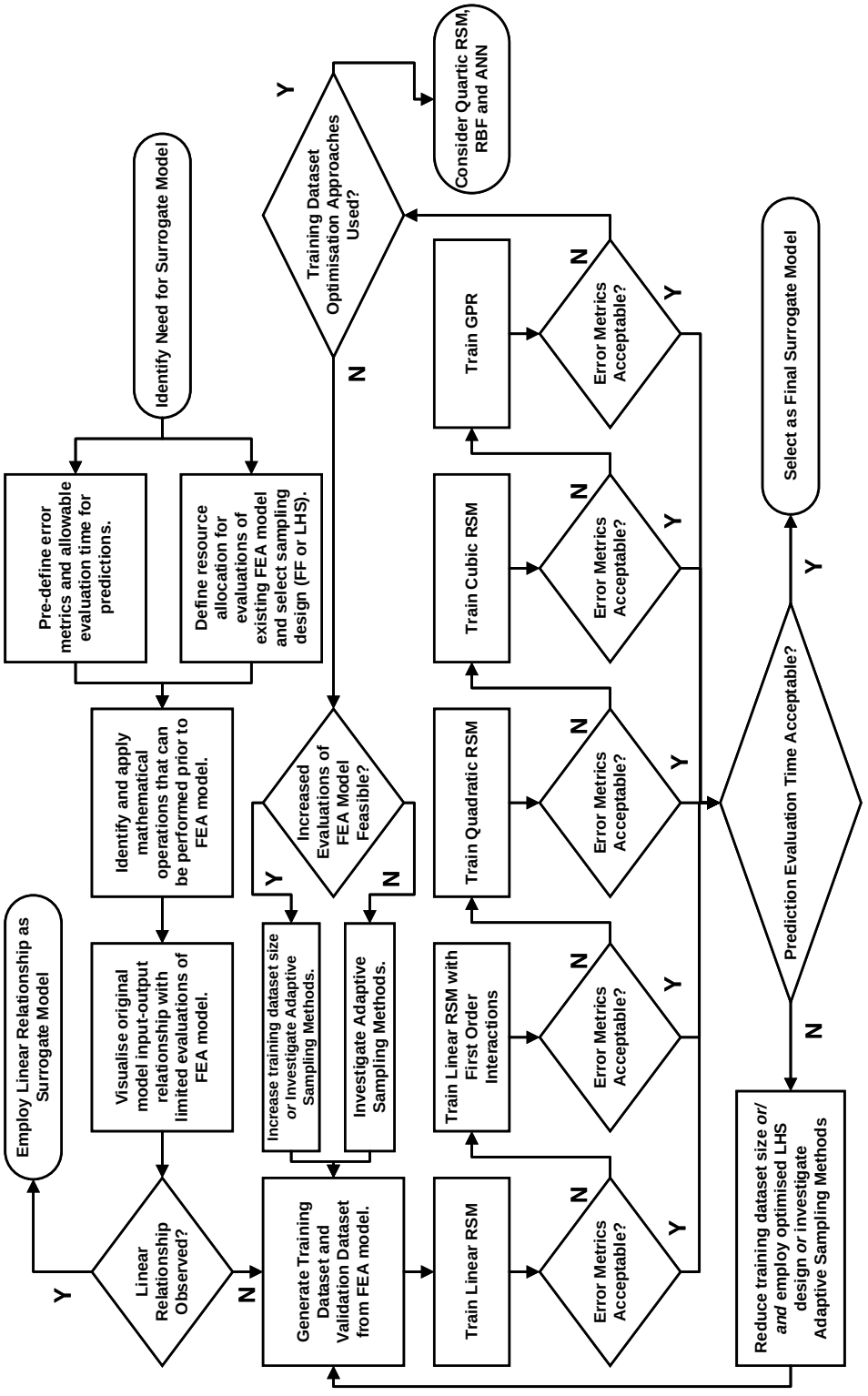

FIGURE 6.18. Proposed surrogate modelling selection process for linear static FEA models based upon the trends in computational expense and accuracy observed when constructing surrogate models for the FEA MLG beam model.

The process shown in Figure 6.18 also aims to capture the knowledge and experience gained over the lower side-stay and drag brace case studies, including the need to consider linear surrogate models in the first instance, and mitigating the effects of large training dataset sizes on surrogate model training and prediction times. The remainder of this section details the individual steps shown in Figure 6.18. The process shown in Figure 6.18 can also be considered as a higher-level representation of the surrogate modelling process shown previously in Figure 6.4.

6.7.1 Problem Definition and Initial Model Exploration

The first stage of surrogate model selection as shown in Figure 6.18 is to define the need for the surrogate model, in terms of the acceptable values for the MAE, MPE and $RMSE$ error metrics and the permitted evaluation time to generate predictions from the surrogate model. At this stage, the available resource (i.e. CPU run-time) to generate the training and validation datasets from the original FEA model should be defined. Where possible, acceptable error metrics should be defined with respect to the output of the process in which the surrogate model will be employed, as discussed in Section 6.4.2.4.

As demonstrated for the lower side-stay case study in Section 6.3, it can be useful at this stage to identify whether any mathematical operations can be applied to the input parameters prior to their evaluation by the FEA model, as this can simplify the input-output relationship that the surrogate model must represent.

The existing FEA model is then explored at a limited number of values for the input parameters (e.g. maximum and minimum combinations from a 2-level FF design). This will permit the overall FEA model response to be visualised for low-dimensionality cases, such as for the lower side-stay component. At this stage, as for the lower side-stay case study in Section 6.3, it may be observed that a simple linear relationship can be defined between the input and output parameters of the FEA model.

6.7.2 Surrogate Model Training and Testing

Following the initial exploration of the FEA model, the training and validation datasets must be constructed. Initially the training dataset sample size will be defined based upon the available computational resource, as this represents a practical engineering start-point for defining the sample size. Further steps to reduce and optimise the training dataset will be discussed in the following subsection. At this stage in the process, the use of either a FF or LHS design must be selected. It is recommended that LHS design is used, as the 'space-filling' nature of LHS ensures training data points are spread across the expected input space for a given sample size and model dimensionality [246], whilst FF design will rapidly constrain the training dataset to contain only maximum/minimum values (i.e. a 2-level FF design) for input parameters as the dimensionality of the model increases (such as for for the drag brace case study in Section 6.4)

[142]. As a result, LHS permits greater flexibility in the selection of the training dataset sample size, potentially reducing the required number of evaluations of the original FEA model and reduced surrogate model training and prediction times due to a reduced training dataset sample size [246]. Additional methods available to optimise training datasets are presented in Section 6.7.2.1.

The surrogate model training and testing process progresses from the simplest linear RSM approach and only increases the complexity of the surrogate model if the current candidate is found to generate unacceptable error metrics. Such a process is proposed as the lower side-stay case study demonstrated that the FEA MLG beam model could be represented using a simple linear RSM, rather than higher order RSMs or non-parametric methods. Consequently, the process shown in Figure 6.18 ensures that the simplest RSM methods are considered in the first instance, to prevent the wasting of computational resources on more complex surrogate modelling methods. As a result, the process shown in Figure 6.18 aims to select the simplest surrogate model with acceptable error metric and prediction time values for linear static FEA models.

6.7.2.1 Optimisation of Training Datasets

During the drag brace case study, the sensitivity of the surrogate model prediction time to the size of the training dataset was observed. Whilst larger training datasets will increase training times, as surrogate models are typically used to reduce the computational expense of evaluating FEA models, the focus of the process shown in Figure 6.18 is to minimise the prediction evaluation time of the surrogate model.

Therefore, if a candidate surrogate model is found to provide acceptable error metrics, its prediction evaluation time is then assessed. Providing the prediction evaluation time is acceptable, the candidate surrogate model is then selected. In the event that the prediction time is unacceptable, it is possible that the training dataset sample size is resulting in the manipulation of large matrices during surrogate model evaluation. Therefore, the training dataset sample size should be reduced. However, as reducing the training dataset sample size is likely to reduce the accuracy of the surrogate model, optimisation of the training dataset must also be considered. Ultimately, training dataset optimisation aims to achieve a uniform distribution of the training dataset values across the expected input space (as for LHS) or the generation of training datapoints at carefully selection locations in the expected input space [143, 247].

Training dataset optimisation therefore concerns not only the training dataset sample size, but also the sampling strategy used to create the training dataset. Beyond FF design, other classical DoE methods could be explored such as Central Composite design [248]. Whilst the dimensionality of the lower drag brace case required the use of LHS design rather than FF design, the sampling design produced by LHS can be further optimised by maximising its 'space-filling' nature by maximising the distance between LHS data points or minimising the correlation between data points across the LHS design [249].

Alternatively, adaptive sampling (also known as sequential design) methods can be used to continually populate the training dataset with new evaluations (known as infill points) of the original FEA model [143, 247]. Adaptive sampling methods continually retrain a surrogate model based on the generated infill points, which are targeted at areas where the surrogate model shows the largest errors [247]. Fuhg and Lin et al provide a comprehensive review of various adaptive sampling approaches for surrogate modelling [247, 248], a number of which are reliant on various optimisation methods to reduce the surrogate model error and targeted sampling approaches, such as focusing training data points at locations where the gradient of the model response is largest, as performed by Singh et al [250]. One evident advantage of adaptive sampling approaches for training surrogate models is that it does not require the *a-priori* definition of the training dataset sample size, as the training dataset is governed by the error observed within the surrogate model [247]. This is of an advantage as it is often challenging to predict the impact of training dataset sample size on the accuracy the resulting surrogate model [247]. Future work could therefore be conducted to assess the suitability and efficiency of applying optimised training datasets to linear static FEA models.

6.7.2.2 Reflection on Surrogate Modelling Selection and Model Complexity

As the majority of fatigue analysis is performed using linear static and linear elastic FEA models [7], it is expected that most surrogate models required for probabilistic fatigue analysis will be RSMs of varying polynomial order. Therefore, it is anticipated that the process shown in Figure 6.18 will be sufficient in guiding future practitioners when performing probabilistic fatigue analysis.

In the event that all of the RSM types are rejected due to unacceptable error metrics, a non-parametric GPR surrogate model is trained. In the event that the GPR surrogate model is also rejected, the training dataset should be revisited. If there is available computational resource, the training dataset size can be increased, providing dataset optimisation is considered (as described in the previous subsection) and that acceptable prediction evaluation times are achieved. More sophisticated surrogate modelling methods (e.g. quartic RSM, RBF or ANN) should be considered after it has been shown that the surrogate model error does not reduce with an optimised training dataset.

Whilst it is anticipated that mostly RSMs will be required to support probabilistic fatigue analysis, the modern engineering sector is often reliant on FEA and simulations that are significantly more complex than the linear elastic and linear static FEA presented within this thesis. For example, computationally intensive non-linear FEA stress analysis which accounts for material plasticity and complex non-linear dynamic loading simulations are now commonplace [7, 221]. Consequently, it is anticipated that the development of probabilistic approaches to design involving such models and simulations will be reliant on sophisticated surrogate modelling. As the underlying response of such models will be more complicated than linear static FEA models,

such applications of surrogate modelling may require a further investigation into the performance of GPR, RBF and ANN surrogate models. Therefore, it is expected that the surrogate modelling complexity will 'match' the increased complexity of the original FEA models.

In addition, non-linear and dynamic FEA models typically present a greater computational demand than the linear static FEA models considered in this chapter. Therefore it is also suggested that surrogate modelling in such contexts will also require the employment of the training dataset optimisation methods described in the previous subsection. It is hoped that future work in the surrogate modelling field will aim to generate a systematic surrogate modelling selection process for such cases, similar in nature to the one presented for linear static FEA models in Figure 6.18.

6.7.3 Current Limitations of Surrogate Models

The load factor values generated within the statistically simulated load-time histories concern the loads measured at the aircraft Centre of Gravity (CoG) [191]. Due to the lack of data concerning aircraft CoG position variability with respect to the MLG, it was assumed that the CoG load factors were applied directly at the MLG tyres. Coupled with the assumption of equal load distribution between the left and right MLGs and across all four tyres of the MLG, along with the lack of torsional loading data for landing gear within the literature, the surrogate models do not account for torsional loads being applied to the MLG. As a result, future work should investigate the development of surrogate models based upon a linear static FEA MLG beam model that does account for the application of torsional loads to the landing gear.

Concerning the candidate surrogate modelling methods, it should be noted that the GPR, RBF and ANN approaches all have different elements of 'architecture' that could be varied prior to training of the surrogate models:

- **GPR:** Kernel functions other than the squared exponential are available:
  - Matérn kernels, which have been suggested to provide good representation of physical processes [227].
  - The incorporation of boundary conditions into kernel functions to better represent physical constraints [251].
- **RBF:** Basis functions other than the MQ basis function are available [144]. Rocha suggests that the basis function should be selected based on minimising the error of the RBF surrogate model [231].
- **ANN:** Beyond the number of neurons in each layer, the number of layers can be varied, along with the transfer function of each neuron and the back-propagation training algorithm used [232].

The definition and training of the ANN for the drag brace in Section 6.4 highlighted significant challenges in selecting the number of neurons within the ANN to achieve an accurate surrogate model. A large number of 'rules of thumb' are presented within reference texts on ANNs, which provide guidance on selecting the training dataset size based upon the number of weights in the ANN and vice-versa [244, 252, 253]. It is recommended that in future investigations into the utilisation of ANNs for surrogate modelling, that such guidance material is used to define ANN architecture, rather than the neuron number sweep proposed in Section 6.2.3.4.

As a result, future work should consider the down-selection of surrogate model architecture prior to training, through assessing the error metrics for different kernel, basis and ANN architectures. Such an approach would also need a systematic process similar to the flowchart shown previously in Figure 6.18. However, as this chapter has demonstrated the capability of the RSM approach, it is anticipated that such a process would be required for complex, non-linear and dynamic FEA models, rather than the linear static FEA models considered within this chapter.

6.8 Summary

Aircraft landing gear loads are typically defined as global loads applied at the landing gear tyres. In order to perform static and fatigue analysis of landing gear components, the global loads must be converted into internal component loads. Due to the complexity of landing gear structural assemblies, which include complex geometries, load paths and many mechanical joints, linear static FEA models of the structural assemblies (comprised of 1D beam elements) must be employed to compute internal component loads.

The reliance on an FEA model to compute internal component loads already presents a significant computational burden in the existing deterministic analysis approach. As a result, the use of FEA beam models represents a prohibitive computational expense when considering a probabilistic fatigue methodology, during which millions of load factor levels will have to be analysed for the thousands of statistically simulated load-time histories. Surrogate modelling methods have been proposed as an approach that generate an accurate representation of the input-output relationship of an existing computationally expensive model, whilst requiring significantly less computational resource to evaluate.

This chapter has demonstrated the application of a wide range of surrogate modelling methods to predict the internal loads in lower side-stay and drag brace landing gear components, which would normally by computed using a linear static FEA model. Through considering RSM, RBF, GPR and ANN surrogate models by using a systematic training and testing process, it was identified that RSM and GPR surrogate models could accurately predict internal loads for the lower side-stay and drag brace components respectively. The utilisation of surrogate modelling methods reduced the CPU run-time required to evaluate internal component loads from 20 seconds to less than a millisecond. As a result, the surrogate models could be employed to

convert a statistically simulated design safe-life load-time history of 50,000 flights in 0.2 seconds. This dramatic reduction in computational expense will permit the inclusion of the statistically simulated load-time histories within the probabilistic fatigue methodology.

The application of surrogate modelling methods to the landing gear beam models also highlighted that the RBF approaches, which are reliant on optimisation methods to define surrogate model parameters or architectures, required a significantly higher computational resource to train and evaluate. Challenges were also encountered in the training of an ANN surrogate model. However, the RBF and ANN surrogate models failed to provide a more accurate surrogate model, when compared to simpler methods such as RSM. As a result, a surrogate model selection process for linear static FEA models has been proposed, which encourages practitioners and those new to the field of surrogate modelling to build simple RSM surrogate models prior to considering more sophisticated methods. The proposed process therefore mitigates the risk of expending significant time and computational resource on training complex surrogate models that may not actually provide an accurate representation of the input-output relationship of the original model.

The 'blockers' to implementing a probabilistic approach to fatigue design overcome by surrogate modelling are shown in Table 6.17. Firstly, the wider utilisation of surrogate modelling methods primarily helps to overcome the *computational expense* blocker, through the dramatic reduction in computational expense when compared to the original FEA model. The proposed surrogate model selection process also reduces the overall computational expense required by focusing on the use of simple surrogate modelling methods, prior to considering more sophisticated methods which have a higher computational resource burden for training.

TABLE 6.17. The blockers to probabilistic design approaches overcome by the wider utilisation of surrogate models.

Blocker	Blockers overcome due to utilisation of surrogate models
Computational Expense	• Surrogate models are significantly faster to evaluate than existing models, drastically reducing the computational expense of a probabilistic methodology. • Proposed surrogate model selection process reduces the risk of 'wasting' resources on inaccurate surrogate models.
Required Assumptions of Existing Process	Surrogate models permit the full potential complexity of the input-output relationship of computationally expensive models to be retained within the probabilistic approach.
Availability of Data	N/A
Accuracy of Data Characterisation	N/A
Required Knowledge	• Surrogate models can be used to support other engineering activities, increasing the return on the resources required to generate surrogate models for a probabilistic approach. • Proposed surrogate model selection process consolidates required knowledge into a single process for new practitioners.

The use of surrogate models also supports the overcoming of the *simplifications/assumptions of deterministic analysis process* blocker, through enabling the full potential complexity of the input-output relationships of linear elastic and static FEA models to be incorporated into the probabilistic fatigue methodology, without requiring direct evaluation of the FEA model within the MCS-SSI probabilistic analysis method. Finally, as highlighted in Chapter 3, once surrogate models have been constructed, they can be used in a wide range of other engineering activities. This increases the useful return on the resources and knowledge required to generate surrogate models for a probabilistic approach, supporting the overcoming of the *required knowledge* blocker. The overcoming of this blocker is also supported by the definition of a systematic surrogate model testing, training and selection process, which consolidates all of the required methods into a single process. Table 6.17 summarises the ways in which extensive surrogate modelling can overcome the blockers to a probabilistic approach to design.

CHAPTER 7

LOWER SIDE-STAY CASE STUDY

This chapter of the thesis considers the application of the probabilistic fatigue methodology to the lower side-stay assembly of the main landing gear of a wide-body civil aircraft. The probabilistic fatigue methodology described in Chapter 3 is applied to the lower side-stay assembly in order to compute the probability of fatigue failure for engineering features of the lower side-stay assembly, along with generating component-level and assembly-level reliability estimates. Whilst the previous chapters of this thesis have concerned data collection, design parameter characterisation and surrogate modelling methods, the current chapter focuses on the adaptation of the existing deterministic safe-life fatigue analysis process within the probabilistic fatigue methodology and the post processing of results from the probabilistic fatigue methodology. Beyond generating probability of failure estimates, extensive sensitivity analysis is performed to identify the fatigue design drivers for the lower side-stay assembly.

7.1 Introduction to Case Studies

The next two chapters will present the implementation of the probabilistic fatigue methodology on landing gear component case studies, along with presenting the subsequent results from the probabilistic analysis and sensitivity analysis. The case studies considered within the following two chapters concern an MLG lower side-stay assembly and an MLG drag brace. The use of two case studies permits the demonstration of the probabilistic fatigue methodology across case studies of differing dimensional, loading and analysis complexity, including analytical and FEA stress analysis.

7.1.1 Selection of Monte Carlo Simulation Iterations

As discussed during the definition of the probabilsitic methodology in Section 3.3.1, the implementation of the MCS-SSI probabilistic fatigue methodology requires the definition of the number of MCS iterations to perform. A common 'benchmark' value proposed within the literature for MCS-based probabilistic analysis methods is $N_{MCS} = 1 \times 10^6$ iterations [46]. Other guidelines recommend utilising an approximation of the expected p_f value, whereby the number of MCS iterations should be in the order of 10^{k+1}, when the expected p_f is in the order of $10^- k$ [114].

The expected p_f for safe-life landing gear components can be assessed from the literature. Firstly, Habermann has reviewed the safety factors currently used for the safe-life fatigue design of military aircraft landing gear components, and has identified that the current safety factors result in a target of $p_f = 2 \times 10^{-4}$ at the component design safe-life [254]. Schmidt has investigated the current in-service failure rate of landing gear components due to fatigue, and as a result has suggested that the current p_f per-flight cycle of landing gear components is 4.7×10^{-8} [16]. For a 50,000 flight design safe-life, this corresponds to a target of $p_f = 2.3 \times 10^{-3}$.

Based upon the expected p_f of safe-life landing gear components, the minimum number of MCS iterations that would need to be considered is $N_{MCS} = 1 \times 10^5$, based on the 10^{k+1} criterion. In order to verify this value of N_{MCS}, Equations 3.2 and 3.3 from Chapter 3 can be used to estimate the statistical uncertainty in $P_{f_{MCS}}$ for different values of N_{MCS}, based upon the expected value of $p_f = 2 \times 10^{-4}$. Table 7.1 shows the $P_{f_{MCS+2\sigma}}$ values for a number of N_{MCS} values.

TABLE 7.1. Convergence of MCS $P_{f_{MCS}}$ for different numbers of N_{MCS} iterations, assuming an expected p_f value of $p_f = 2 \times 10^{-4}$.

N_{MCS}	$P_{f_{MCS+2\sigma}}$ (for $p_f = 2 \times 10^{-4}$)
1×10^4	4.828×10^{-4}
2×10^4	4.000×10^{-4}
1×10^5	2.894×10^{-4}
5×10^5	2.400×10^{-4}
1×10^6	2.283×10^{-4}

Table 7.1 demonstrates that the statistical error in $P_{f_{MCS}}$ reduces rapidly between $N_{MCS} = 2 \times 10^4$ and $N_{MCS} = 1 \times 10^5$. It can also be observed that doubling the number of iterations from $N_{MCS} = 5 \times 10^5$ to $N_{MCS} = 1 \times 10^6$ only resulted in a 5% reduction in the statistical uncertainty from $P_{f_{MCS}}$ estimates. As a result, the conventional benchmark of $N_{MCS} = 1 \times 10^6$ was rejected, as this represented a significant increase in CPU run-time for limited reduction in statistical uncertainty.

As the $P_{f_{MCS}}$ results are only to be used for validation of the $P_{f_{dist}}$ results from the MCS-SSI probabilistic fatigue methodology, the selected benchmark was $N_{MCS} = 1 \times 10^5$, in order to minimise the CPU run-time of the case studies, whilst still satisfying the 10^{k+1} criterion. It should be noted that the opportunity to reduce the value of N_{MCS} for the MCS-SSI probabilistic fatigue methodology and the impact on the accuracy of $P_{f_{dist}}$ estimates will be explored in Section 8.2.

7.1.2 Feature-Based Approach

Due to the use of FEA models to perform linear elastic stress analysis of landing gear components [9], discrete locations on the FEA models must be selected at which to perform the probabilistic fatigue analysis. The locations within the FEA models can be identified and selected using a 'feature-based' approach, which ensures that specific engineering features are represented within the probabilistic fatigue analysis. Engineering features include elements of geometry that are expected to act as 'stress-raisers' in a component, leading to an increased accumulation of D_T damage at such locations. These locations are also known as 'hot-spot' locations [9]. A down-selection process to identify which engineering features are to be included in the probabilistic analysis is also required to reduce the computational memory requirement and run-time as discussed during the definition of the probabilistic fatigue methodology in Section 3.3.1. A thorough demonstration of the methodology is presented later in this thesis in Section 8.1.4.

A systematic feature down-selection process was implemented for the FEA models, in order to identify the features to include in the probabilistic fatigue analysis:

1. Highlight all stress-raising features within the component.

2. Highlight stress hot-spots under maximum loading cases from FEA.

3. If the number of features to include in the probabilistic fatigue analysis from Steps 1 and 2 exceeds the available computational resource:

    - Perform deterministic fatigue analysis using a $PoS = 99\%$ S-N curve and retain all damaged features (these are features that would accumulate damage within existing deterministic safe-life fatigue analysis).

4. If the number of features to include the probabilistic fatigue analysis from Steps 1 to 3 exceeds the available CPU resource:

    - Perform a 'short' MCS ($N_{MCS} = 1{,}000$) and statistically characterise the variability in D_T. Only retain features that demonstrate a quantifiable value of $P_{f_{dist}}$.

Figure 7.1 summaries the feature down-selection process as a flowchart, and the down-selection process is demonstrated for the lower side-stay case study and drag brace case study in Sections 7.2.3 and 8.1.2 respectively.

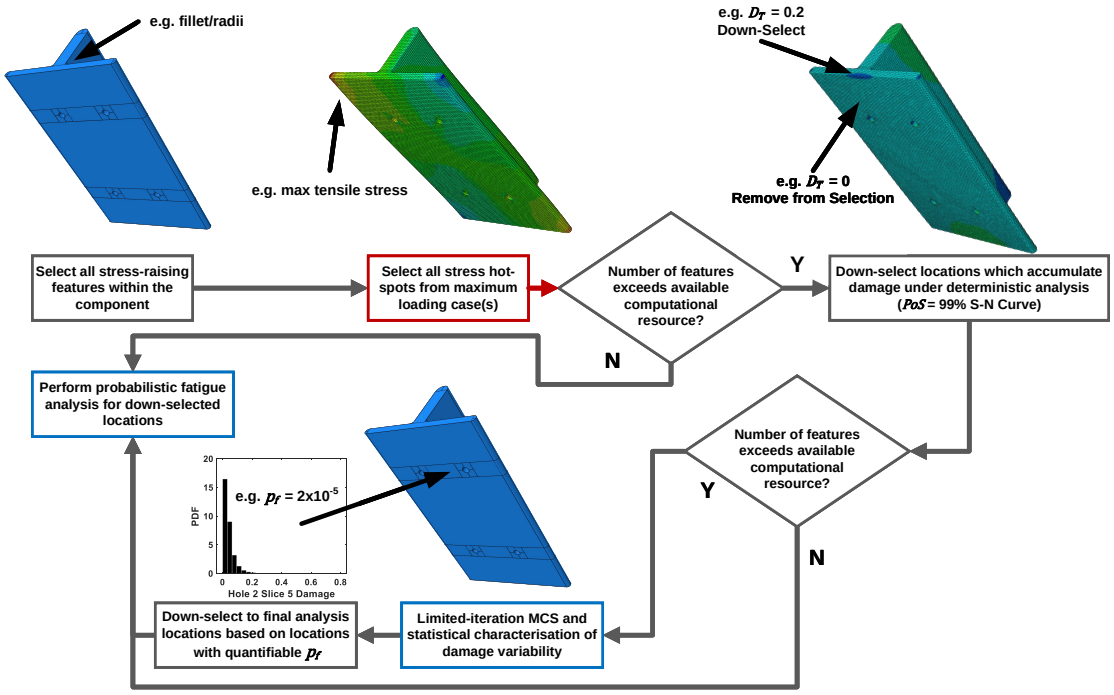

FIGURE 7.1. The feature down-selection process for the probabilistic fatigue methodology.

7.2 Lower Side-Stay Assembly Case Study

This section of the present chapter will detail the implementation of the probabilistic fatigue methodology to the MLG lower side-stay assembly of a civil wide-body aircraft. The following case study considers the application the probabilistic fatigue methodology to components that are analysed using both analytical and FEA stress analysis methods. The probabilistic results and sensitivity analysis cases will also be presented following the implementation of the probabilistic fatigue methodology.

7.2.1 Assembly Overview

The side-stay assembly is attached to the main fitting of the MLG and the landing gear attachment points within the airframe, as shown in Figure 7.2. The purpose of the side-stay is to react side loads applied to the MLG during landing and ground manoeuvres. The side-stay assembly also provides down-locking of the MLG and must also fold to achieve MLG stowage. The side-stay assembly is composed of the components highlighted in Figure 7.2.

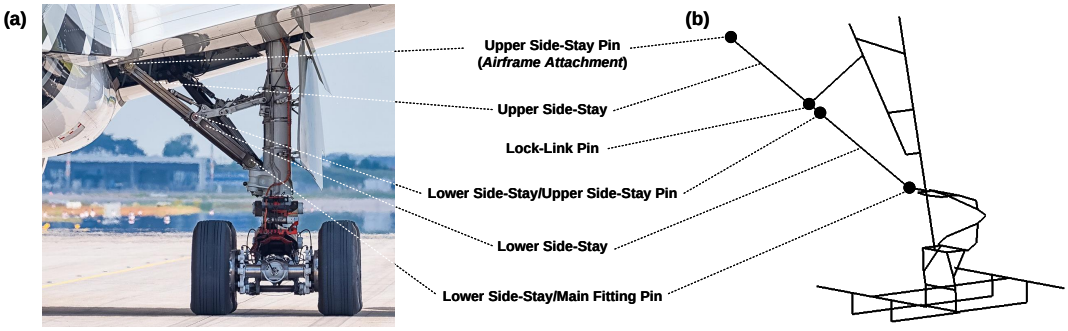

FIGURE 7.2. The location of components in the side-stay assembly, shown on (a) a typical wide-body aircraft landing gear and (b) an FEA MLG beam model.
(a) Original image attributed to Julian Herzog and is used under the GNU Free Documentation License Version 1.2 GFDL and Creative Commons Attribution 4.0 International License CC-BY-4.0. Source: Wikimedia Commons

The case study concerning the side-stay assembly focuses on the lower side-say assembly, which comprises of the lower side-stay, lower side-stay/main fitting pin and the lower side-stay/upper side-stay pin. The design safe-life for the lower side-stay assembly is 50,000 flights.

Loading

As discussed in Chapter 6 and shown previously in Figure 6.8, the lower side-stay only carries F_1 axial loads along the length of the side-stay, as a result of global F_Y side loads from the side load factor n_y. A positive value of n_y results in compression in the side-stay assembly (i.e. negative F_1). Within deterministic analysis, the linear static FEA MLG beam model described in Chapter 6 is employed to convert global loads at the MLG tyres to F_1 side-stay loads.

Lower Side-Stay Component

The lower-side stay component is formed of a simple geometry consisting of a constant H-section, as shown in Figure 7.3. The overall dimensions of the lower side-stay are also shown overleaf in Figure 7.3 and the component is symmetric about the centre lines of the assembly and the H-section. Component dimensions have been sourced from scaling public domain photographs of MLG components. A 3D visualisation of the lower side-stay component is provided in Figure 7.4. The lower side-stay component is manufactured from high-tensile strength 4340 steel [25].

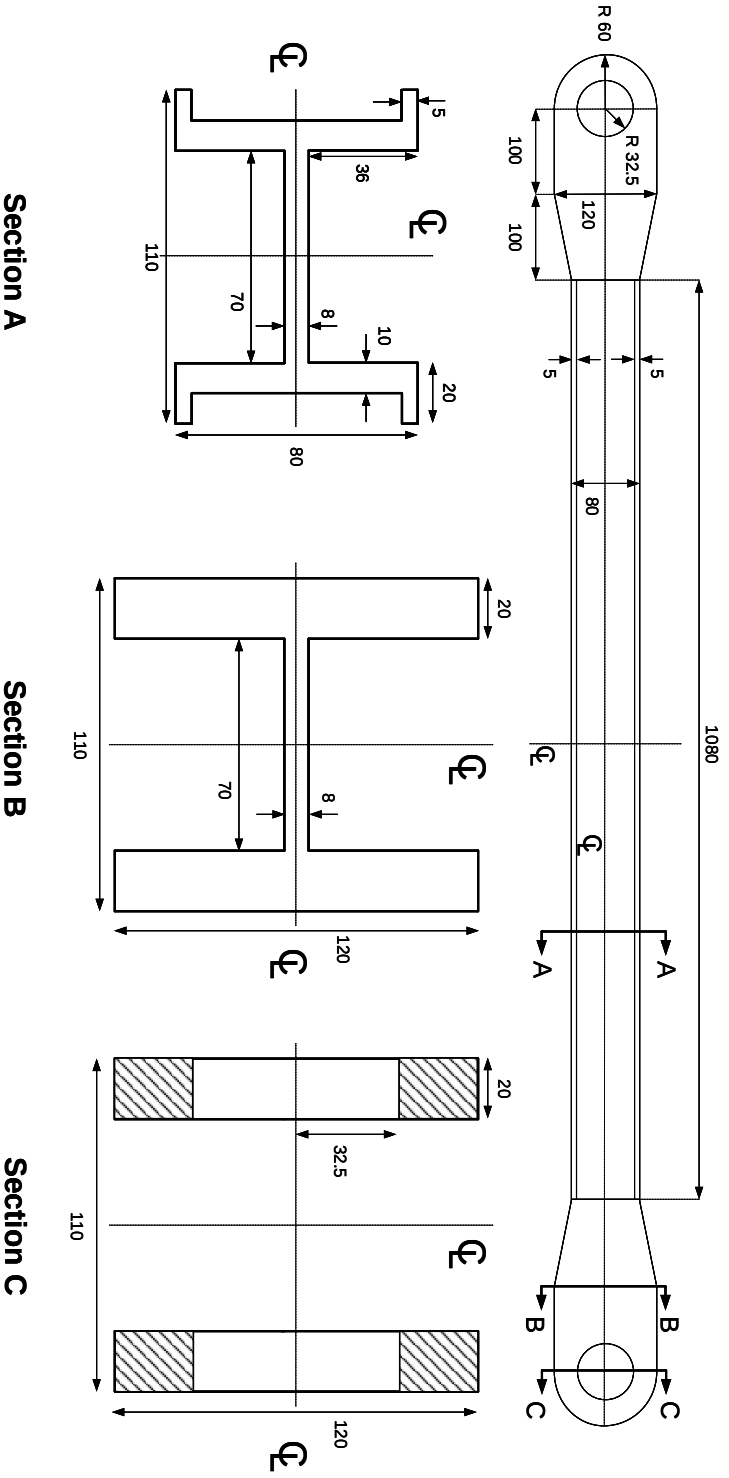

FIGURE 7.3. The dimensional and sectional properties of the lower side-stay component.

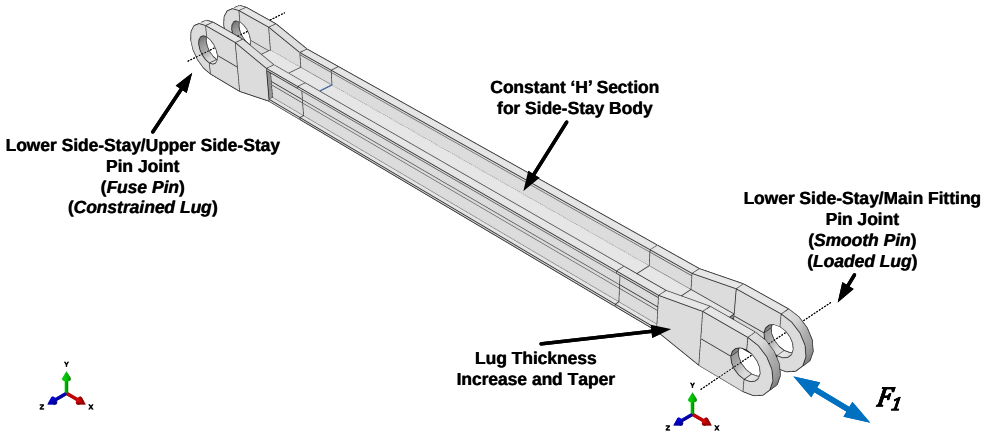

FIGURE 7.4. A 3D model of the lower side-stay component.

At the end of the H-section, the vertical webs are extended to produce a pair of lugs as shown in Figure 7.4. The lugs have an increased thickness and depth compared to the webs of the H-section (see Section B and C in Figure 7.3). The lower side-stay is loaded through the pair of lugs which are in contact with the lower side-stay/main fitting pin joint, as highlighted in Figure 7.4. The loads in the lower side-stay are reacted at the opposite pair of lugs, which are in contact with the lower side-stay/upper side-stay pin joint.

Lower Side-Stay Pins

The lower side-stay component is joined to both the main fitting and the upper side-stay using pin joints, which are both in a clevis (or double shear) arrangement, whereby the lower side-stay provides the outermost lugs as shown in Figure 7.5. Due to the clevis arrangement, both pins are loaded in pure shear resulting from the F_1 axial tension/compression loads. Pure shear loading assumes that no pin bending occurs. In addition, it is assumed that both pins carry the same shear loading, as the side-stay assembly is the only load path in the MLG assembly that can react side loads (see Chapter 6). Figure 7.5 also demonstrates the shear loading on the pins, whereby the F_1 side-stay axial load acts across the circular face of the pins. Due to the clevis arrangement, the maximum shear load occurs at the interface between the two lugs of the clevis joint, and is equal to half the side-stay axial load (i.e. $S = \frac{F_1}{2}$) [245, 255].

The geometry for both side-stay pins is shown in Figure 7.6. Both pins are hollow and are defined by an outer radius 'OR' and an inner radius 'IR' and the length of the pins is equal to the width of the lower side-stay. Component dimensions have been sourced from scaling public domain photographs of MLG components. The pins are manufactured from high-tensile strength 4340 steel [25].

The lower side-stay/upper side-stay pin is a 'fuse pin', which is designed to fail through static overload (i.e. at a specific ultimate 'S' shear load) [255]. Fuse pins are used within landing gear assemblies to ensure that in the event of an overload (e.g. hard landing), the landing gear separates from the airframe in a controlled manner, to ensure the structural integrity of other aircraft structural components and fuel tanks [255]. The control of the overload failure at a given static load is achieved by machining circumferential grooves on the inner surface of the pin at the maximum shear plane location. These grooves result in a stress concentration K_t, and the geometry of the groove (defined by width - 'w_g', depth - 'd_g' and radius - 'r_g') dictates the value of K_t at the fuse groove [256]. The lower side-stay/main fitting pin is not a fuse pin and is therefore referred to as a 'smooth' pin.

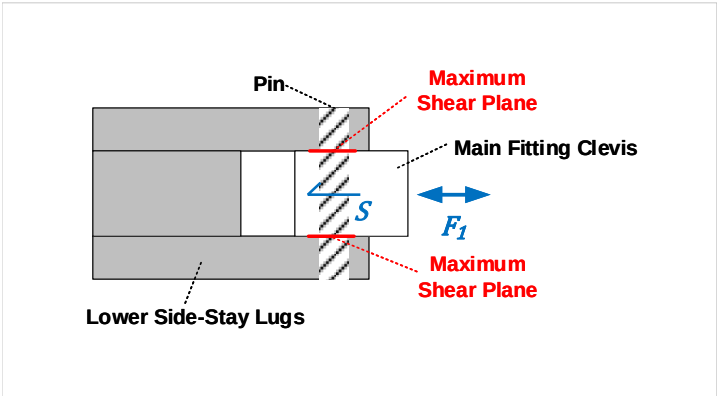

FIGURE 7.5. A clevis / double shear pin joint as typically used in landing gear assemblies, highlighting how the axial load is converted to a pin shear load.

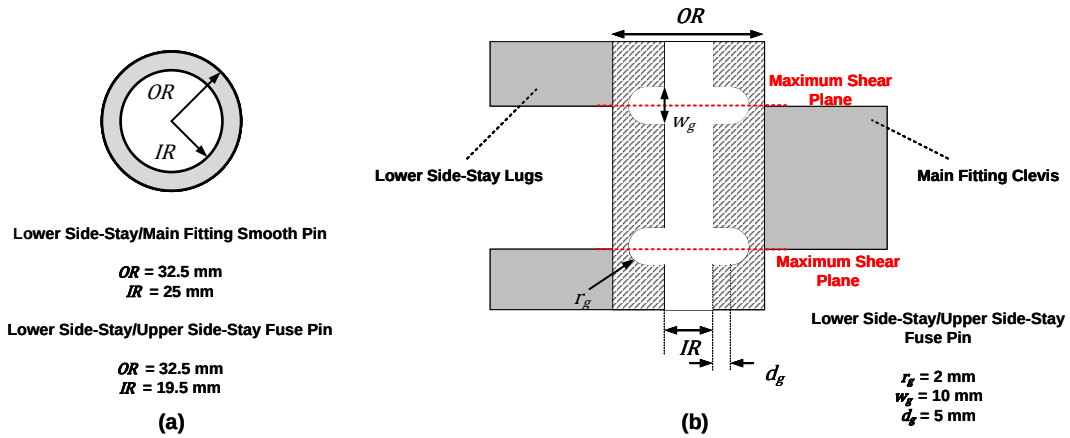

FIGURE 7.6. The dimensions of the (a) smooth and (a, b) fuse pins in the lower side-stay assembly.

7.2.2 Stress Analysis

Within the probabilistic fatigue methodology, the load-time histories of individual components (as computed using the linear static FEA MLG beam model surrogate model based upon the global load-time history) must be converted to stress-time histories using stress analysis. Cyclic stress amplitudes σ_a can then be extracted from the stress-time history using rainflow counting. The stress analysis employed for the components of the lower side-stay will now be presented. Linear elastic stress analysis methods are used exclusively throughout this case study, consistent with existing practice [6, 7] and all loads modelling is based upon a linear static FEA model.

7.2.2.1 Classical Analysis: Lower Side-Stay Pins

Landing gear pins are typically assessed using classical or analytical stress analysis methods [257]. The shear load 'S' applied to the pin can be converted to a shear stress 'τ' using Equation 7.1.

$$\tau = \frac{S}{\pi OR^2 - \pi IR^2} \tag{7.1}$$

A key challenge of performing fatigue analysis of pins is the need to convert from shear stresses to uniaxial stresses, which are typically used to derive S-N datasets and curves. In addition, the shear loading applied to pins can result in complex and multi-axial stress states. Narayan et al and Le-The provide an overview of recent advancements in the multi-axial stress analysis of landing fuse pins [255, 257]. However, for simplicity, the existing practice of employing a shear to uniaxial stress transformation was adopted, such that fatigue analysis could be performed based upon the uniaxially-derived S-N dataset for 4340 steel [25, 255, 257].

The multi-axial stress correction employed within the lower side-stay case study was the "von Mises Equivalent Uniaxial Stress" correction as described by Narayan et al [257]. Assuming pure shear and no pin bending as a result of the clevis arrangement, the shear stress τ in the pin can be converted to the equivalent uniaxial signed von Mises stress 'σ_{eq}' using Equation 7.2 [257]:

$$\sigma_{eq} = \pm\sqrt{3}\tau \tag{7.2}$$

The σ_{eq} value therefore represents the σ stress value to be used in the stress-time history for the pins. In order to estimate the K_t for the fuse pin, Equation 7.3, sourced from Pollack [256] and ESDU data item 79032 [258], can be used in conjunction with the fuse groove geometry. K_t is applied to the value of σ_{eq} and at the nominal fuse dimensions is $K_t = 3.17$.

[REDACTED] (7.3)

7.2.2.2 Finite Element Analysis: Lower Side-Stay Component

The stress analysis of the lower side-stay component is performed using full-field FEA linear elastic stress analysis. The lower side-stay component geometry was constructed as a 3D solid model in ABAQUS®, comprising of linear quadratic 8-node brick elements (C3D8R elements), resulting in the FEA model shown in Figure 7.7. C3D8R elements are first order (i.e. linear) elements with a single integration point at the centre of the element[1], rather than an integration point at every element node (i.e. reduced integration) [259]. A reduced integration element type was selected to reduce the CPU run-time of the linear elastic FEA stress model.

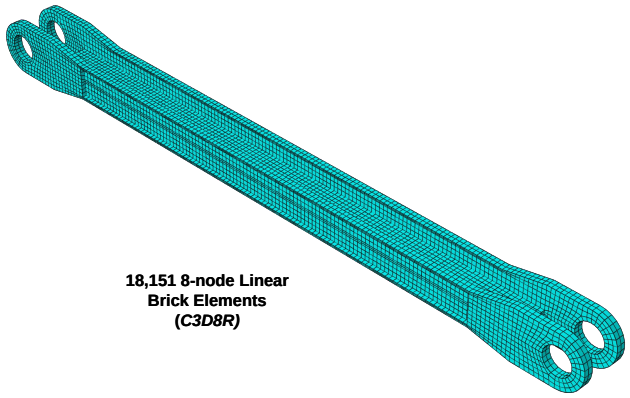

FIGURE 7.7. The linear elastic FEA model of the lower side-stay component.

In order to apply loading to the lower side-stay, the lower side-stay pins and clevis lugs (i.e. main fitting and upper side-stay attachments) were modelled as solid and stiff components. A uniformly-distributed pressure load, equivalent to the required F_1 load, was applied to the main fitting stiff lug, as shown in Figure 7.8a. The corresponding lugs on the lower side-stay are identified as the 'loaded' lugs within the remainder of this thesis. Within ABAQUS®, 'contact pairs' are used to represent the interactions between different components within a structural assembly [259], and a friction coefficient of $\mu_f = 0.1$ was used to represent the typical friction present in landing gear pin joints with bushings [260].

Boundary conditions were applied to the upper side-stay clevis lug to represent the load transfer from the lower side-stay to the upper side-stay. In order to simplify the stress analysis for the probabilistic fatigue methodology case study, the upper side-stay clevis lug was assumed to be pinned, constraining displacements along the direction of loading as shown in Figure 7.8b. The corresponding lugs on the lower side-stay are identified as the 'constrained' lugs within the remainder of this thesis. Whilst it would be expected that the upper side-stay clevis lug would demonstrate displacement under loading, this would require the displacements from the FEA MLG beam model to be captured, rather than the F_1 axial load, complicating the stress analysis.

[1] 'Hourglass' control is applied to C3D8R elements to constrain non-physical element deformation.

Improved approaches to representing boundary conditions for landing gear components will be presented for the drag brace case study in Section 8.1. A visualisation of the lower side-stay FEA stress model under tensile loading is shown in Figure 7.9.

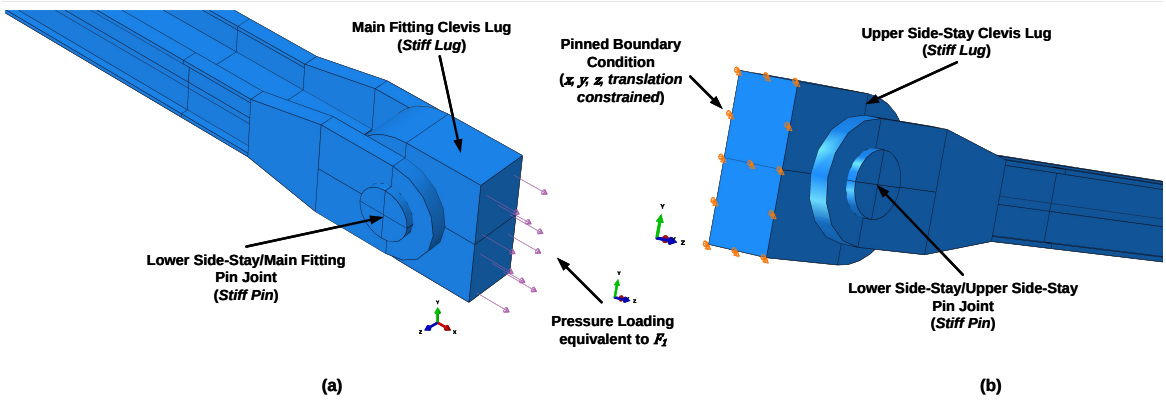

FIGURE 7.8. The (a) loading and (b) boundary conditions of the FEA model of the lower side-stay component.

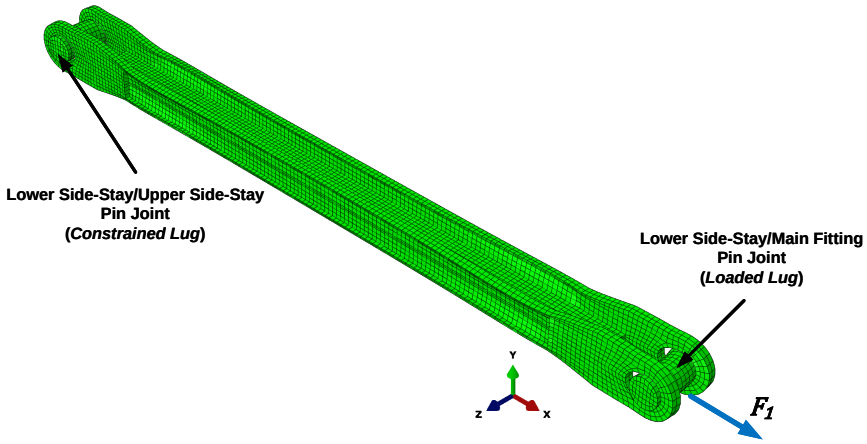

FIGURE 7.9. The deformed lower side-stay component under tensile loading.

Regarding the mesh density of the linear elastic FEA stress model, the mesh density was selected such that it resulted in converged stress estimates at the top and bottom of each lug within the lower side-stay. These locations were selected as they were expected to result in the maximum stresses of the lower side-stay, as maximum or 'hot-spot' stresses occur in such locations when under axial tensile loading, as shown in Figure 7.10.

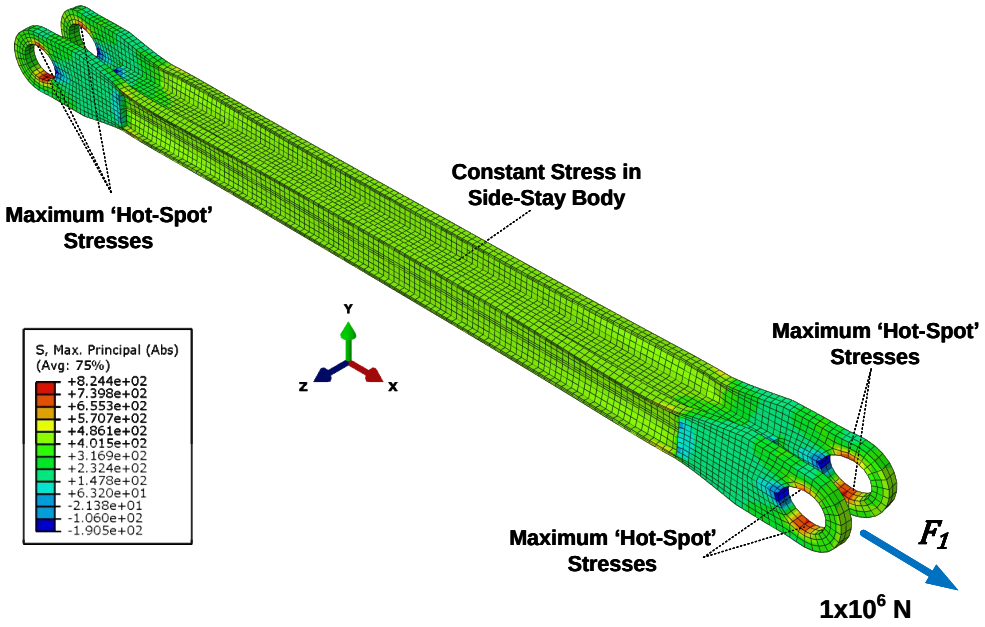

FIGURE 7.10. Hot-spot stresses as a result of tensile loading of the lower side-stay component computed using linear elastic FEA.

In order to verify the mesh density and validate the lower side-stay FEA model, the stress concentration K_t at the loaded lugs was compared to classical estimates for K_t values of round lugs filled with pins from Schijve and Peterson [6, 261]. The K_t from the FEA model was computed by comparing the loaded lug hot-spot stress to a nominal stress value away from the lug under tensile loading as shown in Figure 7.11. The analytical and FEA K_t values are shown in Table 7.2. As can be seen from Table 7.2, there is good agreement between the analytical and FEA-derived K_t values, therefore validating the FEA model. The corresponding mesh density resulted in the lower side-stay comprising of 18,151 C3D8R brick elements, requiring a CPU run-time of 20 seconds[2] to generate σ stress values (using maximum principal stress for the multi-axial stress correction [255]) for a single F_1 axial load[3]. A stress concentration of $K_t = 1.5$ was also applied to the lower side-stay to account for surface finishes applied to the component [27].

TABLE 7.2. Stress concentration factor estimates for the lower side-stay lugs.

Method	K_t
Schijve [6]	2.70
Peterson [261]	2.65
FEA model	2.79

[2]Computer Specifications: 4-core processor (3.40 GHz) with 16.0 GB RAM.

[3]Reduced integration elements can provide inaccurate modelling of stress concentrations as the stress value is provided at the centre of the element, rather than on the element surface. However, Table 7.2 shows that good agreement was achieved between the C3D8R elements and analytically derived K_t values.

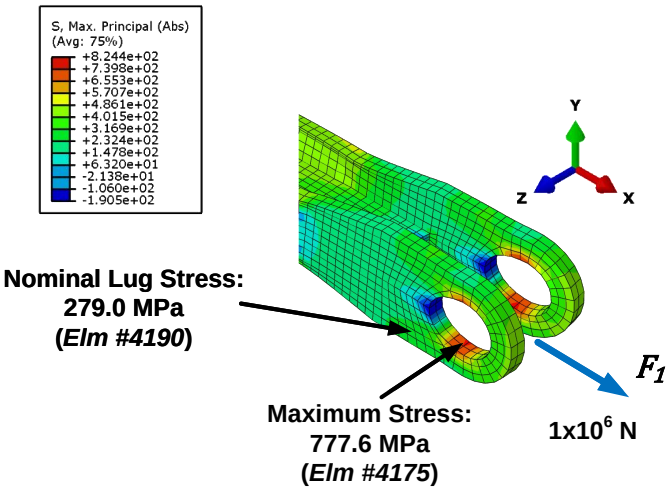

FIGURE 7.11. Lug K_t based upon the lower side-stay component FEA model.

7.2.3 Feature Down-Selection

Based upon the feature down-selection process defined in Section 7.1.2, features of the lower side-stay component were first identified considering all stress-raising features of the component (e.g. lugs, sectional/thickness changes, etc). Hot-spot stress locations were also identified through applying maximum tensile and compressive F_1 loads to the lower side-stay. Figures 7.12 and 7.13 highlight the stress-raising and hot-spot stress locations of the lower side-stay under tensile and compressive loading respectively. The feature down-selection process resulted in each of the following features:

1. a) top, b) bottom, c) body edge and d) free edge locations on all lugs[4].
2. The lug exterior in-line with the F_1 loading at all lugs.
3. The side-stay body in the H-section.
4. Both ends of the horizontal flange.
5. The centre of the thickness increase for the lugs.
6. The web locations where the thickness change occurs between the lugs and side-stay H-section.

[4] i.e. when viewing the lower side-stay from the side, the 12, 6, 9 and 3 o'clock positions on the lug. Under axial tension/compression these were identified to be the locations of maximum and minimum stresses.

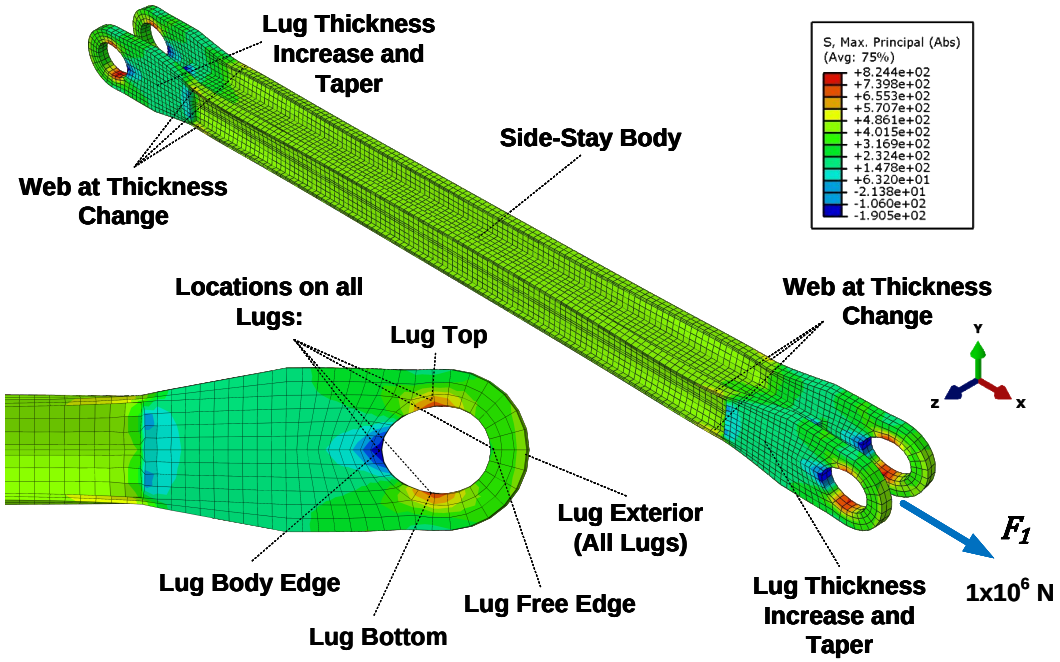

FIGURE 7.12. Selected features from the lower side-stay component due to tensile loading.

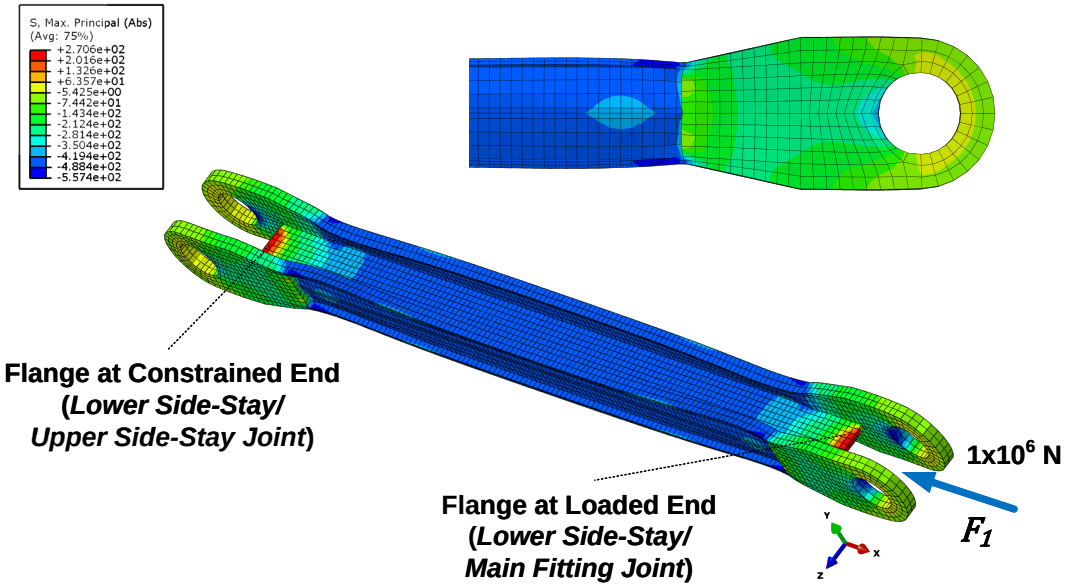

FIGURE 7.13. Selected features from the lower side-stay component due to compressive loading.

Each of the pins also had two features, in-line with the lug interface at the location of maximum shear. Due to the symmetry of the lower side-stay and of the pins, not every feature had to be retained within the feature down-selection process. For example, the stresses at the bottom of the left and right lugs that are loaded by the smooth pin will be the same in both lugs. As a result, only a single lug needs to be analysed, and the probabilistic results can be used to estimate p_f values for both of the lugs. This is the case for all lug features, web thickness changes and the two maximum shear locations in the pins. Figure 7.14 shows the symmetry in stress values across the lower side-stay component. The feature down-selection process ultimately resulted in 19 features being assessed by the probabilistic fatigue methodology, each requiring the generation of an individual stress-time history, rainflow counting results and statistically generated S-N curve for every MCS iteration.

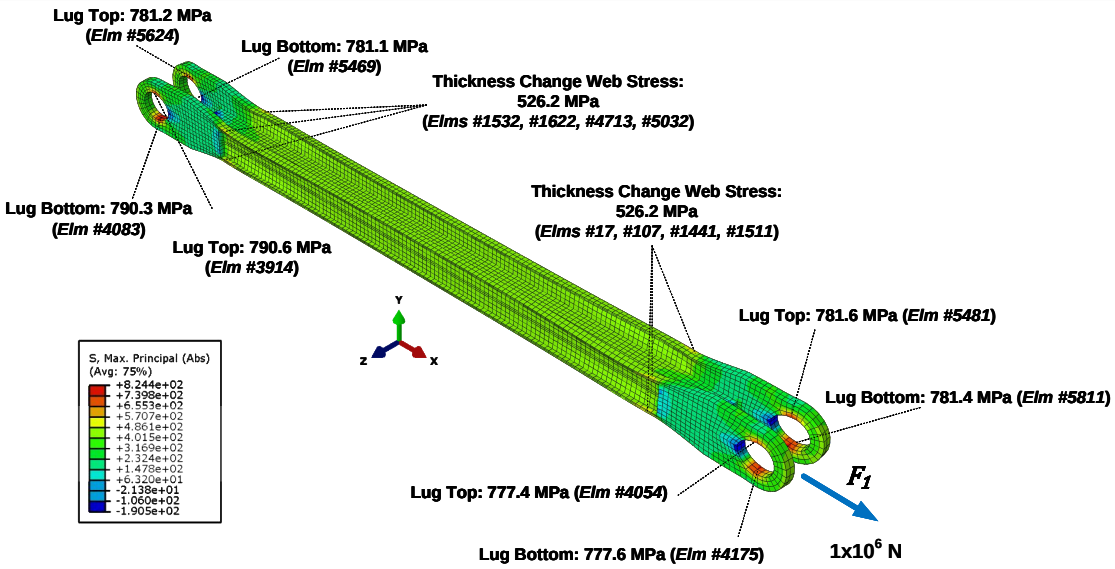

FIGURE 7.14. A visualisation of the symmetric stresses across the lower side-stay component.

Concerning the lower side-stay linear elastic FEA model, the 20 second CPU run-time for each stress evaluation resulted in a prohibitive computational cost. As a result, a surrogate model for the lower side-stay FEA model was required to predict the stress at each feature for a given F_1 loading. An initial investigation into the stress response at each feature (based upon the surrogate modelling process shown in Figure 6.18) highlighted that due to the use of linear elastic stress analysis and the component loading only being a result of F_1, that a bi-linear stress response about the unloaded state was observed with respect to F_1. As a result, the bi-linear relationships shown in Figure 7.15 could be used to predict feature stress values within the probabilistic fatigue methodology, without having to evaluate the original lower side-stay FEA model for every applied F_1 in the load-time history. This approach is similar to the linear superposition approach

proposed by Halfpenny et al [61]. For the side-stay pins, the classical stress analysis defined in Equations 7.1 to 7.3 was directly performed due to the negligible computational expense compared to lower side-stay FEA model.

Figure 7.16 demonstrates how the linear static FEA MLG beam model surrogate model and the lower side-stay stress bi-linear relationships were used to convert a global load-time history into stress-time histories for the down-selected features of the lower side-stay assembly.

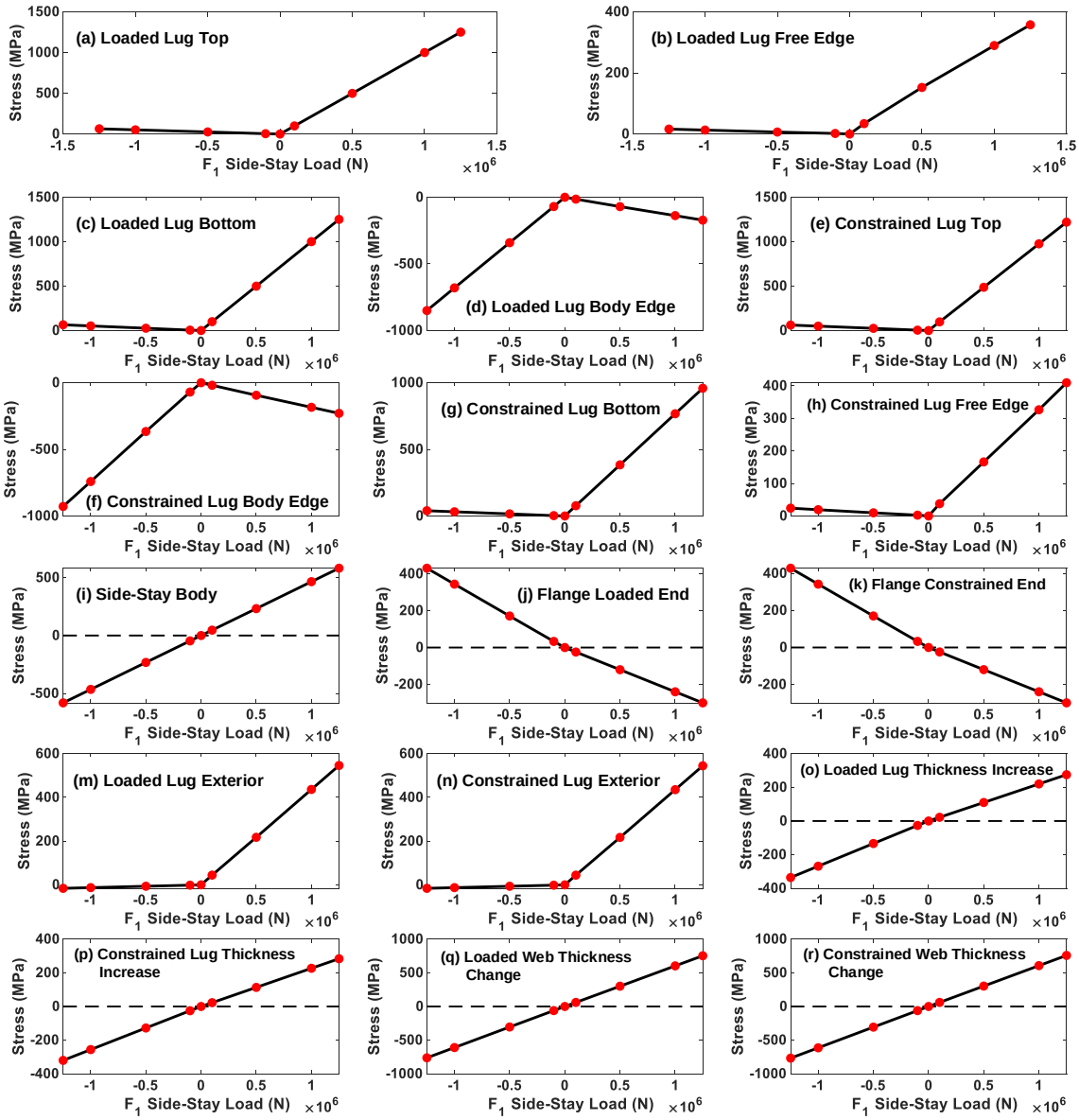

FIGURE 7.15. The bi-linear stress responses for the lower side-stay component features, generated from the linear elastic FEA stress model.

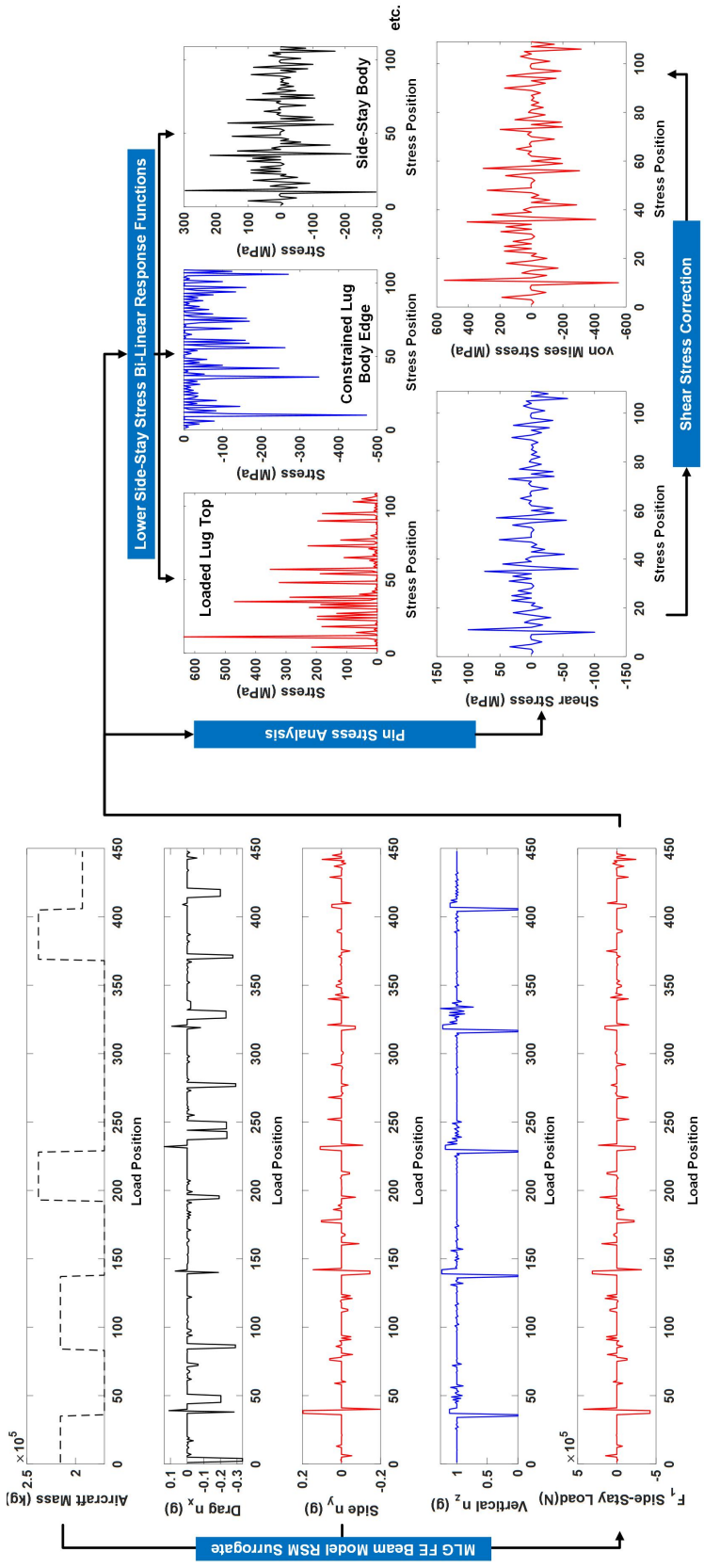

FIGURE 7.16. Conversion of the global load-time history to stress-time histories at lower side-stay component features (*note: figure only shows a segement of five flights out of a statistically simulated 50,000 flight design life*).

It is important to note in Figure 7.16 that the definition of the x-axis unit of 'load position' is as described in Section 5.10.4. As rainflow counting does not account for the actual time (e.g. seconds) between loads, once the load sequence has been converted into a stress sequence using the bi-linear relationships shown in Figure 7.15, only the sequence of stress values is required. Therefore, the x-axes of the stress sequences shown Figure 7.16 refer to the 'stress position' which is the integer value that identifies the order in which each stress value occurs in the sequence. Again, such a sequence is commonly referred to as a 'stress-time history', but it is important to clarify that no time-based effects are accounted for during S-N fatigue analysis. In addition, it is important to note that the stress sequence is pre-processed prior to rainflow counting to remove any stresses that remain at a constant value for more than one step in the stress sequence. Therefore, the stress position number is not guaranteed to be the same as the load position number that results in the stress.

7.2.4 Design Parameter Statistical Characterisation

The variability present within the design parameters of the lower side-stay assembly concern variability within the loading applied to the side-stay assembly, the material properties of the down-selected features and the dimensional parameters of the lower side-stay pins.

As all components within the side-stay assembly are loaded by F_1 axial loads, the statistical characterisation of loading variability was the same for all components within the lower side-stay assembly. Loading variability was represented in the lower side-stay case study using the statistical simulation of global load-time histories as described in Chapter 5. As a result, loading variability was accounted for considering the variability in ground manoeuvre occurrence and sequencing, as well as the variability in the load factor magnitude for each ground manoeuvre and the aircraft mass at pre-takeoff and post-landing taxi phases.

Regarding material property variability, as all components were manufactured from 4340 high-tensile strength steel, the process of statistically generating S-N curves, as demonstrated in Chapter 4, was used to account for variability in S-N datasets. It was assumed that the variability for N_f in the S-N dataset was characterised using the 2P Log-Normal distribution and the σ_{FL} was statistically characterised using a Normal distribution with a mean value of 457 MPa and a standard deviation of 13 MPa [25]. The σ_{UTS} of the high-tensile strength steel was characterised as a Normal distribution with a mean of 1,200 MPa with $c_v = 0.0122$ [29, 262].

The variability in the dimensional parameters of the lower side-stay pins were all characterised using Normal distributions, based on the variability observed for typical manufacturing processes described by Haugen [31]. The variability in the OR and IR parameters of the pins was characterised as a Normal distribution with the mean dimensional values shown previously in Figure 7.6, with $c_v = 0.003$ [31]. The variability in groove dimensions from machining of the fuse pins resulted in the use of Normal distributions, with the mean dimensions shown in Figure 7.6b and a standard deviation of 0.0423 mm [31]. Due to the complexity of incorporating dimensional

changes within the FEA stress model of the lower side-stay component, dimensional variability was not accounted for regarding the lower side-stay component.

7.2.5 Implementation of Probabilistic Fatigue Methodology

The purpose of this section is to briefly demonstrate how the probabilistic fatigue methodology detailed across Chapters 2 and 3 was implemented specifically for the lower side-stay case study. The flowchart of the proposed probabilistic fatigue methodology shown previously in Figure 3.4 in Chapter 3 has been updated in Figure 7.17.

Figure 7.17 highlights how the RSM surrogate model of the linear static FEA MLG beam model is utilised to convert n_y side load factors into F_1 side-stay loads. Figure 7.17 also demonstrates how classical stress analysis for the lower side-stay pins and the bi-linear stress response surrogate models for the lower side-stay component are employed to generate a stress-time history for each down-selected feature. This ultimately results in 19 'channels' of stress-time history, which each must be individually processed using rainflow counting, prior to computing the D_T accumulated damage in each feature at the design safe-life of 50,000 flights. It is important to note that for each MCS iteration, a different S-N curve is statistically generated for each feature (i.e. 19 independent S-N curves are statistically generated during each MCS iteration).

The process visualised in Figure 7.17 is repeated for each MCS iteration, each time storing the D_T accumulated damage values. As described in Chapter 3, statistical characterisation methods are then used to compute p_f estimates for each of the 19 down-selected features.

As justified in Section 7.1.1, $N_{MCS} = 1 \times 10^5$ MCS iterations were performed within the probabilistic fatigue methodology for the lower side-stay case study. Parallel processing across a 4-core processor was used to reduce the computational expense of the probabilistic fatigue methodology, through performing four MCS iterations simultaneously. Through using parallel processing, the CPU run-time to perform $N_{MCS} = 1 \times 10^5$ MCS iterations required 4 days, resulting in each MCS iteration requiring approximately 3.5 seconds[5].

[5]Computer Specifications: 4-core processor (3.40 GHz) with 16.0 GB RAM.

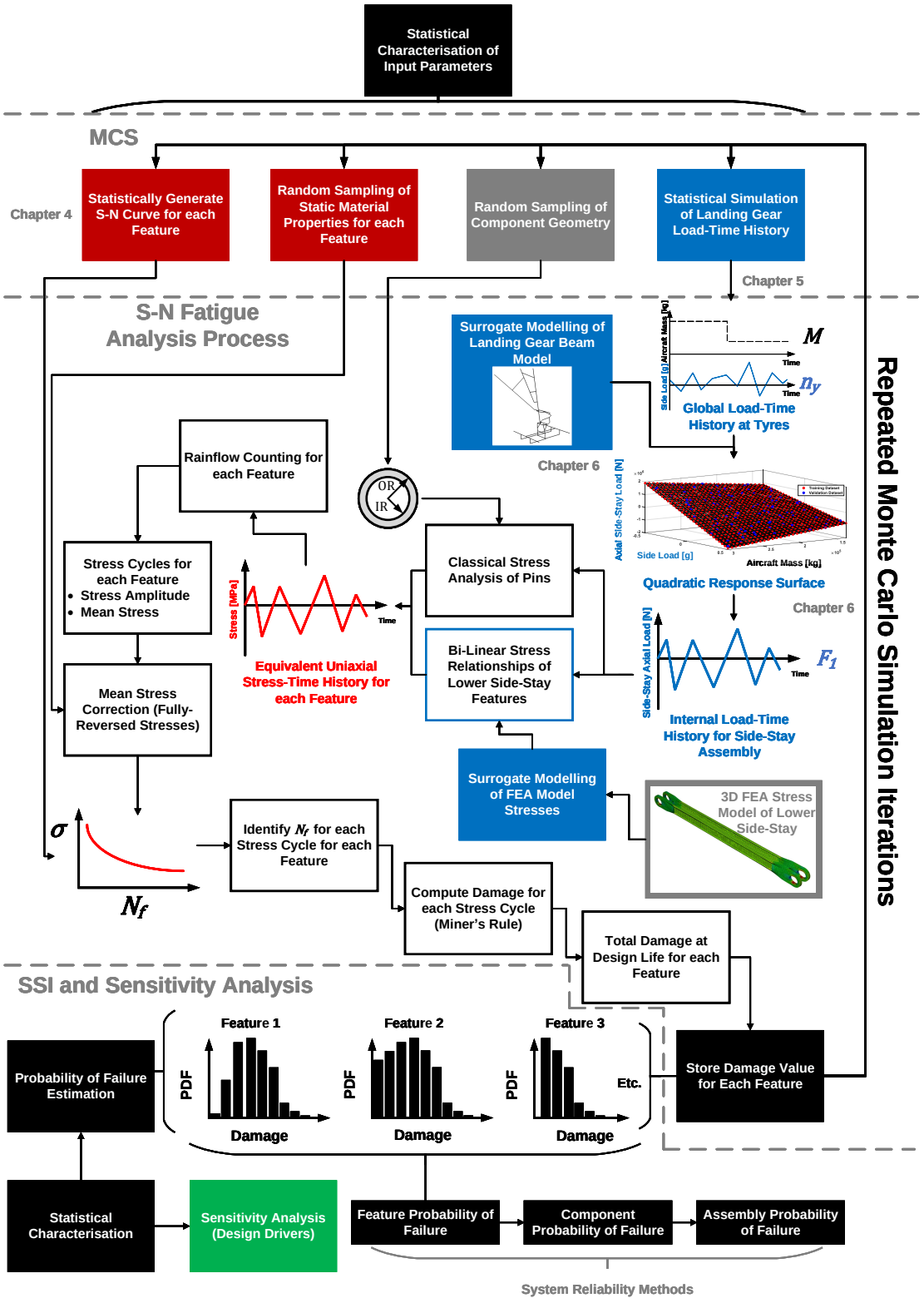

FIGURE 7.17. Flowchart demonstrating the implementation of the probabilistic fatigue methodology to the lower side-stay case study.

7.2.6 Probabilistic Results

The implementation of the probabilistic fatigue methodology enabled the computation of p_f estimates for the various features of the lower side-stay assembly. This subsection presents the results of the probabilistic fatigue methodology for the lower side-stay assembly.

Lower Side-Stay Pins

Following the $N_{MCS} = 1 \times 10^5$ MCS iterations, the D_T accumulated damage values were collected for both the smooth pin and fuse pin maximum shear location features. Figures 7.18a and 7.18b show the D_T histograms for the smooth pin and fuse pin respectively. The histograms have been normalised such that the area under the histogram is equal 1, to enable a direct visual comparison with the fitted candidate distributions (see Appendix B). All D_T histograms throughout the remainder of this thesis show the maximum observed D_T value as the maximum limit of the D_T x-axis.

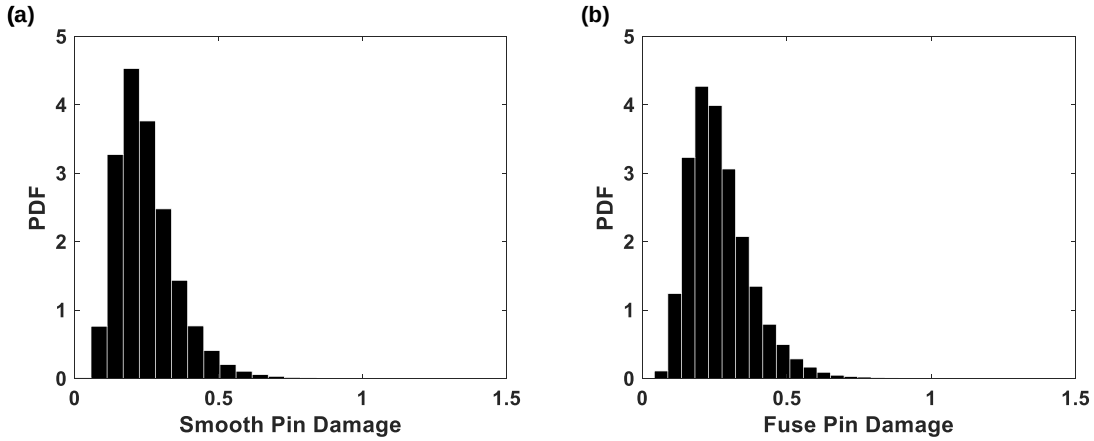

FIGURE 7.18. D_T histograms for the lower side-stay (a) smooth and (b) fuse pin maximum shear locations at a design safe-life of 50,000 flights.

It can be observed from Figure 7.18 that both the smooth pin and fuse pin maximum shear location D_T values demonstrate positive skew with similar magnitudes of D_T at the 50,000 flight design safe-life. The systematic statistical characterisation process detailed in Chapter 4 was employed to statistically characterise the variability in the D_T values, considering candidate distributions capable of showing positive support and positive skew: 2P Log-Normal, 3P Log-Normal, 2P Weibull, 3P Weibull, Gumbel Maximum and Log-Logistic (All distributions types are defined in Appendix B). It is important to note that due to the large sample size resulting from the MCS, the alternative systematic statistical characterisation process shown previously in Figure 4.1 must be employed (i.e. using r and $RMSE$ for GoF testing as described in Steps A, B and C in Section 4.2.2).

Table 7.3 shows the PPLR and MLE distribution parameter estimates for the candidate distributions of the variability in D_T for the smooth pin maximum shear location. The 3P Log-Normal distribution estimated a negative threshold δ value for D_T, inferring negative damage accumulation, which is not physically representative of fatigue as a failure mode. Therefore, the 3P Log-Normal distribution was rejected due to failing to represent the correct support.

TABLE 7.3. Statistical characterisation of the variability in D_T for the smooth pin maximum shear location.

Distribution	Fitting Type	Distribution Parameter Estimate			Skewness	$\gamma = 1.284$	
	(*Rank Equation*)	Threshold δ	Scale σ	Shape λ	Good CDF Fit?	$RMSE$	r
2P Log-Normal	PPLR (*Gumbel*)	-	-1.480	0.409	Y	0.003	**0.9999**
	MLE	-	-1.480	0.409	Y	0.003	-
3P Log-Normal	PPLR predicts zero threshold. 2P Log-Normal distribution fitted. MLE predicts negative threshold. Reject distribution.						
2P Weibull	PPLR (*Mean*)	-	0.275	3.050	N	0.041	0.9731
	MLE	-	0.279	2.475	N	0.039	-
3P Weibull	PPLR (*Hazen*)	0.040	0.231	2.449	N	0.028	0.9892
	MLE	0.040	0.234	2.102	N	0.028	-
Gumbel Max	PPLR (*EV*)	-	0.081	0.200	Y	0.005	0.9996
	MLE	-	0.079	0.201	Y	0.006	-
Log-Logistic	PPLR (*Mean*)	-	-1.480	0.227	N	0.015	0.9961
	MLE	-	-1.478	0.234	N	0.010	-

When comparing the fitted CDFs to the ECDF of the smooth pin maximum shear location D_T values, it was observed that only the 2P Log-Normal and Gumbel Maximum distributions provided an acceptable visual fit to the ECDF, as highlighted by the *Good CDF Fit?* column in Table 7.3. It can also be observed from Table 7.3 that the $RMSE$ values are significantly smaller for the 2P Log-Normal distribution and Gumbel Maximum when compared to the other candidate distributions, supporting the rejection of the other candidate distributions.

Considering the r correlation coefficient from the PPLR distribution parameter estimation process, it can be seen from Table 7.3 that the 2P Log-Normal distribution provided the best-fit to the variability in the smooth pin maximum shear location D_T values. As a result, the statistical characterisation values shown in Table 7.3 suggest that the 2P Log-Normal distribution provides the best-fit to the D_T damage values at the smooth pin maximum shear location. Table 7.3 also shows that there is a negligible percentage difference between the distribution parameter estimates for the 2P Log-Normal distribution from PPLR and MLE, therefore validating the distribution parameter estimates of the statistical characterisation of the smooth pin maximum shear location D_T values.

The fitted 2P Log-Normal distribution for the smooth pin maximum shear location D_T values is shown in Figure 7.19. It can be seen from Figure 7.19 that the 2P Log-Normal distribution provides an acceptable visual fit to both the histogram and ECDF of D_T values.

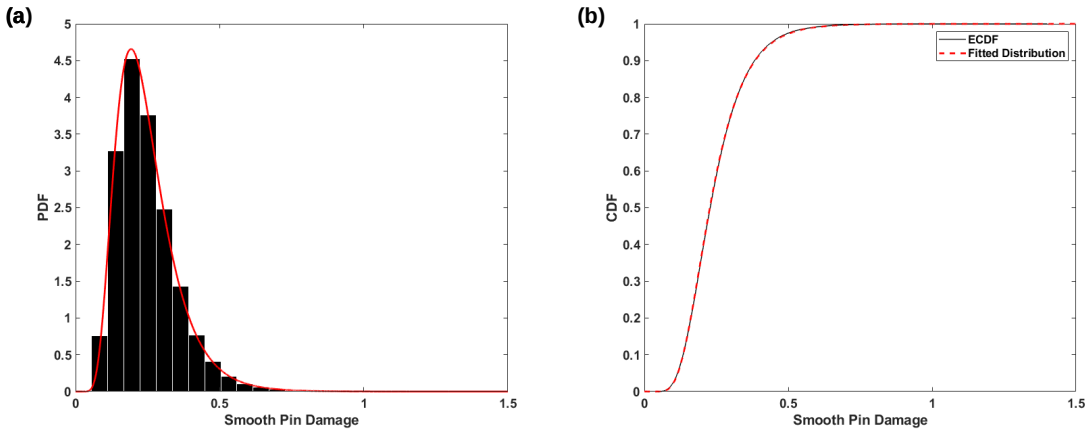

FIGURE 7.19. Fitted 2P Log-Normal distribution to smooth pin maximum shear location D_T damage variability compared to (a) the D_T histogram and (b) the ECDF.

The statistical characterisation process was repeated for the D_T values at the maximum shear location of the fuse pin, shown previously as a histogram in Figure 7.18b. Table 7.4 shows the resulting distribution parameter estimates and $RMSE$ values. Table 7.4 shows that both the 2P Log-Normal distribution and Gumbel Maximum distribution also provided acceptable fits to the variability in the fuse pin maximum shear location D_T values.

TABLE 7.4. Statistical characterisation of the variability in D_T for the fuse pin maximum shear location.

Distribution	Fitting Type (*Rank Equation*)	Distribution Parameter Estimate			Skewness	$\gamma = 1.157$	
		Threshold δ	Scale σ	Shape λ	Good CDF Fit?	$RMSE$	r
2P Log-Normal	PPLR (*Mean*)	-	-1.400	0.396	Y	0.003	**0.9998**
	MLE	-	-1.400	0.396	Y	0.003	-
3P Log-Normal	PPLR predicts zero threshold. 2P Log-Normal distribution fitted. MLE predicts negative threshold. Reject distribution.						
2P Weibull	PPLR (*Mean*)	-	0.296	3.153	N	0.041	0.9736
	MLE	-	0.300	2.579	N	0.038	-
3P Weibull	PPLR (*Hazen*)	0.044	0.249	2.527	N	0.030	0.9890
	MLE	0.044	0.252	2.177	N	0.028	-
Gumbel Max	PPLR (*Mean*)	-	0.084	0.218	Y	0.003	**0.9999**
	MLE	-	0.083	0.218	Y	0.005	-
Log-Logistic	PPLR (*Mean*)	-	-1.399	0.219	N	0.015	0.9956
	MLE	-	-1.397	0.226	N	0.010	-

It should be observed from Table 7.4 that the Gumbel Maximum distribution provides the largest r value from PPLR and the 2P Log-Normal distribution provides the lowest RMSE values. Therefore, in order to down-select the final distribution type for the fuse pin maximum shear location D_T values, $P_{f_{dist}}$ (see Equation 3.1 in Chapter 3) values were computed for both candidate distributions at $D_{fail} = 1$. For the Gumbel Maximum distribution, $P_{f_{dist}} = 8.038 \times 10^{-5}$, whilst for the 2P Log-Normal distribution $P_{f_{dist}} = 2.048 \times 10^{-4}$, a difference of 60%.

The large difference between the two $P_{f_{dist}}$ estimates is as a result of 'tail-sensitivity', whereby $P_{f_{dist}}$ estimates are highly sensitive to the selected probability distribution type, especially when the selected failure criterion lies in the tail of the distributions. Figure 7.20 demonstrates the tail-sensitivity of the $P_{f_{dist}}$ estimates for the fuse pin maximum shear location D_T values. As the 2P Log-Normal distribution provided the most conservative $P_{f_{dist}}$ value, it was selected as the final distribution to characterise the variability in D_T values for the fuse pin maximum shear location as shown in Figure 7.21. Figure 7.21 shows that the 2P Log-Normal distribution provides a good visual fit to the histogram and ECDF of the fuse pin maximum shear location D_T values.

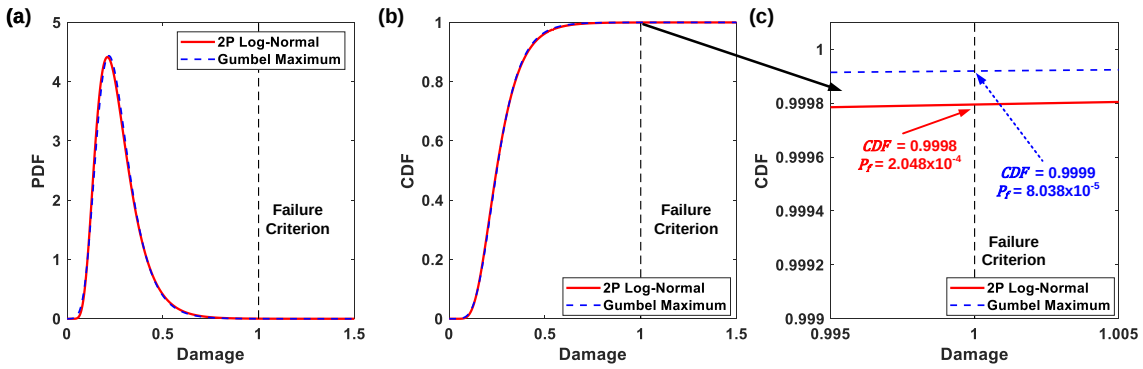

FIGURE 7.20. A demonstration of tail-sensitivity for the fuse pin maximum shear location D_T values, from comparing (a) PDFs, (b) CDFs and (c) the change in $P_{f_{dist}}$ values.

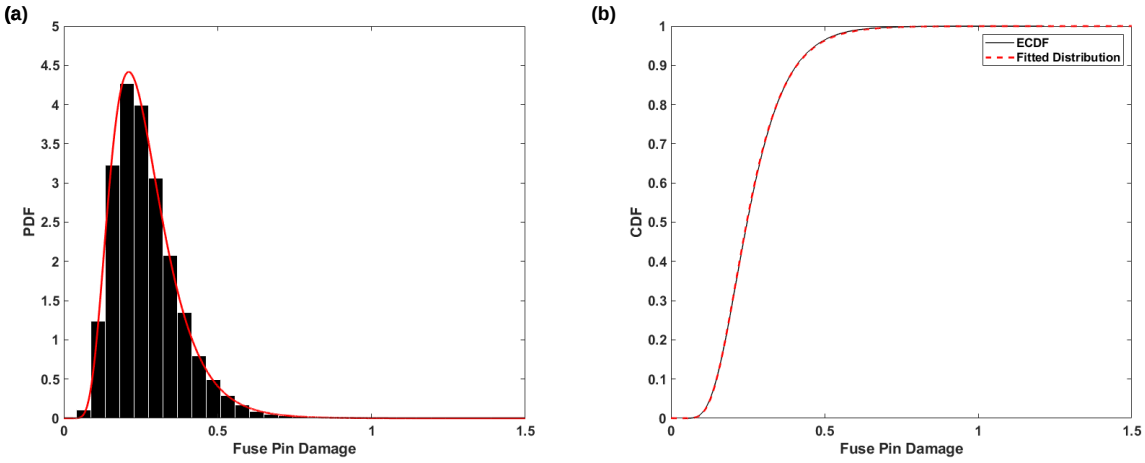

FIGURE 7.21. Fitted 2P Log-Normal distribution to fuse pin maximum shear location D_T damage variability compared to (a) the D_T histogram and (b) the ECDF.

Consistent with the probabilistic fatigue methodology defined in Chapter 3, GPD tail-fitting was also performed based on the upper tails of the D_T histograms shown in Figure 7.18, assuming a tail dataset of $N_t = 474$ (based on the $1.5\sqrt{N_{MCS}}$ criterion [159, 160]). Table 7.5 shows the MLE GPD distribution parameter estimates for the pin maximum shear location D_T values.

TABLE 7.5. GPD distribution parameters for the D_T values of the smooth and fuse pin maximum shear locations of the lower side-stay assembly.

Feature	GPD Parameters		
	Threshold t	Shape λ	Scale σ
Smooth Pin Max Shear	0.647	0.036	0.088
Fuse Pin Max Shear	0.667	-0.042	0.088

The D_T values from the MCS iterations were also inspected to identify the number of N_{fail} 'failure' iterations (i.e. $D_T \geq 1$) for both the smooth and fuse pin maximum shear locations. Table 7.6 show the number of failure observations observed for the pin features after $N_{MCS} = 1 \times 10^5$ MCS iterations.

TABLE 7.6. Number of failure MCS iterations observed for the smooth and fuse pin maximum shear locations from $N_{MCS} = 1 \times 10^5$ MCS iterations.

Feature	N_{fail}
Smooth Pin Max Shear	12
Fuse Pin Max Shear	8

Following the statistical characterisation of the pin maximum shear location D_T values, the p_f estimates could be generated using the methods described in Chapter 3. Table 7.7 shows the p_f estimates for the maximum shear locations of both the smooth and fuse pin.

TABLE 7.7. The p_f estimates for the maximum shear locations on the smooth and fuse pin of the lower side-stay assembly.

Feature	p_f estimation method				
	$P_{f_{dist}}$	$P_{f_{dist}}$ 95% CI	$P_{f_{tail}}$	$P_{f_{MCS}}$	$P_{f_{MCS+2\sigma}}$
Smooth Pin Max Shear	1.485×10^{-4}	1.586×10^{-4}	1.131×10^{-4}	1.200×10^{-4}	1.893×10^{-4}
Fuse Pin Max Shear	2.048×10^{-4}	2.181×10^{-4}	7.697×10^{-5}	8.000×10^{-5}	1.366×10^{-4}

Concerning the smooth pin maximum shear location, it can be observed that the $P_{f_{dist}}$ estimate is larger than both the $P_{f_{tail}}$ and $P_{f_{MCS}}$ estimates. When accounting for statistical uncertainty in p_f estimates, Table 7.7 demonstrates that the 95% confidence interval (CI) value for $P_{f_{dist}}$ is closer to the $P_{f_{dist}}$ value ($\approx 7\%$ increase) compared to the $+2\sigma$ $P_{f_{MCS}}$ value, which is an $\approx 58\%$ increase of the $P_{f_{MCS}}$ value.

Regarding the fuse pin maximum shear location, Table 7.7 again demonstrates that the $P_{f_{dist}}$ estimate is more conservative than the p_f estimates generated using $P_{f_{tail}}$ and $P_{f_{MCS}}$. It is important to highlight that the $P_{f_{MCS}}$ for the fuse pin is significantly lower than the $P_{f_{MCS}}$ for

the smooth pin as shown in Table 7.7. This observation is in contradiction to the $P_{f_{dist}}$ estimates, which suggest that the fuse pin maximum shear location should have a higher p_f than the smooth pin. A higher p_f should also be expected due to the pin geometry and presence of the fuse groove K_t in the fuse pin, which would result in higher stress values and D_T values in otherwise identically loaded pins.

Figure 7.22 shows the superimposition of the original D_T histograms for the smooth and fuse pin maximum shear locations. It can be observed from Figure 7.22 that the fuse pin maximum shear location D_T histogram demonstrates a higher mean value and a heavier right-hand tail, suggesting that a higher p_f would be expected for the fuse pin maximum shear location compared to the smooth pin maximum shear location. These observations suggest that in this instance, $P_{f_{MCS}}$ estimates cannot be used as a reliable estimate for the pin p_f values. As the $P_{f_{tail}}$ estimates are consistent with the $P_{f_{MCS}}$ estimates in Table 7.7, it can also be suggested that the $P_{f_{tail}}$ estimates cannot be reliably used to generate p_f estimates for the smooth and fuse pin.

The histograms in Figure 7.22 also provide support for selecting the 2P Log-Normal distribution over the Gumbel Maximum distribution to characterise the variability in the fuse pin maximum shear location D_T values. The use of a Gumbel Maximum distribution would have resulted in the fuse pin maximum shear location having a lower $P_{f_{dist}}$ estimate than the smooth pin maximum shear location, which again contradicts the histograms shown in Figure 7.22.

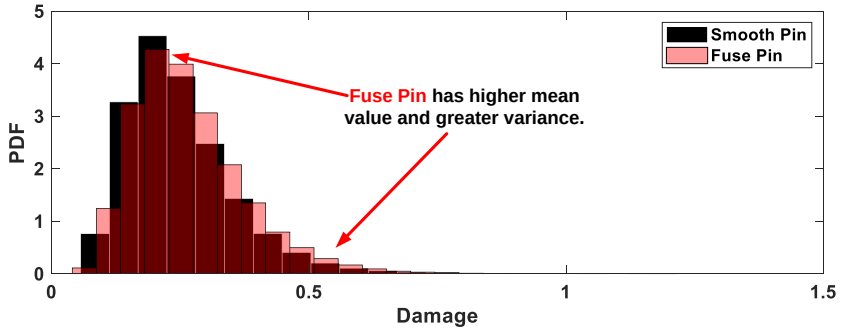

FIGURE 7.22. A comparison of the D_T histograms for the smooth and fuse pins maximum shear locations.

Component-level p_f estimates can be generated for the pins in the lower side-stay assembly using Equation 3.6 in Chapter 3. As there are two maximum shear planes in each pin, and as the damage accumulation is assumed to be independent at each shear plane (as the material properties and dimensional variability are assumed to be statistically independent across the features), the component-level p_f estimates are simply twice the p_f estimates shown in Table 7.7. Table 7.8 shows the component-level p_f estimates for the smooth and fuse pins.

TABLE 7.8. The component-level p_f estimates for the smooth and fuse pin of the lower side-stay assembly.

Component	Component-level p_f Estimation Method				
	$P_{f_{dist}}$	$P_{f_{dist}}$ 95% CI	$P_{f_{tail}}$	$P_{f_{MCS}}$	$P_{f_{MCS+2\sigma}}$
Smooth Pin	2.971×10^{-4}	3.721×10^{-4}	2.261×10^{-4}	2.400×10^{-4}	3.786×10^{-4}
Components per Failure	3,366	3,152	4,421	4,166	2,641
Fuse Pin	4.095×10^{-4}	4.361×10^{-4}	1.539×10^{-5}	1.600×10^{-4}	2.731×10^{-4}
Components per Failure	2,441	2,292	6,496	6,250	3,661

Table 7.8 also shows the 'components per failure', which is simply the inverse of the p_f estimate (i.e. a value of 3,000 represents that, on average, 1 in 3,000 components would be expected to fail by the design safe-life). A typical global fleet size (i.e. all of the aircraft of a given type produced) for a civil wide-body aircraft is between 1,000 and 2,000 aircraft [263]. This suggests that the components per failure values in Table 7.8 demonstrate that less than one pin would be expected to fail in the global fleet of aircraft.

Finally, it can be seen from Table 7.8 that the same observations regarding the maximum shear location p_f estimates in Table 7.7 are applicable to the component-level p_f estimates. Again, when not accounting for statistical uncertainty in p_f estimates, the $P_{f_{dist}}$ estimates provide the most conservative p_f estimates for both the smooth and fuse pins.

Lower Side-Stay Component

Following the $N_{MCS} = 1 \times 10^5$ MCS iterations, the histograms of the D_T accumulated damage values were constructed for each of the features of the lower side-stay component as down-selected in Section 7.2.3. The resulting D_T histograms are shown overleaf in Figure 7.23 and are also shown in relation to their location on the lower side-stay component in Figure 7.24.

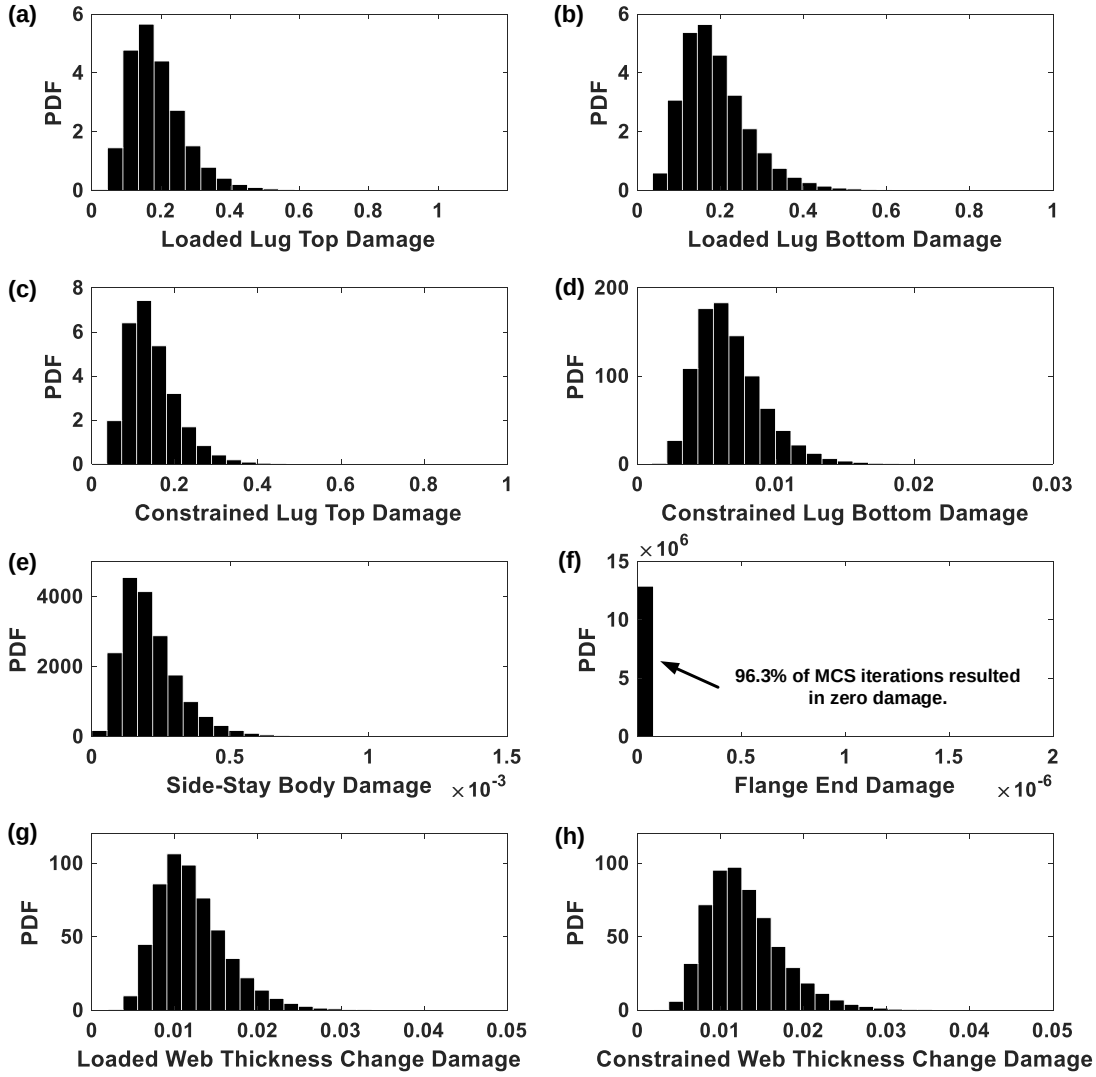

FIGURE 7.23. Histograms of the D_T variability at the lower side-stay component features.

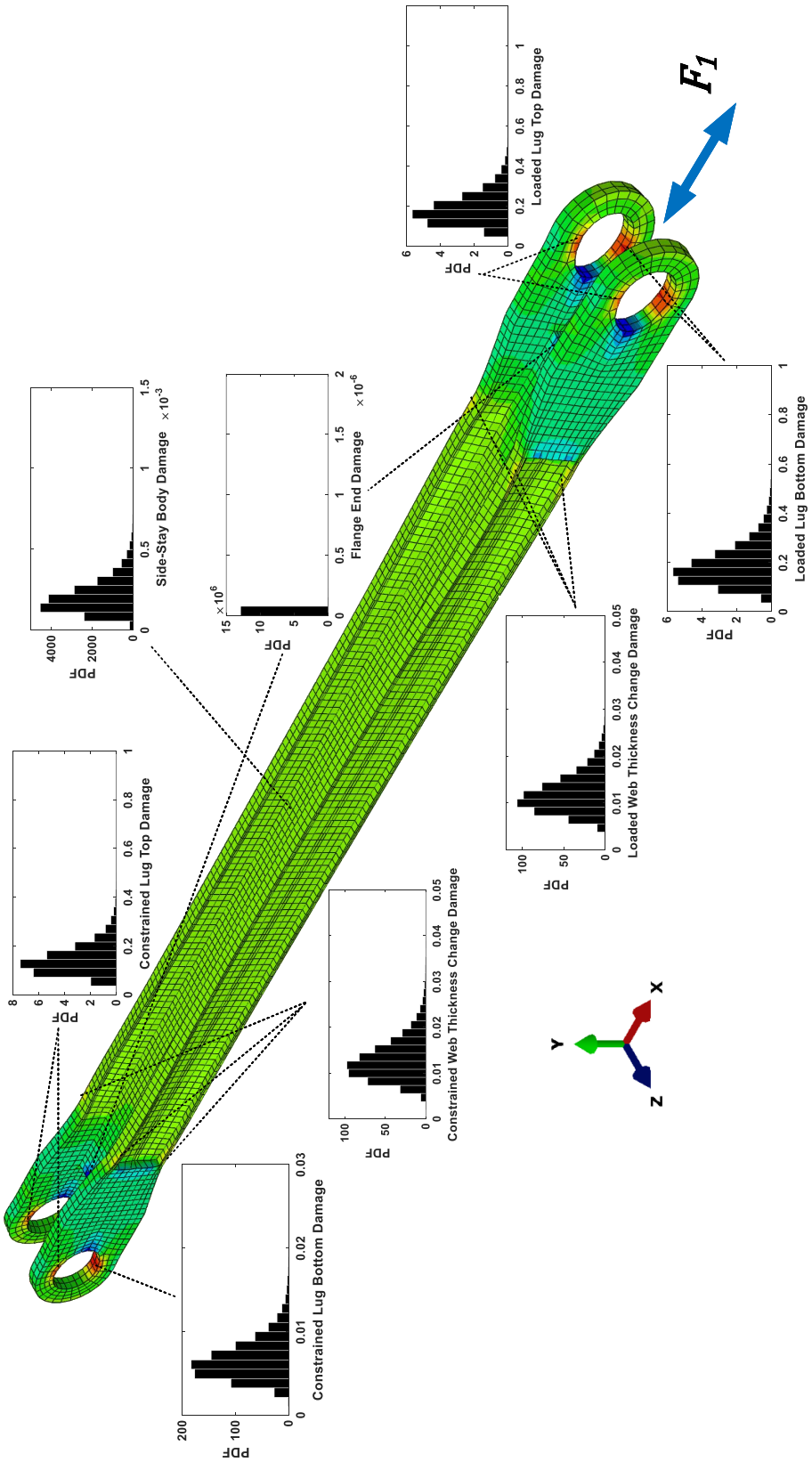

FIGURE 7.24. Location of the D_T variability at the lower side-stay component features.

It can be observed from Figure 7.23 that the majority of features demonstrate a positive skew and that the order of magnitude of the D_T damage values varies significantly across the features, from 10^{-1} at the lugs to 10^{-3} at the side-stay body. Of note is Figure 7.23f, which is representative of the damage D_T at either end of the horizontal flange, in which it can be seen that the majority of MCS iterations resulted in zero fatigue damage being accumulated (i.e. all of the applied stress amplitudes were below the σ_{FL} of the statistically generated S-N curves). In addition, any damage that was accumulated by the horizontal flange ends was in the order of 10^{-6} and as a result, it was assumed that the horizontal flange end features did not contribute to the p_f of the lower side-stay component.

Table 7.9 shows the maximum D_T damage values observed for each feature across the $N_{MCS} = 1 \times 10^5$ MCS iterations. The wide range in the order of magnitude of the damage values across the features is highlighted by Table 7.9, and it can also be seen that the lug free edges, lug body edges and lug exteriors failed to accumulate any fatigue damage across the $N_{MCS} = 1 \times 10^5$ MCS iterations.

TABLE 7.9. Maximum D_T damage values observed for the lower side-stay component over $N_{MCS} = 1 \times 10^5$ MCS iterations.

Feature	Maximum D_T Value Observed
Loaded Lug Top	1.121
Loaded Lug Free Edge	0
Loaded Lug Bottom	0.885
Loaded Lug Body Edge	0
Constrained Lug Top	0.890
Constrained Lug Free Edge	0
Constrained Lug Bottom	0.029
Constrained Lug Body Edge	0
Side-Stay Body	1.361×10^{-3}
Loaded Flange Edge	1.921×10^{-6}
Constrained Flange Edge	2.011×10^{-6}
Loaded Lug Exterior	0
Constrained Lug Exterior	0
Loaded Web Thickness Change	0.046
Constrained Web Thickness Change	0.046

The D_T damage histograms for the lower side-stay component features were then statistically characterised using the same approach as used for the lower side-stay pins. As each of the histograms in Figure 7.23 show positive support and skew, 2P Log-Normal, 3P Log-Normal, 2P Weibull, 3P Weibull, Gumbel Maximum and Log-Logistic distributions were considered as candidate distributions to characterise the D_T variability.

Table 7.10 shows the statistical characterisation results of the loaded lug top feature and it can be observed that both the 2P Log-Normal distribution and the Gumbel Maximum distribution provided acceptable visual fits to the histogram and ECDF. As the 2P Log-Normal distribution had the lowest $RMSE$ values and the highest PPLR r correlation coefficient, the 2P Log-Normal

distribution provided the best-fit to the D_T variability at the loaded lug top feature.

The resulting 2P Log-Normal distribution for the D_T values at the loaded lug top feature is shown in Figure 7.25, where the fitted distribution can be seen to provide an acceptable visual fit to both the histogram and ECDF.

TABLE 7.10. Statistical characterisation of the variability in D_T for the loaded lug top feature of the lower side-stay component.

Distribution	Fitting Type (*Rank Equation*)	Distribution Parameter Estimate			Skewness	$\gamma = 1.302$	
		Threshold δ	Scale σ	Shape λ	Good CDF Fit?	$RMSE$	r
2P Log-Normal	PPLR (*Hazen*)	-	-1.762	0.425	Y	0.005	**0.9997**
	MLE	-	-1.762	0.425	Y	0.005	-
3P Log-Normal	PPLR predicts zero threshold. 2P Log-Normal distribution fitted. MLE predicts negative threshold. Reject distribution.						
2P Weibull	PPLR (*Mean*)	-	0.209	2.939	N	0.039	0.9749
	MLE	-	0.212	2.400	N	0.037	-
3P Weibull	PPLR (*EV*)	0.023	0.183	2.493	N	0.030	0.9872
	MLE	0.024	0.186	2.120	N	0.029	-
Gumbel Max	PPLR (*EV*)	-	0.064	0.151	Y	0.005	0.9994
	MLE	-	0.062	0.151	Y	0.006	-
Log-Logistic	PPLR (*Mean*)	-	-1.762	0.235	N	0.015	0.9960
	MLE	-	-1.758	0.243	N	0.010	-

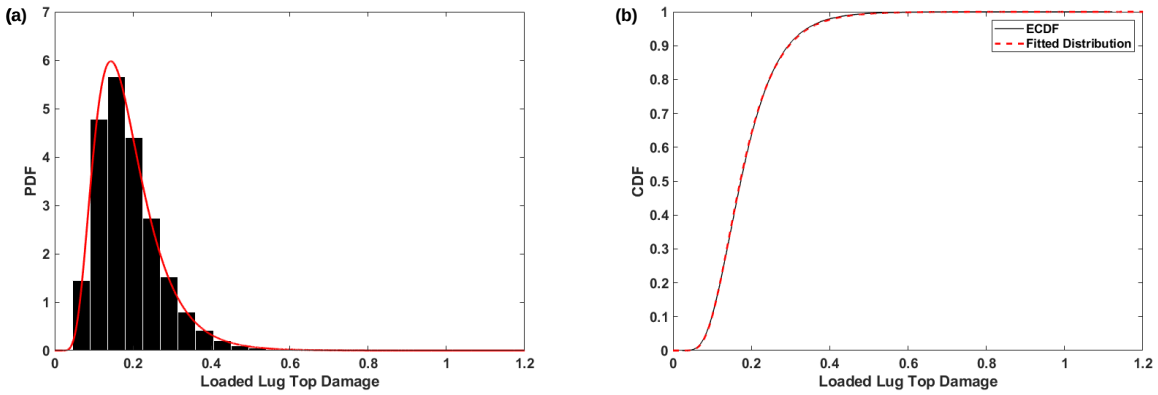

FIGURE 7.25. Fitted 2P Log-Normal distribution to the loaded lug top feature D_T damage variability compared to (a) the D_T histogram and (b) the ECDF.

The remaining features were statistically characterised using the same approach and it was found that the 2P Log-Normal distribution provided the best-fit to the variability in D_T damage values at all of the lower side-stay component features. The full statistical characterisation results are shown in Appendix G and Table 7.11 shows the selected probability distributions. It can be seen from Table 7.11 that the 2P Log-Normal distribution provided the best-fit at all features due to low $RMSE$ values and high r values.

TABLE 7.11. Statistical characterisation of the D_T variability at each feature of the lower side-stay component.

Feature	2P Log-Normal Parameters		$RMSE$	r
	Scale σ	Shape λ		
Loaded Lug Top	-1.762	0.425	0.005	0.9997
Loaded Bottom Lug	-1.753	0.423	0.004	0.9997
Constrained Lug Top	-2.017	0.415	0.004	0.9998
Constrained Lug Bottom	-5.071	0.356	0.001	1
Side-Stay Body	-8.583	0.497	0.006	0.9994
Loaded Web Thickness Change	-4.473	0.345	0.001	1
Constrained Web Thickness Change	-4.407	0.345	0.001	1

Table 7.12 shows the GPD parameter estimates from MLE of the tail datasets extracted from the D_T histograms for each feature, with a tail dataset size $N_t = 474$.

TABLE 7.12. GPD distribution parameters for the D_T values of the lower side-stay component features.

Feature	GPD Parameters		
	Threshold t	Scale σ	Shape λ
Loaded Lug Top	0.501	0.062	0.135
Loaded Lug Bottom	0.503	0.065	0.026
Constrained Lug Top	0.378	0.043	0.132
Constrained Lug Bottom	0.016	0.002	0.041
Side-Stay Body	6.311×10^{-4}	9.611×10^{-5}	0.050
Loaded Web Thickness Change	0.028	0.003	-0.026
Constrained Web Thickness Change	0.030	0.004	-0.126

The MCS damage values were also inspected for each feature to identify the number of 'failure' (i.e. $D_T \geq 1$) iterations. Table 7.13 shows that failure iterations were only observed for the loaded lug top feature within the $N_{MCS} = 1 \times 10^5$ MCS iterations.

TABLE 7.13. Number of failure MCS iterations observed for the lower side-stay component features from $N_{MCS} = 1 \times 10^5$ MCS iterations.

Feature	N_{fail}
Loaded Lug Top	2
Loaded Lug Bottom	0
Constrained Lug Top	0
Constrained Lug Bottom	0
Side-Stay Body	0
Loaded Web Thickness Change	0
Constrained Web Thickness Change	0

The p_f estimates for the lower side-stay component features were computed using the methods shown previously in Chapter 3. The resulting p_f estimates are shown for each feature of the lower side-stay component in Table 7.14. It can be observed from Table 7.14 that the only features that demonstrated a quantifiable p_f for the lower side-stay component were the loaded

lug top, loaded lug bottom and constrained lug top features, as all other features demonstrated a p_f equal to zero for all estimation methods.

TABLE 7.14. The p_f estimates for the lower side-stay component features.

Feature	p_f Estimation Method				
	$P_{f_{dist}}$	$P_{f_{dist}}$ 95% CI	$P_{f_{tail}}$	$P_{f_{MCS}}$	$P_{f_{MCS+2\sigma}}$
Loaded Lug Top	1.717×10^{-5}	1.867×10^{-5}	2.052×10^{-5}	2.000×10^{-5}	4.828×10^{-5}
Loaded Lug Bottom	1.722×10^{-5}	1.872×10^{-5}	4.949×10^{-6}	0	0
Constrained Lug Top	5.954×10^{-7}	6.658×10^{-7}	1.488×10^{-6}	0	0

It can be observed from Table 7.14 that the order of magnitude of the p_f values varies across the component features, from 10^{-5} for the loaded lug features to 10^{-7} for the constrained lug top feature. This variation in p_f values is consistent with the maximum observed damage values shown in Table 7.9, where the most highly damaged values show the greatest p_f values. It can also be observed from Table 7.14 that the order of magnitude of p_f values are significantly lower than the p_f values for the smooth and fuse pins shown previously in Table 7.8. Such a result is also anticipated in the deterministic fatigue analysis of landing gear components, as landing gear pins are typically fatigue critical components which accumulate significantly higher levels of fatigue damage compared to 'bulk' component sections, such as the lower side-stay component [255].

Table 7.14 also shows that there is good agreement in the $P_{f_{dist}}$, $P_{f_{tail}}$ and $P_{f_{MCS}}$ estimates for the loaded top lug feature, therefore providing validation of the $P_{f_{dist}}$ estimate. However, when reviewing the p_f estimates for the loaded lug bottom feature and the constrained lug top feature, the $P_{f_{tail}}$ estimates differ from the $P_{f_{dist}}$ estimates by an order of magnitude, whilst a nil p_f value is estimated using $P_{f_{MCS}}$. Table 7.14 highlights that the $P_{f_{dist}}$ estimates were consistent between the loaded lug top feature and loaded lug bottom feature and therefore, it would be expected that the $P_{f_{tail}}$ and $P_{f_{MCS}}$ estimates would also be consistent between the two features. However, Table 7.14 demonstrates that the $P_{f_{tail}}$ and $P_{f_{MCS}}$ estimates differ significantly between the loaded lug top and loaded lug bottom feature, suggesting that $P_{f_{tail}}$ and $P_{f_{MCS}}$ estimates are sensitive to the observation of high D_T values within the MCS iterations and as a result, are sensitive to the specific D_T values generated during the probabilistic analysis.

Concerning the significantly lower $P_{f_{dist}}$ value for the constrained lug top feature compared to the loaded lug top feature, this observation contradicts the expectation that the p_f estimates would be similar between the two features, due to the similar maximum damage values shown previously in Table 7.9 and the similar geometry and loading of the lugs. The smaller $P_{f_{dist}}$ estimates at the constrained lug top feature can be explained by considering the histograms and ECDF of the D_T values at the feature, as shown in Figure 7.26.

Figure 7.26 shows that smaller p_f values should be expected for the constrained lug top feature due to the variability in D_T demonstrating a smaller mean and lower variance compared to the loaded lug top feature. The reduced variability in the D_T values of the constrained lug

top feature is expected to be as a result of the assumed 'pinned' boundary conditions at the constrained lugs of the lower side-stay. Therefore, Figure 7.26 demonstrates the sensitivity of results from the probabilistic fatigue methodology to the assumptions made within the original deterministic fatigue analysis process.

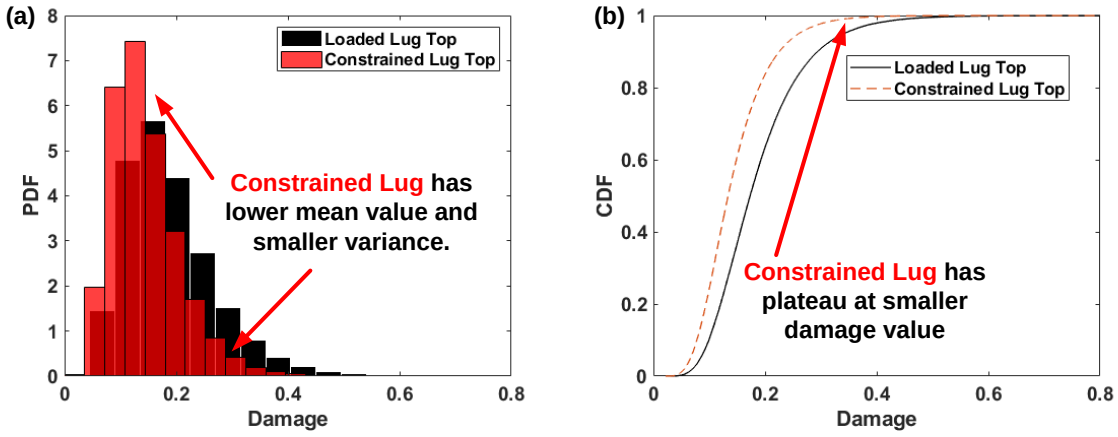

FIGURE 7.26. A comparison of the (a) D_T histograms and (b) CDFs for the loaded lug top and constrained lug top features.

The p_f estimates for each feature can then be combined into a component-level '$p_{f_{component}}$' estimate for the lower side-stay component, using Equation 3.6 shown previously in Chapter 3. Based on the symmetry of the lower side-stay component as discussed in Section 7.2.3, the features to account for in the $p_{f_{component}}$ estimate are:

- 2 × Loaded Lug Top Feature
- 2 × Loaded Lug Bottom Feature
- 2 × Constrained Lug Top Feature
- 2 × Constrained Lug Bottom Feature
- 1 × Side-Stay Body Feature
- 4 × Loaded Web Thickness Change Feature
- 4 × Constrained Web Thickness Change Feature

Table 7.15 shows the resulting lower side-stay component $p_{f_{component}}$ estimates for each p_f estimation method. It can be observed from Table 7.15 that when not accounting for statistical uncertainty, the $P_{f_{dist}}$ estimates provide the most conservative $p_{f_{component}}$ for the lower side-stay

component. When accounting for statistical uncertainty, Table 7.15 demonstrates that $P_{f_{MCS+2\sigma}}$ provides the most conservative estimate. However, it is important to note that the $P_{f_{MCS+2\sigma}}$ estimate for $p_{f_{component}}$ only accounts for the loaded lug top feature, as this was the only feature to demonstrate failure MCS iterations, as shown previously in Table 7.13. Therefore, the $P_{f_{MCS}}$-derived estimates fail to account for the quantifiable p_f observed in other features of the lower side-stay component.

TABLE 7.15. The component-level p_f estimates for the lower side-stay component.

Component	Component-level $p_{f_{component}}$ Estimation Method				
	$P_{f_{dist}}$	$P_{f_{dist}}$ 95% CI	$P_{f_{tail}}$	$P_{f_{MCS}}$	$P_{f_{MCS+2\sigma}}$
Lower Side-Stay	6.998×10^{-5}	7.611×10^{-5}	5.391×10^{-5}	4.000×10^{-5}	9.657×10^{-5}
Components per Failure	14,290	13,139	18,547	25,000	10,355

Table 7.15 also shows the components per failure for the lower side-stay component. Comparing the p_f estimates and components per failure values with the lower side-stay pins in Table 7.8 demonstrates that the probability of failure due to fatigue in the lower side-stay component is significantly lower than that for the lower side-stay pins.

Lower Side-Stay Assembly

The component p_f estimates for the smooth pin, fuse pin and lower side-stay component could then be combined to produce an estimate of the $p_{f_{assembly}}$. This could be achieved using Equation 3.7 shown in Chapter 3, as the lower side-stay assembly is a single load path assembly and is as a result, a 'series' reliability system. The resulting assembly-level $p_{f_{assembly}}$ estimates are shown in Table 7.16.

TABLE 7.16. The assembly-level p_f estimates for the lower side-stay assembly.

Assembly	Assembly-level $p_{f_{assembly}}$ Estimation Method				
	$P_{f_{dist}}$	$P_{f_{dist}}$ 95% CI	$P_{f_{tail}}$	$P_{f_{MCS}}$	$P_{f_{MCS+2\sigma}}$
Lower Side-Stay	7.766×10^{-4}	8.295×10^{-4}	4.340×10^{-4}	4.400×10^{-4}	7.483×10^{-4}
Reliability R	0.9992	0.9992	0.9996	0.9996	0.9993
Assemblies per Failure	1,287	1,205	2,304	2,272	1,336

It can be observed from Table 7.16 that there is good agreement of the $p_{f_{assembly}}$ estimate of the lower side-stay assembly across the different p_f estimation methods, which all show the same order of magnitude of 10^{-4}. Table 7.16 also shows the lower side-stay assemblies per failure value and as a result, it would be expected to observe approximately one failure of the assembly in the typical fleet size of a wide-body civil aircraft of 1,000 to 2,000 aircraft [263].

The $p_{f_{assembly}}$ generated using $P_{f_{dist}}$ provides the most conservative estimate of the lower side-stay assembly at $P_{f_{dist}} = 8.295 \times 10^{-4}$ (at the 95% confidence level), corresponding to an assembly reliability of $R = 0.9992$. As $P_{f_{dist}}$ provides the most conservative estimate of the lower

side-stay $p_{f_{assembly}}$, both when accounting for and neglecting statistical uncertainty, it should be used as the final estimate for the lower side-stay $p_{f_{assembly}}$.

Whilst the values in Table 7.16 suggest that the $P_{f_{tail}}$ and $P_{f_{MCS}}$ estimates provide validation for the $P_{f_{dist}}$ values, it should be recalled that the $p_{f_{assembly}}$ estimates based on $P_{f_{tail}}$ and $P_{f_{MCS}}$ fail to account for all of the features within the lower side-stay component with a quantifiable p_f value. As a result, the $P_{f_{tail}}$ and $P_{f_{MCS}}$ again fail to generate p_f estimates that are representative of all the potential locations of fatigue failure in the assembly.

7.2.7 Sensitivity Analysis

As introduced in Chapter 3, sensitivity analysis methods provide further information to support fatigue design decisions, by ranking design parameters with respect to their relative contribution to the variability observed in the D_T accumulated damage values. The design parameters providing the greatest contribution are known as 'design drivers'.

The density-based K-L sensitivity analysis method introduced in Chapter 3 was applied to the lower side-stay assembly case study. In order to perform K-L sensitivity analysis, repeated MCS-SSI probabilistic analyses had to be performed, each time fixing a specific design parameter to a nominal value. In order to reduce the computational expense of conducting the sensitivity analysis, a reduced number of MCS iterations was used for each sensitivity analysis case. $N_{MCS} = 1 \times 10^4$ MCS iterations (10% of the N_{MCS} used for the estimation of p_f values) was used to conduct the K-L sensitivity analysis. In order to ensure $N_{MCS} = 1 \times 10^4$ iterations would still result in accurate sensitivity analysis results, the distribution parameter estimates for the D_T damage and the resulting $P_{f_{dist}}$ estimates were compared between $N_{MCS} = 1 \times 10^5$ and $N_{MCS} = 1 \times 10^4$ for the fuse pin maximum shear location and loaded lug top feature, as shown in Table 7.17.

TABLE 7.17. Comparison of distribution parameters and $P_{f_{dist}}$ at $N_{MCS} = 1 \times 10^5$ and $N_{MCS} = 1 \times 10^4$ iterations for the fuse pin maximum shear location and loaded lug top features.

Feature	Property	Value		
		$N_{MCS} = 1 \times 10^5$	$N_{MCS} = 1 \times 10^4$	% Difference
Fuse Pin Max Shear	2P Log-Normal σ	-1.399	-1.400	0.050
	2P Log-Normal λ	0.396	0.397	0.311
	$P_{f_{dist}}$	2.048×10^{-4}	2.210×10^{-4}	3.516
Loaded Lug Top	2P Log-Normal σ	-1.762	-1.761	0.025
	2P Log-Normal λ	0.425	0.424	0.323
	$P_{f_{dist}}$	1.717×10^{-5}	1.627×10^{-5}	5.242

Table 7.17 shows that the percentage difference between the distribution parameter estimates and $P_{f_{dist}}$ for the D_T accumulated damage only differ by approximately 5% for both features. As a result, $N_{MCS} = 1 \times 10^4$ provides a sufficient number of MCS iterations to perform K-L sensitivity analysis. The remainder of this section will present the sensitivity analysis results for the fuse pin maximum shear location and the loaded lug top feature of the lower side-stay component.

These features were selected as they provided the most highly damaged features within their respective sections of the lower side-stay assembly.

Fuse Pin

The sensitivity analysis of the fuse pin maximum shear location considered each of the design parameters statistically characterised for the fuse pin case study as described previously in Section 7.2.4. The following sensitivity analysis cases were therefore considered:

- Mean aircraft mass assumed for pre-takeoff taxi and take-off (2.262×10^5 kg [191]) and for landing and post-landing taxi (1.835×10^5 kg [191]).
- Fixed ground manoeuvre occurrence and sequence based on the standardised loading spectrum described in Appendix E.
- All side load factors fixed to $n_y = \pm 0.1$ g.
- Mean S-N curve (i.e. all S-N curves are set to $PoS = 50\%$, with a mean $\sigma_{FL} = 457$ MPa.)
- Mean $\sigma_{UTS} = 1{,}200$ MPa.
- Mean outer radius $OR = 32.5$ mm.
- Mean inner radius $IR = 19.5$ mm.
- Mean groove radius $r_g = 2$ mm.
- Mean groove depth $d_g = 5$ mm.
- Mean groove width $w_g = 10$ mm.

The output from each MCS sensitivity analysis case was statistically characterised using the same process as used in the probabilistic analysis in Section 7.2.6 and the resulting distributions are shown in Table 7.18. It can be observed from Table 7.18 that the removal of variability in specific design parameters can result in a significant change in the probability distribution shape (e.g. an Exponential distribution) compared to the original 'parent' 2P Log-Normal distribution when all design parameter variability is accounted for.

Figure 7.27 shows the deviation from the fuse pin maximum shear location D_T parent distribution for the sensitivity analysis cases concerning the loading on the lower side-stay assembly. It can be observed from Figure 7.27a that the mean aircraft mass values only result in a slight deviation from the parent distribution. The fixing of the variability in the manoeuvre occurrence and sequencing resulted in a Gumbel Maximum distribution that demonstrated increased deviation from the parent distribution, as highlighted by Figure 7.27b. Figure 7.27c shows that the Exponential distribution representing the removal of variability in the n_y load

factor magnitude demonstrated a significant deviation from the parent distribution, qualitatively suggesting that variability in n_y loading magnitude provides a significant contribution to the variability in D_T values at the fuse pin maximum shear location.

TABLE 7.18. Statistical characterisation results for the fuse pin maximum shear location sensitivity analysis cases.

Sensitivity Analysis Case	Distribution Type	Distribution Parameter Estimate		
		Threshold δ	Scale σ	Shape λ
Mean Aircraft Mass	Gumbel Maximum	-	0.076	0.202
Fixed Occurrence and Sequence	Gumbel Maximum	-	0.034	0.086
Fixed n_y	Exponential	-	0.005	-
Mean S-N Curve	3P Log-Normal	0.017	-1.464	0.079
Mean σ_{UTS}	2P Log-Normal	-	-1.405	0.400
Mean OR	2P Log-Normal	-	-1.394	0.396
Mean IR	2P Log-Normal	-	-1.398	0.397
Mean r_g	2P Log-Normal	-	-1.409	0.393
Mean d_g	2P Log-Normal	-	-1.402	0.395
Mean w_g	2P Log-Normal	-	-1.396	0.397
Parent Distribution	2P Log-Normal	-	-1.400	0.396

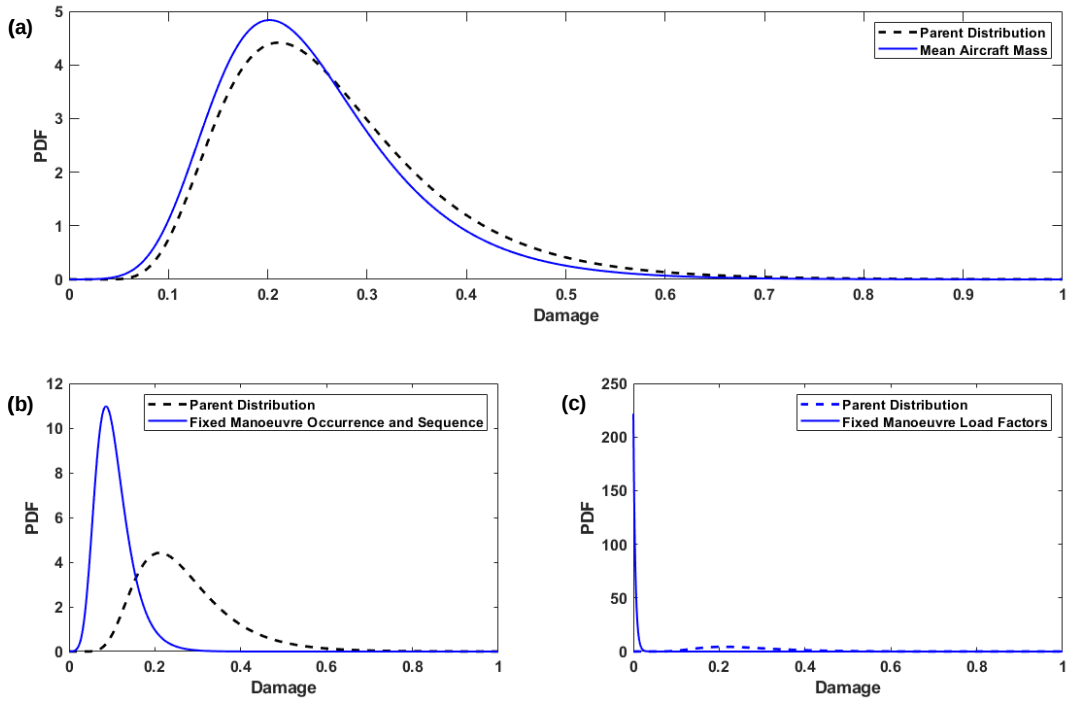

FIGURE 7.27. D_T probability distributions resulting from fuse pin maximum shear location loading sensitivity analysis cases: (a) mean take-off and landing mass, (b) fixed manoeuvre occurrence and sequencing and (c) fixed n_y side load factors.

The distributions of the fuse pin maximum shear location D_T values resulting from the sensitivity analysis cases concerning material properties are shown in Figure 7.28. It can be seen from Figure 7.28a that the use of a mean S-N curve results in a large departure from the original parent distribution, with a significant reduction in the observed skew and variance. On the other hand, Figure 7.28b suggests that removal of the variability in σ_{UTS} only results in a limited change to the D_T distribution, suggesting that σ_{UTS} only has a limited impact on the variability in the fuse pin maximum shear location D_T values.

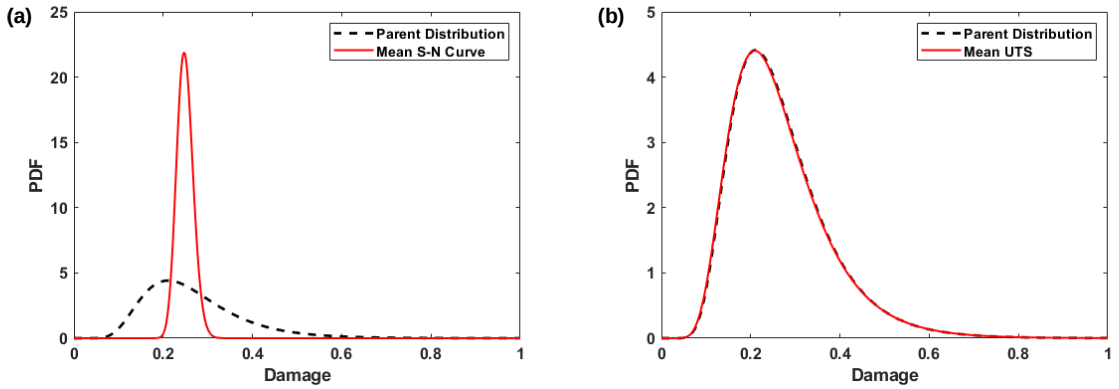

FIGURE 7.28. D_T probability distributions resulting from fuse pin maximum shear location material property sensitivity analysis cases: (a) mean S-N curve and (b) mean σ_{UTS}.

Figure 7.29 shows the distributions resulting from the sensitivity analysis cases that considered the fuse pin dimensional design parameters. It can be observed from Figure 7.29 that there is minimal visual difference between the parent distribution and the distributions from the dimensional parameter sensitivity analysis cases, suggesting that the variability in dimensional design parameters provides a very limited contribution to the variability in the fuse pin maximum shear location D_T values.

In order to quantify the difference between the parent distribution and each of the resulting distributions for the sensitivity analysis cases, the K-L total effect TE sensitivity value can be computed using the K-L sensitivity analysis method described in Chapter 3 and Equation 3.8. The resulting TE values are shown in Table 7.19, where a larger TE value implies that a design parameter provides a greater contribution to the variability in D_T values (i.e. identifying a more 'significant' design parameter or design driver).

Table 7.19 shows that based on K-L sensitivity analysis, the variability in the side load factor n_y for each ground manoeuvre results in the largest TE value and therefore, provides the greatest contribution to the variability in the D_T values for the fuse pin maximum shear location.

This TE value is also significantly larger than any of the other TE values, suggesting that the n_y load factor variability is the primary contributor to the variability in D_T values. As a result, n_y is the fatigue design driver for the fuse pin maximum shear location. As the typical shape of the n_y load factor distributions is Exponential [12], this suggests that it is also the upper-tail and rare or 'extreme' loading events that contribute significantly to the variability in fuse pin maximum shear location D_T values.

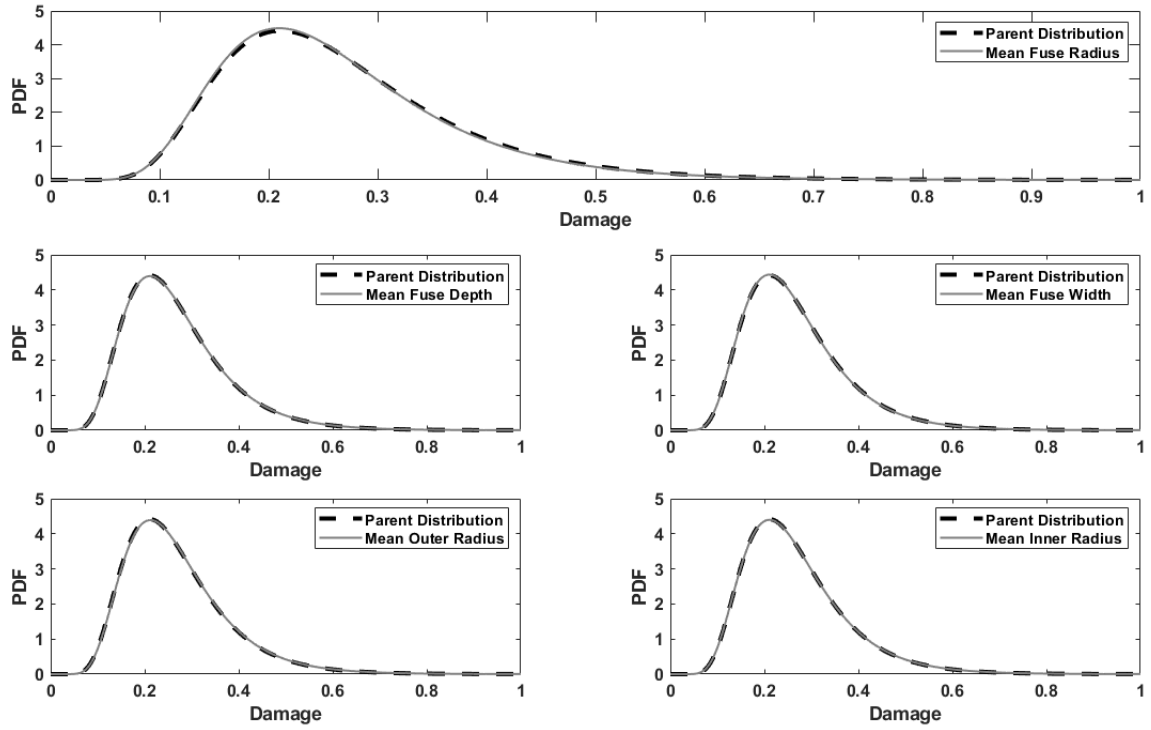

FIGURE 7.29. D_T probability distributions resulting from fuse pin maximum shear location dimensional parameter sensitivity analysis cases: (a) mean r_g, (b) mean d_g, (c) mean w_g, (d) mean OR and (e) mean IR.

The results in Table 7.19 also show that the variability present in the S-N curves also contributes a significant amount of variability to the fuse pin maximum shear location D_T damage values. This result is to be expected due to the significant variability that is present within S-N datasets and N_f values [6]. The removal of manoeuvre occurrence and sequencing variability also resulted in a TE value of a similar magnitude to using mean S-N curves, suggesting that manoeuvre occurrence and sequencing also introduces significant variability in the fuse pin maximum shear location D_T damage values.

The remaining design parameters, including all those related to the dimensional parameters of the fuse pin, demonstrated negligible TE values and therefore provided a limited contribution

to the variability in D_T damage values. As a result, in future probabilistic analyses, there is the potential to 'screen' dimensional variability, by fixing such values to their mean or deterministic values, potentially reducing the computational expense of the probabilistic analysis.

TABLE 7.19. Total Effect TE values for the fuse pin maximum shear location sensitivity analysis cases, computed using the K-L sensitivity analysis method.

Sensitivity Analysis Case	TE
Fixed n_y	54.674
Mean S-N Curve	5.894
Fixed Occurrence and Sequence	3.240
Mean Aircraft Mass	0.156
Mean r_g	0.021
Mean σ_{UTS}	0.013
Mean OR	0.011
Mean d_g	0.006
Mean w_g	0.006
Mean IR	0.003

Loaded Top Lug Feature

Sensitivity analysis was also performed for the loaded lug top feature of the lower side-stay component. The following K-L sensitivity analysis cases based upon $N_{MCS} = 1 \times 10^4$ were performed for the loaded lug top feature:

- Mean aircraft mass assumed for pre-takeoff taxi and take-off (2.262×10^5 kg [191]) and for landing and post-landing taxi (1.835×10^5 kg [191]).
- Fixed ground manoeuvre occurrence and sequence based on the standardised loading spectrum described in Appendix E.
- All side load factors fixed to $n_y = \pm 0.1$ g.
- Mean S-N curve (i.e. all S-N curves are set to $PoS = 50\%$, with a mean $\sigma_{FL} = 457$ MPa).
- Mean $\sigma_{UTS} = 1{,}200$ MPa.

The output from the MCS sensitivity analysis cases was then statistically characterised using the same approach as for the fuse pin sensitivity analysis cases and the resulting distributions are shown in Table 7.20. It should be noted that the sensitivity analysis case concerning fixing all side load factors to $n_y = \pm 0.1$ g only resulted in three MCS iterations accumulating fatigue damage in the loaded lug top feature and as a result, a distribution could not be fitted.

Figure 7.30 shows the distributions for the loaded lug top sensitivity analysis cases related to the lower side-stay loading. Figure 7.30a shows that the removal of variability in aircraft mass only results in a limited deviation from the parent distribution, compared to when the variability

in manoeuvre occurrence and sequencing is removed as shown in Figure 7.30b. Therefore, Figure 7.30 qualitatively suggests that variability in ground manoeuvre occurrence and sequencing provides a greater contribution to the D_T damage value variability compared to the variability in the aircraft mass. As only a limited number of MCS iterations resulted in accumulated damage in the sensitivity analysis case in which n_y side load factor variability was removed, it is therefore suggested that the n_y variability is the design driver for the loaded lug top feature.

TABLE 7.20. Statistical characterisation results for the loaded lug top sensitivity analysis cases.

Sensitivity Analysis Case	Distribution Type	Distribution Parameter Estimate	
		Scale σ	Shape λ
Mean Aircraft Mass	Gumbel Maximum	0.051	0.129
Fixed Occurrence and Sequence	2P Log-Normal	-2.551	0.434
Mean S-N Curve	2P Log-Normal	-1.754	0.061
Mean σ_{UTS}	2P Log-Normal	-1.759	0.418
Parent Distribution	2P Log-Normal	-1.762	0.425

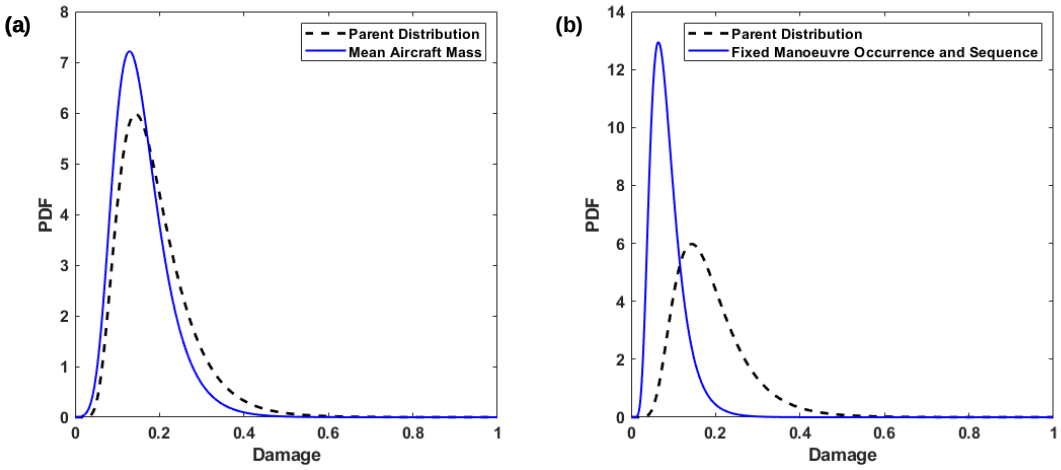

FIGURE 7.30. D_T probability distributions resulting from loaded lug top loading sensitivity analysis cases: (a) mean take-off and landing mass and (b) fixed manoeuvre occurrence and sequencing.

The sensitivity analysis cases concerning the mean S-N curve and mean σ_{UTS} are shown in Figures 7.31a and 7.31b respectively. It can be seen from Figure 7.31 that the mean S-N curve results in a significant deviation from the parent distribution, especially when compared to the limited deviation of the mean σ_{UTS} case. This qualitatively suggests that the mean S-N curve may also be fatigue design driver, whilst the variability in σ_{UTS} only provides a limited contribution to the variability in the loaded lug top D_T damage values.

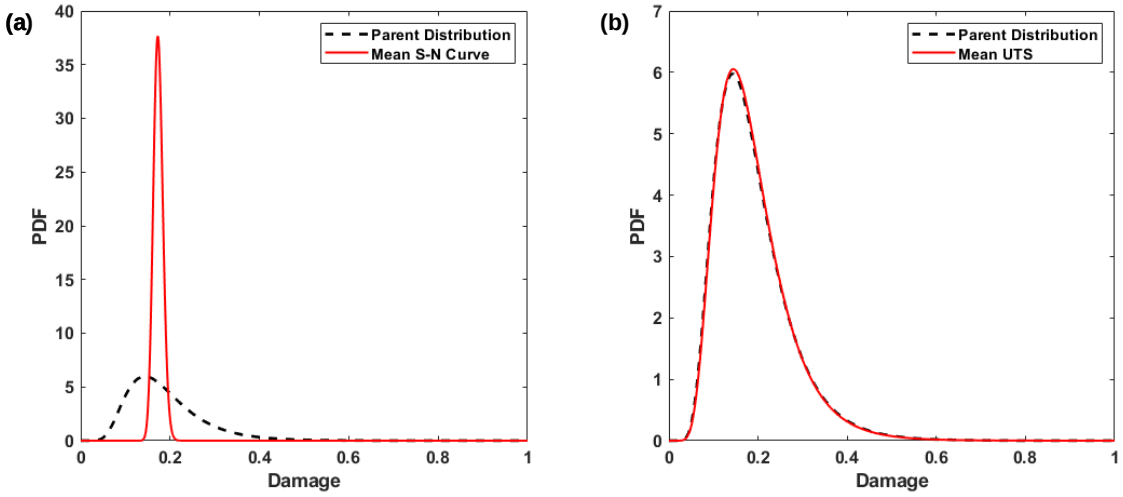

FIGURE 7.31. D_T probability distributions resulting from loaded lug top material property sensitivity analysis cases: (a) mean S-N curve and (b) mean σ_{UTS}.

K-L TE sensitivity values were computed for the loaded lug top sensitivity analysis cases and are shown in Table 7.21. It can be observed from Table 7.21 that the variability in the S-N curve and variability in the manoeuvre occurrence and sequence resulted in greater TE values and hence provided a greater contribution to the variability in the loaded lug top D_T damage values.

TABLE 7.21. Total Effect TE values for the loaded lug top sensitivity analysis cases, computed using the K-L sensitivity analysis method.

Sensitivity Analysis Case	TE
Mean S-N Curve	10.718
Fixed Occurrence and Sequence	2.004
Mean Aircraft Mass	0.332
Mean σ_{UTS}	0.018

Summary of Lower Side-Stay Assembly Sensitivity Analysis

The sensitivity analysis performed for the fuse pin maximum shear location and loaded lug top feature of the lower side-stay assembly highlighted that the following design parameters were design drivers for both features:

- Side load factor n_y for ground manoeuvres.
- S-N curve variability.
- Manoeuvre Occurrence and Sequencing.

The variability in n_y for ground manoeuvres was found to provide the greatest contribution to the variability in the lower side-stay D_T values and therefore, future work would be required to better control or characterise the variability in n_y. Whilst variability in landing gear loads cannot be directly reduced due to the operational environment of aircraft landing gear, future work could be performed to better characterise the variability in n_y side load factors for landing gear, beyond the existing studies presented in the literature [12, 14, 191, 214]. In a similar manner, the variability in ground manoeuvre occurrence and sequencing could be further characterised and incorporated into the existing deterministic safe-life fatigue analysis process, based upon data collection from ADS-B data files as described in Chapter 5.

The variability in S-N datasets and their subsequent S-N curves were also found to be fatigue design drivers for the lower side-stay assembly features. Whilst the inherent scatter in N_f within S-N datasets cannot be reduced, improved statistical characterisation of S-N datasets, as performed in Chapter 4, could reduce the variability in N_f represented within analysis, such as through the use of a 3P Weibull distribution for N_f. This would have the potential to reduce the variability in accumulated D_T damage values and will be explored in the following subsection.

7.2.8 3-Parameter Weibull P-S-N Curves

Chapter 4 demonstrated that whilst the variability in N_f for 4340 steel could be statistically characterised using a 2P Log-Normal distribution, an improved fit to the N_f values in the S-N dataset could be achieved using a 3P Weibull distribution. In order to investigate the impact on the probabilistic analysis and results for the lower side-stay assembly of assuming a 3P Weibull distribution for N_f instead of a 2P Log-Normal distribution, additional MCS iterations were performed of $N_{MCS} = 1 \times 10^4$ using a 3P Weibull distribution for N_f at each σ_0 stress level. The methodology used to statistically simulate 3P Weibull S-N curves was as described previously in Section 4.5.1.

Figure 7.32 shows the resulting D_T histograms for the fuse pin maximum shear location and loaded lug top feature when assuming a 3P Weibull distribution for N_f, compared to the original 'parent' distribution when assuming a 2P Log-Normal distribution for N_f. In both instances the variability in all other design parameters was retained.

The histograms shown in Figures 7.32b and 7.32d show the D_T histograms when assuming a 3P Weibull distribution for N_f for the fuse pin maximum shear location and loaded lug top feature respectively. It can be observed from Figure 7.32 that the resulting histograms from the 3P Weibull S-N curves can be characterised as negatively (i.e. left) skewed with a sharp right-hand tail. The histogram also shows a flattening of the peak of the distribution, compared to the sharp peak of probability density (i.e. central tendency) of the parent distributions in Figures 7.32a and 7.32c.

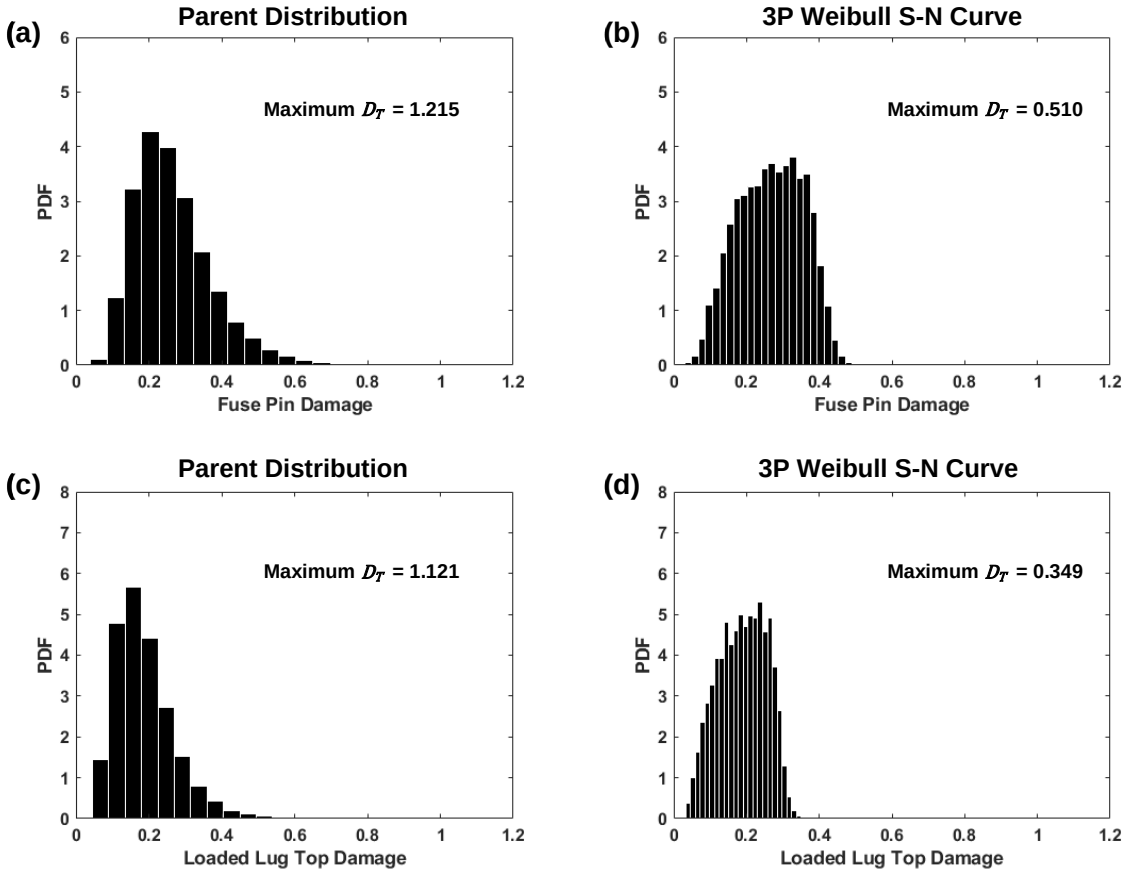

FIGURE 7.32. (a, c) D_T probability distributions resulting from using 2P Log-Normal S-N curves for fuse pin maximum shear location and loaded lug top feature and (b, d) D_T probability distributions resulting from using 3P Weibull S-N curves for fuse pin maximum shear location and loaded lug top feature.

The complex shape of the D_T histograms when employing a 3P Weibull N_f distribution for the S-N curve is expected to be as a result of the shape and support of the 3P Weibull distribution, which features a non-zero δ threshold value and a sharp increase to the maximum value of probability density (see Figure 4.6 in Chapter 4). It should also be noted from Figures 7.32b and 7.32d that the maximum D_T damage values observed were significantly lower when assuming a 3P Weibull N_f distribution. This reduction in maximum damage compared to when using a 2P Log-Normal N_f distribution is as a result of the non-zero δ threshold, which infers that there is a minimum N_f value at each σ_0 stress level, whereas 2P distributions theoretically infer that failure could occur at zero cycles. As a result, it can be suggested that a 3P Weibull distribution could result in reduced p_f estimates, providing the 3P Weibull distribution provides the most accurate fit to the variability in N_f.

In order to identify the change in p_f for the fuse pin maximum shear location and loaded lug top feature when using 3P Weibull N_f distributions, candidate distributions capable of negative skew and positive support were considered to characterise the D_T histograms in Figures 7.32b and 7.32d. The candidate distributions consisted of:

- 2P Weibull.
- 3P Weibull.
- Gumbel Minimum.
- Skew-Normal [264].

Figure 7.33 shows the candidate distributions fitted to the loaded lug top feature D_T histogram and ECDF. It can be seen from Figure 7.33 that none of the candidate distributions provided an acceptable visual fit the D_T histogram or ECDF when 3P Weibull N_f distributions were used, due to the complex shape of the histogram. As a good-fit to the D_T variability could not be achieved, p_f estimates when assuming a 3P Weibull N_f distribution could not be generated. As a result, and in a similar manner to the complexities of employing 3P Weibull distributions to construct P-S-N curves for deterministic fatigue design as described in Section 4.4, the utilisation of 3P Weibull distributions introduces significant complexity in the post processing of the probabilistic analysis. Methodologies that could be employed to overcome this complexity are discussed in Chapter 9.

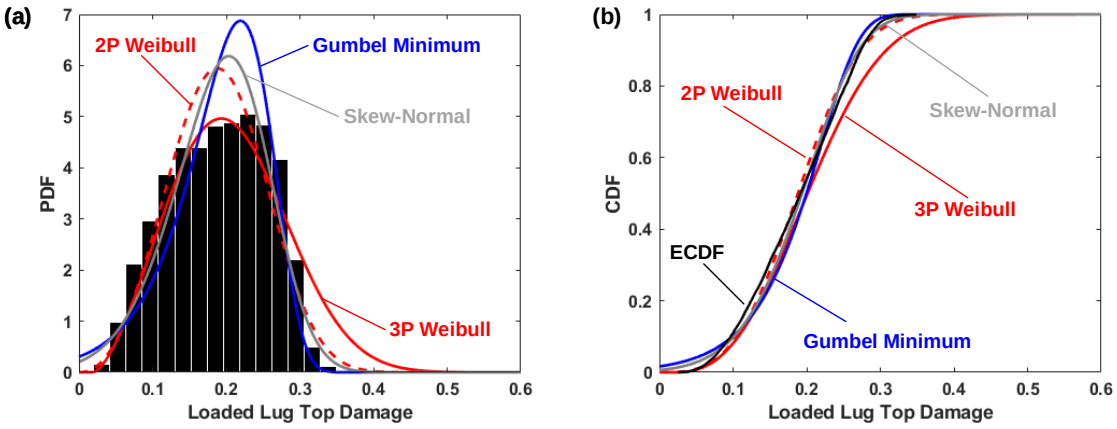

FIGURE 7.33. A visualisation of how all candidate distributions provided a poor-fit to the D_T (a) histogram and (b) ECDF for the loaded lug top feature when using an 3P Weibull N_f S-N curve.

7.3 Summary

This chapter has demonstrated the application of the probabilistic fatigue methodology defined in Chapter 3 to the smooth pin, fuse pin and lower side-stay components of a lower side-stay assembly for a wide-body civil aircraft MLG. The implementation of the probabilistic fatigue methodology permitted p_f estimates to be generated for the various engineering features of the lower side-stay components, along with component-level and assembly-level estimates. The MCS-SSI hybrid probabilistic fatigue methodology was successfully applied to components which are analysed using both classical/analytical and linear elastic FEA stress analysis methods. From the application of the probabilistic fatigue methodology to the lower side-stay assembly, additional observations beyond the successful generation of p_f estimates were made:

- The $P_{f_{dist}}$ estimates provided the most conservative p_f values, whilst the $P_{f_{tail}}$ and $P_{f_{MCS}}$ estimates were found to be sensitive to the specific D_T values observed during the MCS iterations.
- The utilisation of sensitivity analysis methods during the post processing of the results from the case studies identified the following design parameters as fatigue design drivers:
  - Variability in n_y side load factors.
  - Variability in the S-N curve.
  - Variability in the ground manoeuvre occurrence and sequencing.
- The p_f estimates of assemblies are typically dominated by specific components (e.g. the side-stay pins within the lower side-stay assembly) and the p_f estimates of components are typically dominated by specific features (e.g. the lug features of the lower side-stay component). As a result, from the perspective of fatigue reliability, many features of the lower side-stay assembly are potentially over-designed and could be further optimised to reduce component mass.

Due to the relative simplicity of the axial tension/compression loading applied to the lower side-stay assembly, the stress fields resulting in the lower side-stay component and pins were simple to assess and incorporate within the probabilistic fatigue methodology. As a result, an additional case study comprising of a component with a complex geometry that is exposed to complex loading is required in order to perform a critical assessment of the MCS-SSI hybrid probabilistic fatigue methodology defined in Chapter 3. Therefore, the following chapter considers an additional case study concerning a lower drag brace component, which will be assessed using the same probabilistic fatigue methodology and analysis procedures and demonstrated in this chapter.

CHAPTER 8

DRAG BRACE CASE STUDY

The current chapter aims to further extend the application of the probabilistic fatigue methodology to a landing gear component that demonstrates increased geometrical, loading and stress analysis complexity compared to the lower side-stay assembly assessed in Chapter 7. To further investigate the utility and performance of the probabilistic fatigue methodology defined Chapter 3, the methodology is applied to the assessment of a lower drag brace component, which is subjected to a complex combination of global landing gear loads. Beyond performing the probabilistic and sensitivity analysis of the engineering features of the lower drag brace component, this chapter also explores the further exploitation of surrogate modelling methods during the implementation of probabilistic fatigue methodologies. This chapter concludes by identifying observations made across both the lower side-stay assembly and lower drag brace case studies, to support the critical evaluation of the methodology to be performed in Chapter 9.

8.1 Lower Drag Brace Case Study

This chapter of the thesis will detail the implementation of the probabilistic fatigue methodology to the MLG lower drag brace component of a civil wide-body aircraft. The following case study considers the application of the probabilistic fatigue methodology to a component that is loaded in a complex fashion and is analysed using linear elastic FEA stress analysis methods. The probabilistic results and sensitivity analysis cases will also be presented following the implementation of the probabilistic fatigue methodology.

8.1.1 Component Overview

The drag brace is part of the main fitting of the MLG as highlighted in Figure 8.1. The drag brace runs from the main fitting to the forward airframe attachment point as shown in Figure 8.1b and is part of the single-piece forging of the main fitting as highlighted in Figures 8.1a and 8.1c.

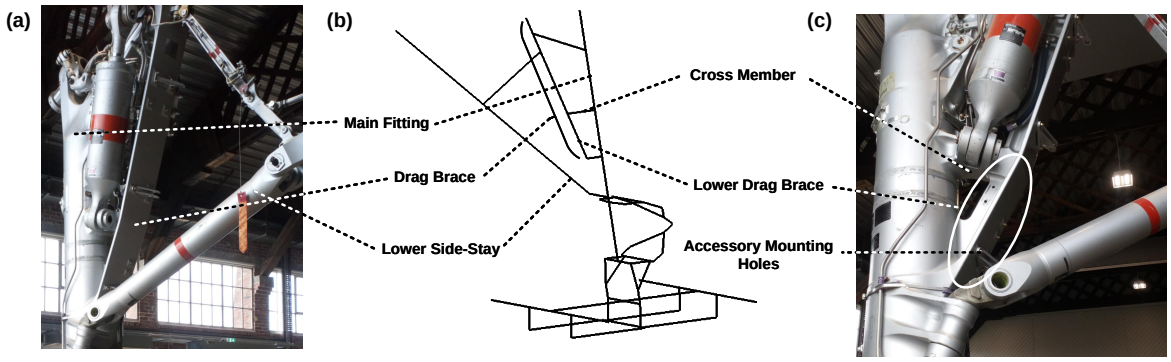

FIGURE 8.1. Overview of the lower drag brace component: (a) drag brace location within main fitting forging, (b) drag brace within FEA MLG beam model and (c) a close-up of the lower drag brace component.

The purpose of the drag brace is to react drag loads applied to the MLG during landing and ground manoeuvres. Drag loads are experienced during braking, pushback, and spin-up/spring-back loads following landing touchdown as described in Chapter 5.

The case study within this section focuses on the lower drag brace component, which is the region of the drag brace highlighted in Figures 8.1c and 8.2. The design safe-life for the lower drag brace component is 50,000 flights.

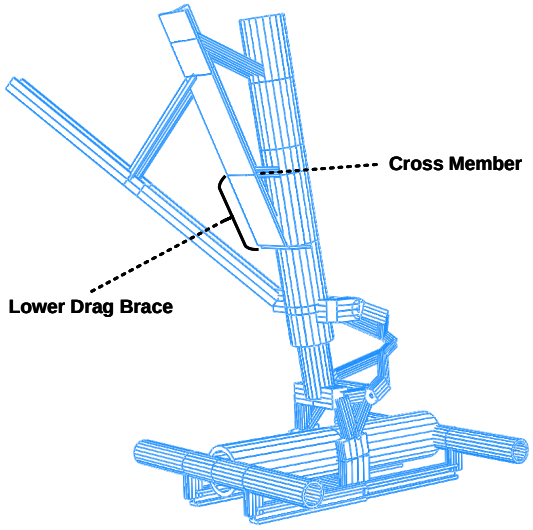

FIGURE 8.2. The lower drag brace component within the MLG assembly.

Loading

As the function of the drag brace is to react drag loads during landing and ground manoeuvres, the drag brace predominately carries loads related to the global drag load factor n_x. However, as the drag brace is part of the single-piece forging of the main fitting, a share of the global vertical F_Z load is also carried by the drag brace. As described extensively in Chapter 6, linear static FEA MLG beam models are used to convert global loads into internal loads at the lower drag brace. As shown previously in Figure 6.13, the internal loads of the lower drag brace consist of axial (F_1), shear (F_2, F_3), bending (F_4, F_5) and torsional (F_6) loads, relative to the T-section of the drag brace. These loads are applied at the base of the lower drag brace and are then transmitted along the drag brace, ultimately being reacted at the forward airframe attachment point.

Component Dimensions

The lower drag brace component is shown in Figure 8.3, comprising of a constant T-section which runs from the main fitting to the first main fitting cross member as shown previously in Figure 8.2. The lower drag brace therefore forms a 'slice' of the overall drag brace component and single-piece main fitting forging. The overall dimensions of the lower drag brace component are shown in Figure 8.4. Component dimensions have been sourced from scaling public domain photographs of MLG components. The drag brace features a number of fillets and radii, along with through-flange thickness holes which serve as accessory mounting holes. Accessory mounts permit items such as landing gear doors and wiring harnesses to be secured to the drag brace. The lower drag brace component is to be manufactured from 4340 high-tensile strength steel [25].

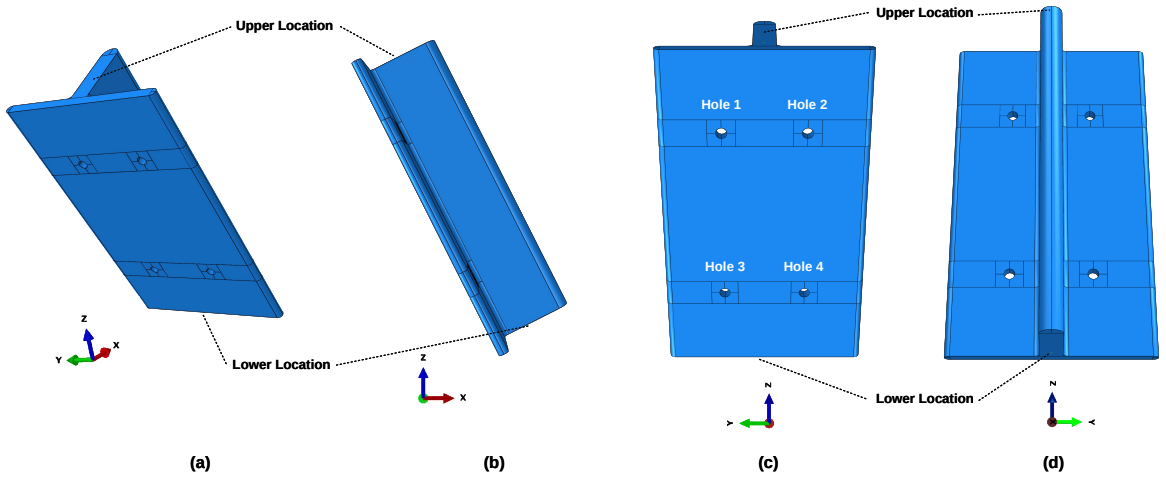

FIGURE 8.3. 3D model of the lower drag brace component aligned to the global coordinate system of the FEA MLG beam model: (a) an overview, (b) side view, (c) front view and (d) rear view.

8.1.2 Stress Analysis: Sub-Modelling and Surrogate Modelling

Within the probabilistic fatigue methodology, the load-time history of individual components must be converted to a stress-time history using stress analysis. This subsection details the stress analysis performed for the lower drag brace.

Finite Element Model

Due to the complexity of the lower drag brace loading and geometry, a linear elastic FEA stress analysis model was used to compute the stresses across the lower drag brace, consistent with existing practice [6, 7]. The lower drag brace component was constructed as a 3D solid model in ABAQUS®, comprising of linear quadratic 8-node brick elements (C3D8R elements), resulting in the linear elastic FEA model shown in Figure 8.5. The justification for using reduced integration elements was to reduce the evaluation time of the FEA model, as described previously in Section 7.2.2.2.

For simplicity, a constant mesh density was used across the component. The mesh density was selected such that it resulted in converged stresses at the accessory holes and fillet locations. These locations were selected as they were expected to be the hot-spot stress locations for the lower drag brace. The resulting mesh density produced an FEA model of the lower drag brace comprised of 69,500 C3D8R elements.

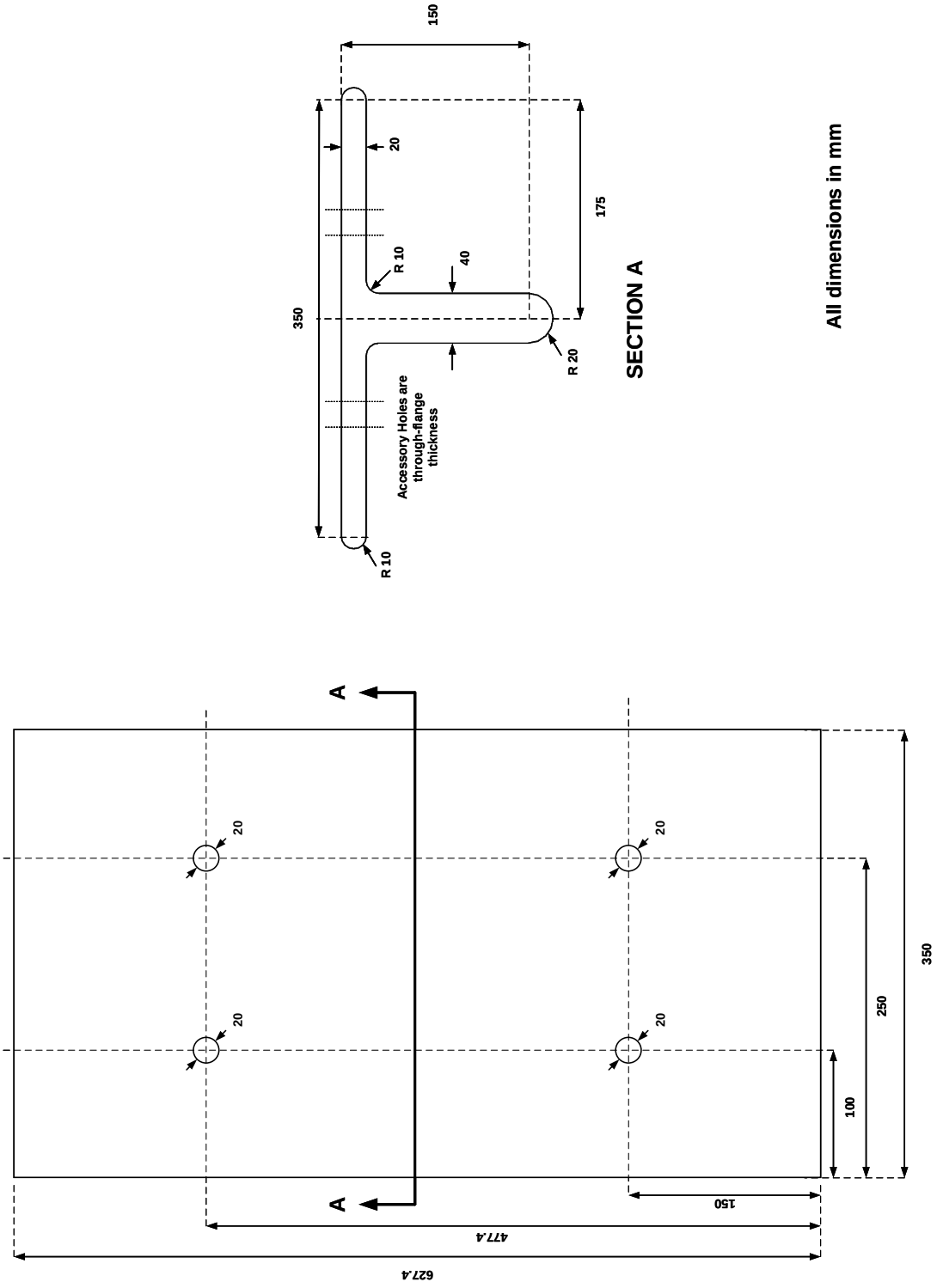

FIGURE 8.4. Dimensional and sectional properties of the lower drag brace component.

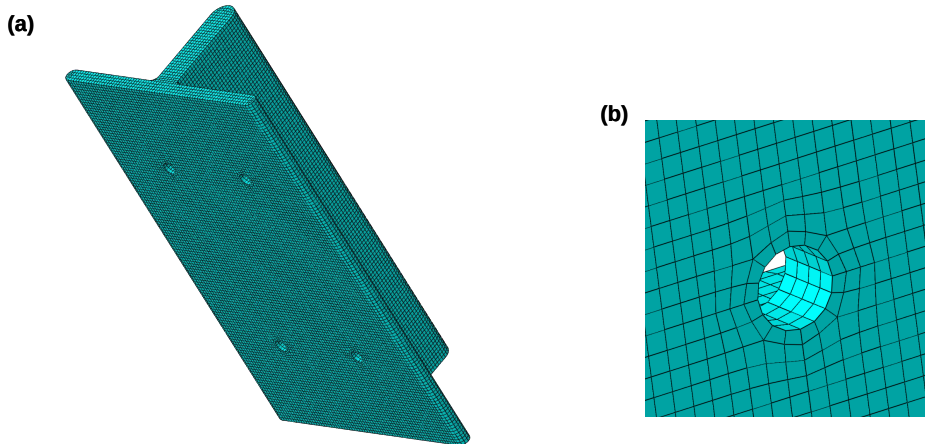

FIGURE 8.5. The 3D linear elastic FEA stress model of the lower drag brace: (a) the overall component and (b) the mesh surrounding an accessory mounting hole showing the elements through the thickness of the flange.

Sub-Modelling Approach

As a result of the complex loading of the drag brace component, coupled with the MLG configuration that results in cross members interrupting the drag brace along its length, it was expected that the boundary conditions at the lower and upper locations of the lower drag brace (i.e. the main fitting attachment and first cross member location respectively) would be challenging to define. It was also expected that the boundary conditions on the lower drag brace section would be dependent on the applied global loading, as the main fitting, drag brace and cross members all carry loads resulting from the n_x and n_z load factors as a result of the single-piece forging used for these components.

Therefore, the approach used for the surrogate modelling of the lower drag brace in Chapter 6 could not be used to directly compute the lower drag brace stresses resulting from global MLG loading. As a result, an alternative approach known as 'sub-modelling' was required.

Sub-modelling is an approach widely used in FEA stress analysis, whereby a specific component feature is modelled as a separate 'detailed' FEA model within a 'coarse' FEA model[1] [265]. Within the lower drag brace case study, the coarse FEA model is the linear static FEA MLG beam model and the detailed or 'sub' model is the 3D linear elastic FEA stress model of the lower drag brace component, as visualised in Figure 8.6. It should be noted that the 3D FEA stress model for the lower drag brace is aligned with the global coordinate system of the FEA MLG beam model.

Within sub-modelling, the displacements and rotations at the interface between the coarse and detailed models are first computed using the coarse model and then 'passed' to the detailed

[1]Sub-modelling permits finer mesh densities at specific model locations or can be used to interface different element types [265].

model [265]. For the lower drag brace component, the displacements and rotations are computed at the lower and upper locations within the linear static FEA MLG beam model and are then passed to the 3D linear elastic FEA stress model of the lower drag brace. Multi Point Constraints (MPCs) were used to apply the displacements and rotations from the FEA MLG beam model to the 3D FEA stress model, as shown in Figure 8.7.

At both the lower and upper locations of the lower drag brace component, there are three displacement values ($U1$, $U2$ and $U3$ - along the X, Y and Z directions of the FEA MLG beam model coordinate system) and three rotation values ($R1$, $R2$ and $R3$ - about the X, Y and Z directions of the FEA MLG beam model coordinate system). When a set of displacement and rotation values are applied at the lower and upper locations of the lower drag brace component, the 3D linear elastic FEA stress model can be evaluated to compute stress values across the model. The maximum principal stress was used to account for multi-axial stress effects [255], and the stress response for various global loading conditions are visualised in Figure 8.8. It was identified that a single evaluation of the 3D solid linear elastic FEA stress model required ≈ 50 seconds of CPU run-time[2]. Due to the utilisation of two FEA models to convert the statistically simulated load-time histories to stress-time histories in the lower drag brace case study, two independent surrogate models were required to reduce the computational expense of performing the probabilistic analysis of the lower drag brace to a feasible CPU run-time.

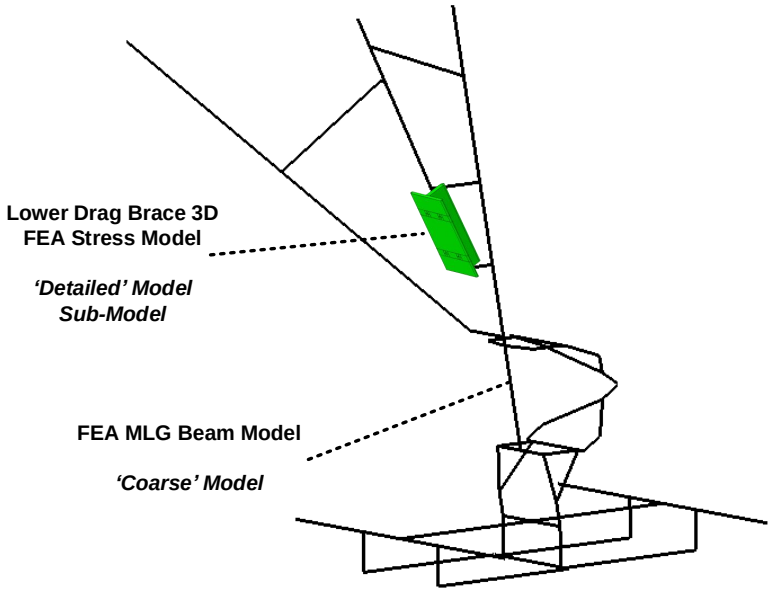

FIGURE 8.6. Sub-modelling approach for the lower drag brace component showing the 3D FEA stress model within the FEA MLG beam model.

[2]Computer Specifications: 4-core processor (3.40 GHz) with 16.0 GB RAM.

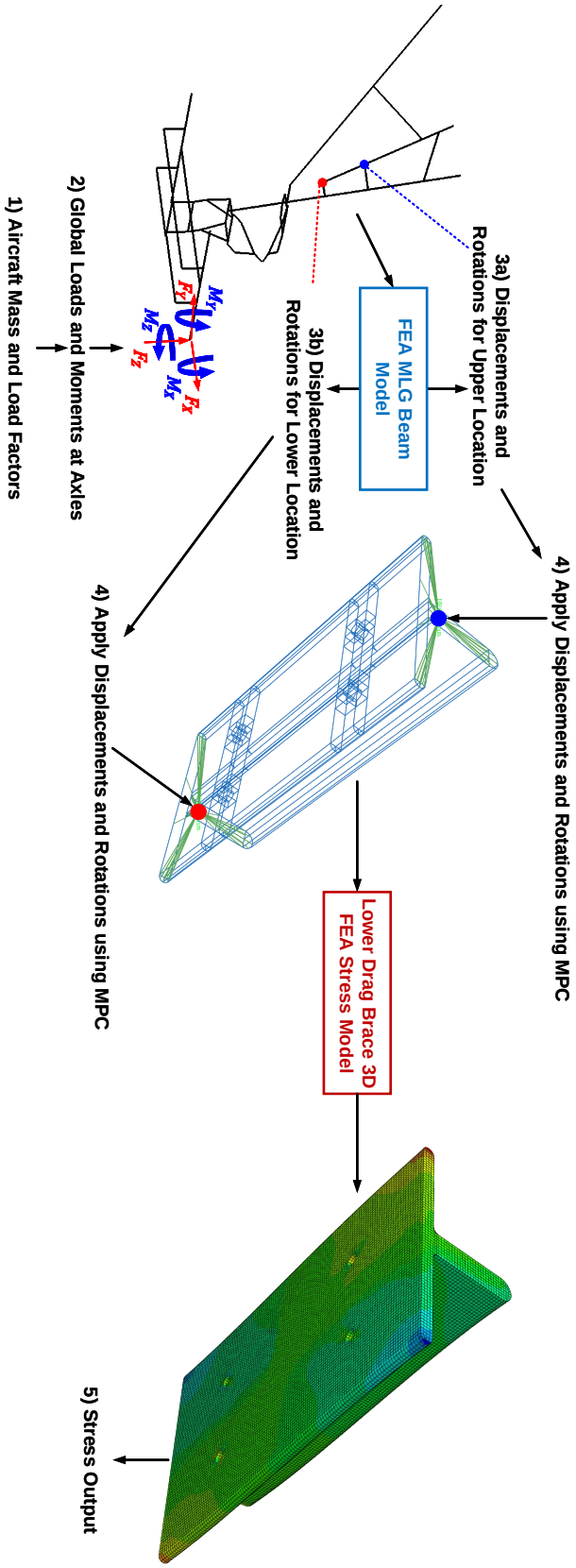

FIGURE 8.7. The sub-modelling process for the lower drag brace using MPCs.

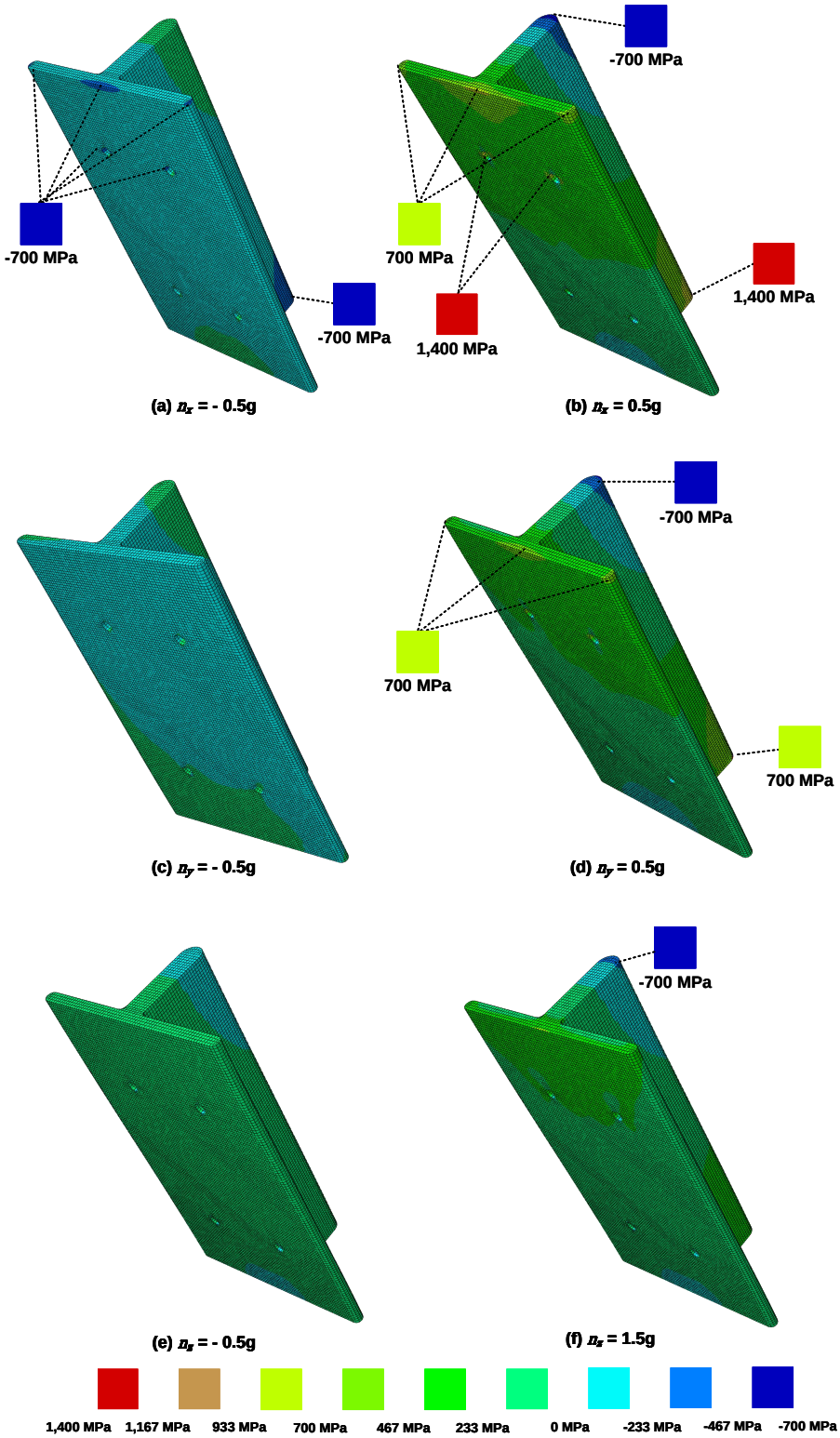

FIGURE 8.8. Example linear elastic FEA stress responses of the lower drag brace component: (a, b) maximum global drag loads, (c, d) maximum global side loads and (e, f) maximum global vertical loads. Peak stress locations are also shown.

FEA MLG Beam Model Surrogate Modelling

The first surrogate model required for the lower drag brace case study was concerned with the linear static FEA MLG beam model. The purpose of this surrogate model was to represent the input-output relationship between the global loading of the MLG (defined by the three global load factors and aircraft mass) and the three displacements and three rotations at the lower and upper locations of the lower drag brace. This resulted in the need to generate a surrogate model with four input parameters and 12 output parameters.

Following the surrogate modelling training process defined in Figure 6.4 in Chapter 6, a training dataset was generated from evaluations of the linear static FEA MLG beam model using a 'caged-LHS' approach of size $S_T = 3,000$ (i.e. a 'half-day' resource block). A validation dataset of $S_V = 600$ was also constructed using an LHS design.

Based on the surrogate modelling selection process proposed in Figure 6.18 in Chapter 6, a cubic RSM surrogate model was proposed for use on the linear static FEA MLG beam model, especially considering the high accuracy achieved by the cubic RSM in the case studies in Chapter 6. Due to the 12 outputs of the FEA MLG beam model, 12 cubic response surfaces were required and each surface was defined by 35 β coefficients. The total training time of the cubic RSM surrogate model was 0.5 seconds using least squares regression[3].

Error metrics (as defined in Chapter 6) are shown for each of the displacements and rotations for both the lower and upper locations of the lower drag brace in Table 8.1. The error metrics are provided for both training and validation datasets, denoted by the subscripts 'T' and 'V' respectively.

TABLE 8.1. Error metrics for both the training and validation datasets of the FEA MLG beam model cubic RSM for displacements and rotations at the lower and upper locations of the lower drag brace.

Error Metric	Lower Location Displacement			Lower Location Rotation		
	$U1$ mm	$U2$ mm	$U3$ mm	$R1$ rad	$R2$ rad	$R3$ rad
MAE_T	5.029×10^{-5}	3.997×10^{-5}	9.672×10^{-6}	3.106×10^{-8}	2.697×10^{-8}	2.290×10^{-8}
MPE_T	0.118%	0.047%	10.647%	0.032%	0.198%	0.020%
MAE_V	4.863×10^{-5}	4.019×10^{-5}	9.554×10^{-6}	3.048×10^{-8}	2.374×10^{-8}	2.046×10^{-8}
MPE_V	0.051%	0.003%	0.084%	0.009%	0.014%	0.002%
Error Metric	Upper Location Displacement			Upper Location Rotation		
	$U1$ mm	$U2$ mm	$U3$ mm	$R1$ rad	$R2$ rad	$R3$ rad
MAE_T	2.530×10^{-5}	2.700×10^{-5}	1.092×10^{-6}	2.753×10^{-8}	2.641×10^{-8}	1.717×10^{-8}
MPE_T	0.015%	0.601%	1.136%	0.096%	0.647%	0.020%
MAE_V	2.571×10^{-5}	2.696×10^{-5}	1.384×10^{-6}	2.812×10^{-8}	2.431×10^{-8}	1.588×10^{-8}
MPE_V	0.019%	0.553%	0.011%	0.135%	0.012%	0.002%

Table 8.1 shows that the MAE values are low and that the MPE values are less than approximately 10%. 10% was considered an acceptable surrogate modelling error, as FEA models are often only capable of achieving an accuracy of between 5 and 10% [61, 229].

[3]Computer Specifications: 4-core processor (3.40 GHz) with 16.0 GB RAM.

The cubic RSM surrogate model was then assessed for the time required to generate 1,000 predictions for the 12 displacement and rotation values. On average, the cubic RSM required 0.012 seconds of CPU run-time to generate 1,000 predictions[4]. For the approximately 5×10^6 load levels within the statistically simulated 50,000 flight load-time history, 1.071 seconds were required to generate the corresponding displacement and rotation values. This CPU run-time represented a dramatic reduction in the 20 seconds required to evaluate the original linear static FEA MLG beam model.

Initial Feature Down-Selection

In order to select the features of the lower drag brace component to be included within the probabilistic analysis, the feature down-selection process defined in Section 7.1.2 was employed. All stress raising features (e.g. radii, fillets, accessory mounting holes, etc.) were identified. Consistent with the feature down-selection process, stress hot-spots were identified by executing the analysis of the linear elastic FEA stress model at maximum load factor values (i.e. $n_x = \pm 0.5$ g, $n_y = \pm 0.5$ g and $n_z = [-0.5 \text{ g}, +1.5 \text{ g}]$) at the maximum aircraft mass. A two-level Full Factorial design was also used to produce maximum and minimum combinations of the load factors to be evaluated by the FEA stress model.

The accessory mounting holes were segregated into slices based upon the FEA stress model mesh as highlighted in Figure 8.9a. The 16 strips around each accessory mounting hole also consisted of four elements through the thickness of the lower drag brace flange, as shown in Figure 8.9b. In order to reduce the number of features within the probabilistic analysis for the sake of computational expense, it was assumed that the maximum absolute stress identified through the flange thickness represented the stress of the specific slice around the accessory hole. This process is demonstrated in Figure 8.9b. Such an assumption was also considered appropriate as due to the short critical crack lengths of high-tensile strength steel, any crack initiation at the hole features would result in a through-flange thickness crack propagating [6, 21].

All slices around the accessory holes were initially selected as features of interest, as the hot-spot stress analysis highlighted complex stress fields around the holes. Combined with the other stress raising features and hot spots on the lower drag brace, this resulted in 95 features; 64 of which were related to the accessory mounting holes. Figure 8.10 highlights the features that were initially down-selected for the lower drag-brace.

[4]Computer Specifications: 4-core processor (3.40 GHz) with 16.0 GB RAM

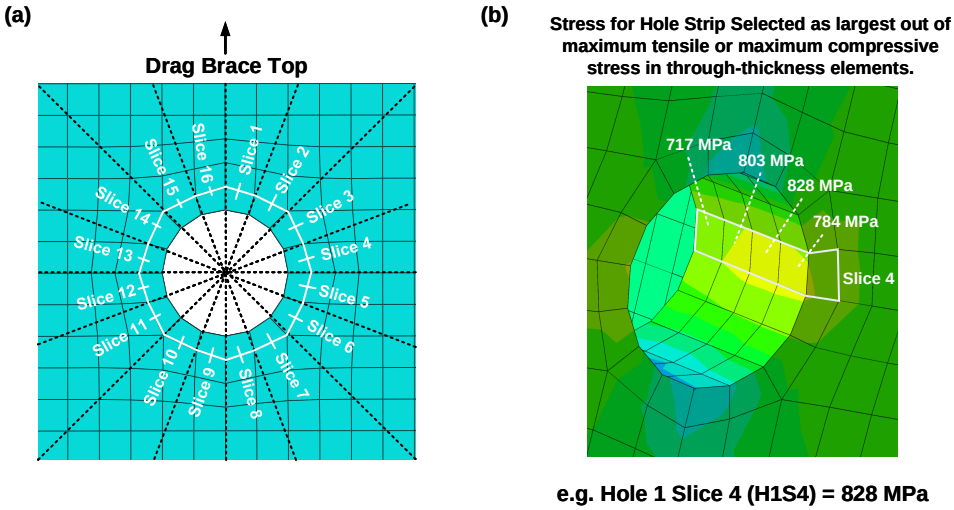

FIGURE 8.9. FEA mesh around the accessory mounting holes of the lower drag brace: (a) the 16 'slices' that partition the holes circumferentially and (b) the identification of the maximum absolute stress from the four through-thickness elements at each slice.

3D FEA Stress Model Surrogate Modelling

In order to negate the 50 second CPU run-time of a single evaluation of the lower drag brace solid linear elastic FEA stress model, a surrogate model was required to convert the displacements and rotations from the linear static FEA MLG beam model to stress values at the 95 lower drag brace features. The surrogate model for the linear elastic FEA stress model would be required to represent 12 inputs (three displacements and three rotations at the lower and upper locations of the lower drag brace) and 95 outputs (i.e. each down-selected feature).

For the generation of training data for the FEA stress surrogate model, a 'full-day' resource block was defined, permitting 3,000 evaluations of the original linear elastic FEA stress model. In order to produce a training dataset that was representative of the combinations of displacement and rotations that could be applied to the lower drag brace, an LHS design of $S_T = 3{,}000$ was generated for the four input parameters of the FEA MLG beam model (n_x, n_y, n_z and aircraft mass). The corresponding displacement and rotation values were then computed using the FEA MLG beam model surrogate model developed previously in this chapter. This resulted in the generation of the input training dataset to be used to train the surrogate model of the FEA stress model. An example of the input training data can be seen in Figure 8.11 for different combinations of displacements and rotations. The original linear elastic FEA stress model was then evaluated to produce the output values of the training data. Examples of such values are shown in Figure 8.12.

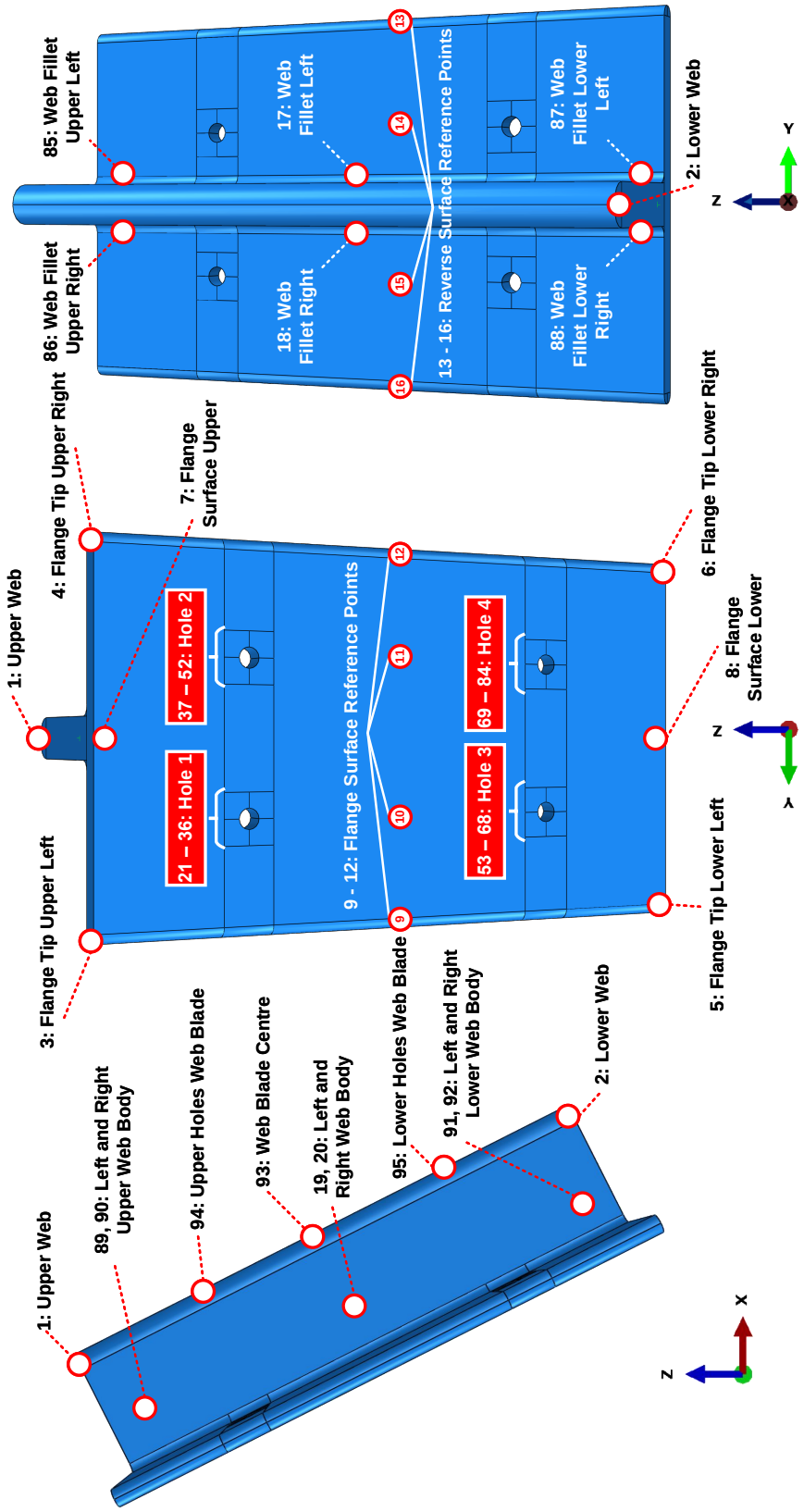

FIGURE 8.10. Initial features of the lower drag brace component to be included in the probabilistic analysis.

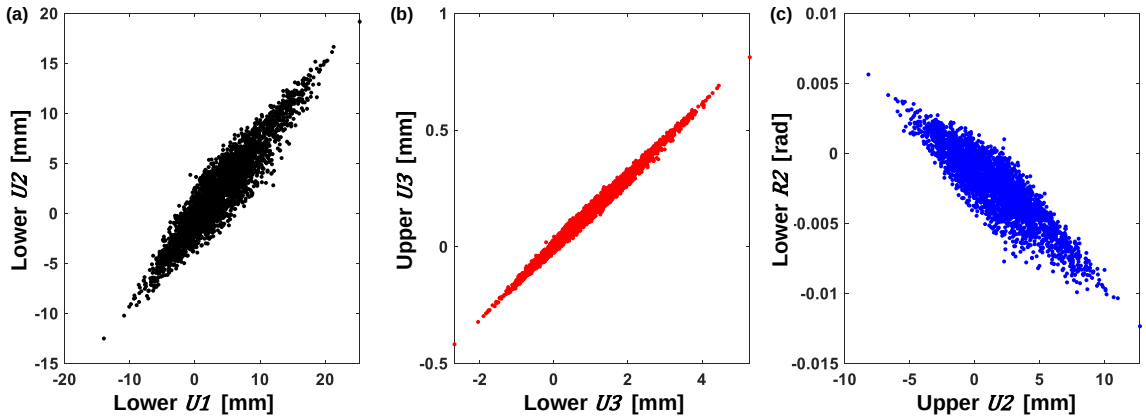

FIGURE 8.11. Load factor training data for the lower drag brace FEA stress model surrogate model, based on an LHS design of the global n_x, n_y, and n_z load factors.

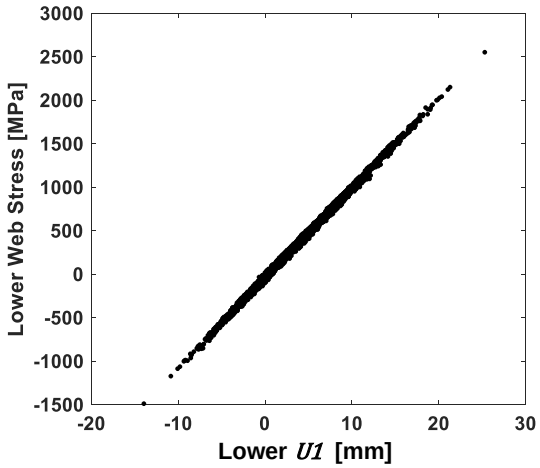

FIGURE 8.12. Stress training data for the lower drag brace linear elastic FEA stress model surrogate model, based on results from the linear static FEA MLG beam model and the LHS design of the global n_x, n_y, and n_z load factors.

In accordance with the surrogate modelling selection process shown previously in Figure 6.18, a quadratic RSM surrogate model was considered as the first candidate for the linear elastic FEA stress model. The quadratic RSM consisted of 91 β coefficients for each component feature and the training of the 95 quadratic RSM surfaces required 0.5 seconds of CPU run-time.

MAE and MPE error metrics were computed for both the training and validation datasets for the quadratic RSM and are shown in Figures 8.13a and 8.13b. The 'Feature ID' values shown in Figure 8.13 correspond to the ID labels shown previously in Figure 8.10. Figure 8.13a shows that the majority of features have $MAE < 20$ MPa, whilst certain specific features show larger MAE values in excess of 50 MPa. Further investigation highlighted that the higher MAE errors were as a result of accessory mounting hole slices where the maximum stress would constantly move across the four through thickness-elements, whilst the lower MAE errors represented accessory mounting hole slices which always demonstrated the maximum stress value at the same through-thickness location. It is expected that this behaviour is observed as a quadratic RSM aims to provide a smooth representation of the stress response, and it is hypothesised that the movement of the maximum stress location across the four through-thickness elements would result in discontinuities in the stress response. In future work, the use of regression trees can be considered to account for discontinuous responses, by providing a different RSM for each through-thickness element [266].

Figure 8.13b shows that the majority of features have MPE values in excess of $MPE > 100\%$. Whilst at first this may appear to be an unacceptable error, plotting the PE values against the predicted stress value, as shown in Figure 8.14 demonstrates that the highest PE values occur around the 'unloaded' or zero-stress state. Therefore, the large MPE values observed for the quadratic RSM are as a result of the sensitivity of the MPE error metric to values close to zero, rather than inaccuracy in the surrogate model.

With a view to reducing the MAE and MPE values, both cubic RSM and GPR surrogate models were trained and evaluated consistent with the proposed surrogate modelling process in Chapter 6. However, it was identified that the cubic RSM and GPR surrogate models resulted in similar MAE and MPE values as the quadratic RSM for each feature. The quadratic RSM required approximately 0.11 seconds of CPU run-time[5] to generate 1,000 predictions, demonstrating a significant reduction in computational expense compared to the original 50 second CPU run-time of the FEA stress model. As a result, the quadratic RSM was selected as the surrogate model for the lower drag brace FEA stress model.

[5]Computer Specifications: 4-core processor (3.40GHz) with 16.0 GB RAM.

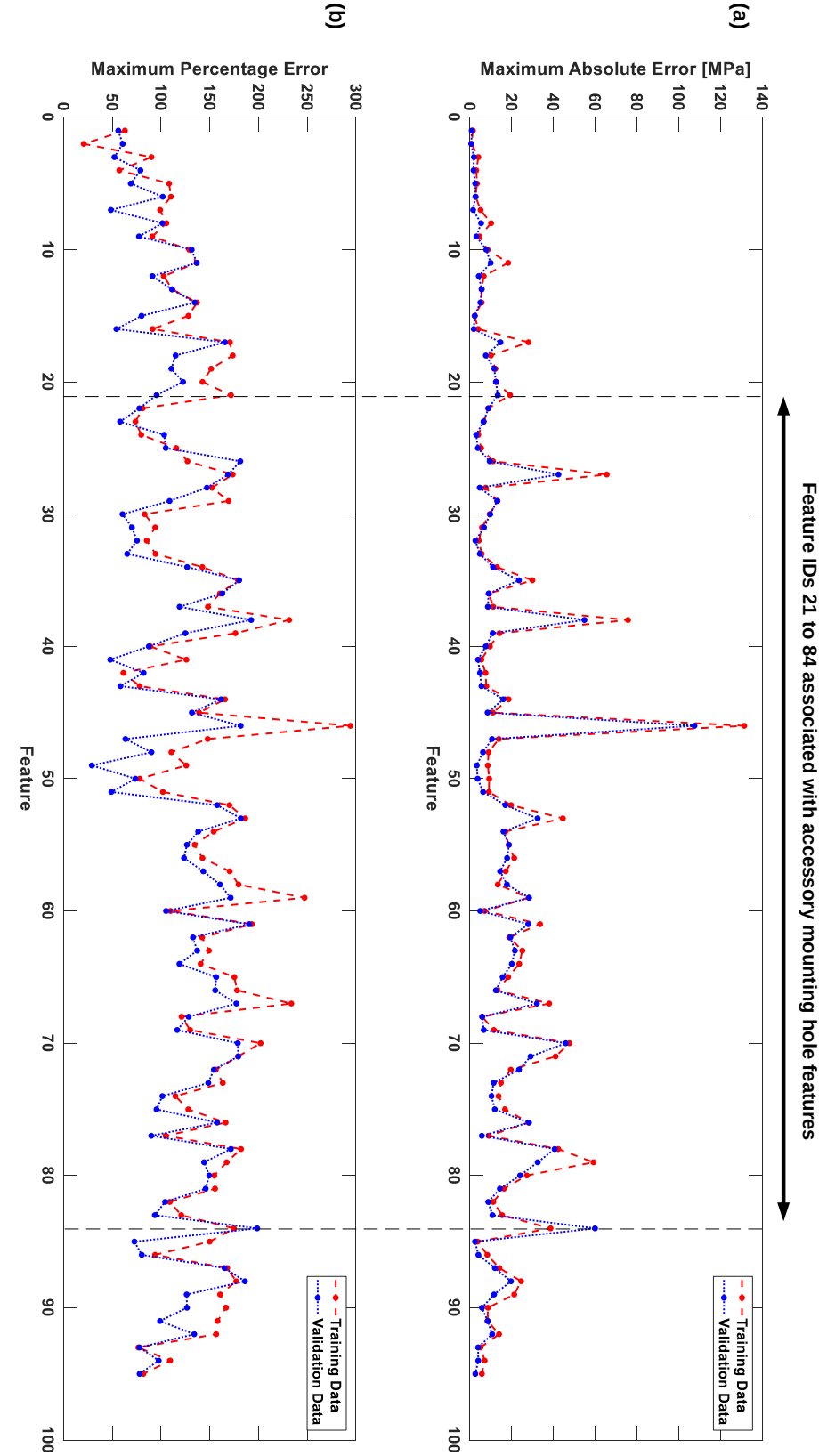

FIGURE 8.13. Error metrics for the quadratic RSM surrogate model of the lower drag brace linear elastic FEA stress model: (a) MAE and (b) MPE for both the training and validation datasets.

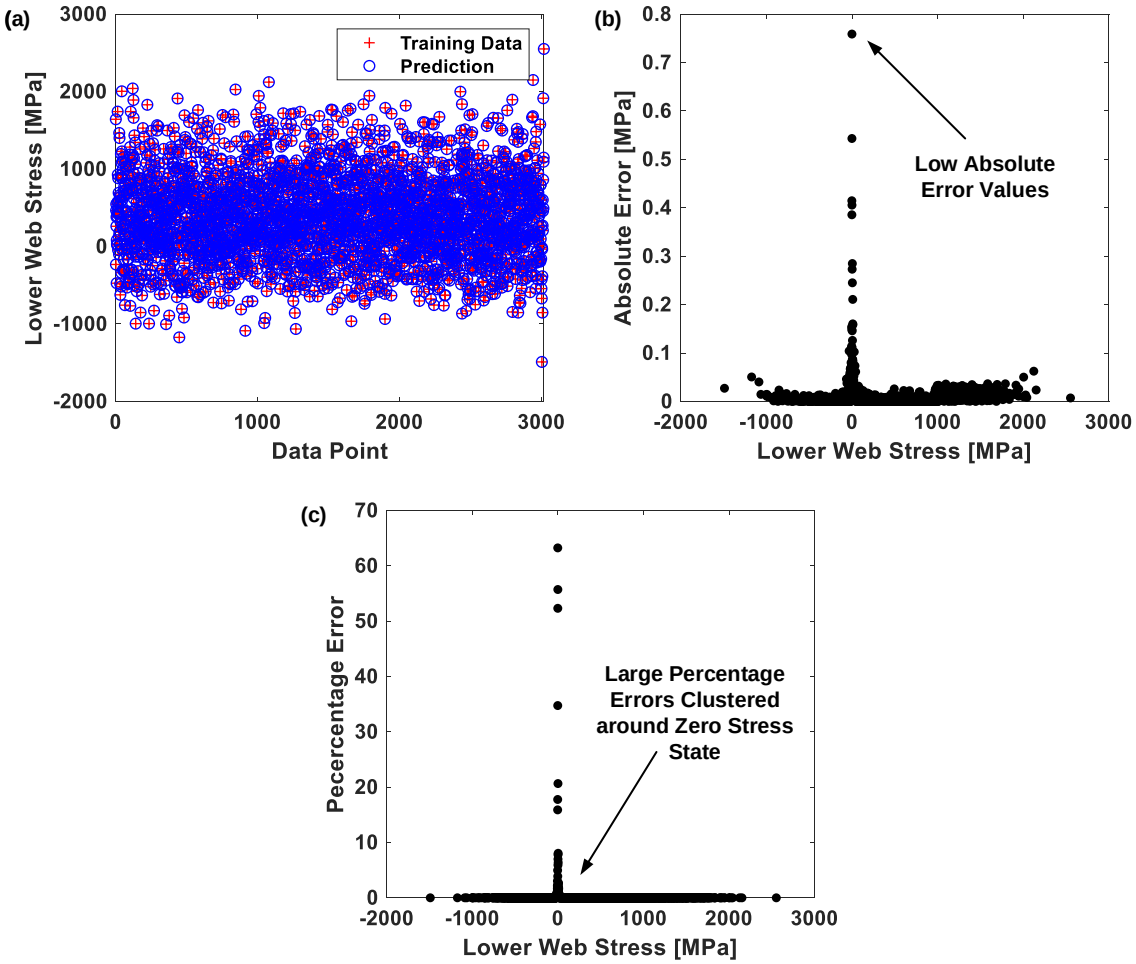

FIGURE 8.14. Example error results for the lower drag brace linear elastic FEA stress quadratic RSM surrogate model: (a) quadratic RSM predictions superimposed on the original training data, (b) AE values and (c) PE values.

8.1.3 Design Parameter Statistical Characterisation

The variability present within the design parameters of the lower drag brace component concern the variability within the loading applied to the component and the material properties of the component. The representation of loading variability is as performed for the lower side-stay case study in Section 7.2, using the statistical simulation of load-time histories described in Chapter 5. The variability in the 4340 steel S-N curve was as characterised in Chapter 4, with variability in N_f being characterised using a 2P Log-Normal distribution at each σ_0 stress level and a Normally-distributed σ_{FL}, with a mean value of 457 MPa and standard deviation of 13 MPa [25].

The σ_{UTS} of the high-tensile steel was characterised as Normally-distributed with a mean of 1,200 MPa with $c_v = 0.0122$ [29, 262].

For the features of the lower drag brace related to the accessory mounting holes, it was assumed that a stress concentration factor K_t was present relating to the surface finish resulting from the machining required to form the holes. Based on work performed by Shigley and Mischke, the variability in K_t was taken as 2P Log-Normally distributed with $\sigma = 1$ and $\lambda = 0.058$ [27].

8.1.4 Implementation of Probabilistic Fatigue Methodology

The purpose of this subsection is to briefly demonstrate how the probabilistic fatigue methodology employed for the lower side-stay case study was adapted for the lower drag brace component. The updated flowchart of the probabilistic analysis framework is shown in Figure 8.15. The similarity between the general probabilistic analysis framework, the framework employed for the lower side-stay case study and the framework for the lower drag brace case study shown in Figure 8.15, highlights the general and application-independent nature of the MCS-SSI methodology.

Figure 8.15 highlights how the cubic RSM surrogate model of the linear static FEA MLG beam model is used to convert the statistically simulated load-time history into displacement/rotation-time histories. The displacement/rotation-time histories are then converted to stress-time histories for each feature using the quadratic RSM surrogate model of the lower drag brace linear elastic FEA stress model. Figure 8.16 demonstrates this process. It should be recalled that the load-time histories are defined as a sequence of load factor values at a given 'load position' as discussed in Section 5.10.4. The loads are then converted into a corresponding sequence of displacement and rotation values. The sequence of these values must be retained across the 12 displacement and rotation values and therefore the sequence is defined using a displacement or rotation 'position', which is an integer value detailing the order of the displacement or rotation value in the overall sequence. Following the conversion of the displacement and rotation values into feature stresses, the resulting stress-time history is only representative of the order in which stresses occur (rather than the actual time been stress values), as described previously in Section 7.2.3. The individual stress-time history for each feature is then processed using rainflow counting, the statistically generated S-N curve for the feature and Miner's rule, to produce an accumulated D_T damage value at the 50,000 flight design safe-life for each MCS iteration.

Parallel processing was again employed to reduce the computational expense of the probabilistic analysis. However, as a result of the large matrices required to store the stress-time histories for each of the features ($\approx 5 \times 10^6$ stress levels per time-history), parallel processing across four CPU cores would effectively represent 380 feature stress-time histories being assessed simultaneously, exceeding the available memory capacity of the hardware used for the case studies of 16 GB RAM. As a result, the number of features to include in the probabilistic analysis of the lower drag brace had to be reduced, following the feature down-selection process defined previously in Section 7.1.2.

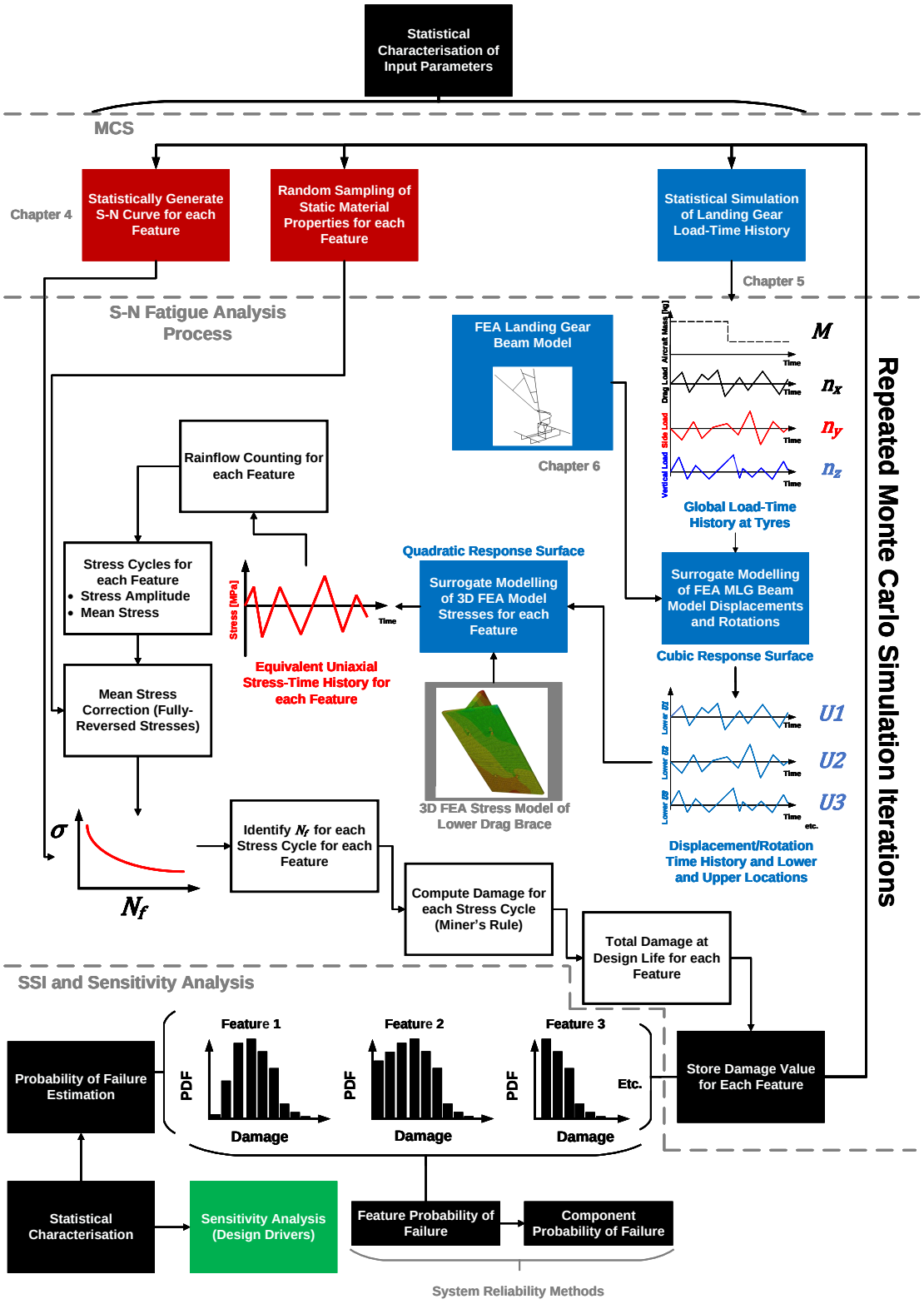

FIGURE 8.15. Flowchart demonstrating the implementation of the probabilistic fatigue methodology to the lower drag brace case study.

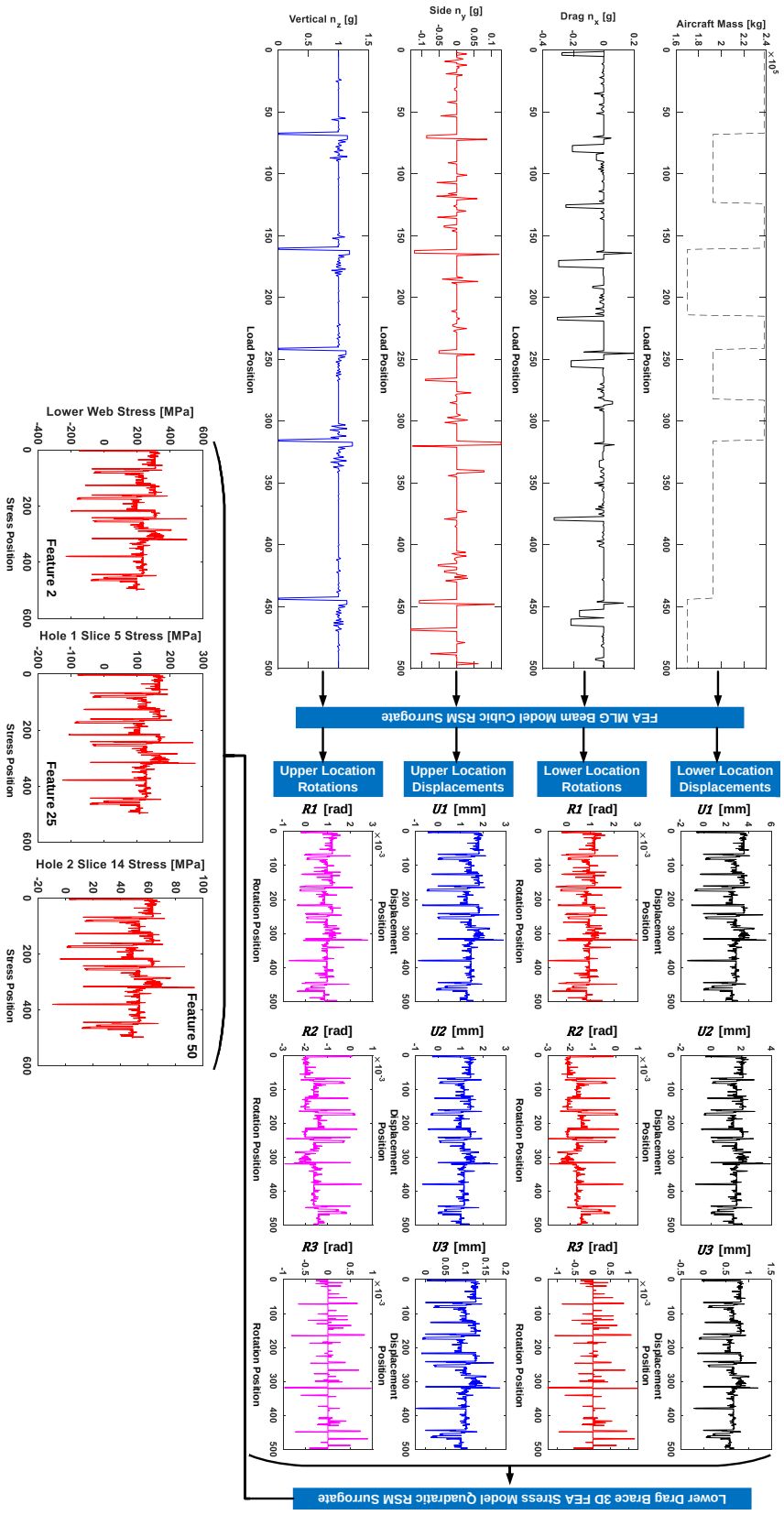

FIGURE 8.16. Conversion of the global MLG load-time history to lower drag brace feature stress-time histories using the surrogate models for the FEA MLG beam model and 3D FEA stress model of the lower drag brace (*note: figure only shows a segement of five flights out of a statistically simulated 50,000 flight design life*).

Final Feature Down-Selection

In order to further down-select the features for the lower drag brace component using the feature down-selection process, deterministic fatigue analysis was performed with a $PoS = 99\%$ S-N curve, as this would highlight features that would remain undamaged during the existing deterministic analysis process. The deterministic analysis highlighted that only 22 of the 95 features accumulated fatigue damage. Unfortunately, this number of features still exceeded the available 16.0 GB RAM memory capacity.

As previously shown in the down-selection process in Figure 7.1, a short probabilistic fatigue analysis (without parallel processing) was performed of $N_{MCS} = 1{,}000$ iterations. The resulting D_T values for each feature were then statistically characterised as shown in Table 8.2. From Table 8.2 it can be observed that 13 features demonstrated a quantifiable p_f and as a result, these features were the final features to be down-selected and included within the probabilistic fatigue analysis of the lower drag brace. The final features are shown overleaf in Figure 8.17

TABLE 8.2. Statistical characterisation and $P_{f_{dist}}$ at $N_{MCS} = 1{,}000$ for lower drag brace feature down-selection from 95 to 22 features. *U = Upper, UL = Upper Left, UR = Upper Right*.

Feature ID	Feature	Distribution	Distribution Parameter Estimate		$P_{f_{dist}}$
			Scale σ	Shape λ	
2	Lower Web	2P Log-Normal	-1.930	0.375	1.3625×10^{-7}
3	Flange Tip UL	2P Weibull	1.529×10^{-7}	0.432	2.032×10^{-5}
4	Flange Tip UR	2P Log-Normal	-12.101	0.830	0
7	Flange Surface U	2P Log-Normal	-11.015	0.815	0
23	Hole 1 Slice 3	2P Log-Normal	-7.662	1.157	1.745×10^{-11}
24	Hole 1 Slice 4	2P Log-Normal	-3.636	0.868	1.413×10^{-5}
25	Hole 1 Slice 5	2P Log-Normal	-5.379	0.946	6.550×10^{-9}
26	Hole 1 Slice 6	2P Weibull	4.112×10^{-8}	0.478	0
31	Hole 1 Slice 11	2P Log-Normal	-8.902	1.306	4.597×10^{-12}
32	Hole 1 Slice 12	2P Log-Normal	-4.138	0.905	2.424×10^{-6}
33	Hole 1 Slice 13	2P Log-Normal	-5.519	0.999	1.672×10^{-8}
34	Hole 1 Slice 14	2P Weibull	1.122×10^{-7}	0.398	0
39	Hole 2 Slice 3	2P Weibull	1.783×10^{-6}	1.163	0
40	Hole 2 Slice 4	2P Log-Normal	-4.914	0.979	2.568×10^{-7}
41	Hole 2 Slice 5	2P Log-Normal	-3.493	0.875	3.260×10^{-5}
42	Hole 2 Slice 6	2P Log-Normal	-7.773	1.177	2.028×10^{-11}
47	Hole 2 Slice 11	2P Weibull	1.122×10^{-7}	0.398	0
48	Hole 2 Slice 12	2P Log-Normal	-4.962	0.948	8.255×10^{-8}
49	Hole 2 Slice 13	2P Log-Normal	-3.121	0.838	9.823×10^{-5}
50	Hole 2 Slice 13	2P Log-Normal	-6.725	1.009	1.314×10^{-11}
73	Hole 4 Slice 5	2P Weibull	1.022×10^{-6}	10.578	0
81	Hole 4 Slice 13	2P Weibull	1.054×10^{-6}	4.572	0

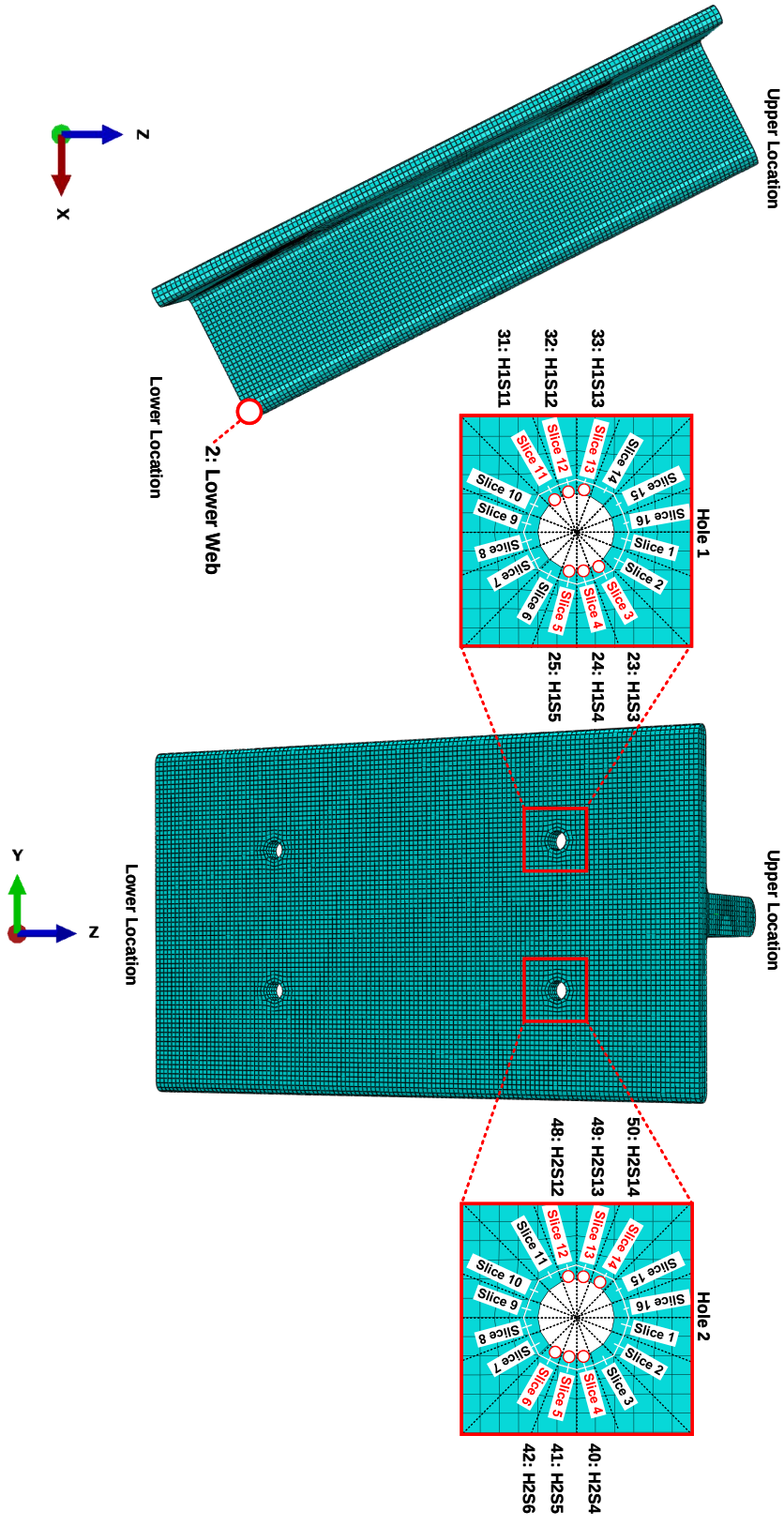

FIGURE 8.17. The final 13 features to be included in the probabilistic fatigue analysis of the lower drag brace.

The final 13 features shown in Figure 8.17 to be included in the lower drag brace probabilistic fatigue analysis were as follows:

- Lower Web (Feature 2)
- Hole 1 Slice 3 (Feature 23)
- Hole 1 Slice 4 (Feature 24)
- Hole 1 Slice 5 (Feature 25)
- Hole 1 Slice 11 (Feature 31)
- Hole 1 Slice 12 (Feature 32)
- Hole 1 Slice 13 (Feature 33)
- Hole 2 Slice 4 (Feature 40)
- Hole 2 Slice 5 (Feature 41)
- Hole 2 Slice 6 (Feature 42)
- Hole 2 Slice 12 (Feature 48)
- Hole 2 Slice 13 (Feature 49)
- Hole 2 Slice 14 (Feature 50)

The down-selection to 13 lower drag brace features reduced the memory demand to the extent that parallel processing over two CPU cores was possible. This enabled two MCS iterations to be performed simultaneously. Using parallel processing, the CPU run-time[6] to perform the required $N_{MCS} = 1 \times 10^5$ MCS iterations for the probabilistic fatigue analysis was 17.5 days. This resulted in each MCS iteration requiring approximately 15.2 seconds of CPU run-time. The greater CPU run-time for each MCS iteration compared to the lower side-stay case study was as a result of the need to use two surrogate models to generate the stress-time histories.

Finally, returning to the quadratic RSM surrogate model of the FEA stress surrogate model, Table 8.3 overleaf shows the MAE values for the final 13 features for both the training and validation dataset. It can be observed from Table 8.3 that the MAE values are all less than 10 MPa, demonstrating that the quadratic RSM provides sufficient accuracy when representing the FEA stress surrogate model in the probabilistic fatigue analysis of the lower drag brace component.

[6]Computer Specifications: 4-core processor (3.40GHz) with 16.0 GB RAM.

TABLE 8.3. MAE values for the final 13 features of the lower drag brace stress model quadratic RSM surrogate model.

Feature ID	Feature	MAE_T (MPa)	MAE_V (MPa)
2	Lower Web	0.759	0.718
23	Hole 1 Slice 3	6.676	6.530
24	Hole 1 Slice 4	4.059	3.036
25	Hole 1 Slice 5	5.403	3.840
31	Hole 1 Slice 11	5.824	6.776
32	Hole 1 Slice 12	4.290	2.660
33	Hole 1 Slice 13	5.660	4.771
40	Hole 2 Slice 4	9.584	7.597
41	Hole 2 Slice 5	5.520	3.893
42	Hole 2 Slice 6	7.497	4.871
48	Hole 2 Slice 12	8.949	6.300
49	Hole 2 Slice 13	8.601	3.302
50	Hole 2 Slice 14	9.254	3.740

8.1.5 Probabilistic Results

Following the $N_{MCS} = 1 \times 10^5$ iterations, the D_T accumulated damage values were collected for the 13 features of the lower drag brace component. Figure 8.18 shows the histograms of the D_T values at 50,000 flights for the Lower Web (Feature 2), Hole 1 Slice 11 (Feature 31) and Hole 2 Slice 13 (Feature 49) in subplots (a), (b) and (c) respectively. The maximum x-axis value shown for all histograms within this chapter represents the maximum D_T value observed for the given feature.

From reviewing Figure 8.18, it can be observed that all features demonstrated positive skew. However, when comparing Hole 1 Slice 11 (Figure 8.18b) to the Lower Web feature (Figure 8.18a), it can be seen that the D_T histogram for the Hole 1 Slice 11 feature appears to start at a maximum value of probability density, whereas the histogram for the Lower Web D_T values shows an increase up to the maximum probability density from zero.

The statistical characterisation process based upon r and $RMSE$ for GoF testing was employed for the lower side-stay case study in Section 7.2.6 and defined previously in Figure 4.1 was also used to down-select candidate distributions for the lower drag brace D_T values. Due to the complex and varying histogram shapes shown in Figure 8.18, additional candidate distributions were considered, including Birnbaum Saunders, Burr and Gamma distributions[7] (All distribution types are fully defined in Appendix B). For D_T histograms where the histogram starts at the maximum probability density value, the Exponential distribution was also considered for down-selection.

[7] All of these additional candidate distributions can only be fitted using MLE methods.

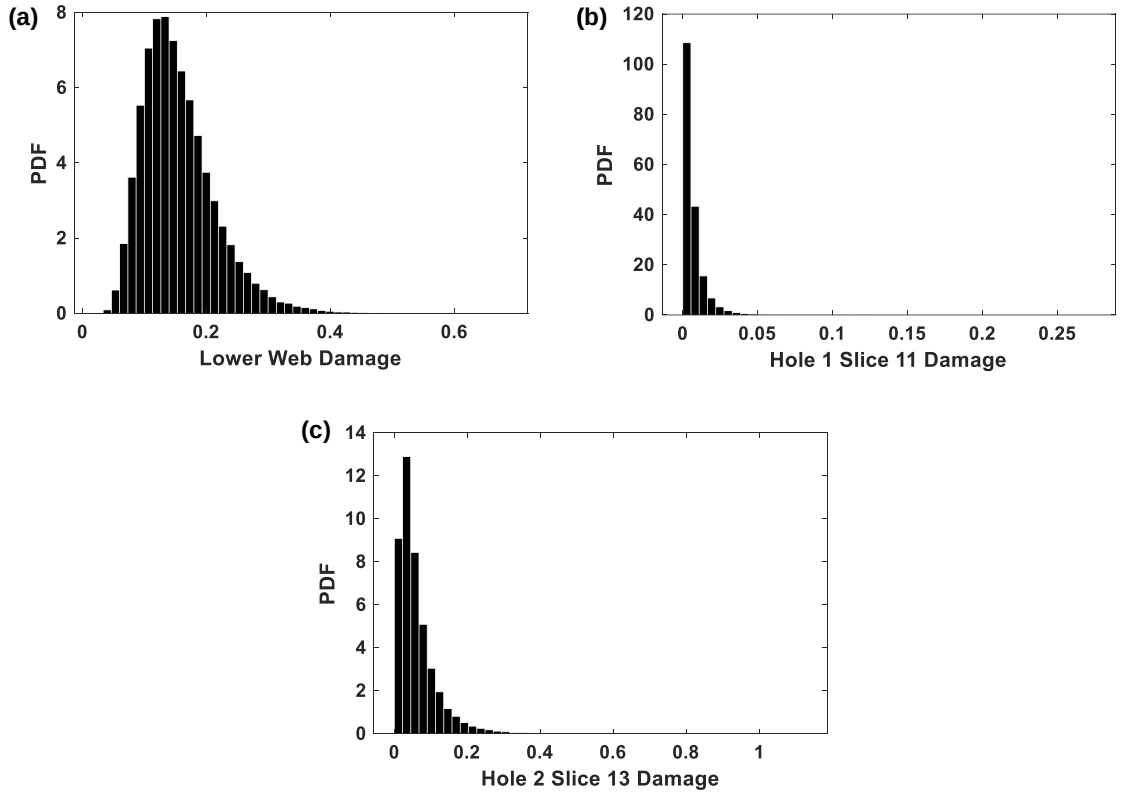

FIGURE 8.18. Examples of D_T damage histograms for features of the lower drag brace: (a) Lower Web, (b) Hole 1 Slice 11 and (c) Hole 2 Slice 13.

Table 8.4 shows the PPLR and MLE distribution parameter estimates for the Lower Web feature. The 3P Log-Normal distribution was rejected due to estimating a negative δ threshold value, which inferred negative fatigue damage accumulation which is not physically representative of fatigue as a failure mode. The GoF for each candidate distribution was assessed using $RMSE$ values between the ECDF and the fitted CDF. PPLR r correlation coefficients were also computed where possible.

Table 8.4 shows that only the 2P Log-Normal, Gumbel Maximum and Birnbaum Saunders distributions provided an acceptable visual fit between the CDF and the ECDF, as supported by the $RMSE$ values which are significantly lower than the other candidate distributions. Table 8.4 demonstrates that the 2P Log-Normal distribution provided the lowest $RMSE$ value and the highest PPLR r value, suggesting that it should be selected as the distribution to characterise the variability in the Lower Web D_T values. Figure 8.19 shows the fitted 2P Log-Normal distribution compared to the D_T histogram and ECDF for the Lower Web feature. A good-fit can be observed for the 2P Log-Normal distribution for both the histogram and the ECDF in Figure 8.19.

TABLE 8.4. Statistical characterisation of the variability in D_T for the Lower Web feature of the lower drag brace.

Distribution	Fitting Type (*Rank Equation*)	Distribution Parameter Estimate			Skewness	$\gamma = 1.151$	
		Threshold δ	Scale σ	Shape λ	Good CDF Fit?	$RMSE$	r
2P Log-Normal	PPLR (*Gumbel*)	-	-1.931	0.371	Y	**0.002**	**1**
	MLE	-	-1.931	0.371	Y	**0.002**	-
3P Log-Normal	PPLR predicts zero threshold. 2P Log-Normal distribution fitted. MLE predicts negative threshold. Reject distribution.						
2P Weibull	PPLR (*Mean*)	-	0.172	3.262	N	0.042	0.9717
	MLE	-	0.174	2.723	N	0.039	-
3P Weibull	PPLR (*Hazen*)	0.028	0.142	2.669	N	0.030	0.9876
	MLE	0.028	0.144	2.276	N	0.029	-
Gumbel Max	PPLR (*EV*)	-	0.046	0.129	Y	0.004	0.9999
	MLE	-	0.046	0.129	Y	0.004	-
Log-Logistic	PPLR (*Mean*)	-	-1.931	0.205	N	0.015	0.9960
	MLE	-	-1.930	0.377	N	0.010	-
Birnbaum Saunders	MLE	-	-0.145	0.377	Y	0.003	-
Burr	MLE	1.189	0.154	4.462	N	0.010	-
Gamma	MLE	-	0.021	7.478	N	0.014	-

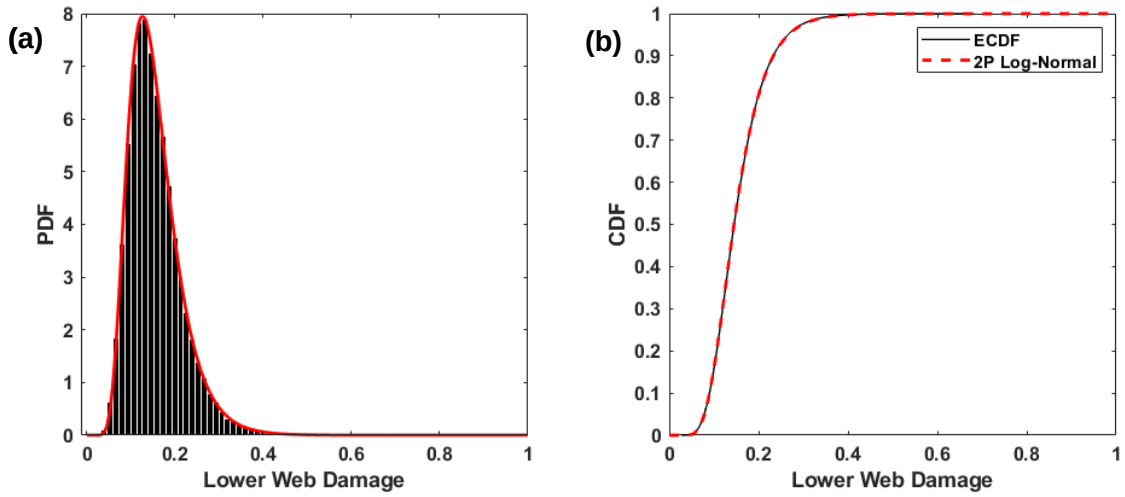

FIGURE 8.19. Statistical characterisation of the D_T variability in the Lower Web feature of the lower drag brace component using a 2P Log-Normal distribution compared to (a) the D_T histogram and (b) the ECDF.

The histogram for the D_T values of the Hole 1 Slice 11 feature shown previously in Figure 8.18b shows the greatest positive skew for all of the lower drag brace features, with $\gamma = 5.537$. Therefore, an Exponential distribution was also considered as a candidate distribution as shown in Table 8.5. Table 8.5 shows that the Burr distribution was the only candidate distribution type to provide an acceptable visual fit to the ECDF, as supported by the $RMSE$ value, which is significantly smaller for the Burr distribution than any of the other candidate distributions.

Table 8.5 also shows that the Exponential distribution failed to provide a good-fit to the D_T value for the Hole 1 Slice 11 feature due to the high $RMSE$ value and low r value.

Figure 8.20 shows the fitted Burr distribution to the D_T histogram and ECDF for the Hole 1 Slice 11 feature. It can be seen from Figure 8.20 that the Burr distribution provides a good-fit to both the histogram and the ECDF.

TABLE 8.5. Statistical characterisation of the variability in D_T for the Hole 1 Slice 11 feature of the lower drag brace.

Distribution	Fitting Type (*Rank Equation*)	Distribution Parameter Estimate			Skewness	$\gamma = 5.537$	
		Threshold δ	Scale σ	Shape λ	Good CDF Fit?	$RMSE$	r
2P Log-Normal	PPLR (*Hazen*)	-	-8.903	1.498	N	0.029	0.9435
	MLE	-	-8.903	1.413	N	0.023	-
3P Log-Normal	PPLR predicts zero threshold. 2P Log-Normal distribution fitted. MLE predicts negative threshold. Reject distribution.						
2P Weibull	PPLR (*Hazen*)	-	2.644×10^{-4}	0.869	N	0.036	0.9573
	MLE	-	2.568×10^{-4}	0.837	N	0.028	-
3P Weibull	PPLR predicts zero threshold. 2P Weibull distribution fitted. MLE predicts negative threshold. Reject distribution.						
Gumbel Max	PPLR (*EV*)	-	6.586×10^{-5}	3.812×10^{-4}	N	0.449	0.8817
	MLE	-	1.499×10^{-4}	1.883×10^{-4}	N	0.146	-
Log-Logistic	PPLR (*Mean*)	-	-8.903	0.820	N	0.022	0.9500
	MLE	-	-8.843	0.741	N	0.012	-
Exponential	PPLR (*EV*)	-	4.587×10^{-4}	-	N	0.433	0.9396
	MLE	-	2.859×10^{-4}	-	N	0.443	-
Birnbaum Saunders	MLE failed to converge. Birnbaum Saunders distribution rejected						
Burr	MLE	2.277	3.913×10^{-4}	1.100	Y	**0.005**	-
Gamma	MLE	-	3.577×10^{-4}	0.799	N	0.044	-

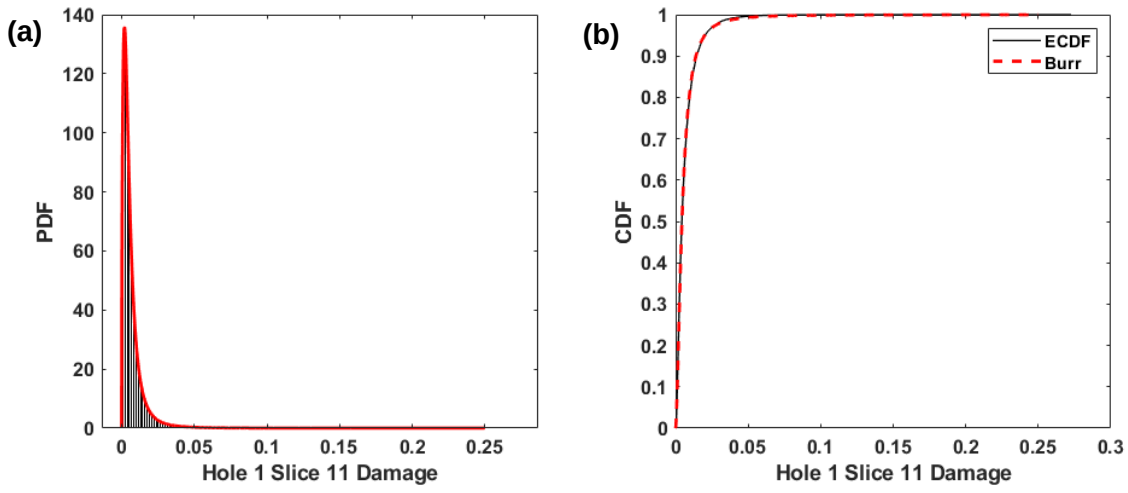

FIGURE 8.20. Statistical characterisation of the D_T variability in the Hole 1 Slice 11 feature of the lower drag brace component using a Burr distribution compared to (a) the D_T histogram and (b) the ECDF.

The final D_T histogram shown previously in Figure 8.18 is for the Hole 2 Slice 13 feature of the lower drag brace. Table 8.6 shows the statistical characterisation results for this feature. It can be observed from Table 8.6 that the 2P Log-Normal distribution provides the lowest $RMSE$ and highest PPLR r values and as a result, was selected as the candidate distribution to characterise the variability in the Hole 2 Slice 13 D_T damage value. Figure 8.21 shows the corresponding good-fit between the fitted 2P Log-Normal distribution and the D_T histogram and ECDF for the Hole 2 Slice 13 feature.

TABLE 8.6. Statistical characterisation of the variability in D_T for the Hole 2 Slice 13 feature of the lower drag brace.

Distribution	Fitting Type (*Rank Equation*)	Distribution Parameter Estimate			Skewness	$\gamma = 2.926$	
		Threshold δ	Scale σ	Shape λ	Good CDF Fit?	$RMSE$	r
2P Log-Normal	PPLR (*Hazen*)	-	-3.114	0.830	Y	**0.007**	**0.9992**
	MLE	-	-3.114	0.829	Y	**0.007**	-
3P Log-Normal	PPLR predicts zero threshold. 2P Log-Normal distribution fitted. MLE predicts negative threshold. Reject distribution.						
2P Weibull	PPLR (*Mean*)	-	0.065	1.513	N	0.037	0.9783
	MLE	-	0.067	1.259	N	0.034	-
3P Weibull	PPLR (*Mean*)	3.410×10^{-4}	0.065	1.497	N	0.038	0.9801
	MLE	3.452×10^{-4}	0.066	1.251	N	0.032	-
Gumbel Max	PPLR (*EV*)	-	0.045	0.036	N	0.065	0.9637
	MLE	-	0.032	0.040	N	0.044	-
Log-Logistic	PPLR (*Mean*)	-	-3.114	0.459	N	0.017	0.9952
	MLE	-	-3.102	0.474	N	0.011	-
Birnbaum Saunders	MLE	-	0.044	0.908	N	0.017	-
Burr	MLE	1.470	0.060	1.881	N	0.009	-
Gamma	MLE	-	0.037	1.670	N	0.028	-

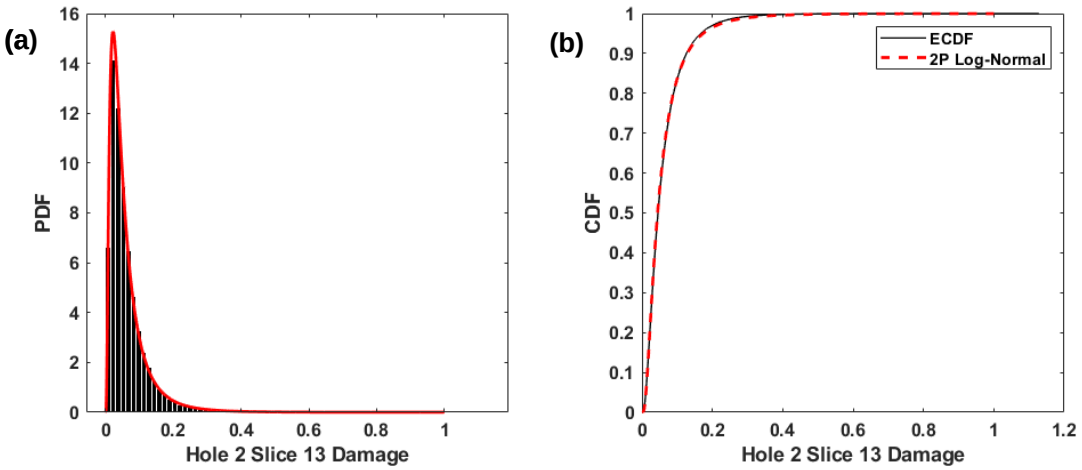

FIGURE 8.21. Statistical characterisation of the D_T variability in the Hole 2 Slice 13 feature of the lower drag brace component using a 2P Log-Normal distribution compared to (a) the D_T histogram and (b) the ECDF.

The statistical characterisation process was repeated for all remaining features of the lower drag brace components, and the full results are presented in Appendix H. Table 8.7 provides a summary of the final distributions used to characterise the variability in D_T damage values at each of the lower drag brace features. It can be observed from Table 8.7 that the features are best characterised by either a 2P Log-Normal distribution or a Burr distribution. The statistical characterisation results in Appendix H demonstrate how for most features, that the 2P Log-Normal distribution and Burr distribution had similar $RMSE$ GoF results. Therefore, it is expected that the p_f estimates for the lower drag brace features may be susceptible to 'tail-sensitivity', as demonstrated for the lower side-stay case study previously in Figure 7.20. A further discussion of tail-sensitivity will be presented in Chapter 9.

TABLE 8.7. Statistical characterisation results for the D_T values of the lower drag brace features.

Feature	Distribution	Distribution Parameter Estimate			$RMSE$
		Threshold δ	Scale σ	Shape λ	
Lower Web	2P Log-Normal	-	-1.931	0.371	0.002
Hole 1 Slice 3	Burr	1.664	8.285×10^{-4}	1.309	0.008
Hole 1 Slice 4	2P Log-Normal	-	-3.629	0.872	0.006
Hole 1 Slice 5	2P Log-Normal	-	-5.373	0.985	0.008
Hole 1 Slice 11	Burr	2.277	3.913×10^{-4}	1.100	0.005
Hole 1 Slice 12	2P Log-Normal	-	-4.169	0.905	0.008
Hole 1 Slice 13	2P Log-Normal	-	-5.477	0.993	0.008
Hole 2 Slice 4	2P Log-Normal	-	-4.929	0.954	0.007
Hole 2 Slice 5	2P Log-Normal	-	-3.523	0.857	0.007
Hole 2 Slice 6	Burr	1.677	7.882×10^{-4}	1.314	0.008
Hole 2 Slice 12	2P Log-Normal	-	-4.956	0.960	0.009
Hole 2 Slice 13	2P Log-Normal	-	-3.114	0.829	0.007
Hole 2 Slice 14	Burr	1.581	0.002	1.420	0.009

Consistent with the probabilistic fatigue methodology described in Chapter 3, GPD tail-fitting was performed using MLE methods based on a tail dataset of size $N_t = 474$. The resulting GPD distribution parameter estimates are shown in Table 8.8.

Finally, the 'raw' MCS D_T damage values were inspected for all features to identify the number of 'failure' (i.e. $D_T \geq 1$) MCS iterations 'N_{fail}'. It was observed that $N_{fail} = 2$ for the Hole 2 Slice 13 feature across the $N_{MCS} = 1 \times 10^5$ iterations. No other lower drag brace features demonstrated failure iterations during the $N_{MCS} = 1 \times 10^5$ MCS.

TABLE 8.8. Tail-fitting results for the D_T values of the lower drag brace features.

Feature	GPD Parameters		
	Threshold t	Scale σ	Shape λ
Lower Web	0.374	0.044	0.058
Hole 1 Slice 3	0.007	0.002	0.170
Hole 1 Slice 4	0.230	0.056	0.189
Hole 1 Slice 5	0.050	0.015	0.171
Hole 1 Slice 11	0.003	9.453×10^{-4}	0.166
Hole 1 Slice 12	0.142	0.043	0.090
Hole 1 Slice 13	0.046	0.013	0.175
Hole 2 Slice 4	0.073	0.022	0.128
Hole 2 Slice 5	0.240	0.072	0.074
Hole 2 Slice 6	0.007	0.003	0.115
Hole 2 Slice 12	0.072	0.021	0.080
Hole 2 Slice 13	0.331	0.078	0.145
Hole 2 Slice 14	0.017	0.006	0.088

Following the statistical characterisation of the MCS probabilistic analysis results, the p_f estimates for the lower drag brace component features could be generated using the methods described in Chapter 3. Table 8.9 shows the $P_{f_{dist}}$, $P_{f_{tail}}$ and $P_{f_{MCS}}$ estimates for each feature of the lower drag brace included in the probabilistic analysis. Table 8.9 shows that the Hole 1 Slice 4, Hole 2 Slice 5 and Hole 2 Slice 13 features are the features with the highest p_f values for the lower drag brace component, with $P_{f_{dist}}$ estimates in the order of 10^{-5}. Figure 8.22 visualises the location of the $P_{f_{dist}}$ values.

It can be observed from Table 8.9 that only three of the lower drag brace features have $P_{f_{dist}}$ estimates higher than the order of 10^{-7}. This therefore suggests the many of the remaining features of the lower drag brace component are over-designed due to their low and in some cases, negligible (i.e. 10^{-9}) p_f estimates[8]. The consequence of over-designing of components will be discussed in Chapter 9. It should be noted that the $P_{f_{dist}}$ values in Table 8.9 demonstrate that specific features of components tend to dominate the overall component-level p_f.

Table 8.9 also shows that the Hole 1 Slice 4, Hole 2 Slice 5 and Hole 2 Slice 13 features also have the highest $P_{f_{tail}}$ estimates using GPDs, with $P_{f_{tail}}$ values in the order of 10^{-6}. The only feature to demonstrate failure MCS iterations was the Hole 2 Slice 13 feature, which is supported by this feature also having the highest $P_{f_{dist}}$ and $P_{f_{tail}}$ estimates. The features showing the highest p_f values in Table 8.9 correlated with the features showing the highest hot-spot stresses previously in Figure 8.8.

[8]It is of course noted that component geometry and features may be driven by other design considerations such as stiffness requirements and manufacturing constraints.

TABLE 8.9. The p_f estimates for the features of the lower drag brace.

Feature (ID)	p_f Estimation Method				
	$P_{f_{dist}}$	$P_{f_{dist}}$ 95% CI	$P_{f_{tail}}$	$P_{f_{MCS}}$	$P_{f_{MCS+2\sigma}}$
Lower Web (2)	9.395×10^{-8}	1.067×10^{-7}	1.535×10^{-7}	0	0
Hole 1 Slice 3 (23)	1.946×10^{-7}	2.526×10^{-7}	4.796×10^{-14}	0	0
Hole 1 Slice 4 (24)	1.589×10^{-5}	1.729×10^{-5}	5.258×10^{-6}	0	0
Hole 1 Slice 5 (25)	2.480×10^{-8}	2.849×10^{-8}	2.623×10^{-9}	0	0
Hole 1 Slice 11 (31)	2.923×10^{-9}	4.454×10^{-9}	1.110×10^{-16}	0	0
Hole 1 Slice 12 (32)	2.068×10^{-6}	2.289×10^{-6}	5.287×10^{-8}	0	0
Hole 1 Slice 13 (33)	1.767×10^{-8}	2.036×10^{-8}	1.587×10^{-9}	0	0
Hole 2 Slice 4 (40)	1.190×10^{-7}	1.349×10^{-7}	2.212×10^{-9}	0	0
Hole 2 Slice 5 (41)	1.992×10^{-5}	2.163×10^{-5}	1.924×10^{-6}	0	0
Hole 2 Slice 6 (42)	1.438×10^{-7}	1.888×10^{-7}	0	0	0
Hole 2 Slice 12 (48)	1.205×10^{-7}	1.365×10^{-7}	2.443×10^{-11}	0	0
Hole 2 Slice 13 (49)	8.621×10^{-5}	9.247×10^{-5}	1.827×10^{-5}	2.000×10^{-5}	4.828×10^{-5}
Hole 2 Slice 14 (50)	8.765×10^{-7}	9.553×10^{-7}	1.110×10^{-16}	0	0

From comparing the results from the various p_f estimation methods across Table 8.9, it can be observed that there is a significant difference between the $P_{f_{dist}}$ and $P_{f_{tail}}$ values for each feature by up to 7 orders of magnitude for specific features (e.g. Hole 1 Slice 3). However, at other features that show higher p_f values (e.g. Hole 2 Slice 13), the $P_{f_{tail}}$ values show a much better agreement with the $P_{f_{dist}}$ values, with both estimates displaying the same order of magnitude. In a similar manner to the lower side-stay case study, this is expected to be as a result of the sensitivity of $P_{f_{tail}}$ estimates to the specific D_T values observed during the MCS. For features with a higher $P_{f_{dist}}$ value, the GPD tail dataset will contain more higher-magnitude D_T values, resulting in $P_{f_{tail}}$ estimates that are similar to the $P_{f_{dist}}$ values. $P_{f_{dist}}$ estimates will show reduced sensitivity to the specific D_T values generated during the MCS compared to $P_{f_{tail}}$ and $P_{f_{MCS}}$, as $P_{f_{dist}}$ estimates are generated using the whole range of D_T values, rather than a few specific D_T values as for $P_{f_{tail}}$ and $P_{f_{MCS}}$.

The sensitivity of the $P_{f_{tail}}$ estimates can be further highlighted by considering the Hole 2 Slice 5 feature from Table 8.9. Hole 2 Slice 5 lies directly opposite the Hole 2 Slice 13 feature, and therefore, it was expected that the estimated p_f values for the two features would be similar, due to the similar stress states at the two locations on Hole 2, as highlighted in Figure 8.23. From Table 8.9, it can be seen that the $P_{f_{dist}}$ estimates show the same order of magnitude for the two features (10^{-5}), whilst the $P_{f_{tail}}$ estimates result in an order of magnitude difference for p_f of 10^{-6} and 10^{-5} for the Hole 2 Slice 5 and Hole 2 Slice 13 features respectively. The difference in $P_{f_{tail}}$ estimate values for the two features, despite their similar stress states shown in Figure 8.23, is expected to be directly as a result of the sensitivity of $P_{f_{tail}}$ estimates to the specific D_T values observed during the MCS.

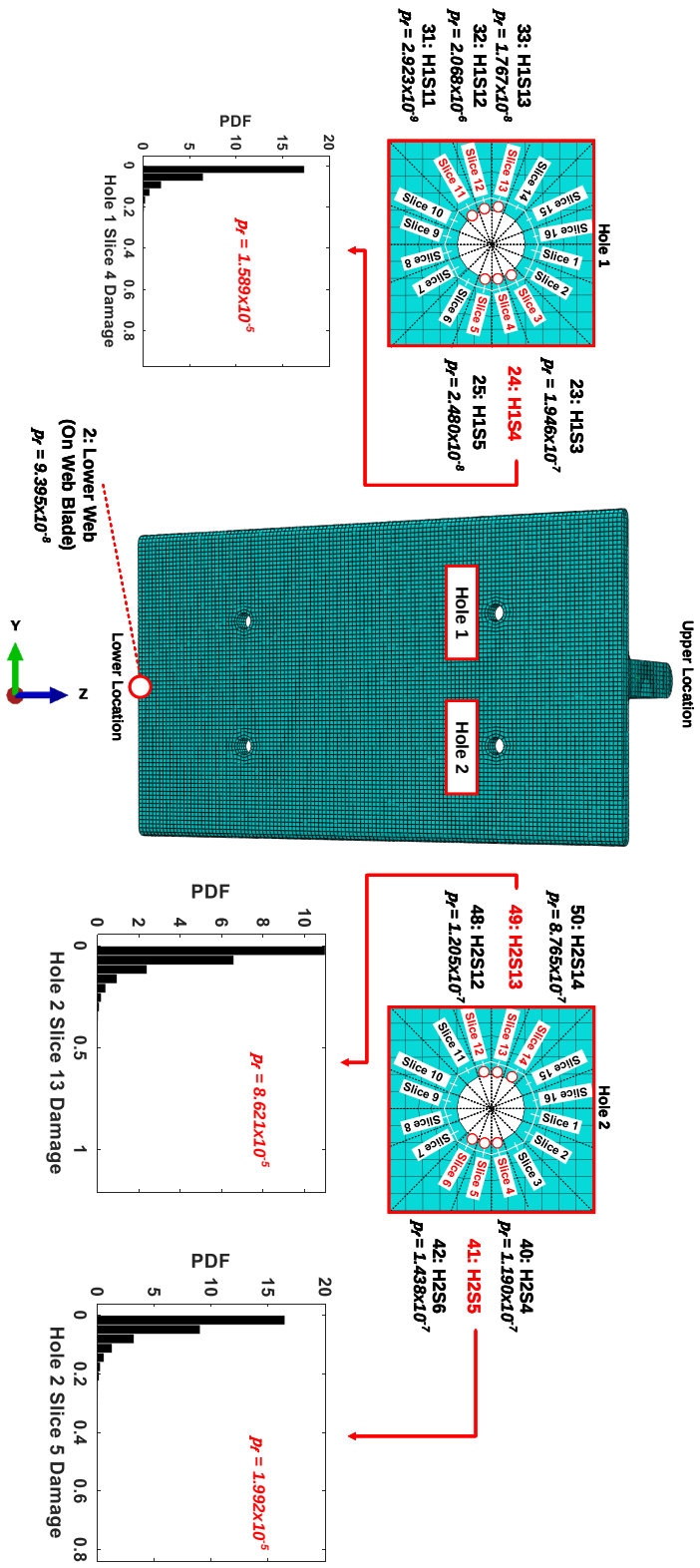

FIGURE 8.22. D_T histograms and $P_{f_{dist}}$ estimates for the lower drag brace features.

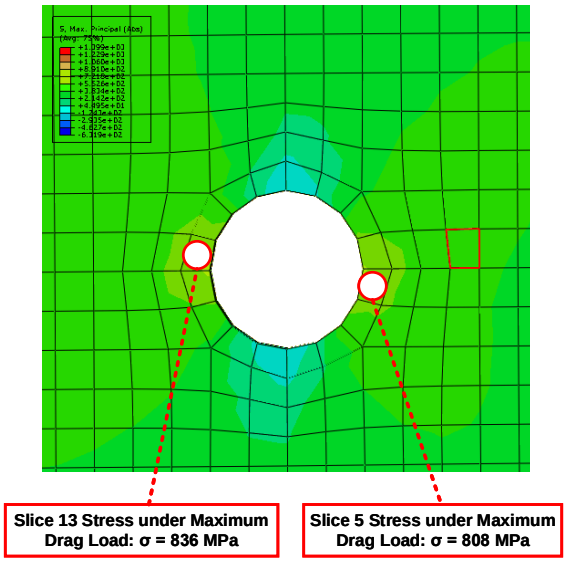

FIGURE 8.23. Approximately equal stresses at opposing hole slices for the accessory mounting holes.

As a result, if $P_{f_{dist}}$ estimates are shown to provide good agreement with the $P_{f_{MCS}}$ and $P_{f_{tail}}$ estimates for a feature with a higher p_f (e.g. at Hole 2 Slice 13 all p_f estimation methods resulted in a p_f with the order of 10^{-5}) , it is expected that the $P_{f_{dist}}$ values will also provide accurate p_f estimates at other features. This effect is due to the lack of sensitivity of $P_{f_{dist}}$ estimates to the specific D_T values observed during the MCS. However, $P_{f_{tail}}$ estimates, will always demonstrate sensitivity to the specific D_T values observed during the MCS. Therefore, GPD-derived $P_{f_{tail}}$ values do not provide a reliable method for generating p_f estimates during the probabilistic fatigue analysis of safe-life components.

Concerning the $P_{f_{MCS}}$ values from Table 8.9, it can be seen that only the Hole 2 Slice 13 feature provides a quantifiable p_f estimate, due to Hole 2 Slice 13 being the only feature to demonstrate failure iterations during the MCS at $N_{MCS} = 1 \times 10^5$. As a result, the $P_{f_{MCS}}$ estimates infer that there is a nil p_f for all other features, which contradicts both the $P_{f_{dist}}$ and $P_{f_{tail}}$ estimates. Therefore, as was the case for the lower side-stay case study, the use of $P_{f_{MCS}}$ estimates would fail to account for the quantifiable p_f of all features within the component at $N_{MCS} = 1 \times 10^5$.

An interesting observation from both Figure 8.16 and Table 8.9 is that the Hole 2 Slice 13 feature demonstrates a significantly higher $P_{f_{dist}}$ compared to the Lower Web feature, despite the Lower Web feature demonstrating a higher mean D_T value as shown previously in Figure 8.16a. As a result, it would be expected that the Lower Web feature could potentially have a higher p_f value than the Hole 2 Slice 13 feature.

However, this observation can be supported by superimposing the two D_T histograms for the Lower Web and Hole 2 Slice 13 feature, as shown in Figure 8.24. It can be seen from Figure 8.24 that whilst the Lower Web feature does display a higher mean D_T value, greater variability is observed for the Hole 2 Slice 13 feature, which can be supported by the 2P Log-Normal distribution λ shape parameter (which controls the 'spread' of the distribution). Considering the value of the shape parameter, $\lambda = 0.371$ for the Lower Web feature, whilst $\lambda = 0.829$ for the Hole 2 Slice 13 feature and as a result, the greater variability in the Hole 2 Slice 13 D_T values would lead to a higher p_f value compared to the Lower Web feature. Deterministic design approaches would often consider the feature with the higher mean D_T value to the be the damage hot-spot of the component and as a result, the Lower Web feature would typically drive the lower drag brace safe-life. However, Figure 8.24 demonstrates an important advantage of probabilistic analysis methods in that through accounting for the variability in design parameters and assessing the component safe-life based on p_f values, the true design drivers or damage hot-spots for a component can be identified.

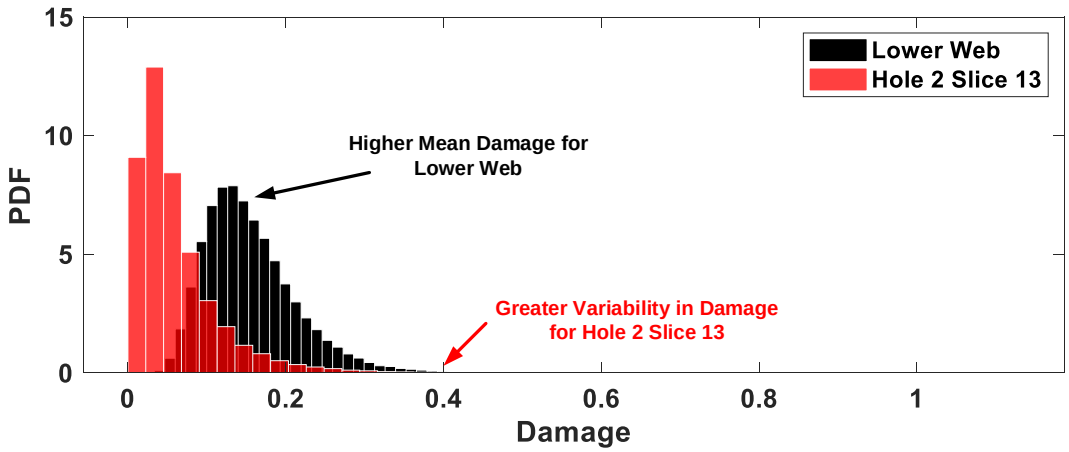

FIGURE 8.24. Comparison of the Lower Web and Hole 2 Slice 13 D_T histograms.

Finally, the results in Table 8.9 demonstrate that again the $P_{f_{dist}}$ estimates provide the most conservative p_f values. When accounting for statistical uncertainty, the values in Table 8.9 also highlight the limited statistical uncertainty in the $P_{f_{dist}}$ estimates[9], especially compared to the statistical uncertainty in the $P_{f_{MCS}}$ estimate for the Hole 2 Slice 13 feature.

[9] 2P Log-Normal 95% CI values could be computed using closed-form equations [33], whilst parametric bootstrap methods were required to generate the 95% CI values for the $P_{f_{dist}}$ estimates resulting from Burr distributions [156, 267].

Component-Level Results

The p_f estimates for each feature can then be combined into a component-level '$p_{f_{component}}$' estimate for the lower drag brace component, using Equation 3.6 shown previously in Chapter 3. As the lower drag brace is a safe-life and single load path component, it is assumed that failure (i.e. crack initiation) of any feature in the component results in the failure of the component, therefore satisfying the 'series' reliability system definition [30, 161]. As a result, the $p_{f_{component}}$ estimates are simply the summation of the p_f estimates for each feature. Table 8.10 shows the $p_{f_{component}}$ values for the lower drag brace, along with the components per failure values.

TABLE 8.10. The component-level p_f estimates for the lower drag brace component.

Component	Component-level $p_{f_{component}}$ Estimation Method				
	$P_{f_{dist}}$	$P_{f_{dist}}$ 95% CI	$P_{f_{tail}}$	$P_{f_{MCS}}$	$P_{f_{MCS+2\sigma}}$
Lower Drag Brace	1.257×10^{-4}	1.335×10^{-4}	2.567×10^{-5}	2.000×10^{-5}	4.828×10^{-5}
Components per Failure	7,956	7,380	38,960	50,000	20,712

Table 8.10 highlights that the $P_{f_{dist}}$ estimates provide a more conservative result than the $P_{f_{tail}}$ and $P_{f_{MCS}}$ results. As a result, it is further recommended that $P_{f_{tail}}$ and $P_{f_{MCS}}$ estimates are not used to generate $p_{f_{component}}$ estimates, as they may produce significantly unconservative estimates, especially for limited values of N_{MCS}. Compared to the lower side-stay assembly assessed in Chapter 7, the lower drag brace can be observed to demonstrate a lower value of p_f.

8.1.6 Sensitivity Analysis

As for the lower side-stay case study, K-L sensitivity analysis was also performed for the lower drag brace component, in order to identify the design drivers which provide the greatest contribution to the variability in D_T values. Due to the increased computational expense of performing the MCS iterations of the lower drag brace case study, the number of MCS iterations to perform the K-L sensitivity analysis (as introduced in Chapter 3) was reduced to $N_{MCS} = 2,500$. To ensure that $N_{MCS} = 2,500$ would still result in accurate K-L sensitivity analysis results, the distribution parameter estimates computed for the D_T damage values were compared between $N_{MCS} = 1 \times 10^5$ (the original probabilistic analysis) and $N_{MCS} = 2,500$, as shown in Table 8.11.

TABLE 8.11. Comparison of distribution parameters and $P_{f_{dist}}$ values at $N_{MCS} = 1 \times 10^5$ and $N_{MCS} = 2{,}500$ iterations for the Lower Web and Hole 2 Slice 13 features of the lower drag brace.

Feature	Property	Value		
		$N_{MCS} = 1 \times 10^5$	$N_{MCS} = 2{,}500$	% Difference
Lower Web	2P Log-Normal σ	-1.931	-1.939	0.400
	2P Log-Normal λ	0.371	0.370	0.044
	$P_{f_{dist}}$	9.395×10^{-8}	8.290×10^{-8}	11.759
Hole 2 Slice 13	2P Log-Normal σ	-3.114	-3.094	0.670
	2P Log-Normal λ	0.829	0.812	2.103
	$P_{f_{dist}}$	8.621×10^{-5}	6.911×10^{-5}	19.838

The Lower Web and Hole 2 Slice 13 features were selected for the lower drag brace sensitivity analysis cases due to being the most highly damaged features and because the two features demonstrate significantly different histogram shapes and skewness, as shown previously in Figures 8.18a and 8.18c. Table 8.11 shows that the distribution parameter estimates only differ by less than 3% for the two features. As the distribution parameter estimates control the 'shape' of probability distributions fitted to the D_T histograms, the K-L TE sensitivity values will show a limited difference between $N_{MCS} = 1 \times 10^5$ and $N_{MCS} = 2{,}500$. As a result, $N_{MCS} = 2{,}500$ provided a sufficient number of MCS iterations to perform accurate sensitivity analysis.

Lower Web Feature

The following $N_{MCS} = 2{,}500$ sensitivity analysis cases were considered for the Lower Web feature[10]:

- Mean S-N curve (i.e. all S-N curves are set to $PoS = 50\%$, with a mean $\sigma_{FL} = 457$ MPa). Additional sub-cases were also performed:
  - Mean N_f values with varying σ_{FL}.
  - Mean σ_{FL} with varying N_f.
- Mean aircraft mass assumed for pre-takeoff taxi and takeoff (2.262×10^5 kg [191]) and for landing and post-landing taxi (1.835×10^5 kg [191]).
- Fixed ground manoeuvre occurrence and sequence based on the standardised loading spectrum described in Appendix E.
- Fixed n_x, n_y and n_z load factors for each ground manoeuvre type as described in Appendix E.

[10]Variability in σ_{UTS} was shown to provide a negligible contribution to the D_T variability during the lower side-stay case study and was therefore 'screened' from the lower drag brace sensitivity analysis.

The output from each sensitivity analysis case was statistically characterised using the same method as for the probabilistic fatigue analysis and the resulting distributions for the Lower Web sensitivity analysis cases are shown in Table 8.12.

TABLE 8.12. Statistical characterisation results for the Lower Web sensitivity analysis cases.

Sensitivity Analysis Case	Distribution Type	Distribution Parameter Estimate	
		Scale σ	Shape λ
Mean S-N	2P Log-Normal	-1.930	0.037
Mean N_f	Gamma	9.320×10^{-4}	155.658
Mean σ_{FL}	2P Log-Normal	-1.935	0.305
Mean Aircraft Mass	2P Log-Normal	-2.178	0.365
Fixed Occurrence and Sequence	2P Log-Normal	-1.923	0.364
Fixed Load Factors	Gamma	0.003	3.067
Parent	2P Log-Normal	-1.931	0.371

Figure 8.25 shows the distributions for the sensitivity analysis cases relating to the variability in the S-N curve for the Lower Web feature. As can be seen from Figure 8.25, the greatest deviation from the parent distribution is when all variability is removed from the S-N curve. When removing only the variability in N_f, Figure 8.25 shows that a symmetric distribution is formed, suggesting that the skewness observed in D_T values is a result of the skewness of the 2P Log-Normal distributions used to characterise the variability of N_f within the S-N dataset. Figure 8.25 also shows that removing the variability in σ_{FL} only results in a limited deviation from the parent distribution, qualitatively suggesting that the variability in N_f provides the greatest contribution to D_T variability when considering the sources of variability present in S-N curves.

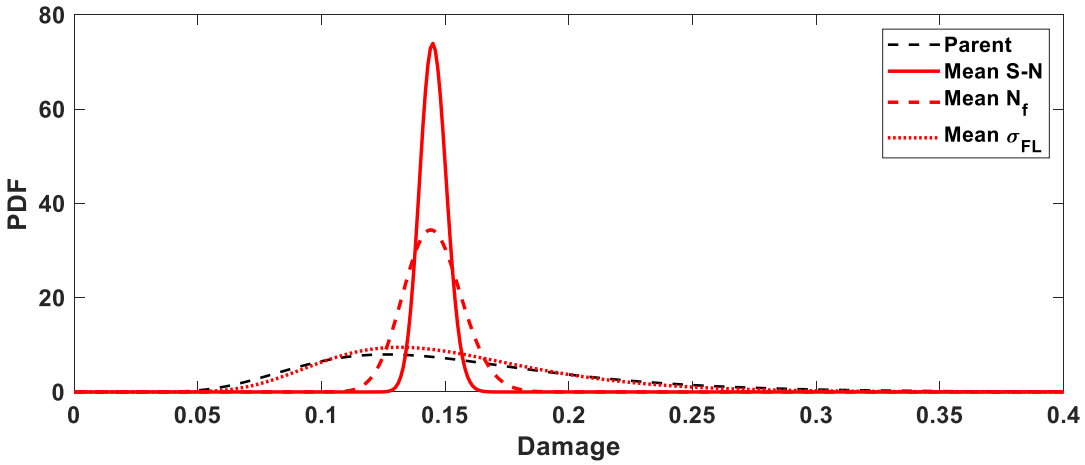

FIGURE 8.25. D_T distributions resulting from the Lower Web S-N curve sensitivity analysis cases.

The distributions shown in Figure 8.26 relate to the loading sensitivity analysis cases for the Lower Web feature. Figure 8.26 shows that fixing the variability in the load factors for each ground manoeuvre resulted in the greatest deviation from the parent distribution, suggesting that the load factor variability is a fatigue design driver for the Lower Web feature. Fixing the aircraft mass to mean values resulted in a reduced deviation from the parent distribution as shown in Figure 8.26. Of note from Figure 8.26 is that removing the variability in ground manoeuvre occurrence and sequencing results in a negligible deviation from the parent distribution.

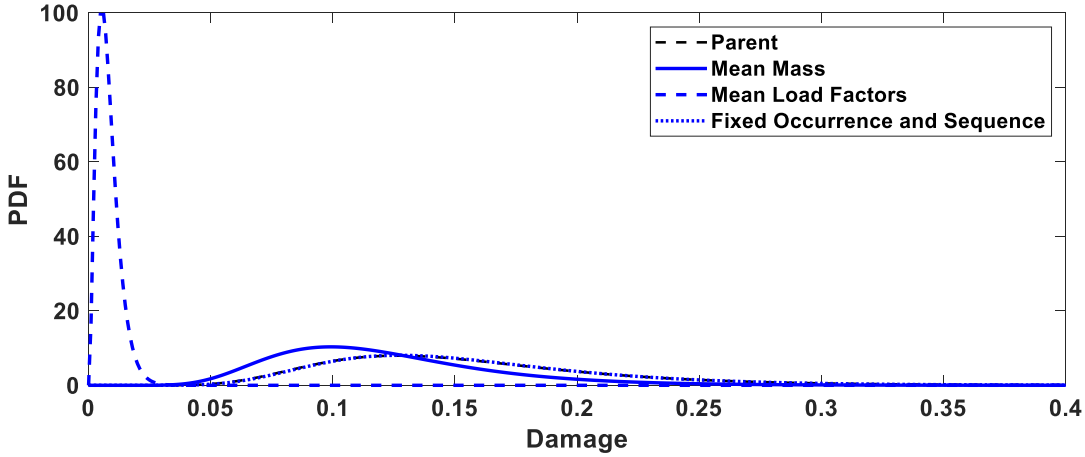

FIGURE 8.26. D_T distributions resulting from the Lower Web loading sensitivity analysis cases.

K-L TE values for each of the Lower Web sensitivity analysis cases were computed and are shown in Table 8.13. It can be observed that the sensitivity analysis cases with the highest TE values are for the mean S-N curve and fixed load factors. As a result, both the variability in the S-N curve and in the load factors can be considered as fatigue design drivers for the Lower Web feature. Table 8.13 also shows the insensitivity of the D_T values to variability in the ground manoeuvre occurrence and sequencing due to the negligible TE value.

TABLE 8.13. Total Effect TE values for the Lower Web sensitivity analysis cases, computed using the K-L sensitivity analysis method.

Sensitivity Analysis Case	TE
Mean S-N Curve	47.263
Fixed Load Factors	47.223
Mean Aircraft Mass	0.575
Fixed Occurrence and Sequence	0.018

Accessory Hole Feature

The following $N_{MCS} = 2{,}500$ sensitivity analysis cases were also considered for the Hole 2 Slice 13 feature:

- Mean S-N curve (i.e. all S-N curves are set to $PoS = 50\%$, with a mean $\sigma_{FL} = 457$ MPa). Additional sub-cases were also performed:
  - Mean N_f values with varying σ_{FL}.
  - Mean σ_{FL} with varying N_f.
- Mean aircraft mass assumed for pre-takeoff taxi and takeoff (2.262×10^5 kg [191]) and for landing and post-landing taxi (1.835×10^5 kg [191]).
- Fixed ground manoeuvre occurrence and sequence based on the standardised loading spectrum described in Appendix E.
- Fixed n_x, n_y and n_z load factors for each ground manoeuvre type as described in Appendix E.
- Mean K_t from accessory mounting hole machining surface finish ($K_t = 1.7$).

Table 8.14 shows the probability distributions fitted to characterise the variability in D_T for each of the sensitivity analysis cases. Table 8.14 highlights that for the fixed load factor sensitivity analysis case, no D_T damage was accumulated in the Hole 2 Slice 13 feature. This result suggests that the variability in load factors provides the greatest contribution to the D_T variability in the Hole 2 Slice 13 feature, as large loading magnitudes are required to accumulate damage in the Hole 2 Slice 13 feature.

TABLE 8.14. Statistical characterisation results for the Hole 2 Slice 13 sensitivity analysis cases.

Sensitivity Analysis Case	Distribution Type	Distribution Parameter Estimate		
		Threshold δ	Scale σ	Shape λ
Mean S-N	2P Log-Normal	-	-3.087	0.743
Mean N_f	Burr	1.694	0.065	2.071
Mean σ_{FL}	2P Log-Normal	-	-3.092	0.787
Mean Aircraft Mass	2P Log-Normal	-	-3.445	0.875
Fixed Occurrence and Sequence	2P Log-Normal	-	-3.083	0.795
Fixed Load Factors	No observed damage.			
Mean K_t	2P Log-Normal	-	-2.785	0.356
Parent	2P Log-Normal	-	-3.114	0.829

Figure 8.27 shows the D_T distributions resulting from the sensitivity analysis cases related to removing variability in the S-N curve. From Figure 8.27 it can be seen that removing the variability in N_f and σ_{FL} resulted in a limited deviation from the parent distribution. A limited deviation is also observed when removing all of the variability present in the S-N curve. Figure 8.27 therefore suggests that the variability in the Hole 2 Slice 13 feature D_T values is insensitive to the variability in the S-N curve.

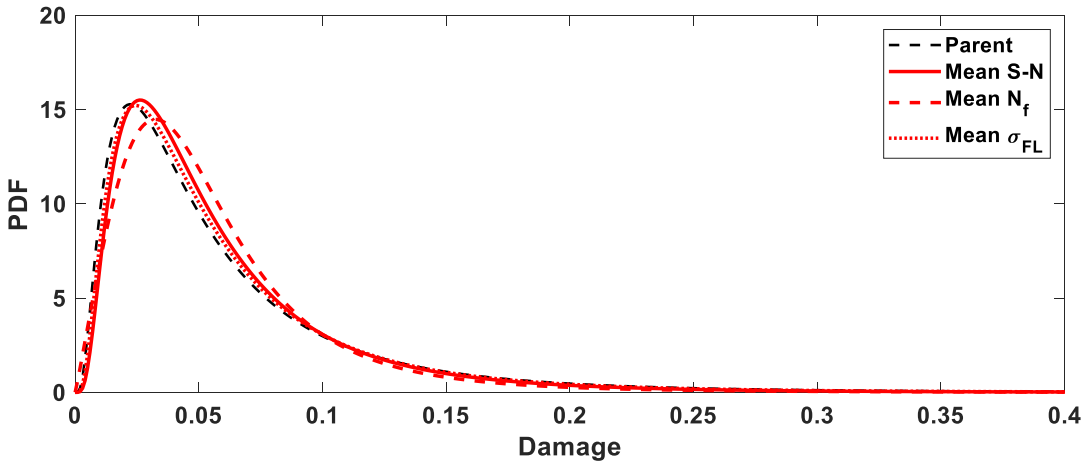

FIGURE 8.27. D_T distributions resulting from the Hole 2 Slice 13 S-N curve sensitivity analysis.

The distributions shown in Figure 8.28 represent the sensitivity analysis cases related to the loading applied to the lower drag brace component. Figure 8.28 shows that removing the variability in the aircraft mass resulted in a deviation from the parent distribution, whilst removing the variability in ground manoeuvre occurrence and sequencing failed to result in a deviation, as also observed for the Lower Web feature. Figure 8.28 also demonstrates that removing the variability in the hole surface finish K_t resulted in a significant departure from the parent distribution, suggesting that the surface finish K_t may be a fatigue design driver. As the removal of variability in the n_x, n_y and n_z load factors failed to result in any D_T damage accumulation at the Hole 2 Slice 13 feature within the sensitivity analysis case, load factor variability can be considered as a fatigue design driver for the Hole 2 Slice 13 load factor.

K-L TE sensitivity values were computed to support the qualitative observations from Figures 8.27 and 8.28 as shown in Table 8.15. Table 8.15 highlights that the hole surface finish is a fatigue design driver for the Hole 2 Slice 13 feature due to having a higher TE value than the other design parameters.

Of specific interest from Table 8.15 is the low TE value for the mean S-N curve sensitivity analysis case, which when coupled with Figure 8.27 suggests that the variability in D_T values for the Hole 2 Slice 13 feature is insensitive to the variability in the S-N curve. As this observation

contradicts the expected result from the sensitivity analysis due to the large variability present in S-N datasets, along with contradicting the sensitivity analysis results for the lower side-stay assembly and the Lower Web feature of the lower drag brace, an investigation into the insensitivity of the D_T variability at the Hole 2 Slice 13 feature to the variability in the S-N curve was performed.

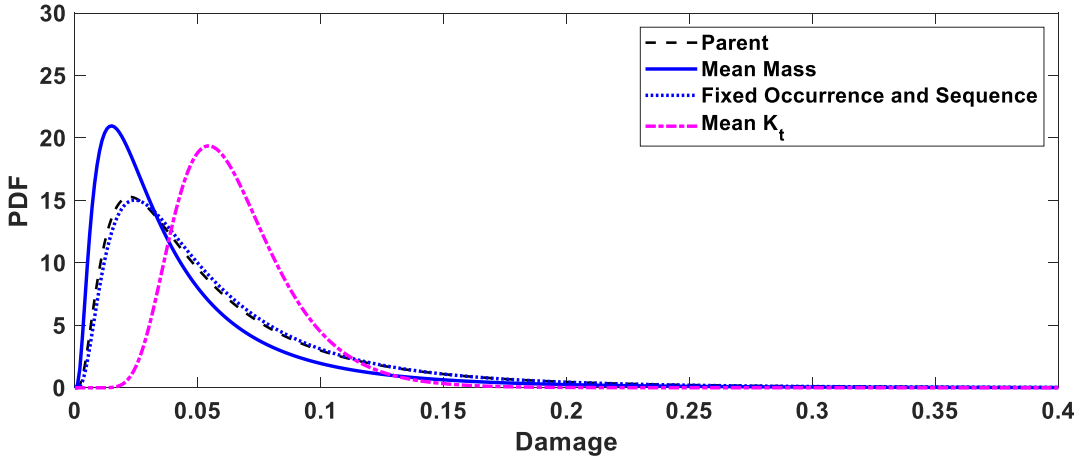

FIGURE 8.28. D_T distributions resulting from Hole 2 Slice 13 S-N curve sensitivity analysis, including the surface finish K_t sensitivity analysis case.

TABLE 8.15. Total Effect TE values for the Hole 2 Slice 13 sensitivity analysis cases, computed using the K-L sensitivity analysis method.

Sensitivity Analysis Case	TE
Fixed Load Factors	No Observed Damage.
Mean K_t	2.359
Mean Aircraft Mass	0.303
Mean S-N Curve	0.118
Fixed Occurrence and Sequence	0.050

From reviewing the stress-time histories generated for the Hole 2 Slice 13 feature, it was identified that fatigue damage would only be accumulated in cases where the MCS sampling resulted in a large surface finish K_t. As a consequence, the K_t value would result in fully-reversed stress amplitudes σ_0 of a sufficient amplitude to localise damage accumulation to regions of the S-N curve where the variability in N_f is minimal (i.e. less than the two orders of magnitude variability typically observed [6]), as shown in Figure 8.29. It can be observed from Figure 8.29 that as D_T damage accumulation only occurs when the nominal stresses (which are below σ_{FL}) are scaled by a high K_t value, the resulting variability in D_T values is a complex interaction between the variability in the load factor values, variability in N_f and the S-N curve shape geometry.

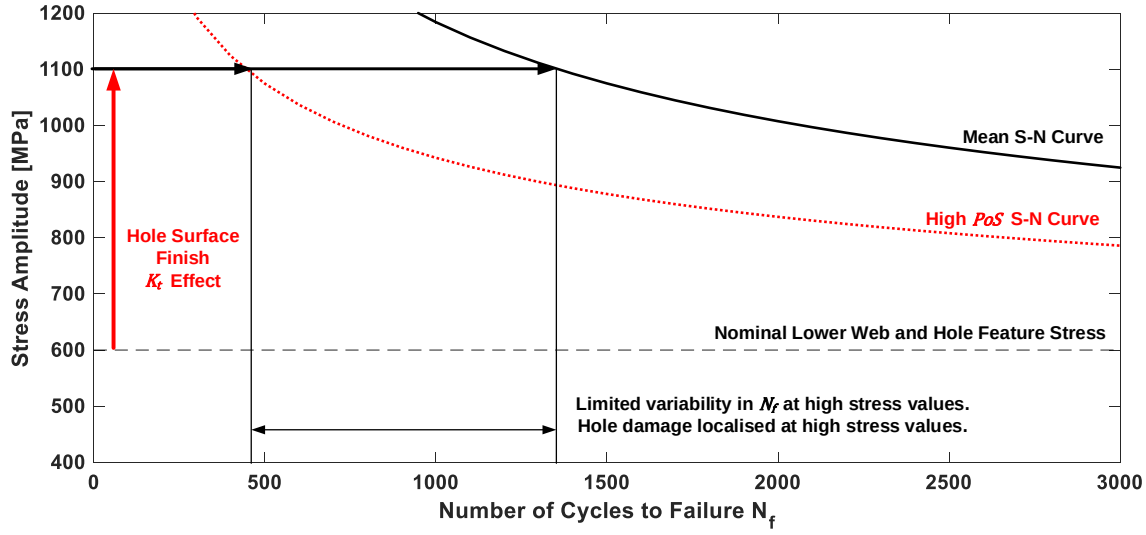

FIGURE 8.29. Insensitivity of the Hole 2 Slice 13 D_T variability to S-N curve variability.

In a similar manner to the K_t resulting from surface finishing, residual stresses are an additional form of stress that is present in unloaded components, which exists directly as a result of the various process required to manufacture the component [6, 22, 29]. The residual stresses present within a component can be expected to show variability [29, 268] and as a result, could be included in future probabilistic analysis cases, as has been performed for the probabilistic crack propagation assessment of engine turbine components by Millwater et al [268]. It is anticipated that the incorporation of residual stresses into the probabilistic fatigue methodology will result in complex interactions with the S-N curve shape, therefore demonstrating similar behaviour to the surface finish K_t shown in Figure 8.29. The inclusion of residual stress variability into the probabilistic fatigue methodology may be of significant importance to safe-life landing gear components, due to the shot-peening and other residual stress inducing manufacturing process used in the construction of landing gear components [9, 269].

Lack of Sensitivity to Manoeuvre Occurrence and Sequence Variability

The identification of the insensitivity of the variability in the D_T values of the lower drag brace features to the variability in ground manoeuvre occurrence and sequencing contradicts the observation that this source of variability was a fatigue design driver for the lower side-stay component features. Therefore, an investigation into the apparent insensitivity of the lower drag brace to ground manoeuvre occurrence and sequencing variability was conducted.

As the lower drag brace features were insensitive to the ground manoeuvre occurrence and sequencing variability, it was hypothesised that the lower drag brace features were only accumulating D_T damage for the following loading conditions:

- As a result of ground manoeuvres that occur for every single flight with the same frequency (i.e. no occurrence variability).
- As a result of ground manoeuvres that occur in the same 'order' or 'position' within every flight (i.e. no sequencing variability).

The ground manoeuvres that satisfy the above criteria for the MLG load-time histories were related to pushback, landing touchdown and the landing roll:

- Pushback:
  - n_x drag load factor when being pushed by tug.
- Landing Touchdown:
  - n_z vertical load factor on touchdown.
  - n_y load factor during touchdown drift.
  - n_x spin-up load factor.
  - n_x spring-back load factor.
- Landing Roll:
  - n_z lift dump load factor.
  - n_x landing roll braking load factor.

From reviewing the feature stress-time histories, it was observed that σ_0 stress amplitudes that were sufficiently large enough to accumulate D_T damage (i.e. $\sigma_0 \geq \sigma_{FL}$) could be traced back to specific peaks in the load-time histories. These peaks were then identified to be as a result of the manoeuvres listed above. In order to identify the specific load factors which provided the greatest contribution to the variability in D_T values, additional $N_{MCS} = 2{,}500$ sensitivity analysis cases were performed for the Lower Web and Hole 2 Slice 13 features of the lower drag brace. Each sensitivity analysis case removed the variability in one of the load factors listed above. Table 8.16 shows the resulting probability distributions for each sensitivity analysis case (the parent distributions are as shown previously in Tables 8.12 and 8.14).

Figure 8.30 shows the resulting distributions for the load factor sensitivity analysis cases for the Lower Web feature and Hole 2 Slice 13 feature in subplots (a, b) and (c, d) respectively. It can be observed from Figures 8.30a and 8.30b that the touchdown n_z, touchdown drift n_y and pushback n_x provide the greatest deviation from the parent distribution for the Lower Web

TABLE 8.16. Statistical characterisation for lower drag brace load factor sensitivity analysis cases.

Load Factor	Distribution	Distribution Parameter Estimate	
		Scale σ	Shape λ
Lower Web Feature			
Pushback n_x	2P Log-Normal	-2.193	0.375
Touchdown n_z	2P Log-Normal	-2.267	0.359
Touchdown Drift n_y	2P Log-Normal	-1.823	0.362
Spin-up n_x	2P Log-Normal	-1.954	0.370
Spring-back n_x	2P Log-Normal	-1.927	0.356
Lift Dump n_z	2P Log-Normal	-1.922	0.364
Landing Braking n_x	2P Log-Normal	-1.954	0.370
Hole 2 Slice 13 Feature			
Pushback n_x	2P Log-Normal	-3.356	0.848
Touchdown n_z	2P Log-Normal	-3.588	0.931
Touchdown Drift n_y	2P Log-Normal	-3.087	0.867
Spin-up n_x	2P Log-Normal	-3.510	0.819
Spring-back n_x	2P Log-Normal	-3.222	0.897
Lift Dump n_z	2P Log-Normal	-3.106	0.827
Landing Braking n_x	2P Log-Normal	-3.135	0.844

feature, whilst Figure 8.30c and 8.30d show that only the touchdown n_z and pushback n_x load factors result in a deviation in the parent distribution for the Hole 2 Slice 13 feature.

The K-L TE values for the load factor sensitivity cases are shown in Table 8.17 for both the Lower Web and Hole 2 Slice 13 feature. It can be observed that the TE values suggest that for the lower drag brace features, the touchdown n_z and pushback n_x load factors are the fatigue design drivers due to having the highest TE values. The investigation into the load factor variability has therefore highlighted the utility of K-L sensitivity analysis at different levels of design parameter granularity. K-L sensitivity analysis therefore enables specific design parameters to be identified as design drivers from groups composed of a large number of individual design parameters, such as the load factors within the statistically simulated load-time histories.

TABLE 8.17. Total Effect TE values for the load factor sensitivity analysis cases, computed using the K-L sensitivity analysis method.

Load Factor	Lower Web TE	Hole 2 Slice 13 TE
Pushback n_x	**0.587**	**0.227**
Touchdown n_z	**0.837**	**0.410**
Touchdown Drift n_y	**0.244**	0.047
Spin-up n_x	0.050	0.036
Spring-back n_x	0.042	0.112
Lift Dump n_z	0.025	0.009
Landing Braking n_x	0.049	0.025

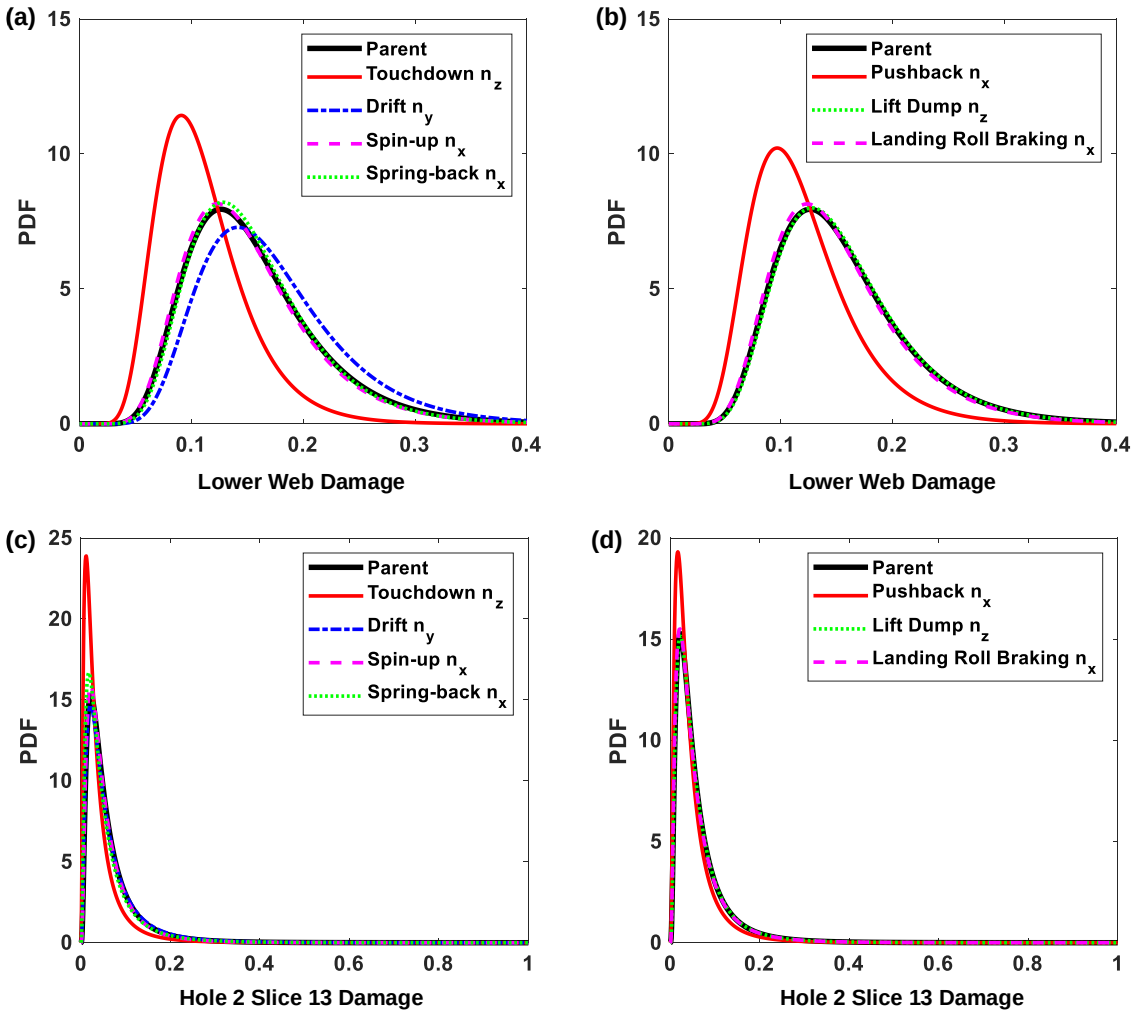

FIGURE 8.30. Load factor sensitivity analysis cases for (a, b) Lower Web feature and (c, d) Hole 2 Slice 13 features of the lower drag brace component.

A final result of interest from Table 8.17 is the high TE value for the touchdown drift n_y load factor for the Lower Web feature. Due to the configuration of the MLG assembly and corresponding linear static FEA MLG beam model shown in Chapter 6, it would be expected that all n_y side load factors and corresponding F_Y global side loads would be reacted solely through the lower side-stay. As a result, n_y load factors were not expected to result in loads or stresses in the main fitting component and therefore, loads originating from n_y load factors should not accumulate D_T damage in the lower drag brace features. However, the fact that the variability in the Lower Web and Hole 2 Slice D_T values changes when the variability in the landing drift n_y is fixed highlights that in fact, side loads were resulting in loading of the drag brace.

From reviewing the linear static FEA MLG beam model under various loading conditions, it was observed that under large n_y load factors, the displacement of the lower and upper side-stay components would result in a load transfer along the lock link component back to the drag brace. This would result in stresses being generated locally in the drag brace and lower drag brace component due to torsional loading. This load redistribution is highlighted in Figure 8.31. This observation also highlights the importance being aware that limitations in the existing deterministic analysis process can impact the probabilistic results from implementing the probabilistic fatigue methodology and this will be discussed further in Chapter 9.

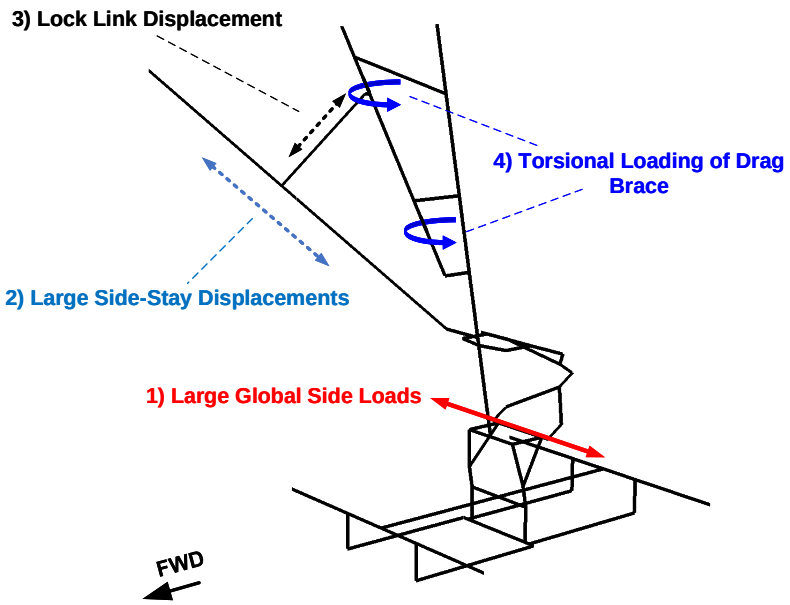

FIGURE 8.31. Demonstration of lock link loading of lower drag brace.

Summary of Lower Drag Brace Sensitivity Analysis

The sensitivity analysis cases performed for the Lower Web and Hole 2 Slice 13 features of the lower drag brace highlighted that the load factor variability (specifically for the touchdown n_z and pushback n_x load factors) was the fatigue design driver for the lower drag brace component. As a result, future work could be targeted at better characterising the variability in the load factors associated with the touchdown and pushback ground manoeuvres, with the view to better characterising the variability in the D_T values of the lower drag brace.

For the Lower Web feature, S-N curve variability was shown to provide a significant contribution to the D_T variability. However, this observation was not the case for the Hole 2 Slice 13 feature and this result therefore highlights that sensitivity analysis results cannot be generalised across individual components and must be performed on a feature-by-feature basis. The

sensitivity analysis cases for the Hole 2 Slice 13 feature also highlighted that surface finish K_t values are a fatigue design driver and as a result, future work should aim to better characterise the variability in K_t values resulting from machining and finishing activities.

When comparing between the sensitivity analysis results for the lower side-stay assembly features and the lower drag brace features, the most significant difference is that the D_T variability in the lower drag brace features was insensitive to the variability in the ground manoeuvre occurrence and sequencing, whilst this source of variability was identified as a design driver for the lower side-stay assembly features. This is as a result of the lower drag brace only accumulating D_T damage for manoeuvres which occur with the same frequency every flight. However, the n_y side-load factors that cause loading of the lower side-stay are mostly as a result of turning manoeuvres, which as described in Chapter 5, show significant variability in their per-flight occurrence and sequencing. As a result, the sensitivity analysis cases performed for the lower side-stay assembly and lower drag brace features have demonstrated that sensitivity analysis results also cannot be generalised across different components of the MLG assembly.

8.1.7 3-Parameter Weibull P-S-N Curves

As for the lower side-stay assembly in Section 7.2.8, an additional probabilistic analysis for the lower drag brace was conducted using the 3P Weibull distribution to statistically characterise the variability in N_f due to its better fit to the S-N dataset as identified previously in Chapter 4. Figure 8.32 shows the resulting D_T histogram from an $N_{MCS} = 2{,}500$ probabilistic analysis for the Lower Web feature of the lower drag brace when using a 3P Weibull S-N curve.

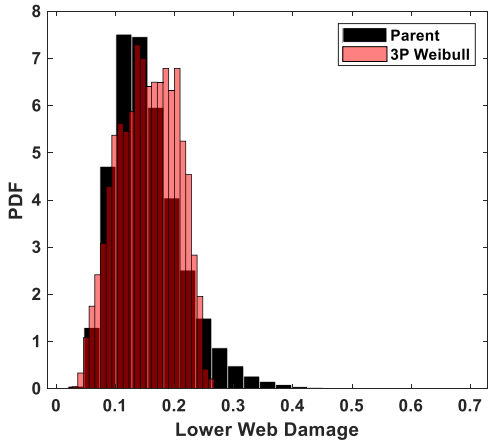

FIGURE 8.32. Lower Web feature D_T histogram when using a 3P Weibull S-N curve.

It can be observed from Figure 8.32 that the D_T histogram again demonstrates negative skew with a sharp right-hand tail and a flat distribution peak, as was observed for the lower side-stay assembly features in Section 7.2.8.

As a result, the utilisation of the 3P Weibull distribution to characterise N_f values has again resulted in a complex histogram shape that cannot be characterised accurately by existing candidate distributions. A further discussion of how the complex D_T histogram shapes resulting from employing 3P Weibull S-N curves can be assessed is presented in Chapter 9.

8.2 Evaluation of Convergence

As described in Section 7.1.1, the $N_{MCS} = 1 \times 10^5$ MCS iterations were selected for the case studies in order to satisfy the 10^{k+1} MCS convergence criterion [114]. As the highest p_f values observed for all features across the lower side-stay and lower drag brace were in the order of 10^{-4}, the 10^{k+1} criterion was therefore satisfied for the most critical features in the case studies. However, in order to further investigate the convergence of the p_f estimates, the lower side-stay assembly case study was repeated for $N_{MCS} = 5 \times 10^5$. It was assumed as both the lower side-stay features and lower drag brace features showed similar p_f values, that any observations resulting from increasing the value of N_{MCS} for the lower side-stay assembly case study were also applicable to the lower drag brace case study. It is important to note that any conclusions relating to convergence are constrained to the computational resource available for the presented case studies and the application of the probabilistic fatigue methodology to components that are assessed using linear static and linear elastic FEA models.

Tables 8.18, 8.19 and 8.20 show the $P_{f_{dist}}$, $P_{f_{tail}}$ and $P_{f_{MCS}}$ values at $N_{MCS} = 1 \times 10^5$ and $N_{MCS} = 5 \times 10^5$ for the lower side-stay assembly features, along with component-level and assembly-level p_f estimates. These tables also show the percentage difference in the p_f estimates between the $N_{MCS} = 1 \times 10^5$ and $N_{MCS} = 5 \times 10^5$ probabilistic analysis cases. For cases where the percentage error metric exhibits a high sensitivity due to the small order of magnitude of the p_f values, a more representative metric based on the order of magnitude shift in the p_f estimates between $N_{MCS} = 1 \times 10^5$ and $N_{MCS} = 5 \times 10^5$ is given.

It can be observed from Table 8.18 that the feature, component-level and assembly-level $P_{f_{dist}}$ values all demonstrated a low percentage error, therefore suggesting that the $P_{f_{dist}}$ estimates had converged at $N_{MCS} = 1 \times 10^5$. On the other hand, Table 8.19 shows that the percentage errors for the $P_{f_{tail}}$ estimates are large between $N_{MCS} = 1 \times 10^5$ and $N_{MCS} = 5 \times 10^5$, with some specific feature p_f values differing by three orders of magnitude. As a result, the sensitivity of $P_{f_{tail}}$ estimates to the specific values observed during the MCS has again been highlighted.

Finally, from Table 8.20, the $P_{f_{MCS}}$ values can be seen to vary significantly between $N_{MCS} = 1 \times 10^5$ and $N_{MCS} = 5 \times 10^5$, therefore suggesting that the $P_{f_{MCS}}$ estimates had not converged at $N_{MCS} = 1 \times 10^5$. Despite the low percentage error for the overall lower side-stay assembly $P_{f_{MCS}}$, it should be recalled that the $P_{f_{MCS}}$ results fail to account for all features of the lower side-stay that demonstrate a quantifiable p_f.

TABLE 8.18. Convergence of the feature, component-level and assembly-level $P_{f_{dist}}$ estimates for the lower side-stay case study at $N_{MCS} = 1 \times 10^5$ and $N_{MCS} = 5 \times 10^5$.

Feature	$P_{f_{dist}}$			
	$N_{MCS} = 1 \times 10^5$	$N_{MCS} = 5 \times 10^5$	% difference	Order Shift
Smooth Pin Max Shear	1.485×10^{-4}	1.422×10^{-4}	**2.991**	0
Fuse Pin Max Shear	2.048×10^{-4}	2.175×10^{-4}	**5.847**	0
Loaded Lug Top	1.717×10^{-5}	1.689×10^{-5}	**1.670**	0
Loaded Lug Bottom	1.722×10^{-5}	1.727×10^{-5}	**0.305**	0
Constrained Lug Top	5.954×10^{-7}	5.835×10^{-7}	**2.043**	0
Component	$P_{f_{dist}}$			
	$N_{MCS} = 1 \times 10^5$	$N_{MCS} = 5 \times 10^5$	% difference	Order Shift
Smooth Pin	2.917×10^{-4}	2.884×10^{-4}	**2.991**	0
Fuse Pin	4.095×10^{-4}	4.349×10^{-4}	**5.847**	0
Lower Side-Stay	6.998×10^{-5}	6.949×10^{-5}	**0.695**	0
Assembly	$P_{f_{dist}}$			
	$N_{MCS} = 1 \times 10^5$	$N_{MCS} = 5 \times 10^5$	% difference	Order Shift
Lower Side-Stay	7.766×10^{-4}	8.015×10^{-4}	**3.113**	0

TABLE 8.19. Convergence of the feature, component-level and assembly-level $P_{f_{tail}}$ estimates for the lower side-stay case study at $N_{MCS} = 1 \times 10^5$ and $N_{MCS} = 5 \times 10^5$.

Feature	$P_{f_{tail}}$			
	$N_{MCS} = 1 \times 10^5$	$N_{MCS} = 5 \times 10^5$	% difference	Order Shift
Smooth Pin Max Shear	1.313×10^{-4}	1.053×10^{-4}	**7.391**	0
Fuse Pin Max Shear	7.697×10^{-5}	8.598×10^{-5}	**10.479**	0
Loaded Lug Top	2.052×10^{-5}	6.386×10^{-6}	**221.306**	1
Loaded Lug Bottom	4.949×10^{-6}	6.421×10^{-6}	**22.914**	0
Constrained Lug Top	1.488×10^{-6}	8.319×10^{-9}	**1.8×10^4**	3
Component	$P_{f_{tail}}$			
	$N_{MCS} = 1 \times 10^5$	$N_{MCS} = 5 \times 10^5$	% difference	Order Shift
Smooth Pin	2.261×10^{-4}	2.106×10^{-4}	**7.391**	0
Fuse Pin	1.539×10^{-4}	1.720×10^{-4}	**10.479**	0
Lower Side-Stay	5.391×10^{-5}	2.563×10^{-5}	**110.351**	0
Assembly	$P_{f_{tail}}$			
	$N_{MCS} = 1 \times 10^5$	$N_{MCS} = 5 \times 10^5$	% difference	Order Shift
Lower Side-Stay	4.340×10^{-4}	4.082×10^{-4}	**6.328**	0

The order shift values shown in Tables 8.18, 8.19 and 8.20 also highlight that the $P_{f_{dist}}$ values were the only p_f estimates converged at $N_{MCS} = 1 \times 10^5$, as the both the $P_{f_{tail}}$ and $P_{f_{MCS}}$ estimates showed changes in the p_f order of magnitude for at least one feature between $N_{MCS} = 1 \times 10^5$ and $N_{MCS} = 5 \times 10^5$.

TABLE 8.20. Convergence of the feature, component-level and assembly-level $P_{f_{MCS}}$ estimates for the lower side-stay case study at $N_{MCS} = 1 \times 10^5$ and $N_{MCS} = 5 \times 10^5$.

Feature	$P_{f_{MCS}}$			
	$N_{MCS} = 1 \times 10^5$	$N_{MCS} = 5 \times 10^5$	% difference	Order Shift
Smooth Pin Max Shear	1.200×10^{-4}	1.120×10^{-4}	**7.143**	0
Fuse Pin Max Shear	8.000×10^{-5}	9.800×10^{-5}	**18.367**	0
Loaded Lug Top	2.000×10^{-5}	6.000×10^{-6}	**233.333**	1
Loaded Lug Bottom	0	0	**-**	-
Constrained Lug Top	0	0	**-**	-
Component	$P_{f_{MCS}}$			
	$N_{MCS} = 1 \times 10^5$	$N_{MCS} = 5 \times 10^5$	% difference	Order Shift
Smooth Pin	2.400×10^{-4}	2.240×10^{-4}	**7.143**	0
Fuse Pin	1.600×10^{-4}	1.960×10^{-4}	**18.367**	0
Lower Side-Stay	4.000×10^{-5}	1.200×10^{-5}	**233.333**	0
Assembly	$P_{f_{MCS}}$			
	$N_{MCS} = 1 \times 10^5$	$N_{MCS} = 5 \times 10^5$	% difference	Order Shift
Lower Side-Stay	4.400×10^{-4}	4.320×10^{-4}	**1.852**	0

As the $P_{f_{dist}}$ estimates were shown to be converged at $N_{MCS} = 1 \times 10^5$, the question of at what value of N_{MCS} do the $P_{f_{dist}}$ estimates converge can be raised. Based upon the reduced N_{MCS} used for the lower side-stay and lower drag brace sensitivity analysis cases, it can be suggested that less than $N_{MCS} = 1 \times 10^5$ iterations may be required for converged $P_{f_{dist}}$ estimates. As shown previously in Table 7.17, reducing the number of MCS iterations to $N_{MCS} = 1 \times 10^4$ for the lower side-stay case study resulted in a maximum error of $\approx 5\%$ for the $P_{f_{dist}}$ values. Likewise, Table 8.11 demonstrated that reducing the number of MCS iterations to $N_{MCS} = 2{,}500$ produced a maximum error of $\approx 20\%$ in the $P_{f_{dist}}$ values. However, the $P_{f_{dist}}$ values generated during feature down-selection as shown in Table 8.2 suggest that there is a lower bound for the value of N_{MCS} to achieve convergence, as the $P_{f_{dist}}$ estimates generated at $N_{MCS} = 1{,}000$ show $P_{f_{dist}}$ values that differ from the converged values by two or more orders of magnitude. These results therefore suggest that accurate and useful p_f estimates could be generated from the probabilistic fatigue methodology with significantly fewer MCS iterations than $N_{MCS} = 1 \times 10^5$. This reduction in $N_{MCS} = 1 \times 10^5$ would ultimately reduce the cost of executing the probabilistic fatigue methodology and the consequences of this will be discussed in Chapter 9.

8.3 Summary

This chapter has presented the application of the probabilistic fatigue methodology defined in Chapter 3 (supported by the technical content of Chapters 4 to 6) to a case study concerning the lower drag brace component of a wide-body civil aircraft MLG. The implementation of the MCS-SSI hybrid probabilistic fatigue methodology to the lower drag brace component permitted the successful implementation of the probabilistic fatigue methodology to compute p_f estimates for a component with a complex geometry subjected to complex loading as assessed using linear

elastic FEA stress analysis. As a result, it can be concluded that the MCS-SSI probabilistic fatigue methodology can be used to generate p_f estimates for safe-life landing gear components of differing geometrical, loading and analysis complexity. Beyond the probabilistic fatigue analysis results, a series of additional observations were made, as identified below. It is interesting to note that the additional observations are similar to those identified for the lower side-stay assembly case study in Chapter 7. This further suggests that the MCS-SSI hybrid probabilistic fatigue methodology is insensitive to the specific component under assessment and the complexity of the existing deterministic analysis process. The additional observations from the lower drag brace case study were:

- The probabilistic fatigue methodology was able to generate p_f estimates for various component features, as well as providing a component-level estimate. As a result, the probabilistic fatigue methodology provides a route for accounting for all component features when defining a component safe-life, which is not currently possible in the deterministic approach as it relies on the identification of a single 'hot-spot' damage.

- The $P_{f_{dist}}$ estimates generated for the hybrid MCS-SSI method provided the most conservative estimates across both case studies and were also found to be converged at $N_{MCS} = 1 \times 10^5$.

- The $P_{f_{tail}}$ and $P_{f_{MCS}}$ estimates were found to be sensitive to the specific D_T values observed during the MCS iterations.

- The successful implementation of the probabilistic fatigue methodology was only feasible as a result of the extensive use of surrogate modelling methods to replace the component linear elastic FEA stress analysis model.

- The utilisation of sensitivity analysis methods during the post processing of the results from the lower drag brace case study identified the following design parameters as fatigue design drivers:

  - Variability in the n_x, n_y and n_z load factors.
  - Variability in the S-N curve, specifically the N_f variability at different σ_0 stress levels.

- The employment of complicated distribution types (e.g. 3P Weibull) to characterise design parameter variability can result in complex D_T histogram shapes that cannot be currently characterised using probability distributions.

- The p_f estimates of components are typically dominated by specific features (e.g. the upper hole features of the lower drag brace component). As a result, from the perspective of fatigue reliability, many features of the lower drag brace component are potentially over-designed and could be further optimised to reduce component mass.

The observations listed above and shown previously in Section 7.3 will be used to support the critical evaluation of the probabilistic fatigue methodology in Chapter 9. The wider consequences for probabilistic design and analysis approaches from the observations made during the case studies will also be discussed in the following chapter, along with the identification of how the results from the case studies contribute to resolving the research questions posed at the start of this thesis in Chapter 1.

Finally, the application of the probabilistic fatigue methodology has demonstrated how the definition of a probabilistic analysis framework in Chapter 3 has further supported the aim of overcoming the blockers to a probabilistic design approach. Despite applying the probabilistic fatigue methodology across two case studies of differing complexity, the overall framework and analysis flow/architecture remained consistent across the two case studies, requiring very little modification for the different landing gear components. Therefore, the probabilistic fatigue methodology is general in nature and can be applied to different analysis and assessment cases. This general nature helps to overcome the *required knowledge* blocker as shown in Table 8.21, by providing a single methodology and framework that be implemented regardless of the specific analysis task required.

TABLE 8.21. The blockers to probabilistic design approaches overcome from applying the probabilistic analysis framework to the landing gear component case studies.

Blocker	Blockers overcome due to application of analysis framework
Computational Expense	N/A
Required Assumptions of Existing Process	N/A
Availability of Data	N/A
Accuracy of Data Characterisation	N/A
Required Knowledge	Framework can be applied to different case studies with minimal modification. This enables the probabilistic fatigue methodology to be insensitive to the specific analysis and assessment case.

CHAPTER 9

DISCUSSION

The preceding chapters of this thesis have presented the novel technical work performed during the development, implementation and demonstration of a probabilistic fatigue methodology for safe-life landing gear components. The penultimate chapter of this thesis aims to highlight how the work performed has answered the original research aim and questions defined in Chapter 1. This chapter also intends to explore the wider impact of the work on the future implementation of probabilistic design approaches, through both the overcoming of the 'blockers' to probabilistic design approaches and the future research and engineering effort required to develop a practical probabilistic fatigue design approach for safe-life landing gear components.

9.1 Critical Evaluation of Probabilistic Fatigue Methodology

The overall research aim of the work presented in this thesis was to "*develop a probabilistic fatigue methodology to support the fatigue design of safe-life components*". This aim was also captured by the first research question posed in Chapter 1:

- *Can a probabilistic fatigue methodology be successfully applied to safe-life landing gear components, in order to compute the probability of failure related to a component safe-life*?

To answer this question, this section aims to critically assess the MCS-SSI hybrid probabilistic fatigue methodology presented in Chapter 3, based upon the application of the methodology to the landing gear component case studies in Chapters 7 and 8. It is important to note that critical evaluation of the probabilistic fatigue methodology is performed with respect to the performance of the methodology when applied to S-N fatigue analysis consisting of linear static loads FEA model and either analytical or linear elastic FEA stress analysis.

Ultimately, the research aim and research question stated above have been satisfied by the successful implementation of the probabilistic fatigue methodology to the landing gear component case studies. During the case studies, the MCS-SSI hybrid methodology produced converged p_f estimates at $N_{MCS} = 1 \times 10^5$ MCS iterations, using the $P_{f_{dist}}$ estimates. The $P_{f_{dist}}$ estimates were derived from the SSI method of fitting a probability distribution to the variability present in the D_T damage values resulting from the MCS. The probabilistic fatigue methodology was also shown across both case studies to be capable of generating p_f estimates across different engineering features, as well as providing component-level and assembly-level reliability estimates. In addition, the MCS-SSI hybrid probabilistic fatigue methodology was shown to be successfully able to generate p_f estimates for differing component geometrical, loading and analysis complexity (i.e. across analytical and linear elastic FEA stress analysis). Therefore, this thesis has presented a probabilistic fatigue methodology that can be used to support the fatigue design of safe-life components, through computing p_f values related to a component safe-life.

Beyond achieving the research aim, the MCS-SSI hybrid probabilistic fatigue methodology was also demonstrated on a novel application of such approaches, through implementing the methodology on safe-life landing gear component case studies. Consequently, the work presented in this thesis has demonstrated the wider utility of probabilistic fatigue methodologies, beyond their more common employment in wind energy, automotive and turbine engine assessments [87, 94, 119]. In addition, as widely discussed in Chapter 2, the most recent applications of probabilistic fatigue methodologies have required the extensive modification or simplification of the existing fatigue analysis approach, either through the adoption of Limit State Approximation (LSA) methodologies or assumptions such as the Equivalent Fatigue Cycle (EFC) [57, 104, 115]. However, the probabilistic fatigue methodology developed within this thesis has been applied directly to the S-N safe-life fatigue analysis process in its original form. The only modification to

the existing process required for the probabilistic fatigue methodology was the representation of FEA loads and stress models using accurate surrogate models. As a result, this thesis has also demonstrated novelty in applying a probabilistic fatigue methodology to an existing and complete analysis process. This is especially the case due to the retention of the complexity of the original analysis processes within the methodology, without making the simplifications required in previous applications of probabilistic fatigue methodologies.

9.1.1 Limitations of Probabilistic Fatigue Methodology

Despite the conclusion that the original research aim has been satisfied by the development and demonstration of the probabilistic fatigue methodology, there are a number of limitations currently present within the proposed MCS-SSI hybrid probabilistic fatigue methodology. These limitations are representative of the challenges faced within the constraints of this work, that is, the available computational resource for the case studies and the application of the methodology to S-N fatigue analysis comprising of linear static FEA loading models and linear elastic FEA stress models.

Firstly, during the definition of the probabilistic fatigue methodology in Chapter 3, it was intended that p_f estimates would also be generated from the 'pure' MCS (i.e. $P_{f_{MCS}}$) and GPD tail-fitting methods (i.e. $P_{f_{tail}}$), in order to provide validation of the $P_{f_{dist}}$ estimates provided by SSI.

The estimates generated by $P_{f_{MCS}}$ failed to converge at $N_{MCS} = 1 \times 10^5$ iterations, suggesting that additional MCS iterations would be required in order to produce reliable $P_{f_{MCS}}$ estimates. This was not feasible due to the significant increase in computational expense that would be incurred, considering that $N_{MCS} = 1 \times 10^5$ required 4 days and 18 days of CPU run-time for the lower side-stay and lower drag brace case studies respectively. Therefore, reliable $P_{f_{MCS}}$ estimates could not be generated, even when satisfying the 10^{k+1} criterion for the component features that demonstrated the highest p_f values (in the order of 10^{-4}). This suggests that a more appropriate convergence criteria for $P_{f_{MCS}}$ is to set N_{MCS} to the order of 10^{k+2} to guarantee convergence, which is in agreement the with recommendations of Sudret [270].

The use of 'pure' MCS $P_{f_{MCS}}$ estimates also failed to provide reliable p_f estimates at a component-level and assembly-level, due to estimating nil p_f values for features which were shown to possess a quantifiable p_f using either $P_{f_{dist}}$ or $P_{f_{tail}}$ methods. As a result, $P_{f_{MCS}}$ results should only be employed for 'hot-spot' probabilistic fatigue analysis of single critical features. Therefore, $P_{f_{MCS}}$ values should not be used to estimate component and assembly p_f estimates when components demonstrate multiple features with quantifiable p_f values that span a wide range of orders of magnitude (e.g. from 10^{-7} to 10^{-4} for the lower side-stay assembly).

The other alternative approach to generating p_f estimates was the GPD tail-fitting values represented by $P_{f_{tail}}$. The p_f estimates resulting from $P_{f_{tail}}$ values were shown to be sensitive to the specific D_T damage values observed during the MCS iterations and as a result, would

provide inconsistent and unreliable p_f estimates as discussed in Chapters 7 and 8. The $P_{f_{tail}}$ estimates, in a similar manner to the $P_{f_{MCS}}$ estimates, also failed to account for all features that demonstrated a quantifiable p_f estimate from $P_{f_{dist}}$ values. It is suggested by Acar that the incorrect definition of the GPD t threshold parameter can significantly affect the $P_{f_{tail}}$ results from GPD tail-fitting and therefore, future work could be performed to investigate the impact of t within the MCS-SSI hybrid probabilistic fatigue methodology [271].

As a result, it is recommended that the GPD $P_{f_{tail}}$ method is not used to generate p_f estimates within a probabilistic fatigue methodology. This recommendation is supported by the limited application of GPD methods for probabilistic fatigue analysis in the literature beyond the original recommendation of the utilisation of tail-fitting methods for p_f estimation by Ramu and Kim [159, 160]. Only three cases of the utilisation of GPD tail-fitting to generate $P_{f_{tail}}$ values have been identified in the literature:

- Wind turbine fatigue analysis by Norouzi [272].
- Fatigue design optimisation performed by Tüten and Acar [273].
- Probabilistic fatigue analysis of steel bridges by Nesterova et al [274].

Whilst Norouzi demonstrates the successful application of GPD $P_{f_{tail}}$ estimates, the work performed by Tüten and Acar and Nesterova et al [273, 274] highlights that currently there has been insufficient experience and validation activities performed on GPD $P_{f_{tail}}$ estimates to assess their reliability and suitability for probabilistic design.

Therefore, validation could not be performed for the $P_{f_{dist}}$ values from the MCS-SSI probabilistic fatigue methodology at all component features. However, it was identified that for the most critical features from a fatigue failure standpoint (i.e. those that demonstrated the highest p_f values), there was good agreement between the $P_{f_{dist}}$, $P_{f_{tail}}$ and $P_{f_{MCS}}$ estimates. Examples of these critical features are the smooth pin maximum shear location and loaded lug top features of the lower side-stay assembly (see Tables 7.7 and 7.14) and the Hole 2 Slice 13 feature of the lower drag brace (see Table 8.9). As a result, only a limited amount of validation of the $P_{f_{dist}}$ estimates has been performed. Coupled with the observation that the $P_{f_{dist}}$ values were the only p_f estimates to be converged at $N_{MCS} = 1 \times 10^5$, as well as providing the most conservative p_f values at all features, $P_{f_{dist}}$ estimates should be used as the approach to generate p_f values using the MCS-SSI hybrid probabilistic fatigue methodology. However, the MCS-SSI hybrid probabilistic fatigue methodology in its current form does also contain further limitations, which will now be discussed.

Computational Expense

The computational expense of the MCS-SSI probabilistic fatigue methodology is currently too large to serve as a practical design tool, due to requiring 4 days to generate converged p_f

estimates for the lower side-stay assembly and 18 days to produce converged p_f estimates for the lower drag brace component[1]. The currently excessive computational expense of the probabilistic fatigue methodology could be reduced by minimising the N_{MCS} MCS iterations required to generate the $P_{f_{dist}}$ estimates. This could be achieved using $P_{f_{dist}}$ convergence studies as described in Section 8.2.

An alternative route to reducing the computational expense of the probabilistic fatigue methodology would be to investigate stratified or targeted sampling approaches, such as Latin Hypercube Sampling (LHS) as performed by Halfpenny et al [61] or Importance Sampling (IS) methods, such as the methods used for the probabilistic fatigue analysis of rotorcraft components by Frewen et al [133]. Convergence studies for $P_{f_{dist}}$ could then be performed to identify the reduction in computational expense for employing these targeted sampling approaches. However, such approaches require additional abstract statistical concepts and as a result, care must be taken to ensure that targeted sampling methods are described and demonstrated in an accessible way for practicing engineers.

Ultimately, if the computational expense could be reduced to such an extent that a 'pure' MCS could generate converged $P_{f_{MCS}}$ estimates for all component features, it is proposed that the SSI element of the methodology could be removed in favour of a pure MCS approach. Such an approach would overcome the existing limitations of the MCS-SSI approach discussed in the following subsections of tail-sensitivity and complex 'stress' distribution types. However, in order to further investigate the convergence of a pure MCS approach, either the computational resource (i.e. allowable run-time) for the case studies would have to be dramatically increased, or the employment of increased computational hardware (such as increased memory and processor specifications or use of High Performance Computing methods) would have to be considered.

Tail-Sensitivity

As highlighted during the lower side-stay case study in Chapter 7, tail-sensitivity can result in significantly different $P_{f_{dist}}$ estimates from two candidate distributions that both provide similar Goodness-of-Fit (GoF) results for the variability in D_T values. Whilst the presence of tail-sensitivity has been widely reported across the previous three decades [42, 45, 275, 276], there has been limited work to identify routes to mitigating tail-sensitivity. Currently, the only recommendation within the literature is to assess the impact of assuming one valid distribution type over another [45, 275]. In the context of the fatigue design of safety-critical structures, it is suggested that this infers that the candidate distribution that provides the most conservative $P_{f_{dist}}$ should be selected.

However, based on the work performed in this thesis, it is proposed that future work by the probabilistic analysis community in developing GoF tests for large sample sizes (i.e. equal to the N_{MCS} values used for the MCS-SSI probabilistic fatigue methodology) could help mitigate tail-

[1]Computer Specifications: 4-core processor (3.40 GHz) with 16.0 GB RAM.

sensitivity. Large sample GoF tests would permit the full systematic statistical characterisation process defined in Chapter 4 to be applied to the D_T histograms generated by the probabilistic fatigue methodology. One potential large sample GoF test that could be investigated is the use of K-L entropy (as used for sensitivity analysis as described in Section 3.5.2) to assess the GoF of fitted distributions to datasets with a large sample size [277]. The application of the systematic statistical characterisation process would therefore provide more evidence for selecting one candidate distribution over another to characterise the D_T variability, as performed for the S-N dataset in Chapter 4.

Complex 'Stress' Distribution Types

Despite Chapter 4 detailing and demonstrating a systematic statistical characterisation process that selected a 3P Weibull distribution to represent the variability of N_f within S-N datasets, it was observed in Chapters 7 and 8 that the improved statistical characterisation of the input design parameter variability resulted in complex histogram shapes for the variability in D_T values. Ultimately, the D_T histograms could not be characterised using common candidate distribution types and as a result, it can be concluded that the consequence of the enhanced statistical characterisation of design parameters is the need to increase the sophistication of the post processing of the output (i.e. the 'stress' distribution within the SSI approach) from the MCS-SSI probabilistic fatigue methodology. The balance of the research focus of this thesis between design parameter characterisation and post processing of the methodology output will be discussed further in Section 9.3.

'Kernel' or 'non-parametric' distributions have been proposed as a method to fit a probability distribution to a dataset, without needing to assume a candidate distribution type [278]. Similar to the non-parametric surrogate modelling methods described in Chapter 6, Kernel distributions provide a 'smooth' fit to the dataset histogram and could therefore be used to fit a probability distribution to D_T values that demonstrate complex histogram shapes. However, from a review of the literature, it is surprising to observe that Kernel distributions are yet to be used for probabilistic fatigue analysis and as a result, it is recommended that such approaches are investigated as a priority for the probabilistic analysis field.

Combining Features and FEA Models

The system reliability approach used to generate component-level and assembly-level p_f estimates demonstrates a limitation when applied to FEA stress models of components. As series system reliability approaches (see Equation 3.6) summate the p_f values of every feature included in the probabilistic analysis, the $p_{f_{component}}$ value effectively becomes sensitive to the mesh density of the FEA model[2]. As a result, future implementation of the probabilistic fatigue methodology

[2] i.e. as the mesh density increases, the $p_{f_{component}}$ will also increase.

would require the application of the approach proposed by Leverant et al [161], which groups FEA elements with a similar p_f into zones of equal p_f, prior to summating the p_f zones to produce $p_{f_{component}}$.

Another challenge raised by FEA models within the probabilistic fatigue methodology is how to account for dimensional variability within FEA models. Whilst it is technically feasible to update FEA model geometries to reflect dimensional variability, it is not currently clear at which location stress values should be taken, either by recording stresses at specific element locations, or as defined in 'free-space' by the FEA model global coordinate system. However, as the sensitivity analysis results for the lower side-stay fuse pin in Chapter 7 suggested that dimensional variability provides only a negligible contribution to the variability in D_T values, the representation of dimensional variability in FEA models may not be necessary when performing probabilistic fatigue analysis. Despite this, the impact of dimensional variability on the magnitude of K_t stress concentration factors should not be ignored, especially in design cases where multiple stress concentrations occur at the same location on a component [261]. Therefore, future applications of the probabilistic fatigue methodology should explore the sensitivity of the D_T variability to dimensional variability in such design cases.

'Strength' Distribution Failure Criterion

The MCS-SSI probabilistic fatigue methodology developed and demonstrated in this thesis has assumed that the Miner's rule failure criterion D_{fail} is deterministic. As a result, the 'strength' distribution within the SSI approach has been modelled as a single value of $D_{fail} = 1$. However, it has been suggested that the due to limitations and assumptions within Miner's rule, such as neglecting the effect of loading sequence, variability is present in D_{fail} [83]. Whilst a probabilistic failure criterion has not been represented within the MCS-SSI probabilistic fatigue methodology, this could be easily implemented by using closed-form, numerical integration or MCS approaches to evaluating the SSI equation shown previously in Equation 2.1 [29, 44].

Unfortunately, there is currently limited data available to quantify the variability in D_{fail} and the statistical characterisation of the variability in D_{fail} has resulted in significantly different results. For example, Ocampo et al recommend that a Normal distribution should be used to characterise D_{fail} variability [39], whilst Wirsching proposed the use of a Log-Normal distribution [83, 279]. Therefore, in order for the MCS-SSI probabilistic fatigue methodology to be truly representative of fatigue as a failure mode, the fatigue design community must make a conscious effort to characterise the variability in D_{fail}.

9.1.2 Exploitation of Probabilistic Fatigue Methodology within Deterministic Fatigue Design and Analysis

The second research question defined in Chapter 1 considered the impact of probabilistic fatigue methodologies on the existing deterministic analysis process and how probabilistic methodologies can support fatigue design activities, in line with the overall research aim:

- *Can a probabilistic fatigue methodology be used to support the existing safe-life fatigue analysis process and fatigue design?*

The fatigue design community has had to account for, and mitigate the effects of, variability in fatigue design parameters since its inception [6, 22, 35], as highlighted by the wide range of conservatism approaches identified previously in Chapter 2. Consequently, the fatigue design process comprises of significant amounts of data generation and design parameter characterisation [6, 35]. As a result, the work performed within this thesis concerning dataset generation and design parameter characterisation can be used to directly support the existing deterministic safe-life fatigue analysis process.

Firstly, the systematic statistical characterisation process defined and demonstrated in Chapter 4 facilitated the selection of a more accurate distribution type for the variability in N_f values within S-N datasets. By providing additional evidence to select a 3P Weibull distribution over the commonly-assumed 2P Log-Normal distribution, it was demonstrated in Section 4.4 that the safe-life of a component designed using 3P Weibull P-S-N curves could be increased by 20%. Such an increase in design life is even more important for safe-life components, which are retired based on usage rather than observation of fatigue crack initiation and propagation, and as a result, cannot benefit from the maintenance actions available for damage tolerant components. Therefore, the robust and systematic statistical characterisation processes required to support a probabilistic fatigue methodology can also be used to directly improve the statistical characterisation required in the existing deterministic fatigue design and analysis process, potentially yielding more efficient components with longer safe-life values.

In addition, Chapter 5 demonstrated how big-data sources could be used to challenge the conservatism currently required in the assumed landing gear load spectra for deterministic fatigue design. Big-data sources permit the relaxation of the often conservative assumptions required in deterministic design through providing data and statistics that were previously unavailable. As big-data sources are becoming more readily available across all engineering sectors [59, 280, 281], it is anticipated that the careful handling of such data sources could be used to challenge assumptions and reduce conservatism throughout the fatigue design community.

As a result, the novel technical work presented in Chapters 4 and 5 has highlighted the direct utility of the methods and approaches required to implement a probabilistic fatigue methodology in supporting the existing deterministic safe-life fatigue design and analysis process. The exploitation of such methods to support existing fatigue design and analysis processes is

expected to provide the most immediate impact on the fatigue design community. Guidance and best practice for successfully implementing probabilistic design and analysis approaches typically recommends that probabilistic methodologies are to be introduced into existing design and analysis processes incrementally [46, 54]. Due to the significant cultural and 'mindset' change required by engineers to adopt probabilistic approaches [23, 30], the demonstration of how probabilistic methods can support the existing design and analysis process provides the first step to increasing the 'buy-in' from engineers that is so vital for the successful implementation and survival of probabilistic methodologies and approaches to design [45, 46]. [REDACTED].

It is also interesting to note that when using the probabilistic fatigue methodology to support the existing deterministic design process, it is *epistemic* uncertainty that is predominately challenged. Concerning big-data sources, the real-time tracking of aircraft provided the required data to overcome the lack-of-knowledge that requires potentially conservative assumptions regarding ground manoeuvre sequencing to be made during deterministic design. In a similar manner, Kiureghian and Ditlevsen highlight that the assumption of a distribution type for design parameters can lead to epistemic uncertainty [42]. Therefore, the systematic statistical characterisation process developed in Chapter 4 helps to reduce epistemic uncertainty in fatigue design approaches, through ensuring a more accurate characterisation of the variability (or aleatoric uncertainty) present in S-N datasets. Ultimately, the support provided by the probabilistic fatigue methodology to the existing deterministic process blurs the distinction between aleatoric and epistemic uncertainty, further supporting the view of Kiureghian and Ditlevsen that it is often challenging to assign sources of uncertainty into either aleatoric or epistemic sources [42].

Concerning landing gear design in general, Chapter 1 highlighted how landing gear are mass-critical structures within aerospace structural design [3, 4]. During the introduction to probabilistic methods in Chapter 1, it was suggested that probabilistic design approaches could reduce over-design and hence, component mass, through challenging the conservatism present in safety factors [8, 45, 48]. Whilst this has not been explicitly performed within this thesis, the application of the probabilistic fatigue methodology to the landing gear component case studies in Chapters 7 and 8 did highlight that component-level p_f estimates were typically dominated by a few specific engineering features. These features demonstrated significantly higher p_f values than the other features on the component. Examples of such fatigue-critical features are the pins in the lower side-stay assembly and the upper hole locations of the lower drag brace. This observation suggests that from the perspective of fatigue reliability, many features on landing gear components are over-designed, resulting in negligible p_f values. As a result, the component geometry at such features could be optimised following the probabilistic analysis, by reducing the component sectional areas in the over-designed features, ultimately reducing the component mass. This in turn would increase the overall efficiency of the landing gear assembly [8].

9.2 Overcoming Blockers to Probabilistic Design

Beyond generating p_f estimates for safe-life landing gear components, the novel technical work performed over Chapters 2 to 8 explored how probabilistic methodologies can be used to overcome the inhibiting factors (or 'blockers') that currently prevent the wider utilisation of probabilistic approaches to design. The blockers to probabilistic design were highlighted in Chapter 1. Figure 9.1 overleaf summarises how the novel elements of the technical work performed in this thesis contribute to overcoming the various blockers to probabilistic design approaches, based on the tables presented in the summary of each chapter (Tables 2.2, 3.1, 4.11, 5.6, 6.17 and 8.21). Whilst the probabilistic fatigue methodology was demonstrated using case studies related to safe-life landing gear components, the summary points presented in Figure 9.1 are general in nature and could apply to any implementation of probabilistic design and analysis. The remainder of this section aims to answer the remaining research questions posed in Chapter 1.

9.2.1 Method Selection and Framework Definition

The penultimate research question defined in Chapter 1 aimed to identify whether the characteristics of the implemented probabilistic analysis method and the probabilistic analysis framework could help to overcome the blockers to probabilistic design approaches:

- *Can careful selection of a probabilistic analysis method, along with the construction of a systematic probabilistic analysis framework, result in a probabilistic fatigue methodology that overcomes the blockers to probabilistic design approaches?*

During the literature review performed in Chapter 2, it was observed that there is limited guidance currently available for selecting the probabilistic analysis method to implement for a new probabilistic analysis case. As a result, the selection of the MCS-SSI probabilistic analysis method could only by driven by the need to overcome the blockers to a probabilistic design approach. Consequently, the selection of an MCS-based probabilistic analysis method enabled the full complexity of the existing safe-life fatigue analysis process and design parameter variability to be retained in the probabilistic methodology. Therefore, the selection of the MCS-SSI probabilistic analysis method contributed to overcoming the *required simplifications/assumptions* and *accuracy of data characterisation* blockers. Likewise, the MCS-SSI probabilistic analysis method was capable of being applied to case studies of varying complexity without modification. This demonstrated that only a single probabilistic fatigue methodology is required to support fatigue design, reducing the knowledge required to perform probabilistic fatigue analysis in different design cases. This is a vital observation, as it is often stated that novel design and analysis methodologies fail to be successfully implemented due to their 'bespoke' nature when created for a specific analysis case [54]. Therefore, the careful selection of the MCS-SSI probabilistic analysis method has helped to overcome the blockers to a probabilistic design approach. Through-

out the development of the methodology, [REDACTED]. However, as the probabilistic fatigue methodology presented in this thesis provides an MCS-SSI method than can be employed when the convergence of a 'pure' MCS cannot be guaranteed, the *computational expense* blocker was also overcome through the selection of an MCS-SSI probabilistic analysis method.

Concerning the novel probabilistic analysis framework defined in Chapter 3, it is important to highlight that such a framework is required to fully exploit the advantages of each element of the methodology. For example, whilst the MCS-SSI probabilistic analysis method can incorporate any distribution type to characterise the variability in design parameters, this is only of benefit if a robust and accurate statistical characterisation process is also available. This thesis has also demonstrated that tens of methods are required to implement a probabilistic methodology and the framework presented in Chapter 3 will help practicing engineers understand how each of the required methods interact with one another.

The consequence of requiring such a large number of individual methods to perform probabilistic fatigue analysis is the large resource burden that would be required to understand, implement and test the required methods within an industrial engineering environment. However, the probabilistic fatigue analysis framework presented in this thesis also demonstrates how each of the individual methods can be utilised to support other engineering activities. This ultimately would increase the return from the resources required to implement a probabilistic approach through facilitating other novel design approaches. The maximisation of the return on resources for implementing the probabilistic fatigue methodology would increase the 'buy-in' from engineers. Therefore, the probabilistic analysis framework developed during this work has helped to overcome the *required knowledge* blocker to probabilistic design approaches.

Finally, it is hoped that the systematic processes for statistical characterisation, surrogate model selection and MCS-SSI implementation defined in this thesis will support other practitioners during the future implementation of probabilistic methodologies to both fatigue and general engineering design and analysis. It is intended that the definition of such processes will make the required methods more accessible for engineers, specifically those who are new to the field or who have a limited statistical background, through consolidation of the vast amount of knowledge required to implement probabilistic methodologies. [REDACTED].

FIGURE 9.1. A matrix summarising how the probabilistic fatigue methodology overcomes the blockers to a probabilistic design approach.

9.2.2 Exploitation of Recent Advances

Over the past decade, new mathematical and statistical approaches have been developed that offer opportunities to increase the accuracy of probabilistic methodologies, along with methods that can reduce the computational expense of such methodologies. Therefore, the final research question of this work was:

- *Can recent advances in probabilistic approaches and aerospace structural design, such as surrogate modelling and 'big-data' sources, assist probabilistic fatigue methodologies in overcoming the blockers to probabilistic design approaches?*

Whilst the most recent applications of probabilistic fatigue methodologies have focused on targeted sampling approaches [57, 133], since the last major interest in the wider implementation of probabilistic design approaches during the 1990s and 2000s [23, 45, 46], the recent advances of big-data sources and surrogate modelling have become available. As a result, the implementation of a probabilistic fatigue methodology to the safe-life fatigue analysis of landing gear components provided an opportune context in which to investigate the utility and exploitation of these recent advances within probabilistic methodologies.

Firstly, Chapter 5 investigated how landing gear ground manoeuvre statistics could be generated from the ADS-B transponder big-data source. Ultimately, the exploitation of a big-data source within the probabilistic fatigue methodology permitted the statistical characterisation of design parameter variability that was not previously characterised due to a lack of available data. As a result, beyond overcoming the *availability of data* blocker, the utilisation of big-data sources can also greatly increase the accuracy of a probabilistic methodology by incorporating design parameter variability which otherwise would have to be neglected or assumed. By a similar nature, the exploitation of big-data sources within probabilistic methodologies greatly increases the accuracy of the characterisation of design parameter variability, by providing larger datasets than would be have been previously available (e.g. global aircraft fleet tracking via ADS-B compared to the in-service monitoring of only a few aircraft). As lack of data and inaccuracy in data characterisation represent a major cause of the scepticism in the results from probabilistic methodologies [23, 45, 46], the employment of big-data sources permits a large number of the blockers to probabilistic design approaches to be easily overcome. Therefore, big-data sources will become a significant part of the future development and implementation of probabilistic design approaches.

Concerning the exploitation of surrogate modelling within the probabilistic fatigue methodology, the successful implementation of the methodology on the landing gear component case studies would simply not have been possible without surrogate modelling. Due to the CPU run-times for single evaluations of the linear static and linear elastic FEA models developed in Chapters 6 to 8, surrogate modelling (specifically RSM approaches) was required to mitigate the prohibitive computational expense of the MCS-SSI probabilistic analysis method. As a result, the

utilisation of surrogate modelling methods is an unavoidable element of performing probabilistic analysis of the complex and simulation-based deterministic analysis approaches employed in the modern engineering sector.

The RSM surrogate models generated within this thesis were for linear static FEA loads and linear elastic FEA stress models, which are the type of FEA models most routinely used for fatigue analysis [7]. It is therefore intended that the extensive utilisation of surrogate modelling methods within this thesis, coupled with the surrogate modelling selection process and simplicity of RSM approaches, will support the wider employment of surrogate modelling methods for structural analysis, across static and fatigue domains, in both deterministic and probabilistic approaches. However, it is also recommended that the linear superposition approaches proposed by Draper and Halfpenny et al are explored further as a route to representing linear FEA models within probabilistic analysis [7, 61].

Beyond reducing the computational expense of the probabilistic fatigue methodology to a feasible level, surrogate modelling methods also permitted the full complexity of the FEA MLG beam model and lower drag brace linear elastic FEA stress model to be incorporated into the probabilistic fatigue methodology. The utilisation of surrogate modelling methods therefore enabled the existing deterministic analysis process to be used 'as-is' within the probabilistic fatigue methodology. As a result, surrogate modelling methods predominately overcome the *required simplifications/assumptions* blocker to a probabilistic design approach. It is an interesting observation that surrogate modelling was vital to facilitate a probabilistic methodology for application to an S-N analysis process that consists of relatively simple FEA models (i.e. linear, static and elastic). Consequently, the need for surrogate modelling is even more critical in the future when considering probabilistic approaches for more complicated design and analysis processes, which may be reliant on non-linear FEA or dynamic loading simulations.

However, the recent advances of big-data sources and surrogate modelling could only support the overcoming of the blockers to probabilistic design approaches through the definition of systematic processes for data collection, surrogate model training and surrogate model selection, along with their inclusion within the probabilistic analysis framework from Chapter 3. As a result, the importance of systematic methods to implement probabilistic methodologies has once again been highlighted. Finally, both big-data sources and surrogate modelling are expected to perform major roles in the ever-growing employment of 'digital twins' for the monitoring of in-service components [58, 282, 283]. The development of digital twins for components should be aligned with the implementation of probabilistic approaches in order to maximise the utility of the resource burden required to develop these two novel design and assessment approaches.

9.3 Outlook for Probabilistic Design Approaches: Future Blockers

The previous sections of this chapter have demonstrated how the probabilistic fatigue methodology and its supporting methods can overcome the following blockers to a probabilistic design approach:

- Computational Expense.
- Required Simplifications/Assumptions of the Existing Deterministic Analysis Process.
- Availability of Data.
- Accuracy of Data Characterisation.
- Required Knowledge.

It is interesting to observe that the novel work performed to overcome these blockers is predominately focused at the 'input' stage of the probabilistic methodology, concerning data generation, statistical characterisation and the adoption of surrogate modelling to represent the existing analysis process. The 'front-loading' of the work performed in this thesis has therefore highlighted that future blockers to probabilistic approaches concern the post processing of the results from the probabilistic fatigue methodology, especially concerning tail-sensitivity and lack-of-fit for candidate distributions as discussed in Section 9.1.1.

In a similar manner, the scope of this thesis has been limited to considering the probabilistic fatigue methodology and has therefore not discussed how the p_f results from the methodology could be used in probabilistic design. To perform probabilistic design, p_f estimates are compared to probabilistic design criteria in order to establish whether a design satisfies the reliability requirements placed upon it [45]. For safe-life components, probabilistic design would set component safe-life values based upon the component demonstrating an acceptable probability of failure '$p_{f_{acc}}$' (i.e. the probability of the component failing to achieve its design safe-life).

Probabilistic design criteria are also known as reliability targets 'R_T'. The definition of R_T values represents one the greatest future challenges in implementing a probabilistic approach to design, as a result of the large number of legal, technical and socioeconomic considerations that must be factored into the development of such values [30, 45]. This is especially the case for safety-critical components and a significant cultural and 'mindset' change is required to accept the finite probability of failure for such components [30].

Currently, $p_{f_{acc}}$ and R_T values do not exist for safe-life landing gear components and therefore, the implementation of a probabilistic fatigue design approach would require extensive engineering effort to define these values. However, the following approaches to defining reliability targets are proposed as future work:

- Assessing the intended reliability derived from existing safety factors, which are based on the safe-life variability from full scale component testing. Habermann suggests that this would represent a $p_{f_{acc}}$ of between 1×10^{-3} and 2×10^{-4} at the component safe-life [254].
- Developed from certification guidelines, such as EASA CS25 for large civil aircraft, which requires systems that could result in a catastrophic failure (i.e. loss of the aircraft) to have a failure rate of no greater than $p_{f_{acc}} = 1 \times 10^{-9}$ per-flight hour [24]. CS25 also defines that landing gear structural components should demonstrate an acceptably low probability of failure due to fatigue, although this value is not currently quantified within the certification specifications [24].
- Based on the number of parts in service, such that the $p_{f_{acc}}$ is less than observing one part failure within the aircraft fleet. This was performed for military helicopters under the 'six-nines' reliability target [114].
- Based on the current in-service failure rate (if deemed to be acceptable), as identified by Schmidt, who showed that the current probability of a civil aircraft landing gear failure due to fatigue is $p_f = 4.7 \times 10^{-8}$ per-flight cycle [16].
- As part of the reliability 'budget' from Failure Mode, Effects and Criticality Analysis (FMECA) [29].

It is expected that the definition of R_T values for safe-life landing gear components would use all of the routes listed above and would require input from aerospace manufacturers, aircraft operators and regulatory bodies. In addition, it is anticipated that there will be numerous challenges regarding the assumptions within R_T values, such as the assumption of an average p_f per-flight cycle, along with how reliability targets are distributed across the components within MLG assemblies. [REDACTED]. Consequently, it is expected that the definition of such values will be the most significant remaining blocker to implementing probabilistic approaches in different industrial sectors. However, despite the challenges facing the future definition of R_T values, they should not be considered insurmountable as reliability targets are included in the regulatory material for Eurocode3 steel structures [77] and the UK nuclear sector is encouraging the adoption of probabilistic approaches for structural integrity based on reliability targets [51].

Over the past four decades, during which the various methods required for probabilistic design approaches have come to maturity, the blockers and inhibiting factors that prevent the wider implementation of such approaches have concentrated on the areas concerning the

probabilistic methodology and the characterisation of design parameter variability. However, the final novel contribution of this thesis is the conclusion that these areas are no longer the blockers to implementing probabilistic design approaches. As discussed throughout this chapter, the development of big-data sources and surrogate modelling methods has greatly reduced the technical challenges related to implementing probabilistic design approaches since the last period of significant interest in probabilistic approaches during the 1990s and 2000s. As a result, the findings of this thesis represent a 'step change' which highlights that whilst technical challenges no longer inhibit probabilistic approaches to design, challenges related to the implementation activities (e.g. definition of reliability targets) and the cultural 'mindset' change required to perform design using p_f estimates remain the final blockers to probabilistic design approaches.

The importance of facilitating the 'mindset' change required to implement probabilistic approaches on a wider scale was demonstrated previously during the 1990s when the SAE guidelines for implementing probabilistic approaches identified that the development of probabilistic design approaches and reliability targets was "*behind the actual possibilities based on new hardware and software developments*" [46]. This statement is even more representative of the blockers to probabilistic design approaches in the present day due to the highly accurate and sophisticated characterisation of design parameter variability that can now be performed, coupled with the retention of the full deterministic analysis complexity achievable with the use of MCS methods.

To further facilitate the mindset change required to successfully implement a probabilistic fatigue design approach, there are additional implementation considerations that must be addressed in order to evolve the probabilistic fatigue methodology into a complete probabilistic design approach. Firstly, extensive training will be required to educate engineers in the utilisation of probabilistic design approaches and the probabilistic fatigue methodology. It is surprising that there is limited guidance in the literature, beyond those cited in this thesis, regarding the training requirements for implementing novel design approaches in industrial environments [23, 46, 54]. The consolidation of knowledge performed by the systematic processes for statistical characterisation, surrogate modelling and probabilistic methodologies developed during this thesis could greatly ease the training burden required to implement a probabilistic approach. In a similar manner, such systematic processes could reduce the cultural and 'mindset' change required to adopt probabilistic approaches. This would be achieved by the various ways in which the processes developed within the presented work increase the 'buy-in' to probabilistic approaches from engineers and management as highlighted throughout the current chapter.

Despite the significant challenges of evolving the probabilistic fatigue methodology to a practical design approach based on reliability targets, there has been recent work in the aerospace sector that has demonstrated the sector's aspiration to transition to a probabilistic approach for structural design. Rosario et al have questioned the conservatism present in the current design criteria used within civil aircraft static structural design using statistical and probabilistic arguments [284]. In addition, Larsen and Raju have also stated the benefits to aerospace static

structural design of transitioning from the existing deterministic process [285]. Concerning fatigue design and analysis, the Federal Aviation Administration (FAA) have recently published probabilistic methodologies for the fatigue assessment of light aircraft structures and engine turbine components [286, 287]. It is hoped that the work performed within this thesis can further support the implementation of probabilistic design approaches within the aerospace structural design community, especially regarding the systematic processes defined for performing statistical characterisation and surrogate modelling, along with the systematic framework for the MCS-SSI probabilistic fatigue methodology.

9.4 Summary

This chapter has demonstrated how the novel contributions of the work presented in this thesis have achieved the research aim. The research questions posed in Chapter 1 were also answered by the following novel elements of work:

- Development and demonstration of a probabilistic fatigue methodology for safe-life landing gear components.
- Development of a systematic statistical characterisation process for design parameters.
- Improved characterisation of landing gear ground manoeuvre variability from 'real-time' tracking of aircraft using a big-data source.
- Extensive surrogate modelling of landing gear linear static FEA loads models and linear elastic FEA stress models.
- Definition of systematic processes for implementing the probabilistic fatigue methodology, including the MCS-SSI analysis framework and surrogate model selection.

When combined, the novel elements of work supported the overcoming of the *computational expense*, *required simplifications/assumptions*, *availability of data*, *accuracy of data characterisation* and *required knowledge* blockers to a probabilistic design approach. However, this chapter has also highlighted that a number of limitations also exist within the presented methodology. These limitations predominately concern the post processing of results from the methodology and the required engineering and research effort required to mature the methodology into a practical probabilistic fatigue design approach. Due to the enhanced design parameter data generation and characterisation approaches presented in this thesis, the final blockers to probabilistic design approaches that now remain are the generation of reliability target values and the facilitation of the cultural and 'mindset' change required to make design decisions using p_f estimates and reliability targets.

Regardless of the remaining blockers to probabilistic approaches, the probabilistic fatigue methodology has supported the future implementation of a probabilistic fatigue design approach for safe-life landing gear components, by providing the mathematical methods and framework required to compute the p_f values required for probabilistic design. The work presented in this thesis has therefore satisfied the research aim to "*develop a probabilistic fatigue methodology to support the fatigue design of safe-life components*". Based on the discussion presented in this chapter, it has been shown that the probabilistic fatigue methodology has supported both deterministic and probabilistic approaches for safe-life fatigue design, as a result of the work required to satisfy the research aim and research questions.

Finally, throughout this work it has been assumed that the existing safe-life fatigue analysis process is physically representative of fatigue as a failure mode. Therefore model-based uncertainties (i.e. the assumptions present within S-N fatigue analysis) have not been challenged as they were considered outside the scope of this thesis. Such examples of model-based uncertainties (also known as epistemic uncertainty [42]) include the type of S-N curve shape used and the assumed correlation between N_f values and σ_{FL} values as discussed in Chapter 4. Other sources of model-based uncertainty include the assumptions present within Miner's rule and any modelling errors present in the original FEA models, as highlighted in Section 8.1.6 [6, 83]. As a result, future investigations into these areas are required, as supported by the extensive discussion the of matter provided by Kiureghian and Ditlevsen [42].

CHAPTER 10

CONCLUSIONS AND FURTHER WORK

10.1 Conclusions

This thesis has presented the development and demonstration of a probabilistic fatigue methodology for safe-life landing gear components. A hybrid methodology consisting of Monte Carlo Simulation and Stress-Strength Interference approaches was successfully implemented on case studies consisting of different levels of component and analysis complexity. The probabilistic fatigue methodology was constructed with the aim of overcoming the inhibiting factors, known as 'blockers', that currently prevent the wider implementation of probabilistic design approaches. The blockers to probabilistic design include:

- Computational Expense.
- Required Simplifications/Assumptions of the Existing Deterministic Analysis Process.
- Availability of Data.
- Accuracy of Data Characterisation.
- Required Knowledge.

This thesis has presented the novel utilisation of big-data sources to generate landing gear loading statistics in order to challenge the *availability of data* blocker. Extensive employment of surrogate modelling methods also reduced the *computational expense* of conducting analysis using the probabilistic fatigue methodology. Coupled with the development of a probabilistic analysis framework and a systematic process for statistical characterisation, the exploitation of the recent developments of big-data sources and surrogate modelling within the fields of aerospace

structural design and probabilistic analysis, resulted in a probabilistic fatigue methodology that overcame the blockers to probabilistic design.

In order to summarise the findings and research contributions of this thesis concerning probabilistic methodologies in general, and number of conclusions can be drawn out from the presented research. It is important to note that such conclusions are made within the constraints of the work performed within this thesis, that is, based upon on the available compuational resource for the case studies and the application of the probabilistic fatigue methodology to stress-life fatigue analysis comprising of linear static and linear elastic finite element models. The conclusions of this thesis are as follows:

- A probabilistic fatigue methodology was successfully defined and developed based upon a hybrid probabilistic analysis method consisting of both Monte Carlo Simulation and Stress-Strength Interference approaches.
- The probabilistic fatigue methodology can be used to produce probability of failure estimates for safe-life landing gear components at a feature, component and assembly-level.
- The proposed probabilistic fatigue methodology is insensitive to the specific assessment case as a result of the probabilistic analysis framework and the use of the Monte Carlo Simulation based method.
- Probability of failure estimates based on 'pure' Monte Carlo Simulation results or tail-fitting approaches fail to provide reliable probability of failure estimates when compared with those generated from Stress-Strength Interference methods.
- Probabilistic fatigue methodologies and their supporting methods can be used to support existing fatigue design practices:
  - Identification of component features that are sub-optimal from the standpoint of fatigue reliability.
  - Use of enhanced statistical characterisation to reduce the conservatism in design parameters relating to material properties.
  - Use of big-data sources to reduce conservatism in the load spectra used for deterministic fatigue analysis.
- The use of systematic statistical characterisation processes, surrogate modelling and big-data sources can overcome the following blockers to probabilistic design approaches:
  - Computational Expense.
  - Required Simplifications/Assumptions of the Existing Deterministic Analysis Process.
  - Availability of Data.

  - Accuracy of Data Characterisation.
  - Required Knowledge.

- The remaining blockers to a probabilistic design approach concern the development of probabilistic design criteria and the cultural and 'mindset' change required to perform design based upon fatigue reliability values.
- Surrogate modelling is vital for implementing probabilistic methodologies on simulation-based analysis processes.
- The knowledge required to implement probabilistic methodologies must be exploited in other engineering activities to reduce the resource burden of developing such approaches.
- Systematic processes, from data collection through to design criteria development, will support the future and wider implementation of probabilistic design approaches.

There are of course conclusions which can also be drawn regarding landing gear fatigue design and analysis based upon the specific case study results presented within this thesis:

- The fatigue design drivers for landing gear components are: variability in stress-life material datasets, variability in ground manoeuvre load factors and variability in the occurrence and sequencing of ground manoeuvres.
- Many engineering features of landing gear components are over-designed from the standpoint of fatigue reliability.
- Extensive research and engineering effort will be required to define fatigue reliability targets for safe-life landing gear components.

10.2 Further Work

This thesis has comprehensively presented the development of a probabilistic fatigue methodology for safe-life landing gear components. Whilst the presented methodology has overcome a large number of the blockers to probabilistic approaches, additional research and engineering activities are required to evolve the methodology into a successfully implemented probabilistic fatigue design approach. As this thesis has focused predominately on data generation, characterisation of design parameter variability and the incorporation of the existing deterministic analysis process into the probabilistic methodology, the recommended further work is aimed at the post processing and utilisation of the results from the probabilistic methodology.

Firstly, due to presence of tail-sensitivity or lack-of-fit when characterising the variability in damage values generated by the probabilistic methodology, further work should consider how probability distributions can be accurately selected and fitted in such cases. It is proposed that

the investigation into, and development of, large sample size Goodness-of-Fit tests could greatly support the characterisation of variability in the probabilistic output. This further work would support the accurate post processing of the probabilistic output, in order to fully benefit from the enhanced statistical characterisation of design parameters afforded by the work shown in this thesis. The utilisation of non-parametric 'Kernel' distributions within probabilistic methodologies could also be explored to combat tail-fitting and lack-of-fit [278].

The greatest challenge remaining for probabilistic approaches is the definition of probabilistic design criteria in the form of reliability targets. Further work must define a systematic and traceable process for generating such values. It is anticipated that the definition of reliability targets will be based upon the existing reliability achieved using safety factors, observed in-service failure rates and extensive dialogue with the relevant regulatory authorities.

Specifically regarding the fatigue design of safe-life landing gear components, the future implementation of a probabilistic design approach should account for the variability in residual stresses and stress concentrations resulting from manufacturing and surface finishing processes. In addition, the fatigue design community must make an active effort to characterise the variability in the failure criterion for Miner's rule.

Finally, it is hoped that the experience and knowledge consolidated within the systematic processes presented within this thesis will support other engineers and practitioners in implementing probabilistic methodologies and their supporting methods throughout engineering design.

REFERENCES

[1] R. K. Schmidt and P. Sartor, "Landing Gear," in *Encyclopedia on Structural Health Monitoring* (C. Boller, F. Chang, and Y. Fujino, eds.), ch. 114, John Wiley & Sons Ltd., 2009.

[2] D. W. Young, "Aircraft landing gears-the past, present and future," *Proceedings of the Institution of Mechanical Engineers, Part D: Journal of Automobile Engineering*, vol. 200, pp. 75–92, 1986.

[3] H. G. Conway, *Landing Gear Design*.
Chapman & Hall, 1958.

[4] S. J. Greenbank, "Landing gear-the aircraft requirement," *Proceedings of the Institution of Mechanical Engineers, Part G: Journal of Aerospace Engineering*, vol. 205, pp. 27–34, 1991.

[5] S. F. N. Jenkins, "Landing gear design and development," *Proceedings of the Institution of Mechanical Engineers, Part G: Journal of Aerospace Engineering*, vol. 203, pp. 67–73, 1989.

[6] J. Schijve, *Fatigue of Structures and Materials*.
Springer, 2nd ed., 2010.

[7] J. Draper, *Modern Metal Fatigue Analysis*.
EMAS Publishing, 2008.

[8] S. Suresh, *Fatigue of Materials*.
Cambridge University Press, 2nd ed., 1998.

[9] J. X. Tao, S. Smith, and A. Duff, "The effect of overloading sequences on landing gear fatigue damage," *International Journal of Fatigue*, vol. 31, pp. 1837–1847, 2009.

[10] W. Schütz, "A History of Fatigue," *Engineering Fracture Mechanics*, vol. 54, no. 2, pp. 263–300, 1996.

[11] J. F. Darlington, *Concept Design for Fatigue Resistance*.
PhD, University of Bristol, 2006.

[12] O. Buxbaum, "Landing Gear Loads of Civil Transport Airplanes," in *Aircraft Fatigue in the Eighties, Proceedings of the 11th ICAF-Symposium*, (Noordwijkerhout, The Netherlands), 1981.

[13] A. I. Gustavsson and A. F. Blom, "Long Time Measurements of Landing Gear Loads on SAAB SF-340 Commuter Aircraft," in *Conference Proceedings on Landing Gear Design Loads, AGARD-CP-484*, 1990.

[14] V. Ladda and H. Struck, "Operational Loads on Landing Gear," in *Conference Proceedings on Landing Gear Design Loads, AGARD-CP-484*, 1990.

[15] P. Beaudet and M. Roth, "Failure Analysis Case Histories of Canadian Forces Aircraft Landing Gear Components," in *Conference Proceedings on Landing Gear Design Loads, AGARD-CP-484*, 1990.

[16] R. K. Schmidt, *Is 'Safe-Life' Safe Enough?*
MSc, Cranfield University, 2017.

[17] Air Accident Investigation Branch, "AAIB Bulletin: 2/2010 G-BXAR EW/C2009/02/03," 2010.

[18] L. Werfelman, "Gear Collapse," *Journal of Flight Safety Foundation*, no. March, 2010.

[19] BBC News, "BA jobs go after plane write-off," *http://news.bbc.co.uk/1/hi/scotland/edinburgh_and_east/8067315.stm*, 2009.

[20] Office of the Inspector General Department of Defense, "C-17 Landing-Gear Durability and Parts Support Report No. 99-193," 1999.

[21] D. F. O. Braga, S. M. O. Tavares, L. F. M. Da Silva, P. M. G. P. Moreira, and P. M. S. T. De Castro, "Advanced design for lightweight structures: Review and prospects," *Progress in Aerospace Sciences*, vol. 69, pp. 29–39, 2014.

[22] C. C. Osgood, *Fatigue Design*.
Pergamon Press Ltd., 2nd ed., 1982.

[23] Y. M. Goh, C. A. McMahon, and J. D. Booker, "Improved utility and application of probabilistic methods for reliable mechanical design," *Proceedings of the Institution of Mechanical Engineers, Part O: Journal of Risk and Reliability*, vol. 223, no. 3, pp. 199–214, 2009.

[24] European Aviation Safety Agency, "CS-25 Certification Specifications and Acceptable Means of Compliance for Large Aeroplanes Amendment 18," 2016.

[25] Engineering Sciences Data Unit, "ESDU 04019: Endurance of high-strength steels," 2006.

[26] B. J. Greenland, *Resolution of Indeterminate Landing Gear Structure Design*. MEng, Ryerson University, 2007.

[27] J. E. Shigley and C. R. Mischke, *Mechanical Engineering Design*. McGraw-Hill, Inc., 6^{th} ed., 2001.

[28] J. N. Siddall, *Probabilistic Engineering Design*. Marcel Dekker, Inc., 1983.

[29] J. Booker, M. Raines, and K. Swift, *Designing Capable and Reliable Products*. Butterworth-Heinemann, 2001.

[30] M. Lemaire, *Structural Reliability*. John Wiley & Sons, Inc., 2009.

[31] E. B. Haugen, *Probabilistic Mechanical Design*. John Wiley & Sons, Inc., 1980.

[32] I. Elishakoff, *Safety Factors and Reliability: Friends or Foes?* Kluwer Academic Publishers, 2004.

[33] K. Bury, *Statistical Distributions in Engineering*. Cambridge University Press, 1999.

[34] P. H. Wirsching, "Probabilistic Fatigue Analysis," in *Probabilistic Structural Mechanics Handbook: Theory and Industrial Applications* (C. Sundararajan, ed.), ch. 7, pp. 146–165, Chapman & Hall, 1995.

[35] R. A. Heller, *Probabilistic Aspects Of Fatigue ASTM STP511*. American Society for Testing and Materials, 1971.

[36] J. Schijve, "Statistical distribution functions and fatigue of structures," *International Journal of Fatigue*, vol. 27, no. 9, pp. 1031–1039, 2005.

[37] P. H. Wirsching, "Statistical Summaries of Fatigue Data for Design Purposes NASA Contractor Report 3697," 1983.

[38] T. Svensson and P. Johannesson, "Reliable fatigue design, by rigid rules, by magic or by enlightened engineering," *Procedia Engineering*, vol. 66, pp. 12–25, 2013.

[39] J. Ocampo, H. Millwater, G. Singh, H. Smith, F. Abali, M. Nuss, M. Reyer, and M. Shiao, "Development of a Probabilistic Linear Damage Methodology for Small Aircraft," *Journal of Aircraft*, vol. 48, no. 6, pp. 2090–2106, 2011.

[40] Federal Aviation Administration, "A Comparison of Landing Parameters from Manual and Automatic Landings of Airbus A-320 Aircraft," 2001.

[41] J. K. Williams, "The airworthiness approach to structural fatigue," in *Fatigue Design Procedures* (E. Gassner and W. Schütz, eds.), ch. 2, pp. 91–131, Pergamon Press Ltd., 1969.

[42] A. D. Kiureghian and O. Ditlevsen, "Aleatory or epistemic? Does it matter?," *Structural Safety*, vol. 31, no. 2, pp. 105–112, 2009.

[43] D. Sandberg, R. Mansour, and M. Olsson, "Fatigue probability assessment including aleatory and epistemic uncertainty with application to gas turbine compressor blades," *International Journal of Fatigue*, vol. 95, pp. 132–142, 2017.

[44] C. Sundararajan and F. J. Witt, "Stress-Strength Interference Method," in *Probabilistic Structural Mechanics Handbook: Theory and Industrial Applications* (C. Sundararajan, ed.), ch. 2, Chapman & Hall, 1995.

[45] Federal Aviation Administration, "Probabilistic Design Methodology for Composite Aircraft Structures DOT/FAA/AR-99/2," 1999.

[46] SAE International, "AIR5080: Integration of Probabilistic Methods into the Design Process," 1997.

[47] F. Safie and E. P. Fox, "A Probabilistic Design Analysis Approach for Launch Systems," in *AIAA/SAE/ASME 27th Joint Propulsion Conference*, (Sacramento, CA, USA), 1991.

[48] G. Cavallini and R. Lazzeri, "A probabilistic approach to fatigue risk assessment in aerospace components," *Engineering Fracture Mechanics*, vol. 74, pp. 2964–2970, 2007.

[49] R. D'Ippolito, H. Hack, S. Donders, H. Van der Auweraer, N. Tzannetakis, L. Farkas, and W. Desmet, "Robust and Reliable Fatigue Design of Automotive and Aerospace Structures," in *Proceedings of 6th International Conference on Durability and Fatigue (Fatigue 2007)*, (Cambridge, UK), 2007.

[50] Y. T. Tsai, K. H. Lin, and Y. Y. Hsu, "Reliability design optimisation for practical applications based on modelling processes," *Journal of Engineering Design*, vol. 24, no. 12, pp. 849–863, 2013.

[51] Nuclear Structural Integrity Probabilistic Working Group, "Nuclear Structural Integrity Probabilistic Working Principles," 2019.

[52] Y. M. Goh, J. Booker, and C. McMahon, "A Comparison of Methods in Probabilistic Design Based on Computational and Modelling Issues," in *5th International Conference on Integrated Design and Manufacturing in Mechanical Engineering*, (Bath, UK), 2004.

[53] NAFEMS, *Why do - Probabilistic Finite Element Analysis?*
NAFEMS Ltd., 2008.

[54] J. Booker, "A survey-based methodology for prioritising the industrial implementation qualities of design tools," *Journal of Engineering Design*, vol. 23, no. 7, pp. 507–525, 2012.

[55] Health & Safety Executive, "Comparison of Fatigue Provisions in Codes and Standards, Offshore Technology Report 2001/083," 2001.

[56] F. M. Safie, "The role of Probabilistic Design Analysis Methods in Safety and Affordability," in *2016 Annual Reliability and Maintainability Symposium*, (Tuscon, Arizona, USA), 2016.

[57] B. Echard, N. Gayton, and A. Bignonnet, "A reliability analysis method for fatigue design," *International Journal of Fatigue*, vol. 59, pp. 292–300, 2014.

[58] K. Graham, M. Artim, and D. Daverschot, "Aircraft Fatigue Analysis in the Digital Age," in *International Committee on Aeronautical Fatigue and Structural Integrity (ICAF) 36th Conference and 29th Symposium*, (Nagoya, Japan), 2017.

[59] V. E. Badea, A. Zamfiroiu, and R. Boncea, "Big Data in the Aerospace Industry," *Informatica Economica*, vol. 22, no. 1, pp. 17–24, 2018.

[60] M. Z. Li and M. S. Ryerson, "Reviewing the DATAS of aviation research data: Diversity, availability, tractability, applicability, and sources," *Journal of Air Transport Management*, vol. 75, pp. 111–130, 2019.

[61] A. Halfpenny, M. Bonato, A. Chabod, P. Czapski, J. Aldred, and K. Munson, "Probabilistic Fatigue and Reliability Simulation," in *NAFEMS World Congress 2019*, (Quebec City, Canada), 2019.

[62] T. Xiaojiang, *The Investigation of Reliability in Landing Gear Structure Design*. MSc, Cranfield University, 2010.

[63] P. Sartor, K. Worden, and R. K. Schmidt, "Bayesian sensitivity analysis of flight parameters that affect main landing gear yield locations," *The Aeronautical Journal*, vol. 118, no. 1210, pp. 1481–1497, 2014.

[64] R. S. Langley, "The application of level II reliability theory," *Proceedings of the Institution of Mechanical Engineers*, vol. 209, pp. 291–298, 1995.

[65] D. Yadav and N. C. Nigam, "Reliability Analysis of Landing Gear Fatigue Life," in *Probabilistic Methods in the Mechanics of Solids and Structures. International Union of Theorhetical and Applied Mehcanics Symposium 1984* (S. Eggwertz and N. C. Lind, eds.), (Stokholm, Sweden), pp. 569–577, Springer Berlin Heidelberg, 1985.

[66] E. Castillo and A. Fernández-Canteli, *A Unified Statistical Methodology for Modeling Fatigue Damage*.
Springer, 2009.

[67] V. Rathod, O. P. Yadav, A. Rathore, and R. Jain, "Probabilistic Modeling of Fatigue Damage Accumulation for Reliability Prediction," *International Journal of Quality, Statistics, and Reliability*, 2011.

[68] D. Paolino and M. Cavatorta, "On the application of the stochastic approach in predicting fatigue reliability using Miner's damage rule," *Fatigue & Fracture of Engineering Materials & Structures*, vol. 37, no. 1, pp. 107–117, 2014.

[69] Y. Liu and S. Mahadevan, "Stochastic fatigue damage modeling under variable amplitude loading," *International Journal of Fatigue*, vol. 29, no. 6, pp. 1149–1161, 2007.

[70] H. Shen, J. Lin, and E. Mu, "Probabilistic model on stochastic fatigue damage," *International Journal of Fatigue*, vol. 22, no. 7, pp. 569–572, 2000.

[71] W. F. Wu and T. H. Huang, "Prediction of fatigue damage and fatigue life under random loading," *International Journal of Pressure Vessels and Piping*, vol. 53, no. 2, pp. 273–298, 1993.

[72] Federal Aviation Administration, "Fatigue, Fail-Safe, and Damage Tolerance Evaluation of Metallic Structure for Normal, Utility, Acrobatic, and Commuter Category Airplanes AC23-13A," 2005.

[73] Sandia National Laboratories, "Evaluation of Conservatisms and Environmental Effects in ASME Code, Section III, Class 1 Fatigue Analysis SAND94-0187," 1994.

[74] British Standards Institute, "BS EN 61400-1:2005+A1:2010 Wind Turbines, Part 1: Design Requirements," 2016.

[75] DNV GL, "Fatigue Design of Offshore Steel Structures DNV-RP-C203," 2014.

[76] DNV GL, "Design of Offshore Steel Structures, General LRFD Method DNVGL-OS-C101," 2015.

[77] British Standards Institute, "BS EN 1993-1-9:2005, Eurocode 3: Design of Steel Structures - Part 1-9: Fatigue," 2010.

[78] Sandia Corporation, "Factors for One-sided Tolerance Limits and for Variables Sampling Plans SCR-607," 1963.

[79] N. Micone and W. De Waele, "Comparison on Fatigue Design Codes with Focus on Offshore Structures," in *Proceedings of the ASME 2015 34th International Conference on Ocean, Offshore and Arctic Engineering OMAE2015*, (St. John's, Newfoundland, Canada), 2015.

[80] J. Shi, L. Wei, C. Faidy, A. Wasylyk, and N. Prinja, "A Comparison of Different Design Codes on Fatigue Life Assessment Methods," in *Proceedings of the ASME 2016 Pressure Vessels and Piping Conference PVP2016*, (Vancouver, British Columbia, Canada), 2016.

[81] N. Doorn and S. O. Hansson, "Should Probabilistic Design Replace Safety Factors?," *Philosophy & Technology*, vol. 24, pp. 151–168, 2011.

[82] L. Min, X. Xiaofei, and Y. Qing-Xiong, "Cumulative fatigue damage dynamic interference statistical model," *International Journal of Fatigue*, vol. 17, no. 8, pp. 559–566, 1995.

[83] P. H. Wirsching, "Fatigue Reliability for Offshore Structures," *Journal of Structural Engineering*, vol. 110, no. 10, pp. 2340–2356, 1984.

[84] P. H. Wirsching and Y.-N. Chen, "Considerations of probability-based fatigue design for marine structures," *Marine Structures*, vol. 1, pp. 23–45, 1988.

[85] A. Bignonnet, "An Overview on Fatigue Problems in the Car Industry," in *ECF12 - Fracture From Defects*, (Sheffield, UK), pp. 17–22, 1998.

[86] J. J. Thomas, G. Perroud, A. Bignonnet, and D. Monnet, "Fatigue design and reliability in the automotive industry," in *Fatigue design and reliability, European Structural Integrity Society Vol. 23* (G. Marquis and J. Solin, eds.), pp. 1–11, Elsevier, 1999.

[87] J. J. Thomas, "Fatigue Modeling for Automotive Applications SAE Technical Paper 2002-01-0655," 2002.

[88] Y. X. Zhao, "Methodology for strain-based fatigue reliability analysis," *Reliability Engineering and System Safety*, vol. 70, no. 2, pp. 205–213, 2000.

[89] J. Zhao, J. Tang, and H. C. Wu, "A Generalized Random Variable Approach for Strain-Based Fatigue Reliability Analysis," *Journal of Pressure Vessel Technology*, vol. 122, no. 2, pp. 156–161, 2000.

[90] S. Beretta and S. Foletti, "A simple format for failure probability under LCF and its application to a complex component," *Procedia Materials Science*, vol. 3, pp. 2098–2103, 2014.

[91] S. Beretta, S. Foletti, E. Rusconi, A. Riva, and D. Socie, "A log-normal format for failure probability under LCF: Concept, validation and definition of design curve," *International Journal of Fatigue*, vol. 82, pp. 2–11, 2016.

[92] S. Beretta and D. Regazzi, "Probabilistic fatigue assessment for railway axles and derivation of a simple format for damage calculations," *International Journal of Fatigue*, vol. 86, pp. 13–23, 2016.

[93] S.-P. Zhu, H.-Z. Huang, W. Peng, H.-K. Wang, and S. Mahadevan, "Probabilistic PoF-based Framework for Fatigue Life Prediction of Aircraft Gas Turbine Discs," in *18^{th} AIAA Non-Deterministic Approaches Conference*, (San Diego, California, USA), 2016.

[94] S.-P. Zhu, S. Foletti, and S. Beretta, "Probabilistic framework for multiaxial LCF assessment under material variability," *International Journal of Fatigue*, vol. 103, pp. 371–385, 2017.

[95] S.-P. Zhu, Q. Liu, Z. Y. Yu, and Y. Liu, "Fatigue reliability analysis of a turbine disc under multi-source uncertainties," *Procedia Structural Integrity*, vol. 5, pp. 967–972, 2017.

[96] S.-P. Zhu, Q. Liu, and H. Z. Huang, "Probabilistic Modeling of Damage Accumulation for Fatigue Reliability Analysis," *Procedia Structural Integrity*, vol. 4, pp. 3–10, 2017.

[97] S.-P. Zhu, Q. Liu, W. Peng, and X. C. Zhang, "Computational-experimental approaches for fatigue reliability assessment of turbine bladed disks," *International Journal of Mechanical Sciences*, vol. 142-143, pp. 502–517, 2018.

[98] S.-P. Zhu, Q. Liu, J. Zhou, and Z. Y. Yu, "Fatigue reliability assessment of turbine discs under multi-source uncertainties," *Fatigue and Fracture of Engineering Materials and Structures*, vol. 41, pp. 1291–1305, 2018.

[99] S.-P. Zhu, Q. Liu, and Q. Lei, "Probabilistic fatigue life prediction and reliability assessment of a high pressure turbine disc considering load variations," vol. 27, no. 10, pp. 1569–1588, 2018.

[100] C. Roux, X. Lorang, H. Maitournam, and M. L. Nguyen-Tajan, "Fatigue design of railway wheels: A probabilistic approach," *Fatigue and Fracture of Engineering Materials and Structures*, vol. 37, no. 10, pp. 1136–1145, 2014.

[101] A. S. R. Murty and V. N. A. Naikan, "Machinery selection – process capability and product reliability dependence," *International Journal of Quality & Reliability Management*, vol. 14, no. 4, pp. 381–390, 1997.

[102] J. Zhou, H. Z. Huang, Y. F. Li, and J. Guo, "A framework for fatigue reliability analysis of high-pressure turbine blades," *Annals of Operations Research*, 2019.

[103] C. Zhang, J. Wei, H. Jing, C. Fei, and W. Tang, "Reliability-Based Low Fatigue Life Analysis of Turbine Blisk with Generalized Regression," *Materials*, vol. 12, no. 1545, 2019.

[104] M. Ferlin, A. Pyre, F. Lefebvre, S. Oriol, and A. Bignonnet, "DEFFI project for a new concept of fatigue design in the aerospace domain," in *50^{th} AIAA/ASME/ASCE/ASC Structures, Structural Dynamics, and Materials Conference*, (Palm Springs, California, USA), 2009.

[105] S. Bucas, P. Rumelhart, N. Gayton, and A. Chateauneuf, "Stress-strength interference method applied for the fatigue design of tower cranes," *Procedia Engineering*, vol. 66, pp. 500–507, 2013.

[106] A. S. Nowak and K. R. Collins, *Reliability of Structures*.
CRC Press, 2^{nd} ed., 2013.

[107] P. H. Wirsching, T. Y. Torng, and W. S. Martin, "Advanced fatigue reliability analysis," *International Journal of Fatigue*, vol. 13, no. 5, pp. 389–394, 1991.

[108] Y. T. Wu, H. R. Millwater, and T. A. Cruse, "An advanced probabilistic structural analysis method for implicit performance functions," *AIAA Journal*, vol. 28, no. 9, pp. 1663–1669, 1990.

[109] Y. T. Wu and P. H. Wirsching, "New Algorithm for Structural Reliability Estimation," *Journal of Engineering for Gas Turbines and Power*, vol. 113, no. 9, pp. 1319–1336, 1987.

[110] H. Karadeniz, "Uncertainty modeling in the fatigue reliability calculation of offshore structures," *Reliability Engineering and System Safety*, vol. 74, no. 3, pp. 323–335, 2001.

[111] I. Lotsberg, *Fatigue Design of Marine Structures*.
Cambridge University Press, 2016.

[112] K. Kwon and D. M. Frangopol, "Bridge fatigue reliability assessment using probability density functions of equivalent stress range based on field monitoring data," *International Journal of Fatigue*, vol. 32, no. 8, pp. 1221–1232, 2010.

[113] T. Guo, D. M. Frangopol, and Y. Chen, "Fatigue reliability assessment of steel bridge details integrating weigh-in-motion data and probabilistic finite element analysis," *Computers and Structures*, vol. 112-113, pp. 245–257, 2012.

[114] J. Zhao, D. O. Adams, and C. T. Stratford, "Achieving Six-Nine's Reliability Using an Advanced Fatigue Reliability Assessment Model," in *American Helicopter Society 66^{th} Annual Forum*, (Phoenix, Arizona, USA), 2010.

[115] B. Sudret and Z. Guédé, "Probabilistic assessment of thermal fatigue in nuclear components," *Nuclear Engineering and Design*, vol. 235, no. 17-19, pp. 1819–1835, 2005.

[116] H. Sutherland and P. Veers, "Fatigue case study and reliability analyses for wind turbines," in *ASME/JSME/JSES International Solar Energy Conference*, (Maui, Hawaii), 1995.

[117] Sandia National Laboratories, "Probabilistic Fatigue Methodology and Wind Turbine Reliability SAND96-1246," 1996.

[118] D. Veldkamp, *Chances in Wind Energy: A Probabilistic Approach to Wind Turbine Fatigue Design*.
PhD, Delft University, 2006.

[119] D. Veldkamp, "A probabilistic evaluation of wind turbine fatigue design rules," *Wind Energy*, vol. 11, no. 6, pp. 655–672, 2008.

[120] C. Watson, D. Beardsmore, and K. Wright, "A Comparison of the Deterministic and Probabilistic Aspects of the ASME III Fatigue Evaluation Procedures," in *Proceedings of the ASME 2014 Pressure Vessels & Piping Conference PVP2014*, (Anaheim, California, USA), 2014.

[121] Y. M. Asri, E. A. Azrulhisham, A. W. Dzuraidah, A. Shahrir, A. Shahrum, and Z. Azami, "Fatigue Life Reliability Prediction of Stub Axle Using Monte Carlo Simulation," *International Journal of Automotive Technology*, vol. 12, no. 5, pp. 713–719, 2011.

[122] G. Narayanan, K. Rezaei, and U. Nackenhorst, "Fatigue life estimation of aero engine mount structure using Monte Carlo simulation," *International Journal of Fatigue*, vol. 83, pp. 53–58, 2015.

[123] National Aeronautics and Space Administration, "Probabilistic Fatigue Methodology for Six Nines Reliability NASA Technical Memorandum 102757," 1990.

[124] U.S. Army Materials Technology Laboratory, "Assessment of Helicopter Component Statistical Reliability Computations MTL TR 92-71," 1992.

[125] S. Moon, D. Menon, and G. Barndt, "Fatigue life reliability based on measured usage, flight loads and fatigue strength variations," in *American Helicopter Society 52nd Annual Forum*, (Washington DC, USA), pp. 366–389, 1996.

[126] S. Moon, D. Menon, and G. Barndt, "Fatigue Life Reliability Based on Measured Usage, Flight Loads, and Fatigue Strength Variations," *Journal of the American Helicopter Society*, vol. 56, no. 3, pp. 1–18, 2011.

[127] Y. C. Tong, R. A. Antoniou, and C. H. Wang, "A Critical Analysis of the Six-Nines Reliability Methodology," *Journal of the American Helicopter Society*, vol. 48, no. 4, pp. 278–286, 2003.

[128] N. Toulas and P. E. Irving, "Safety Factors and Risk in Usage Monitoring and Fatigue Substantiation of Helicopter Components," in *American Helicopter Society 59th Annual Forum Volume 1*, (Phoenix, Arizona, USA), pp. 374–375, 2003.

[129] S. Dekker, G. Wurzel, and R. Alderliesten, "Reliability modelling for rotorcraft component fatigue life prediction with assumed usage," *The Aeronautical Journal*, vol. 120, no. 1232, pp. 1658–1692, 2016.

[130] J. D. Ocampo, H. R. Millwater, H. Smith, E. Meyer, M. Nuss, M. Reyer, F. Abali, and M. Shiao, "Probabilistic Risk Assessment for Small Airplanes," in *51st AIAA/ASME/ASCE/AHS/ASC Structures, Structural Dynamics, and Materials Conference*, (Orlando, Florida, USA), 2010.

[131] N. A. Zentuti, J. D. Booker, R. A. W. Bradford, and C. E. Truman, "A review of probabilistic techniques: towards developing a probabilistic lifetime methodology in the creep regime," *Materials at High Temperatures*, vol. 34, no. 5-6, pp. 333–341, 2017.

[132] B. Echard, N. Gayton, M. Lemaire, and N. Relun, "A combined Importance Sampling and Kriging reliability method for small failure probabilities with time-demanding numerical models," *Reliability Engineering and System Safety*, vol. 111, pp. 232–240, 2013.

[133] T. A. Frewen and M. R. Gurvich, "An Alternative Probabilistic Approach for Reliability Assessment of Rotorcraft Structures," in *Vertical Flight Society 75th Annual Forum & Technology Display*, (Philadelphia, Pennsylvania, USA), 2019.

[134] G. Holmes, P. Sartor, S. Reed, P. Southern, K. Worden, and E. Cross, "Prediction of landing gear loads using machine learning techniques," *Structural Health Monitoring: An International Journal*, vol. 15, no. 5, pp. 568–582, 2016.

[135] E. Cross, P. Sartor, K. Worden, and P. Southern, "Prediction of Landing Gear Loads Using Machine Learning Techniques," in *6th European Workshop on Structural Health Monitoring*, (Dresden, Germany), 2012.

[136] G. Venter, R. Haftka, and M. Chirehdast, "Response Surface Approximations for Fatigue Life Prediction," in *38th Structures, Structural Dynamics, and Materials Conference*, (Kissimmee, Florida, USA), pp. 1383–1396, 1997.

[137] Q. Huchet, C. Mattrand, P. Beaurepaire, N. Relun, and N. Gayton, "Cost effective strategy using Kriging surrogates to compute fatigue at multiple locations of a structure: Application to offshore wind turbine certification," in *12th International Fatigue Congress (Fatigue2018)*, (Poitiers, France), 2018.

[138] R. Teixeira, M. Nogal, A. O'Connor, J. Nichols, and A. Dumas, "Stress-cycle fatigue design with Kriging applied to offshore wind turbines," *International Journal of Fatigue*, vol. 125, pp. 454–467, 2019.

[139] R. Teixeira, A. O'Connor, and M. Nogal, "Fatigue reliability using a multiple surface approach," in *13th International Conference on Applications of Statistics and Probability in Civil Engineering, ICASP 2019*, (Seoul, South Korea), 2019.

[140] G. Singh, J. Ocampo, C. A. Acosta, and H. Millwater, "Distributed Computing for Probabilistic Structural Integrity Analysis of Aircraft Structures," in *51st AIAA/ASME/ASCE/AHS/ASC Structures, Structural Dynamics, and Materials Conference*, (Orlando, Florida, USA), 2010.

[141] N. Cross, "Developing design as a discipline," *Journal of Engineering Design*, vol. 29, no. 12, pp. 691–708, 2018.

[142] T. W. Simpson, J. D. Poplinski, P. N. Koch, and J. K. Allen, "Metamodels for Computer-based Engineering Design: Survey and recommendations," *Engineering with Computers*, vol. 17, no. 2, pp. 129–150, 2001.

[143] A. I. J. Forrester and A. J. Keane, "Recent advances in surrogate-based optimization," *Progress in Aerospace Sciences*, vol. 45, no. 1-3, pp. 50–79, 2009.

[144] A. Forrester, A. Sóbester, and A. Keane, *Engineering Design via Surrogate Modelling: A Practical Guide*.
John Wiley & Sons Ltd., 2008.

[145] M. Cortina, J. Ocampo, and H. Millwater, "Sensitivity analysis for general Aviation risk assessment," in *53rd AIAA/ASME/ASCE/AHS/ASC Structures, Structural Dynamics and Materials Conference 2012*, (Honolulu, Hawaii).

[146] S. Saltelli, A., Ratto, M., Andres, T., Campolongo, F., Cariboni, J., Gatelli, D., Saisana, M., Tarantola, *Global Sensitivity Analysis-The Primer*.
John Wiley & Sons Ltd., 2008.

[147] F. Pianosi, K. Beven, J. Freer, J. W. Hall, J. Rougier, D. B. Stephenson, and T. Wagener, "Sensitivity analysis of environmental models: A systematic review with practical workflow," *Environmental Modelling & Software*, vol. 79, pp. 214–232, 2016.

[148] B. Iooss and P. Lemaître, "A review on global sensitivity analysis methods," in *Uncertainty management in Simulation-Optimization of Complex Systems: Algorithms and Applications* (G. Dellino and C. Meloni, eds.), ch. 5, pp. 101–122, Springer, 2015.

[149] A. Saltelli, P. Annoni, I. Azzini, F. Campolongo, M. Ratto, and S. Tarantola, "Variance based sensitivity analysis of model output. Design and estimator for the total sensitivity index," *Computer Physics Communications*, vol. 181, no. 2, pp. 259–270, 2010.

[150] J. Hoole, P. Sartor, and J. E. Cooper, "Safe-Life Fatigue and Sensitivity Analysis: A Pathway Towards Embracing Uncertainty?," in *Royal Aeronautical Society 5th Aircraft Structural Design Conference*, (Manchester, UK), 2016.

[151] J. McFarland and D. Riha, "Uncertainty Quantification Methods for Helicopter Fatigue Reliability Analysis," in *American Helicopter Society 65th Annual Forum*, (Grapevine, Texas, USA), pp. 2730–2737, 2009.

[152] H. Liu and W. Chen, "Probabilistic Sensitivity Analysis Methods for Design under Uncertainty," in *10th AIAA/ISSMO Multidisciplinary Analysis and Optimization Conference*, (Albany, New York, USA), 2004.

[153] H. Liu and W. Chen, "Relative Entropy Based Method for Probabilistic Sensitivity Analysis in Engineering Design," *Journal of Mechanical Design*, vol. 128, pp. 326–336, 2006.

[154] "flightradar24 Live Air Traffic," *https://www.flightradar24.com*.

[155] B. P. Smarslok, R. T. Haftka, L. Carraro, and D. Ginsbourger, "Improving accuracy of failure probability estimates with separable Monte Carlo," *International Journal of Reliability and Safety*, vol. 4, no. 4, pp. 393–414, 2010.

[156] D. Montgomery and G. Runger, *Applied Statistics and Probability for Engineers*. John Wiley & Sons, Inc., 6$^{\text{th}}$ ed., 2014.

[157] E. Castillo, *Extreme Value Theory in Engineering*. Academic Press, Inc., 1988.

[158] J. Beirlant, Y. Goegebeur, J. Segers, and J. Teugels, *Statistics of Extremes - Theory and Applications*. John Wiley & Sons Ltd., 2004.

[159] N. H. Kim, P. Ramu, and N. V. Queipo, "Tail Modeling in Reliability-Based Design Optimization for Highly Safe Structural Systems," in *47th AIAA/ASME/ASCE/AHS/ASC Structures, Structural Dynamics, and Materials Conference*, (Newport, Rhode Island, USA), 2006.

[160] P. Ramu, N. H. Kim, and R. T. Haftka, "System Reliability Analysis Using Tail Modeling," in *11th AIAA/ISSMO Multidisciplinary Analysis and Optimization Conference*, (Portsmouth, Virginia, USA), 2006.

[161] G. R. Leverant, D. L. Littlefield, R. C. McClung, H. R. Millwater, and J. Y. Wu, "A Probabilistic Approach to Aircraft Turbine Rotor Material Design," in *International Gas Turbine & Aeroengine Congress & Exhibition*, (Orlando, Florida, USA), 1997.

[162] R. Teixeira, A. O'Connor, and M. Nogal, "Probabilistic sensitivity analysis of offshore wind turbines using a transformed Kullback-Leibler divergence," *Structural Safety*, vol. 81, 2019.

[163] C.-L. Shen, *The Statistical Analysis of Fatigue Data*.
PhD, University of Arizona, 1994.

[164] N. R. Mann, N. D. Singpurwalla, and R. E. Schafer, *Methods for Statistical Analysis of Reliability and Life Data*.
John Wiley & Sons, Inc., 1974.

[165] P. D. Toasa Caiza and T. Ummenhofer, "Consideration of the runouts and their subsequent retests into S-N curves modelling based on a three-parameter Weibull distribution," *International Journal of Fatigue*, vol. 106, pp. 70–80, 2018.

[166] A. Brot, "Weibull or Log-Normal Distribution to Characterize Fatigue Life Scatter - Which Is More Suitable?," in *ICAF 2019 - Structural Integrity in the Age of Additive Manufacturing*, pp. 551–561, Springer, 2019.

[167] Y.-X. Zhao, Q. Gao, and J.-N. Wang, "An approach for determining appropriate assumed distribution of fatigue life under limited data," *Reliability Engineering & System Safety*, vol. 67, pp. 1–7, 2000.

[168] Z. Wei, L. Luo, L. Gao, and K. Nikbin, "Statistical and probabilistic analysis of fatigue life data with two- and three-parameter Weibull distribution functions," in *ASME 2016 Pressure Vessel and Piping Conference*, (Vancouver, Canada), 2016.

[169] M. J. Khameneh and M. Azadi, "Reliability prediction, scatter band analysis and fatigue limit assessment of high-cycle fatigue properties in EN-GJS700-2 ductile cast iron," in *12^{th} International Fatigue Congress (Fatigue2018)*, (Poitiers, France), 2018.

[170] W. Nelson, *Applied Life Data Analysis*.
John Wiley & Sons, Inc., 1982.

[171] S. Bisgaard, "Teaching Statistics to Engineers," *The American Statistician*, vol. 45, no. 4, pp. 274–283, 1991.

[172] C. Chatfield, "Avoiding Statistical Pitfalls," *Statistical Science*, vol. 6, no. 3, pp. 240–268, 1991.

[173] R. B. D'Agostino and M. A. Stephens, *Goodness-of-fit techniques*.
Marcel Dekker, Inc., 1986.

[174] ASTM International, "Standard Practice for Statistical Analysis of Linear or Linearized Stress-Life (S-N) and Strain-Life (E-N) Fatigue Data ASTM E739-10," 2015.

[175] United States Department of Agriculture, "Two- and three-parameter Weibull goodness-of-fit tests FPL-RP-493," 1989.

[176] W. Stute, W. G. Manteiga, and M. P. Quindimil, "Bootstrap based goodness-of-fit tests," *Metrika: International Journal for Theoretical and Applied Statistics*, vol. 40, pp. 243–256, 1993.

[177] Martin-Löf, "The Notion of Redundancy and Its Use as a Quantitative Measure of the Discrepancy between a Statistical Hypothesis and a Set of Observational Data," *Scandinavian Journal of Statistics*, vol. 1, no. 1, pp. 3–18, 1974.

[178] M. Lin, H. C. Lucas, and G. Shmueli, "Too Big to Fail: Large Samples and the p-Value Problem," *Information Systems Research*, vol. 24, no. 4, pp. 906–917, 2013.

[179] A. Bag, D. Delbergue, P. Bocher, M. Lévesque, and M. Brochu, "Statistical analysis of high cycle fatigue life and inclusion size distribution in shot peened 300M steel," *International Journal of Fatigue*, vol. 118, pp. 126–138, 2019.

[180] J. F. Lawless, *Statistical Models and Methods for Lifetime Data*.
John Wiley & Sons, Inc., 1982.

[181] R. M. Wetzel, *Fatigue under complex loading: analyses and experiments*.
Society of Automotive Engineers Inc., 1977.

[182] Altair Engineering Inc., "eFatigue - SAE Keyhole Test Program," *https://www.efatigue.com/benchmarks/SAE_keyhole/SAE_keyhole.html*, 2020.

[183] H. J. Sutherland and P. S. Veers, "The Development of Confidence Limits for Fatigue Strength Data," in *ASME Wind Energy Symposium*, (Reno, Nevada, USA), 2000.

[184] P. Sartor, D. A. Bond, W. J. Staszewski, and R. K. Schmidt, "Value of an Overload Indication System Assessed Through Analysis of Aviation Occurrences," *Journal of Aircraft*, vol. 46, no. 5, pp. 1692–1705, 2009.

[185] Federal Aviation Administration, "Statistical Loads Data for the Airbus A-320 Aircraft in Commercial Operations DOT/FAA/AR-02/35," 2002.

[186] Defence Science and Technology Organisation, "Importance of Reliability Assessment to Helicopter Structural Component Fatigue Life Prediction DSTO-TN-0462," 2002.

[187] J. M. Potter and R. T. Watanabe, *Development of Fatigue Loading Spectra*. ASTM International, 1989.

[188] SAE International, "AIR5914: Landing Gear Fatigue Spectrum Development For Part 25 Aircraft," 2014.

[189] Air Accident Investigation Branch, "Report on the accident to McDonnell-Douglas MD-83, EC-FXI at Liverpool Airport on 10 May 2001 - Aircraft Accident Report 4/2003," 2003.

[190] E. Mangortey, J. Gilleron, G. Dard, O. J. Pinon, and D. N. Mavris, "Development of a Data Fusion Framework to support the Analysis of Aviation Big Data," in *AIAA SciTech Forum*, (San Diego, California, USA), 2019.

[191] Federal Aviation Administration, "Statistical Loads Data for the Boeing 777-200ER Aircraft in Commercial Operations," 2006.

[192] M. Schäfer, M. Strohmeier, V. Lenders, I. Martinovic, and M. Wilhelm, "Bringing up OpenSky: A large-scale ADS-B sensor network for research," in *IPSN 2014 - Proceedings of the 13th International Symposium on Information Processing in Sensor Networks*, pp. 83–94, April, 2014.

[193] A. Rodríguez-Díaz, B. Adenso-Díaz, and P. L. González-Torre, "Minimizing deviation from scheduled times in a single mixed-operation runway," *Computers & Operations Research*, vol. 78, pp. 193–202, 2017.

[194] M. Weiszer, J. Chen, and P. Stewart, "A real-time Active Routing approach via a database for airport surface movement," *Transportation Research Part C*, vol. 71, pp. 127–145, 2016.

[195] K. Benlic, U., Brownlee, A. E. I., Burke, "Heuristic search for the coupled runway sequencing and taxiway routing problem," *Transportation Research Part C*, vol. 71, pp. 333–355, 2016.

[196] A. E. I. Brownlee, M. Weiszer, J. Chen, J. R. Ravizza, S., Woodward, and E. K. Burke, "A fuzzy approach to addressing uncertainty in Airport Ground Movement Optimisation," *Transportation Research Part C*, vol. 92, pp. 150–175, 2018.

[197] A. Lange, J. Sieling, and G. Gonzalez Parra, "Convergence in airline operations: The case of ground times," *Journal of Air Transport Management*, vol. 77, pp. 39–45, 2019.

[198] J. Zhang, J. Liu, R. Hu, and H. Zhu, "Online four dimensional trajectory prediction method based on aircraft intent updating," *Aerospace Science and Technology*, vol. 77, pp. 774–787, 2018.

[199] G. Anderienko, N. Andrienko, G. Fuchs, and J. M. C. Garcia, "Clustering Trajectories by Relevant Parts for Air Traffic Analysis," *IEEE Transactions on Visualization and Computer Graphics*, vol. 24, no. 1, pp. 34–44, 2018.

[200] R. Alligier and D. Gianazza, "Learning aircraft operational factors to improve aircraft climb prediction: A large scale multi-airport study," *Transportation Research Part C*, vol. 96, pp. 72–95, 2018.

[201] J. Sun, J. Ellerbroek, and J. Hoekstra, "Flight Extraction and Phase Identification for Large Automatic Dependent Surveillance Broadcast Datasets," *Journal of Aerospace Information Systems*, vol. 14, no. 10, pp. 566–572, 2017.

[202] J. Sun, J. Ellerbroek, and J. Hoekstra, "Large-Scale Flight Phase Identification from ADS-B Data Using Machine Learning Methods," in *Proceedings of 7^{th} International Conference on Research in Air Transportation*, (Philadelphia, Pennsylvania, USA), 2016.

[203] M. E. O'Kelly, "Air freight hubs in the FedEx System: Analysis of fuel use," *Journal of Air Transport Management*, vol. 36, pp. 1–12, 2014.

[204] P. Ren and L. Li, "Characterizing air traffic networks via large-scale aircraft tracking data: A comparison between China and the US networks," *Journal of Air Transport Management*, vol. 67, pp. 181–196, 2018.

[205] J. A. Becco and D. Joyce, "Automated aircraft tracking for park and landscape planning," *Landscape and Urban Planning*, vol. 186, pp. 103–111, 2019.

[206] L. A. Sanchez-Perez, L. P. Sanchez-Fernandez, A. Shaout, and S. Suarez-Guerra, "Airport take-off noise assessment aimed at identify responsible aircraft classes," *Science of the Total Environment*, vol. 542, pp. 562–577, 2016.

[207] M. Nowacki and D. Olejniczak, "Analysis of Boeing 737 MAX 8 Flight, in Terms of the Exhaust Emission for the Selected Flight," *Transportation Research Procedia*, vol. 35, pp. 158–165, 2018.

[208] Y. Yu, M. Yang, and B. Nuseibeh, "Live Blackboxes: Requirements for Tracking and Verifying Aircraft in Motion," in *4^{th} Software Challenges in Aerospace Symposium*, (Grapevine, Texas, USA), 2017.

[209] X. Olive and P. Bieber, "Quantitative Assessments of Runway Excursion Precursors using Mode S data," in *Proceedings of ICRAT – International Conference for Research in Air Transportation*, (Castelldefels, Spain), 2018.

[210] E. K. Stone, "A comparison of Mode-S Enhanced Surveillance observations with other in situ aircraft observations," *Quarterly Journal of the Royal Meteorological Society*, vol. 144, pp. 695–700, 2018.

[211] R. Trüb, D. Moser, M. Schäfer, R. Pinheiro, and V. Lenders, "Monitoring Meteorological Parameters With Crowdsourced Air Traffic Control Data," in *Proceedings of the 17th ACM/IEEE International Conference on Information Processing in Sensor Networks (IPSN'18)*, (New York, USA), pp. 25–36, 2018.

[212] J. Sun, J. Ellerbroek, and J. M. Hoekstra, "WRAP: An open-source kinematic aircraft performance model," *Transportation Research Part C*, vol. 98, pp. 118–138, 2019.

[213] H. Khadilkar and H. Balakrishnan, "A Multi-Modal Unscented Kalman Filter for Inference of Aircraft Position and Taxi Mode from Surface Surveillance Data," in *Proceedings of the 11th AIAA Aviation Technology, Integration and Operations (ATIO) Conference*, (Virginia Beach, Virginia, USA), 2011.

[214] Federal Aviation Administration, "Side Load Factor Statistics From Commercial Aircraft Ground Operations," 2003.

[215] A. Tabassum and W. Semke, "UAT ADS-B Data Anomalies and the Effect of Flight Parameters on Dropout Occurrences," *Data*, vol. 19, no. 3, pp. 1–21, 2018.

[216] B. S. Ali, W. Schuster, W. Ochieng, and A. Majundar, "Analysis of anomalies in ADS-B and its GPS data," *GPS Solutions*, vol. 20, pp. 429–438, 2016.

[217] B. S. Ali, W. Y. Ochieng, and A. Majumdar, "ADS-B: Probabilistic Safety Assessment," *The Journal of Navigation*, vol. 70, pp. 887–906, 2017.

[218] A. Tabassum and W. Semke, "Assessing the Effect of ADS-B Message Drop-Out in Detect and Avoid of Unmanned Aircraft System Using Monte Carlo Simulation," *Safety*, vol. 49, no. 4, pp. 1–18, 2018.

[219] T. L. Verbraak, J. Ellerbroek, J. Sun, and J. Hoekstra, "Large Scale ADS-B Data and Signal Quality Analysis," in *Proceedings of 12th USA/Europe Air Traffic Management Research and Development Seminar*, (Seattle, Washington, USA), 2017.

[220] J. Zhang, W. Liu, and Z. Y., "Study of ADS-B Data Evaluation," *Chinese Journal of Aeronautics*, vol. 24, pp. 461–466, 2011.

[221] F. Caputo, A. De Luca, A. Grecco, S. Maietta, A. Marro, and A. Apicella, "Investigation on the static and dynamic structural behaviours of a regional aircraft main landing gear by a new numerical methodology," *Frattura ed Integrita Strutturale*, vol. 12, no. 43, pp. 191–204, 2018.

[222] F. Caputo, A. De Luca, A. Grecco, A. Marro, A. Apicella, R. Sepe, and E. Armentani, "Established Numerical Techniques for the Structural Analysis of a Regional Aircraft Landing Gear," *Advances in Materials Science and Engineering*, 2018.

[223] *ABAQUS 6.14 Scripting Reference Guide*.
Dassualt Systems, 2014.

[224] G. M. Puri, *Python Scripts for ABAQUS - Learn by Example*.
Gautam Puri, 2011.

[225] P. van Ginneken, *Development of an Optimization Framework for Landing Gear Design*.
MSc, Delft University of Technology, 2016.

[226] N. Heerens, *Landing gear design in an automated design environment*.
MSc, Delft University of Technology, 2014.

[227] C. E. Rasmussen and C. K. I. Williams, *Gaussian Processes for Machine Learning*.
MIT Press, 2nd ed., 2006.

[228] Y. F. Li, S. H. Ng, M. Xie, and T. N. Goh, "A systematic comparison of metamodeling techniques for simulation optimization in Decision Support Systems," *Applied Soft Computing Journal*, vol. 10, pp. 1257–1273, 2010.

[229] H. Smith, "Applications in Aircraft Structures," in *Probabilistic Structural Mechanics Handbook: Theory and Industrial Applications* (C. Sundararajan, ed.), ch. 23, pp. 558–574, Chapman & Hall, 1995.

[230] J. C. Lagarias, J. A. Reeds, M. H. Wright, and P. E. Wright, "Convergence Properties of the Nelder-Mead Simplex Method in Low Dimensions," *SIAM Journal of Optimization*, vol. 9, no. 1, pp. 112–147, 1998.

[231] H. Rocha, "On the selection of the most adequate radial basis function," *Applied Mathematical Modelling*, vol. 33, no. 3, pp. 1573–1583, 2009.

[232] M. Demuth, H., Beale, *Neural Network Toolbox For Use with MATLAB*.
The Maths Works Inc., 3rd ed., 1998.

[233] R. Teixeira, A. O'Connor, M. Nogal, N. Krishnan, and J. Nichols, "Analysis of the design of experiments of offshore wind turbine fatigue reliability design with Kriging surfaces," *Procedia Structural Integrity*, vol. 5, pp. 951–958, 2017.

[234] S. Brandt, M. Broggi, J. Hafele, C. Guillermo Gebhardt, R. Rolfes, and M. Beer, "Metamodels for fatigue damage estimation of offshore wind turbines jacket substructures," *Procedia Engineering*, vol. 199, pp. 1158–1163, 2017.

[235] Q. Huchet, C. Mattrand, P. Beaurepaire, N. Relun, and N. Gayton, "AK-DA: An efficient method for the fatigue assessment of wind turbine structures," *Wind Energy*, vol. 22, pp. 638–652, 2019.

[236] K. Müller and P. W. Cheng, "A surrogate modeling approach for fatigue damage assessment of floating wind turbines," in *Proceedings of the ASM 2018 37th International Conference on Ocean, Offshore and Arctic Engineering OMAE2018*, (Madrid, Spain), 2018.

[237] L. K. Song, G. C. Bai, C. W. Fei, and J. Wen, "Reliability-Based Fatigue Life Prediction for Complex Structure with Time-Varying Surrogate Modeling," *Advances in Materials Science and Engineering*, 2018.

[238] E. J. Cross, P. Sartor, K. Worden, and P. Southern, "Prediction of Landing Gear Loads from Flight Test Data Using Gaussian Process Regression," in *Structural Health Monitoring 2013: A Roadmap to Intelligent Structures* (F.-K. Chang, ed.), pp. 1452–1459, DEStech Publications, Inc., 2013.

[239] I. Tartaruga, J. E. Cooper, M. H. Lowneberg, P. Sartor, and Y. Lemmens, "Uncertainty and Sensitivity Analysis of Bifurcation Loci Characterizing Nonlinear Landing-Gear Dynamics," *Journal of Aircraft*, vol. 55, no. 1, pp. 162–172, 2018.

[240] P. Sartor, W. Becker, K. Worden, R. K. Schmidt, and D. Bond, "Bayesian Sensitivity Analysis of Flight Parameters in a Hard-Landing Analysis Process," *Journal of Aircraft*, vol. 53, no. 5, pp. 1317–1331, 2016.

[241] R. H. Myers, A. I. Khuri, and W. H. Carter, "Response Surface Methodology: 1966-1988," *Technometrics*, vol. 31, no. 2, pp. 137–157, 1989.

[242] W. B, *Reliability Analysis of Dynamic Systems: Efficient Probabilistic Methods and Aerospace Applications*.
Elsevier and Shanghai Jiao Tong University Press Aerospace Series, 2014.

[243] W. M. Hoffman, M. E. Riley, and B. W. Spencer, "Surrogate Model Development and Validation for Reliability Analysis of Reactor Pressure Vessels," in *ASME 2016 Pressure Vessels and Piping Conference*, (Vancouver, British Columbia, Canada), 2016.

[244] H. I. Park, "Study for Application of Artificial Neural Networks in Geotechnical Problems," in *Artificial Neural Networks: Application* (C.-L. Leung, ed.), pp. 303–331, InTech, 2011.

[245] M. C. Y. Niu, *Airframe Stress Analysis and Sizing*.
Hong Kong Conmilit Press Ltd, 2nd ed., 2001.

[246] A. Afzal, K.-Y. Kim, and J.-w. Seo, "Effects of Latin hypercube sampling on surrogate modeling and optimization," *International Journal of Fluid Machinery and Systems*, vol. 10, no. 3, pp. 240–253, 2017.

[247] J. N. Fuhg, *Adaptive Surrogate Models for Parametric Studies*.
MSc, Leibniz University Hannover, 2019.

[248] H. Liu, Y.-S. Ong, and J. Cai, "A survey of adaptive sampling for global metamodelling in support of simulation-based complex engineering design," *Structural and Multidisciplinary Optimization*, vol. 57, pp. 393–416, 2018.

[249] V. R. Joseph and Y. Hung, "Orthogonal-Maximum Latin Hypercube Designs," *Statistica Sinica*, vol. 18, pp. 171–186, 2008.

[250] P. Singh, D. Deschrijver, and T. Dhaene, "A Balanced Sequential Design Strategy for Global Surrogate Modeling," in *Proceedings of the 2013 Winter Simulations Conference* (R. Pasupathy, S.-H. Kim, A. Tolk, R. Hill, and M. E. Kuhl, eds.), IEEE, 2013.

[251] E. J. Cross, T. J. Rogers, and T. J. Gibbons, "Grey-box modelling for structural health monitoring: Physical constraints on machine learning algorithms," in *Structural Health Monitoring 2019: Enabling Intelligent Life-Cycle Health Management for Industry Internet of Things (IIOT) - Proceedings of the 12th International Workshop on Structural Health Monitoring, Vol. 2* (F.-K. Chang, A. G$\acute{}$uemes, and F. Kopsaftopoulos, eds.), pp. 2136–2145, DEStech Publications Inc., 2019.

[252] K. L. Priddy and P. E. Keller, *Artificial Neural Networks: An Introduction*.
SPIE Press, 2005.

[253] G. D. Garson, *Neural Networks: An Introductory Guide for Social Scientists*.
Sage Publishing, 1998.

[254] G. Habermann, "On the Selection of Test Factors For The Determination of Safe-Life," in *Proceedings of the 24th Symposium of the International Committee on Aeronautical Fatigue and Structural Integrity (ICAF2007)*, (Naples, Italy), 2007.

[255] Q.-V. Le-The, *Application of Multiaxial Fatigue Analysis Methodologies for the Improvement of the Life Prediction of Landing Gear Fuse Pins*.
MSc, Carelton University, 2016.

[256] P. Pollack, *Designing for Strength: Principles and Practical Aspects of Stress Analysis for Engineers and Students*.
Macmillian International Higer Education, 1982.

[257] P. Narayan, K., Behdinan, K., Vanderpol, "An Equivalent Uniaxial Fatigue Stress Model for Analyzing Landing Gear Fuse Pins," *Strength of Materials*, vol. 38, no. 3, pp. 278–288, 2006.

[258] Engineering Sciences Data Unit, "ESDU 79032: Stress concentrations at grooves for retaining rings or seals (with notes on design against fatigue)," 2000.

[259] *ABAQUS 6.14 Analysis User's Guide*.
Dassualt Systems, 2014.

[260] J. Zhu, S. Pugh, and R. S. Dwyer-Joyce, "Model and experiments to determine lubricant film formation and frictional torque in aircraft landing gear pin joints," *Proceedings of the Institution of Mechanical Engineers Part: J*, vol. 226, no. 4, pp. 315–327, 2012.

[261] W. D. Pilkey and D. F. Pilkey, *Peterson's Stress Concentration Factors*.
John Wiley & Sons, 3rd ed., 2008.

[262] C. H. R. Boller and T. Seeger, *Materials Data for Cyclic Loading Part B: Low-Alloy Steels*.
Elsevier Science Publishers B.V., 1987.

[263] DVB Bank SE Aviation Research, "An Overview of Commercial Aircraft 2018-2019," 2017.

[264] F. Figueiredo and M. I. Gomes, "The skew-normal distribution in SPC," *Revstat Statistical Journal*, vol. 11, no. 1, pp. 83–104, 2013.

[265] D. Baguley and D. R. Hose, *How to - Model with Finite Elements*.
NAFEMS Ltd., 1997.

[266] K. Worden and E. J. Cross, "On switching response surface models, with applications to the structural health monitoring of bridges," *Mechanical Systems and Signal Processing*, vol. 98, pp. 139–156, 2018.

[267] A. C. Davison and D. V. Hinkley, *Bootstrap Methods and their Application*.
Cambridge University Press, 1997.

[268] H. Millwater, J. Larsen, and R. John, "Effects of residual stresses on probabilistic lifing of engine disk materials," *Materials Science and Engineering A*, vol. 468-470, pp. 129–136, 2007.

[269] N. Jayaraman, P. Prevey, N. Ontko, M. Shepard, R. Ware, and J. Coate, "Comparison of mechanical suppression by shot peening and low plasticity burnishing to mitigate SCC and corrosion fatigue failures in 300m landing gear steel," *International Conference on Shot Peening*, vol. 5, no. 259, pp. 247–251, 2005.

[270] B. Sudret, "Meta-models for structural reliability and uncertainty quantification," in *Fifth Asian-Pacific Symposium on Structural Reliability and its Applications (5APSSRA)* (K. K. Phoon, M. Beer, S. T. Quek, and S. D. Pang, eds.), Research Publishing, 2012.

[271] E. Acar, "Guided tail modelling for efficient and accurate reliability estimation of highly safe mechanical systems," *Proceedings of the Institution of Mechanical Engineers, Part C: Journal of Mechanical Engineering Science*, vol. 225, no. 5, pp. 1237–1251, 2011.

[272] M. Norouzi, *An Efficient Method to Assess Reliability under Dynamic Stochastic Loads*. PhD, University of Toledo, 2012.

[273] N. Tüten and E. Acar, "Weight Optimization and Reliability Prediction of an Automobile Torque Arm Subjected to Cyclic Loading," *International Journal of Computational and Experimental Science and Engineering*, vol. 1, no. 2, pp. 16–19, 2015.

[274] M. Nesterova, F. Schmidt, E. Brühwiler, and C. Soize, "Generalized Pareto distribution for reliability of bridges exposed to fatigue," in *IABMAS Conference on Bridge Maintenance, Safety and Management*, (Melbourne, Australia), 2018.

[275] Health & Safety Executive, "Probabilistic methods: Uses and abuses in structural integrity," 2001.

[276] O. Ditlevsen, "Structural reliability codes for probabilistic design - A debate paper based on elementary reliability and decision analysis concepts," *Structural Safety*, vol. 19, no. 3, pp. 253–270, 1997.

[277] A. Evren and E. Tuna, "On Some Properties of Goodness of Fit Measures Based on Statistical Entropy," *International Journal of Research and Reviews in Applied Sciences*, vol. 13, no. 1, pp. 192–205, 2012.

[278] A. W. Bowman and A. Azzalini, *Applied Smoothing Techniques for Data Analysis - The Kernel Approach with S-Plus Illustrations*.
Oxford University Press, 1997.

[279] P. H. Wirsching, "Fatigue Reliability in Welded Joints of Offshore Structures," *International Journal of Fatigue*, vol. April, pp. 77–83, 1980.

[280] L. Wang and C. A. Alexander, "Big data in design and manufacturing engineering," *American Journal of Engineering and Applied Sciences*, vol. 8, no. 2, pp. 223–232, 2015.

[281] M. Rogalewicz and R. Sika, "Methodologies of knowledge discovery from data and data mining methods in mechanical engineering," *Management and Production Engineering Review*, vol. 7, no. 4, pp. 97–108, 2016.

[282] S. O. Erikstad, "Merging Physics, Big Data Analytics and Simulation for the Next-Generation Digital Twins," in *HIPER 2017, High-Performance Marine Vehicles*, (Zevenwacht, South-Africa), pp. 139–148, 2017.

[283] D. J. Wagg, P. Gardner, R. J. Barthorpe, and K. Worden, "On Key Technologies for Realising Digital Twins for Structural Dynamics Applications," in *Model Validation and Uncertainty Quantification, Volume 3, Proceedings of the 37th IMAC, A Conference*

and Exposition on Structural Dynamics 2019 (R. Barthorpe, ed.), ch. 30, pp. 267–272, Springer, 2020.

[284] Z. del Rosario, G. Iaccarino, and R. W. Fenrich, "When are Design Allowables Conservative ?," in *AIAA SciTech Forum 2020*, (Orlando, Florida, USA), 2020.

[285] C. E. Larsen and I. S. Raju, "Moving Aerospace Structural Design Practice to a Load and Resistance Factor Approach," in *57th AIAA/ASCE/AHS/ASC Structures, Structural Dynamics, and Materials Conference*, (San Diego, California, USA), 2016.

[286] Federal Aviation Administration, "Probabilistic Structural Risk Assessment and Risk Management for Small Airplanes DOT/FAA/AR-11/14," 2017.

[287] Federal Aviation Administration, "Probabilistic Integrity and Risk Assessment of Turbine Engines DOT/FAA/TC-17/15," 2018.

[288] K. J. Marsh, *Full-scale fatigue testing of components*. Butterworth & Co., 1988.

[289] M. P. McLaughlin, *Compendium of Common Probability Distributions*. 2016.

All web-based references checked for access on 5$^{\text{th}}$ February 2020.

APPENDIX A: CONSERVATISM CASE STUDY

Please note: *This appendix contains material sourced from "Evaluating the Impact of Conservatism in Industrial Fatigue Analysis of Life-Limited Components" as highlighted in Section 1.3.1.*

SAE Keyhole Benchmark Case Study

In order to quantify the reduction of a component safe-life resulting from the different conservatism approaches shown in Section 2.2 in Chapter 2, a case study was developed. The case study is identical to the SAE keyhole benchmark shown previously in Figure 4.8 in Chapter 4 [181] and applies the 'transmission' load-time history to the SAE keyhole geometry. The ESDU S-N dataset for 4340 steel was used to represent the material properties [25].

The component safe-life was computed for each conservatism approach shown in Figure 2.3 in Chapter 2 using an S-N analysis approach. Where PoS/CL P-S-N curves were required, the appropriate curve coefficient 'P' and exponent 'q' were sourced from Table A.1. The corresponding S-N curves were shown previously in Figure 2.2.

Table A.1. Statistically reduced 4340 PoS/CL P-S-N curves.

PoS/CL	P Coefficient	q Exponent	σ_{FL}
50/50 Mean	15,020	-0.425	457.0
99/95	4,523	-0.328	421.6
97.7/95	5,073	-0.338	426.5
97.7/75	6,206	-0.352	429.3
95/75	6,993	-0.362	434.1

Impact of Conservatism Approach on Component Safe-Life

The case study component safe-life values (e.g. the number of times that the 'transmission' load-time history can be applied) resulting from each conservatism approach is shown in Table A.2. The total accumulated damage from Miner's rule 'D_T' and the percentage reduction in the safe-life from the 'baseline' case (i.e. the mean S-N curve and no conservatism applied) is also shown.

Table A.2. Safe-Life reduction for the SAE keyhole geometry.

Industrial Sector	D_T	Safe-Life	Reduction in Safe-Life
Baseline	3.02×10^{-5}	33,157	-
Large Aircraft	1.02×10^{-4}	3,273	90.13%
Light Aircraft	2.41×10^{-4}	4,144	87.50%
Nuclear	1.06×10^{-2}	94	99.72%
Wind Turbines	2.47×10^{-3}	404	98.78%
Offshore	7.00×10^{-4}	1,428	95.69%
Steel Structures	1.63×10^{-3}	615	98.15%

Discussion

As can be seen from Table A.2, the baseline component safe-life of 33,157 cycles is significantly reduced following the application of the conservatism approaches, with a maximum safe-life of 4,144 cycles for light aircraft structures, whilst the minimum safe-life was 94 cycles for nuclear components under the ASME III conservatism approach. Therefore, the conservatism approach that has the largest impact on the component safe-life is that used by the nuclear sector, reducing the safe-life by 99.7%. It is interesting to note that the conservatism impact for both large aircraft and light aircraft structures are similar in magnitude, producing a reduction in the component safe-life of 90.1% and 87.5% respectively.

These results from the aerospace sector contrast with the results from the remaining 'land' based sectors, which all show consistency in the percentage reduction of the safe-life value. These values range from 95.7% for offshore steel structures, 98.1% for Eurocode 3 steel structures, 98.8% for wind turbine components and 99.7% for nuclear components. This trend suggests that the conservatism approaches of the aerospace sectors introduce a smaller magnitude of conservatism compared to all other sectors. This may result from the requirement to minimise weight and the stringent characterisation of materials and loading data performed within aerospace design [245].

In addition, the aerospace sectors are the only sectors that require a full-scale test of the complete structure, whilst due to the structural size and economic considerations in other sectors, only full-scale testing of components (e.g. welded joints in the offshore sector) is performed [288]. As the full-scale test provides a "safety-net" for the fatigue analysis, this could also permit the aerospace sectors to introduce reduced conservatism.

Previous work by Sutherland [183] highlights that the different industrial sectors have different fatigue design cases. For example, wind turbine components have long target design lives (30+years) and are exposed to many fatigue cycles due to the rotational nature of components (e.g. blade hubs) [183]. Offshore structures, with a 20-year design life, are exposed to significant cyclic loading from wave and wind loads [75]. Nuclear components can have longer design lives (40 years) and are also safety-critical [73]. On the other hand, aerospace structural components, whilst having typical design lives of 20 years [245] (which is lower than all other sectors), will also be exposed to a lower level of cycling, due to the reduced rotational nature of components.

These comparisons are shown in Figure A.1, after [183]. As can be seen in Figure A.1, a trend exists between the more severe fatigue design cases (i.e. long design lives and highly cycled components) and the conservatism introduced by each sector. Superimposed on Figure A.1 are the percentage reductions in safe-life, showing that as the target design life or the cyclic nature of loading increases, the percentage reduction in the component safe-life also increases. It can therefore be suggested that sectors which anticipate more severe fatigue design cases introduce increased conservatism into S-N fatigue analysis. A final trend that could be explored in the future is the link between the conservatism impact and the production volumes of each sector, which vary from potentially thousands in the aerospace sector to one-off components in the nuclear sector.

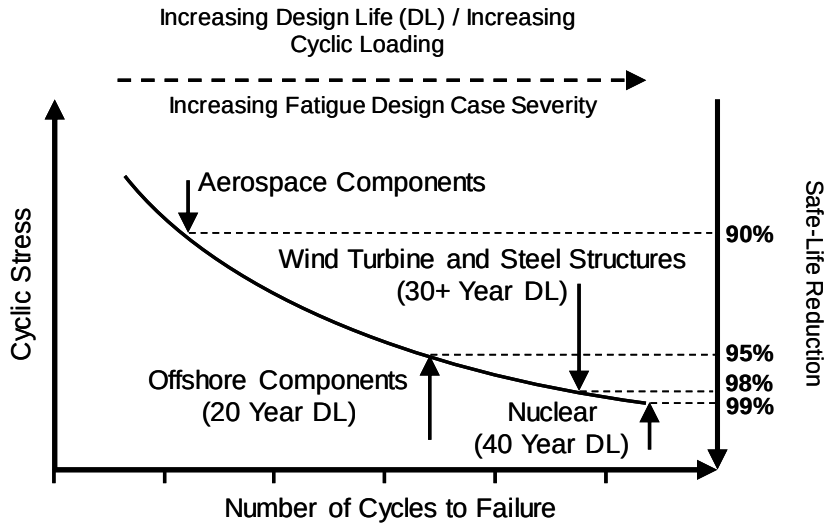

Figure A.1. A comparison of the fatigue design case and percentage reduction in safe-life for each sector, modified from [183].

Deterministic Safety Factors vs. Statistical Reduction Factors

As discussed in Chapter 2, a number of the industrial sectors reviewed in Figure 2.3 use a mixture of both safety factors and statistical reduction factors within their conservatism approaches. Figure A.2 shows the breakdown of the percentage reduction in the safe-life between the safety factors and statistical reduction factors.

Figure A.2 shows that for large aircraft, offshore structures and steel structures, the majority of the safe-life reduction originates from the use of PoS/CL P-S-N curves. Wind turbine components however, receive 97.7% of the safe-life reduction from deterministic safety factors applied

to stress values. This shows the significant impact that a safety factor applied to cyclic stress magnitudes can have. This impact is as a result of increasing the number of stress amplitudes that will lie above the fatigue limit 'σ_{FL}'. A similar effect is introduced through reducing σ_{FL} by using either a PoS/CL P-S-N curve or a deterministic safety factor on the S-N curve. This effect is highlighted in Table A.3, whereby the different conservatism approaches are compared regarding the number of damaging stress cycles above σ_{FL} extracted from rainflow counting. Table A.3 also shows the sensitivity of the reduction in component safe-life to the reduction in σ_{FL}.

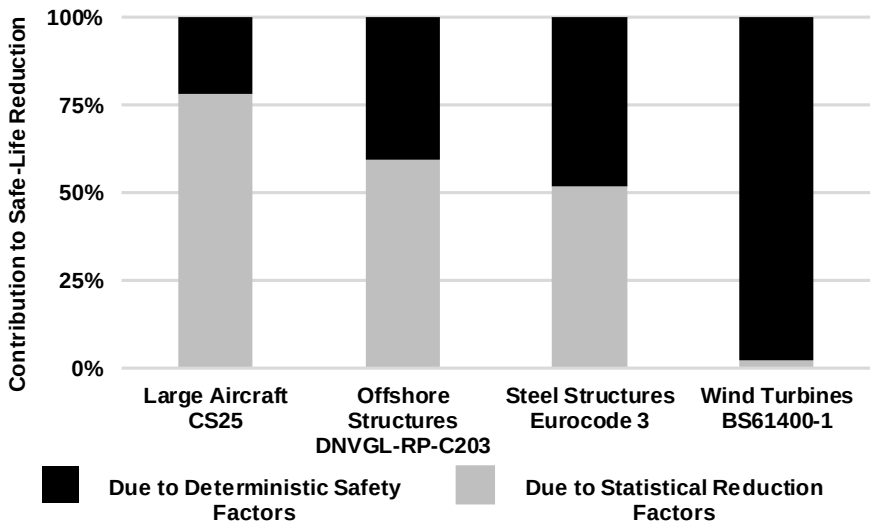

Figure A.2. Breakdown of safe-life reduction into contribution from statistical reductions and safety factors.

Table A.3. Impact on reduction in safe-life of deterministic safety factors on stress.

Industrial Sector	Safety Factor on Stress	Number of Damaging Cycles	Reduction in Safe-Life
Baseline	-	10	-
Large Aircraft	Statistically reduced σ_{FL}	21	90.13%
Nuclear	Stress factor on S-N curve	112	99.72%
Wind Turbines	Factor on applied stress, Statistically reduced σ	66	98.78%
Offshore	Statistically reduced σ_{FL}	19	95.69%
Steel Structures	Statistically reduced σ_{FL}, Stress factor on S-N curve	57	98.15%

Regarding safety factors and statistical reductions in general, statistical reductions are a more 'flexible' approach to applying conservatism than deterministic safety factors. This is because they are based upon the datasets of the specific component design and parameters, rather than

the ‘general’ nature of deterministic safety factors. It is interesting to note that the two industrial sectors that produced the minimum and maximum safe-life reductions (light aircraft and nuclear respectively) are both sectors that use only deterministic safety factors. This suggests that the introduction of conservatism through statistical reductions will be more representative of the specific design case at hand, potentially reducing the risk of under or over-conservative design. As a result, increased use of statistical reductions as conservatism approaches within fatigue design is recommended to mitigate against un-safe or inefficient components.

Identifying the Most Influential Area of Variability

From the share of the reduction in component safe-life between deterministic safety factors and statistical reductions shown in Figure A.2, it can be seen that in most instances the statistical reductions accounted for at least 50% of the reduction in the component safe-life. Referring back to the conservatism approaches in Figure 2.3, it can be seen that statistical reductions are only applied to account for variability within S-N datasets. It can also be observed that when PoS/CL P-S-N curves are used in conjunction with safety factors, the safety factors are applied to account for multiple areas of variability.

As a result, these observations demonstrate that for most industrial sectors, the majority of design conservatism is applied to account for S-N dataset variability. This suggests that the various industrial sectors consider S-N dataset variability to be the most influential source of variability within fatigue design. Therefore, improved and enhanced statistical characterisation of S-N datasets, as performed in Chapter 4, could support a potential reduction in the conservatism currently required in the fatigue design of safe-life components.

APPENDIX B: STATISTICAL PRIMER

This appendix aims to provide the necessary statistical background required to understand and implement the probabilistic fatigue methodology defined in this thesis. The statistical primer in this appendix aims to cover essential information regarding variability, probability distributions and Goodness-of-Fit testing.

Data, Random Variables and Probability

Design parameters demonstrate variability as a result of the variability or 'scatter' observed in the raw data used to define the value of the design parameter [33]. Raw data is known as a *dataset* and is composed of individual *data points* 'x_i'. Design parameters that can take a range of values (with an associated probability of a given value being taken) are known as *random variables* [156]. The simplest way of characterising the variability in a dataset or random variable is to compute the mean 'μ' and standard deviation 'σ' of the dataset. The parameters μ and σ are known as *statistics* of the dataset, as they quantify different attributes of the dataset variability [156]. The μ and σ of a dataset can be computed using the following equations, where 'N' is the number of data points within the dataset, known as the *sample size* [156]:

$$\mu = \frac{1}{N}\sum_{i=1}^{N} x_i \tag{B.1}$$

$$\sigma = \sqrt{\frac{\sum_{i=1}^{N}(x_i - \mu)^2}{N-1}} \tag{B.2}$$

The value of μ is a measure of the average value of the dataset and the standard deviation represents the 'spread' or variability within the dataset [156]. The coefficient of variation 'c_v' can be defined for a dataset, based upon the values of μ and σ:

$$c_v = \frac{\sigma}{\mu} \tag{B.3}$$

Often within statistical characterisation, a dataset must be ordered from the smallest value to the largest value. This results in the dataset being defined as '$x_1, x_2, ..., x_i, ...$' where 'i' represents the i^{th} *order statistic* [164, 170]. The ordered dataset is known as a *ranked dataset* and therefore, 'i' is also known as the *rank* of the data point [29].

Probability

Probability is the measure of the likelihood (or 'chance') of a given event occurring. Probability can take any value between zero (i.e. the event will never happen) and 1 (i.e. the event will certainly happen). Equation B.4 demonstrates how probability is mathematically represented.

$$\text{Probability of event '}X\text{' occurring } = P[X] \tag{B.4}$$

The 'event' in Equation B.4 could represent the probability of observing a given value within a dataset, or the probability of a random variable taking a specific value. The probability of two events (e.g. 'X' and 'Y') occurring follows a set of different conditions [156]:

- $P[X|Y]$ - *Conditional probability*: The probability that 'X' occurs given that event 'Y' has occurred.
- $P[X \cup Y]$ - *Union*: The probability that either event 'X' or 'Y' will occur.
- $P[X \cap Y]$ - *Intersection*: The probability that both event 'X' and 'Y' will occur.
- *Mutually Exclusive*: Events 'X' and 'Y' cannot both occur (i.e. the result of a coin toss cannot be both heads and tails).
- *Statistically Independent*: The occurrence of event 'Y' does not influence the probability of event 'X' occurring (i.e. $P[X|Y] = P[X]$). For statistically independent events:
  1. $P[X \cup Y] = P[X] + P[Y]$
  2. $P[X \cap Y] = P[X] \times P[Y]$

Continuous Probability Distributions

Whilst μ and σ provide an initial characterisation of the variability in a dataset, the most common way to represent variability is in the form of a *probability distribution*. Probability distributions represent how the probability of a random variable or dataset taking a specific value varies [33].

Histograms and Probability Density Functions

In order to visualise the variability in datasets, *histograms* can be used to demonstrate how the frequency of observed data points within the dataset varies with the value of the data point [29]. An example of a histogram is shown in Figure B.1.

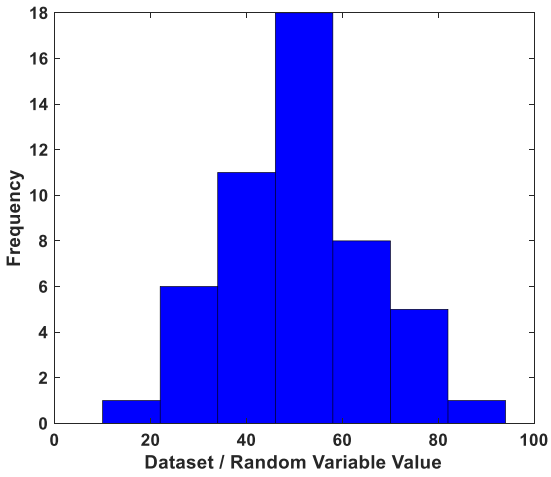

Figure B.1. A histogram of 7 bins for a sample size of $N = 50$.

Histograms are constructed by partitioning the range of values within the dataset into 'bins'. Various rules are available for defining the number of bins 'n_{bin}' and within this thesis, Equation B.5 has been used [29]:

$$n_{bin} = 1 + 3.22 log_{10}(N) \tag{B.5}$$

From the definition of n_{bin}, the width of each bin is computed assuming an equal bin width across the range of values within the dataset [29]. The dataset is then worked through and the data points are placed into the bin which contains the data point value. Figure B.1 therefore shows the frequency of observed data points within each bin. Histograms enable qualitative properties of the dataset variability to be established, such as skewness, support and any multi-modal behaviour.

Histograms can be normalised by the total observed frequency, to give a histogram of relative frequency for each bin, as shown in Figure B.2a [29]. Histograms can be further normalised by dividing the area of the bar for each bin by the total histogram area, as shown in Figure B.2b. This normalisation process results in the histogram representing the frequency density of observations.

Figure B.2b therefore gives rise to the definition of probability density. Probability density represents how the relative probability of observing a specific value for a random variable varies with the value of the random variable. Probability density is often defined using a Probability Density Function (PDF), which is a continuous mathematical function, as shown in Figure B.3 [33]. PDFs are often referred to directly as probability distribution types or 'shapes', such as the Normal distribution shown in Figure B.3. The PDF for the Normal distribution is shown in Equation B.6 and consists of the μ and σ parameters defined in Equations B.1 and B.2 [29, 33].

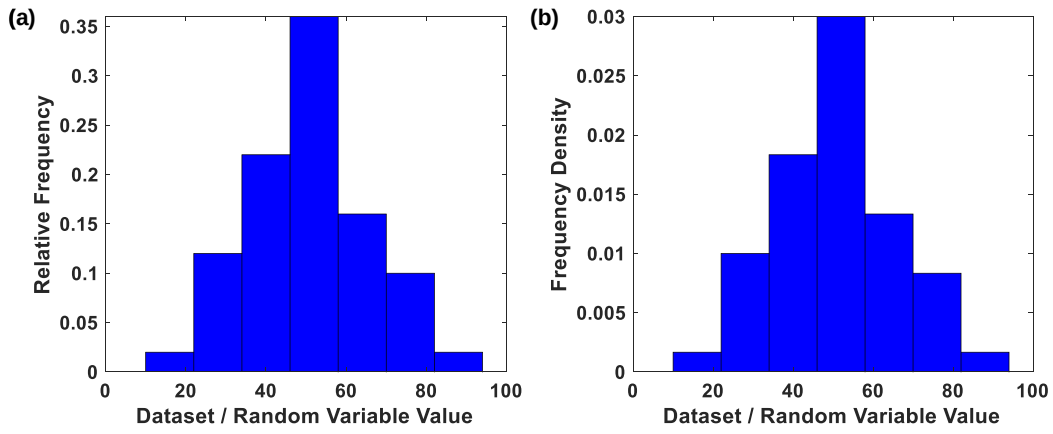

Figure B.2. (a) Relative frequency and (b) frequency density normalised histograms from the histogram shown previously in Figure B.1.

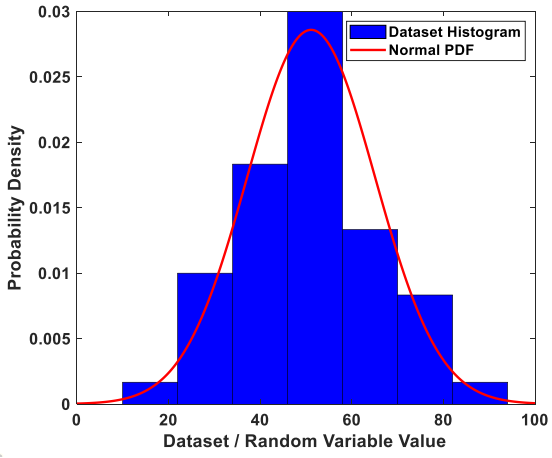

Figure B.3. A Normal PDF compared with the frequency density histogram from Figure B.2.

$$f(x) = \frac{1}{\sqrt{2\pi\sigma^2}} \exp\left(-\frac{(x-\mu)^2}{2\sigma^2} \right) \tag{B.6}$$

Different probability distribution types and PDFs can display different variability characteristics. Firstly, *skewness* is a quantification of how unsymmetrical a distribution is [33]. For example the Normal distribution shown previously in Figure B.3 is symmetric about the mean value and therefore has zero skewness [33]. However, distributions such as the Weibull distribution shown in Figure B.4 can demonstrate either positive skew or negative skew. Positive skew results in a long right-hand tail to the distribution, whilst negative skew results in a long left-hand tail to the distribution as shown in Figure B.4.

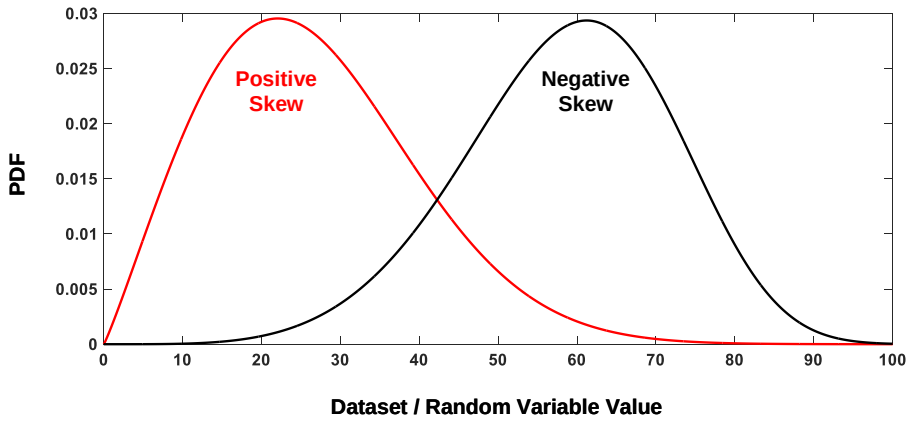

Figure B.4. A visualisation of probability distribution skew behaviour.

Support is the definition of the possible range of values that a PDF can represent. Outside of the support, a PDF will be equal to zero [33]. The Normal PDF shown in Figure B.3 has a support of $[-\infty, +\infty]$ as a random variable defined by a Normal PDF can theoretically take any value. However, many engineering design parameters are not able to take negative values and known bounds or limits may exist for specific design parameters [29, 33]. As a result, commonly required PDF supports are (examples of the supports are shown in Figure B.5) [29, 33]:

- $[0, +\infty]$: The PDF and random variable can only take positive values.
- $[a, +\infty]$: The PDF can only take values from 'a' to $+\infty$. 'a' is known as the *threshold* of the PDF and random variable.
- $[a, b]$: The PDF and random variable can only take values between 'a' and 'b'.

The continuous functions used to define PDFs typically consist of one or more of the following types of parameters (an example of each parameter type is shown in Figure B.6) [29, 33]:

- **Location/Threshold:** These parameters can represent where the 'peak' of the PDF lies, such as the value of μ for a Normal distribution. For distributions that represent a $[a, +\infty]$ support, the location parameter can also define the 'a' threshold value.
- **Scale:** This parameter represents the 'spread' of the PDF, such as the value of σ for the Normal distribution.
- **Shape:** This parameter controls the overall shape of the distribution and PDF, such as the skewness of the distribution. For certain distribution types, shape parameters also define the 'peak' location of the PDF.

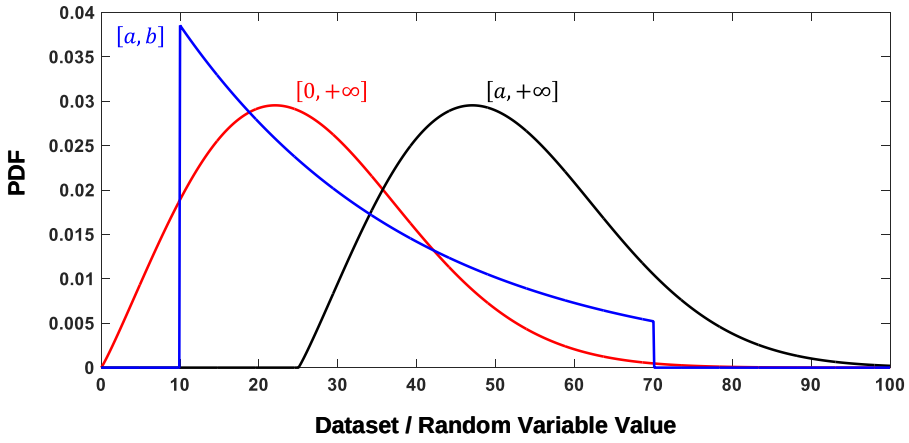

Figure B.5. A visualisation of probability distribution support behaviour.

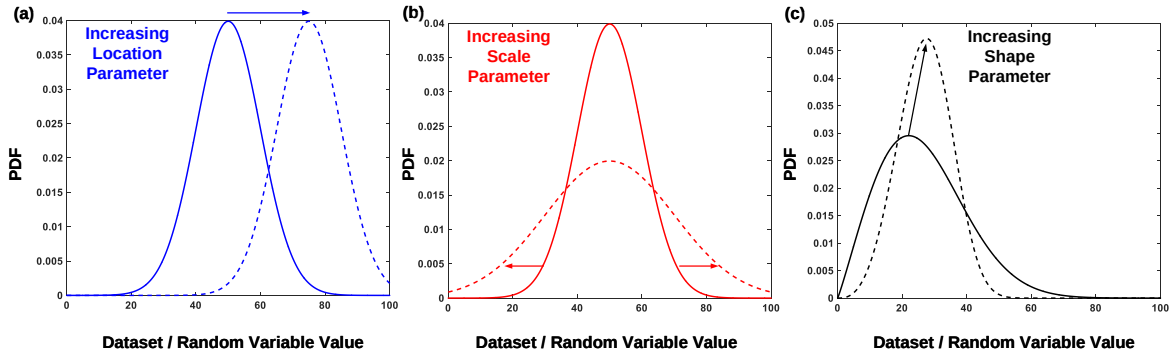

Figure B.6. A visualisation of probability distribution behaviour for a change in: (a) location parameter, (b) scale parameter and (c) shape parameter.

Cumulative Frequencies and Cumulative Density Functions

The relative frequency values shown in Figure B.2a can be used to produce a histogram that represents cumulative relative frequency 'R_c' [29]. An example of an R_c histogram is shown in Figure B.7 and it can be observed that the values for R_c run from zero to one.

The histogram of R_c is equivalent to the Cumulative Density Function (CDF) of a probability distribution [29]. The CDF is a mathematical function whose value is equivalent to the area under the corresponding PDF for the probability distribution [33, 156]. An example of a Normal CDF generated from a Normal PDF is shown in Figure B.8. The area under a PDF can be used to compute the probability of random variable 'X' taking a value that is equal to or less than the specified value 'x'. Therefore, a CDF can be used to compute $P[X \leq x]$. Mathematically, the CDF is the integral of the PDF [29, 33].

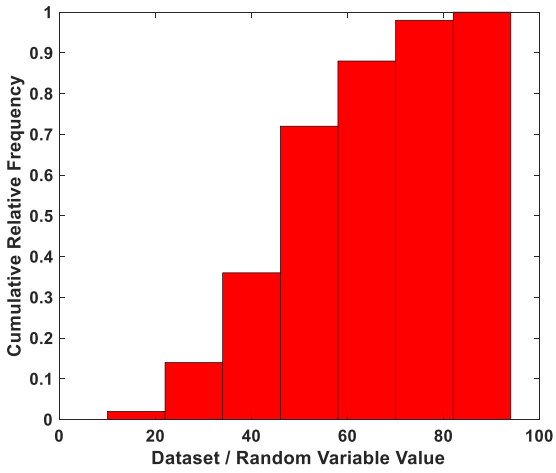

Figure B.7. A cumulative relative frequency histogram for the histogram shown in Figure B.1.

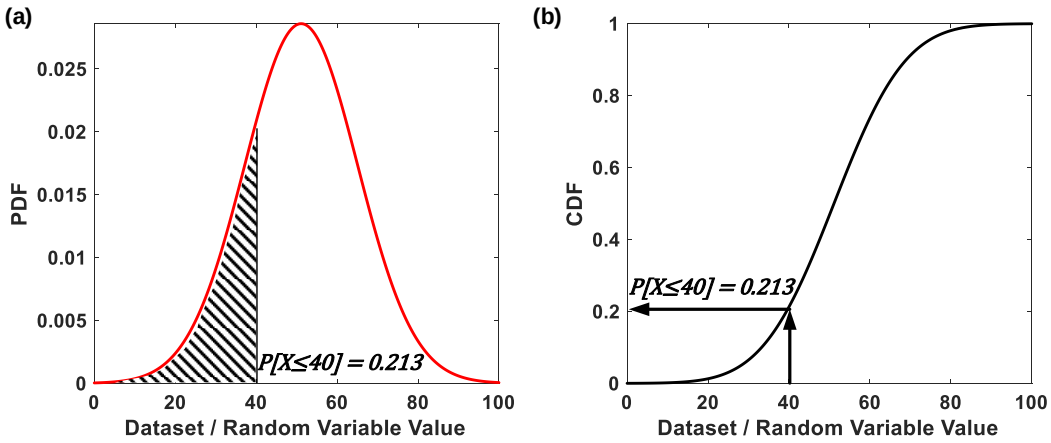

Figure B.8. A demonstration of the relationship between an (a) PDF and (b) CDF.

Whilst the histogram of R_c provides an indication of the dataset CDF, it has been suggested that *ranking equations* can be used to give a better approximation of the R_c for data points within a dataset under different conditions [29, 35]. Ranking equations take the form shown in Equation B.7, using the f_1 and f_2 coefficients given in Table B.1 [29]. When employing ranking equations, the dataset must be ordered from the smallest data point to the largest data point. An example of the Mean Rank for the dataset shown previously in Figure B.8 is given in Figure B.9.

$$R_{c_i} = \frac{i - f_1}{N + f_2} \tag{B.7}$$

Table B.1. Ranking equations and f_1 and f_2 values to be used to compute relative frequency [29].

Ranking Equation (*Abbreviation*)	f_1	f_2
Large Sample (*LS*)	0	0
Hazen Formula (*Hazen*)	0.5	0
Mean Rank (*Mean*)	0	1
Gumbel (*Gumbel*)	0.4	0.2
Extreme Value (*EV*)	0.35	0
Median Rank (*Median*)	0.3	0.4
Normal (*Normal*)	0.3175	0.365

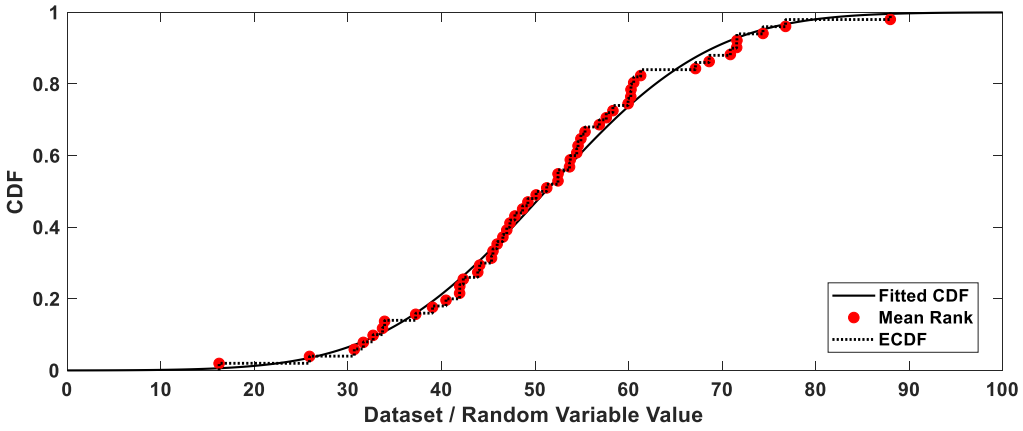

Figure B.9. A visualisation of how Mean Rank values can be compared with the fitted CDF and the ECDF of a dataset.

For large datasets, the Empirical Cumulative Density Function (ECDF) can be plotted as a step-function to provide a representation of the CDF. It is useful to note that the ECDF produces equivalent ranking values to employing the Large Sample ranking equation for a dataset.

Distribution Fitting

In order to estimate the location/threshold, shape and scale parameters of a chosen probability distribution type, distribution fitting methods must be employed. Distribution fitting methods generate distribution parameter estimates based directly on the values of data points contained within the dataset.

The first form of distribution fitting is Probability Plotting and Linear Rectification (PPLR). As PPLR is discussed and demonstrated extensively in Chapter 4, this section only intends to highlight the transformation equations and linear rectification equations required to generate probability distribution estimates when performing PPLR.

In order to perform PPLR and uncover the linear relationships between data point values and R_c, transformation equations must be used. For example, considering a 2-Parameter (2P)

Weibull distribution, the data point values 'x_i' must be transformed using Equation B.8a, whilst the R_{c_i} values for each data point must be transformed using Equation B.8b [29]. Transformation equations are available for different distribution types in reference texts [29, 33, 35].

$$x_{t_i} = ln(x_i) \tag{B.8a}$$

$$R_{c,t_i} = ln\left(ln\left(\frac{1}{1-R_{c_i}}\right)\right) \tag{B.8b}$$

Once the linear regression for the x_{t_i} and R_{c,t_i} transformed values has been performed, the $A0$ intercept and $A1$ slope values must be converted to distribution parameter estimates using linear rectification equations. For example, the σ scale and λ shape parameters for the 2P Weibull distribution can be computed using Equations B.9a and B.9b respectively [29]. Linear rectification equations are available for different distribution types in reference texts [29, 33, 35].

$$\sigma = \exp\left(-\frac{A0}{A1}\right) \tag{B.9a}$$

$$\lambda = A1 \tag{B.9b}$$

An alternative to PPLR is Maximum Likelihood Estimation (MLE). MLE selects distribution parameter estimates that maximise the probability of randomly sampling (or 'observing') the available dataset from the fitted distribution [33]. The probability of observing the dataset is known as the *likelihood* [33, 156]. The likelihood for a given dataset and set of distribution parameter estimates is given by the Likelihood Function (LF) of the chosen distribution type [33]. An example of an LF for a Normal distribution is shown in Equation B.10 [33]:

$$LF = \sigma^{-N}(2\pi)^{-\frac{N}{2}}\exp\left\{-\frac{1}{2}\sum_{i=1}^{N}\left(\frac{x_i-\lambda}{\sigma}\right)^2\right\} \tag{B.10}$$

The maximum likelihood value can be identified by differentiating Equation B.10 with respect to each distribution parameter type and setting the resulting equation to zero. This process results in Maximum Likelihood (ML) equations, such as those for a Normal distribution shown in Equations B.11a and B.11b [33].

$$\lambda_{ML} = \frac{1}{N}\sum_{i=1}^{N} x_i \tag{B.11a}$$

$$\sigma_{ML} = \sqrt{\frac{\sum_{i=1}^{N}(x_i-\lambda_{ML})^2}{N-1}} \tag{B.11b}$$

It is interesting to note that the ML equations for a Normal distribution are identical to the formulas used to compute the μ and σ of a dataset shown previously in Equations B.1 and B.2. ML equations are available in reference texts for a wide range of distribution types [33, 164]. It

should be noted however, that some distributions are defined by three or more ML equations, which must be solved simultaneously [164]. Such situations are reliant on complex optimisation and numerical solution approaches [33].

Confidence Intervals

It should be noted that the true purpose of fitting a distribution to a dataset is to infer the statistical characteristics of a *population* [33, 156]. A population represents a complete set of 'items'. However, within engineering, it is often uneconomical, or even impossible to work with the population, so the datasets used to characterise design parameter variability are typically a *sample* of the population [29].

Figure B.10 shows how a sample, such as the datasets used to characterise the variability in N_f within an S-N datasets relates to a population (i.e. all of the specific material ever manufactured). Often when constructing S-N curves, only a single sample dataset is available from the coupon test results of a single test campaign. However, if the coupon testing was repeated, a completely different sample dataset would be generated (i.e. the coupons would fail at different values of N_f compared to the first sample). Therefore, the distribution parameter estimates for the second sample would be expected to differ slightly from the first. Subsequent datasets would also show different distribution parameter estimates.

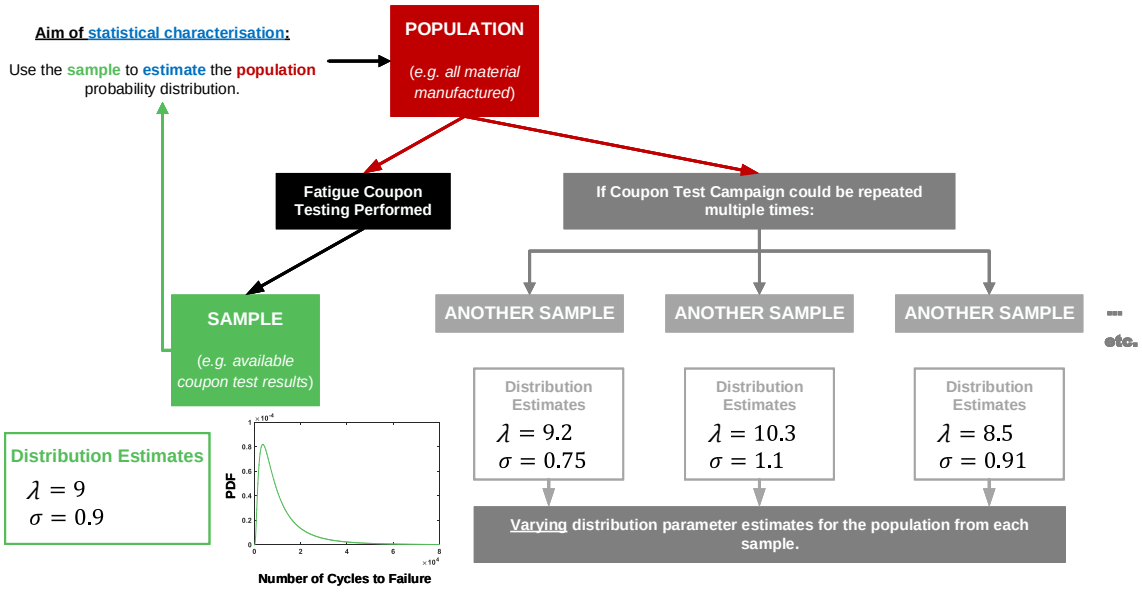

Figure B.10. A demonstration of why distribution parameter estimates exhibit variability.

As a result, distribution parameter estimates only ever provide an estimate of the statistical characteristics of a population [33]. Therefore, when fitting distributions to a dataset, the distribution parameter estimates must also be expected to show variability. The statistical characterisation of the variability in distribution parameter estimates is often called *sample statistics* [156].

As only one sample from a population is typically available, the distribution parameter estimates generated by PPLR and MLE fitting methods are known as *point estimates* [156]. The error between the sample distribution parameter estimates and those of the population is known as *bias* [33, 156]. Ideally, it is preferable to generate *unbiased estimates*.

Confidence Intervals (CI) can be used to highlight and quantify the variability present in distribution parameter estimates [33, 156]. The CI provides a plausible range of the sample distribution parameter estimates that bracket the true population distribution parameters [156]. CIs can be constructed using closed-form equations or numerical simulation approaches such as parametric bootstrapping [33, 176]. The CI is constructed at a *Confidence Level* (CL). A $CL = 95\%$ represents that if many samples could be drawn from a population, the computed CI would bracket the population distribution parameter for 95% of the sample datasets [156].

Goodness-of-Fit Testing

Goodness-of-Fit (GoF) tests provide a selection of methods that enable the assessment and quantification of how well a specific distribution type fits a sample dataset [29].

The first example of a GoF test is the Anderson-Darling (A-D) test, which compares between the expected frequency from the dataset and the fitted CDF [33, 173]. The A-D test statistic 'A^2' is computed using Equation B.12, where '$F(x)$' is the CDF of the fitted distribution [33, 173].

$$A^2 = -N - \left(\frac{1}{N}\right)\sum_{i=1}^{N}(2i-1)[ln(F(x_i)) + ln(1-F(x_{N+1-i}))] \tag{B.12}$$

The A^2 statistic is then compared to a critical value 'A_c^2', which is available in tabulated form or via parametric bootstrap methods [173, 176]. The fitted distribution is rejected if $A^2 \geq A_c^2$. Critical values for GoF tests are defined at a specific *significance level* 'α'. In a similar case to the variability present in distribution parameter estimates, GoF test statistics would also show variability if multiple samples were available from the same population [156]. Therefore, the A^2 statistic will also demonstrate variability, as highlighted by the probability distribution in Figure B.11.

As the A^2 test statistic demonstrates variability, setting a single-valued critical value of A_c^2 will result in the potential that a 'correct' distribution type is rejected as its A^2 test statistic could lie within the rejected tail area of Figure B.11. The probability of falsely rejecting a correct distribution is known as the significance level [156]. A typical significance level value is 5%, presenting a probability of $P = 0.05$ for falsely rejecting the correct distribution type.

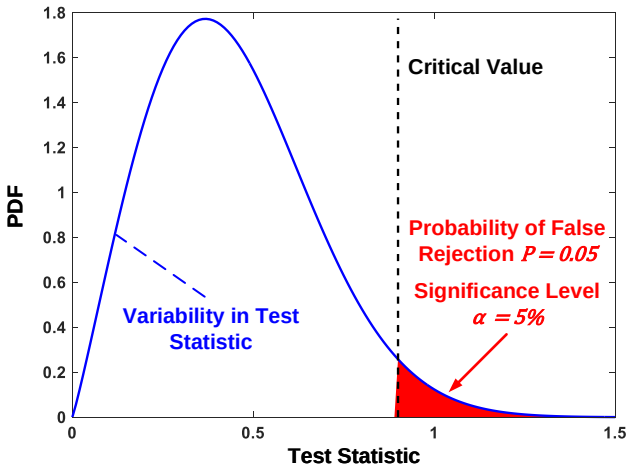

Figure B.11. A visualisation of the definition of the α significance level.

The other GoF test presented within this thesis is the Chi-Squared (χ^2) test. The χ^2 test is similar to the A-D GoF test as it compares the observed frequency of values within a dataset with the expected frequency of the same values from the fitted CDF [156, 173]. Again, a test statistic is generated 'χ^2_s' and compared to a critical value 'χ^2_c', which must also be defined at a specific significance level, conventionally $\alpha = 5\%$.

The χ^2 GoF test differs from the A-D GoF test as the dataset is first partitioned into bins. It is recommended that the number of bins n_{bin} is computed using Equation B.13 when performing the χ^2 GoF test at the $\alpha = 5\%$ significance level [173].

$$n_{bin} = 2N^{\frac{2}{5}} \tag{B.13}$$

The width of each bin is then defined such that each bin range represents a value range that has an equal probability of being observed (i.e. a set of parameter ranges that result in the area under the fitted PDF being divided into equal portions) [173]. The required probability in each bin is computed using Equation B.14. The minimum and maximum values (b_{min} and b_{max}) of each bin can be identified using Equation B.15, where 'F^{-1}' is the Inverse Cumulative Density Function (ICDF) of the fitted distribution. For a given bin, b_{min} is equal to the b_{max} value of the previous bin.

$$P_{bin} = \frac{1}{n_{bin}} \tag{B.14}$$

$$b_{max} = F^{-1}(P_{bin}) + F(b_{min}) \tag{B.15}$$

The data points in the sample dataset are then sorted into each bin 'j' and the observed frequency 'O_j' of data points in each bin is identified [156, 173]. It is a common requirement to have at least five data points in each bin (i.e. $O_j \geq 5$) [173] and therefore, bins are often merged with neighbouring bins. Following the binning of data points, the χ_s^2 test statistic can be computed using Equation B.16, where 'E_j' represents the expected frequency for the bin based upon the fitted CDF. Equation B.17 is used to compute E_j for each bin.

$$\chi_s^2 = \sum_{j=1}^{n_{bin}} \frac{(O_j - E_j)^2}{E_j} \tag{B.16}$$

$$E_j = N[F(b_{max_j}) - F(b_{min_j})] \tag{B.17}$$

The χ_s^2 statistic is then compared to tabulated values of the χ_c^2 critical value [156]. The χ_c^2 value is defined at an α significance level. The χ_c^2 value is also based on the 'degrees of freedom' of the χ^2 GoF test 'ν', which can be computed using Equation B.18 [156, 173]. The fitted distribution is rejected if $\chi_s^2 \geq \chi_c^2$ [156, 173].

$$\nu = n_{bin} - \text{Number of distribution parameters estimated} \tag{B.18}$$

Probability of Failure Estimates from Tail-Fitting

Generation of $P_{f_{tail}}$ estimates using Generalised Pareto Distributions (GPDs) was conceptually described in Section 3.5.1.1. This section provides the equations required to generate $P_{f_{tail}}$ estimates from the output of an MCS [159, 160]. The process is also visualised in Figure B.12.

Following an MCS, a tail dataset is extracted from the MCS output by defining a lower threshold to the tail 't', such that the sample size of the dataset 'N_t' is equal to $1.5\sqrt{N_{MCS}}$ as shown in Figures B.12a and B.12b. The proportion of the of the MCS output that lies in the tail dataset (i.e. above t) '$F(t)$' is estimated using Equation B.19 as also shown in Figure B.12a.

$$F(t) = 1 - \frac{N_t}{N_{MCS}} \tag{B.19}$$

A GPD is then fitted to the tail dataset using maximum likelihood estimation methods, as shown in Figure B.12c. The GPD is evaluated at the failure criterion (e.g. D_{fail}) to give the value of '$F_{GPD}(D_{fail})$', as shown in Figure B.12d. Consequently, an estimation of the proportion of the MCS output that lies above the failure criterion (i.e. above D_{fail}) '$F(D_{fail}$' can be generated using Equation B.20.

$$F(D_{fail}) = F_{GPD}(D_{fail})[1 - F(t)] + F(t) \tag{B.20}$$

The probability of failure estimate '$P_{f_{tail}}$' is then computed using Equation B.21.

$$P_{f_{tail}} = 1 - F(D_{fail}) \tag{B.21}$$

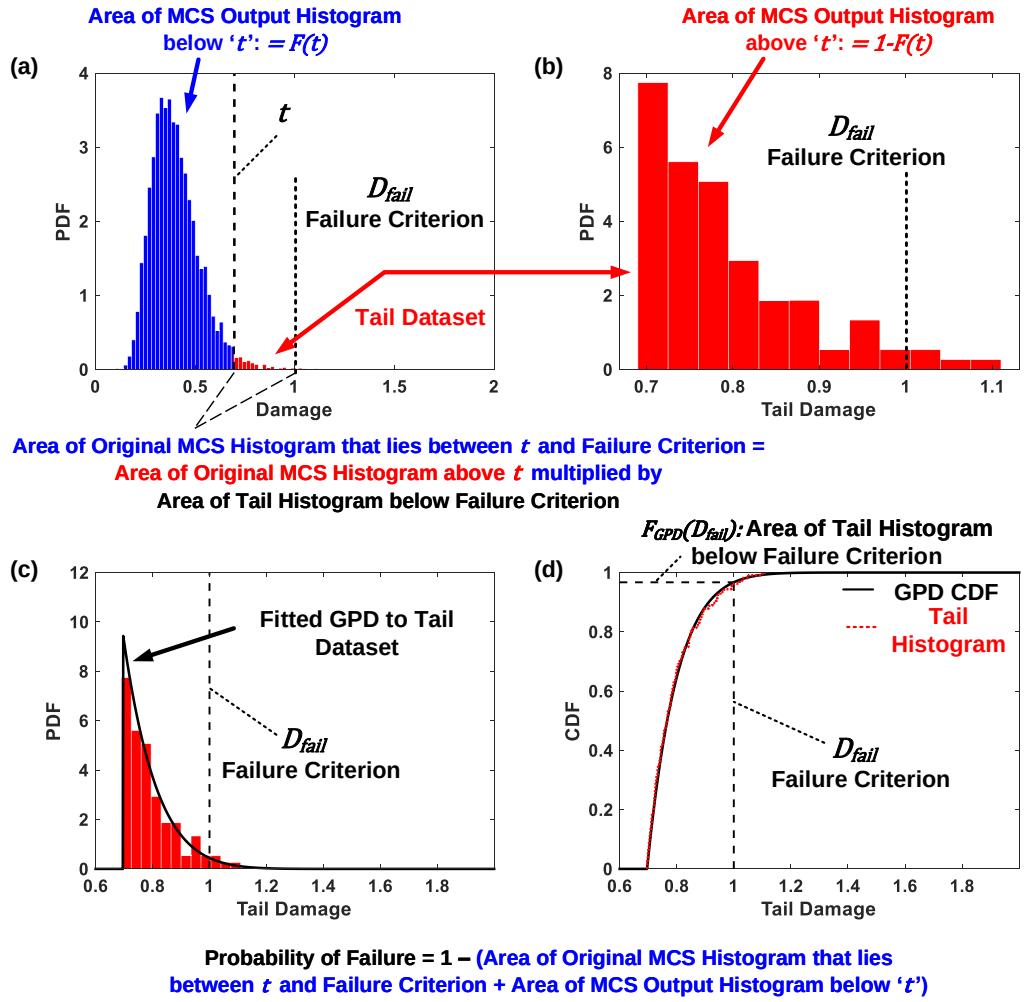

Figure B. 12. Computation of the $P_{f_{tail}}$ estimate by (a, b) defining the tail dataset, (c) fitting a GPD to the tail dataset and (d) evaluating F_{GPD} using the fitted GPD.

Distribution Type Catalogue

This section presents the PDFs, CDFs, support and skew of the distributions presented within this thesis, sourced from various reference texts [29, 33, 289]. The PDFs and CDFs require additional mathematical functions such as the error function 'erf', the gamma function 'Γ', the SND PDF 'ϕ_{SND}' and Owen's T function 'T'. The distribution catalogue also includes figures showing key properties of each distribution type. Reference texts provide the origin and typical application of each distribution type [29, 33, 289]. *Distribution catalogue has been redacted due to copyright. Please see reference texts.*

APPENDIX C: GROUND MANOEUVRE CONTINGENCY TABLES

This appendix provides the contingency tables generated to investigate the correlation between the occurrence of turning and braking manoeuvres for wide-body civil aircraft. The contingency tables in this appendix support Figures 5.21 and 5.22 in Chapter 5 and show the frequency of specific combinations of turning and braking occurrences observed in the 1,265 flights of the ADS-B dataset.

Table C.1. Observed frequency of flights with specific combinations of pre-takeoff left turn and pre-takeoff right turn occurrences.

		Number of Left Turns Pre-Takeoff													
1265 Flights		0	1	2	3	4	5	6	7	8	9	10	11	12	13
Number of Right Turns Pre-Takeoff	0	23	46	20	3	2	0	0	0	0	0	0	0	0	0
	1	75	**227**	127	42	12	0	0	0	0	0	0	0	0	0
	2	38	136	113	59	17	3	1	1	0	0	0	0	0	0
	3	22	45	56	38	16	4	8	0	2	0	0	0	0	0
	4	6	6	21	27	13	3	1	2	0	0	0	0	0	0
	5	0	1	8	6	6	5	3	1	1	0	0	0	0	0
	6	0	0	1	0	3	4	1	0	0	0	0	0	0	0
	7	0	0	0	0	2	0	2	0	1	0	0	0	0	0
	8	0	0	0	0	2	0	0	0	0	0	0	0	0	0
	9	0	0	0	0	0	1	0	0	0	0	0	0	0	0
	10	0	0	0	0	0	0	0	1	0	0	0	0	0	0
	11	0	0	0	0	0	0	0	0	0	0	0	0	0	0
	12	0	0	0	0	0	0	0	0	0	0	0	0	0	0
	13	0	0	0	0	0	0	0	0	0	0	0	0	0	1

Table C.2. Observed frequency of flights with specific combinations of pre-takeoff turn and pre-takeoff braking occurrences.

		Total Number of Turns Pre-Takeoff																	
1265 Flights		0	1	2	3	4	5	6	7	8	9	10	11	12	13	14	15	16	17	26
Total Number of Braking Occurrences Pre-Takeoff	0	0	6	10	5	2	3	2	0	0	0	0	0	0	0	0	0	0	0	0
	1	7	28	28	21	7	7	4	0	0	0	1	0	0	0	0	0	0	0	0
	2	9	19	**55**	36	24	11	6	2	2	1	0	0	0	0	0	0	0	0	0
	3	2	26	51	48	30	14	5	5	2	2	1	0	0	0	0	0	0	0	0
	4	3	22	45	48	31	5	11	7	2	1	0	0	0	1	0	0	0	0	0
	5	1	9	29	34	32	16	12	5	2	3	1	0	0	0	0	0	0	0	0
	6	0	6	21	29	24	15	6	7	1	4	1	2	2	0	0	0	0	1	0
	7	0	3	18	36	16	20	3	6	1	3	0	2	0	0	0	0	0	0	0
	8	1	1	12	11	17	12	5	8	4	0	3	0	0	1	0	0	0	0	0
	9	0	1	6	7	8	10	6	5	4	0	0	2	0	0	0	0	0	0	0
	10	0	0	1	5	5	6	4	1	5	0	1	2	0	0	0	0	0	0	0
	11	0	0	7	5	6	6	3	3	1	1	0	0	0	1	0	0	0	0	0
	12	0	0	0	2	1	1	6	2	0	1	0	3	1	0	0	0	0	0	0
	13	0	0	2	0	2	2	2	2	0	0	0	1	0	0	1	0	0	0	0
	14	0	0	0	0	2	1	0	0	0	0	1	0	1	0	0	0	0	0	0
	15	0	0	0	0	1	0	1	0	1	1	0	0	0	0	0	1	0	0	0
	16	0	0	0	0	0	3	0	1	0	0	0	0	0	0	0	0	0	0	0
	17	0	0	0	0	0	0	1	0	0	0	0	1	0	0	0	0	0	0	0
	18	0	0	0	1	0	0	0	0	0	0	0	0	0	0	0	0	0	0	0
	19	0	0	0	0	0	0	0	0	0	0	0	0	0	0	0	0	0	0	0
	20	0	0	0	0	0	0	0	0	0	1	0	0	0	0	0	0	0	0	0
	21	0	0	0	0	0	1	0	0	0	0	0	0	0	0	0	0	0	0	1

Table C.3. Observed frequency of flights with specific combinations of post-landing left turn and post-landing right turn occurrences.

1265 Flights	Number of Left Turns Post-Landing								
Number of Right Turns Post-Landing	0	1	2	3	4	5	6	7	8
0	55	109	38	14	1	1	0	0	0
1	84	**244**	140	32	13	4	1	0	0
2	27	100	96	65	26	5	2	0	0
3	6	25	34	39	13	7	1	0	0
4	0	4	12	15	9	2	0	0	0
5	0	0	5	8	3	1	0	1	0
6	0	0	0	3	7	3	0	0	0
7	0	0	1	0	2	1	2	0	1
8	0	0	0	0	1	0	0	2	0

Table C.4. Observed frequency of flights with specific combinations of post-landing turn and post-landing braking occurrences.

1265 Flights	Total Number of Turns Post-Landing															
Total Number of Braking Occurrences Post-Landing	0	1	2	3	4	5	6	7	8	9	10	11	12	13	14	15
0	6	4	4	4	2	0	1	0	0	0	0	0	0	0	0	0
1	14	24	28	17	3	1	2	3	0	0	0	0	0	0	0	0
2	7	40	52	27	10	10	5	1	0	1	0	0	0	0	0	0
3	13	44	54	50	30	16	7	3	3	1	1	1	0	0	0	0
4	7	37	**66**	49	24	10	7	4	2	1	0	0	0	0	0	0
5	4	25	47	39	21	12	8	3	5	0	2	1	0	0	0	0
6	4	8	30	30	21	15	15	3	0	2	1	1	0	0	0	0
7	0	6	13	17	16	16	13	6	3	1	0	1	0	0	0	1
8	0	3	8	7	8	14	9	3	0	0	1	0	0	0	0	0
9	0	2	3	9	9	9	0	2	5	0	0	0	2	0	0	0
10	0	0	1	4	3	4	2	3	2	1	1	0	0	0	0	0
11	0	0	2	5	2	2	5	4	1	0	1	0	0	0	0	0
12	0	0	1	0	3	4	3	1	0	0	0	1	0	0	0	0
13	0	0	0	2	2	1	0	3	1	0	0	0	0	0	0	0
14	0	0	0	0	0	0	1	0	2	1	1	0	0	0	0	1
15	0	0	0	0	0	2	0	0	0	0	0	0	0	1	0	0
16	0	0	0	0	0	0	0	0	1	0	0	0	0	0	0	0
17	0	0	0	0	0	0	3	0	0	0	0	0	0	0	0	1
18	0	0	0	0	0	1	0	0	1	1	0	0	0	0	0	0
19	0	0	0	0	0	0	0	0	0	0	0	0	1	0	0	0
20	0	0	0	0	0	0	0	0	0	0	0	0	0	1	0	0
21	0	0	0	0	0	0	0	0	0	0	0	0	0	0	0	0
22	0	0	0	0	0	0	0	0	0	0	0	0	0	0	0	0
23	0	0	0	0	0	0	0	0	0	0	0	0	0	0	0	0
24	0	0	0	0	0	0	0	0	0	0	0	0	0	0	0	0
25	0	0	0	0	0	0	0	0	0	0	0	0	0	0	0	0
26	0	0	0	0	0	0	0	0	0	0	0	0	0	0	0	0
27	0	0	0	0	0	0	0	0	0	1	0	0	0	0	0	0

APPENDIX D: MILESTONE MANOEUVRE SEQUENCING STATISTICS

This appendix presents the ADS-B results from the identification of manoeuvres following and preceding the milestone manoeuvres as described in Chapter 5:

- Manoeuvre after pushback.
- Manoeuvre before runway entry.
- Manoeuvre after runway exit.
- Manoeuvre before turn onto stand.

Figure D.1a shows the proportion of manoeuvres after a tail-left pushback, where the majority of following manoeuvres are straight taxi. This observation is also made for the manoeuvres following a tail-right pushback in Figure D.1b. Figure D.1 shows that the proportional share of manoeuvres following pushback is insensitive to the pushback direction.

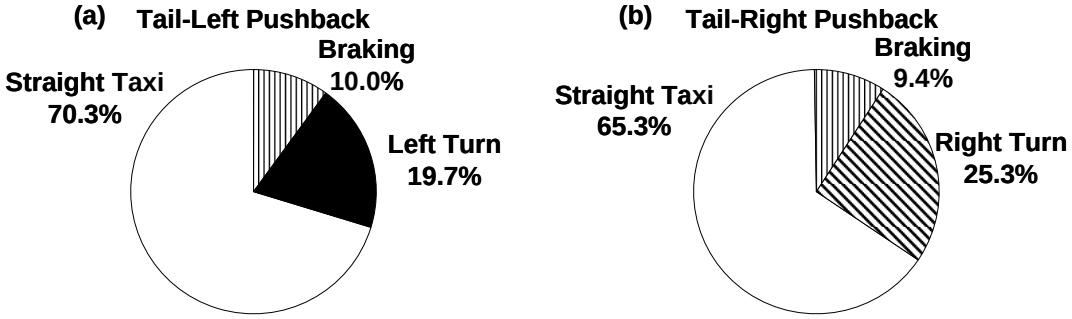

Figure D.1. Proportional share of manoeuvres following a (a) tail-left pushback and (b) tail-right pushback.

Figure D.2 shows the proportional share of manoeuvres occurring before a standard runway entry. For both left and right standard runway entry turns, Figure D.2 shows that the majority of manoeuvres preceding the runway entry are straight taxi manoeuvres. This observation could be as a result of typical airport geometries, where the runway entry taxiway is perpendicular to the runway. A significant number of the preceding manoeuvres to the runway entry are braking manoeuvres, as shown in Figure D.2 and this is expected to be as a result of aircraft braking to

'hold-short' of the runway at the designated hold-short locations. Figure D.2 also shows that the proportional share of manoeuvres preceding a runway entry is insensitive to the runway entry direction.

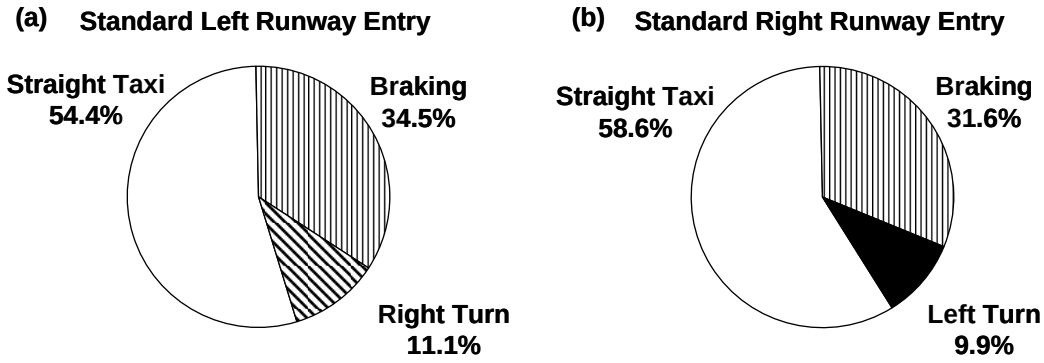

Figure D.2. Proportional share of manoeuvres before a (a) left standard runway entry and (b) right standard runway entry.

The manoeuvres preceding backtrack runway entries are shown in Figure D.3. It can be observed from Figure D.3 that for the majority of both left and right 180° backtrack turns, that the preceding manoeuvre was a turn in the opposite direction. This is expected to be the turn that offsets the aircraft from the runway centreline prior to performing the 180° turn.

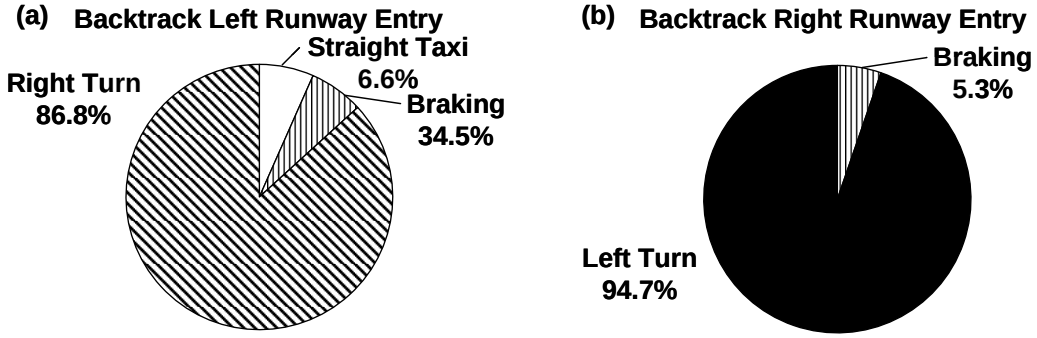

Figure D.3. Proportional share of manoeuvres before a (a) left backtrack runway entry and (b) right backtrack runway entry.

The manoeuvres occurring after a standard runway exit are shown in Figure D.4. Figure D.4 demonstrates that the proportional share of manoeuvres occurring after a standard runway exit is insensitive to the runway exit direction. The greatest proportion of manoeuvres following standard runway exits are straight taxi and braking. This is as a result of airport geometries, which typically have taxiways perpendicular to the runway and 'hold-short' locations prior to the aircraft joining the taxiway after vacating the runway.

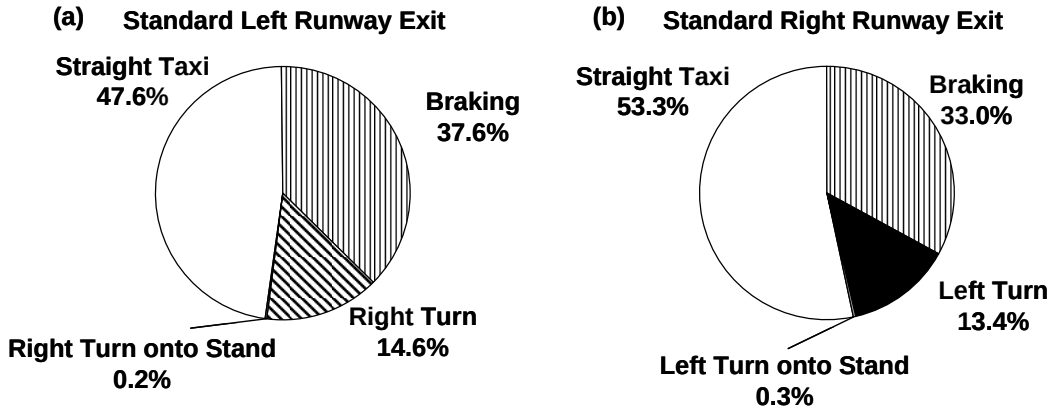

Figure D.4. Proportional share of manoeuvres after a (a) left standard runway exit and (b) right standard runway exit.

Figure D.4 also shows that in less than 1% of cases for each runway exit direction that the aircraft was able to turn directly onto the arrival stand. A turn onto stand following a runway exit is only possible at smaller airports, which represent a small proportion of the airports that the wide-body civil aircraft studied in this thesis operates at.

Figure D.5 shows the manoeuvres occurring after a high speed runway exit. It can be observed that for both left and right high speed exits that the proportional share of manoeuvres following the exit is in good agreement with the values shown for standard runway exits in Figure D.4. The manoeuvre sequencing following runway exits is therefore insensitive to the runway exit direction regardless of whether a standard or high speed exit is performed. This is to be expected as airport geometries tend to result in standard and Rapid Exit Taxiways (RETs) leading the aircraft to the same taxiway parallel to the runway.

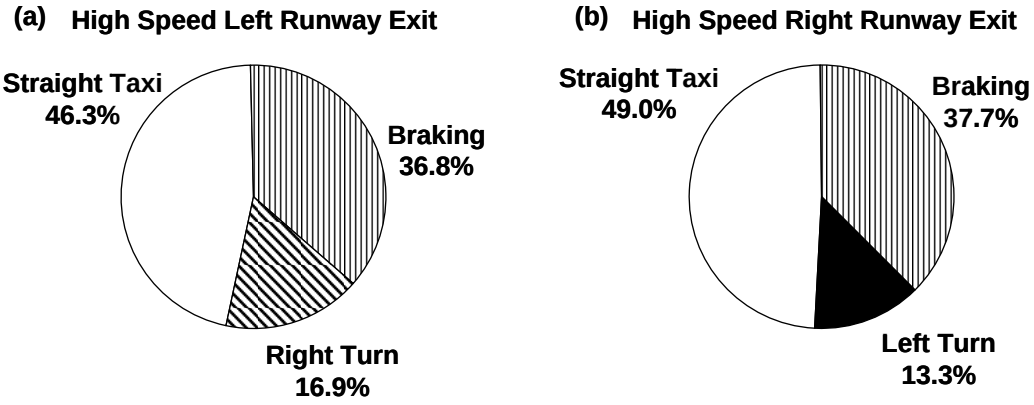

Figure D.5. Proportional share of manoeuvres after a (a) left high speed runway exit and (b) right high speed runway exit.

Finally, Figure D.6 shows the proportional share of manoeuvres preceding both a left and right turn onto stand. It can be seen from Figure D.6 that the two pie charts are visually indistinguishable, suggesting that the proportional share of manoeuvres preceding a turn onto stand is insensitive to the turn onto stand direction. The greater proportion of braking manoeuvres occurring before the turn onto stand is expected to be as a result of the aircraft typically decelerating before performing the tight/pivot turn onto stand.

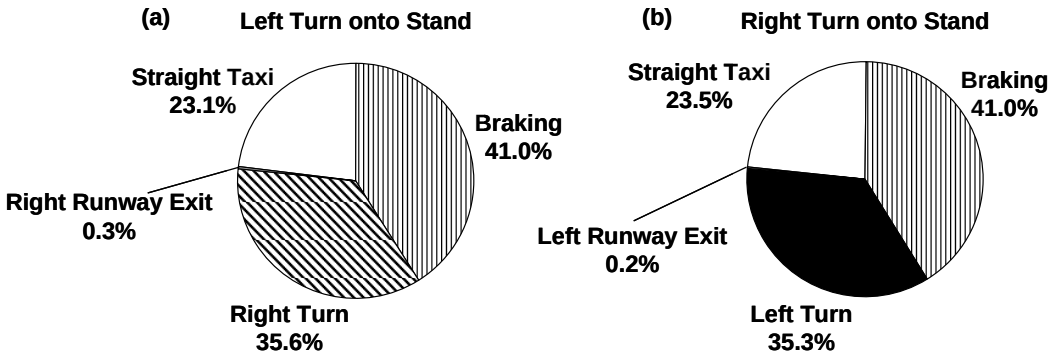

Figure D.6. Proportional share of manoeuvres preceding a (a) left turn onto stand and (b) right turn onto stand.

Summary

This appendix has demonstrated the sequencing variability of manoeuvres following and preceding the milestone manoeuvres. It has been demonstrated that airport geometries dictate the sequencing of such manoeuvres. The most important observation from this appendix is that the proportional share of manoeuvres following or preceding a given milestone manoeuvre is insensitive to the direction of the milestone manoeuvre.

APPENDIX E: STANDARDISED LOADING SPECTRUM

This appendix details the loading spectrum (i.e. manoeuvre occurrence and sequencing) and load factors used to support the sensitivity analysis cases presented in Chapters 7 and 8.

Standard Loading Spectrum

The standard loading spectrum is used to provide a landing gear load-time history that has a fixed manoeuvre sequence of a constant number of manoeuvre occurrences, which does not vary from flight-to-flight during the statistical simulation of load-time histories. The occurrences for the ground manoeuvres within the standard loading spectrum are based upon the mode occurrence values identified for turning and braking manoeuvres in Chapter 5. The sequencing of manoeuvres is based upon existing design practice [188]. The standard loading spectrum is as follows:

1. Pushback (tail-left or tail-right).
2. Straight Taxi.
3. Pre-takeoff Turn (left or right).
4. Straight Taxi.
5. Pre-takeoff Turn (left or right).
6. Pre-runway Entry Queuing:
    a) Straight Taxi.
    b) Braking.
    c) Straight Taxi.
    d) Braking.
    e) Straight Taxi.
7. Runway Entry Turn (left or right).
8. Takeoff Roll.
9. Landing Touchdown (left or right drift).
10. Landing Roll and Braking.
11. Runway Exit Turn (left or right).
12. Braking.
13. Post-landing Turn (left or right).
14. Straight Taxi.
15. Braking.
16. Post-landing Turn (left or right).
17. Straight Taxi.
18. Braking.
19. Turn onto Stand (left or right).

The standard loading spectrum sequence shown above still provides the possibility that turning manoeuvres may either be to the left or to the right. As it was observed in Chapter 5 that the turning direction for all manoeuvres was equally shared between left and right turns, the above sequence was generated for all possible combinations of turning directions, resulting in

512 different flight types. The sequence of 512 flights was then repeated until the design safe-life of 50,000 flights was achieved.

Available Landing Gear Load Exceedance Curves

This appendix section provides the full list of the exceedance curves used within the statistical simulation of load-time histories for each of the ground manoeuvre load-time profiles, as discussed in Chapter 5. The exceedance curves listed below are sourced from the in-service loads monitoring of different types of wide-body civil aircraft:

FAA Statistical Loads Programme [191]

- Longitudinal (drag) load factor during taxi-out (pre-takeoff) and taxi-in (post-landing):
  - used to provide n_x braking drag load variability.
- Longitudinal (drag) load factor during landing roll with thrust reversers:
  - used to provide n_x braking drag load variability during first section of landing roll:
- Longitudinal (drag) load factor during landing roll without thrust reversers:
  - used to provide n_x braking drag load variability during second section of landing roll or for flights where thrust reversers are not deployed.
- Lateral (side) load factor at touchdown:
  - used to provide n_y side load variability during landing drift.
- Lateral (side) load factor during runway turnoff (exit):
  - used to provide n_y side load variability during runway exits (standard and high speed).
- Lateral (side) load factor during ground turns for taxi-out (pre-takeoff) and taxi-in (post-landing):
  - used to provide n_y side load variability during turns (including runway entry, pushback turn and turn onto stand).
- Vertical load factor during taxi-out (pre-takeoff) and taxi-in (post-landing):
  - used to provide n_z vertical load factor variability for bump load during taxiing.
- Vertical load factor during takeoff roll:
  - used to provide n_z vertical load factor variability for bump load during takeoff roll.

- Vertical load factor at touchdown:
  - used to provide n_z vertical load factor variability at landing touchdown.
- Vertical load factor at spoiler deployment:
  - used to provide n_z vertical load factor variability at lift dump.
- Vertical load factor during landing roll:
  - used to provide n_z vertical load factor variability for bump load during landing roll.

Ladda and Struck, Buxbaum [12, 14]

- Longitudinal (drag) load factor during spin-up and spring-back:
  - used to provide n_x drag load variability for spin-up and spring-back loads at touchdown.

Fixed Load Factor Values

In order to remove the load factor variability in the sensitivity analysis cases shown in Chapters 7 and 8, nominal load factor values were defined for each of the ground manoeuvres in the statistically simulated load-time histories. Nominal load factors were defined by identifying the approximate load factor that resulted in an $F_{ECDF} = 0.5$ value for the histogram generated by fine blocking for each exceedance curve. The nominal load factors are as follows (note: drag n_x load factors are defined in the opposite sense in the FEA MLG beam model as described in Chapter 6):

Longitudinal, drag, n_x, load factors:

- Pushback: -0.25 g
- Taxi braking: -0.02 g
- Spin-up: -0.1 g
- Spring-back: 0.1 g
- Landing braking with thrust reversers: -0.25 g
- Landing braking without thrust reversers: -0.15 g

Lateral, side, n_y load factors:

- Pre-takeoff turn and runway entry turn: ±0.05 g
- Touchdown drift: 0.1 g
- Runway exit turn: ±0.075 g
- Post-landing turn: ±0.05 g

Vertical, n_z load factors:

- Taxi bump: 0.01 g
- Takeoff roll bump: 0.025 g
- Touchdown: 0.25 g
- Lift dump: 0.1 g
- Landing roll bump: 0.05 g

APPENDIX F: STATISTICAL SIMULATION OF MANOEUVRE SEQUENCE

This appendix details the necessary processes required to statistically simulate the occurrences and sequencing of ground manoeuvres within the statistical simulation of load-time histories described in Chapter 5. The processes required to statistically simulate ground manoeuvre occurrences and sequencing were reliant on correlated random sampling and conditional sampling. This appendix provides worked examples of both correlated sampling and conditional sampling using the pie charts and contingency tables across Chapter 5 and Appendices C and D. The processes detailed in this section were performed using MATLAB® scripts during the statistical simulation of load-time histories. This section relies on assuming values for random numbers '*RN*', which naturally would vary with every statistically simulated flight.

Correlated Random Sampling from Contingency Tables

Correlated random sampling is required to represent the correlation shown in Chapter 5 that exists between the occurrences of left and right turns, along with the correlation that exists between the total number of turns and total number of braking occurrences, within each taxi phase. Correlated random sampling is also required for the takeoff and landing mass of the aircraft.

Correlated random sampling can be performed using the contingency tables shown in Appendix C. To represent the correlation between the number of left and right turns in the post-landing taxi phase, the contingency table in Table C.3 can be converted to a joint probability table [156], as shown in Table F.1. Table F.1 shows the probability of observing a specific combination of left and right turn occurrences in the post-landing taxi phase, and is generated by dividing the contingency table values by the total observed frequency (e.g. the 1,265 flights collected during the ADS-B study in Chapter 5).

At the bottom of the joint probability table in Table F.1, the 'marginal probability' for the number of left turns during the post-landing taxi phase is shown. This value represents the probability of observing a post-landing taxi phase with the given number of left turns, irrespective of what the number of right turns is. The marginal probability is simply the sum of the joint probability values for each column representing a specific number of left turns [156].

Table F.1. Joint probability table for left and right turns in the post-landing taxi phase.

		Number of Left Turns Post-Landing								
	1265 Flights	0	1	2	3	4	5	6	7	8
Number of Right Turns Post-Landing	0	0.043	0.086	0.030	0.011	0.001	0.001	0.000	0.000	0.000
	1	0.066	0.193	0.111	0.025	0.010	0.003	0.001	0.000	0.000
	2	0.021	0.079	0.076	0.051	0.021	0.004	0.002	0.000	0.000
	3	0.005	0.020	0.027	0.031	0.010	0.006	0.001	0.000	0.000
	4	0.000	0.003	0.009	0.012	0.007	0.002	0.000	0.000	0.000
	5	0.000	0.000	0.004	0.006	0.002	0.001	0.000	0.001	0.000
	6	0.000	0.000	0.000	0.002	0.006	0.002	0.000	0.000	0.000
	7	0.000	0.000	0.001	0.000	0.002	0.001	0.002	0.000	0.001
	8	0.000	0.000	0.000	0.000	0.001	0.000	0.000	0.002	0.000
	Marginal Probability	*0.136*	*0.381*	*0.258*	*0.139*	*0.059*	*0.019*	*0.005*	*0.002*	*0.001*
	Cumulative Marginal Probability	**0.136**	**0.517**	**0.775**	**0.914**	**0.973**	**0.992**	**0.997**	**0.999**	**1.000**

The marginal probability values can then be converted into cumulative marginal probability values [156]. A random number 'RN' is then generated from a uniform random number generator. For example, $RN = 0.690$. This value can then be used to identify the number of left turns, through identifying the cumulative marginal probability bin that it falls into [156]. As $0.517 < RN \leq 0.775$, the randomly sampled number of left turns is 2.

Knowing that the number of post-landing left turns is 2, a conditional probability table can be constructed to randomly sample the corresponding number of right turns. Conditional probabilities represent the probability of observing an event, when the value (or outcome) of an additional event is already known [156]. Concerning the original contingency table in Table C.3, the column of right turn frequencies relating to the case where there are 2 left turns are isolated, as shown on the left-hand side of Table F.2. These frequencies are then normalised by the frequency of flights observed to contain two left turns in the post-landing phase, irrespective of the number of right turns (e.g. 326 flights). This results in the 'conditional probability' column in Table F.2 [156], which shows the probability of observing a specific number of right turns, knowing that the taxi phase also contains 2 left turns.

Table F.2. Conditional probability table for right turns in the post-landing taxi phase, when the number of left turns is two.

		Conditional Probabilities when Number of Left Turns = 2		
	326 Flights	Original Frequency	Conditional Probability	Cumulative Conditional Probability
Number of Right Turns Post-Landing	0	38	0.117	0.117
	1	140	0.429	0.546
	2	96	0.294	0.840
	3	34	0.104	0.945
	4	12	0.037	0.982
	5	5	0.015	0.997
	6	0	0.000	0.997
	7	1	0.003	1.000
	8	0	0.000	1.000

The conditional probability values in Table F.2 can then be converted to cumulative conditional probability values [156]. An additional RN value can be generated, for example $RN = 0.250$. This value is then used to randomly sample the number of right turns to be included with the 2 left turns for the post-landing taxi phase. As $0.117 < RN \leq 0.546$, the value of RN falls into the 1 right turn bin. Consequently, a correlated random sample for the post-landing turning occurrences has been generated consisting of 2 left turns and 1 right turn. Random sampling in this manner retains the correlation structure observed for the turning occurrences (see Chapter 5) by accounting for the conditional probability values [156].

Correlated random sampling is also performed to identify the number of braking occurrences within the statistically simulated manoeuvre sequence. In the example above, the total number of turns in the post-landing taxi phase is 3. A conditional probability table for the number of post-landing braking occurrences when there are 3 post-landing turns can be constructed based upon the contingency table in Table C.4.

Statistical Simulation of Manoeuvre Sequence: Worked Example

This section will provide a worked example of how a ground manoeuvre sequence is statistically simulated based on the ground manoeuvre statistics shown in Chapter 5 and Appendices C and D. Using the demonstration of correlated random sampling in the previous section, the post-landing ground manoeuvre sequence will be simulated. An identical process is used for the statistical simulation of the pre-takeoff taxi phase ground manoeuvre sequence.

Number of Post-Landing Braking Manoeuvres

The previous section used a correlated random sample to generate the number left and right turns for the post-landing taxi phase (2 left turns and 1 right turn). This random sampling resulted in a total of 3 post-landing turns to be included in the sequence. The number of post-landing braking occurrences can be randomly sampled from the contingency table shown previously in Table C.4. A correlated random sample for the number of braking occurrences is generated based on the value of 3 post-landing turns. Table F.3 shows the conditional probability table for post-landing braking occurrences when the total number of post-landing turns is 3, based on the frequencies shown in Table C.4.

An RN value is generated, which in this example is $RN = 0.200$. As $0.185 < RN \leq 0.377$, the RN value falls into the 3 braking manoeuvres bin. Therefore, the correlated random sample has resulted in the post-landing taxi phase consisting of 2 left turns, 1 right turn and 3 braking manoeuvres.

Table F.3. Conditional probability table for post-landing braking occurrences when the total number of post-landing turns is three.

		Conditional Probabilities when Total Number of Turns = 3		
Number of Post-Landing Braking Occurrences	260 Flights	Original Frequency	Conditional Probability	Cumulative Conditional Probability
	0	4	0.015	0.015
	1	17	0.065	0.081
	2	27	0.104	0.185
	3	50	0.192	0.377
	4	49	0.188	0.565
	5	39	0.150	0.715
	6	30	0.115	0.831
	7	17	0.065	0.896
	8	7	0.027	0.923
	9	9	0.035	0.958
	10	4	0.015	0.973
	11	5	0.019	0.992
	12	0	0.000	0.992
	13	2	0.008	1.000

Post-Landing Milestone Manoeuvres and Initial Sequencing

The next step is to randomly sample the milestone manoeuvres of the post-landing taxi phase, which includes the runway exit type and turn onto stand direction. An RN value is generated for each of these cases. Based on the cumulative probability values shown in Tables F.4 and F.5, the milestone manoeuvres can be identified. The cumulative probability values in Tables F.4 and F.5 are sourced from the pie charts for the milestone manoeuvres shown in Chapter 5.

Table F.4. Runway exit type cumulative probability table based on the pie chart shown in Figure 5.23d.

Runway Exit Type	% Share	Probability	Cumulative Probability
Standard Left Exit	38.7%	0.387	0.387
Standard Right Exit	42.1%	0.421	0.808
High Speed Left Exit	10.8%	0.108	0.916
High Speed Right Exit	7.8%	0.078	0.994
Left Backtrack Exit	0.6%	0.006	1

Table F.5. Turn onto Stand direction cumulative probability table based on the pie chart shown in Figure 5.23b.

Turn onto Stand Direction	% Share	Probability	Cumulative Probability
Left	54.3%	0.543	0.543
Right	45.7%	0.457	1

For the runway exit type, the RN value is 0.850, therefore selecting a high speed left runway exit from Table F.4 as $0.808 < RN \leq 0.916$. For the turn onto stand Direction, $RN = 0.050$, resulting in a left turn onto stand from Table F.5 as $0 \leq RN \leq 0.543$. The post-landing phase is

now defined as containing a high speed left runway exit, 2 left turns, 1 right turn, 3 braking occurrences and a left turn onto stand.

The initial sequencing of manoeuvres is then performed. This stage identifies the manoeuvres preceding or following the post-landing milestone manoeuvres using the pie charts shown in Appendix D. Table F.6 shows the cumulative probability of the manoeuvres **following** a high speed left runway exit, based on the pie chart shown in Figure D.5a. An $RN = 0.575$ results in a braking manoeuvre being sequenced after the high speed left runway exit. This also reduces the number of available braking manoeuvres for the remainder of the post-landing taxi phase to 2.

Table F.6. Cumulative probability table of manoeuvre following a high speed left runway exit based on the pie chart shown in Figure D.5a.

Manoeuvre Following High Speed Left Exit	% Share	Probability	Cumulative Probability
Straight Taxi	46.3%	0.463	0.463
Braking	36.8%	0.368	0.831
Right Turn	16.9%	0.169	1

The manoeuvre **preceding** the left turn onto stand is then identified using the cumulative probability values shown in Table F.7. An RN value of 0.690 results in a right turn preceding the left turn onto stand, reducing the number of available right turns in the post-landing taxi phase to zero. The number of available right turns is therefore exhausted.

Table F.7. Cumulative probability table of manoeuvre preceding a left turn onto stand based on the pie chart in Figure D.6a.

Manoeuvre Preceding Left Turn onto Stand	% Share	Probability	Cumulative Probability
Straight Taxi	23.2%	0.232	0.232
Braking	41.1%	0.411	0.643
Right Turn	35.7%	0.357	1

As a result, an initial manoeuvre sequence can be defined for the post-landing taxi phase, as shown by the sequence in Figure F.1. The manoeuvres have been replaced with their respective ID codes, where: *11 - right turn, 41 - braking, 722 - high speed left exit, 82 - left turn onto stand, 333 - landing touchdown* and *444 - landing roll*.

Manoeuvre ID	333	444	722	41	*Post-landing Taxi*	11	82

Figure F.1. Initial ground manoeuvre sequence generated from milestone manoeuvres.

Remaining Manoeuvre Sequence

Following the initial post-landing taxi phase manoeuvre sequence, the remaining post-landing taxi manoeuvres can be sequenced. This is performed in a sequential manner starting from the manoeuvre following the runway exit (in this example a braking manoeuvre), until all of the remaining turn and braking manoeuvres are exhausted. Within this example, there are 2 left turns and 2 braking manoeuvres remaining to populate the post-landing taxi.

Starting with the braking manoeuvre following the runway exit, Table F.8 shows the cumulative probability for manoeuvres following a post-landing braking manoeuvre, based upon the pie chart shown in Figure 5.25d. As no right turns are available, and there is a taxi phase prior to the turn onto stand, the pie chart in Figure 5.25d must be modified such that it only contains straight taxi and left turn options, as shown in Table F.8.

Table F.8. Cumulative probability table of manoeuvre following post-landing braking with zero right turns and no turn onto stand.

Manoeuvre Following Post-landing Braking	Original % Share	Modified % Share	Probability	Cumulative Probability
Straight Taxi	63.7%	80.3%	0.803	0.803
Left Turn	15.6%	19.7%	0.197	1

An $RN = 0.900$ is sampled, resulting in a left turn following the braking manoeuvre. This reduces the number of available left turns to 1, whilst there are still 2 braking manoeuvres available. In order to sample the manoeuvre following the left turn, the pie chart shown in Figure 5.24c must be modified to account for the unavailable right turns and turn onto stand, as shown in Table F.9. A random sample of $RN = 0.150$ results in a straight taxi manoeuvre following the left turn.

Table F.9. Cumulative probability table of manoeuvre following post-landing left turn with zero right turns and no turn onto stand.

Manoeuvre Following Post-landing Left Turn	Original % Share	Modified % Share	Probability	Cumulative Probability
Straight Taxi	49.1%	69.8%	0.698	0.698
Braking	21.3%	30.2%	0.302	1

Table F.10 shows the cumulative probability of manoeuvres following a post-landing straight taxi when no right turns are available and the turn onto stand has already been defined. An RN sample of 0.445 results in a braking manoeuvre following the straight taxi manoeuvre, reducing the number of available braking occurrences to 1.

To sample the manoeuvre following the braking manoeuvre, the cumulative probability values in Table F.8 can be used again as left turns are still available. An $RN = 0.125$ results in a straight taxi manoeuvre. As 1 braking manoeuvre and 1 left turn are still available, Table F.10 can also be used to identify the manoeuvre following the most recent straight taxi manoeuvre.

Table F.10. Cumulative probability table of manoeuvre following post-landing straight taxi with zero right turns and no turn onto stand.

Manoeuvre Following Post-landing Straight Taxi	Original % Share	Modified % Share	Probability	Cumulative Probability
Braking	68.3%	82.5%	0.825	0.825
Left Turn	14.5%	17.5%	0.175	1

An $RN = 0.500$ results in a braking manoeuvre, exhausting the available braking manoeuvres for the post-landing taxi phase. To sample the manoeuvre following the final braking manoeuvre, Table F.8 can be used as a single left turn is still available. An $RN = 0.960$ results in the selection of a left turn.

As this exhausts the turn manoeuvres available for the post-landing taxi phase, and as the right turn and braking manoeuvres have been previously exhausted, the sequencing of the ground manoeuvres has been completed. To summarise the results above, the post-landing taxi manoeuvre sequence becomes:

1. 12 - Left Turn
2. 66 - Straight Taxi
3. 41 - Braking
4. 66 - Straight Taxi
5. 41 - Braking
6. 12 - Left Turn

The post-landing taxi ground manoeuvre sequence listed above can then be inserted into the initial post-landing ground manoeuvre sequence, as shown in Figure F.2. This ultimately defines the post-landing taxi manoeuvre sequence and the subsequent load-time history can then be statistically simulated based upon this sequence as described in Chapter 5.

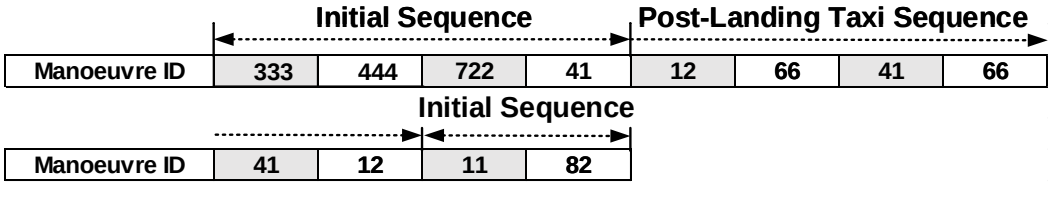

Figure F.2. Final post-landing taxi phase ground manoeuvre sequence.

Manoeuvre Occurrence and Sequencing Statistical Simulation Errors

Tables F.11 and F.12 provide the percentage errors for the verification of the statistical simulation of ground manoeuvre occurrence and sequencing respectively. The percentage errors were computed by comparing the values in the pie charts and contingency tables across Chapter 5 and Appendices C and D to the statistics generated from 250,000 statistically simulated flights. For example, in the original pie chart in Figure 5.24a, it is shown that a left turn followed a pre-takeoff straight taxi in 14.2% of cases, whilst the 250,000 statistically simulated flights resulted in a left turn following a pre-takeoff straight taxi in 17.6% of cases. This would correspond to a percentage error of 23.9% (i.e. the error in the percentage of cases).

Within Tables F.11 and F.12, 'sampling error' is used to highlight error values that could be reduced with a greater number of simulated flights. For example, specific occurrences and combination of manoeuvre occurrences were rarely observed within the original contingency tables (see Appendix C) and as a result, the percentage error results for each category can be highly sensitive to the under or over-observation of these manoeuvre occurrences. Within the case studies presented in Chapters 7 and 8, 5×10^9 individual flights were statistically simulated, due to the use of $N_{MCS} = 1 \times 10^5$ MCS iterations of 50,000 flights. Therefore, it expected that the percentage errors for manoeuvre occurrence and sequencing will be significantly lower for the case studies. Critical analysis of the percentage errors of the statistical simulation approach is provided in Chapter 5.

Table F.11. Percentage error results for verification of the statistical simulation of ground manoeuvre occurrences.

Occurrence Variability	Percentage Error	Error Description
Takeoff and Landing Mass	10.70%	Sampling error. Maximum percentage error occurs for an event with a probability of 0.033. All other errors are below 10%.
Takeoff Left and Right Turns	12.50%	Sampling error. Maximum percentage error occurs for an event with a probability of 0.0174. All other errors are below 10%.
Total Takeoff Turns and Braking	32.20%	Sampling error. Maximum percentage error occurs for an event with a probability of 0.0190.
Landing Left and Right Turns	28.40%	Sampling Error. Maximum percentage error occurs for an event with a probability of 0.0213.
Total Landing Turns and Braking	18.40%	Sampling error. Maximum percentage error occurs for an event with a probability of 8×10^{-4}.
Pushback Direction	1.90%	Sampling error.
Runway Entry Direction	2.10%	Sampling error.
Runway Exit Direction	1.40%	Sampling error.
Turn onto Stand Direction	0.40%	Sampling error.

Table F.12. Percentage error results for verification of the statistical simulation of ground manoeuvre sequencing.

Sequencing Variability	Percentage Error	Error Description
After Left Pushback	12.20%	Error regards left turns occurring after left pushback. Lower error value suggests sampling error.
After Right Pushback	9.40%	Error regards right turns occurring after right pushback. Lower error value suggests sampling error.
Before Left Runway Entry	11.40%	Error regards right turns occurring before a left runway entry. Lower error value suggests sampling error.
Before Right Runway Entry	15.50%	Error regards left turns occurring before a right runway entry. Lower error value suggests sampling error.
After Left Runway Exit	17.50%	Error regards right turns occurring after a left runway exit. Lower error value suggests sampling error.
After Right Runway Exit	13.50%	Error regards left turns occurring after a right runway exit. Lower error value suggests sampling error.
After Left High Speed Exit	16.10%	Error regards right turns occurring after a left high speed runway exit. Lower error value suggests sampling error.
After Right High Speed Exit	13.90%	Error regards left turns occurring after a right high speed runway exit. Lower error value suggests sampling error.
Before Left Turn onto Stand	20.10%	Error regards straight taxi occurring before left turn onto stand. Error expected as a result of separating same-direction turns with a 'straight' taxi manoeuvre resulting in an over-sample of straight taxi manoeuvres before a left turn onto stand.
Before Right Turn onto Stand	17.80%	Error regards straight taxi occurring before right turn onto stand. Error expected as a result of separating same-direction turns with a 'straight' taxi manoeuvre resulting in an over-sample of straight taxi manoeuvres before a right turn onto stand.
After Pre-takeoff Straight Taxi	26.80%	Error regards right turns occurring after straight taxi (23.70% error for left turns). Error expected to be as a result of the separation of turns in the same direction with a straight taxi manoeuvre.
After Pre-takeoff Left Turn	34.60%	Error regards right turns occurring after left turns. Error (under-sampling of right turns) is expected to be as a result of pre-defining turn manoeuvres after and before 'milestone' manoeuvres, removing the availability of turns within the pre-takeoff taxi phase.
After Pre-takeoff Right Turn	37.50%	Error regards left turns occurring after right turns. Error (under-sampling of left turns) is expected to be as a result of pre-defining turn manoeuvres after and before 'milestone' manoeuvres, removing the availability of turns within the pre-takeoff taxi phase.
After Pre-takeoff Braking	34.50%	Error regards left turns occurring after braking. Error (under-sampling of left turns) is expected to be as a result of pre-defining turn manoeuvres after and before 'milestone' manoeuvres, removing the availability of turns within the pre-takeoff taxi phase.

Table F.12 (*continued*). Percentage error results for verification of the statistical simulation of ground manoeuvre sequencing.

Sequencing Variability	Percentage Error	Error Description
After Post-landing Straight Taxi	11.90%	Error regards right turns occurring after straight taxi (11.90% error for right turns). Lower error value suggests sampling error.
After Post-landing Left Turn	31.70%	Error regards right turns occurring after left turns. Error (under-sampling of right turns) is expected to be as a result of pre-defining turn manoeuvres after and before 'milestone' manoeuvres, removing the availability of turns within the post-landing taxi phase.
After Post-landing Right Turn	31.20%	Error regards left turns occurring after right turns. Error (under-sampling of left turns) is expected to be as a result of pre-defining turn manoeuvres after and before 'milestone' manoeuvres, removing the availability of turns within the post-landing taxi phase.
After Post-landing Braking	34.20%	Error regards left turns occurring after braking. Error (under-sampling of left turns) is expected to be as a result of pre-defining turn manoeuvres after and before 'milestone' manoeuvres, removing the availability of turns within the post-landing taxi phase.

APPENDIX G: LOWER SIDE-STAY STATISTICAL CHARACTERISATION

This appendix presents the statistical characterisation results for the remaining features of the lower side-stay component to support the case study presented in Chapter 7.

Table G.1. Statistical characterisation of the variability in D_T for the loaded lug bottom feature of the lower side-stay component.

Distribution	Fitting Type	Distribution Parameter Estimate			Skewness	$\gamma = 1.255$	
	(*Rank Equation*)	Threshold δ	Scale σ	Shape λ	Good CDF Fit?	$RMSE$	r
2P Log-Normal	PPLR (*Gumbel*)	-	-1.753	0.423	Y	0.004	**0.9997**
	MLE	-	-1.753	0.423	Y	0.004	-
3P Log-Normal	PPLR predicts zero threshold. 2P Log-Normal distribution fitted.						
	MLE predicts negative threshold. Reject distribution.						
2P Weibull	PPLR (*Mean*)	-	0.211	2.954	N	0.040	0.9751
	MLE	-	0.214	2.419	N	0.037	-
3P Weibull	PPLR (*EV*)	0.023	0.185	2.511	N	0.030	0.9872
	MLE	0.024	0.188	2.138	N	0.029	-
Gumbel Max	PPLR (*Hazen*)	-	0.064	0.152	Y	0.005	0.9997
	MLE	-	0.062	0.153	Y	0.006	-
Log-Logistic	PPLR (*Mean*)	-	-1.753	0.234	N	0.015	0.9960
	MLE	-	-1.749	0.242	N	0.010	-

Table G.2. Statistical characterisation of the variability in D_T for the constrained lug top feature of the lower side-stay component.

Distribution	Fitting Type	Distribution Parameter Estimate			Skewness	$\gamma = 1.243$	
	(*Rank Equation*)	Threshold δ	Scale σ	Shape λ	Good CDF Fit?	$RMSE$	r
2P Log-Normal	PPLR (*Gumbel*)	-	-2.017	0.415	Y	0.004	**0.9998**
	MLE	-	-2.017	0.415	Y	0.004	-
3P Log-Normal	PPLR predicts zero threshold. 2P Log-Normal distribution fitted.						
	MLE predicts negative threshold. Reject distribution.						
2P Weibull	PPLR (*Mean*)	-	0.161	3.008	N	0.040	0.9743
	MLE	-	0.164	2.460	N	0.038	-
3P Weibull	PPLR (*EV*)	0.022	0.138	2.463	N	0.029	0.9889
	MLE	0.022	0.139	2.114	N	0.028	-
Gumbel Max	PPLR (*EV*)	-	0.048	0.117	Y	0.006	0.9997
	MLE	-	0.047	0.117	Y	0.004	-
Log-Logistic	PPLR (*Mean*)	-	-2.017	0.230	N	0.015	0.9957
	MLE	-	-2.014	0.237	N	0.010	-

Table G.3. Statistical characterisation of the variability in D_T for the constrained lug bottom feature of the lower side-stay component.

Distribution	Fitting Type (*Rank Equation*)	Distribution Parameter Estimate			Skewness	$\gamma = 1.116$	
		Threshold δ	Scale σ	Shape λ	Good CDF Fit?	$RMSE$	r
2P Log-Normal	PPLR (*Hazen*)	-	-5.071	0.356	Y	0.001	**1**
	MLE	-	-5.071	0.415	Y	0.001	-
3P Log-Normal	PPLR predicts zero threshold. 2P Log-Normal distribution fitted. MLE predicts negative threshold. Reject distribution.						
2P Weibull	PPLR (*Mean*)	-	0.007	3.497	N	0.044	0.9702
	MLE	-	0.007	2.824	N	0.041	-
3P Weibull	PPLR (*Hazen*)	0.001	0.006	2.819	N	0.033	0.9847
	MLE	0.001	0.006	2.378	N	0.031	-
Gumbel Max	PPLR (*Hazen*)	-	0.002	0.006	Y	0.002	1
	MLE	-	0.002	0.006	Y	0.003	-
Log-Logistic	PPLR (*Mean*)	-	-5.071	0.197	N	0.015	0.9958
	MLE	-	-5.071	0.204	N	0.010	-

Table G.4. Statistical characterisation of the variability in D_T for the side-stay body feature of the lower side-stay component.

Distribution	Fitting Type (*Rank Equation*)	Distribution Parameter Estimate			Skewness	$\gamma = 1.436$	
		Threshold δ	Scale σ	Shape λ	Good CDF Fit?	$RMSE$	r
2P Log-Normal	PPLR (*Hazen*)	-	-8.583	0.497	Y	0.006	**0.9994**
	MLE	-	-8.583	0.497	Y	0.006	-
3P Log-Normal	PPLR predicts zero threshold. 2P Log-Normal distribution fitted. MLE predicts negative threshold. Reject distribution.						
2P Weibull	PPLR (*Mean*)	-	2.355×10^{-4}	2.521	N	0.040	0.9773
	MLE	-	2.394×10^{-4}	2.085	N	0.034	-
3P Weibull	PPLR (*Mean*)	1.166×10^{-5}	2.225×10^{-4}	2.343	N	0.034	0.9836
	MLE	1.179×10^{-5}	2.260×10^{-4}	1.974	N	0.030	-
Gumbel Max	PPLR (*EV*)	-	8.404×10^{-5}	1.628×10^{-4}	N	0.012	0.9982
	MLE	-	7.825×10^{-5}	1.664×10^{-4}	Y	0.013	-
Log-Logistic	PPLR (*Mean*)	-	-8.583	0.275	N	0.016	0.9956
	MLE	-	-8.583	0.284	N	0.011	-

Table G.5. Statistical characterisation of the variability in D_T for the loaded web thickness change feature of the lower side-stay component.

Distribution	Fitting Type (*Rank Equation*)	Distribution Parameter Estimate			Skewness	$\gamma = 1.087$	
		Threshold δ	Scale σ	Shape λ	Good CDF Fit?	$RMSE$	r
2P Log-Normal	PPLR (*Mean*)	-	-4.473	0.345	Y	0.001	**1**
	MLE	-	-4.473	0.345	Y	0.001	-
3P Log-Normal	PPLR predicts zero threshold. 2P Log-Normal distribution fitted. MLE predicts negative threshold. Reject distribution.						
2P Weibull	PPLR (*Mean*)	-	0.013	3.608	N	0.043	0.9701
	MLE	-	0.014	2.911	N	0.041	-
3P Weibull	PPLR (*Hazen*)	0.003	0.011	2.720	N	0.030	0.9884
	MLE	0.003	0.011	2.329	N	0.028	-
Gumbel Max	PPLR (*Mean*)	-	0.003	0.010	Y	0.003	1
	MLE	-	0.003	0.010	Y	0.002	-
Log-Logistic	PPLR (*Mean*)	-	-4.473	0.191	N	0.015	0.9960
	MLE	-	-4.473	0.197	N	0.010	-

Table G.6. Statistical characterisation of the variability in D_T for the constrained web thickness change feature of the lower side-stay component.

Distribution	Fitting Type (*Rank Equation*)	Distribution Parameter Estimate			Skewness	$\gamma = 1.043$	
		Threshold δ	Scale σ	Shape λ	Good CDF Fit?	$RMSE$	r
2P Log-Normal	PPLR (*Mean*)	-	-4.407	0.345	Y	0.001	**1**
	MLE	-	-4.407	0.345	Y	0.001	-
3P Log-Normal	PPLR predicts zero threshold. 2P Log-Normal distribution fitted. MLE predicts negative threshold. Reject distribution.						
2P Weibull	PPLR (*Mean*)	-	0.014	3.609	N	0.043	0.9711
	MLE	-	0.014	2.927	N	0.040	-
3P Weibull	PPLR (*Hazen*)	0.002	0.012	2.831	N	0.032	0.9868
	MLE	0.002	0.012	2.411	N	0.029	-
Gumbel Max	PPLR (*Mean*)	-	0.004	0.011	Y	0.004	0.9998
	MLE	-	0.004	0.011	Y	0.003	-
Log-Logistic	PPLR (*Mean*)	-	-4.407	0.191	N	0.015	0.9958
	MLE	-	-4.406	0.197	N	0.010	-

APPENDIX H: DRAG BRACE STATISTICAL CHARACTERISATION

This appendix presents the statistical characterisation results for the remaining features of the lower drag brace component to support the case study presented in Chapter 8.

Table H.1. Statistical characterisation of the variability in D_T for the Hole 1 Slice 3 feature of the lower drag brace.

Distribution	Fitting Type (*Rank Equation*)	Distribution Parameter Estimate			Skewness	$\gamma = 4.711$	
		Threshold δ	Scale σ	Shape λ	Good CDF Fit?	$RMSE$	r
2P Log-Normal	PPLR (*Hazen*)	-	-7.667	1.170	N	0.011	0.9973
	MLE	-	-7.667	1.167	N	0.011	-
3P Log-Normal	PPLR predicts zero threshold. 2P Log-Normal distribution fitted. MLE predicts negative threshold. Reject distribution.						
2P Weibull	PPLR (*Mean*)	-	7.981×10^{-4}	1.082	N	0.035	0.9843
	MLE	-	8.269×10^{-4}	0.914	N	0.031	-
3P Weibull	PPLR (*Mean*)	5.658×10^{-8}	7.980×10^{-4}	1.082	N	0.035	0.9844
	MLE	6.280×10^{-8}	8.270×10^{-4}	0.914	N	0.031	-
Gumbel Max	PPLR (*EV*)	-	0.001	2.765×10^{-4}	N	0.104	0.9019
	MLE	-	5.486×10^{-4}	4.780×10^{-4}	N	0.077	-
Log-Logistic	PPLR (*Mean*)	-	-7.667	0.647	N	0.017	0.9951
	MLE	-	-7.639	0.661	N	0.011	-
Exponential	PPLR (*EV*)	-	0.001	-	N	0.139	0.9554
	MLE	-	8.687×10^{-4}	-	N	0.046	-
Birnbaum Saunders	MLE	-	4.016×10^{-4}	1.476	N	0.056	-
Burr	MLE	1.664	8.285×10^{-4}	1.309	Y	**0.008**	-
Gamma	MLE	-	9.239×10^{-4}	0.940	N	0.041	-

Table H.2. Statistical characterisation of the variability in D_T for the Hole 1 Slice 4 feature of the lower drag brace.

Distribution	Fitting Type (*Rank Equation*)	Distribution Parameter Estimate			Skewness	$\gamma = 3.504$	
		Threshold δ	Scale σ	Shape λ	Good CDF Fit?	$RMSE$	r
2P Log-Normal	PPLR (*Hazen*)	-	-3.629	0.873	Y	**0.006**	**0.9994**
	MLE	-	-3.629	0.872	Y	**0.006**	-
3P Log-Normal	PPLR predicts zero threshold. 2P Log-Normal distribution fitted. MLE predicts negative threshold. Reject distribution.						
2P Weibull	PPLR (*Mean*)	-	0.040	1.437	N	0.041	0.9775
	MLE	-	0.041	1.188	N	0.036	-
3P Weibull	PPLR (*Mean*)	3.641×10^{-4}	0.039	1.408	N	0.035	0.9811
	MLE	3.663×10^{-4}	0.040	1.173	N	0.032	-
Gumbel Max	PPLR (*EV*)	-	0.031	0.020	N	0.079	0.9496
	MLE	-	0.021	0.024	N	0.049	-
Log-Logistic	PPLR (*Mean*)	-	-3.629	0.483	N	0.015	0.9956
	MLE	-	-3.618	0.498	N	0.010	-
Birnbaum Saunders	MLE	-	0.026	0.965	N	0.018	-
Burr	MLE	1.407	0.035	1.810	N	0.009	-
Gamma	MLE	-	0.025	1.515	N	0.032	-

Table H.3. Statistical characterisation of the variability in D_T for the Hole 1 Slice 5 feature of the lower drag brace.

Distribution	Fitting Type (*Rank Equation*)	Distribution Parameter Estimate			Skewness	$\gamma = 4.015$	
		Threshold δ	Scale σ	Shape λ	Good CDF Fit?	$RMSE$	r
2P Log-Normal	PPLR (*Hazen*)	-	-5.373	0.986	Y	**0.008**	**0.9989**
	MLE	-	-5.373	0.985	Y	**0.008**	-
3P Log-Normal	PPLR predicts zero threshold. 2P Log-Normal distribution fitted. MLE predicts negative threshold. Reject distribution.						
2P Weibull	PPLR (*Mean*)	-	0.007	1.275	N	0.028	0.9799
	MLE	-	0.008	1.064	N	0.046	-
3P Weibull	PPLR (*Mean*)	3.582×10^{-5}	0.007	1.259	N	0.028	0.9825
	MLE	3.600×10^{-5}	0.007	1.058	N	0.025	-
Gumbel Max	PPLR (*EV*)	-	0.007	0.003	N	0.099	0.9318
	MLE	-	0.004	0.004	N	0.043	-
Log-Logistic	PPLR (*Mean*)	-	-5.373	0.546	N	0.017	0.9952
	MLE	-	-5.355	0.562	N	0.011	-
Birnbaum Saunders	MLE	-	1.123	0.004	N	0.025	-
Burr	MLE	1.533	0.007	1.570	N	0.009	-
Gamma	MLE	-	0.006	1.235	N	0.034	-

Table H.4. Statistical characterisation of the variability in D_T for the Hole 1 Slice 12 feature of the lower drag brace.

Distribution	Fitting Type (*Rank Equation*)	Distribution Parameter Estimate			Skewness	$\gamma = 3.518$	
		Threshold δ	Scale σ	Shape λ	Good CDF Fit?	$RMSE$	r
2P Log-Normal	PPLR (*Hazen*)	-	-4.169	0.906	Y	**0.008**	**0.9991**
	MLE	-	-4.169	0.905	Y	**0.008**	-
3P Log-Normal	PPLR predicts zero threshold. 2P Log-Normal distribution fitted. MLE predicts negative threshold. Reject distribution.						
2P Weibull	PPLR (*Mean*)	-	0.023	1.386	N	0.032	0.9788
	MLE	-	0.024	1.152	N	0.032	-
3P Weibull	PPLR (*Mean*)	2.259×10^{-4}	0.023	1.354	N	0.032	0.9830
	MLE	2.275×10^{-4}	0.024	1.152	N	0.032	-
Gumbel Max	PPLR (*EV*)	-	0.019	0.012	N	0.080	0.9459
	MLE	-	0.013	0.014	N	0.049	-
Log-Logistic	PPLR (*Mean*)	-	-4.169	0.502	N	0.016	0.9954
	MLE	-	-4.154	0.517	N	0.011	-
Birnbaum Saunders	MLE	-	1.010	0.015	Y	0.020	-
Burr	MLE	1.490	0.022	1.719	Y	0.009	-
Gamma	MLE	-	0.016	1.427	N	0.031	-

Table H.5. Statistical characterisation of the variability in D_T for the Hole 1 Slice 13 feature of the lower drag brace.

Distribution	Fitting Type (*Rank Equation*)	Distribution Parameter Estimate			Skewness	$\gamma = 4.210$	
		Threshold δ	Scale σ	Shape λ	Good CDF Fit?	$RMSE$	r
2P Log-Normal	PPLR (*Hazen*)	-	-5.477	10.995	Y	**0.008**	**0.9989**
	MLE	-	-5.477	0.993	Y	**0.008**	-
3P Log-Normal	PPLR predicts zero threshold. 2P Log-Normal distribution fitted. MLE predicts negative threshold. Reject distribution.						
2P Weibull	PPLR (*Mean*)	-	0.007	1.264	N	0.051	0.9795
	MLE	-	0.007	1.503	N	0.038	-
3P Weibull	PPLR (*Mean*)	1.432×10^{-5}	0.007	1.256	N	0.050	0.9807
	MLE	1.459×10^{-5}	0.007	1.049	N	0.038	-
Gumbel Max	PPLR (*EV*)	-	0.006	0.003	N	0.090	0.9286
	MLE	-	0.004	0.004	N	0.064	-
Log-Logistic	PPLR (*Mean*)	-	-5.477	0.550	N	0.017	0.9954
	MLE	-	-5.460	0.567	N	0.011	-
Exponential	PPLR (*EV*)	-	0.008	-	N	0.065	0.9723
	MLE	-	0.007	-	N	0.034	-
Birnbaum Saunders	MLE	-	0.004	1.139	Y	0.026	-
Burr	MLE	1.504	0.006	1.564	Y	0.009	-
Gamma	MLE	-	0.005	1.214	N	0.035	-

Table H.6. Statistical characterisation of the variability in D_T for the Hole 2 Slice 4 feature of the lower drag brace.

Distribution	Fitting Type (*Rank Equation*)	Distribution Parameter Estimate			Skewness	$\gamma = 3.752$	
		Threshold δ	Scale σ	Shape λ	Good CDF Fit?	$RMSE$	r
2P Log-Normal	PPLR (*Gumbel*)	-	-4.929	0.995	Y	**0.007**	**0.9991**
	MLE	-	-4.929	0.954	Y	**0.007**	-
3P Log-Normal	PPLR predicts zero threshold. 2P Log-Normal distribution fitted. MLE predicts negative threshold. Reject distribution.						
2P Weibull	PPLR (*Mean*)	-	0.011	1.316	N	0.032	0.9790
	MLE	-	0.012	1.095	N	0.041	-
3P Weibull	PPLR (*Mean*)	6.974×10^{-5}	0.011	1.295	N	0.033	0.9820
	MLE	7.010×10^{-5}	0.011	1.084	N	0.027	-
Gumbel Max	PPLR (*EV*)	-	0.010	0.005	N	0.091	0.9380
	MLE	-	0.006	0.007	N	0.065	-
Log-Logistic	PPLR (*Mean*)	-	-4.929	0.529	N	0.016	0.9953
	MLE	-	-4.914	0.545	N	0.011	-
Birnbaum Saunders	MLE	-	0.007	1.077	Y	0.022	-
Burr	MLE	1.490	0.010	1.631	Y	0.009	-
Gamma	MLE	-	0.009	1.301	N	0.033	-

Table H.7. Statistical characterisation of the variability in D_T for the Hole 2 Slice 5 feature of the lower drag brace.

Distribution	Fitting Type (*Rank Equation*)	Distribution Parameter Estimate			Skewness	$\gamma = 3.249$	
		Threshold δ	Scale σ	Shape λ	Good CDF Fit?	$RMSE$	r
2P Log-Normal	PPLR (*Hazen*)	-	-3.523	0.858	Y	**0.007**	**0.9993**
	MLE	-	-3.523	0.857	Y	**0.007**	-
3P Log-Normal	PPLR predicts zero threshold. 2P Log-Normal distribution fitted. MLE predicts negative threshold. Reject distribution.						
2P Weibull	PPLR (*Mean*)	-	0.044	1.462	N	0.039	0.9779
	MLE	-	0.045	1.210	N	0.035	-
3P Weibull	PPLR (*Mean*)	4.868×10^{-4}	0.043	1.428	N	0.034	0.9819
	MLE	4.893×10^{-4}	0.044	1.193	N	0.032	-
Gumbel Max	PPLR (*EV*)	-	0.033	0.023	N	0.075	0.9541
	MLE	-	0.022	0.027	N	0.049	-
Log-Logistic	PPLR (*Mean*)	-	-3.523	0.475	N	0.015	0.9956
	MLE	-	-3.511	0.489	N	0.010	-
Birnbaum Saunders	MLE	-	0.029	0.945	Y	0.018	-
Burr	MLE	1.424	0.039	1.837	Y	0.009	-
Gamma	MLE	-	0.027	1.565	N	0.030	-

Table H.8. Statistical characterisation of the variability in D_T for the Hole 2 Slice 6 feature of the lower drag brace.

Distribution	Fitting Type (*Rank Equation*)	Distribution Parameter Estimate			Skewness	$\gamma = 4.923$	
		Threshold δ	Scale σ	Shape λ	Good CDF Fit?	$RMSE$	r
2P Log-Normal	PPLR (*Hazen*)	-	-7.723	1.162	Y	0.012	0.9975
	MLE	-	-7.723	1.160	Y	0.012	-
3P Log-Normal	PPLR predicts zero threshold. 2P Log-Normal distribution fitted. MLE predicts negative threshold. Reject distribution.						
2P Weibull	PPLR (*Mean*)	-	7.520×10^{-4}	1.088	N	0.034	0.9842
	MLE	-	7.790×10^{-4}	0.918	N	0.030	-
3P Weibull	PPLR (*Mean*)	2.350×10^{-7}	7.517×10^{-4}	1.087	N	0.034	0.9845
	MLE	2.410×10^{-7}	7.786×10^{-4}	0.918	N	0.030	-
Gumbel Max	PPLR (*EV*)	-	9.676×10^{-4}	2.575×10^{-4}	N	0.104	0.8991
	MLE	-	5.137×10^{-4}	4.507×10^{-4}	N	0.076	-
Log-Logistic	PPLR (*Mean*)	-	-7.723	0.643	N	0.017	0.9952
	MLE	-	-7.695	0.657	N	0.011	-
Exponential	PPLR (*EV*)	-	0.001	-	N	0.139	0.9526
	MLE	-	8.161×10^{-4}	-	N	0.045	-
Birnbaum Saunders	MLE	-	3.908×10^{-4}	1.435	Y	0.049	-
Burr	MLE	1.677	7.882×10^{-4}	1.314	Y	**0.008**	-
Gamma	MLE	-	8.599×10^{-4}	0.949	N	0.040	-

Table H.9. Statistical characterisation of the variability in D_T for the Hole 2 Slice 12 feature of the lower drag brace.

Distribution	Fitting Type (*Rank Equation*)	Distribution Parameter Estimate			Skewness	$\gamma = 3.618$	
		Threshold δ	Scale σ	Shape λ	Good CDF Fit?	$RMSE$	r
2P Log-Normal	PPLR (*Hazen*)	-	-4.956	0.961	Y	**0.009**	**0.9988**
	MLE	-	-4.956	0.960	Y	**0.009**	-
3P Log-Normal	PPLR predicts zero threshold. 2P Log-Normal distribution fitted. MLE predicts negative threshold. Reject distribution.						
2P Weibull	PPLR (*Mean*)	-	0.011	1.310	N	0.037	0.9803
	MLE	-	0.011	1.095	N	0.028	-
3P Weibull	PPLR (*Mean*)	2.369×10^{-5}	0.011	1.302	N	0.037	0.9814
	MLE	2.430×10^{-5}	0.011	1.080	N	0.029	-
Gumbel Max	PPLR (*EV*)	-	0.010	0.005	N	0.092	0.9405
	MLE	-	0.006	0.007	N	0.071	-
Log-Logistic	PPLR (*Mean*)	-	-4.956	0.532	N	0.017	0.9952
	MLE	-	-4.938	0.547	N	0.011	-
Exponential	PPLR (*EV*)	-	0.012	-	N	0.048	0.9803
	MLE	-	0.011	-	N	0.037	-
Birnbaum Saunders	MLE	-	6.765×10^{-3}	1.088	Y	0.025	-
Burr	MLE	1.556	0.011	1.607	Y	0.009	-
Gamma	MLE	-	8.370×10^{-3}	1.297	N	0.032	-

Table H.10. Statistical characterisation of the variability in D_T for the Hole 2 Slice 14 feature of the lower drag brace.

Distribution	Fitting Type (*Rank Equation*)	Distribution Parameter Estimate			Skewness	$\gamma = 4.283$	
		Threshold δ	Scale σ	Shape λ	Good CDF Fit?	$RMSE$	r
2P Log-Normal	PPLR (*Hazen*)	-	-6.690	1.084	Y	0.009	0.9985
	MLE	-	-6.690	1.083	Y	0.009	-
3P Log-Normal	PPLR predicts zero threshold. 2P Log-Normal distribution fitted. MLE predicts negative threshold. Reject distribution.						
2P Weibull	PPLR (*Mean*)	-	0.002	1.162	N	0.031	0.9812
	MLE	-	0.002	0.975	N	0.025	-
3P Weibull	PPLR (*Mean*)	6.474×10^{-6}	0.002	1.150	N	0.031	0.9836
	MLE	6.520×10^{-6}	0.002	0.969	N	0.025	-
Gumbel Max	PPLR (*EV*)	-	0.002	8.190×10^{-4}	N	0.094	0.9166
	MLE	-	0.001	0.001	N	0.048	-
Log-Logistic	PPLR (*Mean*)	-	-6.690	0.600	N	0.017	0.9952
	MLE	-	-6.669	0.617	N	0.011	-
Exponential	PPLR (*EV*)	-	0.003	-	N	0.100	0.9656
	MLE	-	0.002	-	N	0.034	-
Birnbaum Saunders	MLE	-	0.001	1.275	Y	0.032	-
Burr	MLE	1.581	0.002	1.420	Y	**0.009**	-
Gamma	MLE	-	0.002	1.055	N	0.037	-